Physics of the Solid State, Vol. 45, No. 10, 2003, pp. 1815–1828. Translated from Fizika Tverdogo Tela, Vol. 45, No. 10, 2003, pp. 1729–1741.

The Relativistic Theory of Fluctuation Electromagnetic Interactions of Moving Neutral Particles with a Flat Surface

G. V. Dedkov and A. A. Kyasov

Kabardino-Balkar State University, ul. Chernyshevskogo 173, Nalchik, 360004 Russia

e-mail: gv_dedkov@mail.ru

Received January 28, 2003

Abstract—The problem concerning the fluctuation electromagnetic interaction of a neutral particle moving parallel to the boundary of a semi-infinite homogeneous isotropic medium characterized by a permittivity and permeability dependent on the frequency is considered in terms of the fluctuation electrodynamic theory within the relativistic formalism. It is assumed that, in the general case, the particle and the medium have different temperatures. Within the proposed approach, general expressions are derived both for conservative (normal to the boundary of the medium) and nonconservative (tangential) forces of the interaction between the particle and the medium and for the thermal heating (cooling) rate of the particle. In the nonrelativistic limit ($c \longrightarrow \infty$), the derived relationships coincide with nonrelativistic analogs available in the literature. It is demonstrated that the tangential force acting on the particle can be either accelerating or decelerating. There can occur a situation when the hot moving particle will be heated and the cold medium will be cooled. The interaction of the high-conductivity medium with a high-conductivity particle is analyzed numerically. The asymptotics of the radiative contributions to the heat flux and the tangential force is investigated. It is shown that the inclusion of the relativistic effects leads to a substantial increase in the tangential force and the heat flux at distances greater than 1 μm (as compared to the nonrelativistic case); however, the corresponding dependences exhibit a monotonic decreasing behavior over the entire range of studied distances (from zero to several hundreds of microns).

1. INTRODUCTION

The fluctuation electromagnetic interaction between neutral particles and a medium is governed by quantum and thermal fluctuations of the polarization and magnetization inducing fluctuation electromagnetic fields both inside and outside the particles and the medium. The fluctuation electromagnetic interaction is associated with conservative van der Waals forces [1–3], conservative Casimir forces [3–6], tangential (nonconservative) forces [7–14], heat exchange effects [15–18], and a number of other interesting phenomena [6].

The purpose of this work is to develop a consistent relativistic theory for calculating the heating rate and the fluctuation force acting on a small-sized neutral spherical particle moving parallel to a flat boundary of a polarization medium under vacuum. Consideration is given to the conservative (normal) and nonconservative (tangential) components of the fluctuation electromagnetic interaction force.

The current state of the art in the study of the nonrelativistic problem was analyzed in our recent review [14]. The results of relativistic investigations were briefly outlined in [19, 20]. In the framework of the rigorous relativistic approach, the dynamic force of fluctuation electromagnetic interaction between a small-sized particle and a surface was calculated for the first time in our previous work [21], in which we derived general formulas for normal and tangential components of the fluctuation force. Dorofeyev *et al.* [22] investigated a similar problem but restricted their consideration to the case of a nonrelativistic relative velocity V and obtained (to the first order in V) the following dependence of the tangential force on the velocity V: $F_x \sim V/c^2$, where c is the velocity of light in free space.

The related problem of calculating the tangential forces of the fluctuation electromagnetic interaction between two semi-infinite media separated by a plane vacuum space has been treated in a number of earlier works [8–10]. However, the relationships deduced in those works are inconsistent with each other and with their nonrelativistic analogs at $c \longrightarrow \infty$ [11, 12], because, in this limit, they lead to a zero tangential force within an approximation linear in velocity. It should be noted that Pendry [11] and Volokitin and Persson [12] took into account the retardation effects but restricted their consideration to the case of nonrelativistic relative motion. After appropriate transformations of the expression for the tangential stress between semi-infinitive media, Volokitin and Persson [12] derived a relationship describing the interaction of a small-sized particle and a flat surface.

Unlike the relationships derived in the aforementioned works, the expressions obtained in our recent studies [19–21] completely coincide with nonrelativistic formulas at $c \longrightarrow \infty$ not only within an approximation linear in velocity V. As a result, considerable

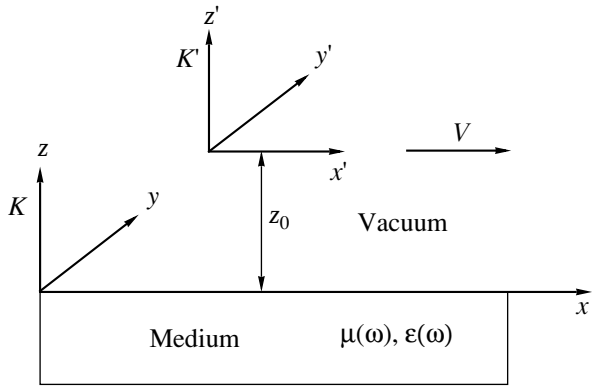

Fig. 1. Coordinate systems *K* and *K*' related to the surface at rest and a moving particle.

advances have been achieved in the description of dynamic fluctuation electromagnetic interactions, even though the relativistic solution of the problem of interaction between a small-sized particle and a surface cannot be directly extended to the case of a different geometry and, in particular, to the geometry of two semi-infinite media (and vice versa).

Our calculation technique is based on the equations of classical and fluctuation electrodynamics (including spontaneous and induced components of the fields and currents caused by fluctuations) and the formalism of fluctuation dissipative relationships. It should be noted that no additional simplifying assumptions were made in the course of our calculations.

This paper is organized as follows. In Section 2, we formulate the problem and derive general expressions for calculating the forces and thermal effects. In Section 3, the essence of the method used is demonstrated within the nonrelativistic approach (the results obtained are necessary for providing deeper insight into the relativistic approach). The regular solution of the Maxwell equations for the electromagnetic field components induced by a moving particle in the vacuum region is found in Section 4. The relativistic relationships for correlators of the physical quantities and components of the retarded Green's functions for radiation in the medium are deduced in Section 5. The final formulas describing the fluctuation medium and the thermal heating rate of the particle are given in Section 6. The results of numerical calculations are presented in Section 7. The main conclusions are summarized in Section 8. Computational details are described in the Appendix. Note that, in this work, we use the Gaussian system of units.

2. FORMULATION OF THE PROBLEM AND BASIC EXPRESSIONS

Let us consider a small-sized neutral spherical particle that moves parallel to the boundary of a semi-infinite medium at a distance z_0 from this boundary under vacuum (Fig. 1). The half-space $z \le 0$ is filled with a medium characterized by a complex permittivity ε and complex permeability μ dependent on the frequency ω. It is assumed that the particle is nonmagnetic in the intrinsic coordinate system and possesses an electric dipole polarizability $\alpha(\omega)$ and (or) a permittivity $\varepsilon_1(\omega)$. The real and imaginary parts of these functions (and their derivatives) are designated by one and two primes, respectively. The laboratory coordinate system *K* is related to the surface at rest, and the coordinate system *K*' is related to the moving particle. In the coordinate system *K*, the *z* axis is perpendicular to the interface and the *x* axis coincides with the direction of the particle velocity *V*. Under the assumption that $z_0 \gg R$ (where *R* is the characteristic particle size), the particle can be considered a point fluctuating electric dipole with the moment $\mathbf{d}(t)$.

It should be noted that, within the relativistic approach, the nonmagnetic particle having only the electric dipole moment in the coordinate system *K*' possesses the magnetic dipole moment $\mathbf{m}(t)$ in the coordinate system *K*. Therefore, in the coordinate system *K*, the vectors of the electric and magnetic polarizations induced by the moving particle can be written in the form

$$\mathbf{P}(x, y, z, t) = \delta(x - Vt)\delta(y)\delta(z - z_0)\mathbf{d}(t), \quad (1)$$

$$\mathbf{M}(x, y, z, t) = \delta(x - Vt)\delta(y)\delta(z - z_0)\mathbf{m}(t). \quad (2)$$

Correspondingly, in the coordinate system *K*' (in the general case), we have

$$\mathbf{P}'(x', y', z', t') = \delta(x')\delta(y')\delta(z')\mathbf{d}'(t'), \quad (3)$$

$$\mathbf{M}'(x', y', z', t') = \delta(x')\delta(y')\delta(z')\mathbf{m}'(t)'. \quad (4)$$

The coordinates (x, y, z, t) and (x', y', z', t') in both systems are related by the Lorentz transformations

$$x' = \gamma(x - \beta ct), \quad t' = \gamma(t - \beta x/c), \quad y' = y, \quad z' = z, \quad (5)$$

where $\beta = V/c$ and $\gamma = (1 - \beta^2)^{-1/2}$. The formulas of the Lorentz transformations for the moments $\mathbf{d}(t)$ and $\mathbf{m}(t)$ can be derived from similar formulas for the polarization vectors **P** and **M** specified by the components parallel and perpendicular to the direction of the particular velocity *V* [23]:

$$\mathbf{P}_\parallel = \mathbf{P}'_\parallel, \quad \mathbf{P}_\perp = \gamma\left(\mathbf{P}'_\perp + \frac{1}{c}[\mathbf{V}\mathbf{M}']\right), \quad (6)$$

$$\mathbf{M}_\parallel = \mathbf{M}'_\parallel, \quad \mathbf{M}_\perp = \gamma\left(\mathbf{M}'_\perp - \frac{1}{c}[\mathbf{V}\mathbf{P}']\right). \quad (7)$$

By using relationships (1)–(7) and the identity $\delta(\alpha x) = \delta(x)/|\alpha|$ and assuming that $\mathbf{m}'(t') = 0$, we obtain

$$d_x(t) = \gamma^{-1}d_x(t'), \quad d_y(t) = d'_y(t'), \quad d_z(t) = d'_z(t'),$$
$$m_x(t) = 0, \quad m_y(t) = \beta d'_y(t'), \quad m_z(t) = -\beta d'_z(t'). \quad (8)$$

Note that the variables t and t' in expressions (8) are related by transformation (5). The formulas necessary for the transformations of the moments **d** and **m** for the case when the particle velocity has an arbitrary direction and $\mathbf{m}'(t') \neq 0$ are given in [24].

The fluctuation force acting on the particle can be determined from the generalized formula for the Lorentz force:

$$\mathbf{F} = \int \langle \rho \mathbf{E} \rangle d^3 r + \frac{1}{c} \int \langle [\mathbf{j}\mathbf{H}] \rangle d^3 r, \quad (9)$$

where ρ and **j** are the charge and current densities of the particle, respectively; **E** and **H** are the electric and magnetic field strengths, respectively; and the angle brackets $\langle \ldots \rangle$ indicate the complete quantum-statistical averaging. The integrals are taken over the particle volume. As is usually done in the fluctuation electromagnetic theory, all vector quantities are treated as Heisenberg operators.

By definition, we have $\rho = -\mathrm{div}\mathbf{P}$ and $\mathbf{j} = \partial\mathbf{P}/\partial t + c\,\mathrm{curl}\mathbf{M}$, where **P** and **M** are determined by relationships (1) and (2), respectively. Substitution of the relevant expressions into relationship (9) gives

$$\mathbf{F}^e = \int \langle \rho \mathbf{E} \rangle d^3 r = \langle \nabla(\mathbf{d}\mathbf{E}) \rangle + \frac{1}{c} \langle [\mathbf{d}\partial\mathbf{H}/\partial t] \rangle, \quad (10)$$

$$\mathbf{F}^m = \frac{1}{c} \int \langle \mathbf{j}\mathbf{H} \rangle d^3 r = \langle \nabla(\mathbf{m}\mathbf{H}) \rangle - \frac{1}{c} \langle [\mathbf{d}\partial\mathbf{H}/\partial t] \rangle. \quad (11)$$

By summing expressions (10) and (11), we obtain

$$\mathbf{F} = \mathbf{F}^e + \mathbf{F}^m = \langle \nabla(\mathbf{d}\mathbf{E} + \mathbf{m}\mathbf{H}) \rangle. \quad (12)$$

Then, we explicitly separate the contributions of spontaneous (sp) and induced (in) fluctuations:

$$\begin{aligned} \mathbf{F} &= \langle \nabla(\mathbf{d}^{\mathrm{sp}}\mathbf{E}^{\mathrm{in}} + \mathbf{m}^{\mathrm{sp}}\mathbf{H}^{\mathrm{in}}) \rangle \\ &+ \langle \nabla(\mathbf{d}^{\mathrm{in}}\mathbf{E}^{\mathrm{sp}} + \mathbf{m}^{\mathrm{in}}\mathbf{H}^{\mathrm{sp}}) \rangle. \end{aligned} \quad (13)$$

Equation (13) is most convenient for subsequent calculations of the fluctuation force. It should be noted that the differentiation in this equation should be carried out prior to the substitution of the current coordinates of the particle $(V, t, 0, z_0)$. The normal component of the force **F** describes the dynamic van der Waals interaction.

Now, we analyze the work done by the fluctuation electromagnetic field on the particle in a unit time. This work is determined by the dissipation integral $\int \langle \mathbf{j}\mathbf{E} \rangle d^3 r$. Taking into account the Lorentz transformations of the current density, the charge density, and the electric field strength in the coordinate systems K and K',

$$j_x' = \gamma(j_x - \rho c\beta), \quad j_y' = j_y,$$

$$j_z' = j_z, \quad \rho' = \gamma(\rho - \beta j_x),$$

$$E_x' = E_x, \quad E_y' = \gamma(E_\gamma - \beta H_z), \quad E_z' = \gamma(E_z + \beta H_y),$$

and the relationship between the volume elements in these systems $d^3r = \gamma^{-1} d^3 r'$, we obtain

$$\int \langle \mathbf{j}'\mathbf{E}' \rangle d^3 r' = \gamma^2 \left[\int \langle \mathbf{j}\mathbf{E} \rangle d^3 r - F_x V \right], \quad (14)$$

where

$$F_x = \int \langle \rho E_x \rangle d^3 r + \frac{1}{c} \int \langle [\mathbf{j}\mathbf{H}]_x \rangle d^3 r. \quad (15)$$

On the other hand, with allowance made for relationships (3), (4), $\rho = -\mathrm{div}\mathbf{P}$, $\mathbf{j} = \partial\mathbf{P}/\partial t + c\,\mathrm{curl}\mathbf{M}$, and $\mathbf{m}' = 0$, we have

$$\begin{aligned} \int \langle \mathbf{j}'\mathbf{E}' \rangle d^3 r' &= \int \left\langle \frac{\partial \mathbf{P}'}{\partial t'} \mathbf{E}' \right\rangle d^3 r' \\ = \int \langle \delta(x')\delta(y')\delta(z')\dot{\mathbf{d}}'\mathbf{E}' \rangle d^3 r' &= \langle \dot{\mathbf{d}}'\mathbf{E}' \rangle. \end{aligned} \quad (16)$$

By using relationships (8) and $dt' = \gamma^{-1} dt$, expression (16) can be rearranged to give

$$\int \langle \mathbf{j}'\mathbf{E}' \rangle d^3 r' = \langle \dot{\mathbf{d}}'\mathbf{E}' \rangle = \gamma^2 [\langle \dot{\mathbf{d}}\mathbf{E} \rangle - \beta \langle [\dot{\mathbf{d}}\mathbf{H}]_x \rangle]. \quad (17)$$

Finally, from formulas (14), (16), and (17), we derive the following expression:

$$\begin{aligned} \int \langle \mathbf{j}\mathbf{E} \rangle d^3 r &= F_x V + \langle \dot{\mathbf{d}}\mathbf{E} \rangle - \beta \langle [\dot{\mathbf{d}}\mathbf{H}]_x \rangle \\ &\equiv F_x V + dQ/dt. \end{aligned} \quad (18)$$

It is evident that the derivative dQ/dt can be treated as the heating (cooling) rate of the particle. It should be emphasized that all the quantities entering into expression (18) refer to the laboratory coordinate system K. By analogy with the transformation of formula (9) for the fluctuation force, the derivative dQ/dt can be written in the more compact form

$$\begin{aligned} \dot{Q} &= \langle \dot{\mathbf{d}}\mathbf{E} \rangle - \frac{V}{c} \langle [\dot{\mathbf{d}}\mathbf{H}]_x \rangle = \langle \dot{\mathbf{d}}\mathbf{E} + \dot{\mathbf{m}}\mathbf{H} \rangle \\ &= \langle \dot{\mathbf{d}}^{\mathrm{sp}}\mathbf{E}^{\mathrm{in}} + \dot{\mathbf{m}}^{\mathrm{sp}}\mathbf{H}^{\mathrm{in}} \rangle + \langle \dot{\mathbf{d}}^{\mathrm{in}}\mathbf{E}^{\mathrm{sp}} + \dot{\mathbf{m}}^{\mathrm{in}}\mathbf{H}^{\mathrm{sp}} \rangle. \end{aligned} \quad (19)$$

In the nonrelativistic case, it is obvious that $\dot{Q} = \langle \dot{\mathbf{d}}\mathbf{E} \rangle$. Hence, if the particle is considered a system of coupled charges, it is easy to show that the work done by the fluctuation electric field on the particle in a unit time is equal to the sum of the power of the tangential force applied to the center of mass of the particle and the rate of heating that leads to an increase in the root-mean-square velocities of charges constituting the particle. This is a direct consequence of the energy conservation law (in the absence of radiation)

$$-\frac{dW}{dt} = \int \langle \mathbf{j}\mathbf{E} \rangle d^3 r = F_x V + dQ/dt. \quad (20)$$

The left-hand side of this equation represents the energy loss rate of the fluctuation electromagnetic field. The heating of a molecule (nanoparticle) results in an increase in its temperature, whereas the heating of a

neutral atom can be interpreted as a Lamb shift of the levels due to the interaction with the surface.

Relationships (18) and (20) are of fundamental importance for understanding the interaction between the particle and the surface. In particular, we ignored the term dQ/dt in relationship (20) in our earlier work [25] and, as a consequence, obtained an incorrect asymptotic relationship for the tangential force at $T \longrightarrow 0$. On the other hand, the tangential force for charged particles and multipoles with a permanent moment, is quite correctly expressed in terms of the dissipation integral, because $dQ/dt = 0$. Virtually the same error was made by Dorofeyev *et al.* [22], who determined the tangential force from the series expansion of the dissipation integral in powers of the velocity. In this case, to the first order in the velocity (for the force F_x), the corresponding term of the expansion is proportional to V^2. In contrast to identity (18), this approach makes it impossible to separate explicitly the power of the tangential force from the heating rate of the particle and to obtain more general results when the dependence on the velocity exhibits a nonlinear behavior.

At $\dot{Q} \neq 0$, the heat flux is localized in the space, because it is associated with the volume of the small particle. However, the dissipation of the electromagnetic field energy on the surface and in the bulk of the medium at rest leads to heating of the medium even at $\dot{Q} = 0$ (due to the motion of charges and multipoles with a permanent moment). In this case, the thermal effect arises in the medium at a later stage owing to the relaxation motion of multipoles to which the translational energy of the particle is transferred. At $\dot{Q} < 0$, when the heat flux is directed from the particle to the surface and the particle is retarded, the total heating of the medium is determined by the right-hand side of Eq. (20), which accounts for both types of dissipation of the fluctuation field energy. Mathematically, this is equivalent to the dissipation integral taken over the volume of the medium at rest.

Therefore, in order to calculate the fluctuation force and the heat flux, it is necessary to perform statistical averaging in expressions (13) and (18). Unlike the computational schemes used in [8–10], our technique is clear physically and efficient computationally.

3. THE NONRELATIVISTIC CASE

It is expedient to consider the simpler nonrelativistic problem with the aim of demonstrating the general scheme of calculations and comparing the obtained results with relativistic formulas. In this case, the terms involving the contribution of the magnetic field should be omitted from expressions (13) and (18). The dipole moments can be represented as Fourier integral transforms with the time factor $\exp(-i\omega t)$, and the electric field components can be written in the form of expansions in terms of the components of the two-dimensional wave vector $\mathbf{k} = (k_x, k_y)$ and the frequency. The induced electric field $\mathbf{E}^{in}$ is expressed through the scalar potential φ, which is the solution of the Poisson equation $\nabla^2\varphi = -4\pi\rho$ with additional continuity conditions for the scalar potential φ and the normal component of the electric induction at the boundary $z = 0$. The quantity ρ is defined by the equation $\rho = -\mathrm{div}\mathbf{P}$ and, with due regard for expression (1), can also be represented as a Fourier transform. The corresponding calculations are described in detail in [26, 27]. After performing the statistical averaging in expressions for $\langle\nabla\mathbf{d}^{sp}\mathbf{E}^{in}\rangle$ and $\langle\nabla\mathbf{d}^{in}\mathbf{E}^{sp}\rangle$, we obtain the relationships for the normal and tangential components of the fluctuation force. The former component is conveniently related to the conservative (van der Waals) potential of attraction for the surface with the use of the expression $F_z = -\partial U/\partial z$. As a result, we have [14]

$$U(z_0, V) = \frac{\hbar}{\pi^2}\int d\omega dk_x dk_y k e^{-2kz_0} \times \{C(T_1, \omega)\alpha''(\omega)[\Delta'(\omega - Vk_x) + \Delta'(\omega + Vk_x)] + C(T_2, \omega)\Delta''(\omega)[\alpha'(\omega - Vk_x) + \alpha'(\omega + Vk_x)]\}, \quad (21)$$

$$F_x = \langle(\mathbf{d}^{sp}\nabla)E_x^{in}\rangle + \langle(\mathbf{d}^{in}\nabla)E_x^{sp}\rangle = -\frac{2\hbar}{\pi^2}\int d\omega dk_x dk_y k_x k e^{-2kz_0} \times \{C(T_1, \omega)\alpha''(\omega)[\Delta''(\omega + Vk_x) - \Delta''(\omega - Vk_x)] + C(T_2, \omega)\Delta''(\omega)[\alpha''(\omega + Vk_x) - \alpha''(\omega - Vk_x)]\}, \quad (22)$$

where

$$C(T, \omega) = \coth\left(\frac{\hbar\omega}{2kT}\right),$$

$$\Delta(\omega) = \Delta' + i\Delta'' = \frac{\varepsilon(\omega) - 1}{\varepsilon(\omega) + 1}$$

is the dielectric-response function of the surface and T_1 is the particle temperature, which, in the general case, differs from the surface temperature T_2 (for the neutral atom, $T_1 = 0$).

Note that integration over all the variables is carried out in the interval $(0, \infty)$ and the negative sign corresponds to the decelerating (dissipative) tangential force.

For subsequent comparison with relativistic formulas, relationship (22) can be conveniently rewritten in an equivalent form, which can be obtained by transforming the frequency arguments in the first term in the curly brackets with allowance made for the analytical

properties of the integrands. After manipulations, we obtain

$$F_x = -\frac{2\hbar}{\pi^2}\int d\omega dk_x dk_y k_x k e^{-2kz_0} \times [\Xi(\omega, V) - \Xi(\omega, -V)], \quad (23)$$

where

$$\Xi(\omega, V) = \Delta''(\omega)\alpha''(\omega + k_x V)[C(T_2, \omega) - C(T_1, \omega + k_x V)].$$

From relationships (21)–(23), it is easy to derive all standard formulas that describe both the attraction of the spherical particle to the surface and the tangential force. Specifically, in the limit of low velocities, we have

$$F_x = -\frac{3\hbar V}{2\pi z_0^5}\left[\int_0^\infty d\omega [n(T_1, \omega) - n(T_2, \omega)]\alpha(\omega)\frac{d\Delta''(\omega)}{d\omega} - \frac{\hbar}{kT_2}\int_0^\infty d\omega \alpha''(\omega)\Delta''(\omega)n(T_2, \omega)[1 + n(T_2, \omega)]\right], \quad (24)$$

$$n(T, \omega) = \frac{1}{e^{\hbar\omega/kT} - 1}.$$

For $T_1 = T_2 = T$, from expression (24), we deduce the formula [28]

$$F_x = \frac{3\hbar V}{2\pi z_0^5}\int_0^\infty \alpha''(\omega)\Delta''(\omega)\frac{d}{d\omega}n(T, \omega)d\omega, \quad (25)$$

according to which the dissipative force at $T \longrightarrow 0$ is absent to the first order in the velocity. In a more general case, from relationship (23) in the limit $T_1 \longrightarrow 0$ and $T_2 \longrightarrow 0$, we obtain

$$F_x = \frac{4\hbar}{\pi^2}\int_0^\infty k_x dk_x \int_0^\infty dk_y k e^{-2kz_0} \times \int_0^{k_x V} d\omega \Delta''(\omega)\alpha''(\omega - Vk_x). \quad (26)$$

From expression (26), at $V \longrightarrow 0$, we derive the relationship $F_x \sim V^3/z_0^7$.

The heat flux $\dot{Q}$ can be calculated in the same manner. As a result, we have [14]

$$\dot{Q} = \langle \dot{\mathbf{d}}\mathbf{E}\rangle = \langle \dot{\mathbf{d}}^{sp}E^{in}\rangle + \langle \dot{\mathbf{d}}^{in}E^{sp}\rangle = -\frac{2\hbar}{\pi^2}\int d\omega dk_x dk_y k e^{-2kz_0} \times \{C(T_1, \omega)\alpha''(\omega)[\omega\Delta''(\omega + Vk_x)'' + \omega\Delta''(\omega - Vk_x)] - C(T_2, \omega)\Delta''(\omega)[(\omega + Vk_x)\alpha''(\omega + Vk_x) + (\omega - Vk_x)\alpha''(\omega - Vk_x)]\}. \quad (27)$$

By analogy with expression (23), relationship (27) can be rearranged to the equivalent form

$$\dot{Q} = -\frac{2\hbar}{\pi^2}\int d\omega dk_x dk_y k e^{-2kz_0}\Delta''(\omega) \times \{(\omega + Vk_x)\alpha''(\omega + Vk_x)[C(T_1, \omega + Vk_x) - C(T_2, \omega)] + (\omega - Vk_x)\alpha''(\omega - Vk_x) \times [C(T_1, \omega - Vk_x) - C(T_2, \omega)]\}. \quad (28)$$

By expanding expression (27) in terms of the velocity and retaining the first two terms, we obtain

$$\dot{Q} = -\frac{\hbar}{\pi z_0^3}\int_0^\infty d\omega\omega\alpha''(\omega)\Delta''(\omega)[n(T_1, \omega) - n(T_2, \omega)] - \frac{3\hbar V^2}{8\pi z_0^5}\int_0^\infty d\omega\left\{C(T_1, \omega)\omega\alpha''\frac{d^2\Delta''}{d\omega^2} - C(T_2, \omega)\Delta''\left(2\frac{d\alpha''}{d\omega} + \omega\frac{d^2\alpha''}{d\omega^2}\right)\right\}. \quad (29)$$

Even a cursory examination of formulas (23), (24), (28), and (29) demonstrates that, in general, the tangential force and the heat flux between the particle and the surface can be different in sign. Polevoĭ [9] was the first to call attention to this fact in the study of the tangential forces between semi-infinite media. Now, we turn to an analysis of the relativistic problem.

4. SOLUTION OF THE MAXWELL EQUATIONS FOR INDUCED COMPONENTS OF THE ELECTROMAGNETIC FIELD

The relativistic problem can be efficiently solved within the formalism of the Hertz vectors $\mathbf{\Pi}^e(\mathbf{r}, t)$ and $\mathbf{\Pi}^m(\mathbf{r}, t)$. The Fourier transformers of these vectors obey the equations [29]

$$\left(\Delta + \frac{\omega^2}{c^2}\varepsilon(\omega)\mu(\omega)\right)\mathbf{\Pi}^e_{\omega\mathbf{k}}(z) = -\frac{4\pi}{\varepsilon(\omega)}\mathbf{P}_{\omega\mathbf{k}}(z), \quad (30)$$

$$\left(\Delta + \frac{\omega^2}{c^2}\varepsilon(\omega)\mu(\omega)\right)\mathbf{\Pi}^m_{\omega\mathbf{k}}(z) = -\frac{4\pi}{\mu(\omega)}\mathbf{M}_{\omega\mathbf{k}}(z),$$
$$\Delta = -k_x^2 - k_y^2 + \frac{\partial^2}{\partial z^2}. \quad (31)$$

The boundary conditions corresponding to the formulated problem for the Hertz vectors and the solutions of Eqs. (30) and (31) are given in Appendix A. The amplitudes of the electric and magnetic fields can be expressed through the Hertz vectors with the use of the relationships [29]

$$\mathbf{E}_{\omega\mathbf{k}} = \mathrm{graddiv}\mathbf{\Pi}^e_{\omega\mathbf{k}} + \frac{\omega^2}{c^2}\varepsilon(\omega)\mu(\omega)\mathbf{\Pi}^e_{\omega\mathbf{k}} + \frac{i\omega}{c}\mu(\omega)\mathrm{curl}\mathbf{\Pi}^m_{\omega\mathbf{k}}, \quad (32)$$

$$\mathbf{H}_{\omega\mathbf{k}} = \mathrm{graddiv}\mathbf{\Pi}^m_{\omega\mathbf{k}} + \frac{\omega^2}{c^2}\varepsilon(\omega)\mu(\omega)\mathbf{\Pi}^m_{\omega\mathbf{k}} - \frac{i\omega}{c}\varepsilon(\omega)\mathrm{curl}\mathbf{\Pi}^e_{\omega\mathbf{k}}. \quad (33)$$

From expressions (32), (33), and (A3)–(A8), we obtain (for the vacuum region $z \geq 0$)

$$E^{\mathrm{in}}_{x,\,\omega\mathbf{k}}(z) = \Theta(z)\Big[-k_x(k_xd_x + k_yd_y)(\Delta_m - \Delta_{em}) - ik_xq_0d_z\Delta_e + \frac{\omega^2}{c^2}d_x\Delta_m + \frac{i\omega}{c}\Big(-\Delta_{em}\frac{k_y}{q_0}(k_xm_x + k_ym_y) + ik_ym_z\Delta_m + q_0m_y\Delta_e\Big)\Big], \quad (34)$$

$$E^{\mathrm{in}}_{y,\,\omega\mathbf{k}}(z) = \Theta(z)\Big[-k_y(k_xd_x + k_yd_y)(\Delta_m - \Delta_{em}) - ik_yq_0d_z\Delta_e + \frac{\omega^2}{c^2}d_y\Delta_m - \frac{i\omega}{c}\Big(-\Delta_{em}\frac{k_x}{q_0}(k_xm_x + k_ym_y) + ik_xm_z\Delta_m + q_0m_x\Delta_e\Big)\Big], \quad (35)$$

$$E^{\mathrm{in}}_{z,\,\omega\mathbf{k}}(z) = \Theta(z)\Big[\frac{ik_xd_x + ik_yd_y}{q_0}(k^2\Delta_{em} - q_0^2\Delta_m) + k^2d_z\Delta_e + \frac{i\omega}{c}(ik_xm_y\Delta_e - ik_ym_x\Delta_e)\Big]. \quad (36)$$

Here,

$$\Theta(z) = \frac{2\pi}{q_0}\exp[-q_0(z + z_0)],$$

$$H^{\mathrm{in}}_{x,\,\omega\mathbf{k}}(z) = \Theta(z)\Big[-k_x(k_xm_x + k_ym_y)(\Delta_e - \Delta_{em}) - ik_xq_0m_z\Delta_m + \frac{\omega^2}{c^2}m_x\Delta_e - \frac{i\omega}{c}\Big(-\Delta_{em}\frac{k_y}{q_0}(k_xd_x + k_yd_y) + ik_yd_z\Delta_e + q_0d_y\Delta_m\Big)\Big], \quad (37)$$

$$H^{\mathrm{in}}_{y,\,\omega\mathbf{k}}(z) = \Theta(z)\Big[-k_y(k_xm_x + k_ym_y)(\Delta_e - \Delta_{em}) - ik_yq_0m_z\Delta_m + \frac{\omega^2}{c^2}m_y\Delta_e + \frac{i\omega}{c}\Big(-\Delta_{em}\frac{k_x}{q_0}(k_xd_x + k_yd_y) + ik_xd_z\Delta_e + q_0d_x\Delta_m\Big)\Big], \quad (38)$$

$$H^{\mathrm{in}}_{z,\,\omega\mathbf{k}}(z) = \Theta(z)\Big[\frac{ik_xm_x + ik_ym_y}{q_0}(k^2\Delta_{em} - q_0^2\Delta_e) + k^2m_z\Delta_m + \frac{\omega}{c}(k_xd_y\Delta_m - k_yd_x\Delta_m)\Big], \quad (39)$$

where the projections d_i and m_i ($i = x, y, z$) are represented by formulas (A9),

$$q_0 = (k^2 - \omega^2/c^2)^{1/2}, \quad q = (k^2 - \varepsilon(\omega)\mu(\omega)\omega^2/c^2)^{1/2}, \quad k^2 = k_x^2 + k_y^2, \quad (40)$$

$$\Delta_m(\omega) = \frac{\mu(\omega)q_0 - q}{\mu(\omega)q_0 + q}, \quad (41)$$

$$\Delta_e(\omega) = \frac{\varepsilon(\omega)q_0 - q}{\varepsilon(\omega)q_0 + q}, \quad (42)$$

$$\Delta_{em}(\omega) = \frac{2q_0^2(\varepsilon(\omega)\mu(\omega) - 1)}{(\varepsilon(\omega)q_0 + q)(\mu(\omega)q_0 + q)}. \quad (43)$$

Note also that the functions Δ_m, Δ_e, and Δ_{em} are related by the expression

$$k^2\Delta_{em} - q_0^2\Delta_e - q_0^2\Delta_m = 0. \quad (44)$$

5. CORRELATORS OF THE PHYSICAL QUANTITIES

When determining the contributions of spontaneous and induced fluctuations to the force and the heating rate, it is necessary to express the Fourier components of the fields and dipole moments of the particle in the

coordinate system K. For the induced field components, we have

$$\mathbf{E}^{\text{in}}(\mathbf{r}, t) = \frac{1}{(2\pi)^3}\int d\omega dk_x dk_y \mathbf{E}^{\text{in}}_{\omega\mathbf{k}}(z) \times \exp(i(k_x x + k_y y - \omega t)), \quad (45)$$

$$\mathbf{H}^{\text{in}}(\mathbf{r}, t) = \frac{1}{(2\pi)^3}\int d\omega dk_x dk_y \mathbf{H}^{\text{in}}_{\omega\mathbf{k}}(z) \times \exp(i(k_x x + k_y y - \omega t)). \quad (46)$$

Making allowance for expressions (5) and (8), the spontaneous components of the vectors $\mathbf{d}^{\text{sp}}(t)$ and $\mathbf{m}^{\text{sp}}(t)$ can be written in the form

$$d_x^{\text{sp}}(t) = \gamma\int_{-\infty}^{+\infty}\frac{d\omega}{2\pi}d_x'^{\text{sp}}(\gamma\omega)\gamma^{-1}e^{-i\omega t},$$

$$d_y^{\text{sp}}(t) = \gamma\int_{-\infty}^{+\infty}\frac{d\omega}{2\pi}d_y'^{\text{sp}}(\gamma\omega)e^{-i\omega t},$$

$$d_z^{\text{sp}}(t) = \gamma\int_{-\infty}^{+\infty}\frac{d\omega}{2\pi}d_z'^{\text{sp}}(\gamma\omega)e^{-i\omega t},$$

$$m_x^{\text{sp}}(t) = 0,$$

$$m_y^{\text{sp}}(t) = \gamma\beta\int_{-\infty}^{+\infty}\frac{d\omega}{2\pi}d_z'^{\text{sp}}(\gamma\omega)e^{-i\omega t},$$

$$m_z^{\text{sp}}(t) = -\gamma\beta\int_{-\infty}^{+\infty}\frac{d\omega}{2\pi}d_y'^{\text{sp}}(\gamma\omega)e^{-i\omega t}. \quad (47)$$

It should be noted that the left-hand and right-hand sides of relationships (47) involve the "laboratory" time t.

Upon substituting formulas (45)–(47) into the first terms of expressions (13) and (19), there appears a correlator of the dipole moment of the particle in its own rest system. This correlator can be represented in the following form [21]:

$$\langle d_i'^{\text{sp}}(\gamma\omega')d_k'^{\text{sp}}(\gamma(\omega - Vk_x))\rangle = \frac{2\pi\hbar}{\gamma}\delta_{ik}\delta(\omega' + \omega - Vk_x)\alpha''(\gamma\omega')\coth\left(\frac{\gamma\hbar\omega'}{2kT_1}\right). \quad (48)$$

In order to calculate the second terms in formulas (13) and (19), the induced components of the dipole moment of the particle should be expressed in the laboratory coordinate system. For this purpose, we will use a standard nonrelativistic integral relationship between $\mathbf{d}^{\text{in}}$ and $\mathbf{E}^{\text{sp}}$. In the rest system K' of the particle, this relationship can be written as

$$\mathbf{d}'^{\text{in}}(t') = \int_{-\infty}^{t'}\alpha(t' - \tau')\mathbf{E}'^{\text{sp}}(\mathbf{r}_0'\tau')d\tau'.$$

Next, we rewrite this relationship with due regard for the Fourier transform of the expansion of $\mathbf{E}'^{\text{sp}}$ in terms of spatial and time variables with the use of expressions (5) and (8) and the Lorentz transformations for the field amplitudes and derive the sought formulas

$$d_x^{\text{in}} = \frac{\gamma^{-1}}{(2\pi)^3}\int d\omega dk_x dk_y \alpha(\gamma(\omega - Vk_x))E^{\text{sp}}_{x\omega\mathbf{k}}(z_0) \times \exp(-i(\omega - Vk_x)t),$$

$$d_y^{\text{in}} = \frac{\gamma}{(2\pi)^3}\int d\omega dk_x dk_y \alpha(\gamma(\omega - Vk_x)) \times [E^{\text{sp}}_{y\omega\mathbf{k}}(z_0) - \beta H^{\text{sp}}_{z\omega\mathbf{k}}(z_0)]\exp(-i(\omega - Vk_x)t),$$

$$d_z^{\text{in}} = \frac{\gamma}{(2\pi)^3}\int d\omega dk_x dk_y \alpha(\gamma(\omega - Vk_x)) \times [E^{\text{sp}}_{z\omega\mathbf{k}}(z_0) + \beta H^{\text{sp}}_{y\omega\mathbf{k}}(z_0)]\exp(-i(\omega - Vk_x)t),$$

$$m_x^{\text{in}} = 0,$$

$$m_y^{\text{in}} = \frac{\beta\gamma}{(2\pi)^3}\int d\omega dk_x dk_y \alpha(\gamma(\omega - Vk_x)) \times [E^{\text{sp}}_{z\omega\mathbf{k}}(z_0) + \beta H^{\text{sp}}_{y\omega\mathbf{k}}(z_0)]\exp(-i(\omega - Vk_x)t),$$

$$m_z^{\text{in}} = -\frac{\beta\gamma}{(2\pi)^3}\int d\omega dk_x dk_y \alpha(\gamma(\omega - Vk_x)) \times [E^{\text{sp}}_{y\omega\mathbf{k}}(z_0) - \beta H^{\text{sp}}_{z\omega\mathbf{k}}(z_0)]\exp(-i(\omega - Vk_x)t). \quad (49)$$

Substitution of formulas (49) and the spontaneous field components of the surface into the second terms in expressions (13) and (19) leads to the appearance of correlators of the electric and magnetic field amplitudes. By virtue of the stationarity of the fluctuations, these correlators can be expressed through the spectral densities [30, 31]:

$$\langle U^{\text{sp}}_{i,\omega\mathbf{k}}V^{\text{sp}}_{j,\omega'\mathbf{k}'}\rangle = (2\pi)^3\delta(\omega + \omega')\delta(k_x + k_x') \times \delta(k_y + k_y')(U_i^{\text{sp}}V_j^{\text{sp}})_{\omega\mathbf{k}}, \quad (50)$$

where $U_i^{\text{sp}} = E_i^{\text{sp}}$ and $V_i^{\text{sp}} = B_i^{\text{sp}}$ $(i = x, y, z)$.

In turn, the spectral densities of the amplitudes can be expressed through the components of the retarded

Green's function for radiation in the medium with the use of the relationships [2, 27]

$$(E_i^{sp}(z)E_k^{sp}(z'))_{\omega\mathbf{k}} = i\frac{\omega^2}{2c^2}C(T,\omega) \times [D_{ik}(\omega\mathbf{k}; zz') - D_{ki}^*(\omega\mathbf{k}; z'z)], \quad (51)$$

$$(B_i^{sp}(z)B_k^{sp}(z'))_{\omega\mathbf{k}} = i\frac{1}{2}C(T,\omega)\mathrm{curl}_{il}\mathrm{curl}'_{km} \times [D_{lm}(\omega\mathbf{k}; zz') - D_{ml}^*(\omega\mathbf{k}; z'z)], \quad (52)$$

$$(E_i^{sp}(z)B_k^{sp}(z'))_{\omega\mathbf{k}} = -\frac{\omega}{2c}C(T,\omega)\,\mathrm{curl}'_{km} \times [D_{im}(\omega\mathbf{k}; zz') - D_{mi}^*(\omega\mathbf{k}; z'z)]. \quad (53)$$

The calculation of the Green's functions is described in detail in Appendix B. Substitution of the Green's functions into formula (50) with allowance made for relationships (51)–(53) makes it possible to determine all the required correlators.

6. FLUCTUATION FORCE AND THE HEATING RATE OF A PARTICLE

The results obtained in Sections 4 and 5 and Appendices A and B allow statistical averaging in relationships (13) and (19). In this case, the formulas derived in [20, 21] for the fluctuation force can be simplified after the frequency arguments of the integrands are transformed in the same manner as in the derivation of expressions (23) and (28). As a result, the components of the fluctuation force and the heating rate of the particle are represented by the following relationships:

$$F_x = -\frac{\hbar\gamma}{\pi^2}\int\limits_{k>\omega/c} d\omega dk_x dk_y k_x \frac{\exp(-2q_0z_0)}{q_0} \times [(C(T_2,\omega) - C(T_1,\gamma(\omega + Vk_x)))\alpha''(\gamma(\omega + Vk_x)) \times [\chi_e^{(+)}(\omega,\mathbf{k})\Delta_e''(\omega) + \chi_m^{(+)}(\omega,\mathbf{k})\Delta_m''(\omega)] - (C(T_2,\omega) - C(T_1,\gamma(\omega - Vk_x)))\alpha''(\gamma(\omega - Vk_x)) \times [\chi_e^{(-)}(\omega,\mathbf{k})\Delta_e''(\omega) + \chi_m^{(-)}(\omega,\mathbf{k})\Delta_m''(\omega)]] + \frac{\hbar\gamma}{\pi^2}\int\limits_{k<\omega/c} d\omega dk_x dk_y k_x \frac{\sin(2\tilde{q}_0z_0)}{q_0} \times \{\Delta_e, \Delta_m \longrightarrow \tilde{\Delta}_e, \tilde{\Delta}_m\}, \quad (54)$$

$$F_z = -\frac{\hbar\gamma}{\pi^2}\int\limits_{k>\omega/c} d\omega dk_x dk_y \exp(-2q_0z_0) \times \{C(T_1,\gamma(\omega + Vk_x))\alpha''(\gamma(\omega + Vk_x)) \times [\chi_e^{(+)}(\omega,\mathbf{k})\Delta_e'(\omega) + \chi_m^{(+)}(\omega,\mathbf{k})\Delta_m'(\omega)] + C(T_1,\gamma(\omega - Vk_x))\alpha''(\gamma(\omega - Vk_x)) \times [\chi_e^{(-)}(\omega,\mathbf{k})\Delta_e'(\omega) + \chi_m^{(-)}(\omega,\mathbf{k})\Delta_m'(\omega)] + C(T_2,\omega)\alpha'(\gamma(\omega + Vk_x)) \times [\chi_e^{(+)}(\omega,\mathbf{k})\Delta_e''(\omega) + \chi_m^{(+)}(\omega,\mathbf{k})\Delta_m''(\omega)] + C(T_2,\omega)\alpha'(\gamma(\omega - Vk_x)) \times [\chi_e^{(-)}(\omega,\mathbf{k})\Delta_e''(\omega) + \chi_m^{(-)}(\omega,\mathbf{k})\Delta_m''(\omega)]\} - \frac{\hbar\gamma}{\pi^2}\int\limits_{k<\omega/c} d\omega dk_x dk_y \cos(2\tilde{q}_0z_0) \times \{\Delta_e, \Delta_m \longrightarrow \tilde{\Delta}_e, \tilde{\Delta}_m\}, \quad (55)$$

$$\dot{Q} = -\frac{\hbar\gamma}{\pi^2}\int\limits_{k>\omega/c} d\omega dk_x dk_y \frac{\exp(-2q_0z_0)}{q_0} \times \{[C(T_1,\omega + Vk_x) - C(T_2,\omega)] \times (\omega + Vk_x)\alpha''(\gamma(\omega + Vk_x)) \times [\chi_e^{(+)}(\omega,\mathbf{k})\Delta_e''(\omega) + \chi_m^{(+)}(\omega,\mathbf{k})\Delta_m'(\omega)] + [C(T_1,\omega - Vk_x) - C(T_2,\omega)] \times (\omega - Vk_x)\alpha''(\gamma(\omega - Vk_x)) \times [\chi_e^{(-)}(\omega,\mathbf{k})\Delta_e''(\omega) + \chi_m^{(-)}(\omega,\mathbf{k})\Delta_m'(\omega)]\} - \frac{\hbar\gamma}{\pi^2}\int\limits_{k<\omega/c} d\omega dk_x dk_y\left[-\frac{\sin(2\tilde{q}_0z_0)}{\tilde{q}_0}\right] \times \{\Delta_e, \Delta_m \longrightarrow \tilde{\Delta}_e, \tilde{\Delta}_m\}. \quad (56)$$

Here, we introduced the designations

$$q_0 = (k^2 - \omega^2/c^2)^{1/2}, \quad \tilde{q}_0 = (\omega^2/c^2 - k^2)^{1/2},$$

$$q = (k^2 - \varepsilon\mu\omega^2/c^2)^{1/2}, \quad \tilde{q} = (\varepsilon\mu\omega^2/c^2 - k^2)^{1/2},$$

$$\chi_e^{(\pm)}(\omega,\mathbf{k}) = 2(k^2 - \beta^2k_x^2)(1 - \omega^2/k^2c^2) + \frac{(\omega \pm Vk_x)^2}{c^2},$$

$$\chi_m^{(\pm)}(\omega,\mathbf{k}) = 2\beta^2k_y^2(1 - \omega^2/k^2c^2) + \frac{(\omega \pm Vk_x)^2}{c^2}.$$

It should be noted that the functions $\tilde{\Delta}_e$ and $\tilde{\Delta}_m$ are defined by formulas (41) and (42) with the replacement

$q(q_0) \longrightarrow \tilde{q}(\tilde{q}_0)$ and integration over the frequency, as is the case in expressions (21) and (22), is performed in the interval from 0 to ∞. The integrals taken over the frequencies $\omega > ck$ and $\omega < ck$ correspond to the contributions from the radiative and nonradiative modes of the fluctuation electromagnetic field, respectively.

7. DISCUSSION AND RESULTS OF NUMERICAL CALCULATIONS

First and foremost, let us consider relationships (54)–(56) in the nonrelativistic limit $c \longrightarrow \infty$. In this case, we have $\chi_e^{(\pm)}(\omega, \mathbf{k}) = 2k^2$ and $\chi_m^{(\pm)}(\omega, \mathbf{k}) = 0$. Hence, it follows that relationships (54) and (56) transform into expressions (23) and (28) and relationship (55) transforms into formula (21) with allowance made for the expression $F_z = -\partial U/\partial z$.

Note that an analysis of the relativistic motion of the particle with due regard for the retardation effect is of practical importance. For numerical calculations, we consider contact between homogeneous nonmagnetic metals ($\mu = 1$) when the bulk dielectric functions are defined by the expression $\varepsilon(\omega) = 1 + 4\pi\sigma i/\omega \equiv 1 + ai$, where σ is the frequency-independent conductivity. Let us introduce new variables: $\dot{t} = kc/\omega$ and $u^2 = |1 - \dot{t}^2|$, where $u^2 = \dot{t}^2 - 1$ for nonradiative modes ($\omega < kc$) and $u^2 = 1 - \dot{t}^2$ for radiative modes ($\omega > kc$). On this basis, from formulas (41) and (42), we obtain the following relationships for the imaginary parts of the response functions:

(a) For nonradiative modes [the upper signs in relationships (57) and (58)], we have

$$\Delta_e''(u, a) = -\frac{u}{a[a^2u^4 + (2u^2 + 1)^2]}[a^2u(2u^2 - 1) + (2 - a^2)u(2u^2 + 1) \mp (aA_1 + (2a^2u^2 + 2u^2 + 1)A_2)], \quad (57)$$

$$\Delta_m''(u, a) = -\frac{2u^2}{a} \pm \frac{2u}{a}A_2, \quad (58)$$

$$A_1 = \left(\frac{\sqrt{a^2 + u^4} - u^2}{2}\right)^{1/2}, \quad (59)$$

$$A_2 = \left(\frac{\sqrt{a^2 + u^4} + u^2}{2}\right)^{1/2}. \quad (60)$$

(b) For radiative modes [the lower signs in relationships (57) and (58)], formulas (57) and (58) are modified by the replacement $2u^2 + 1 \rightleftharpoons 2u^2 - 1$. Compared to the relevant expressions deduced in our earlier work [32], expressions (57)–(60) are derived without invoking the additional simplifying assumption $a \gg 1$.

It should be noted that, in the designations used in [11–13], the response functions Δ_e and Δ_m coincide with the Fresnel reflection coefficients (R_P and R_S) of electromagnetic waves with the *P* and *S* polarizations for which the electric vector lies either in the same plane with the wave vector and the vector normal to the surface (*P* wave) or in the perpendicular plane (*S* wave). Note that the *P* and *S* waves are predominantly electrostatic and magnetic in character, respectively.

For a small-sized spherical particle of radius *R*, the polarizability can be approximated in the following two ways:

$$\alpha(\omega) = R^3\frac{\varepsilon(\omega) - 1}{\varepsilon(\omega) + 2}, \quad (61a)$$

$$\alpha(\omega) = R^3 \times\left(1 + \frac{3(1 - \kappa R\coth(\kappa R))}{2(\varepsilon(\omega) - 1)(1 - \kappa R\coth(\kappa R) + \varepsilon(\omega)(\kappa R)^2)}\right), \quad (61b)$$

where $\kappa^2 = (4/\pi)(9\pi/4)^{1/3}/r_s$ and r_s is the parameter (in atomic units) of the jellium model. Relationship (61b) is derived within the Thomas–Fermi approximation for a metallic cluster and accounts for the screening of the electron gas [33]. Setting $R = 10$ nm (typical radius of a tip of probe microscopes), we obtain $\kappa R \gg 1$ for normal metals. Consequently, from expressions (61a) and (61b) in the low-frequency limit, we have

$$\alpha''(\omega) \approx \frac{3R^3}{a} = \frac{3R^3}{4\pi\sigma}, \quad (62a)$$

$$\alpha''(\omega) \approx \frac{3}{2}\frac{R^3}{(\kappa R)}\frac{1}{a^3} = \frac{3}{2}\frac{R^3}{(\kappa R)}\frac{\omega^3}{(4\pi\sigma)^3}. \quad (62b)$$

By omitting the relativistic terms of the order of β^2 in relationships (54) and (56) and also in the formulas for $\chi_e^{(\pm)}(\omega, \mathbf{k})$ and $\chi_m^{(\pm)}(\omega, \mathbf{k})$ in the case when the polarizability is given by expression (62a), we obtain the following expressions:

$$F_x = \frac{3R^3\hbar V}{4\pi^2\sigma}\int_0^\infty\left(\frac{\omega}{c}\right)^5 d\omega \int_{0 \le u < \infty,\, 0 \le u \le 1}(1 \pm u^2)du \times[\exp(-2\omega uz_0/c), \sin(-2\omega uz_0/c)] \times\{(A(\theta_1) - A(\theta_2))[(\pm 2u^2 + 3)\Delta_e''(u, a) + 3\Delta_m''(u, a)] - B(\theta_1)[(\pm 2u^2 + 1)\Delta_e''(u, a) + \Delta_m''(u, a)]\}, \quad (63)$$

$$\dot{Q} = -\frac{3R^3\hbar}{2\pi^2\sigma}\int_0^\infty\left(\frac{\omega}{c}\right)^3\omega^2 d\omega \int_{0 \le u < \infty,\, 0 \le u \le 1} du \times[\exp(-2\omega uz_0/c), \sin(-2\omega uz_0/c)] \times\{(A(\theta_1) - A(\theta_2))[(\pm 2u^2 + 1)\Delta_e''(u, a) + \Delta_m''(u, a) + \beta^2(1 \pm u^2)((\pm 2u^2 + 5)\Delta_e''(u, a) + 5\Delta_m''(u, a))] \quad (64)$$

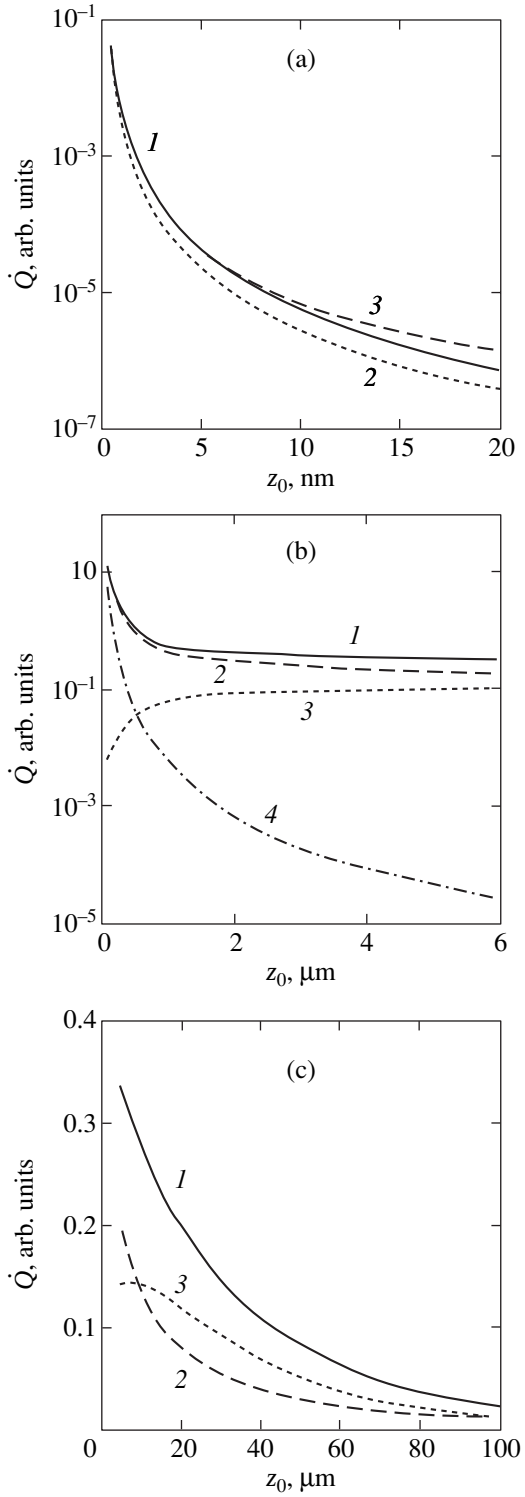

Fig. 2. Dependences of the heat flux on the distance at (a) (*1*) $\alpha = 10^4$ and $T = 300$ K, (*2*) $\alpha = 2 \times 10^4$ and $T = 300$ K, (*3*) $\alpha = 10^4$ and $T = 1200$ K and (b) (*1–3*) $\alpha = 10^4$ and $T = 300$ K. (b) (*1*) The sum of the radiative and nonradiative contributions, (*2*) the contribution of nonradiative modes, (*3*) the contribution of radiative modes, and (*4*) the nonrelativistic approximation. The magnitude of the heat flux (in erg/s) can be obtained by multiplying the ordinate by the quantity $\kappa\hbar/\sigma(kT/\hbar)^3R^3$, where κ = (a) 2×10^{19} and (b, c) 2×10^{10}.

$$- \beta^2 4B(\theta_1)(1 \pm u^2)[(1 \pm u^2)\Delta_e''(u, a) + \Delta_m''(u, a)]\},$$

$$A(x) = \frac{1}{e^x - 1}, \quad B(x) = \frac{xe^x}{(e^x - 1)^2},$$

$$\theta_{1,2} = \frac{\hbar\omega}{kT_{1,2}}.$$

Here, the upper signs, the functions $\exp(-2\omega u z_0/c)$ in the square brackets of the integrands in expressions (63) and (64), and the integration interval $0 \le u < \infty$ correspond to the contribution from the nonradiative modes of the electromagnetic field, whereas the contribution from the radiative modes of the electromagnetic field is calculated for the lower signs, the functions $\sin(-2\omega u z_0/c)$, and the integration interval $0 \le u \le 1$.

After introducing the dimensionless parameters $\alpha = 4\pi\sigma\hbar/kT$ and $b = 2kT(z_0/\hbar c)$, we transform the double integrals in relationships (63) and (64) into the universal functions of α and b, which can be determined by numerical integration (see below). For normal metals ($\sigma = 10^{17}$ s^{-1}) at temperatures $T \le 300$ K, we have $\alpha \ge 30\,000$ and $b \le 0.26 z_0$ (μm). The parameter b serves as a measure of the retardation effect, which is more pronounced at smaller distances from the surface with an increase in the temperature. In the absence of retardation, we set $c = \infty$ and $b = 0$. In passing to the limit $c \longrightarrow \infty$, formulas (57) and (58) are reduced to $\Delta_e'' = 2/a$ and $\Delta_m'' = 0$, respectively.

It follows from expression (64) that, even under isothermal conditions ($T_1 = T_2 = T$), the moving particle is heated by the surface ($\dot{Q} > 0$). However, this effect is relativistic, because $\dot{Q} \sim (V/c)^2$. At $T_1 \ne T_2$, there is a more significant velocity-independent contribution to the heat flux that leads to heating of the particle at $T_1 > T_2$ ($\dot{Q} < 0$) and its cooling at $T_1 < T_2$ ($\dot{Q} > 0$).

Relationship (63) predicts a negative (decelerating) tangential force acting on the moving particle. However, the general expression (56) admits of the occurrence of an accelerating force. The same inferences follow from the nonrelativistic formulas (27) and (31). Physically, the fluctuation acceleration becomes possible owing to the internal degrees of freedom of the neutral particle. By contrast, the tangential forces can be only decelerating when charged particles or multipoles with a permanent moment execute motion. More detailed discussion of this problem is beyond the scope of the present work, because it would require consideration of dielectric functions characterized by a resonance structure of the absorption peaks of the particle and surface materials.

For a small retardation $b = 2kT(z_0/\hbar c) \ll 1$, from relationships (63) and (64), it is easy to derive analytical expressions for the radiative contributions, because the inner integrals are well approximated by functions

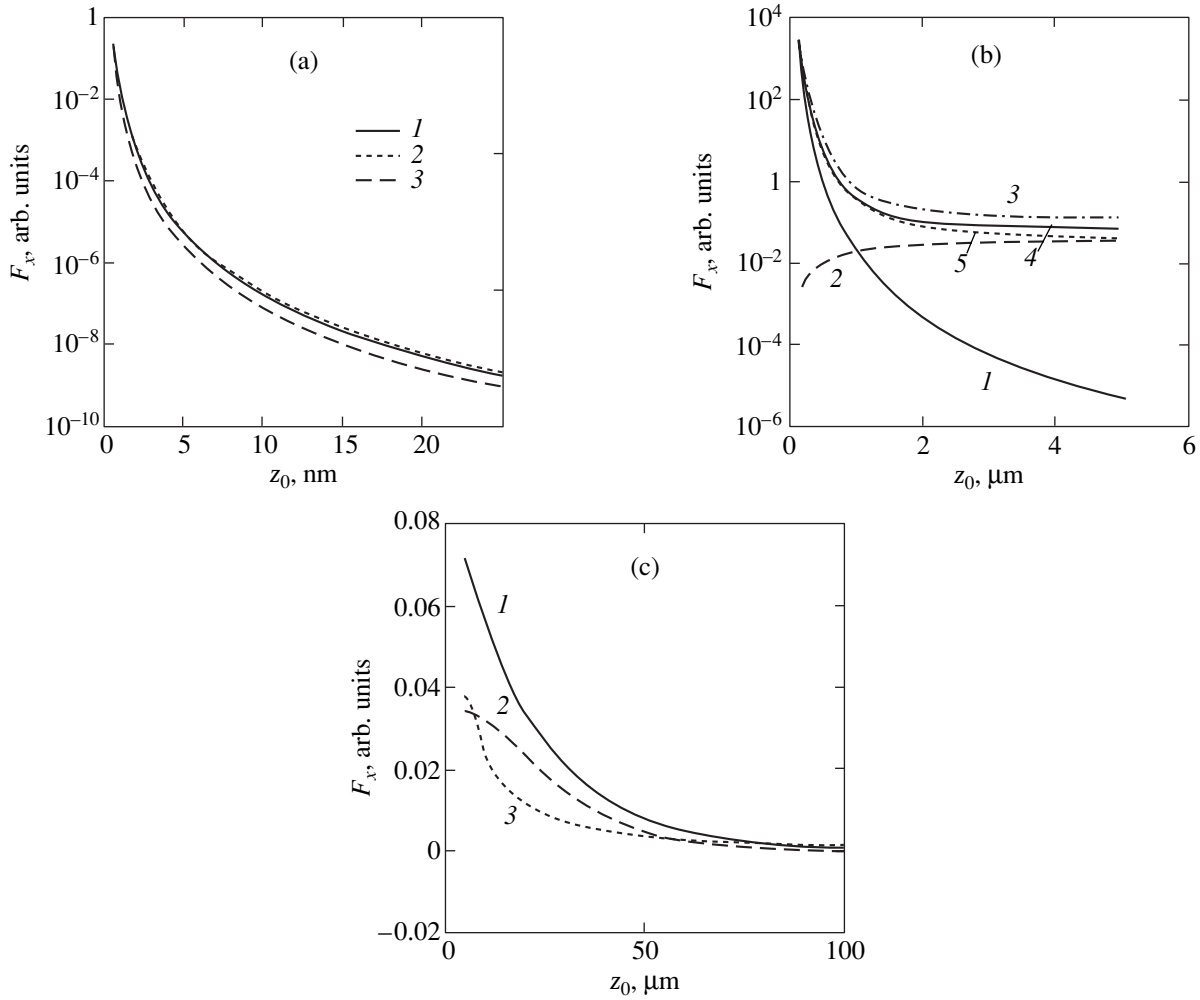

Fig. 3. Dependences of the tangential (decelerating) force on the distance for different parameters α, particle temperatures T_1, and medium temperatures T_2. (a) (*1*) $\alpha = 10^4$ and $T = 300$ K, (*2*) $\alpha = 10^4$ and $T = 1200$ K, (*3*) $\alpha = 2 \times 10^4$ and $T = 300$ K at particle temperatures $T_1 = T$ and medium temperature $T_2 = 0$. (b) (*1*) The nonrelativistic approximation at $\alpha = 10^4$ and $T_1 = T_2 = T = 300$ K; (*2*) the radiative contribution, (*3*) the nonradiative contribution, and (*4*) the sum of the radiative and nonradiative contributions at $\alpha = 10^4$, $T_1 = 300$ K, and $T_2 = 0$; and (*5*) the curve corresponding to $\alpha = 10^4$ and $T_1 = T_2 = T = 300$ K. (c) (*1*) The sum of the radiative and nonradiative contributions, (*2*) the radiative contribution, and (*3*) the nonradiative contribution at $\alpha = 10^4$, $T_1 = 300$ K, and $T_2 = 0$. The magnitude of the tangential force (in dyn) can be obtained by multiplying the ordinate by the quantity $\kappa(R^3VkT/\sigma)$, where κ = (a) 2.4×10^{32} and (b, c) 2.4×10^{17}.

of the type $C(x/\alpha)^{1/2}$, where $x = \omega\hbar/kT$ and C is a numerical constant. After integration, we obtain

$$F_x^{(\mathrm{rad})} \approx -720\frac{\hbar V R^3 z_0}{\sigma^{3/2} c^6}\left(\frac{kT}{\hbar}\right)^{15/2}, \qquad (65)$$

$$\dot{Q}^{(\mathrm{rad})} \approx -170\frac{\hbar R^3 z_0}{\sigma^{3/2} c^4}\left(\frac{kT}{\hbar}\right)^{15/2}(1-\beta^2). \qquad (66)$$

Figures 2 and 3 present the results of numerical calculations of the tangential force F_x and the heat flux $\dot{Q}$ from relationships (63) and (64) for small ($0 < z_0 < 20$ nm, Figs. 2a, 3a), medium ($0.1\ \mu\mathrm{m} < z_0 < 5\ \mu\mathrm{m}$, Figs. 2b, 3b), and large ($5\ \mu\mathrm{m} < z_0 < 100\ \mu\mathrm{m}$, Figs. 2c, 3c) distances from the surface. The retardation effects are negligible at small distances. However, the quantities F_x and $\dot{Q}$ at larger distances considerably increase compared to those obtained in the nonrelativistic approximation (see Figs. 2b, 3b). The presence of the portions in which the contributions $F_x^{(\mathrm{rad})}$ and $\dot{Q}^{(\mathrm{rad})}$ linearly increase with an increase in the distance z_0 according to formulas (65) and (66) leads to their local predominance over the contributions of nonradiative modes in the range $10\ \mu\mathrm{m} \le z_0 \le 60\ \mu\mathrm{m}$ for $F_x^{(\mathrm{rad})}$ and $10\ \mu\mathrm{m} \le z_0 \le 90\ \mu\mathrm{m}$ for $\dot{Q}^{(\mathrm{rad})}$ (Figs. 2c, 3c). At the same time, the total dependences of the tangential force and the heat flux exhibit a monotonic decreasing behavior over the entire range of distances under investigation. The calculations also demonstrate that the fluctuation electromagnetic interaction is

enhanced with an increase in the resistivity of a material (see, for example, Figs. 2a, 3a).

The above inferences are in agreement with the results of our preliminary calculations [32] and the data obtained by Pendry [17], who noted that the contribution of the *S* mode to the heat flux is negligible (for nonmagnetic materials) at nanometer distances. In contrast, Volokitin and Persson [13, 18] argued that, even at distances of 1–10 nm, the inclusion of the *S* mode and the retardation effects (for normal metals) leads to a substantial increase in the heat flux and the tangential force as compared to those calculated within the nonrelativistic approximation (accounting only for the contribution of the *P* mode). In this respect, we note that, in their calculations of the tangential force, Volokitin and Persson [13] disregarded the contribution of the magnetic-polarization current ($\mathbf{j}_m = c\,\mathrm{curl}\,\mathbf{M}$). However, this current in the laboratory coordinate system is observed even for a particle possessing only the fluctuation electric dipole moment in the intrinsic coordinate system (see Section 3). Moreover, it should also be noted that, in [17, 18], the heat flux was calculated only in the specific case of a zero relative velocity.

Let us return to the results of our calculations. The asymptotic dependence $\dot{Q}(z_0)$ calculated at $z_0 \longrightarrow \infty$ does not exhibit distance-independent contributions characteristic of black-body radiation. This is quite consistent with the fact that the heat flux is associated just with the fluctuation electromagnetic interaction between the particle and the surface and, hence, should disappear in the limit $z_0 \longrightarrow \infty$ when the objects do not interact. A comparison of the heat flux $\dot{Q}(z_0)$ with the black-body radiation intensity $\dot{Q}_{\mathrm{BR}}$ in vacuum shows that $\dot{Q}(z_0)/\dot{Q}_{\mathrm{BR}} = p \sim R$ and $p \gg 1$ even at very large distances from the surface. Specifically, according to the data presented in Fig. 2, at $T_1 = 300$ K, $T_2 = 0$, $\sigma = 10^{17}$ s^{-1}, and $R = 1$ nm, we have $p = 2 \times 10^8$ at $z_0 = 5$ nm and $p = 2 \times 10^4$ at $z_0 = 1$ μm. Only at distances of several hundreds of microns do we obtain $p \leq 1$.

The tangential force F_x and the heat flux $\dot{Q}$ numerically estimated using the polarizability determined by formula (62b) are appreciably smaller than those obtained with formula (62a), because formula (62b) involves the small truncating factor $(\kappa R)^{-1}(\omega/4\pi\sigma)^2$. As a consequence, the dependences calculated with formula (62b) are similar to those depicted in Figs. 2 and 3, but the magnitudes of the quantities are less by a factor of $\sim 10^2(\kappa R)^{-1}\alpha^{-2} \ll 1$ and the formulas analogous to expressions (63)–(66) include an additional temperature factor T^2. Therefore, the inclusion of the screening leads to a drastic decrease in the calculated values of F_x and $\dot{Q}$.

8. CONCLUSIONS

Thus, we developed a consistent relativistic theory of dynamic fluctuation electromagnetic interaction of a small-sized particle with a flat surface. This theory provides correct passage to nonrelativistic formulas in the limit $c \longrightarrow \infty$. Within the proposed approach, general relationships were derived for the dissipative-loss integral, the thermal heating (cooling) rate, and the power of the tangential force. The derived relationships account for the difference between the temperatures of the particle and the surface and (in the general form) their dielectric and magnetic properties.

The results of the numerical calculations for high-conductivity materials demonstrated that the largest values of the tangential forces and the heat fluxes (larger at lower conductivities) are obtained at nanometer distances between the particle and the surface at which the nonradiative modes of the electromagnetic field make a dominant contribution. For distances exceeding 1 μm, the tangential force and the heat flux are considerably larger than those calculated in the nonrelativistic approximation. This can be explained by the relativistic retardation effect and an increase in the contribution of the radiative modes, which leads to a decrease (in magnitude) in the exponents of the corresponding dependences. The range of distances at which the contribution of the radiative modes is dominant depends on the product z_0T and reaches several tens of microns. For $z_0 > 100$ μm, the nonradiative modes again make a dominant contribution. The tangential force and the heat flux, which are associated with the fluctuation electromagnetic interaction, monotonically decrease with an increase in the distance between the particle and the surface over the entire range of distances under investigation (0–1 mm). The inclusion of the screening results in a substantial weakening of the fluctuation electromagnetic interaction due to the decrease in the particle polarizability. In the case when the temperatures of the particle and the surface are equal to each other, the heat flux is directed toward the particle and is proportional to the dynamic factor $(V/c)^2$.

APPENDIX A

1. FOURIER COMPONENTS OF THE ELECTRIC AND MAGNETIC POLARIZATION VECTORS

From relationships (1) and (2), with due regard for formulas (5) and (8), we obtain the following expressions for the projections of the Fourier transforms of the electric and magnetic polarization vectors:

$$P_{x,\,\omega\mathbf{k}}(z) = \gamma\delta(z - z_0)d_x^{\mathrm{sp}}(\gamma(\omega - Vk_x))\gamma^{-1},$$

$$P_{y,\,\omega\mathbf{k}}(z) = \gamma\delta(z - z_0)d_y^{\mathrm{sp}}(\gamma(\omega - Vk_x)),$$

$$P_{z,\omega\mathbf{k}}(z) = \gamma\delta(z-z_0)d_z^{\mathrm{sp}}(\gamma(\omega-Vk_x)),$$
$$M_{x,\omega\mathbf{k}}(z) = 0,$$
$$M_{y,\omega\mathbf{k}}(z) = \gamma\beta\delta(z-z_0)d_z^{\mathrm{sp}}(\gamma(\omega-Vk_x)), \quad \text{(A1)}$$
$$M_{z,\omega\mathbf{k}}(z) = -\gamma\beta\delta(z-z_0)d_y^{\mathrm{sp}}(\gamma(\omega-Vk_x)),$$

where $d_i^{\mathrm{sp}}(\ldots)$ are the Fourier components of the spontaneous dipole moment of the particle in the rest system of coordinates K' ($i = x, y, z$).

2. BOUNDARY CONDITIONS FOR THE HERTZ VECTORS

The necessary relationships can be obtained from the continuity conditions of the tangential components of the electric and magnetic fields at $z = 0$. The relevant equations should be written separately for each of the Hertz vectors $\mathbf{\Pi}^e$ and $\mathbf{\Pi}^m$. With the use of expression (33), it is easy to show that the following quantities should be continuous:

$$\varepsilon(\omega)\mu(\omega)\Pi_i^{(e,m)} \quad (i = x, y),$$
$$ik_x\Pi_x^e + ik_y\Pi_y^e + \frac{\partial\Pi_z^e}{\partial z},$$
$$ik_x\Pi_x^m + ik_y\Pi^m + \frac{\partial\Pi_z^m}{\partial z}, \quad \text{(A2)}$$
$$\varepsilon(\omega)\frac{\partial\Pi_i^e}{\partial z} \quad (i = x, y), \quad \varepsilon(\omega)\Pi_z^e,$$
$$\mu(\omega)\frac{\partial\Pi_i^m}{\partial z} \quad (i = x, y).$$

3. SOLUTION OF EQUATIONS (30) AND (31)

The solution of Eqs. (30) and (31) for the induced components of the Hertz vectors under additional continuity conditions (A2) for the vacuum region ($z, z' \geq 0$) is given by the expressions

$$\Pi_{x,\omega\mathbf{k}}^e(z) = \Gamma(z)\frac{\mu q_0 - q}{\mu q_0 + q}d_x(\omega), \quad \text{(A3)}$$

$$\Pi_{y,\omega\mathbf{k}}^e(z) = \Gamma(z)\frac{\mu q_0 - q}{\mu q_0 + q}d_y(\omega), \quad \text{(A4)}$$

$$\Pi_{z,\omega\mathbf{k}}^e(z) = \Gamma(z)\left[i\frac{2q_0^2(\varepsilon\mu-1)}{q_0(\varepsilon q_0+q)(\mu q_0+q)}\right.$$
$$\left.\times(k_xd_x(\omega)+k_yd_y(\omega)) + \frac{\varepsilon q_0 - q}{\varepsilon q_0 + q}d_z(\omega)\right], \quad \text{(A5)}$$

$$\Pi_{x,\omega\mathbf{k}}^m(z) = \Gamma(z)\frac{\varepsilon q_0 - q}{\varepsilon q_0 + q}m_x(\omega), \quad \text{(A6)}$$

$$\Pi_{y,\omega\mathbf{k}}^m(z) = \Gamma(z)\frac{\varepsilon q_0 - q}{\varepsilon q_0 + q}m_y(\omega), \quad \text{(A7)}$$

$$\Pi_{z,\omega\mathbf{k}}^m(z) = \Gamma(z)\left[i\frac{2q_0^2(\varepsilon\mu-1)}{q_0(\varepsilon q_0+q)(\mu q_0+q)}\right.$$
$$\left.\times(k_xm_x(\omega)+k_ym_y(\omega)) + \frac{\mu q_0 - q}{\mu q_0 + q}m_z(\omega)\right], \quad \text{(A8)}$$

$$\Gamma(z) = \frac{2\pi}{q_0}\exp(-q_0(z+z_0)),$$

$$d_x(\omega) = \gamma d_x^{\mathrm{sp}}(\gamma(\omega-Vk_x))\gamma^{-1},$$
$$d_y(\omega) = \gamma d_y^{\mathrm{sp}}(\gamma(\omega-Vk_x)),$$
$$d_z(\omega) = \gamma d_z^{\mathrm{sp}}(\gamma(\omega-Vk_x)),$$
$$m_x(\omega) = 0,$$
$$m_y(\omega) = \gamma\beta d_z^{\mathrm{sp}}(\gamma(\omega-Vk_x)), \quad \text{(A9)}$$
$$m_z(\omega) = -\gamma\beta d_y^{\mathrm{sp}}(\gamma(\omega-Vk_x)).$$

It should be noted that, in relationships (A9), all projections of the spontaneous dipole moment of the particle $d_i^{\mathrm{sp}}(\omega')$ [where $\omega' = (\omega - k_xV)/\sqrt{1-V^2/c^2}$ and $i = x$ and y] are the Fourier transforms in the rest system K'.

APPENDIX B: CALCULATION OF THE RETARDED GREEN'S FUNCTIONS OF RADIATION IN A MEDIUM

The retarded Green's function of electromagnetic radiation in a homogeneous isotropic medium obeys the standard equation [2, 31]

$$\left(\mathrm{curl}_{ik}\mathrm{curl}_{kl} - \frac{\omega^2}{c^2}\varepsilon(\omega)\mu(\omega)\delta_{il}\right)D_{lj}(\omega, \mathbf{r}, \mathbf{r}')$$
$$= -4\pi\hbar\mu(\omega)\delta_{ij}\delta(\mathbf{r}-\mathbf{r}'). \quad \text{(B1)}$$

The solution of Eq. (B1) does not differ radically from the solution of Eqs. (30) and (31). Let us use the analogy with the equation for the electric field induced by a point dipole $d_i(\omega)$ localized at the point $\mathbf{r} = \mathbf{r}'$; that is,

$$\left(\mathrm{curlcurl} - \frac{\omega^2}{c^2}\varepsilon(\omega)\mu(\omega)\right)\mathbf{E}_\omega(\mathbf{r})$$
$$= 4\pi\mu(\omega)\frac{\omega^2}{c^2}\delta(\mathbf{r}-\mathbf{r}')\mathbf{d}(\omega). \quad \text{(B2)}$$

A comparison of Eqs. (B1) and (B2) shows that the retarded Green's function is equivalent to the electric field of the point dipole with the dipole moment

$$d_i(\omega) = \left(-\frac{\hbar c^2}{\omega^2}\right)\delta_{ij}. \quad \text{(B3)}$$

On this basis, with allowance made for relationships (34)–(36) and (B1)–(B3), we directly obtain all components $D_{ij}(\omega\mathbf{k}; z, z')$ of the renormalized Green's function in the vacuum region ($z, z' \geq 0$):

$$D_{xx} = -\Phi(z, z')[k_x^2(1-\xi^2)\Delta_e(\omega) + (\xi k_y)^2\Delta_m(\omega)], \quad \text{(B4)}$$

$$D_{yy} = -\Phi(z, z')[k_y^2(1-\xi^2)\Delta_e(\omega) + (\xi k_x)^2\Delta_m(\omega)], \quad \text{(B5)}$$

$$D_{zz} = -\Phi(z, z')k^2\Delta_e(\omega), \quad \text{(B6)}$$

$$D_{xy} = D_{yx} = -\Phi(z, z')k_x k_y \times [(1-\xi^2)\Delta_e(\omega) - \xi^2\Delta_m(\omega)], \quad \text{(B7)}$$

$$D_{zx} = -D_{xz} = -\Phi(z, z')ik_x q_0\Delta_e(\omega), \quad \text{(B8)}$$

$$D_{zy} = -D_{yz} = -\Phi(z, z')ik_y q_0\Delta_e(\omega),$$

$$\Phi(z, z') = \frac{2\pi\hbar c^2}{q_0\omega^2}\exp(-q_0(z+z')), \quad \xi = \omega/ck. \quad \text{(B9)}$$

REFERENCES

1. E. M. Lifshitz, Zh. Éksp. Teor. Fiz. **29**, 94 (1955) [Sov. Phys. JETP **2**, 73 (1955)].
2. Yu. S. Barash, *Van der Waals Forces* (Nauka, Moscow, 1988).
3. I. E. Dzyaloshinskiĭ, E. M. Lifshitz, and L. P. Pitaevskiĭ, Usp. Fiz. Nauk **73**, 381 (1961) [Sov. Phys. Usp. **4**, 153 (1961)].
4. H. B. G. Casimir, Proc. K. Ned. Acad. Wet. **51**, 793 (1948).
5. V. M. Mostepanenko and N. N. Trunov, *The Casimir Effect and Its Applications* (Clarendon, Oxford, 1997).
6. M. Kardar and R. Golestanian, Rev. Mod. Phys. **71**, 1233 (1999).
7. W. L. Schaich and J. Harris, J. Phys. F: Met. Phys. **11**, 65 (1981).
8. L. S. Levitov, Europhys. Lett. **8**, 488 (1989).
9. V. G. Polevoĭ, Zh. Éksp. Teor. Fiz. **98**, 1990 (1990) [Sov. Phys. JETP **71**, 1119 (1990)].
10. V. E. Mkrtchian, Phys. Lett. **207**, 299 (1995).
11. J. B. Pendry, J. Phys.: Condens. Matter **9**, 10301 (1997).
12. A. I. Volokitin and B. N. J. Persson, J. Phys.: Condens. Matter **11**, 345 (1999).
13. A. I. Volokitin and B. N. J. Persson, Phys. Rev. B **65**, 115419 (2002).
14. G. V. Dedkov and A. A. Kyasov, Fiz. Tverd. Tela (St. Petersburg) **44** (10), 1729 (2002) [Phys. Solid State **44**, 1809 (2002)].
15. D. Polder and M. A. van Hove, Phys. Rev. B **4**, 3303 (1971).
16. M. L. Levin, V. G. Polevoĭ, and S. M. Rytov, Zh. Éksp. Teor. Fiz. **79**, 2087 (1980) [Sov. Phys. JETP **52**, 1054 (1980)].
17. J. B. Pendry, J. Phys.: Condens. Matter **11**, 6621 (1999).
18. A. I. Volokitin and B. N. J. Persson, Phys. Rev. B **63**, 205404 (2001).
19. A. A. Kyasov and G. V. Dedkov, Phys. Low-Dimens. Semicond. Struct. **5/6**, 58 (2002).
20. G. V. Dedkov and A. A. Kyasov, Pis'ma Zh. Tekh. Fiz. **29** (1), 36 (2003) [Tech. Phys. Lett. **29**, 16 (2003)].
21. A. A. Kyasov and G. V. Dedkov, Nucl. Instrum. Methods Phys. Res. B **195**, 247 (2002).
22. I. A. Dorofeyev, H. Fuchs, B. Gotsmann, and J. Jersch, Phys. Rev. B **64**, 35403 (2001).
23. W. Pauli, *The Theory of Relativity* (Pergamon, Oxford, 1958; Nauka, Moscow, 1983).
24. V. V. Batygin and I. N. Toptygin, *Problems in Electrodynamics*, 2nd ed. (Nauka, Moscow, 1970; Academic, London, 1978).
25. G. V. Dedkov and A. A. Kyasov, Phys. Lett. A **259**, 38 (1999); Pis'ma Zh. Tekh. Fiz. **25** (12), 10 (1999) [Tech. Phys. Lett. **25**, 466 (1999)].
26. G. V. Dedkov and A. A. Kyasov, Pis'ma Zh. Tekh. Fiz. **28** (8), 79 (2002) [Tech. Phys. Lett. **28**, 346 (2002)].
27. A. A. Kyasov and G. V. Dedkov, Surf. Sci. **463**, 11 (2000).
28. M. S. Tomassone and A. Widom, Phys. Rev. B **56**, 4938 (1997).
29. M. B. Vinogradova, O. V. Rudenko, and A. P. Sukhorukov, *The Theory of Waves* (Nauka, Moscow, 1982).
30. L. D. Landau and E. M. Lifshitz, *Statistical Physics*, 3rd ed. (Nauka, Moscow, 1976; Pergamon, Oxford, 1980), Part 1.
31. E. M. Lifshitz and L. P. Pitaevskiĭ, *Course of Theoretical Physics*, Vol. 5: *Statistical Physics* (Nauka, Moscow, 1978; Pergamon, New York, 1980), Part 2.
32. G. V. Dedkov and A. A. Kyasov, Pis'ma Zh. Tekh. Fiz. **28** (23), 50 (2002) [Tech. Phys. Lett. **28**, 997 (2002)].
33. M. B. Smirnov and V. P. Krainov, Laser Phys. **9**, 943 (1999).

Translated by O. Borovik-Romanova

Physics of the Solid State, Vol. 45, No. 10, 2003, pp. 1829–1859. Translated from Fizika Tverdogo Tela, Vol. 45, No. 10, 2003, pp. 1742–1769.

REVIEWS

Band Structure and Properties of Superconducting MgB_2 and Related Compounds (A Review)

A. L. Ivanovskiĭ

Institute of Solid-State Chemistry, Ural Division, Russian Academy of Sciences, Pervomaĭskaya ul. 91, Yekaterinburg, 620219 Russia

e-mail: ivanovskii@ihim.uran.ru

Received March 13, 2003

Abstract—This paper presents an overview of the current state of the art in research into the electronic structure and properties of a new superconductor, namely, MgB_2, and a large number of related compounds by computational methods of the band theory. Consideration is given to the specific features of the surface states of magnesium diboride, the electron and hole doping effects in this compound, and the concentration dependences of the band structure and the properties of $Mg_{1-x}Me_xB_2$ and $MgB_{2-y}X_y$ solid solutions and a number of superstructures. The electronic properties of AlB_2-like phases, boron, higher borides, a series of ternary layered boron-containing phases, and compounds with structures of the antiperovskite type ($MgCNi_3$ and others) are discussed in terms of their superconducting characteristics. The results obtained in modeling nanotubes and fullerene-like nanoparticles based on MgB_2 and related borides are analyzed. © *2003 MAIK "Nauka/Interperiodica".*

1. INTRODUCTION

The discovery of the critical transition ($T_c \sim 39$ K) in layered magnesium diboride in 2001 [1] and subsequent systematic investigations of this diboride and a large number of related compounds have made a considerable contribution to the development of the concept of superconductivity in anisotropic materials and led to the revision of many previously obtained results and models.

The critical temperature of MgB_2 is nearly twice as high as the maximum critical temperature T_c of classical binary superconductors, such as transition-metal compounds and alloys with high-symmetry structures of the *B*1 (NbN, $T_c \sim 17.3$ K) or *A*15 (Nb_3Ge, $T_c \sim 23$ K [2]) type, in which the superconductivity is governed by the electron state of the *d* metals.

Among the anisotropic superconductors, magnesium diboride MgB_2 bears the closest similarity to quasi-two-dimensional intercalated graphite compounds ($LiC_{6–8}$, KC_8, etc.). Note that the superconductivity in the intercalated graphite compounds ($T_c \sim 0.55$–5.0 K) is due to interaction of carbon π bands with phonon modes of planar networks composed of carbon atoms [3–5]. A similar mechanism based on the dominant role played by carbon π bands is also characteristic of superconducting fullerides [6]. However, the type of occupation of the energy bands (partially occupied σ bands, see below) in MgB_2 differs radically from that in the above compounds.

It should be noted that, among the boron-containing phases, the MgB_2 diboride is not the sole superconductor (Table 1). Low-temperature superconductivity ($T_c \leq 0.5$–4.5 K) is observed in a number of binary *d* metal borides [2, 7] and a group of ternary ($LnRuB_2$ and $LnRh_4B_4$) and pseudoternary [$(Ln_{1-x}Ln'_y)Rh_4B_4$] borides [8]. High critical temperatures T_c (~ 16–23 K) were revealed for intermetallic borocarbides [9, 10], namely, layered quaternary phases of the $LuNi_2B_2C$ type (see reviews [11, 12]).

Since 2001, the properties of the MgB_2 diboride have been investigated thoroughly. In particular, it has been established that the characteristics of this compound are stable in magnetic fields and under irradiation. The critical transport currents in MgB_2 are large in magnitude and relatively insensitive to contact with intercrystalline boundaries. These properties and a number of other superconductivity characteristics of MgB_2 are very attractive for practical applications (see reviews [13–16]).

A large number of investigations have been performed in the field of materials science of superconducting MgB_2. This compound has been prepared in the form of single crystals, porous and compact ceramics, films, long wires, tapes, and composites (see [13–16]). Moreover, MgB_2-based nanostructures, such as nanostructured thin films [17] and compact nanoceramics [18], have been synthesized recently. At present, researchers have continued to actively search for new superconducting phases related to MgB_2.

Apart from the solution of problems in materials science, basic concepts regarding the nature of superconductivity in the MgB_2 diboride and related compounds

Table 1. Critical temperatures and structural types of superconducting binary semiborides Me_2B, monoborides MeB, diborides MeB_2, and higher borides of metals [14]

Boride	T_c, K	Structure	Boride	T_c, K	Structure
Ta_2B	3.12		$MoB_{2.5}$	8.1	AlB_2
Mo_2B	4.75–5.97*	θ-$CuAl_2$	$ReB_{1.8–2}$	4.5–6.3	
W_2B	3.10–3.22	θ-$CuAl_2$	YB_6	7.1	CaB_6
Re_2B	2.8		LaB_6	5.7	CaB_6
ZrB	2.8–3.4		ThB_6	0.74	CaB_6
NbB	8.25	α-TlI	NbB_6	3.0	
MoB	0.5		ScB_{12}	0.39	UB_{12}
HfB	3.1		YB_{12}	4.7	UB_{12}
TaB	4.0	α-TlI	ZrB_{12}	5.82	UB_{12}
MgB_2	40	AlB_2	LuB_{12}	0.48	UB_{12}
$BeB_{2.75}$	0.7				
ZrB_2	0–5.5	AlB_2			
NbB_2	0–0.62	AlB_2			
$NbB_{2.5}$	6.4	AlB_2			

* According to the data obtained by different authors [14].

have been rapidly developed, to a large extent, owing to recent progress in research into the electronic properties of these phases. The obtained data on the electronic structure are widely used to interpret or to calculate different physicochemical properties of these objects.

In my opinion, the amount of new data obtained since 2001 on the electronic structure of metal borides and related phases is comparable to the amount of information amassed throughout history.

In this review, an attempt is made to generalize the data obtained in 2001 and 2002 on the electronic structure of a new superconductor, namely, MgB_2, with the use of theoretical quantum calculations and spectroscopic methods. Consideration is given to the electron and hole doping effects in the MgB_2 diboride, the band structure, and the properties of $Mg_{1-x}M_xB_2$ and $MgB_{2-y}X_y$ solid solutions and a number of superstructures. This paper also reports on the results obtained in simulating the electronic properties of the MgB_2 surface and nanostructures, such as nanotubes and fullerene-like nanoclusters based on MgB_2 and related diborides. New data on the electronic states of AlB_2-like phases, boron, higher borides, a number of ternary layered boron-containing phases, and compounds with an antiperovskite structure ($MgCNi_3$ and others) are discussed in terms of their superconducting characteristics.

2. MAGNESIUM DIBORIDE MgB_2: ENERGY BANDS, INTERATOMIC INTERACTIONS, AND PROPERTIES

As is known, the MgB_2 diboride has a hexagonal structure (AlB_2 structural type, space group D^1_{6h}–$P6/mm$). The unit cell contains one formula unit ($Z = 1$). Boron atoms are located at the centers of magnesium trigonal prisms, which are shared by all faces and form a three-dimensional packing. The Mg and B atoms have the $[MgB_{12}Mg_8]$ and $[BMg_6B_3]$ coordination polyhedra, respectively. The coordination number is equal to 20 for the Mg atom and 9 for the B atom. In the unit cell, the atoms occupy the following positions: 1 Mg(a) (0, 0, 0) and 2 B(d) (1/3, 2/3, 1/2) and (2/3, 1/3, 1/2). The unit cell parameters are $a = 0.30834$ nm, $c = 0.35213$ nm, and $c/a = 1.142$. The interatomic distances are as follows: B–B ($a/\sqrt{3}$), 0.1780 nm; B–Mg ($\sqrt{a^2/3 + c^2/4}$), 0.2503 nm; Mg–Mg (a in a layer), 0.3083 nm; and Mg–Mg (between layers), 0.3520 nm [14]. The MgB_2 structure can also be represented as consisting of planar hexagonal magnesium networks and graphite-like boron networks alternating in the order …$Mg/B_2/Mg/B_2$… (Fig. 1).

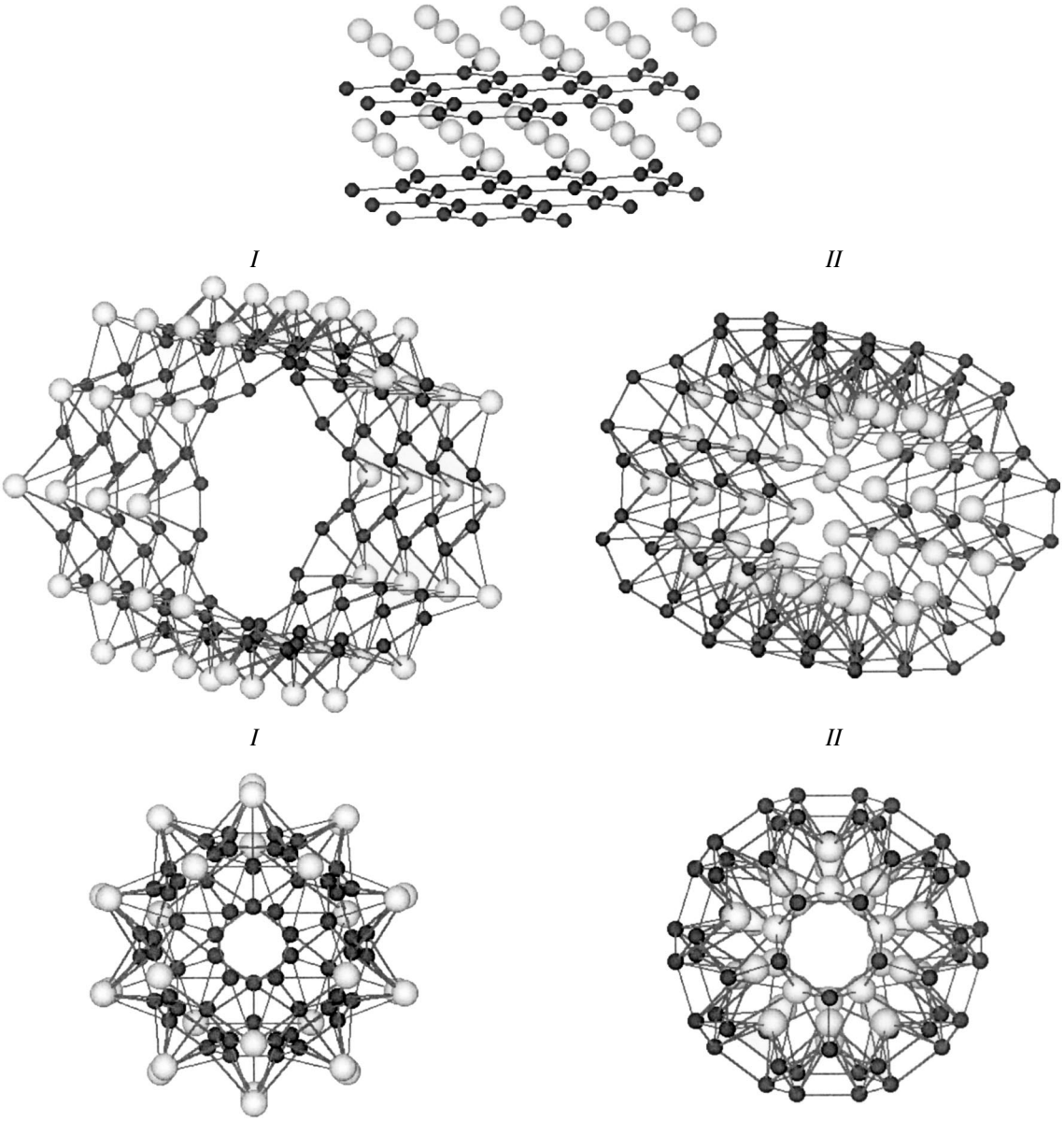

Fig. 1. Crystal structure of hexagonal MgB_2 (at the top) and structures of a nonchiral armchair (11, 11) MgB_2 nanotube and an $Mg_{30}B_{60}$ cage (fullerene-like) molecule for possible atomic configurations: the metallic shell is located (*I*) outside and (*II*) inside the shell formed by boron atoms.

2.1. Band Structure of Magnesium Diboride

Prior to the discovery of superconductivity in MgB_2, the electronic structure of this compound was investigated by the semiempirical method of linear combination of atomic orbitals in the basis set of *sp* orbitals [19], the tight-binding band method [20], and the nonself-consistent orthogonalized plane wave method [21]. It was noted the valence bands of MgB_2 and graphite are similar to each other. The main contribution to the valence band of magnesium diboride is made by a combination of boron $p_{\sigma,\pi}$ states. Charge transfer occurs in the direction Mg $\longrightarrow$ B. The bottom edge of the conduction band is predominantly determined by the B p_π orbitals.

The first *ab initio* calculations performed in the framework of the full-potential linearized muffin-tin orbital (FLMTO) method [22] revealed that the energy bands of MgB_2 are formed as a result of strong B–B interactions in the planes of graphite-like networks. It was found that the density of states is characterized by the B 2*p* peak at the Fermi level E_F. The interatomic interactions in MgB_2 were analyzed and compared with those in isostructural diborides AlB_2 and TiB_2. Among the known metal diborides, titanium diboride TiB_2 possesses extreme thermal and strength characteristics [7].

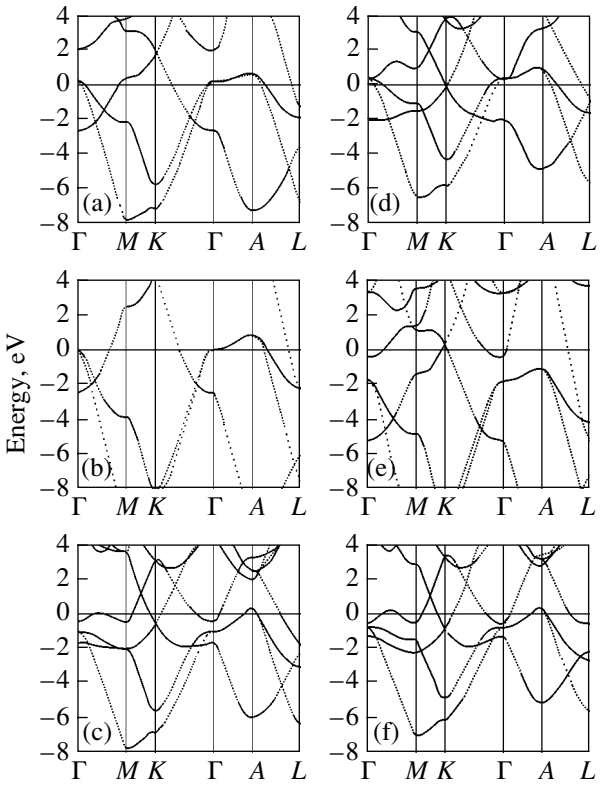

Fig. 2. Energy bands of (a) MgB_2, (b) BeB_2, (c) ScB_2, (d) CaB_2, (e) AlB_2, and (f) YB_2 according to FLMTO calculations [29].

It was shown that, for the boron networks, the overlap of the B–B wave functions decreases in the following order: $MgB_2 \longrightarrow AlB_2 \longrightarrow TiB_2$. The effect of interplanar covalent *Me*–B bonds is most pronounced in TiB_2 and weakest in MgB_2. The cohesion energies E_{coh} (characterizing the total energy effect of interatomic bonds in the system) and the energies of individual (B–B, *Me*–B, *Me*–*Me*) bonds were calculated by the method proposed in [23]. It was demonstrated that the maximum contribution to the cohesion energy E_{coh} is made by the B–B bonds (68%); the contributions of the other bonds are considerably smaller (B–Mg, 23%; Mg–Mg, 9%). In the case of the transition $MgB_2 \longrightarrow AlB_2$, an increase in the cohesion energy E_{coh} is associated with the substantial enhancement of the *Me*–*Me* interactions and the relative constancy of the energies of the *Me*–*Me* and *Me*–B bonds. This is the fundamental difference between the phases under consideration and diborides of *d* metals, for which the cohesion energy E_{coh} is governed by the interlayer *Me*–B interactions (see below).

After the discovery of superconductivity, the specific features of the band structure of MgB_2 were investigated in a large number of works with the use of virtually all known band calculation methods [24–48]. The basic results obtained in these investigations can be summarized as follows.

(1) The valence band of MgB_2 (Fig. 2) is determined by the B 2*p* states, which form four $\sigma(2p_{x,y})$ and two $\pi(2p_z)$ bands. Their dispersion curves $E(k)$ differ significantly.

(2) For the B $2p_{x,y}$ bands, the dispersion $E(k)$ is maximum in the $k_{x,y}$ (Γ–*K*) direction. These bands reflect the distribution of electron states of boron in graphite-like networks, are of the quasi-two-dimensional (2*D*) type, and form flat regions aligned along the k_z (Γ–*A*) direction. Two B $2p_{x,y}$ bands intersect the Fermi level, appreciably contribute to the total density of states at the Fermi level $N(E_F)$ (~ 30%, Fig. 3), and are responsible for the metal-like properties of the diboride. The Fermi level E_F is located in the region of bonding states.

(3) One of the most important features of the electronic spectrum of MgB_2 is the energy position of the B $2p_{x,y}$ bands. At the Γ point of the Brillouin zone, these bands lie above the Fermi level and form hole-type cylindrical elements of the Fermi surface (Fig. 4).

(4) The B $2p_z$ states (of the three-dimensional type) are oriented perpendicularly to the boron networks and are responsible for the weak interlayer π bonds. Both π bands intersect the Fermi level and are characterized by the maximum dispersion along the k_z (Γ–*A*) direction. The Mg *s*, Mg *p*, and B *s* states are admixed to the system of B 2*p* bands in the vicinity of the valence band edge and in the conduction band.

These results provided the basis for the development of modern models explaining the nature of superconductivity in the MgB_2 diboride.

2.2. Electronic Structure and Some Properties of MgB_2

There exist a number of alternative models proposed for explaining the superconducting properties of MgB_2. For example, Hirsch [49] interpreted this effect in the framework of the hole-type superconductivity model [50], according to which carriers are paired as a result of the Coulomb interaction. However, the methods predicted in [49] for increasing the superconducting transition temperature of magnesium diboride (doping with Al or hydrostatic compression of the lattice) turned out to be in direct opposition to both experimental data and the theoretical conclusions based on the electron–phonon mechanism of superconductivity [13–16]. Zaĭtsev [51] developed the concept of strong cation–anion interactions. Volkova *et al.* [52] proposed a scheme of correlations between the critical temperature T_c and crystal chemical parameters for the family of AlB_2-like diborides. Within the proposed approach, the superconductivity of MgB_2 is explained by the lattice instability of this phase.

Kortus *et al.* [26] were the first to attempt to estimate the critical temperature T_c for MgB_2 semiquantitatively

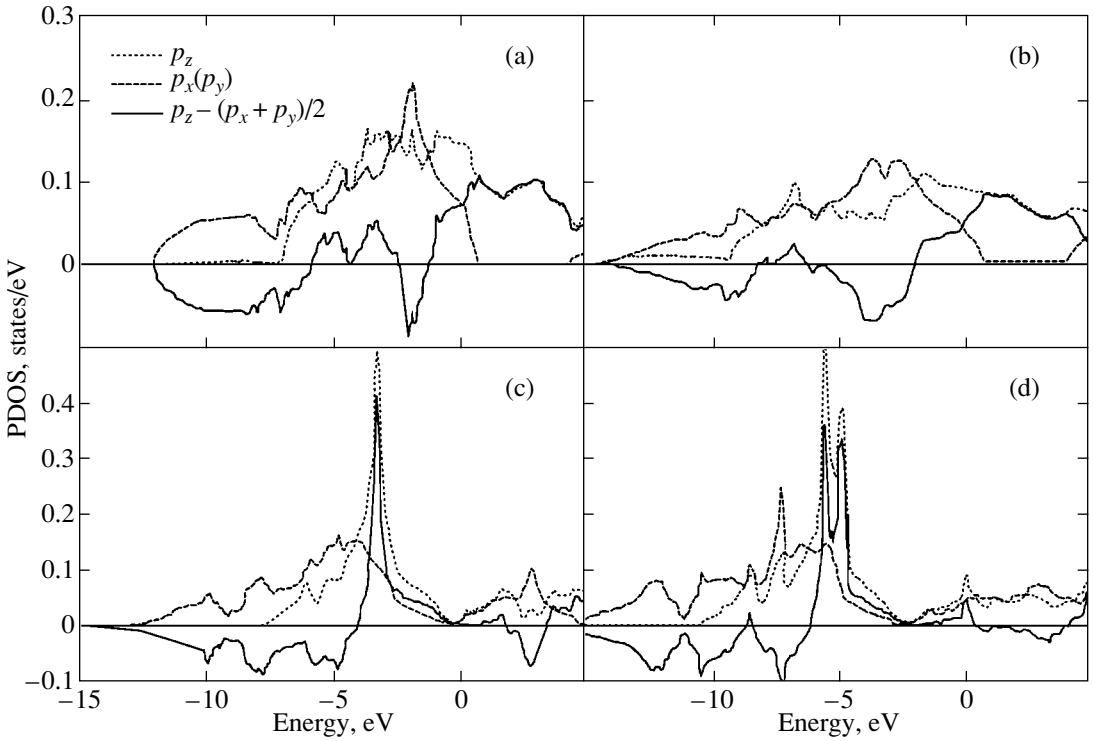

Fig. 3. Partial densities of B p_{xy} (dashed lines) and B p_z (dotted lines) states and their differences (solid lines) for (a) MgB_2, (b) BeB_2, (c) TiB_2, and (d) TaB_2 [80].

by modeling the band structure of the diboride within the electron–phonon interaction formalism. These authors emphasized that strong interactions ($\lambda \sim 0.9$–1.0) of the near-Fermi B σ bands with high-frequency (~300, 700 cm^{-1}) phonon modes of graphite-like boron layers play a decisive role. The effects of the electron–phonon interaction were discussed in more detail in [25, 28, 33, 38–42, 45, 48]. In particular, the calculations performed by Rosner *et al.* [45] showed that the electron–phonon coupling constants λ for different groups of states (σ and π) are strongly anisotropic: $\lambda_\sigma \sim 1.3$ and $\lambda_\pi \sim 0.4$. The *ab initio* calculations of the phonon spectra of magnesium diboride [53–56] proved the dominant role of optical phonons corresponding to the vibrational E_g modes in the plane of boron layers (Fig. 5).

The problem concerning the determination of the type and magnitude of the superconducting gap in magnesium diboride was discussed in a number of works [38, 39, 42, 45–48]. The calculations carried out by Choi *et al.* [47] revealed the presence of a two-gap structure in the σ and π sections of the Fermi surface of MgB_2 (Fig. 4). The gap widths (at $T = 4$ K) were estimated at ~ 6.4–7.2 and 1.2–3.7 meV, respectively. The total superconducting gap is of the *s* type. The temperature dependences of the superconducting gaps due to the σ and π states exhibit substantially different behaviors. This makes it possible to explain the observed anomalies in the low-temperature heat capacity of

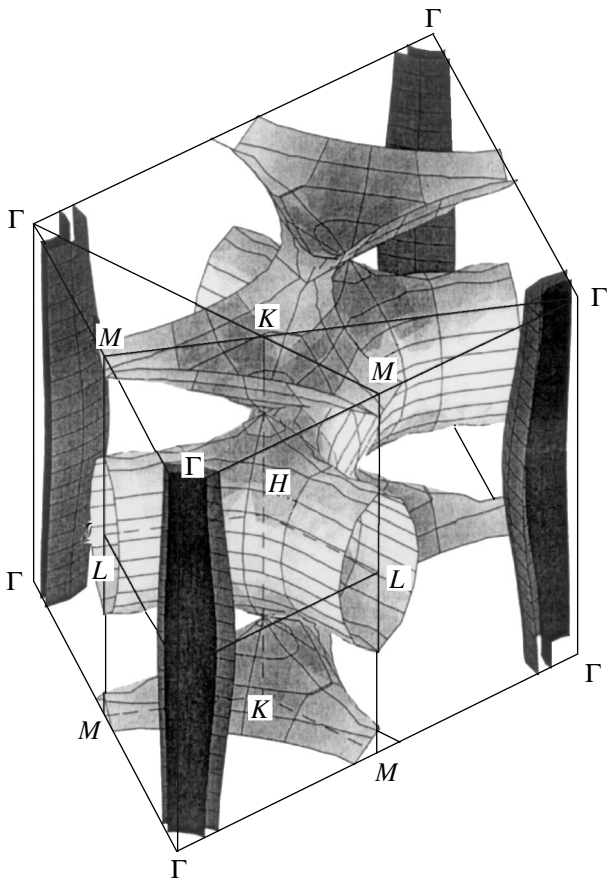

Fig. 4. Fermi surface of MgB_2 [47].

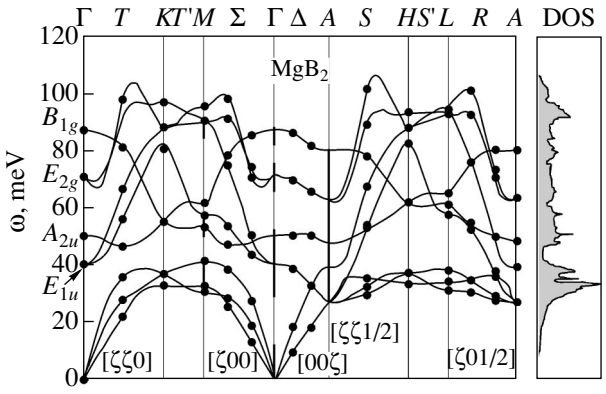

Fig. 5. Phonon spectrum of MgB_2: dispersion curves and densities of states [55].

MgB_2 [57–59]. The superconducting gap widths estimated in [47] are comparable to the experimental values obtained using tunneling microscopy, point-contact spectroscopy, and high-resolution photoelectron spectroscopy [60–66]. According to these studies, the energy spectrum of MgB_2 involves two superconducting gaps with widths of 5.5–8.0 and 1.5–3.5 meV.

In addition to theoretical investigations [24–48], the specific features of the electronic structure of MgB_2 were experimentally studied in detail using photoelectron [62, 63, 67], x-ray emission, x-ray absorption [68–73], and electron energy loss [74, 75] spectroscopy. The experimental data obtained are in excellent agreement with the results of calculations (Fig. 6), which confirms the general concept regarding the correlation between the superconducting properties of MgB_2 and the relative arrangement of the σ and π bands and the occurrence of the σ hole states. The spectral lines also exhibit a number of resonances, which indicates that protective films containing boron oxides are formed on the surface of samples after exposure to air.

A number of fine features in the electronic structure of MgB_2 were revealed in experimental NMR investigations of the spin–lattice relaxation and the Knight shift [76–79] and in theoretical calculations of these parameters, hyperfine interactions, and electric-field gradients at B and Mg nuclei [80, 81]. In particular, Medvedeva *et al.* [80] established that the electric-field gradient at B nuclei in MgB_2 reflects strong anisotropy of the spatial distribution of valence states and that the change in the electric-field gradient in a series of isostructural metal diborides (Table 2) depends primarily on the hybridization of the *p–d* states.

Considerable attention has been given to the theoretical interpretation of the effect of pressure treatment of MgB_2 on the superconducting properties and also to calculations of the mechanical characteristics of this diboride [24, 27, 30–32, 37, 38, 80, 82–87]. It is known (see review [14]) that the critical temperature T_c of MgB_2 under external compression decreases as $dT_c/dP \sim -1.6$ K/GPa. The evolution of the band structure of a compressed magnesium diboride crystal is illustrated in Fig. 7. As can be seen from this figure, the compression leads to an insignificant decrease in the concentration of σ holes (by ~ 0.005 at $P = 10$ GPa) owing to a change in the position of the B $2p_{x,y}$ bands along the Γ–*A* direction in the Brillouin zone and to a weak change in the density of states at the Fermi level $N(E_F)$ (a decrease by ~ 0.02 states/eV). At the same time, the Hopfield parameter η increases with an increase in the pressure ($d\eta/dP \sim 0.55\%$/GPa [80]). The main reason for the decrease in the critical temperature under pressure is the change in the phonon frequencies.

The results of band calculations were also used to interpret the de Haas–van Alphen effect [42, 86].

Table 2. Tensor components V_{zz} (10^{21} V/m) of the electric-field gradient at boron nuclei for MgB_2 and a number of isostructural diborides of *s–d* metals according to theoretical and experimental data [80]

Diboride	$*V_{zz}^{el}$	$*V_{zz}^{lat}$	$\lvert V_{zz}^B \rvert$	$\lvert V_{zz}^B \rvert$ exp
MgB_2	–1.94	0.06	1.88	1.69
BeB_2	–2.43	0.33	2.10	–
AlB_2	–1.17	0.18	0.99	1.08
ScB_2	–0.75	0.13	0.60	–
TiB_2	–0.66	0.31	0.35	0.37
VB_2	–0.76	0.38	0.38	0.43
CrB_2	–1.01	0.42	0.59	0.63
MoB_2	–0.55	0.32	0.23	0.23
TaB_2	–0.21	0.25	0.04	0.02

* V_{zz}^{el} and V_{zz}^{lat} are the electronic and lattice contributions to the electric-field gradient tensor, respectively. The experimental data are obtained by different authors (see [80]).

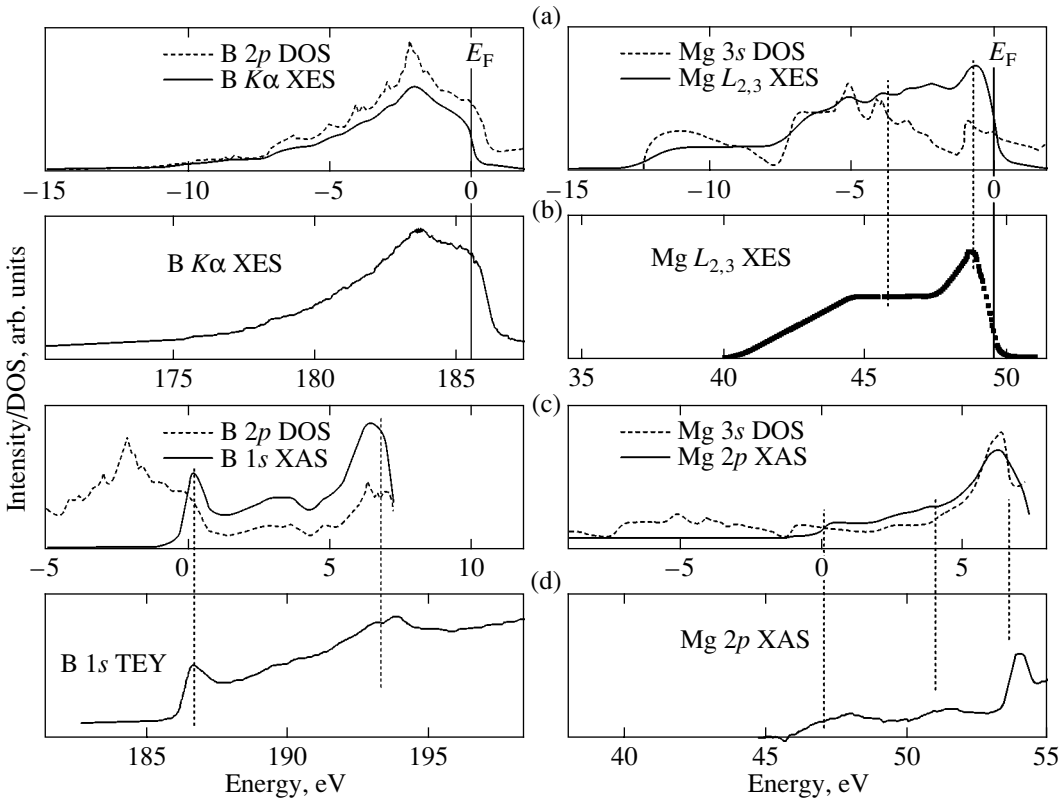

Fig. 6. (a, c) Theoretical and (b, d) experimental emission and absorption spectra of MgB_2 (B *K* line at the left and Mg *L* line at the right) [68].

2.3. Electronic Properties of the MgB_2 Surface

The considerable interest expressed in the specific features of surface electron states of superconducting MgB_2 is particularly associated with the development of methods for the reproducible synthesis of thin superconducting films for use in different electronic devices (see [13–16]). Magnesium boride films have been prepared using two main techniques [87–95], which involve *ex situ* processes (synthesis of boron films followed by their saturation with magnesium) or *in situ* methods (direct preparation of MgB_2 films). The morphology of MgB_2 films (including epitaxially oriented films [96–100]) and a number their properties, such as the conductivity, the Hall effect, the surface resistivity, and optical characteristics [87–108], have been studied in sufficient detail to date. Strong anisotropy of the conductivity was found and the upper critical fields were determined for oriented films.

The methods of the band theory were applied to describe the electronic properties of both magnesium-terminated (Mg-*t*) and boron-terminated (B-*t*) ideal hexagonal MgB_2(0001) surfaces [109–112]. The calculations revealed a number of surface resonances and a pronounced increase in the density of near-Fermi states for outer layers (especially for the B-*t* surface; Fig. 8). According to [109], this behavior is favorable for an increase in the critical temperature of films as compared to that of bulk materials. The band structure in the vicinity of the Fermi level E_F can be different depending on the type of outer monolayer. This region involves B σ and B π bands for the B-*t* surface and only π bands for the Mg-*t* surface. The relaxation effects are rather weak: they amount to –2.1 and –3.7% between two outer monolayers for the B-*t* and Mg-*t* surfaces, respectively, and virtually disappear at a depth of five or six monolayers [110].

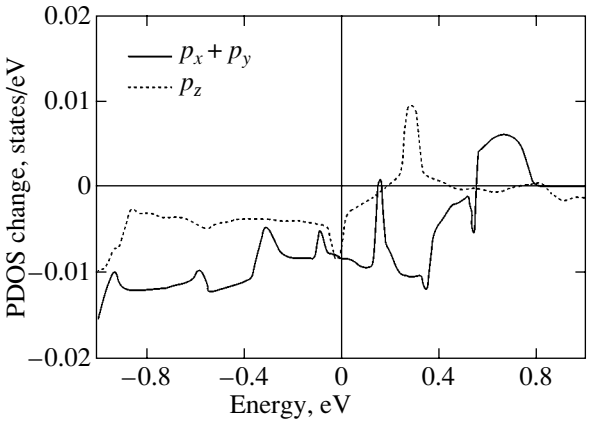

Fig. 7. Changes in the partial densities of B $2p_{xy}$ (solid line) and B $2p_z$ (dashed line) states of MgB_2 under a pressure of 10 GPa [80].

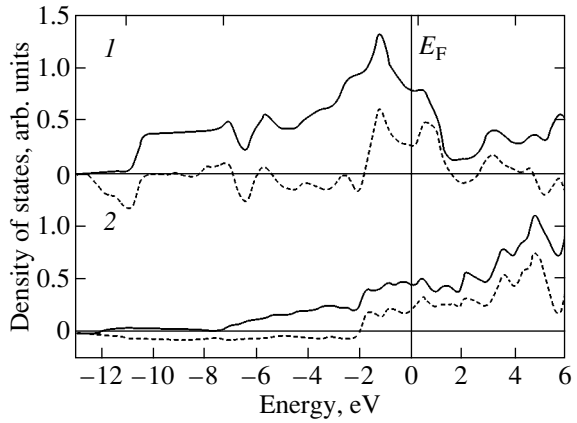

Fig. 8. Densities of states of (*1*) boron and (*2*) magnesium outer monolayers for the $MgB_2(0001)$ surface (solid lines). Differential densities of states corresponding to outer and inner monolayers (dashed lines) are given. LDA calculations for a model of a 13-atom supercell [109].

According to the calculations performed by Servedio *et al.* [112] in the framework of the Korringa–Kohn–Rostoker method, the MgB_2 surface is characterized by a number of surface states corresponding to fine features of the angle-resolved photoelectron spectra of magnesium diboride single crystals [113]. The estimates made by Li *et al.* [111] for the energies of formation of the surfaces terminated by different atoms showed that the system involving an outer monolayer composed of more reactive Mg atoms has a higher stability. The work functions of the B-*t* and Mg-*t* surfaces were calculated to be 5.95 and 4.25 eV, respectively.

It should be emphasized that, in [109–112], the diboride surface was modeled by the (0001) face of a perfect crystal. In actual fact, the situation is more complex. Vasques *et al.* [114] carried out special x-ray photoelectron spectroscopic investigations of the elemental composition of the MgB_2 surface and found that at least three regions with different compositions are formed in the vicinity of the surface. The first region directly on the surface involves an oxide film and is appreciably enriched in magnesium (Mg/B ~ 0.80). By contrast, the near-surface region is depleted in magnesium (Mg/B ~ 0.34); in this case, the nonstoichiometry with respect to metal favors a decrease in the electron density in layers of boron atoms. Only the third region is characterized by the stoichiometric ratio (Mg/B = 0.50) corresponding to the bulk magnesium diboride.

3. DOPING EFFECTS, SOLID SOLUTIONS AND SUPERSTRUCTURES BASED ON MgB_2, AND RELATED TERNARY PHASES

Immediately after the discovery of superconductivity in MgB_2, theoretical and experimental investigations were undertaken with the aim of modifying the properties of magnesium diboride and searching for related superconductors. Within the former direction, researchers have sought to extend the class of possible superconductors through the doping or preparation of different solid solutions and superstructures based on the MgB_2 phase. The latter direction involves searching for the superconductivity effect among the large variety of binary or multicomponent phases whose structural or chemical units are similar to those of MgB_2. The synthesis procedures, crystallographic data for the synthesized materials, and a number of materials science aspects regarding these objects are described in reviews [13–16]. Let us now consider the results obtained in modeling the band structure of the above systems.

Before proceeding further, we recall that, in the early stages of investigations, the rigid-band model was frequently used in the design of many experiments and in interpreting the data obtained for impurity systems and solid solutions. By postulating the identity of the densities of states for doped systems and the initial matrix (MgB_2), investigators only took into account that different dopants can serve as heteroelectronic or isoelectronic impurities and, hence, either lead or do not lead to a change in the electron concentration in the system. Within this model, hole dopants (for example, Be impurities in the boron sublattice or Li, Na, and Cu impurities in the Mg sublattice) should decrease the electron concentration in the system and lead to an increase in the density of hole states in the σ band and to a shift of the Fermi level E_F toward the high-energy range with an increase in the density of states at the Fermi level $N(E_F)$. Both factors are favorable for superconductivity (see above). Contrastingly, electron dopants (Al and *d* metal impurities in the Mg sublattice or C, N, and O impurities in the boron sublattice) affect the occupation of the σ band, result in a decrease in the density of states at the Fermi level $N(E_F)$, and should have a negative effect on the superconducting properties. The role of isoelectronic substitutions (Be, Ca $\longrightarrow$ Mg) remains unclear in terms of the rigid-band model.

It should be noted that, for the majority of systems, the properties predicted on the basis of the aforementioned rigid-band model appear to be in error. For example, the experimental data on the critical temperatures T_c of $Mg_{0.97}Me_{0.03}B_2$ alloys [115] indicate that the critical temperature of the alloy with *Me* = Mn decreases to 33.1 K, whereas the critical temperatures of the alloys with *Me* = Fe, Co, Ni, and Zn are equal to 37.8, 35.7, 37.8, and 38.4 K, respectively. However, according to the rigid-band model, the critical temperature of $Mg_{1-x}Me_xB_2$ alloys should monotonically decrease with an increase in the atomic number *Z* of the *Me* impurity. A number of other examples are given in reviews [13–16]. Numerical calculations made it possible to propose a more correct interpretation for the effects caused by the doping of MgB_2.

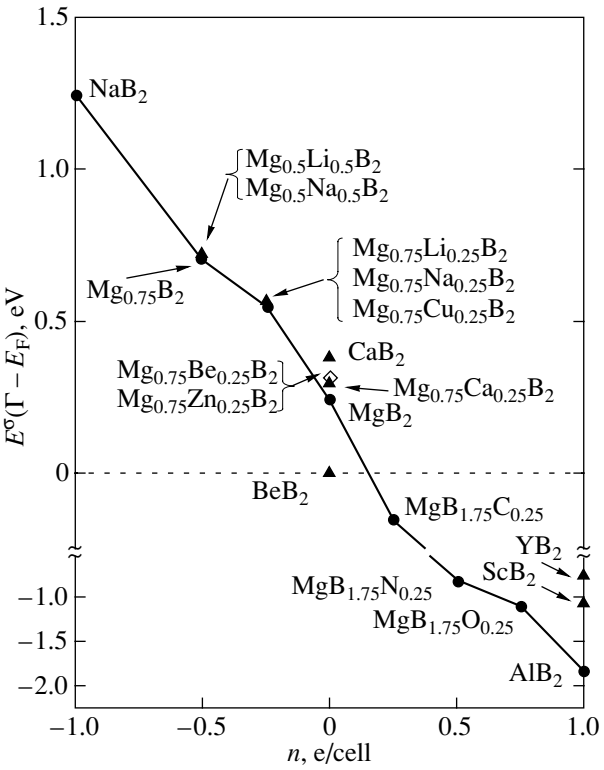

Fig. 9. Dependence of the energy of the B $\sigma(p_{xy})$ band at the Γ point of the Brillouin zone (with respect to the energy of the corresponding band of MgB_2) on the electron concentration n (e/cell) for a number of binary and ternary AlB_2-like diborides according to the FLMTO calculations [116].

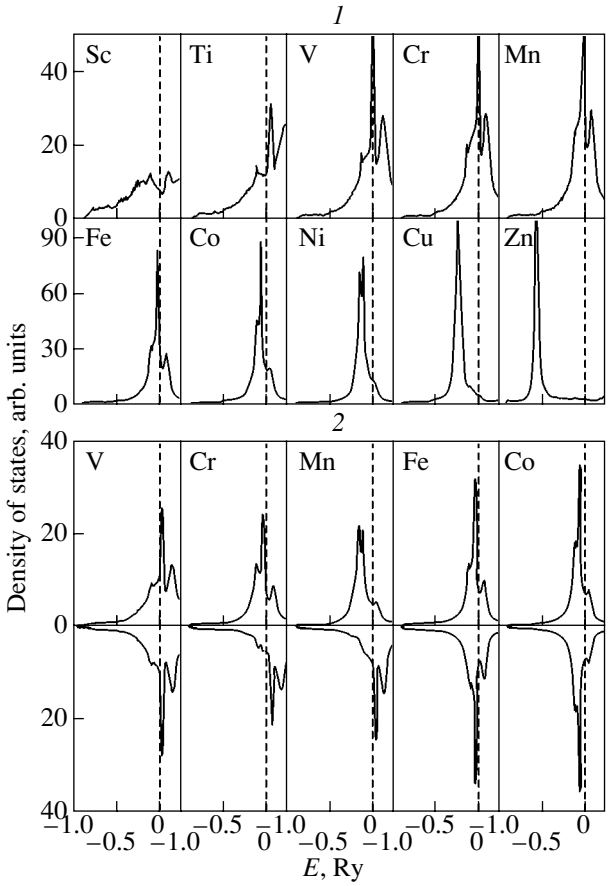

Fig. 10. Densities of states of 3*d* metal impurities in MgB_2. The results of the spin-polarized calculations [117] are given at the bottom.

3.1. Doping of the Metal Sublattice in MgB_2

For the most part, attempts to control the electron and hole concentrations in MgB_2 were reduced to the introduction of different dopants into the cation sublattice of magnesium diboride. Experimental data demonstrate (see [13–16]) that the replacement of Mg by other elements (Li, Na, Be, Al, *d* metals) leads to a decrease in the critical temperature T_c of the system (except for systems with Zn and, possibly, Li), a change in the lattice constants, and, in a number of cases, phase transitions attended by a change in the type of crystal structure.

The first systematic investigations into the regularities of chemical modification of the electronic structure of MgB_2 upon doping of the cation sublattice with Be, Ca, Li, Na, Zn, and Cu impurities were carried out by the first-principles FLMTO method in [116]. It was found that, for $Mg_{1-x}Me_xB_2$ systems (where *Me* = Be, Ba, Li, Na, Cu, Zn), the main features in the band spectra are identical to those in the band spectrum of MgB_2 and the energy positions and the occupation of the near-Fermi σ bands (Fig. 9) and the density of states at the Fermi level $N(E_F)$ are determined by the type and concentration of impurities.

The tendency toward the formation of electronic and magnetic states of 3*d* metal impurities (*Me* = Sc, Ti, V, …, Cu, Zn) in cation positions of MgB_2 as a function of the atomic number Z of metals was analyzed by Singh and Joseph [117], who investigated the $Mg_{0.97}Me_{0.03}B_2$ systems in the framework of the Korringa–Kohn–Rostoker coherent-potential approximation (KKR–CPA). The specific features in the localization of impurity states in the band spectrum of the matrix are illustrated in Fig. 10. These features are characteristic of 3*d* impurities in many metals, alloys, and chemical compounds (see [118–125]). In particular, it can be seen from Fig. 10 that an increase in the atomic number Z of the impurity leads to occupation of the *Me* 3*d* band, which gradually shifts toward the low-energy range. This band for *Me* = Cr and Mn is located in the near-Fermi region of the matrix and is responsible for the high density of states at the Fermi level $N(E_F)$ and the spin splittings with the formation of local magnetic moments at *Me* atoms, which are maximum for Cr (2.43 μ_B) and Mn (2.87 μ_B). For Cu and Zn, the *d* states are completely occupied and form narrow quasi-atomic bands below the Fermi level E_F.

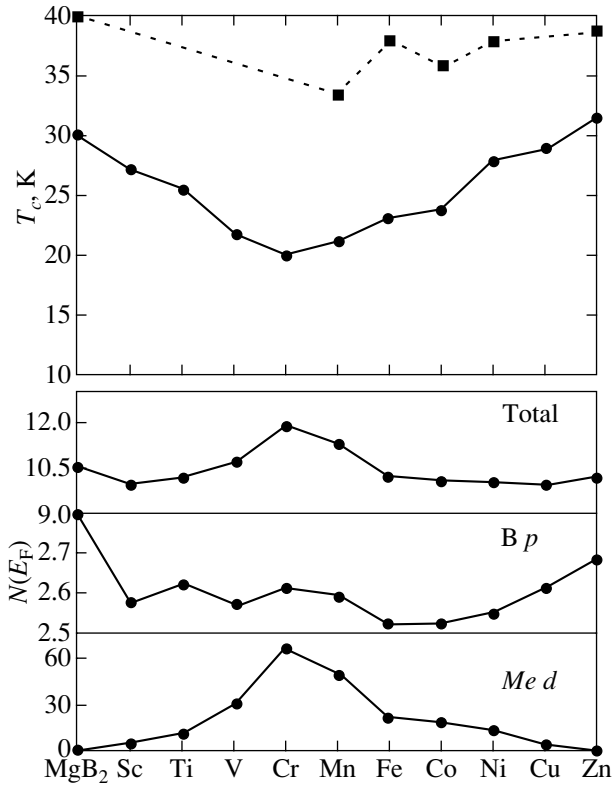

Fig. 11. Dependences of the critical temperature T_c (at the top) and the total and partial densities of states at the Fermi level $N(E_F)$ (at the bottom) on the *Me* impurity type for $Mg_{0.97}Me_{0.03}B_2$ alloys. Circles are the results of calculations, and squares are experimental data [117].

According to estimates, the dependence of the critical temperature T_c on the atomic number Z of the metal in $Mg_{0.97}Me_{0.03}B_2$ alloys exhibits a nonmonotonic behavior. The critical temperature T_c decreases (with respect to T_c for MgB_2) for *Me* atoms in the middle of the 3*d* period, reaches a minimum for $Mg_{0.97}Cr_{0.03}B_2$, then noticeably increases (for elements at the end of the period), and reaches a maximum for $Mg_{0.97}Zn_{0.03}B_2$. This behavior correlates with the dependence of the density of states at the Fermi level $N(E_F)$ on the atomic number of the metal impurity and is in reasonable agreement with the experimental data [115] (Fig. 11). The observed dependence of the superconducting properties on the atomic number Z of the impurity in the $Mg_{0.97}Me_{0.03}B_2$ alloys is explained in [117] by the nonmonotonic filling of the upper bands of the alloys and the magnetic effects (for the impurities in the middle of the 3*d* period) preventing pairing.

Table 3. Lattice parameters (au), total densities of states at the Fermi level $N(E_F)$, and contributions of B 2*p* states to the total density of states (1/Ry spin) for $Mg_{1-x}Ta_xB_2$ alloys according to KKR–CPA calculations [117]

Alloy	a	c/a	$N(E_F)$	B 2*p*
MgB_2	5.834	1.141	3.331	2.834
$Mg_{0.8}Ta_{0.2}B_2$	8.833	1.124	3.116	1.785
$Mg_{0.6}Ta_{0.4}B_2$	5.831	1.106	0.466	0.616
$Mg_{0.4}Ta_{0.6}B_2$	5.830	1.088	1.734	0.663
$Mg_{0.8}Ta_{0.2}B_2$	5.829	1.070	2.979	0.833
TaB_2	5.828	1.052	4.980	1.455

In addition to the MgB_2 : *Me* impurity systems, the electronic structure of $Mg_{1-x}Me_xB_2$ alloys was investigated over a wide range of Mg/*Me* ratios for *d* metals.

Joseph and Singh [126] studied the band structure of $Mg_{1-x}Ta_xB_2$ alloys ($0 \le x \le 1$) by the KKR–CPA method and also estimated the values of λ and T_c for the compositions given in Table 3. As the Ta content increases to 40 at. %, the critical temperature T_c decreases to zero and the $Mg_{1-x}Ta_xB_2$ alloys at 40 at. % $\le x \le$ 80 at. % are not superconductors. At $x >$ 80 at. % Ta, the critical temperature T_c increases and reaches ~ 1.8 K for TaB_2. This behavior was explained by the nonmonotonic change in the contributions of the B 2*p* states to the density of states at the Fermi level $N(E_F)$ as a function of the ratio Mg/Ta (Table 3), i.e., by the same factors that are responsible for the conduction mechanism characteristic of MgB_2. However, the substitution Mg $\longrightarrow$ Ta leads to a radical change in the structure and composition of the near-Fermi bands and in the topology of the Fermi surface (see below). As a result, the *d* states of the transition metal are dominant for the $Mg_{1-x}Ta_xB_2$ alloys enriched in tantalum and, hence, the explanation offered in [126] for the change in the critical temperature T_c of the $Mg_{1-x}Ta_xB_2$ alloys turns out to be controversial.

The concentration dependences of the energy of the σ bands for $Mg_{1-x}Al_xB_2$ and $Mg_{1-x}Na_xB_2$ solid solutions (x = 0, 1/3, 2/3, 1.0) were investigated by Suzuki *et al.* [127] in terms of the supercell model. It was found that, for all compositions of the $Mg_{1-x}Na_xB_2$ solid solutions, the top of the B p_{xy} band at the Γ point lies above the Fermi level E_F; i.e., the electronic criterion for superconductivity holds. For the $Mg_{1-x}Al_xB_2$ solid solutions, this condition is satisfied at $x < 0.06$ and, at larger x, the hole states at the center of the Brillouin zone disappear. The dependences of the concentration n_h of σ holes on the solid solution composition are represented in the form $n_h = (0.8 + 0.8x) \times 10^{23}$ cm^{-3} for the $Mg_{1-x}Al_xB_2$ solid solutions and $n_h = (0.8 - 1.4x) \times 10^{23}$ cm^{-3} for the $Mg_{1-x}Na_xB_2$ solid solutions. The concentration of holes is maximum (~1.6×10^{22} cm^{-3}) for NaB_2. In the series $NaB_2 \longrightarrow Mg_{1-x}Na_xB_2 \longrightarrow MgB_2 \longrightarrow Mg_{1-x}Al_xB_2 \longrightarrow AlB_2$, the cohesion energy changes almost monotonically.

Mehl *et al.* [128] performed calculations for the MgB_2 : (Cu, C) system and made the inference that the double doping (Mg ⟶ Cu, B ⟶ C) can lead to an increase in the critical temperature T_c to ~ 50 K.

3.2. Doping of the Boron Sublattice in MgB_2

The MgB_2–C system has been studied most extensively. It was established that, upon substitution of carbon for boron, $Mg(B_{1-x}C_x)_2$ single-phase compounds are formed in a limited range of carbon concentrations (at $x < 0.2$) and an increase in the ratio C/B results in a rapid decrease in the critical temperature T_c and an increase in the superconducting transition range [129–135]. The band calculations for the MgB_2 diboride doped with C, N, and O atoms (in the boron sublattice) [29, 116] demonstrated that the σ band is completely occupied (Fig. 9), whereas the density of states at the Fermi level $N(E_F)$ in the series $MgB_{1.75}C_{0.25}$ ⟶ $MgB_{1.75}N_{0.25}$ ⟶ $MgB_{1.75}O_{0.25}$ changes nonmonotonically and increases at the end of the series. This effect is associated with the occupation of antibonding states. Note also the results obtained in band calculations for ternary phases, namely, layered borocarbide MgB_2C_2 [28] and layered boronitride Mg_3BN_3 [136] (the structure of the latter phase involves layers formed by different metalloids B and N). It was shown that the energy spectrum of MgB_2C_2 exhibits a metal-like nature and MgB_2BN_3 is a semiconductor with a band gap of ~0.88 eV.

3.3. Superstructures

The effects of long-range atomic order for impurity elements in MgB_2 (formation of superstructures) are of interest from the viewpoint of revealing factors that can stabilize metastable ternary alloys, which (for example, in the MgB_2–CaB_2 system [116]), as expected, should possess improved superconducting properties. Moreover, investigations of these effects can elucidate the mechanism of decomposition of $Mg_xMe_yB_2$ solid solutions at different concentrations.

At present, the above effects are best understood for the Mg–Al–B system. It was found that the $Mg_{1-x}Al_xB_2$ solid solutions are unstable at $0.09 < x < 0.25$ and $x \sim 0.7$, at which the system is in a heterogeneous state [137–139]. According to [138–140], superstructures with ordered motifs in the arrangement of Al atoms along the *c* axis of the crystal are formed at $x \sim 0.5$.

A microscopic model of the superstructure formation was proposed by Barabash and Stroud [141] on the basis of energy calculations (the Vienna *Ab Initio* Simulation Package with inclusion of the lattice relaxation). These authors calculated a number of supercells used as models of superstructures with allowance made for the possible segregation of Al and Mg atoms into their "own" atomic layers (Fig. 12). The analysis of

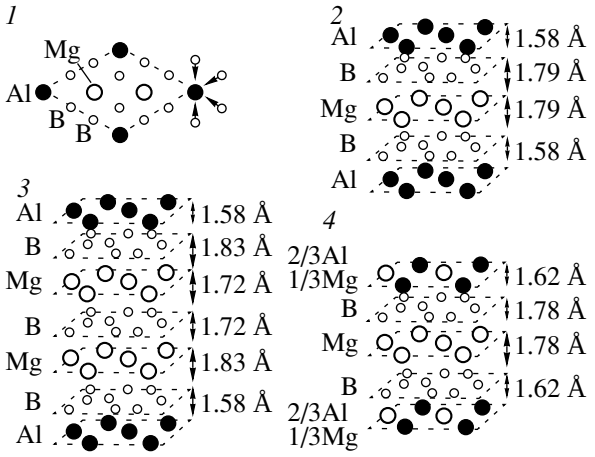

Fig. 12. (*1–4*) Variants of superstructures in the $Mg_{1-x}Al_xB_2$ system [141].

each composition of the $Mg_{1-x}Al_xB_2$ system was based on the parameter $\Delta E(x) = E_1(x) - E_2(x)$, where $E_1(x)$ and $E_2(x)$ are the energy of states of the superstructure and the corresponding disordered solid solution, respectively. It was revealed that the atomic segregation into layers is energetically favorable not only for the stoichiometric composition $x = 0.5$ [138–140] but also for a number of other compositions. The transformation of the system into a heterophase state was explained in [141] within a model allowing for the energy estimates and the contribution of the configurational entropy. As follows from this model, the critical points of the decomposition of the solid solutions correspond to the compositions with $x = 0.25$ and 0.75. It should be noted that the inclusion of the superstructural ordering of the $Mg_{1-x}Al_xB_2$ solid solutions does not affect the interpretation of the decrease in the critical temperature T_c with an increase in *x* due to the occupation of the σ hole bands and the decrease in the density of states at the Fermi level $N(E_F)$.

3.4. Ternary AlB_2-Like Phases

Among ternary layered phases, lithium borocarbide LiBC has attracted the most attention as a possible analog of the superconducting magnesium diboride. The structure of the LiBC lithium borocarbide can be represented as a result of the substitution of the carbon atom for one boron atom and Mg ⟶ Li in the MgB_2 unit cell [142]. The packing of borocarbide networks is of the … *A*/*B*/*A*/*B* … type. The nearest environment of boron atoms consists of carbon atoms and vice versa. Unlike MgB_2, stoichiometric LiBC is an insulator. As follows from the semiempirical calculation [143] for hypothetical borocarbide composed of charged layers $(BC)^{-1}$ with empty cation positions, the band gap between the bounding and antibonding $\pi(p_z)$ bands is approximately equal to 4.3 eV.

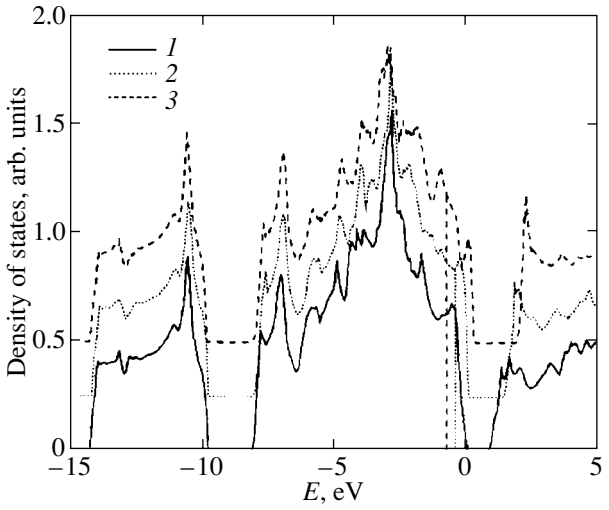

Fig. 13. Densities of states of Li_xBc at x = (*1*) 1.0, (*2*) 0.75, and (*3*) 0.5. Vertical lines indicate the Fermi level [144].

According to the full-potential nonorthogonal-orbital linearized muffin-tin orbital (LMTO) calculations [144], LiBC is an indirect-band-gap (Γ–*H* transition) semiconductor with a band gap of ~ 1.0 eV. The energy spectrum of LiBC changes depending on the packing of BC layers: for a hypothetical crystal with the interlayer packing … *A*/*A*/*A* … (the total energy of this crystal differs from that of the real phase by ~0.35 meV), the p_z band (along the Γ–*K* direction) appears to be partially occupied and the phase becomes a semimetal. The energy spectrum of a virtual crystal LiB_2 [where B is an intermediate atom (C + B)/2 with Z = 5.5] is similar to that of MgB_2.

The cation nonstoichiometry (hole doping; compositions Li_xBC at x = 0.75, 0.50) leads to partial depletion of the σ bands (Fig. 13). The frequencies of the mode E_{2g} for Li_xBC and MgB_2 are sufficiently close to each other [144]. A very high critical temperature T_c ~ 115 K for the $Li_{0.5}BC$ borocarbide was determined from the electron–phonon coupling constant λ ~ 1.75 (λ ~ 0.82 for MgB_2). Interpolation to the composition range $0 < x < 0.5$ demonstrated that the Li_xBC borocarbide can have a critical temperature $T_c \geq 40$ K at $x \geq 0.25$. In order to obtain the required concentration of σ holes, it was proposed to use field doping similar to that applied in [145] to achieve the superconducting state in a hole-doped C_{60}/Br fulleride. The calculations carried out by Dewhurst *et al.* [146] showed that the electron–phonon coupling constant λ for Li_xBC monotonically increases with a decrease in x. In this case, the critical temperature T_c ~ 65 K was predicted for $Li_{0.5}BC$. An *et al.* [147] performed *ab initio* calculations of the dispersion of the phonon modes and the Eliashberg function and noted that a small part (<2%) of the phonon modes is involved in extremely strong interaction.

However, up to now, attempts to reveal the predicted superconducting properties of Li_xBC have not been successful [148, 149]. In particular, this failure was explained by irregular packing of BC layers [149]. The study of an LiBC single crystal by polarized Raman spectroscopy proved that the crystal structure has the symmetry group $P3m1$ and involves puckered BC planes [150].

Mehl *et al.* [128] studied a hypothetical ternary crystal, copper borocarbide CuBC, which is isoelectronic and isostructural to MgB_2. According to the estimates, the maximum critical temperature T_c of this crystal can be as high as 50 K.

Medvedeva *et al.* [151] searched for possible superconducting analogs of the MgB_2 diboride among ternary borides of the $YCrB_4$ and Y_2ReB_6 structural types, which are characterized by two-dimensional motifs in the arrangement of boron atoms. Note that, in AlB_2-like diborides, boron networks are formed by B_6 regular hexagons. Similar boron networks involve B_5 pentagons and B_7 heptagons in the $YCrB_4$ structure (space group *Pbam*) and all three types of polygons (B_5, B_6, B_7) in the Y_2ReB_6 structure (space group *Pbam*). The calculations demonstrated that the $YCrB_4$ boride is a narrow-band-gap semiconductor (with a band gap of 0.05 eV) and its transformation into a metal-like state (due to hole or electron doping) should be associated with the change in the type of occupation of the Cr 3*d* bands [151]. The Fermi level in the energy spectrum of the metal-like Y_2ReB_6 boride lies in the region of the lower edge of the pseudogap between the bonding and antibonding B 2*p* states. However, their density in the vicinity of the Fermi level E_F is very low and the Re 5*d* states make a maximum contribution to the density of states at the Fermi level $N(E_F)$. Consequently, by analogy with Re_3B, in which the critical transition occurs at T_c = 4.7 K [152], only low-temperature superconductivity can be expected for the Y_2ReB_6 boride.

4. BAND STRUCTURE AND PROPERTIES OF *s*, *p*, AND *d* METAL DIBORIDES AND RELATED AlB_2-LIKE PHASES. NONSTOICHIOMETRY EFFECTS

4.1. AlB_2-Like Metal Diborides

Before the discovery of superconductivity in the MgB_2 diboride, the available data on the superconducting properties of other metal diborides were very scarce [7, 14, 153–157]. According to the first systematic investigation of MeB_2 compounds (*Me* = Ti, Zr, Hf, V, Nb, Ta, Cr) [157], they had a critical temperature T_c = 0.7 K.

An analysis of recent results revealed a rather ambiguous pattern. There are data on sufficiently high critical temperatures T_c for ZrB_2 (5.5 K) [158], TaB_2 (9.5 K) [159], and NbB_2 (5.2 K) [160]. It is worth not-

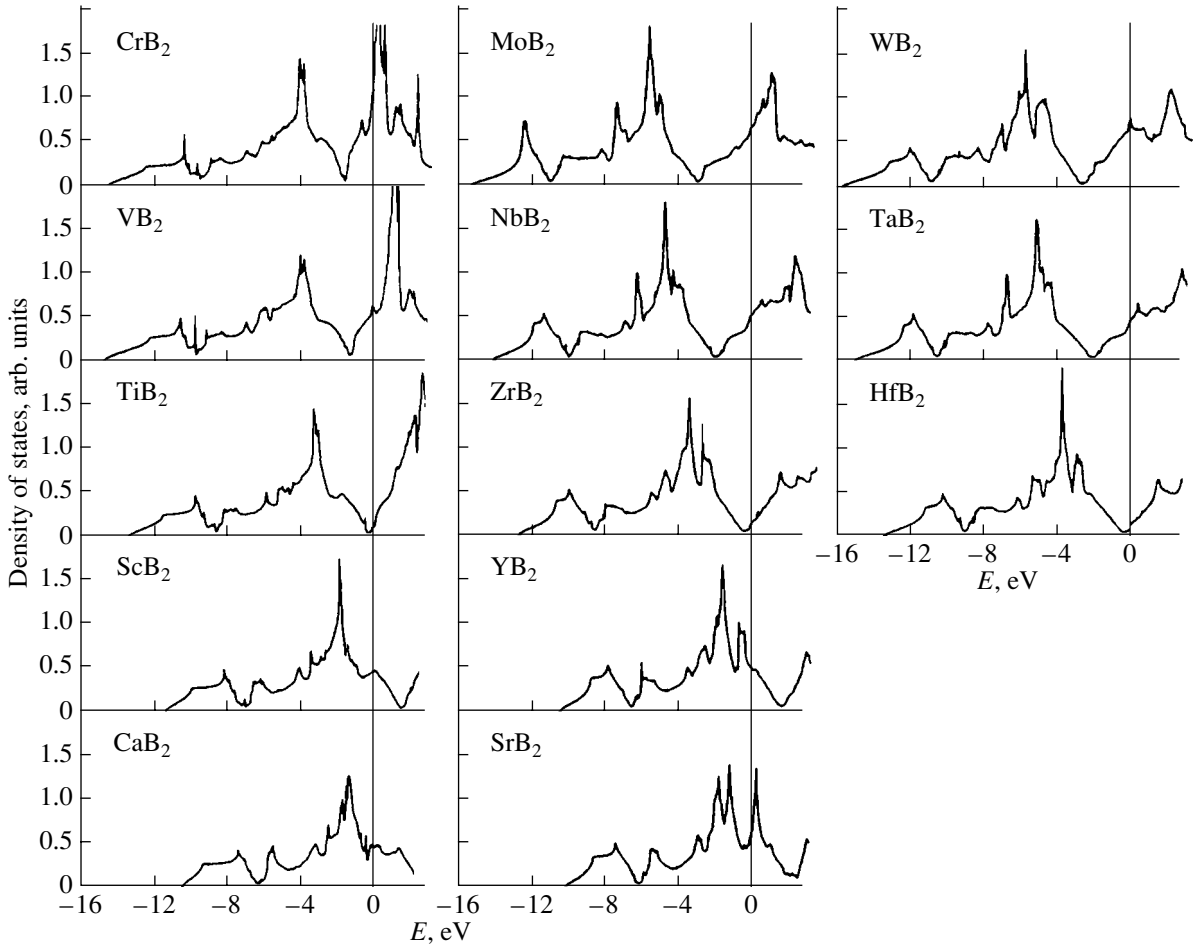

Fig. 14. Densities of states of metal diborides with an AlB_2-like structure [170].

ing that, although different research groups have investigated identical series of diborides (for example, TiB_2, ZrB_2, HfB_2, VB_2, NbB_2, and TaB_2 in [158] and ZrB_2, NbB_2, and TaB_2 in [159], each group discovered its own superconductor (ZrB_2 [158] or TaB_2 [159]), whereas all the other MeB_2 phases were considered to be nonsuperconducting. Subsequent investigations of the TaB_2 diboride showed that the superconducting transition in this compound is not observed down to $T \sim 1.5$ K. The estimated parameters of the electron–phonon interaction allowed the conclusion that the ZrB_2 diboride should be in a nonsuperconducting state [160], whereas the superconducting transitions can be observed at $T_c \sim 0.1$ K in the TaB_2 diboride [161, 162] and $T_c \sim 3$ K in the NbB_2 diboride [163].

The critical transitions were revealed in Re_3B (4.7 K) [152] and a new phase of beryllium boride (0.72 K, $BeB_{2.75}$, the unit cell contains 110.5 atoms) [164]. The occurrence of inclusions of a superconducting titanium boride phase of unknown composition with a maximum critical temperature $T_c \sim 110$–115 K in TiB_k diffuse layers on metallic titanium was reported in [165]. However, to the best of my knowledge, there has been no work done to reproduce the results obtained in [165].

A number of theoretical and experimental systematic investigations into the band structure of stable and metastable Li, Na, Be, Ca, Se, Al, Sc, Y, Ti, Zr, Hf, V, Nb, Ta, Cr, Mo, W, Tc, Ru, Rh, Pd, Ag, and Au diborides have been performed in recent years [28, 29, 34, 36, 116, 127, 166–170]. The total densities of states calculated by the self-consistent full-potential linearized augmented-plane-wave (FLAPW) method [170] for the majority of stable MeB_2 phases are presented in Fig. 14. The electronic structure of a number of compounds (for the most part, diborides of Group IV and V *d* metals) was repeatedly studied earlier (these results are discussed in monograph [155]).

In the majority of the above works, the most attention was focused on the fine features in the near-Fermi states and their influence on the superconducting properties. The absence of superconductivity in the BeB_2 boride was explained by the low-energy shift of the σ bands and the absence of hole states at the Γ point (Fig. 2). This leads to a change in the topology of the Fermi surface: cylinders (along the Γ–*A*) direction)

Table 4. Elastic moduli B_0 (Mbar), their first derivatives B_0', heats of formation ΔH (kJ/mol), cohesion energies E_{coh} (Ry/atom), width ratios of the occupied (V_0) and valence (V_v) bands, melting temperatures T_m (K), densities of states at the Fermi level $N(E_F)$ (1/Ry), and low-temperature susceptibility coefficients γ (mg/mol K^2) for 3*d*–5*d* metal diborides according to LMTO calculations [169] and experimental data

Phase	B_0	B_0^*	B_0'	$-\Delta H$	$-\Delta H^*$	E_{coh}	V_0/V_v	T_m	$N(E_F)$	γ
ScB_2	1.19	–	1.85	231.52	307	1.17	0.87	2523	11.99	2.08
TiB_2	2.13	2.02	2.1	308.38	323	1.32	1.01	3253–3498	4.27	0.74
VB_2	1.75	–	1.67	208.14	206	1.01	1.10	2673–3020	15.86	2.48
CrB_2	1.56	–	1.68	181.93	133	0.98	1.11	2473	34.88	6.05
MnB_2	2.1	–	1.65	140.04	120	0.88	1.09	2261	108.94	18.89
FeB_2	2.3	–	1.69	113.71	94.14	0.79	1.10	–	37.28	6.46
YB_2	1.41	–	2.05	101.68	105	0.88	0.86	2373	11.68	2.03
ZrB_2	1.95	2.15	1.94	296.81	322.59	1.25	1.05	3313–3518	3.84	0.67
NbB_2	1.01	–	1.67	192.73	197	0.94	1.17	3173–3309	13.95	2.42
MoB_2	1.6	–	1.71	131.61	–	0.83	1.23	2373–2648	20.01	3.47
HfB_2	2.16	2.1	1.35	244.20	335.98	1.21	1.05	3373–3653	3.688	0.64
TaB_2	1.81	–	1.78	179.15	209.20	0.98	1.12	3310–3473	12.92	2.24

* Experimental data (see references in [169]).

transform into cones. The occupation of the σ bands in the AlB_2 boride (due to an increase in the concentration of valence electrons) is responsible for its nonsuperconducting state. For the ScB_2 and YB_2 borides, the p_{xy} bands at the *A* point lie above the Fermi level E_F; however, the concentration of hole carriers is insignificant. In the case of the TiB_2, ZrB_2, and HfB_2 diborides, the Fermi level E_F is located in the pseudogap (Fig. 14). An increase in the electron concentration (diborides of Group V and VI *d* metals) results in occupation of the *d* band, and an increase in the density of states at the Fermi level $N(E_F)$ can lead to an increase in the critical temperature T_c. It is important that, unlike MgB_2, for the aforementioned diborides, the *d* states of the metal make a substantial contribution to the density of states at the Fermi level $N(E_F)$ [166–170].

An analysis of the band structure of the metastable Li, Na, Ca, Al, Ag, and Au diborides demonstrates that CaB_2 corresponds to the optimum configuration and the type of occupation of the σ and π bands, which are characteristic of the MgB_2 diboride. The estimated enthalpy of formation of CaB_2 (–0.12 eV/formula unit) [116] indicates that synthesis of this compound is quite possible. The phase can be stabilized by doping (with isoelectronic or hole dopants, such as Mg, Li, and Na).

Apart from the parameters of the electronic structure, the results of the calculations carried out in [166–170] made it possible to analyze a large number of physicochemical properties for diborides. In particular, consideration was given to the conditions required for the appearance of magnetism. Moreover, the low-temperature electronic heat capacity coefficients γ, the lattice constants, and the thermodynamic and thermomechanical parameters (such as the elastic moduli, their derivatives, etc.) were calculated for a number of diborides (Table 4). Important information on the cohesion characteristics and the energies of formation was obtained for MeB_2 diborides. These data made it possible to reveal the fundamental regularities of the interrelation between the electronic properties and the conditions for the stabilization of the structural type (AlB_2) for metal diborides. Specifically, in the framework of the first-principles band calculations [170], the theoretical heats of formation of the MeB_2 phases were determined from the formula

$$\Delta E = E(Me) + 2E(\mathrm{B}) - E(MeB_2),$$

where $E(Me)$, $E(\mathrm{B})$, and $E(MeB_2)$ are the total energies (per unit cell) of the metal, elemental boron (α-B_{12}), and diboride, respectively. The cohesion energy was calculated from the relationship

$$E_c = E_c(Me) + 2E_c(\mathrm{B}) + E_c(MeB_2),$$

where

$$E_c(Me, \mathrm{B}) = E(Me, \mathrm{B}) - E_{at}(Me, \mathrm{B}),$$

$$E_c(MeB_2)$$

$$= E_c(MeB_2) - E_{at}(Me) - 2E_{at}(\mathrm{B}) - E_c(MeB_2).$$

Here, $E_{at}(Me)$ and $E_{at}(\mathrm{B})$ are the total energies of metal and boron free atoms, respectively. Some of the results obtained are compared with the experimental data in Fig. 15. It can be seen from this figure that the stability of the diboride phases directly depends on the metal valence (occupancy of the valence bands) and is maximum for the Ti, Zr, and Hf diborides. For these com-

pounds, the optimum condition of the band occupation is satisfied: all the bonding states are occupied and all the antibonding states are vacant. An increase or decrease in the electron concentration for diborides of the Group V–VII or III metals leads to occupation of antibonding bands or depletion of the bonding bands, which results in a decrease in the stability of these phases.

4.2. Nonstoichiometry Effects in Diborides: Cation Vacancies

Unlike many interstitial phases (carbides, nitrides, oxides of metals [7, 19]), the majority of diborides do not exhibit nonstoichiometry effects: under equilibrium conditions, the deviation of the phase composition from the "ideal" ratio B/*Me* = 2 does not exceed tenths of an atomic percent [153–155]. As a consequence, the presence of vacancies in the metal or boron sublattices, as a rule, is ignored in the discussion of experimental data and in theoretical models.

In this respect, of particular interest are the results of recent experiments on the high-pressure synthesis of $Ta_{1-x}B_2$ and $Nb_{1-x}B_2$ nonstoichiometric (in the metal sublattice) diborides with extended regions of homogeneity $0 < x < 0.48$ [171]. It was found that the presence of *Me* vacancies can lead to a considerable change in the superconducting properties of phases. For example, a change in the atomic ratio B/Nb results in an increase in the critical temperature T_c, which reaches a maximum (~9 K) for the composition $Nb_{\sim 1.76}B_2$. Cooper *et al.* [172] also observed superconductivity in a number of metal-rich borides of nominal compositions $NbB_{2.5}$ (64 K) and $MoB_{2.5}$ (8.1 K).

The first investigation into the influence of *Me* vacancies (□) on the band spectrum of the $Me_{0.75}B_2$ diborides (*Me* = Nb, Zr, Y) was performed by the FLMTO method with 12-atom supercells ($Me_3\square B_8$) [173]. It was established that the effect of *Me* vacancies on the band structure of diborides can differ fundamentally depending on the type of metal sublattice (or the type of occupation of the energy bands). For $Nb_{0.75}B_2$ and $Ta_{0.75}B_2$, the density of states at the Fermi level $N(E_F)$ insignificantly decreases (as compared to that for stoichiometric phases). The presence of Nb vacancies in NbB_2 gives rise to a new peak in the density of states and brings about a change in the contributions of the Nb 4*d* and B 2*p* states in the vicinity of the Fermi level E_F. The states of vacancies are located below the Fermi level E_F and do not affect the density of states at the Fermi level $N(E_F)$. The nonstoichiometry effect is most pronounced for the ZrB_2 diboride. In this case, lattice defects lead to the appearance of an intense peak in the density of states in the vicinity of the pseudogap. As a result, the density of states at the Fermi level $N(E_F)$ for $Zr_{0.75}B_2$ increases drastically and the contribution of the B 2*p* states increases by approximately one order of magnitude (Table 5). Therefore, the presence of Zr vacancies can be one of the factors responsible for the critical transition experimentally observed in ZrB_2 [157].

The opposite effect of *Me* vacancies on the band structure is observed for the YB_2 diboride. The presence

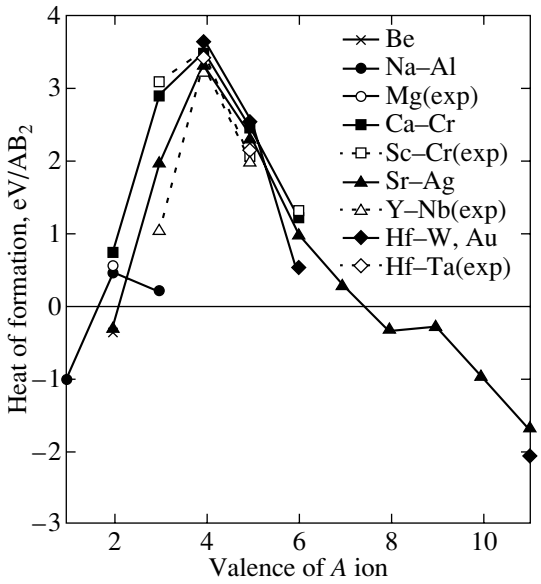

Fig. 15. Theoretical and experimental heats of formation of AlB_2-like metal diborides as a function of the valence of metal *A* [170].

Table 5. Densities of states at the Fermi level $N(E_F)$ (states/eV formula unit) and energies of formation (ΔH), cohesion (E_{coh}), and formation of *Me* vacancies (E_{vf}) for stoichiometric and nonstoichiometric diborides of Nb, Zr, and Y (in Ry/formula unit) [173]

Diboride	$N(E_F)$							E_{coh}	ΔH	E_{vf}
	total	M_s	M_p	M_d	M_f	B_s	B_p			
NbB_2	1.012	0.002	0.012	0.653	0.036	0.009	0.125	1.82	0.27	
$Nb_{0.75}B_2$	0.993	0.009	0.021	0.544	0.022	0.010	0.146	1.57	0.19	0.08
ZrB_2	0.300	0.001	0.003	0.170	0.009	0.000	0.042	1.72	0.35	
$Zr_{0.75}B_2$	1.220	0.005	0.027	0.426	0.019	0.018	0.331	1.46	0.22	0.13
YB_2	0.900	0.008	0.018	0.364	0.014	0.002	0.136	1.42	0.26	
$Y_{0.75}B_2$	0.409	0.004	0.012	0.121	0.004	0.002	0.080	1.23	0.16	0.10

of vacancies results in depletion of the bonding states. For $Y_{0.75}B_2$, the Fermi level is located at a local minimum in the density of states and the value of $N(E_F)$ and the contributions of the Y 4*d* and B 2*p* states decrease sharply. Consequently, no superconductivity can be expected in nonstoichiometric yttrium diborides.

Shein *et al.* [173] estimated the changes in the stability of MeB_2 phases due to the presence of defects. For this purpose, the authors calculated the energies of cohesion and formation (ΔH) for MeB_2 and $Me_{0.75}B_2$ phases. The energy of formation ΔH was calculated from the expressions

$$\Delta H^{MeB_2} = (E_{tot}^{Me} + 2E_{tot}^{B}) - E_{tot}^{MeB_2},$$

$$\Delta H^{Me_{0.75}B_2} = (0.75E_{tot}^{Me} + 2E_{tot}^{B}) - E_{tot}^{Me_{0.75}B_2},$$

where E_{tot}^{Me} and E_{tot}^{B} are the total energies of the pure metal and α-boron crystals, respectively. As can be seen from Table 5, the energies of formation ΔH^{MeB_2} decrease in the order $\Delta H(ZrB_2) > \Delta H(NbB_2) > \Delta H(YB_2)$, which is in agreement with the results of other calculations and the available experimental data on the enthalpy of formation of stoichiometric diborides [7, 153–155, 166–170]. The presence of *Me* vacancies leads to a substantial decrease in the stability of borides. An important energy parameter that characterizes the probability of generating vacancies is the energy of their formation:

$$E_{vf} = E_{tot}^{MeB_2} - E_{tot}^{Me_{0.75}B_2} - 0.25E_{tot}^{Me}.$$

An analysis of the results presented in Table 5 shows that the energy of formation E_{vf} of *Me* vacancies in NbB_2 is less than that in ZrB_2 and YB_2. Therefore, it is more difficult to introduce vacancies into ZrB_2 and the effects of nonstoichiometry (in the *Me* sublattice) are more characteristic of diborides of the Group III and V *d* metals.

4.3. Nonboride AlB_2-Like Phases

At present, more than one hundred binary phases with structures of the AlB_2 type are known. Among these are *s*–*d* metal diborides and MeX_2 phases, in which graphite-like networks are formed by different elements *X* = Be, Si, Ga, Hg, Zn, Cd, Al, Cu, Ag, and Au. As was noted above, the $\sigma(p_{x,y})$ hole bands in the planes of boron networks play a decisive role in the pairing mechanism of superconductivity in MgB_2. It is quite evident that, when searching for potential superconductors, the aforementioned analogies with MgB_2 can be expected for nonboride AlB_2-like phases with networks formed by *sp* elements. In recent years, band calculations have been performed for a number of these systems that involve networks composed of silicon, beryllium, and gallium.

Satta *et al.* [34] examined calcium disilicide. Under equilibrium conditions, $CaSi_2$ is a nonsuperconducting semimetal with a rhombohedral structure. The compound undergoes a polymorphic transition to a phase of the AlB_2 structural type upon heat treatment under pressure. It was found that the band structure of this phase involves the Ca *d* states in the vicinity of the conduction band edge. The π* antibonding bands are partially occupied, which explains the structural instability of the layered phase under normal conditions. According to [34], the replacement of Si atoms (r_{Si} = 1.34 Å) by atoms of a smaller radius (Be; r_{Be} = 1.13 Å; CaSiBe hypothetical compound) should induce a "chemical pressure" favorable for forming a structure of the AlB_2 type in the system. A further factor stabilizing this phase is the partial depletion of the π* states upon a decrease in the electron concentration, which should be reduced by ~ 0.7 e in the system.

The band calculations for $CaGa_2$ demonstrated that the σ and π bands intersect at the Γ point and lie below the Fermi level E_F [174]. The σ hole states at a low density are observed in the vicinity of the *A* point. As a result, the Fermi surfaces for MgB_2 and $CaGa_2$ differ in topology: hole-type cylinders (lying along the Γ–*A* direction for MgB_2) degenerate into cones in $CaGa_2$. A similar band structure was obtained for isoelectronic and isostructural BeB_2 [175], which is not a superconductor. In $CaGa_2$, the Ca states make a dominant contribution (~61%) to the density of states at the Fermi level.

For the AlB_2-like beryllides $ZrBe_2$ and $HfBe_2$ [174, 176], the top of the valence band is determined by the strong hybrid interactions of the Zr (Hf) *d* and Be *sp* states. The Be σ bands have a noticeable dispersion along the Γ–*A* direction, and the hole states are absent. According to the type of energy bands, their composition, and the occupancy, the Zr and Hf beryllides are similar to isostructural and isoelectronic ScB_2 and YB_2, in which superconductivity is not observed down to $T <$ 1.4 K.

The first representatives of a new class of chemically more complex layered (AlB_2-like) phases, namely, $Sr(Ga_xSi_{1-x})_2$ [177], $Ca(Al_{0.5}Si_{0.5})$ [178], and $(Ca,Sr,Ba)(Ga_xSi_{1-x})$ [179, 180], have been synthesized recently. Their hexagonal sublattice is formed by alkaline-earth metal atoms, and the graphite-like networks are composed of Ga and Si or Al and Si atoms. The superconducting transitions in the silicides occur at the critical temperatures T_c ~ 3.3–7.7 K. The exception is the $Ba(Al_xSi_{1-x})_2$ silicide, which is not a superconductor at temperatures above 2 K. Investigation of $(Ca,Sr,Ba)(Al_xSi_{1-x})_2$ phases with a variable Al/Si content ($0.6 < x < 1.2$) indicated that the critical temperatures T_c are maximum at the stoichiometric ratio 1 : 1 : 1 [181].

An analysis of the transport and magnetic properties [177–180] made it possible to assign these silicides to type-II superconductors, and the data on the Seebeck

coefficients suggest that electrons are the majority carriers in (Ca,Sr,Ba)$(Al_xSi_{1-x})_2$ phases [181].

The first band calculations were performed by the FLMTO method for the $Sr(Ga_xSi_{1-x})_2$ phases at x = 0.375, 0.5, and 0.625 [182] and all the known 1 : 1 : 1 ternary phases [$Me(A_{0.5}Si_{0.5})_2$; *Me* = Ca, Se, Ba; *A* = Al, Ga] [183]. The main features of the band structure can be illustrated by using $Ca(Al_{0.5}Si_{0.5})_2$ as an example (Fig. 16). The valence band of the silicide is governed by the Al and Si 3*p* states, which form four $\sigma(3p_{x,y})$ and two $\pi(3p_z)$ bands. For the $3p_{x,y}$ bands, the dispersion is maximum along the $k_{x,y}$ (Γ–*K*) direction. These bands reflect a two-dimensional distribution of the Al and Si *p* states in graphite-like networks and form pseudoflat regions aligned along the k_z (Γ–*A*) direction. The $p_{x,y}$ bands contribute to the density of states over the whole width of the valence band with a maximum at approximately 2.6 eV below the Fermi level E_F. The Al and Si $3p_z$ states (responsible for the interlayer bonds) have a considerable dispersion along the k_z (Γ–*A*) direction. The σ and π bands intersect at the Γ point of the Brillouin zone. It is important that the Al and Si 3*p* bands lie below the Fermi level E_F and do not contain hole states, as is the case in the aluminum diboride [isoelectronic to $Ca(Al_{0.5}Si_{0.5})_2$], which is not a superconductor. The main contribution (~59%) to the density of states at the Fermi level $N(E_F)$ for the $Ca(Al_{0.5}Si_{0.5})_2$ silicide is made by the Ca 3*d* states, which determine the *n*-type conductivity of this phase. The contributions of the Al and Si 3*p* states to the density of states at the Fermi level $N(E_F)$ do not exceed ~ 9 and 10%, respectively.

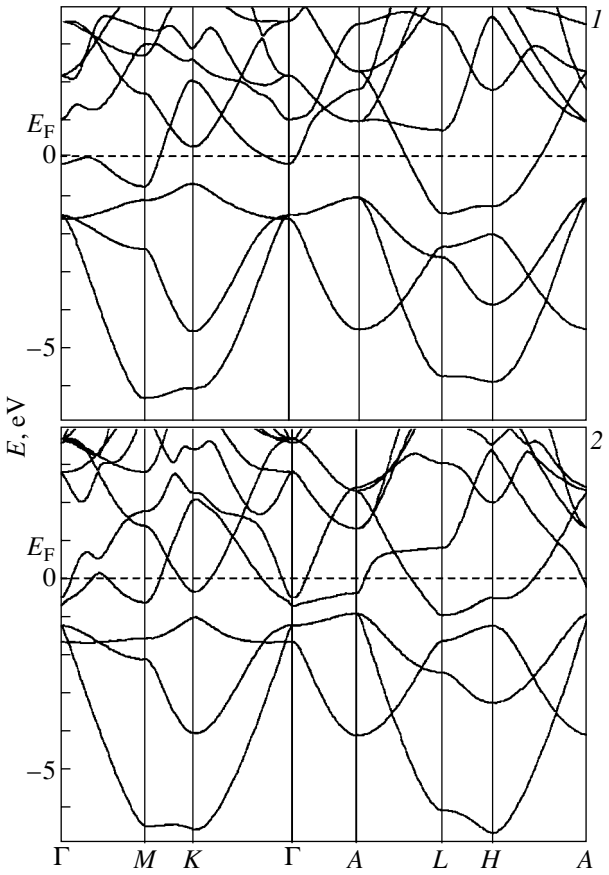

Fig. 16. Energy bands of (*1*) $Ca(Al_{0.5}Si_{0.5})_2$ and (*2*) $Sr(Ga_{0.5}Si_{0.5})_2$ according to FLMTO calculations.

In the series $Ca(Al_{0.5}Si_{0.5})_2 \longrightarrow Sr(Al_{0.5}Si_{0.5})_2 \longrightarrow Ba(Al_{0.5}Si_{0.5})_2$, the change in the type of alkaline-earth metal leads to a change in the position and dispersion of the lower cation *d* bands: the Sr and Ba *d* states form quasi-flat bands (aligned along the *L*–*H* direction), which coincide with the Fermi level E_F. This results in the appearance of sharp peaks in the density of the Sr and Ba *d* states with an admixture of Al and Si *p* orbitals, which are separated by the pseudogap from the bounding *p* bands. In the case of the transition from $Ca(Al_{0.5}Si_{0.5})_2$ to $Ba(Al_{0.5}Si_{0.5})_2$, the density of states at the Fermi level $N(E_F)$ increases by a factor of more than two. It should be noted that the increase in the density of states at the Fermi level $N(E_F)$ is caused by the increase in the contributions from virtually all valence states of the atoms involved in the silicide.

As a whole, the band structures of $Me(Al_{0.5}Si_{0.5})_2$ and $Me(Ga_{0.5}Si_{0.5})_2$ are similar to each other. The main differences reside in the increase in the dispersion of the σ and π bands along the *A*–*L*–*H* direction and the decrease in the band gap (by ~ 1.0–0.9 eV) between the *s* and *p* bands for $Me(Ga_{0.5}Si_{0.5})_2$. The change in the type of alkaline-earth metal (Ca $\longrightarrow$ Sr $\longrightarrow$ Ba) leads to an increase in the density of states at the Fermi level $N(E_F)$ for the $Me(Ga_{0.5}Si_{0.5})_2$ silicides. Note that the *Me* *d* states are dominant in the near-Fermi region.

It can be seen that, compared to the band structure of the MgB_2 superconductor, the band structure of the ternary AlB_2-like silicides has a number of fundamental differences. These differences are as follows: (i) occupation of $p_{x,y}$ bonding bands and the absence of σ hole states, (ii) an enhancement of the covalent interaction between the (Al,Si) [or (Ga,Si)] and alkaline-earth metal layers, and (iii) a change in the orbital composition of the density of states $N(E_F)$, to which the *d* states of alkaline-earth metals make the dominant contribution. The last feature is characteristic of a large number of low-temperature superconducting compounds of *p* and *d* elements (NbN, V_3Si, etc.) [2], for which the critical temperatures T_c can be adequately described by the McMillan equation $T_c \sim \langle\omega\rangle \exp\{f(\lambda)\}$, where $\langle\omega\rangle$ are averaged phonon frequencies (inversely proportional to the atomic masses), $\lambda = N(E_F)\langle I^2\rangle/\langle M\omega^2\rangle$ is the electron–phonon coupling constant, $\langle I^2\rangle$ are the electron–phonon matrix elements, and the quantities $\langle M\omega^2\rangle$ do not depend on the atomic masses and are determined by the force constants.

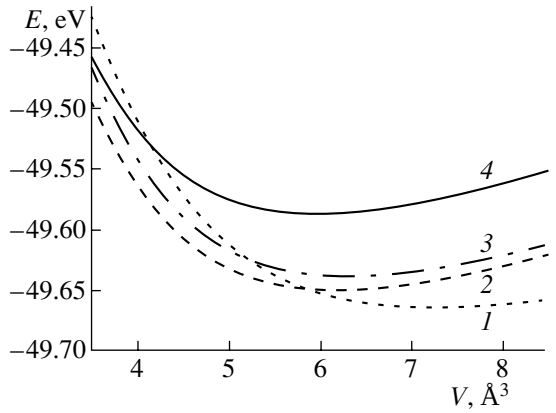

Fig. 17. Dependences of the total energy E (eV) on the unit cell volume V (Å^3) for (*1*) α-B_{12} and hypothetical structures of elemental boron (*2*) BB_{12}, (*3*) □B_{12}, and (*4*) face-centered cubic B (see text).

According to the experimental data [177–181], the critical temperature T_c of the $Me(Al_{0.5}Si_{0.5})_2$ silicides monotonically decreases with an increase in the atomic number of cations. On the other hand, the critical temperature T_c of the $Me(Ga_{0.5}Si_{0.5})_2$ silicides changes insignificantly (in the range 3.9–5.1 K) and is maximum (5.1 K) for the $Sr(Ga_{0.5}Si_{0.5})_2$ silicide. As follows from the calculations performed in [182, 183], the density of states at the Fermi level $N(E_F)$ [like the contributions of the *Me d* and Si, Al, and Ga *p* states to the value of $N(E_F)$] for the $Me(Al_{0.5}Si_{0.5})_2$ and $Me(Ga_{0.5}Si_{0.5})_2$ silicides monotonically increases with a change in the alkaline-earth metal from Ca to Ba (i.e., changes oppositely to the critical temperature T_c). Furthermore, the densities of states $N(E_F)$ for $Me(Al_{0.5}Si_{0.5})_2$ are higher than those for $Me(Ga_{0.5}Si_{0.5})_2$, which also disagrees with the observed ratio of their critical temperatures. Consequently, the direct correlation $T_c \sim N(E_F)$ proposed in [180] for strictly stoichiometric (1 : 1 : 1) compositions $Me(Al_{0.5}Si_{0.5})_2$ is invalid. Apparently, the main factor responsible for the change in the critical temperature T_c for the $Me(Al_{0.5}Si_{0.5})_2$ compounds is the variation in the phonon frequencies dependent on atomic mass. One more reason for the change in the density of states [and, hence, in the value of $N(E_F)$] is the disordering of Al (Ga) and Si atoms in planar networks. As a consequence, alkaline-earth metal atoms reside in a chemically nonequivalent trigonal–prismatic environment, which in part leads to splitting of the near-Fermi bands and a decrease in the density of states at the Fermi level $N(E_F)$. This effect should be most pronounced for the Sr and Ba silicides, because the value of $N(E_F)$ for these compounds in the ordered state is determined by narrow intense peaks in the density of states. The possible chemical disordering in planar networks was also noted in [183].

The band calculations for the $Sr(Ga_xSi_{1-x})_2$ phases with a variable Ga/Si content [182] showed that an increase in the electron concentration from 8.75 (at x = 0.375) to 9.25 e/formula unit (at x = 0.625) results in a drastic change in the profile of the near-Fermi density of states (predominantly, owing to the Sr 4*d* states) and a nonmonotonic dependence of the density of states at the Fermi level $N(E_F)$ with a minimum at x = 0.5. Therefore, the simplified rigid-band model cannot be applied to describe these systems.

5. ENERGY BANDS AND SUPERCONDUCTIVITY OF BORON AND HIGHER BORIDES

An analysis of different classes of binary (semiborides Me_2B, monoborides MeB, diborides MeB_2, tetraborides MeB_4, and a number of higher borides, such as hexaborides MeB_6, dodecaborides MeB_{12}, and MeB_{66}-like borides), ternary, and quaternary borides (see review [14]) has demonstrated that the superconducting properties, as a rule, are observed for phases with a relatively low boron content ($B/Me \leq 2.0$–2.5, Table 1). The structure of these phases contains boron in the form of isolated atoms or linear and planar elements (chains or networks of boron atoms).

The superconducting properties are less pronounced in higher borides ($B/Me \geq 6$), whose structure is formed by stable polyhedral groupings of boron atoms, namely, octahedra B_6 (MeB_6), icosahedra B_{12} (MeB_{12}), or their combinations (MeB_{66}). For example, among the large number of metal hexaborides involving B_6 polyhedra and metal dodecaborides containing B_{12} polyhedra, the low-temperature superconductivity is found only for eight phases, including four MeB_6 phases (*Me* = Y, La, Th, Nd) and four MeB_{12} phases (*Me* = Sc, Y, Zr, Lu) [14].

It should be noted that the most stable crystalline modifications of elemental boron (α-B_{12}, β-B_{105}), in which the main structural units are boron polyhedra (icosahedra or giant icosahedra B_{84}), are semiconductors under normal conditions [155, 184–186]. Recent experiments on compression under ultrahigh pressures have revealed that rhombohedral β-B_{105} transforms into a superconducting state ($T_c \sim 11.2$ K) at pressures above 250 GPa [187]. Papaconstantopoulos and Mehl [188] explained this effect as resulting from the pressure-induced phase transition of β-boron to a phase with a simple face-centered cubic structure. The band structure of face-centered cubic boron was calculated within the local-electron-density (LDA) approach, and the estimated critical temperature T_c was in reasonable agreement with the experimental data [187].

According to another scenario of the transformation of β-boron under high pressures [189], the metallization is caused by the distortion of the crystal structure and (or) partial destruction of its constituent B_{12} polyhedra, during which part of the boron atoms occupy intericosahedral sites. The calculations performed for hypothetical boron crystals simulated through the

removal of *Me* atoms from the MeB_{12} lattice ($\square B_{12}$, where $\square$ is a metal vacancy) or the substitution of boron atoms for *Me* atoms (BB_{12}) indicated that the energy spectra of these phases exhibit a metal-like nature and a considerable density of the near-Fermi states. The solution of the equation of state for the aforementioned alternative structures of superconducting boron (Fig. 17) suggests that the energy stability of the polyhedral structure is higher than the stability of the simple face-centered cubic boron postulated in [188]. The mechanism of structural distortion proposed in [189] was experimentally confirmed by Sanz *et al.* [190], who found that, as the pressure P increases, the initial structure of β-boron is retained to $P \sim 100$ GPa (in this case, distortions become stronger) and then transforms into an amorphous state.

Among superconducting hexaborides, the band spectrum was studied for YB_6 in [155, 191]. This phase belongs to borides of the CaB_6 structural type (space group O_h^1–$Pm3m$), whose lattice can be represented as a simple cubic lattice (CsCl type) in which cations occupy cesium sites and the B_6 octahedra are centered at chlorine sites. The unit cell contains seven atoms ($Z = 1$) with the following coordinates: *Me* (*a*) 0, 0, 0 and 6B (*f*) 1/2, 1/2, *z*. The structure involves two types of B–B interatomic distances that correspond to interoctahedral and intraoctahedral nonequivalent B–B bonds.

The valence band of YB_6 (with a width of ~ 11.8 eV) contains ten occupied bands involving the hybrid B 2*s* and B 2*p* states, which form the above system of B–B bonds between and inside B_6 clusters. A similar band structure is observed for CaB_6-like alkali and alkaline-earth metal hexaborides, which are either narrow-band-gap semiconductors or semimetals [155, 192–195]. For example, the band calculations for metastable cubic MgB_6 (the optimized lattice parameter was determined to be $a = 0.4115$ nm) demonstrated that this hypothetical hexaboride is a narrow-band-gap semiconductor with an indirect transition (band gap, ~ 0.2 eV; $E \longrightarrow R$ transition) [191]. The upper occupied band (forming a flat region aligned along the X–Γ direction) contains B $2p_{x,y}$ orbitals that participate in the interoctahedral interactions. The lower empty band has a considerable k dispersion and involves contributions from cation states.

For superconducting YB_6, the upper completely occupied B $p_{x,y}$ bands are characterized by an appreciable k dispersion along the Γ–X direction and reflect the formation of Y–B bonds. Moreover, there is a partially occupied band with a considerable contribution from delocalized Y *d* states. Analysis of the composition of the density of states at the Fermi level $N(E_F)$ demonstrates that the decrease in the critical temperatures T_c for the series of higher yttrium borides from 7.1 K for YB_6 to 4.7 K for YB_{12} can be qualitatively explained by the appreciable decrease in the contributions of the Y 4*d* states from 0.798 states/eV cell (~71%) for YB_6 to 0.538 states/eV cell (~35%) for YB_{12} [189].

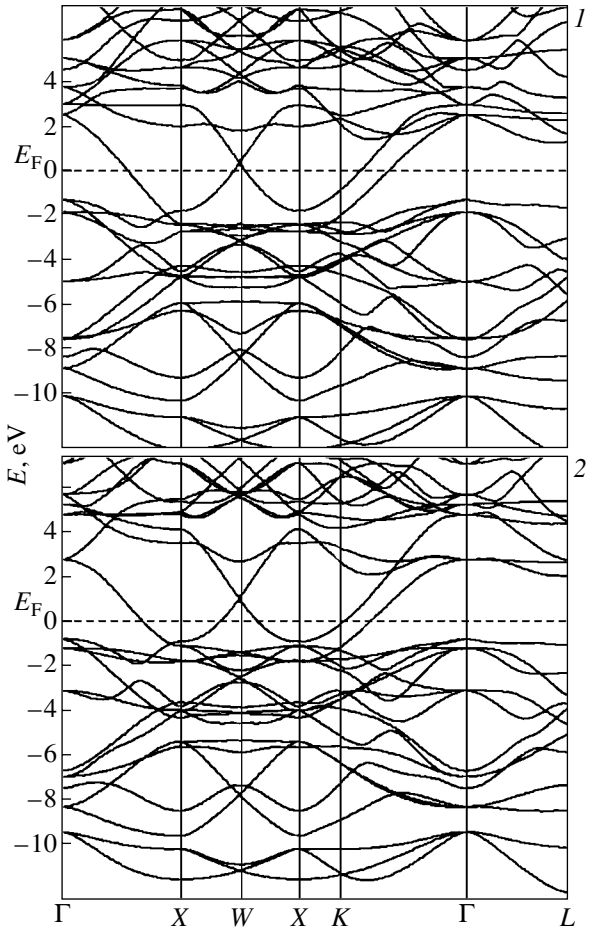

Fig. 18. Energy bands of (*1*) ZrB_{12} and (*2*) YB_{12}.

The energy spectra of the superconducting YB_{12} and ZrB_{12} dodecaborides (UB_{12} type, space group O_h^5–$Fm3m$, the unit cell contains 52 atoms) were studied by the FLMTO method in [189]. Their valence bands involve a complex system of energy bands responsible for the formation of different types of interatomic bonds in the crystal. The bands with dominant contributions from boron states can be divided into three types. Bands of the first type are composed of the B 2*s* and B *p* bonding states, which participate in the formation of three-center B–B bonds in planes of the icosahedron faces. These bonds are responsible for the stabilization of individual B_{12} polyhedra and depend only slightly on their type of packing in the crystal (symmetry of the B_{12} sublattice) (Fig. 18). Similar bands are revealed in polymorphic modifications of elemental boron, whose lattices are formed by B_{12} icosahedra [155, 184–187], and virtually retain their form in YB_{12} and ZrB_{12}.

The second type of bands involves B 2*s* and B *p* bonding states responsible for the formation of intericosahedral B_{12}–B_{12} bonds. Bands of the third type are formed by the B 2*s* and B 2*p* states hybridized with outer Y (Zr) *s*, *p*, and *d* states. The width of the valence band in YB_{12} is approximately equal to 12.98 eV. The valence band involves two groups of completely occupied B 2*s* and B 2*p* bands separated by a pseudogap. The band widths are equal to 2.82 and 8.89 eV, respectively. Near-Fermi bands of the hybrid Y–B type possess a considerable energy dispersion (Fig. 18).

Upon the transition $YB_{12} \longrightarrow ZrB_{12}$, the band structure, as a whole, changes insignificantly. The main effect is associated with the band occupation due to an increase in the electron concentration. According to [189], an increase in the critical temperature T_c from 4.7 K for YB_{12} to 5.8 K for ZrB_{12} [14] can be explained by the increase in the contributions of the *Me* 4*d* states from 0.538 states/eV cell for YB_{12} to 0.743 states/eV cell for ZrB_{12} to the density of states at the Fermi level $N(E_F)$. Note that the Fermi level E_F for YB_{12} and ZrB_{12} is located in the region of a plateau in the profile of the density of states between the bonding and antibonding bands formed by the B 2*s* and B 2*p* states [189]. The change in the metal sublattice type ($YB_{12} \longrightarrow ZrB_{12}$) affects both the total profile of the density of states for these phases and the value of $N(E_F)$ only slightly. The density of states at the Fermi level $N(E_F)$ increases by no more than ~ 16%, and the dominant contribution to the density of states $N(E_F)$ is made by the *Me* 4*d* states. In [189], the inference was drawn that doping of binary dodecaborides (for example, when preparing $Y_xZr_{1-x}B_{12}$ solid solutions) for the purpose of optimizing their superconducting properties, which is very efficient for controlling the critical temperature T_c of other borides (see above), will be inefficient for MeB_{12} phases. However, the specific features of the electronic spectrum of the MeB_{12} phases indicate that their superconducting properties are stable to changes in the chemical composition of the system. In other words, the synthesis conditions for MeB_{12} low-temperature superconductors should not impose rigid requirements on the stoichiometry of the prepared samples, unlike the synthesis of the MgB_2 or YNi_2B_2C superconductors (see reviews [11, 13–16]).

6. ELECTRONIC PROPERTIES OF NEW SUPERCONDUCTORS WITH STRUCTURES OF THE ANTIPEROVSKITE TYPE

A further promising direction in the search for new superconductors is associated with the recent discovery of superconductivity (T_c ~ 8 K) in the $MgCNi_3$ perovskite-like intermetallic compound [196]. Several factors attach special significance to this discovery.

Among its structural analogs, namely, cubic perovskite-like phases, the $MgCNi_3$ compound is the first oxygen-free superconductor. Moreover, $MgCNi_3$ is the first superconductor among ternary carbide (nitride) phases. Ternary carbide (nitride) phases of the general formula $X(C,N)Me_3$, where *Me* is a metal and *X* is an *s* or *d* element, exhibit a variety of interesting physical properties that differ fundamentally depending on their composition (see review [197]). For example, ternary carbides of the $XC(Mn,Fe)_3$ type (*X* = Al, Ga, In, Ge, Sn, *d* metals) are magnets; possess ferromagnetic, antiferromagnetic, and more complex magnetic orderings; and undergo magnetic phase transitions dependent on the temperature. Perovskite-like phases based on alkaline-earth metals, such as $XNCa_3$ (*X* = Ge, Sn, Pb, P, As, Sb, Bi), have an ionic character of chemical bonding [198–200]. Among them, $(Bi,Pb)NCa_3$ is the so-called ionic metal [201]. The $AsNMg_3$ and $SbNMg_3$ intermetallic compounds [202], which are ionic semiconductors [203], have been synthesized recently. On the other hand, phases based on Group III–V metals [$AlCSc_3$, $SnCSc_3$, $X(C,N)Ti_3$, where *X* = Al, Ga, In, etc.] exhibit metallic properties and are high-valence compounds [204–207]. Therefore, the $MgCNi_3$ compound is a phase intermediate between the groups of perovskite-like superconductors (oxides) and nonsuperconducting oxygen-free $X(C,N)Me_3$ phases.

Among its chemical analogs, the $MgCNi_3$ compound is most similar to the aforementioned intermetallic borocarbides, including the $LuNi_2B_2C$ and YNi_2B_2C nickel-containing phases. However, intermetallic borocarbides are magnetic superconductors and have an anisotropic (quasi-two-dimensional) structure. It should be emphasized that the nickel content in intermetallic borocarbides is considerably lower than that in the $MgCNi_3$ compound.

Among low-temperature superconductors, the $MgCNi_3$ compound also occupies a special place, because this phase is rich in nickel, which is a magnetic metal. The occurrence of superconductivity in this system is very unusual; this makes it similar to the so-called ferromagnetic superconductors discovered recently: UGe_2, URhGe [208–210], ZnS_2 [211], and Sr_2RuO_4 oxide characterized by surface ferromagnetic ordering [212, 213]. A number of theories based on the paramagnon and magnon exchange models and other approaches have been proposed for explaining the nature of ferromagnetic superconductivity [214–217]. Consequently, the $MgCNi_3$ compound (as a phase close to the boundary of the magnetic-instability region) can be treated as an intermediate phase between the groups of classical nonmagnetic and ferromagnetic superconductors.

Owing to the above specific features, particular interest has been expressed by researchers in the $MgCNi_3$ compound, primarily, as a superconductor in the vicinity of the critical point of a ferromagnetic transition. A sufficiently large number of works have been devoted to investigating the basic physical (predomi-

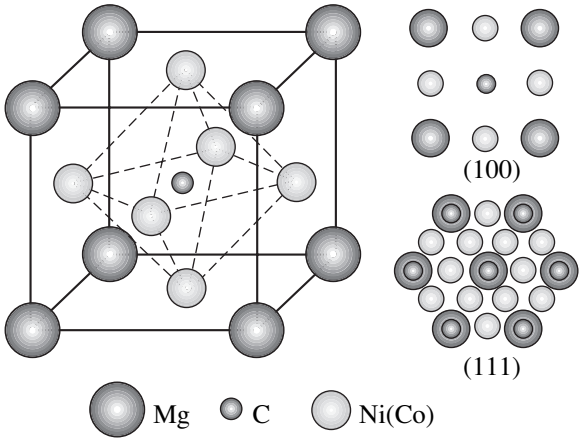

Fig. 19. Structure of the $MgCNi_3$ antiperovskite.

nantly, low-temperature) properties of this compound [196, 218–227]. These properties and the main procedures for synthesizing the $MgCNi_3$ compound and a number of $MgCNi_3$-based solid solutions are described in review [228]. Now, we consider the results obtained in modeling the $MgCNi_3$ compound and related phases in the framework of the band theory.

The band calculations for the electronic spectrum of the ideal $MgCNi_3$ antiperovskite (Fig. 19) were carried out in [229–245]. It was found that the Mg states only slightly participate in the formation of the valence band (the total width is approximately equal to 7.2 eV), which is determined by the contributions of the C 2*p* and Ni 3*d* orbitals. The C states lie below the Ni states and are partially mixed with them. The most important feature of the spectrum is a narrow intense peak in the density of states with a maximum located ~ 45 meV below the Fermi level E_F (Fig. 20). This peak is associated with the quasi-flat Ni 3*d* band (aligned along the *X*–*M* and *M*–Γ directions in the Brillouin zone). The Fermi level E_F is located at the high-energy slope of the above peak. The density of states at the Fermi level $N(E_F)$ is comparable to those for other BCS superconductors that have a cubic structure and are formed with the participation of *d* metals [2]. The maximum contribution (~ 88%) to the density of states at the Fermi level $N(E_F)$ is made by the Ni 3*d* states. The Ni 3*d* bands have a substantial dispersion $E(k)$ in the vicinity of the Fermi level E_F and are responsible for the high velocity of carriers (2×10^5 m s^{-1} [231]) and the metallic properties of the antiperovskite.

The nature of the near-Fermi peak that reflects the Van Hove singularity of the Ni 3*d* bands is considered in detail in [232]. The Ni 3*d* holes forming superconducting pairs have a very large mass. The contributions to the Van Hove singularity are made only by Ni atoms (and, partially, C atoms) located in the *xy* planes. This means that the wave functions can be considered "layered." In order to analyze this effect in more detail, Rosner *et al.* [234] calculated the band spectrum of a $\square^{2+}CNi_3$ hypothetical crystal. It was revealed that the difference between the band spectra of this crystal and $MgCNi_3$ is reduced to a change in the position of the Fermi level E_F.

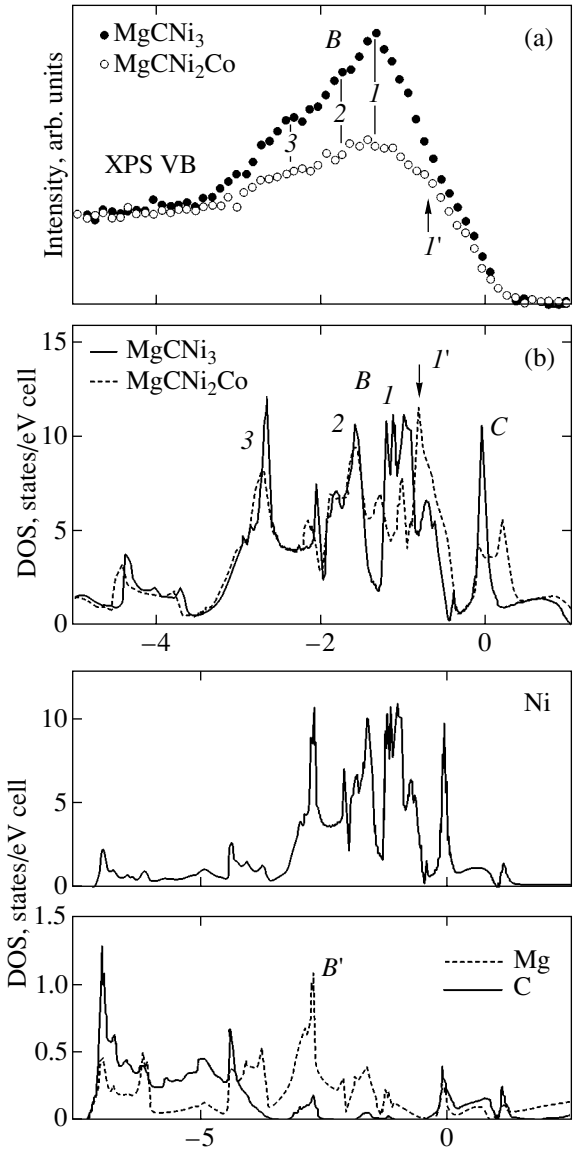

Fig. 20. (a) Photoelectron spectra and (b) total densities of states of $MgCNi_3$ and $MgCNi_2Co$. Partial densities of states of $MgCNi_3$ are given at the bottom [242].

Two bands intersecting the Fermi level E_F form the Fermi surface of the $MgCNi_3$ compound (Fig. 21). The Fermi surface involves electron-type spheroids in the vicinity of the Γ point and small sheets aligned along the faces and corners of the Brillouin zone. The flatter Ni 3*d* band exhibits lobe-type features with the center at the *X* point on the faces of the Brillouin zone and cigar-shaped elements along the Γ–*R* direction.

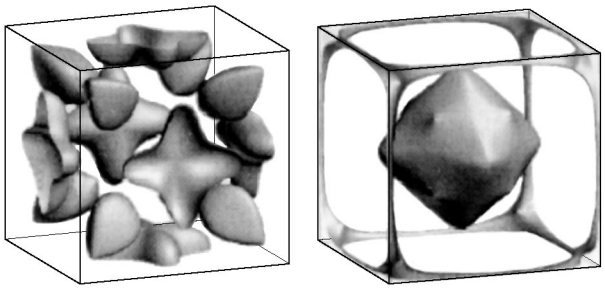

Fig. 21. Fermi surface of $MgcNi_3$ [225].

The interatomic interactions in the $MgCNi_3$ compound were analyzed using the tight-binding method in terms of the crystal orbital overlap populations [239]. The crystal orbital overlap populations were determined to be equal to 0.298, 0.027, and 0.039 e/bond for the Ni–C, Ni–Ni, and Ni–Mg interactions, respectively. This implies that the Ni–C bonds play a dominant role.

In [231, 232, 234], considerable attention was given to the interrelation between the superconductivity and the magnetic instability of $MgCNi_3$. The Stoner parameter S [231] was estimated at ~0.43, which is far from the ferromagnetic limit (~1). The calculations within the rigid-ion model (at the Debye temperature for pure nickel $\Theta_D \sim 455$ K and the constant $\lambda \sim 0.89$) indicated a strong electron–phonon interaction.

In the absence of carbon (at the center of an Ni_6 octahedron), the structure of the $MgCNi_3$ compound coincides with the face-centered cubic structure of Ni, in which one out of four Ni atoms is replaced by an Mg atom. The band calculations for an $Mg\square Ni_3$ hypothetical phase demonstrated that $S(Mg\square Ni_3) = 1.54$ and $\lambda = 0.41$ [231]. Consequently, upon hole doping of $MgCNi_3$, the Fermi level E_F can coincide with the maximum of the near-Fermi Ni 3*d* peak. According to the estimates made in [231], coincidence is achieved when approximately 0.5 holes are introduced into the system. In this case, the density of states at the Fermi level $N(E_F)$ increases by a factor of more than two and the parameter S turns out to be close to unity. The calculations for an $Mg_{0.5}Li_{0.5}CNi_3$ hypothetical phase showed that this phase is in a ferromagnetic state [234]. Similar investigations were carried out for $Mg_{1-x}Na_xCNi_3$ solid solutions [234].

Wang *et al.* [240] attempted to take into account strong electron–electron correlations of the Ni 3*d* states in the framework of one-center correction for Coulomb interactions (LDA + U method). In the LDA approximation (FLAPW method), the magnetic moments (MM) of Ni atoms are negligible (~ 0.014 μ_B), whereas the LDA + U method leads to magnetic moments of ~0.661 μ_B; in the density of states, the narrow peak due to the Ni 3*d* states in the vicinity of the Fermi level E_F disappears. Voelker and Sigrist [241] proposed to consider the $MgCNi_3$ compound as a multiband superconductor in which, apart from the standard mechanism of *s*-wave pairing, there exists an unusual type of states characterized by a specific order parameter of phase relations between particular bands.

An important problem associated with elucidating the microscopic nature of the superconducting and magnetic properties of the $MgCNi_3$ compound is to determine the effect of hole or electron doping on its characteristics. Possible variants of a change in the electron concentration in $MgCNi_3$ through the introduction of structural vacancies (nonstoichiometry in the Mg or C sublattices) or the replacement of atoms in intermetallic sublattices by atoms of a different sort were modeled using band calculations.

In [229, 230, 234–236, 242, 243], the doping of the Ni sublattice was analyzed with the use of 3*d* elements (Cu, Co, Fe, Mn) as impurities ($Me \longrightarrow$ Ni). For ter-

Table 6. Total densities of states at the Fermi level $N(E_F)$ (states/eV), Stoner parameters S, electron–phonon coupling constants λ (at T = 300 and 400 K) [233], energies of magnetization ΔE (meV), and atomic magnetic moments MM [235] for antiperovskite phases (derivatives of superconducting $MgCNi_3$)

Phase	$N(E_F)$	S	λ (300 K)	λ (400 K)	Phase	ΔE	$N^M(E_F)$*	MM (μ_B)
$MgCNi_3$	5.56	0.67	1.36	0.76	$MgCNi_2Co$	+0.2	1.2	–
$MgBNi_3$	5.26	0.60	0.44	0.25	$MgCNiCo_2$	0.0	0.7	–
$MgB_{0.5}C_{0.5}Ni_3$	4.61	0.53	0.78	1.11	$MgCCo_3$	–30.4	2.0	0.39 (Co)
$MgC_{0.5}N_{0.5}Ni_3$	2.84	0.34	0.59	0.33	$MgCNi_2Fe$	0.0	0.5	–
$MgNNi_3$	4.01	0.51	1.16	0.65	$MgCNiFe_2$	–271.6	2.9	0.08 (Ni)
$LiCNi_3$	20.43	2.43	2.86	1.61				1.19 (Fe)
$Li_{0.5}Mg_{0.5}CNi_3$	15.27	1.87	2.15	1.21	$MgCFe_3$	–379.1	3.4	1.42 (Fe)
$Mg_{0.5}Al_{0.5}CNi_3$	1.81	0.21	0.39	0.22	MgC(FeCoNi)	–60.6	2.6	0.97 (Fe)
$AlCNi_3$	2.61	0.29	0.52	0.29				0.24 (Co)
								0.03 (Ni)

* $N^{Me}(E_F)$ are the contributions of transition-metal atoms to the total density of states at the Fermi level $N(E_F)$.

nary substituted intermetallic compounds $MgCCo_3$ and $MgCCu_3$, it was found that the ground state of $MgCCo_3$ is magnetic and the Fermi level E_F in $MgCCu_3$ shifts toward the region of antibonding states with a drastic decrease in the density of states at the Fermi level $N(E_F)$. The doping of $MgCNi_3$ with Fe and Co atoms results in suppression of the superconductivity. Note that the suppression is more efficient upon introduction of iron (Table 6). In [235], the considerable decrease in the critical temperature T_c for $MgCNi_{3-x}Co_x$ ($0 < x < 2$) was explained by the decrease in the density of states at the Fermi level $N(E_F)$ with an increase in the cobalt content (i.e., with a decrease in the electron concentration) and the transformation of the near-Fermi Ni 3*d* and Co 3*d* bands. The doping effect was also studied using the x-ray photoelectron and C K_α ($1s \longrightarrow 2p$), Ni $L_{2,3}$ ($3d \longrightarrow 2p$), and Co $L_{2,3}$ ($4s \longrightarrow 2p$) x-ray emission spectra of $MgC_{1.45}Ni_3$, $MgC_{1.55}Ni_3$, and $MgC_{1.45}Ni_{1-x}Co_x$ [242]. The magnetic moments of V, Cr, Mn, Fe, and Co impurities at the Ni site in $MgCNi_3$ were estimated within the simplified Hartree–Fock approximation [243]. It was revealed that Co is in a nonmagnetic state and the magnetic moments for the other metals fall in the range 0.4–3.0 μ_B.

The doping and nonstoichiometry effects in the C and Mg sublattices were considered in [230, 231, 233, 234, 244]. Dugdale and Jarlborg [231] offered an explanation for the decrease in the critical temperature T_c of $MgC_{1-x}Ni_3$ with an increase in the deviation x from carbon stoichiometry. An increase in x leads to a substantial increase in the density of states at the Fermi level $N(E_F)$ and the Stoner parameter S and an enhancement of spin fluctuations, which result in the breaking of Cooper pairs and the suppression of superconductivity. When modeling the doping of the C and Mg sublattices with B, N [233], Li, and Al [244] atoms, it was assumed that since the near-Fermi edge of the electronic spectrum of $MgCNi_3$ is predominantly formed by the Ni 3*d* states, the replacement of atoms in other (Mg or C) sublattices does not appreciably affect the density of states in the vicinity of the Fermi level E_F and the main effect is reduced to a shift of the Fermi level E_F depending on the electron concentration. The calculations (Table 6) demonstrated that the introduction of B and N impurities into the C sublattice is accompanied by a decrease in the values of $N(E_F)$ and λ. This suggests that similar attempts to improve the superconducting properties of the initial intermetallic compound will be inefficient. The substitution of aluminum (electron donor) for magnesium also leads to a decrease in the values of $N(E_F)$ and λ, and the presence of lithium (hole dopant) at the Mg sites results in the transformation of the system into a magnetic state.

In addition to the band spectra of the $MgCNi_3$ compound and $MgCNi_3$-based solid solutions, the band calculations were performed for a number of actually existing or hypothetical related intermetallic compounds with an antiperovskite structure. In particular, among boron-containing phases, $ScBNi_3$ and $InBNi_3$ are the closest isoelectronic and isostructural analogs of the $MgCNi_3$ compound. In [231], it was shown that the Fermi level E_F for the $ScBNi_3$ and $InBNi_3$ phases is shifted (compared to the Fermi level E_F in $MgCNi_3$) toward the high-energy range and the density of states at the Fermi level $N(E_F)$ decreases sharply. It has been assumed that the superconductivity in boron-containing antiperovskites can be induced either upon introduction of hole dopants or in the presence of structural vacancies. Kumary *et al.* [245] evaluated the energy states for a number of hypothetical antiperovskites with the aim of predicting conditions for their subsequent synthesis. By substituting Ca, Sr, or Ba for Mg and Mn, Fe, or Co for Ni in the $MgCNi_3$ compound, it was revealed that $MgCMn_3$, $MgCFe_3$, and $MgCCo_3$ should be stable phases. According to [245], the $CaCNi_3$, $MgCFe_3$, and $SrCCo_3$ phases should possess magnetic properties, whereas $SrCNi_3$, $BaCNi_3$, and $CaCCo_3$ should be nonmagnetic materials.

By assessing the general role of the discovery of superconductivity in the $MgCNi_3$ compound, He *et al.* [196] noted that this can be an important step toward reinitiating the class of intermetallic compounds as promising superconductors in the context of a "renewed chemical paradigm."

7. MODELING OF THE STRUCTURE AND ELECTRONIC PROPERTIES OF MgB_2 NANOMATERIALS AND RELATED BORIDES

In the search for new superconductors promising for practical applications, two groups of nanomaterials have particularly attracted the attention of researchers. One of these groups contains molecular crystals based on quasi-zero-dimensional (0*D*) fullerene-like nanoparticles, the so-called fullerides. The second group involves quasi-one-dimensional (1*D*) nanotubular systems. The most known representatives of these systems are carbon nanotubes (CNTs) [246–254], which, as was found in [255, 256], undergo a superconducting transition ($T_c \sim 0.55$ K). The theoretical interpretation of the observed effect was proposed by Gonzales [257]. New hybrid (0*D* + 1*D*) carbon nanostructures (the so-called peapods), which consist of fullerene molecules encapsulated inside C_{60}@C nanotubes, have been considered promising high-temperature superconductors [258].

As is known, the majority of non-carbon nanotubes were synthesized (and predicted) for materials that, like carbon, have layered (2*D*) crystalline modifications (see review [259]). For this reason, AlB_2-like phases can provide a basis for designing a new class of inorganic nanotubes that can possess superconducting properties [260, 261]. In this respect, the MgB_2 compound is of special interest as a phase close to the

Table 7. Total energies E_{tot} (eV) and indices of interatomic bonds (crystal orbital overlap populations, COOPs) for (6, 6), (11, 11), and (20, 0) MeB_2 single-walled nanotubes

Nanotube	*Me*	$-E_{tot}$	COOP, e	
			B–B	*Me*–B (*Me*–*Me*)
(6,6)MeB_2 (*I*)*	Mg	1263.27	0.956	0.095
	Al	1425.88	0.842	0.154
	Sc	1405.85	0.828	0.161
	Ti	1610.41	0.606	0.236
(6,6)MeB_2 (*II*)	Mg	1274.55	0.928	0.007
	Al	1427.05	0.967	0.043
	Sc	1428.08	0.780	0.003
	Ti	1636.04	0.752	0.072
(11,11)MeB_2 (*I*)	Mg	2320.33	0.938	0.040 (0.063)
	Al	2620.04	0.884	0.122 (0.040)
	Sc	2578.46	0.845	0.141 (–0.03)
	Ti	2945.32	0.662	0.206 (0.120)
(11,11)MeB_2 (*II*)	Mg	2340.17	0.933	0.050 (0.178)
	Al	2636.75	0.920	0.057 (0.274)
	Sc	2597.82	0.850	0.035 (0.141)
	Ti	2965.25	0.758	0.087 (0.390)
(20,0)MeB_2 (*I*)	Mg	4198.78	0.857	0.088 (0.127)
	Al	4693.19	0.844	0.190 (0.230)
(20,0)MeB_2 (*II*)	Mg	4202.57	0.852	0.054 (0.126)
	Al	4674.83	0.884	0.124 (0.164)

* Nanotube configurations: (*I*) the metallic cylinder is located outside the boron tube and (*II*) the metallic cylinder is located inside a boron tube (Fig. 1).

boundary of lattice instability of AlB_2-like structures [163].

Note that elemental boron has no direct analogs in carbon nanostructures (nanotubes and fullerene-like molecules). Possible boron nanostructures formed from small-sized boron clusters, for example, pentagonal and hexagonal pyramids B_6 and B_7, were theoretically modeled in [262–270]. This made it possible to determine the mechanisms and conditions of formation and the relative stabilities of a series of new (non-carbon) quasi-planar tubular and spherical boron nanostructures.

7.1. Nanotubes Based on Metal Diborides and LiBC

The structural and energy parameters of a number of MgB_2 and ZrB_2 hypothetical nanotubes were determined by the molecular dynamics technique [261]. It was found that armchair diboride nanotubes (the structural classification of nanotubes is described in [246–249]) with the minimum strain energy have a higher stability. It is believed that diborides can form single-walled and multi-walled nanotubes, for example, (7, 7)@(11, 11)@(15, 15) MeB_2 nanotubes.

The first calculations of the band structure for a number of cylindrical structures—prototypes of AlB_2 nanotubes—were performed by Quandt *et al.* [260]. It was revealed that all tubes possess metallic conductivity.

Ivanovskaya *et al.* [271, 272] applied the tight-binding band method to analyze the electronic structure and the nature of interatomic interactions in armchair (6, 6) and (11, 11) and zigzag (20, 0) MeB_2 single-walled nanotubes (*Me* = Mg, Al, Sc, Ti); (3, 3)@(6, 6), (6, 6)@(12, 12), and (3, 3)@(6, 6)@(12, 12) MgB_2 multi-walled nanotubes; and tubes prepared from lithium borocarbide, which is assumed to be a promising superconductor (see above).

A single-walled nanotube of the formal stoichiometry MeB_2 is modeled by two coaxial cylinders formed upon the rolling-up of adjacent (in a crystal) planar networks, namely, an *Me* hexagonal network and a graphite-like boron network. Two types of tube configurations are possible: a metallic cylinder can be located either outside (*I*) or inside (*II*) of a tube composed of boron atoms (Fig. 1). The estimates of the total energy for the alternative configurations of the MeB_2 nanotubes (Table 7) suggest a higher stability of tubular

structures that contain the metallic cylinder inside the tube composed of boron atoms and are characterized by stronger B–B and *Me*–*Me* bonds.

The MgB_2 nanotubes have a metal-like electronic spectrum in which the Fermi level E_F lies in the region of the B 2*p* states (Fig. 22). The Mg 3*s* and Mg 3*p* states insignificantly contribute to the valence band. The nanotube geometry (the nanotube diameter and the orientation of B–B bonds with respect to the *c* axis of the tubulene) has a considerable effect on the density of states. In particular, for the armchair (11, 11) nanotube (a number of B–B bonds are perpendicular to the *c* axis), the Fermi level E_F coincides with a local minimum in the density of states. In contrast, for the zigzag (20, 0) nanotube (a number of B–B bonds are aligned along the *c* axis), the Fermi level E_F is located in the region of a maximum in the density of states with a high density of B 2*p* states. It is obvious that these MgB_2 nanotubes should be more attractive for searching for materials with improved electrical (specifically, superconducting) properties.

According to [272], with an increase in the number of walls [(3, 3) ⟶ (3, 3)@(6, 6) ⟶ (6, 6)@(12, 12) ⟶ (3, 3)@(6, 6)@(12, 12)] in MgB_2 multi-walled nanotubes, the metallic conductivity is retained and the valence band, as a whole, changes insignificantly. The main effect is associated with the change in the density of near-Fermi states, namely, the increase in the density of B 2*p* states in the vicinity of the Fermi level E_F. The dominant contribution to this region is made by the states of boron atoms of an outer tube with a maximum diameter. As the number of walls in the MgB_2 multi-walled nanotube increases, the valence band becomes similar to that of the crystal.

The evolution of the band structure of MeB_2 nanotubes as a function of the metal type (in the series MgB_2 ⟶ AlB_2 ⟶ ScB_2 ⟶ TiB_2) is governed by two factors: (i) an increase in the number of electrons in the unit cell (i.e., the occupancy of bands) and (ii) changes in the spectrum of nanotubes due to the change in the *Me*–*Me* and *Me*–B interactions. For example, upon the transition MgB_2 ⟶ AlB_2, the Al 3*s* and Al 3*p* states make a considerable contribution to the band of occupied B 2*s* and B 2*p* states. In the case of ScB_2 and TiB_2 nanotubes, there arise intense peaks in the density of Sc (Ti) 3*d* states in the vicinity of the Fermi level E_F. In this series of nanotubes, the B–B bonds play a decisive role and the populations of *Me*–*Me* and *Me*–B bonds increase noticeably.

The calculations performed for the (6, 6), (11, 11), and (20, 0) borocarbide nanotubes based on LiBC and $Li_{0.5}BC$ demonstrated that a change in the composition of the nonmetallic cylinder (B_2 ⟶ BC) results in the appearance of a band gap (for particular atomic configurations of nanotubes) between the occupied and empty C 2*p* and B 2*p* bands [271]. Specifically, the (6, 6) and (11, 11) LiBC nanotubes possess metal-like properties,

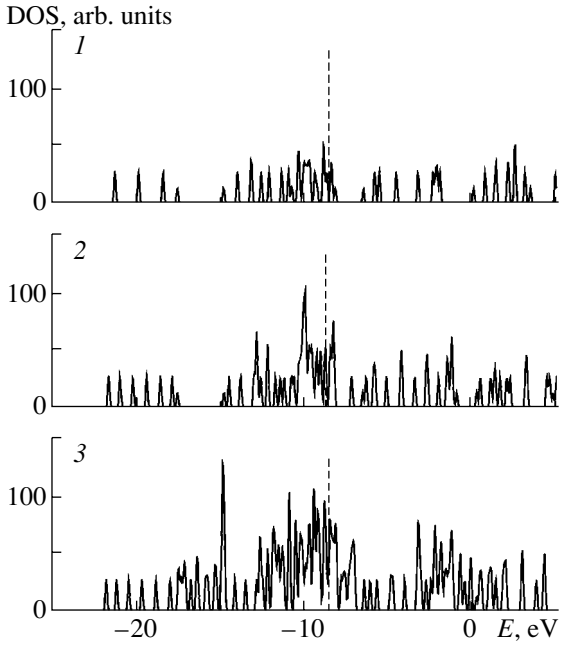

Fig. 22. Total densities of states of (*1*) (6, 6), (*2*) (11, 11), and (*3*) (20, 0) MgB_2 nanotubes with type-*II* configurations (Fig. 1 [271]). Vertical lines indicate the Fermi level.

whereas the (20, 0) LiBC nanotube possesses semiconductor properties. With a decrease in the number of electrons (LiBC ⟶ $Li_{0.5}BC$), all borocarbide nanotubes exhibit metallic properties. In the LiBC and $Li_{0.5}BC$ nanotubes, the C–B interactions play a dominant role and the other bonds (Li–Li, Li–B, Li–C) make a negligible contribution.

At present, experimental data on the synthesis of nanotubes based on MgB_2 and other diborides are unavailable in the literature. Judging from the modern practice of synthesizing inorganic nanotubular structures (see review [259]), we can assume that a possible way of preparing MgB_2 nanotubes is the so-called template method, which has already been applied with advantage to synthesize nanotubular composites, i.e., multi-walled nanotubes containing walls of different chemical compositions. According to this method, stable carbon tubes used as a matrix are covered with layers of different compounds. In the given case, it is clear that the main problem consists in designing a particular technique for applying *in situ* magnesium diboride layers to the surface of carbon nanotubes.

A variant of this technique involves the formation of an elemental-boron nanolayer on carbon nanotubes, followed by treatment of boron–carbon nanotubular composites in magnesium vapors. A similar procedure is successfully used for preparing superconducting MgB_2 wires through annealing amorphous-boron filaments in Mg vapors [273]. The use of recently produced crystalline-boron nanowires [274] as a matrix

can prove promising for the development of techniques for synthesizing nanotubes from metal borides.

Another method of preparing MeB_2 nanotubes is the technique of rolling-up films [275–277]). This technique allows one to prepare nanotubes from thin films of the corresponding materials. In this case, the thickness of the nanotube walls, i.e., the number of walls in multi-walled nanotubes, depends only on the method of applying the film to a substrate. The technique is free of restrictions on the chemical composition of individual walls in nanotubes and can be used to fabricate tubular composites from multilayer films of different compositions. Considering the progress in the preparation of thin MgB_2 films (see [13–16]), the use of this approach in the synthesis of nanotubes seems to be quite justified.

The above synthesis procedures can be used for preparing both pure MeB_2 multi-walled nanotubes and nanotubular composites containing tubular layers of different metal diborides (MeB_2@$Me'B_2$, etc.). In the latter case, it can be expected that such materials will exhibit unusual properties due to the presence of interfaces between adjacent tubes of different chemical nature.

In [272], the modeling of the first representative of composite nanotubes was carried out using a (6, 6)AlB_2@(12, 12)MgB_2 double-walled nanotube as an example. This nanotube has a metal-like spectrum. The B 2*p* states of the outer (12, 12) MgB_2 tube are located in the vicinity of the Fermi level E_F. An increase in the electron concentration [with respect to a pure (6, 6)MgB_2@(12, 12)MgB_2 nanotube] leads to an increase in the band occupation. As a result, the Fermi level E_F is located in the vicinity of a local minimum in the density of states and the density of states at the Fermi level $N(E_F)$ is reduced substantially.

Shein *et al.* [182] considered the electronic properties of tubular structures formed by $Sr(Ga_xSi_{1-x})_2$ and $Ca(Al_xSi_{1-x})_2$ ternary silicides also belonging to AlB_2-like layered superconductors. These authors modeled nonchiral (11, 11) and (20, 0) nanotubes of the formal stoichiometry $Ca(Al_{0.5}Si_{0.5})_2$ = CaAlSi and $Sr(Ga_{0.5}Si_{0.5})_2$ = SrGaSi. The nanotubes retain the metal-like properties inherent in the crystalline phases. However, depending on the geometry and composition of the nanotubes, their near-Fermi densities of states can differ substantially up to the appearance of a pseudogap for the (11, 11) SrGaSi nanotube. In silicide nanotubes, a partial electron transfer Ca $\longrightarrow$ AlSi and Sr $\longrightarrow$ GaSi takes place, bonds in AlSi and GaSi play a dominant role, bonds in Ca and Sr cylinders are comparable, and covalent intertubular bonds (of the van der Waals type [246–249]) between dissimilar coaxial cylinders, as in multi-walled carbon nanotubes, are weak. The configurations of silicide nanotubes involving alkaline-earth metal cylinders inside AlSi or GaSi tubes have a higher stability. In turn, the stability of SrGaSi nanotubes is higher than that of CaAlSi nanotubes.

Chernozatonskiĭ [261] proposed models of the so-called terminal structures for closed MeB_2 nanotubes. Their caps are represented as truncated bifullerenes in the form of double hemispheres formed by metal and boron atoms and involving topological defects in *Me* and B shells.

7.2. Fullerene-Like Nanoclusters Based on Metal Diborides

The structural models of quasi-zero-dimensional molecular forms of diborides—fullerene-like cage particles—were discussed in [261, 278]. Molecules $Me_{n\pm2}B_{2n}$ consist of concentric polyhedra, namely, the inner polyhedron $Me_{n\pm2}$ and the outer polyhedron B_{2n}. According to the estimates of their energy states, the structures that correspond to the stoichiometric compositions $B/Me = 2$ and contain two metal vacancies in two *Me* pentagons have a higher stability.

Bamburov *et al.* [278] calculated the electronic structure and the parameters of interatomic bonds for a number of polyhedral molecules Me_nB_{2n} (n = 10, 30, 90, 120, 160) based on diborides of *s* (MgB_2), *p* (AlB_2), and *d* (ScB_2, TiB_2) metals (Fig. 1) and also more complex cage nanoparticles (of the carbon onion type) composed of two concentric Me_nB_{2n} molecules of identical ($Me_{10}B_{20}$@$Me_{90}B_{180}$) and mixed compositions [$Me_{10}B_{20}$@$Me'_{90}B_{180}$ (*Me*, *Me*' = Mg, Al)].

For all the particles, atomic configurations with outer boron polyhedra have a higher stability. The exception is provided by Al_nB_{2n} molecules. The optimization of their structure leads to a partial destruction of the inner Al_n polyhedron and "diffusion" of part of the aluminum atoms through the outer boron shell with the formation of distorted three-layer structures of the $Al_{n-x}B_{2n}Al_x$ type.

With an increase in the diameter, the total energy E_{tot} of cage molecules varies in a different way depending on the metal type. For Mg_nB_{2n} and Sc_nB_{2n}, the total energy increases, which suggests that their stability increases with a decrease in the radius of curvature (i.e., when the molecular geometry becomes similar to the geometry of a planar layer). Among the Ti_nB_{2n} molecules under consideration, the $Ti_{30}B_{60}$ molecule appears to be most stable.

It seems likely that, in the immediate future, theoretical research on boride nanostructures will deal with the development of structural models and analysis of the electronic properties (including the superconducting properties) of new materials, such as different associates of quasi-zero-dimensional and quasi-one-dimensional boride nanostructures, for example, in the form of molecular crystals composed of fullerene-like molecules or bundles of boride nanotubes.

ACKNOWLEDGMENTS

This work was supported by the Russian Foundation for Basic Research, project no. 02-03-32971.

REFERENCES

1. J. Nagamatsu, N. Nakagawa, T. Muranaka, *et al.*, Nature **410**, 63 (2001).
2. S. V. Vonsovskiĭ, Yu. A. Izyumov, and É. Z. Kurmaev, *Superconductivity of Transition Metals, Their Alloys, and Compounds* (Nauka, Moscow, 1977).
3. N. B. Brandt, S. M. Chudinov, and Ya. G. Ponomarev, *Modern Problems in Condensed Matter Physics* (North-Holland, Amsterdam, 1988).
4. I. T. Belash, A. D. Bronnikov, O. V. Zharikov, and A. P. Pal'nichenko, Synth. Met. **36**, 283 (1990).
5. K. Luders, Mater. Sci. Forum **191**, 119 (1995).
6. K. Tanigaki, T. W. Ebbesen, S. Saito, *et al.*, Nature **352**, 222 (1991).
7. G. V. Samsonov and I. M. Vinitskiĭ, *Handbook of Refractory Compounds* (Metallurgiya, Moscow, 1976; Plenum, New York, 1980).
8. *Superconductivity in Ternary Compounds*, Vol. 1: *Structural, Electronic, and Lattice Properties*, Vol. 2: *Superconductivity and Magnetism*, Ed. by M. B. Maple and O. Fischer (Springer-Verlag, Berlin, 1982).
9. R. J. Cava, H. Takagi, B. Batlogg, *et al.*, Nature **367**, 146 (1994).
10. R. J. Cava, H. Takagi, H. W. Zandbergen, *et al.*, Nature **367**, 252 (1994).
11. A. L. Ivanovskiĭ, Usp. Khim. **67**, 403 (1998).
12. K. H. Muller and V. N. Narozhnyi, Rep. Prog. Phys. **64**, 943 (2001).
13. A. L. Ivanovskiĭ, Usp. Khim. **70**, 811 (2001).
14. C. Buzea and T. Yamashita, Supercond. Sci. Technol. **14**, R115 (2001).
15. P. C. Canfield and S. L. Buk'ko, Phys. World **15**, 29 (2002).
16. A. L. Ivanovskiĭ, N. I. Medvedeva, V. G. Zubkov, and V. G. Bamburov, Zh. Neorg. Khim. **47**, 661 (2002).
17. H. Y. Zhai, H. M. Christen, C. W. White, *et al.*, Appl. Phys. Lett. **80**, 4786 (2002).
18. A. Gumbel, J. Eckert, G. Fuchs, *et al.*, Appl. Phys. Lett. **80**, 2725 (2002).
19. D. Armstrong and P. G. Perkins, J. Chem. Soc., Faraday Trans. 2 **75**, 12 (1979).
20. J. K. Burdett and G. J. Miller, Chem. Mater. **2**, 12 (1989).
21. I. I. Tupitsyn, I. I. Lyakhovskaya, and M. S. Nakhmanson, Fiz. Tverd. Tela (Leningrad) **16**, 2915 (1975) [Sov. Phys. Solid State **16**, 1885 (1975)].
22. A. L. Ivanovskiĭ and N. I. Medvedeva, Zh. Neorg. Khim. **45**, 1234 (2000).
23. A. L. Ivanovskii, N. I. Medvedeva, and J. E. Medvedeva, Mendeleev Commun. **4**, 129 (1998).
24. I. Loa and K. Syassen, Solid State Commun. **118**, 279 (2001).
25. J. M. An and W. E. Pickett, Phys. Rev. Lett. **86**, 4366 (2001).
26. J. Kortus, I. I. Mazin, K. D. Belashchenko, *et al.*, Phys. Rev. Lett. **86**, 4656 (2001).
27. V. Milman and M. C. Warren, J. Phys.: Condens. Matter **13**, 5585 (2001).
28. P. Ravindran, P. Vajeeston, R. Vidya, *et al.*, Phys. Rev. B **64**, 224509 (2001).
29. N. I. Medvedeva, Yu. E. Medvedeva, A. L. Ivanovskiĭ, *et al.*, Pis'ma Zh. Éksp. Teor. Fiz. **73**, 378 (2001) [JETP Lett. **73**, 336 (2001)].
30. W. H. Xie and D. S. Xue, J. Phys.: Condens. Matter **13**, 11679 (2001).
31. F. N. Islam, A. K. Islam, and M. N. Islam, J. Phys.: Condens. Matter **13**, 11661 (2001).
32. A. K. Islam, F. N. Islam, and S. Kabir, J. Phys.: Condens. Matter **13**, L641 (2001).
33. K. Kodayashi and K. Yamamoto, J. Phys. Soc. Jpn. **70**, 1861 (2001).
34. G. Satta, G. Profeta, F. Bernardini, *et al.*, Phys. Rev. B **64**, 104507 (2001).
35. D. A. Papaconstantopoulos and M. J. Mehl, Phys. Rev. B **64**, 172510 (2001).
36. G. Profeta, A. Continenza, F. Bernardini, and S. Massidda, Phys. Rev. B **65**, 054502 (2002).
37. X. G. Wan, J. M. Dong, H. M. Weng, and D. Y. Xing, Phys. Rev. B **65**, 012502 (2002).
38. K. Kobayashi and K. Yamamoto, J. Phys. Soc. Jpn. **71**, 397 (2002).
39. A. A. Golubov, J. Kortus, O. V. Dolgov, *et al.*, J. Phys.: Condens. Matter **14**, 1353 (2002).
40. D. Bagayoko and G. L. Zhao, Int. J. Mod. Phys. **16**, 571 (2002).
41. P. P. Singh, Phys. Rev. Lett. **87**, 087004 (2001).
42. I. I. Mazin and J. Kortus, Phys. Rev. B **65**, 180510 (2002).
43. G. Profeta, A. Continenza, F. Bernardini, *et al.*, Int. J. Mod. Phys. **16**, 1563 (2002).
44. P. Modak, R. S. Rao, B. K. Godwal, and S. K. Sikka, Pramana J. Phys. **58**, 881 (2002).
45. H. Rosner, J. M. An, W. E. Pichett, and S. L. Dreshsler, cond-mat/0203030 (2002).
46. H. Harima, cond-mat/0201452 (2002).
47. H. J. Choi, D. Roundy, H. Sun, *et al.*, Nature **418**, 758 (2002).
48. H. L. Choi, D. Roundy, H. Sun, *et al.*, Phys. Rev. B **66**, 020513 (2002).
49. J. E. Hirsch, cond-mat/0102115 (2001).
50. J. E. Hirsch, Physica C (Amsterdam) **341–348**, 213 (2000).
51. R. O. Zaĭtsev, Pis'ma Zh. Éksp. Teor. Fiz. **73**, 373 (2001) [JETP Lett. **73**, 331 (2001)].
52. L. M. Volkova, S. A. Polyshchuk, S. A. Magarill, and F. E. Herbeck, J. Supercond. **14**, 639 (2001).
53. T. Yildirim, O. Gulsersen, J. W. Lynn, *et al.*, Phys. Rev. Lett. **87**, 37001 (2001).
54. A. Y. Liu, I. I. Mazin, and J. Kortus, cond-mat/0103570 (2001).
55. K. P. Bohnen, R. Heid, and B. Renker, Phys. Rev. Lett. **86**, 5771 (2001).

56. Y. Kong, O. V. Dolgov, O. Jepsen, and O. K. Andersen, Phys. Rev. B **64**, R20501 (2001).
57. H. D. Yang, J. Y. Lin, H. H. Li, *et al.*, Phys. Rev. Lett. **87**, 167003 (2001).
58. F. Bouquet, R. Fisher, P. A. Phillips, *et al.*, J. Supercond. **15**, 469 (2002).
59. Y. Wang, T. Plakowski, and A. Junod, Physica C (Amsterdam) **355**, 179 (2001).
60. X. Chen, M. Konstantinovi, J. C. Irwin, and D. D. Lawie, Phys. Rev. Lett. **87**, 167002 (2001).
61. P. Szabo, P. Samuely, J. Kacmarcik, *et al.*, Phys. Rev. Lett. **87**, 137005 (2001).
62. S. Tsuda, T. Yokoya, T. Kiss, *et al.*, Phys. Rev. Lett. **87**, 177006 (2001).
63. S. Tsuda, T. Yokoya, T. Kiss, *et al.*, Physica B (Amsterdam) **312**, 150 (2002).
64. F. Giubileo, D. Roditchev, W. Sacks, *et al.*, Europhys. Lett. **58**, 764 (2002).
65. M. Pissas, G. Papavassiliou, M. Karayanni, *et al.*, Phys. Rev. B **65**, 184514 (2002).
66. Y. Bugoslavsky, Y. Miyoshi, G. K. Perkins, *et al.*, Supercond. Sci. Technol. **15**, 526 (2002).
67. T. Takahashi, T. Sato, S. Suoma, *et al.*, Phys. Rev. Lett. **86**, 4915 (2001).
68. E. Z. Kurmaev, I. I. Lyakhovskaya, J. Kortus, *et al.*, Phys. Rev. B **65**, 134509 (2002).
69. J. Nakamura, M. Wanatane, T. Oguchi, *et al.*, J. Phys. Soc. Jpn. **71**, 408 (2002).
70. J. Nakamura, N. Yamada, K. Kuroki, *et al.*, Phys. Rev. B **64**, 174504 (2001).
71. T. A. Callcott, L. Lin, G. T. Woods, *et al.*, Phys. Rev. B **64**, 132504 (2001).
72. C. McGuinness, K. E. Smith, S. M. Butorin, *et al.*, Europhys. Lett. **56**, 112 (2001).
73. K. D. Tsuei, H. J. Lin, L. C. Lin, *et al.*, Int. J. Mod. Phys. B **16**, 1618 (2002).
74. R. C. Yu, S. C. Li, Y. Q. Wang, *et al.*, Physica B (Amsterdam) **363**, 184 (2001).
75. X. Kong, Y. Q. Wang, H. Li, *et al.*, Appl. Phys. Lett. **80**, 778 (2002).
76. A. P. Gerashenko, K. N. Mikhalev, S. V. Verkhovskii, *et al.*, Appl. Magn. Reson. **21**, 157 (2001).
77. T. J. Bastow, Solid State Commun. **124**, 269 (2002).
78. G. Papavassiliou, M. Pissas, M. Karayanni, *et al.*, Phys. Rev. B **66**, 140514 (2002).
79. R. Mali, J. Roos, A. Shengelaya, *et al.*, Phys. Rev. B **65**, 100518 (2002).
80. N. I. Medvedeva, A. L. Ivanovskii, J. E. Medvedeva, *et al.*, Phys. Rev. B **65**, 052501 (2002).
81. E. Pavarini and I. I. Mazin, Phys. Rev. B **64**, 140504 (2001).
82. K. Kunc, I. Loa, K. Syassen, *et al.*, J. Phys.: Condens. Matter **13**, 9945 (2001).
83. A. K. Islam and F. N. Islam, Physica C (Amsterdam) **363**, 189 (2001).
84. R. Abd-Shukor, Solid State Commun. **122**, 503 (2002).
85. X. J. Chen, H. Zhang, and H. U. Habermeier, Phys. Rev. B **65**, 144514 (2002).
86. S. Elzaggar, P. M. Oppeneer, S. I. Drechsler, *et al.*, Solid State Commun. **122**, 463 (2002).
87. H. Kim, W. N. Kang, and E. M. Choi, J. Korean Phys. Soc. **40**, 416 (2002).
88. A. Brikman, D. Mijatovich, G. Rijneders, *et al.*, Physica C (Amsterdam) **353**, 1 (2001).
89. D. Blank, H. Hilgenkamp, A. Brikman, *et al.*, Appl. Phys. Lett. **79**, 394 (2001).
90. H. M. Christen, H. Y. Zhai, C. Cantoni, *et al.*, Physica C (Amsterdam) **353**, 157 (2001).
91. S. R. Sinde, S. B. Ogale, R. L. Greene, *et al.*, cond-mat/0103542 (2001).
92. C. B. Eom, M. K. Lee, J. H. Choi, *et al.*, Nature **411**, 558 (2001).
93. M. Paranthaman, C. Cantoni, H. Y. Zhai, *et al.*, Appl. Phys. Lett. **78**, 3669 (2001).
94. G. Grassano, W. Ramadan, V. Ferrando, *et al.*, cond-mat/0103572 (2001).
95. H. Y. Zhai, H. M. Chirsten, L. Zhang, *et al.*, Appl. Phys. Lett. **79**, 2603 (2001).
96. W. N. Kang, H. Kim, E. M. Choi, *et al.*, Phys. Rev. B **65**, 134508 (2002).
97. M. H. Jung, M. Jaime, and A. H. Lacerda, Chem. Phys. Lett. **343**, 4447 (2001).
98. S. Patnaik, L. D. Cooley, A. Gurevich, *et al.*, Supercond. Sci. Technol. **14**, 315 (2001).
99. H. Y. Zhai, H. M. Christen, L. Zhang, *et al.*, J. Mater. Res. **16**, 2759 (2001).
100. W. Tian, X. Q. Pan, S. D. Bu, *et al.*, Appl. Phys. Lett. **81**, 685 (2002).
101. Z. W. Zhao, S. L. Li, Y. M. Ni, *et al.*, Phys. Rev. B **65**, 064512 (2002).
102. S. F. Wang, S. Y. Dai, Y. L. Zhou, *et al.*, Supercond. Sci. Technol. **14**, 952 (2001).
103. X. D. Zeng, A. Sukiasyan, X. Xi, *et al.*, Appl. Phys. Lett. **79**, 1840 (2001).
104. A. H. Li, X. L. Wang, M. Ionescu, *et al.*, Physica C (Amsterdam) **361**, 73 (2001).
105. H. Y. Zhai, H. M. Christen, L. Zhang, *et al.*, Supercond. Sci. Technol. **14**, 425 (2001).
106. S. Y. Lee, J. H. Lee, J. S. Ryu, *et al.*, Appl. Phys. Lett. **79**, 3299 (2001).
107. R. Jin, M. Paranthaman, H. Y. Zhai, *et al.*, Phys. Rev. B **64**, 220506 (2001).
108. J. J. Tu, G. L. Carr, V. Perebeinos, *et al.*, Phys. Rev. Lett. **87**, 277001 (2002).
109. V. M. Silkin, E. V. Chulkov, and P. M. Echenique, Phys. Rev. B **64**, 172512 (2001).
110. I. G. Kim, J. I. Lee, B. I. Min, and A. J. Freeman, Phys. Rev. B **64**, 020508 (2001).
111. Z. Li, J. Yang, J. Hou, and Q. S. Zhou, Phys. Rev. B **65**, 100507 (2002).
112. V. Servedio, S. L. Drechsler, and T. Mishonov, Int. J. Mod. Phys. **16**, 1613 (2002).
113. H. Uchiyama, K. M. Shen, S. Lee, *et al.*, Phys. Rev. Lett. **88**, 157002 (2002).
114. R. P. Vasques, C. U. Jung, M. Park, *et al.*, cond-mat/0103215 (2001).
115. Y. Moritomo and S. Xu, cond-mat/0104568 (2001).

116. N. I. Medvedeva, A. L. Ivanovskii, J. E. Medvedeva, and A. J. Freeman, Phys. Rev. B **64**, 020502 (2001).
117. P. Singh and P. J. Joseph, cond-mat/0202285 (2002).
118. V. I. Anisimov, V. A. Antropov, V. A. Gubanov, A. L. Ivanovskiĭ, É. Z. Kurmaev, A. I. Likhtenshteĭn, and A. V. Postnikov, *Electronic Structure of Impurities and Defects in Transition Metals, Their Alloys, and Compounds* (Nauka, Moscow, 1989).
119. V. A. Gubanov, A. L. Ivanovskii, and V. P. Zhukov, *Electronic Structure of Refractory Carbides and Nitrides* (Cambridge Univ. Press, Cambridge, 1994).
120. V. A. Gubanov and A. L. Ivanovskii, in *Density Functional Theory of Molecules, Clusters, and Solids*, Ed. by D. E. Ellis (Kluwer Academic, Dordrecht, 1994).
121. A. L. Ivanovskii, V. I. Anisimov, A. I. Lichtenstein, and V. A. Gubanov, J. Phys. Chem. Solids **49**, 479 (1988).
122. A. L. Ivanovskiĭ and V. A. Gubanov, Metallofizika (Kiev) **12**, 18 (1990).
123. A. L. Ivanovskiĭ, V. I. Anisimov, and V. A. Gubanov, Zh. Strukt. Khim. **30**, 19 (1989).
124. A. L. Ivanovskii and G. P. Shveikin, Phys. Status Solidi B **181**, 251 (1994).
125. V. M. Cherkashenko, S. Z. Nazarova, A. I. Gusev, and A. L. Ivanovskiĭ, Zh. Strukt. Khim. **42**, 1195 (2001).
126. P. J. Joseph and P. Singh, Solid State Commun. **121**, 467 (2002).
127. S. Suzuki, S. Higai, and K. Nakao, J. Phys. Soc. Jpn. **70**, 1206 (2001).
128. M. J. Mehl, D. A. Papaconstantopoulos, and S. Singh, Phys. Rev. B **64**, 140509 (2001).
129. T. Takenobu, T. Ito, D. H. Chi, *et al.*, Phys. Rev. B **64**, 134513 (2001).
130. M. Paranthaman, J. R. Thompson, and D. K. Christen, Physica C (Amsterdam) **355**, 1 (2001).
131. Z. H. Cheng, B. G. Shen, J. Zhang, *et al.*, J. Appl. Phys. **91**, 7125 (2002).
132. I. Maurin, S. Margadonna, K. Prassides, *et al.*, Physica B (Amsterdam) **318**, 392 (2002).
133. W. Mickelson, J. Cumings, W. Q. Han, and A. Zettl, Phys. Rev. B **65**, 052505 (2002).
134. A. Bharathi, S. J. Balaselvi, and S. Kalavathi, Physica C (Amsterdam) **370**, 211 (2002).
135. K. Papagelis, J. Arvantidis, and S. Margadonna, J. Phys.: Condens. Matter **14**, 7363 (2002).
136. N. I. Medvedeva, Yu. E. Medvedeva, and A. L. Ivanovskiĭ, Dokl. Akad. Nauk **379**, 72 (2001).
137. J. S. Slusky, N. Rogado, K. A. Regan, *et al.*, Nature **410**, 343 (2001).
138. J. Y. Xiang, D. N. Zheng, J. Q. Li, *et al.*, cond-mat/0104366 (2001).
139. J. Q. Li, I. Li, and F. M. Liu, Phys. Rev. B **65**, 132505 (2002).
140. H. W. Zandbergen, M. Y. Wu, H. Jiang, *et al.*, Physica C (Amsterdam) **366**, 221 (2002).
141. S. V. Barabash and D. Stroud, cond-mat/0111392 (2002).
142. M. Worle and R. Nesper, J. Alloys Compd. **216**, 75 (1994).
143. R. Ramirez, Z. Naturforsch. A **42**, 670 (1987).
144. H. Rosner, A. Kitaigorodsky, and W. E. Pickett, Phys. Rev. Lett. **88**, 127001 (2002).
145. J. H. Schon, Ch. Kloc, and B. Batlogg, Science **293**, 2434 (2001).
146. J. K. Dewhurst, S. Sharma, C. Ambrosch-Draxl, and B. Johansson, cond-mat/0210704 (2002).
147. J. M. An, S. Y. Savrasov, H. Rosner, and W. E. Pickett, cond-mat/0207542 (2002).
148. D. Souptel, Z. Hossain, G. Behr, *et al.*, cond-mat/0208346 (2002).
149. A. Bharathi, S. J. Balaselvi, M. Premila, *et al.*, cond-mat/0207448 (2002).
150. J. Hlinka, J. Gregora, A. V. Pronin, and A. Loidl, cond-mat/0207683 (2002).
151. R. I. Medvedeva, Yu. E. Medvedeva, and A. L. Ivanovskiĭ, Dokl. Akad. Nauk **383**, 75 (2002).
152. G. K. Strukova, V. F. Degtyareva, D. V. Shivkun, *et al.*, cond-mat/0105293 (2001).
153. G. V. Samsonov, T. I. Serebryakova, and V. A. Neronov, *Borides* (Atomizdat, Moscow, 1975).
154. T. I. Serebryakova, V. A. Neronov, and P. D. Peshev, *High-Temperature Borides* (Metallurgiya, Moscow, 1991).
155. T. A. Serebryakova, J. Less-Common Met. **67**, 499 (1979).
156. A. L. Ivanovskiĭ and G. P. Shveĭkin, *Quantum Chemistry in Materials Science: Boron, Its Compounds, and Alloys* (Ural. Otd. Ross. Akad. Nauk, Yekaterinburg, 1998).
157. L. Leyarovska and E. Leyarovski, J. Less-Common Met. **67**, 249 (1979).
158. V. A. Gasparov, N. S. Sidorov, I. I. Zver'kova, and M. P. Kulakov, cond-mat/0104323 (2001).
159. D. Kaczorowski, J. Klamut, and A. J. Zaleski, cond-mat/0104479 (2001).
160. N. Ogita, T. Kariya, H. Hiraoka, *et al.*, cond-mat/0106147 (2001).
161. H. Rosner, J. M. An, W. E. Pickett, and S. Drechsler, Phys. Rev. B **66**, 24521 (2002).
162. H. Rosner and W. E. Pickett, cond-mat/0106062 (2001).
163. P. P. Singh, cond-mat/0210091 (2002).
164. D. P. Young, P. W. Adams, J. Y. Chan, and F. R. Fronczek, cond-mat/0104063 (2001).
165. V. V. Volkov, K. G. Myakishev, P. P. Bezverkhniĭ, and E. V. Matizen, Pis'ma Zh. Éksp. Teor. Fiz. **75**, 684 (2002) [JETP Lett. **75**, 566 (2002)].
166. A. L. Ivanovskiĭ, N. I. Medvedeva, Yu. E. Medvedeva, *et al.*, Metallofiz. Noveishie Tekhnol. **20**, 41 (1998).
167. A. L. Ivanovskiĭ, N. I. Medvedeva, and Yu. E. Medvedeva, Metallofiz. Noveishie Tekhnol. **21**, 19 (1999).
168. I. R. Shein, N. I. Medvedeva, and A. L. Ivanovskiĭ, Fiz. Tverd. Tela (St. Petersburg) **44**, 1752 (2002) [Phys. Solid State **44**, 1833 (2002)].
169. P. Vajeeston, P. Ravindran, C. Ravi, and R. Asokamani, Phys. Rev. B **63**, 045115 (2001).
170. T. Oguchi, J. Phys. Soc. Jpn. **71**, 1495 (2002).
171. A. Yamamoto, Y. C. Takao, T. Masui, *et al.*, cond-mat/0208331 (2002).

172. A. S. Cooper, E. Corenzwit, and L. Longinotti, Proc. Natl. Acad. Sci. USA **67**, 313 (1970).
173. I. R. Shein, K. I. Shein, N. I. Medvedeva, and A. L. Ivanovskii, cond-mat/0211247 (2002).
174. I. R. Shein, N. I. Medvedeva, and A. L. Ivanovskiĭ, Fiz. Tverd. Tela (St. Petersburg) **43**, 2121 (2001) [Phys. Solid State **43**, 2213 (2001)].
175. I. R. Shein and A. L. Ivanovskii, Phys. Status Solidi A **227**, R11 (2001).
176. I. R. Shein, N. I. Medvedeva, and A. L. Ivanovskii, cond-mat/0109445 (2001).
177. M. Imai, E. Abe, J. Ye, *et al.*, Phys. Rev. Lett. **87**, 77003 (2001).
178. M. Imai, K. Nishida, T. Kimura, and H. Abe, Appl. Phys. Lett. **80**, 1019 (2002).
179. M. Imai, K. Nishida, T. Kimura, and H. Abe, Physica C (Amsterdam) **377**, 96 (2002).
180. M. Imai, K. Nishida, T. Kimura, *et al.*, cond-mat/0210692 (2002).
181. B. Lorenz, J. Lenzi, J. Cmaidalka, *et al.*, cond-mat/0208341 (2002).
182. I. R. Shein, V. V. Ivanovskaya, N. I. Medvedeva, and A. L. Ivanovskiĭ, Pis'ma Zh. Éksp. Teor. Fiz. **76**, 223 (2002) [JETP Lett. **76**, 189 (2002)].
183. I. R. Shein, N. I. Medvedeva, and A. L. Ivanovskii, cond-mat/0212047 (2002).
184. S. Lee, D. M. Bylander, and L. Kleinman, Phys. Rev. B **42**, 1316 (1990).
185. C. Maihiot, J. B. Grant, and A. K. McMahan, Phys. Rev. B **42**, 9033 (1990).
186. D. Li, Y. Xu, and W. Y. Ching, Phys. Rev. B **45**, 5895 (1992).
187. M. L. Eremets, V. V. Struzhkin, H. Mao, and R. J. Hemley, Science **293**, 272 (2001).
188. D. A. Papaconstantopoulos and M. J. Mehl, Phys. Rev. B **65**, 172510 (2002).
189. I. R. Shein, S. V. Okatov, N. I. Medvedeva, and A. L. Ivanovskii, cond-mat/0202015 (2002).
190. D. N. Sanz, P. Loubeyre, and M. Mezouar, Phys. Rev. Lett. **89**, 245501 (2002).
191. S. V. Okatov, A. L. Ivanovskii, N. I. Medvedeva, and J. E. Medvedeva, Phys. Status Solidi A **225**, R3 (2001).
192. H. Hasegawa and A. Yanase, J. Phys. C **12**, 5431 (1979).
193. Y. Ripplinger, K. Schwarz, and P. Blaha, J. Solid State Chem. **133**, 51 (1997).
194. S. Massidda, A. Continenza, T. M. DePascale, and R. Monnier, Z. Phys. B: Condens. Matter **102**, 83 (1997).
195. A. L. Ivanovskii and S. V. Okatov, Mendeleev Commun. **11**, 8 (2001).
196. T. He, Q. Huang, A. P. Ramirez, *et al.*, Nature **411**, 54 (2001).
197. A. L. Ivanovskiĭ, Usp. Khim. **64**, 499 (1995).
198. F. J. DiSalvo, Science **247**, 649 (1990).
199. M. Y. Chern, D. A. Vennos, and F. J. DiSalvo, Solid State Chem. **96**, 415 (1992).
200. M. Y. Chern, F. J. DiSalvo, J. B. Parise, and A. J. Goldstone, Solid State Chem. **96**, 426 (1992).
201. D. A. Papaconstantopoulos and W. E. Pickett, Phys. Rev. B **45**, 4008 (1992).
202. E. O. Chi, W. S. Kim, N. S. Hur, and D. Jung, Solid State Commun. **121**, 309 (2002).
203. I. R. Chein and A. L. Ivanovskii, J. Solid State Chem. (2003) (in press).
204. A. L. Ivanovskii and N. I. Medvedeva, Mendeleev Commun. **9**, 36 (1999).
205. A. L. Ivanovskiĭ, N. I. Medvedeva, and D. L. Novikov, Fiz. Tverd. Tela (St. Petersburg) **39**, 1035 (1997) [Phys. Solid State **39**, 929 (1997)].
206. A. L. Ivanovskiĭ, N. I. Medvedeva, A. N. Skazkin, and G. P. Shveĭkin, Zh. Neorg. Khim. **44**, 1543 (1999).
207. A. L. Ivanovskiĭ, A. I. Gusev, and G. P. Shveĭkin, *Quantum Chemistry in Materials Science: Ternary Carbides and Nitrides of Subgroup III and V Transition Metals and Elements* (Ural. Otd. Ross. Akad. Nauk, Yekaterinburg, 1996).
208. S. Saxena, P. Agarwal, K. Ahilan, *et al.*, Nature **406**, 587 (2000).
209. A. Huxley, I. Sheikin, E. Ressouche, *et al.*, Phys. Rev. B **63**, 144519 (2001).
210. D. Aoki, A. Huxley, E. Ressouche, *et al.*, Nature **413**, 613 (2001).
211. C. Pfeiderer, M. Uhlarz, S. M. Hayden, *et al.*, Nature **412**, 58 (2001).
212. R. Matzdorf, Z. Fang, A. Ismail, *et al.*, Science **289**, 746 (2000).
213. K. Shen, A. Damascelli, D. H. Lu, *et al.*, Phys. Rev. B **64**, 180502 (2001).
214. T. Kirkpatrick, D. Belitz, T. Vojta, and R. Narayanan, Phys. Rev. Lett. **87**, 127033 (2001).
215. M. W. Walker and K. V. Samokhin, Phys. Rev. Lett. **88**, 207001 (2001).
216. K. Machida and T. Ohmi, Phys. Rev. Lett. **86**, 850 (2001).
217. N. Karchev, cond-mat/0212520 (2002).
218. Z. A. Ren, G. C. Che, S. L. Jia, *et al.*, Physica C (Amsterdam) **371**, 1 (2002).
219. J. Q. Li, L. J. Wu, J. L. Li, and Y. Zhu, Phys. Rev. B **65**, 052506 (2002).
220. S. Y. Li, X. H. Fan, X. D. Chen, *et al.*, Phys. Rev. B **64**, 132505 (2001).
221. L. D. Cooley, X. Song, J. Jiang, *et al.*, Phys. Rev. B **65**, 214518 (2002).
222. Q. Huang, T. He, K. A. Regan, *et al.*, Physica C (Amsterdam) **363**, 215 (2001).
223. S. Y. Li, W. Q. Mo, M. Yu, *et al.*, Phys. Rev. B **65**, 064534 (2002).
224. M. Q. Tan, X. M. Tao, X. J. Xu, *et al.*, Acta Phys. Sin. **52**, 463 (2003).
225. A. Waelte, H. Rosner, M. D. Johannes, *et al.*, cond-mat/0208364 (2002).
226. G. Kinoda, M. Nishiyama, Y. Zhao, *et al.*, Jpn. J. Appl. Phys., Part 2 **40**, L1365 (2001).
227. M. Singer, T. Imai, T. He, *et al.*, Phys. Rev. Lett. **87**, 257601 (2001).
228. A. L. Ivanovskiĭ and V. G. Bamburov, Inzh. Fiz., No. 1, 50 (2003).
229. A. Szajek, J. Phys.: Condens. Matter **13**, L595 (2001).

230. I. R. Shein, N. I. Medvedeva, and A. L. Ivanovskiĭ, Pis'ma Zh. Éksp. Teor. Fiz. **74**, 127 (2001) [JETP Lett. **74**, 122 (2001)].
231. S. B. Dugdale and T. Jarlborg, Phys. Rev. B **64**, 100508 (2001).
232. D. J. Singh and I. I. Mazin, Phys. Rev. B **64**, 140507 (2001).
233. J. H. Shim, S. K. Kwon, and B. I. Min, Phys. Rev. B **64**, 180510 (2001).
234. H. Rosner, R. Weht, M. D. Johannes, *et al.*, Phys. Rev. Lett. **88**, 027001 (2002).
235. I. G. Kim, J. I. Lee, and A. J. Freeman, Phys. Rev. B **65**, 064525 (2002).
236. J. L. Wang, Y. Xu, Z. Zeng, *et al.*, J. Appl. Phys. **91**, 8504 (2002).
237. M. A. Hayward, M. K. Haas, A. P. Ramirez, *et al.*, Solid State Commun. **119**, 491 (2001).
238. Z. Ren, G. Che, S. L. Jia, *et al.*, Sci. China, Ser. A **44**, 1205 (2001).
239. I. R. Shein and A. L. Ivanovskiĭ, Zh. Strukt. Khim. **43**, 180 (2001).
240. X. G. Wang, H. M. Weng, and L. M. Dong, Chin. Phys. Lett. **19**, 1522 (2002).
241. K. Voelker and M. Sigrist, cond-mat/0208367 (2002).
242. I. R. Shein, A. L. Ivanovskii, E. Z. Kurmaev, *et al.*, Phys. Rev. B **66**, 024520 (2002).
243. C. M. Granada, C. da Silva, and A. A. Gomes, Solid State Commun. **122**, 269 (2002).
244. J. H. Shim, S. K. Kwon, and B. I. Min, cond-mat/0110448 (2001).
245. T. G. Kumary, J. Janaki, A. Mani, *et al.*, Phys. Rev. B **66**, 064510 (2002).
246. M. S. Dresselhaus, G. Dresselhaus, and P. C. Eklund, *Science of Fullerenes and Carbon Nanotubes* (Academic, San Diego, 1996).
247. R. Saito, G. Dresselhaus, and M. S. Dresselhaus, *Physical Properties of Carbon Nanotubes* (Imperial College Press, London, 1998).
248. *The Science and Technology of Carbon Nanotubes*, Ed. by K. Tanaka, T. Yamabe, and K. Fuku (Elsevier, Oxford, 1999).
249. P. J. F. Harris, *Carbon Nanotubes and Related Structures: New Materials for the Twenty-First Century* (Cambridge Univ. Press, Cambridge, 1999).
250. A. L. Ivanovskiĭ, *Quantum Chemistry in Materials Science: Nanotubular Forms of Matter* (Ural. Otd. Ross. Akad. Nauk, Yekaterinburg, 1999).
251. P. Moriarty, Rep. Prog. Phys. **64**, 297 (2001).
252. A. V. Eletskiĭ, Usp. Fiz. Nauk **172**, 401 (2002).
253. P. M. Ajayan and O. Z. Zhou, Carbon Nanotubes **80**, 391 (2001).
254. R. Tenne, Prog. Inorg. Chem. **50**, 269 (2001).
255. M. Kociak, A. Y. Kasumov, S. Gueron, *et al.*, Phys. Rev. Lett. **86**, 2416 (2001).
256. Z. K. Tang, L. Zhang, N. Wang, *et al.*, Science **292**, 2463 (2001).
257. J. Gonzales, Phys. Rev. Lett. **88**, 76403 (2002).
258. R. F. Service, Science **292**, 45 (2001).
259. A. L. Ivanovskiĭ, Usp. Khim. **71**, 203 (2002).
260. A. Quandt, A. Y. Liu, and I. Boustani, Phys. Rev. B **64**, 125422 (2001).
261. L. A. Chernozatonskiĭ, Pis'ma Zh. Éksp. Teor. Fiz. **74**, 369 (2001) [JETP Lett. **74**, 335 (2001)].
262. I. Boustani, Int. J. Quantum Chem. **52**, 1081 (1994).
263. I. Boustani, Surf. Sci. **370**, 355 (1997).
264. I. Boustani, Phys. Rev. B **55**, 16426 (1997).
265. I. Boustani and A. Quandt, Europhys. Lett. **39**, 527 (1997).
266. I. Boustani, J. Solid State Chem. **133**, 182 (1997).
267. I. Boustani and A. Quandt, Comput. Mater. Sci. **11**, 132 (1998).
268. M. K. Sabra and I. Boustani, Europhys. Lett. **42**, 611 (1998).
269. I. Boustani, A. Quandt, and A. Rubio, J. Solid State Chem. **154**, 269 (2000).
270. I. Boustani, A. Rubio, and J. A. Alonso, Chem. Phys. Lett. **311**, 21 (1999).
271. V. V. Ivanovskaya, A. N. Enyachin, A. A. Sofronov, *et al.*, J. Mol. Struct.: THEOCHEM **625**, 9 (2003).
272. V. V. Ivanovskaya, A. N. Enyashin, A. A. Sofronov, *et al.*, Teor. Éksp. Khim. **39**, 33 (2003).
273. P. C. Canfield, D. K. Finnemore, S. L. Bud'ko, *et al.*, Phys. Rev. Lett. **86**, 2423 (2001).
274. C. J. Otten, O. R. Lourie, M. F. Yu, *et al.*, J. Am. Chem. Soc. **124**, 4564 (2002).
275. O. G. Schmidt and K. Eberl, Nature **410**, 168 (2001).
276. V. Y. Prinz, A. V. Chekhovskiy, V. V. Preobrazhenskii, *et al.*, Nanotechnology **13**, 321 (2002).
277. C. Deneke, C. Muller, N. Y. Jin-Phillipp, and O. G. Schmidt, Semicond. Sci. Technol. **17**, 1278 (2002).
278. V. G. Bamburov, V. V. Ivanovskaya, A. N. Enyashin, *et al.*, Dokl. Akad. Nauk **388**, 1 (2003).

Translated by O. Borovik-Romanova

Physics of the Solid State, Vol. 45, No. 10, 2003, pp. 1860–1865. Translated from Fizika Tverdogo Tela, Vol. 45, No. 10, 2003, pp. 1770–1775.

METALS AND SUPERCONDUCTORS

Nonlinear Waves in Bismuth

V. G. Skobov* and A. S. Chernov**

** Ioffe Physicotechnical Institute, Russian Academy of Sciences, Politekhnicheskaya ul. 26, St. Petersburg, 194021 Russia*

*** Moscow State Institute of Engineering Physics, Kashirskoe sh. 31, Moscow, 115409 Russia*

Received January 21, 2003; in final form, March 18, 2003

Abstract—The propagation of short radio waves in a bismuth crystal in a constant magnetic field **H** aligned parallel to the bisecting axis oriented normally to the surface of the crystal plate is investigated theoretically. In this geometry, spatial inhomogeneity of the wave field has a weak effect on electrons and a strong effect on holes. It is demonstrated that, in a certain range of magnetic field strengths *H*, the bismuth crystal is characterized by two modes, namely, a helicon and a doppleron, whose damping is governed by cyclotron absorption of holes. For small amplitudes of the wave field in a linear regime, the damping lengths of both modes are relatively short due to cyclotron absorption. In a nonlinear regime, the magnetic field of the radio wave captures holes responsible for cyclotron absorption. As a result, the absorption is suppressed and the damping lengths of the helicon and the doppleron increase drastically. The excitation of these modes in the bismuth plate results in the fact that the dependence of the impedance of the plate on the magnetic field strength *H* exhibits resonance behavior and the transmittance of the plate increases by more than two orders of magnitude. It is shown that this effect should manifest itself at frequencies of the order of a few megahertzes in relatively weak magnetic fields (of the order of a few tens of oersteds). © *2003 MAIK "Nauka/Interperiodica".*

1. The propagation of radio waves through metals in a linear regime can differ significantly from that in a nonlinear regime. For example, Voloshin *et al.* [1] showed that the capture of electrons by a magnetic field of a large-amplitude wave in cadmium leads to strong suppression of the cyclotron absorption and decreases the damping of the hole doppleron, which results in a sharp increase in the amplitude of impedance oscillations. More recently, it was demonstrated that the capture of carriers by a wave field suppresses collisionless damping of helicons and dopplerons in many metals and increases their transparency with respect to these modes [2–4]. Moreover, suppression of the collisionless absorption can lead to the propagation of specific nonlinear waves [3–6] that have no analogs in a linear regime.

It should be noted that the aforementioned works have been concerned with the wave properties of typical metals with high conductivity and nonlinearity observed at relatively low frequencies, i.e., in the long-wavelength and medium-wavelength ranges. The carrier concentration in bismuth is five orders of magnitude less than that in typical metals. Consequently, the nonlinear regime in bismuth can be achieved at higher frequencies. In this work, we theoretically investigated the propagation of short radio waves with a large amplitude in bismuth.

In a strong constant magnetic field *H*, the Alfvén velocity in the bismuth electron–hole plasma is higher than the Fermi velocity of carriers. In this case, the nonlocal effects are insignificant and the Alfvén waves can propagate at frequencies ω exceeding the characteristic frequency ν of carrier collisions (see, for example, [7, 8]). In the frequency range of interest ($\omega \ll \nu$), the conduction is governed by carrier scattering, the propagation of waves becomes impossible, and the skin effect is observed in bismuth in the linear regime. In weaker magnetic fields, the conductivity increases, the skin depth decreases, and the nonlocal effects begin to play an increasingly important role. This implies that, in magnetic fields in which the maximum displacement of carriers over the cyclotron period appears to be larger than the skin depth, the collisionless cyclotron absorption becomes dominant. This range of field strengths is of primary interest to us, because it is in this range that the nonlinear effects most clearly manifest themselves.

2. Let us consider a geometry in which a constant magnetic field **H** and the normal to the surface of the bismuth plate are aligned parallel to the bisecting axis of the crystal [9]. For this orientation of the magnetic field **H**, the cross-sectional areas of all three electron ellipsoids in the plane perpendicular to the vector **H** are one order of magnitude less than the cross-sectional area of the hole ellipsoid. As a result, the cyclotron mass of electrons turns out to be one order of magnitude less than that of holes and the maximum displacement of electrons over the cyclotron period is approximately 30 times shorter than the maximum displacement of holes. Hence, there is a sufficiently wide range of wavelengths in which the radio wavelength in a metal is considerably less than the maximum displacement of holes but is substantially greater than the maximum displacement of electrons. In this range of wave vectors **k**, the nonlocal effects do not affect the electron component of the transverse conductivity but contribute significantly to the hole component. Consequently,

the contribution of electrons to the conductivity can be adequately described in the local approximation, whereas the contribution of holes should be calculated with allowance made for the spatial inhomogeneity of the wave field.

The dependence of the hole energy ε on the hole momentum $\mathbf{p}$ can be represented by the equation

$$\varepsilon(\mathbf{p}) = \frac{p_x^2}{2m_1} + \frac{p_y^2 + p_z^2}{2m_2}, \quad m_1 = 0.54m, \quad m_2 = 0.06m. \tag{1}$$

Here, the x axis is aligned parallel to the trigonal axis of the crystal and m is the mass of a free electron. The cross-sectional area of the hole ellipsoid $\varepsilon(\mathbf{p}) = \varepsilon_F$ in the plane p_z = const can be written in the form

$$S(\varepsilon_F, p_z) = 2\pi\sqrt{m_1 m_2}\left(\varepsilon_F - \frac{p_z^2}{2m_2}\right), \tag{2}$$

where ε_F is the Fermi energy of holes.

As follows from expression (2), the cyclotron mass of holes is determined by the relationship

$$m_c \equiv \frac{1}{2\pi}\frac{\partial S}{\partial \varepsilon_F} = \sqrt{m_1 m_2} \simeq 0.18m, \tag{3}$$

the longitudinal component p_z of the hole momentum at the reference point of the ellipsoid can be obtained from the expression

$$p_{z\max} = \sqrt{2m_2\varepsilon_F}, \tag{4}$$

and the magnitude of the momentum p can be found from the formula

$$p \equiv \frac{1}{2\pi}\left|\frac{\partial S}{\partial p_z}\right|_{\max} = \sqrt{2m_1\varepsilon_F}. \tag{5}$$

The Fermi energy ε_F and the hole concentration n are related by the expression

$$\varepsilon_F = \frac{1}{2}\left(\frac{3\pi^2\hbar^3 n}{\sqrt{m_1 m_2}}\right)^{2/3}. \tag{6}$$

For bismuth, we have $n = 3 \times 10^{17}$ cm^{-3}. Substitution of this concentration and the masses m_1 and m_2 into relationships (5) and (6) gives

$$\varepsilon_F = 2 \times 10^{-14} \text{ erg}, \quad p = 0.45 \times 10^{-20} \text{ g cm/s}. \tag{7}$$

In this work, we are interested in circularly polarized waves propagating in bismuth. The sense of rotation of the field of these waves coincides with that of electrons in the magnetic field (i.e., we deal with the "minus" polarization). The dispersion relation for these modes has the form

$$k^2c^2 = 4\pi i\omega\sigma_-(k, \omega), \tag{8}$$

where

$$\sigma_- \equiv \sigma_{xx} - i\sigma_{yx} = \sigma_-^{(e)} + \sigma_-^{(h)}, \tag{9}$$

$\sigma_{\alpha\beta}$ are the conductivity tensor components, and the superscripts e and h refer to the electron and hole contributions to the conductivity σ_-, respectively. Since the vectors $\mathbf{k}$ and $\mathbf{H}$ are aligned with one of the major axes of the hole ellipsoid, the expression for the nonlocal conductivity σ_- has the same form as in the case of the spherical Fermi surface [10]:

$$\sigma_-^{(h)}(k, \omega, H) = i\frac{nec}{H}\frac{F(t)}{1 + (\omega + i\nu)/\omega_c}, \tag{10}$$

$$F(t) = \frac{3}{2t^2}\left[1 + \frac{t^2 - 1}{2t}\left(\ln\frac{t+1}{t-1} - i\pi\right)\right], \tag{11}$$

$$t = \frac{q}{1 + (\omega + i\nu)/\omega_c}, \quad q = \frac{kcp}{eH}, \quad \omega_c = \frac{eH}{m_c c}, \tag{12}$$

where e is the magnitude of the elementary charge, c is the velocity of light, ω is the circular wave frequency, and ν is the frequency of hole collisions with scatterers. The only difference between our case and the case of the Fermi sphere is that the formula for q involves not the radius p_F of the Fermi sphere but the parameter p determining the displacement of holes at the reference point of the ellipsoid over the cyclotron period.

Note that the radio frequencies are small compared to the hole collision frequency ν. For this reason, hereafter, the dependence of the conductivity σ_- on the frequency ω will be ignored. Moreover, we assume that the magnetic field H is strong enough for the ratio ν/ω_c to be small; that is,

$$\gamma \equiv \frac{\nu}{\omega_c} \ll 1. \tag{13}$$

Under this condition, the expression for the hole conductivity takes the form

$$\sigma_-^{(h)} = i\frac{nec}{H(1 + i\gamma)}F\left(\frac{q}{1 + i\gamma}\right). \tag{14}$$

Our interest is in the situation where the radio wavelength $2\pi/k$ in bismuth is small compared to the maximum displacement of holes over the cyclotron period $2\pi cp(eH)$ ($q \gg 1$) but is large compared to the maximum displacement of electrons over the same period. This situation is quite possible, because, in the geometry under consideration, the maximum displacement of electrons is approximately 30 times shorter than that of holes. In this case, the dependence of $\sigma_-^{(e)}$ on k is insignificant and the relationship for $\sigma_-^{(e)}$ can be reduced to the local Hall conductivity:

$$\sigma_-^{(e)} = -i\frac{nec}{H}. \tag{15}$$

As a result, the dispersion relation (8) can be rewritten in the form of the following equation with respect to the dimensionless variable q:

$$D(q) = 0, \tag{16}$$

where

$$D(q) = q^2 - \xi s(q), \tag{17}$$

$$s(q) = 1 - \frac{1}{1+i\gamma}F\left(\frac{q}{1+i\gamma}\right), \tag{18}$$

$$\xi = \frac{4\pi\omega n p^2 c c}{eH^3}. \tag{19}$$

Now, we analyze the solutions to Eq. (16). For this purpose, we consider the range of field strengths H corresponding to $\xi \gg 1$. In this range, the roots of Eq. (17) are large compared to unity. Approximate solutions can be obtained using an asymptotic expression for the function F at $q \gg 1$ in the form

$$F \simeq -\frac{3\pi i}{4|q|} + \frac{3}{q^2}. \tag{20}$$

On the right-hand side of expression (20), the first term associated with the collisionless cyclotron absorption of the wave by holes is dominant. The collisional terms proportional to the small quantity γ make an insignificant contribution. The second right-hand term in expression (20) corresponds to the nondissipative component of the hole conductivity, which, at $q \gg 1$, appears to be small compared to the electron Hall conductivity. From the physical standpoint, this result can be explained by the fact that holes move in a wave field which changes many times along their trajectory over the course of one cyclotron period. Therefore, on average, the wave field has a relatively weak effect on holes. At the same time, the wave field is nearly uniform for electrons and they efficiently interact with this field.

By substituting expression (20) into relationship (18), we can write the dispersion relation as follows:

$$q^2 = \xi\left[1 + \frac{3}{q^2}\left(\frac{i\pi}{4}|q| - 1\right)\right]. \tag{21}$$

This equation has two roots q_1 and q_2 with positive imaginary parts. Let us introduce the designations

$$h = \frac{H}{H_0}, \quad H_0 = \left(\frac{\pi\omega n p^2 c}{3e}\right)^{1/3}, \tag{22}$$

and rewrite the dispersion relation (21) in the form

$$q^2 - \frac{12}{h^3}\left[1 - \frac{3}{q^2}\left(1 - \frac{i\pi}{4}|q|\right)\right] = 0. \tag{23}$$

The solution to this equation will be sought using the method of successive approximations. First, we omit the imaginary term. As a result, the biquadratic equation has the roots $\pm q_H$ and $\pm q_D$, which can be written as

$$q_H \frac{\sqrt{6}}{h^{3/2}}\left(1 + \sqrt{1-h^3}\right)^{1/2}, \tag{24}$$

$$q_D = -\frac{\sqrt{6}}{h^{3/2}}\left(1 - \sqrt{1-h^3}\right)^{1/2}. \tag{25}$$

Both roots are real in the field range $H < H_0$ (where $h < 1$) and complex in the field range $H > H_0$. Hence, it follows that the quantity H_0 has the meaning of the upper limit of the range of magnetic field strengths at which the wave can propagate. For $H > H_0$, both modes are characterized by strong damping. On this basis, hereafter, we will consider only the range $H < H_0$.

Now, we replace $|q|$ by q_H in the imaginary term in expression (23) and solve the appropriate equation. As a result, we obtain

$$q_1 = \frac{\sqrt{6}}{h^{3/2}}\left[1 + \sqrt{1 - h^3\left(1 - i\frac{\pi}{4}q_H\right)}\right]^{1/2}. \tag{26}$$

With due regard for expression (12) relating q to k, the complex wave vector k_1 can be represented in the form

$$k_1 = \left(\frac{2\pi\omega ne}{cH}\right)^{1/2} \times \left[1 + \sqrt{1 - \left(\frac{H}{H_0}\right)^3\left(1 - i\frac{\pi}{4}q_H\right)}\right]^{1/2}. \tag{27}$$

This root of the equation is related to the helicon, whose spectrum is determined by the Hall conductivity and damping is due to cyclotron absorption of the wave by holes. As was noted above, the region of existence of the helicon in bismuth is limited by the upper threshold of the magnetic field. This distinguishes helicons in bismuth from those in alkali metals, which have no upper threshold. Another important difference is that helicon damping due to cyclotron absorption is enhanced with an increase in the field strength H.

Similarly, we can find the second root

$$q_2 = -\frac{\sqrt{6}}{h^{3/2}}\left[1 - \sqrt{1 - h^3\left(1 + i\frac{\pi}{4}q_D\right)}\right]^{1/2}. \tag{28}$$

This root is associated with the Doppler-shifted cyclotron resonance of holes. With a decrease in q^2, the hole contribution to the Hall conductivity increases and becomes larger than the electron contribution as q approaches unity; as a result, the Hall conductivity reverses sign. Therefore, the dispersion relation possesses the root $q_2 \simeq -\sqrt{3}$ at $h^3 \ll 1$. Since this root is associated with the Doppler-shifted cyclotron resonance, the corresponding mode can be referred to as the doppleron.

It is significant that both roots lie in the range $q^2 > 1$, which corresponds to cyclotron absorption. As a consequence, the imaginary parts of these roots are relatively large in magnitude (of the order of unity). Therefore, both modes are damped through a distance of the order of several displacements of holes over the cyclotron period. Thus, it is unlikely that these modes can be observed in bismuth in a linear regime.

3. The situation can be different in a nonlinear regime. For large amplitudes of the exciting field, the magnetic field of the radio wave can capture holes responsible for cyclotron absorption. The captured holes execute oscillations in the direction of wave propagation, which prevents absorption of the wave energy. The frequency Ω of these oscillations can be defined by the formula [1]

$$\Omega = \omega_c \left[\frac{H_\omega}{H} \sqrt{\frac{S(p_z)}{\pi}} \frac{\partial^2 S}{\partial p_z^2} \left(\frac{\partial S}{\partial p_z} \right)^{-1} \right]^{1/2} \Bigg|_{p_z = p_c}. \quad (29)$$

Here, H_ω is the amplitude of the magnetic field of the wave and

$$p_c = \frac{m_2 \omega_c}{k} \quad (30)$$

is the longitudinal momentum of the holes responsible for cyclotron absorption. By substituting the function $S(p_z)$ given by expression (2) and the longitudinal momentum (30) into formula (29), we obtain

$$\Omega = \omega_c \left[\frac{H_\omega}{H} \left(\frac{m_1}{m_2} \right)^{1/4} (q^2 - 1)^{1/2} \right]^{1/2}. \quad (31)$$

In the case when the frequency of oscillation of the captured holes is considerably higher than the frequency ν of hole collisions, the cyclotron absorption decreases by a factor of Ω/ν. This means that the function $F(t)$ in relationship (10) for the hole conductivity $\sigma_-^{(h)}$ can be replaced by the function

$$F_n(t) = \frac{3}{2t^2} \left[1 + \frac{t^2 - 1}{2t} \left(\ln \frac{t+1}{t-1} - i\pi \frac{\nu}{\Omega} \operatorname{sgn} t \right) \right]. \quad (32)$$

Therefore, in a strongly nonlinear regime, the roots $q_{1,2}$ can be written in the following form:

$$q_1 = \frac{\sqrt{6}}{h^{3/2}} [1 + \sqrt{1 - h^3(1 - i\Gamma_H)}]^{1/2}, \quad (33)$$

$$q_2 = -\frac{\sqrt{6}}{h^{3/2}} [1 - \sqrt{1 - h^3(1 - i\Gamma_D)}]^{1/2}, \quad (34)$$

$$\Gamma_H = \frac{\pi\gamma}{4} \left(\frac{q_H}{\sqrt{3}} \frac{H}{H_\omega} \right)^{1/2}, \quad (35)$$

$$\Gamma_D = \frac{\pi\gamma}{4} \left(-\frac{q_D}{\sqrt{3}} \frac{H}{H_\omega} \right)^{1/2}. \quad (36)$$

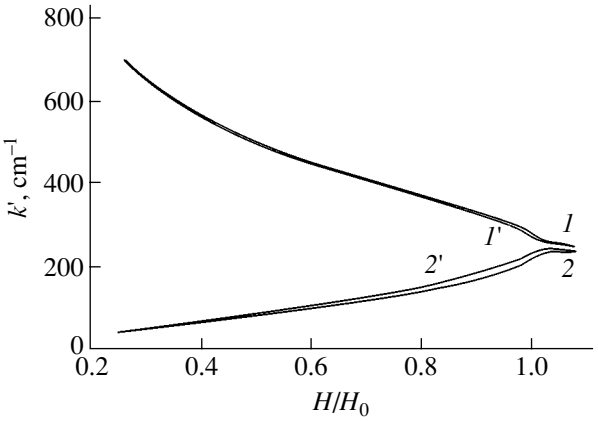

Fig. 1. Dependences of the wave vectors on the magnetic field strength H for (*1*, *1*') helicon and (*2*, *2*') doppleron.

Figure 1 shows the dependences $k'_{1,2} = \pm \mathrm{Re} k_{1,2}(H/H_0)$ in the range of magnetic strengths H from $0.3H_0$ to H_0. The calculation was performed at the frequency $\omega/2\pi$ = 10 MHz, collisional frequency $\nu = 10^8$ s^{-1} (the mean free path of holes is approximately equal to 2 mm), and exciting-field amplitude H_ω = 2 Oe. For this frequency ω, we have the threshold field H_0 = 30 Oe and the quantity $\gamma \approx 0.03$ at $H = H_0$; hence, the condition $\gamma \ll 1$ is well satisfied in the above range of field strengths H. The inequality $\xi \gg 1$ is also satisfied at $H < H_0$, because $\xi = 12(H_0/H)^3$. In Fig. 1, curves *1*, *1*' and *2*, *2*' refer to the helicon and the doppleron, respectively. Curves *1* and *2* were obtained from the numerical solution of the exact dispersion relation, and curves *1*' and *2*' were constructed according to formulas (33)–(36) based on the asymptotic expression for the hole conductivity at large values of q. It can be seen that curves *1* and *1*' almost coincide with each other, whereas curve *2*' lies slightly above curve *2*. This is quite reasonable, because the doppleron root is less than the helicon root and the use of the asymptotic formula for the hole conductivity $\sigma_-^{(h)}$ at $q^2 \gg 1$ leads to a larger error for the doppleron. However, even for the doppleron, the error is less than 10%.

The curves $k''_1 = \mathrm{Im} k_1(H/H_0)$ for the helicon damping are plotted in Fig. 2. Curves *1* and *2* represent the results of numerical calculations for a strongly nonlinear regime (at $H = 0.3H_0$ and H_ω = 2 Oe, the ratio ν/Ω is less than 0.1 and decreases with an increase in the magnetic field strength H) and a linear regime, respectively. The dependence of k''_2 on H for a nonlinear regime also fits curve *1* well. It can be seen that, at the given parameters, the capture of holes by the magnetic field of the radio wave very strongly suppresses cyclotron damping at $H < H_0$.

4. Let us now consider the case of excitation of a helicon and a doppleron in bismuth. The spatial distribution of the electric field $E(z)$ in a semi-infinite metal

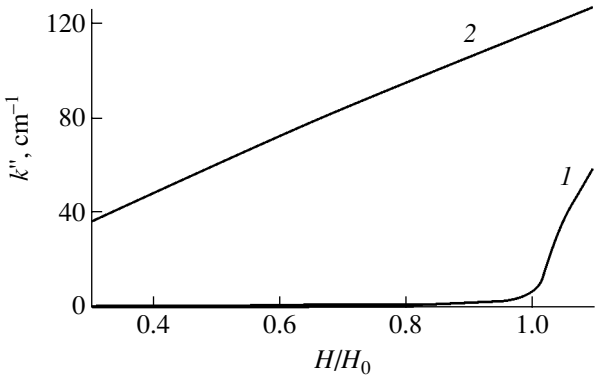

Fig. 2. Dependences of the helicon damping k_1'' on the magnetic field strength H for (*1*) nonlinear and (*2*) linear regimes.

upon specular reflection of carriers from the surface can be represented by the expression [11]

$$E(z) = -\frac{E'(0)}{\pi}\int_{-\infty}^{\infty}\frac{\exp(ikz)dk}{k^2 - 4\pi i\omega\sigma(k)/c^2}, \qquad (37)$$

where $E'(0)$ is the derivative dE/dz at the metal surface for $z = 0$.

Next, we change over to integration with respect to the dimensionless variable q and rewrite integral (37) in the form

$$E(z) = -\frac{E'(0)}{\pi}\frac{cp}{eH}\int_{-\infty}^{\infty}\frac{dq}{D(q)}\exp\left(iq\frac{eH}{cp}z\right), \qquad (38)$$

where $D(q)$ is given by formula (17).

The integrand in expression (38) has poles at the points q_1 and q_2 and the branch point $q = 1 + i\gamma$. If the contour of integration is closed in the upper half-plane q, integral (38) can be represented as the sum of two pole residues and the integral over banks of the cut passing from the branch point to infinity. The residues at the poles q_1 and q_2 represent the helicon and doppleron fields, and the integral over the banks of the cut is the Gantmakher–Kaner nonexponential component, which rapidly decays with an increase in the distance. We are interested in the penetration of the radio-frequency field through the bismuth plate, i.e., the electric field strength at considerable distances from the surface (at $z = d$, where d is the plate thickness). For these distances, the amplitude of the Gantmakher–Kaner component is negligible compared to the helicon and doppleron amplitudes. Therefore, at distances $z \gg cp/eH$, the field $E(z)$ consists of helicon and doppleron components:

$$E(z) = -2iE'(0)\frac{cp}{eH}\sum_{i=1}^{2}\frac{\exp(ik_i z)}{D'(q_i)}, \qquad (39)$$

where

$$D'(q_i) = \left.\frac{dD(q)}{dq}\right|_{q=q_i}. \qquad (40)$$

The surface impedance Z for a semi-infinite metal is proportional to the ratio of $E(0)$ to $E'(0)$; that is,

$$Z = \frac{4\pi i\omega}{c^2}\frac{E(0)}{E'(0)}. \qquad (41)$$

For a plate of thickness d, the impedance is determined by a similar expression whose numerator involves the electric field strength $E_d(0)$ at the surface of the metal plate. This quantity can be expressed through the helicon and doppleron components that have passed through the plate. In the case when the multiple specular reflections of carriers from the surfaces are ignored, the quantity $E_d(0)$ upon antisymmetric excitation (the plate is placed in a radio-frequency coil) is equal to the difference between the strength of the field excited on one surface of the plate and the strength of the field that has passed through the plate on the other surface:

$$E_d(0) = E(0) - E(d), \qquad (42)$$

where $E(0)$ and $E(d)$ are the values of function (39) at $z = 0$ and d, respectively. Consequently, the field strength at the plate surface can be written in the form

$$E_d(0) = -2iE'(0)\frac{cp}{eH}\sum_{i=1}^{2}\frac{1 - \exp(ik_i z)}{D'(q_i)}. \qquad (43)$$

Making allowance for the multiple reflections of carriers from the plate surface, each term in sum (43) includes an additional factor, that is,

$$[1 + \exp(ik_i z)]^{-1}.$$

As a result, the expression for the function $E_d(0)$ takes the form

$$E_d(0) = -2iE'(0)\frac{cp}{eH}\sum_{i=1}^{2}\frac{1}{D'(q_i)}\frac{1 - \exp(ik_i z)}{1 + \exp(ik_i z)}. \qquad (44)$$

Consequently, the impedance Z_d of the plate can be written in the following form:

$$Z_d = \frac{8\pi\omega p}{ceH}\sum_{i=1}^{2}\frac{1}{D'(q_i)}\frac{1 - \exp(ik_i z)}{1 + \exp(ik_i z)}. \qquad (45)$$

The results of numerical calculations of the surface resistance $R = \mathrm{Re}\,Z_d$ for the above parameters and thickness $d = 0.05$ cm are presented in Fig. 3. The dependence $R(H)$ exhibits maxima for magnetic field strengths H at which the plate thickness is a multiple of an odd number of helicon or doppleron half-waves and a standing wave is excited in the sample. Mathematically, this manifests itself in a drastic decrease in the denominator in the corresponding term in expression (45). An analysis demonstrates that the first maximum is associated with the

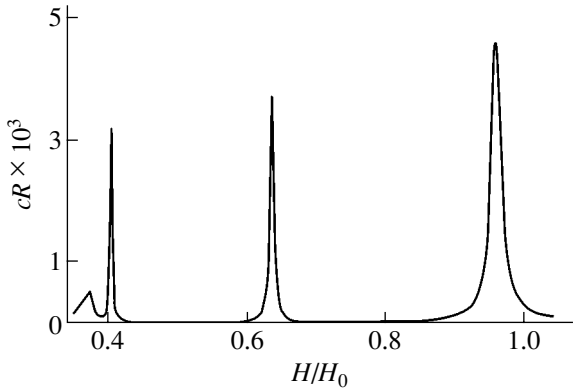

Fig. 3. Dependence of the surface resistance $R(H)$ of a bismuth plate in the strongly nonlinear regime at a frequency of 10 MHz ($H_0 \simeq 30$ Oe).

excitation of the doppleron, the second and third maxima are due to the excitation of the helicon, and the fourth maximum is a superposition of the helicon and doppleron signals.

The nonlinear effect described above appears to be extremely strong; specifically, the curve $R(H)$ in the linear case virtually merges with the abscissa axis in Fig. 3. Thus, the suppression of the cyclotron absorption in the nonlinear regime leads to the fact that the transmittance of the plate at the maxima increases by more than two orders of magnitude.

REFERENCES

1. I. F. Voloshin, G. A. Vugal'ter, V. Ya. Demikhovskiĭ, *et al.*, Zh. Éksp. Teor. Fiz. **73** (4), 1503 (1977) [Sov. Phys. JETP **46**, 790 (1977)].
2. V. G. Skobov and A. S. Chernov, Pis'ma Zh. Éksp. Teor. Fiz. **61** (12), 980 (1995) [JETP Lett. **61**, 1012 (1995)].
3. V. G. Skobov and A. S. Chernov, Zh. Éksp. Teor. Fiz. **109** (3), 992 (1996) [JETP **82**, 535 (1996)].
4. V. G. Skobov and A. S. Chernov, Zh. Éksp. Teor. Fiz. **114** (2), 725 (1998) [JETP **87**, 396 (1998)].
5. A. S. Chernov and V. G. Skobov, Phys. Lett. A **205**, 81 (1995).
6. V. G. Skobov and A. S. Chernov, Zh. Éksp. Teor. Fiz. **119** (2), 388 (2001) [JETP **92**, 338 (2001)].
7. E. A. Kaner and V. G. Skobov, Adv. Phys. **17**, 605 (1968).
8. V. S. Édel'man, Usp. Fiz. Nauk **102** (1), 55 (1970) [Sov. Phys.–Usp. **13**, 583 (1970)].
9. A. P. Cracknell and K. C. Wong, *The Fermi Surface: Its Concept, Determination, and Use in the Physics of Metals* (Clarendon, Oxford, 1973; Atomizdat, Moscow, 1978).
10. O. V. Konstantinov and V. I. Perel', Zh. Éksp. Teor. Fiz. **38**, 161 (1960) [Sov. Phys. JETP **11**, 117 (1960)].
11. G. E. Reuter and E. H. Sondheimer, Proc. R. Soc. London, Ser. A **195**, 336 (1946).

Translated by O. Borovik-Romanova

Physics of the Solid State, Vol. 45, No. 10, 2003, pp. 1866–1873. Translated from Fizika Tverdogo Tela, Vol. 45, No. 10, 2003, pp. 1776–1783.

METALS AND SUPERCONDUCTORS

Transport and Magnetic Properties of $Y_{3/4}Lu_{1/4}Ba_2Cu_3O_7 + Y_3Fe_5O_{12}$ Composites Representing a Josephson-Type Superconductor–Ferrimagnet–Superconductor Weak-Link Network

K. A. Shaĭkhutdinov, D. A. Balaev, S. I. Popkov, and M. I. Petrov

Kirensky Institute of Physics, Siberian Division, Russian Academy of Sciences, Akademgorodok, Krasnoyarsk, 660036 Russia

e-mail: smp@iph.krasn.ru

Received February 25, 2003

Abstract—$Y_{3/4}Lu_{1/4}Ba_2Cu_3O_7 + Y_3Fe_5O_{12}$ composites with different volume ratios of the starting components were synthesized. The composites model an S–F–S Josephson junction network, where S stands for a superconductor and F, for a ferrimagnet. A study of the transport characteristics of the composites revealed that the temperature behavior of the electrical resistivity $\rho(T)$ below the superconducting transition point T_C is different in two regions separated by a temperature T_m. Below T_m, the current–voltage characteristics of the composites are nonlinear, while in the interval from T_C to T_m the values of $\rho(T)$ do not depend on the transport current j and magnetic field H. This behavior of $\rho(T, j)$ and $\rho(T, H)$ is assigned to specific features of the tunneling of superconducting carriers through the ferrimagnetic layers separating HTSC grains in the composite. Magnetic measurements showed the diamagnetic response of HTSC grains to be lower in composites with a ferrimagnet. © *2003 MAIK "Nauka/Interperiodica".*

1. INTRODUCTION

Two-phase composite materials based on high-temperature superconductors (HTSCs) are of considerable interest from both a practical [1–8] and a scientific [2, 3, 5, 6, 9–14] viewpoint. The latter is due to these objects representing a Josephson-coupled weak-link network. The second, nonsuperconducting, component of the composite (insulator, semiconductor, normal metal) acts as an artificially created weak link between HTSC grains. By properly varying the volume concentration ratio of the starting components in such composites, one can vary the effective extent (or "strength") of the weak link within a broad range.

Obviously enough, a single Josephson junction would be an ideal object for investigation, but the small coherence length and the strong chemical reactivity of HTSCs make fabrication and study of such structures a difficult task. However, as shown earlier [10, 11, 14, 15], the transport characteristics (the temperature dependences of electrical resistivity $\rho(T)$ and of the critical current $j_C(T)$, the current–voltage curves) of HTSC-based two-phase composite materials reflect the main features of superconducting carrier flow through a single Josephson junction of a certain effective extension in space, while the relative simplicity of fabrication of such materials makes them attractive objects for studies and for possible applications [7, 8].

We recently studied the transport properties of composites with magnetic impurities in a nonsuperconducting composite (HTSC + $Cu_{1-x}Ni_xO$ ($0 < x < 0.06$) [15], HTSC + $BaPb_{0.9}Fe_{0.1}O_3$, HTSC + $BaPb_{0.9}Ni_{0.1}O_3$ [16]) and found that the superconducting properties of such composites are strongly suppressed by the interaction of the spins of superconducting carriers with magnetic moments during their crossing of the nonsuperconducting layer. Investigation of the transport properties of the composite HTSC + paramagnetic insulator ($NiTiO_3$) [17, 18] revealed not only a strong suppression of superconducting properties but also an anomalous behavior of the temperature dependences of electrical resistivity. Within the temperature interval from the onset of the superconducting transition in the HTSC grains (at T_C) to a certain temperature T_m, the electrical resistivity does not depend on the magnitude of the transport current and applied magnetic field (the I–V curves are linear) and becomes a function of these quantities only below T_m, a feature characteristic of Josephson-type weak links. This anomalous behavior of the temperature dependence of electrical resistivity of the HTSC + $NiTiO_3$ composites was attributed to exchange interaction of superconducting-carrier spins with the magnetic moments of nickel in the paramagnetic phase. This interaction results in an anomaly in the temperature behavior of electrical resistivity at the melting temperature of the Abrikosov vortex lattice in HTSC grains [17, 18].

The next step in investigating composites with magnetically active nonsuperconducting components was a study of HTSC + ferrimagnet composites. Single S–F–S structures (S stands for a superconductor, and F, for a

ferro- or ferrimagnet) have become a subject of intense current research, both theoretical [19–26] and experimental [27–29], because they exhibit interesting phenomena, such as a nonmonotonic dependence of the critical current on temperature [25], a manifestation of π coupling [19, 24, 25], a reduction of superconducting properties, and a characteristic behavior of magnetoresistance [27]. Of the large family of ferro- and ferrimagnetic compounds, we chose $Y_3Fe_5O_{12}$ (classical yttrium–iron garnet), an insulator which interacts weakly enough with the 1-2-3 HTSC structure. To establish the effect of ferrimagnetic ordering in the insulating spacer on the transport properties of composites, we also prepared and studied HTSC + $Y_3Al_5O_{12}$ reference composites, because the $Y_3Al_5O_{12}$ compound is isostructural to $Y_3Fe_5O_{12}$ and nonmagnetic.

2. EXPERIMENTAL

The $Y_{3/4}Lu_{1/4}Ba_2Cu_3O_7$ polycrystalline HTSC was prepared using standard ceramic technology. The nonsuperconducting components of the composites, namely, $Y_3Fe_5O_{12}$ and $Y_3Al_5O_{12}$, were synthesized from Y_2O_3 and Fe_3O_4, $Al(OH)_3$, accordingly, at a temperature of 1250°C for 48 h with three intermediate grindings. After that, the starting components of the composites to be obtained were taken in correct proportion, ground thoroughly in an agate mortar, and pelletized. The pellets were put into preliminarily heated boats and placed in a furnace heated to 910°C for 2 min. They were subsequently kept in another furnace for 3 h at t = 350°C and cooled with the furnace. This method of rapid sintering [11] was employed to prepare composite samples with different volume contents of the HTSC and nonsuperconducting components $Y_3Fe_5O_{12}$ and $Y_3Al_5O_{12}$. We denote our composite materials by S + *V*YIG and S + *V*YAlG, where S stands for the $Y_{3/4}Lu_{1/4}Ba_2Cu_3O_7$ HTSC and *V* is the volume concentration of $Y_3Fe_5O_{12}$ (YIG) or $Y_3Al_5O_{12}$ (YAlG).

The transport characteristics [$\rho(T)$ and I–V curves] were measured by the standard four-probe technique. The critical current was derived from the initial part of the I–V curve using the standard 1 μV/cm criterion [30]. The measurement of the transport characteristics in magnetic fields of up to 500 Oe was performed with a copper solenoid and in magnetic fields above 500 Oe, with a superconducting coil. The transport current j was passed through the sample perpendicular to the magnetic field H. The magnetic measurements were conducted on an automated vibrating-sample magnetometer [31].

3. RESULTS AND DISCUSSION

3.1. Characterization of the Composites

X-ray diffraction measurements of the $Y_{3/4}Lu_{1/4}Ba_2Cu_3O_7 + Y_3Fe_5O_{12}$ and $Y_{3/4}Lu_{1/4}Ba_2Cu_3O_7 + Y_3Al_5O_{12}$ composite samples revealed the existence of two phases only, with the 1-2-3 and garnet structures; no foreign reflections were present (within the accuracy of the x-ray analysis). The relative reflection intensities due to the $Y_{3/4}Lu_{1/4}Ba_2Cu_3O_7$ and $Y_3Fe_5O_{12}$, $Y_3Al_5O_{12}$ phases were in agreement with the volume content of the starting components in the composites. A study of the temperature dependences of the composite magnetization $M(T)$ showed the superconducting-transition onset temperature T_C to be the same for all samples, 93.5 K, which coincides with the value of T_C of the starting HTSC $Y_{3/4}Lu_{1/4}Ba_2Cu_3O_7$. The diamagnetic response decreases with increasing volume content of the nonsuperconducting component ($Y_3Fe_5O_{12}$, $Y_3Al_5O_{12}$) in the composite. Thus, x-ray diffraction and magnetic measurements permit the conclusion that HTSC-based composite materials prepared by fast sintering are indeed two-phase materials with no foreign phases present.

3.2. Transport Properties of the Composites

Figure 1 shows plots of the electrical resistivity $\rho(T)$ of the composite samples obtained in the 4.2- to 300-K temperature interval. The abrupt decrease in resistivity occurring at T_C = 93.5 K signals the transition of HTSC grains to the superconducting state. Above the transition point, the $\rho(T)$ curves are quasi-semiconducting in character. The ratio ρ(93.5 K)/ρ(300 K) grows with increasing volume content of the nonsuperconducting component in the composites. This behavior of the $\rho(T)$ relations suggests that the transport current flows through both HTSC and nonsuperconducting grains.

Below T_C, the course of the $\rho(T)$ dependences is determined by the superconducting transition in Josephson-type weak links [10, 11, 14–18]. In the reference composites HTSC + $Y_3Al_5O_{12}$, this part of the $\rho(T)$ curves exhibits a strong dependence on transport current j and external magnetic field H. Figure 2 displays $\rho(T, j)$ and $\rho(T, H)$ dependences (Figs. 2a, 2b, accordingly) obtained on the S + 15YAlG sample. We readily see that the temperature T_{C0} at which the electrical resistivity ρ becomes negligibly small ($<10^{-6}$ Ω cm) decreases as the transport current j and magnetic field H grow. This behavior of the $\rho(T, j)$ and $\rho(T, H)$ dependences is typical of the Josephson-type superconductor–insulator–superconductor (S–I–S) weak-link network; it was observed earlier on composite samples HTSC + CuO [10] and HTSC + $MgTiO_3$ [17] and has been accounted for in terms of the thermally activated phase slippage (TAPS) [32] and thermally activated vortex flow mechanisms [33]. The pattern of the $\rho(T, j)$ dependence observed in the HTSC + $Y_3Al_5O_{12}$ insulator composites under study has also been described by the TAPS mechanism [32], but its relevant analysis is beyond the scope of the present communication.

According to the thermally activated vortex flow model [33], the resistive-transition width ΔT_{C0} of S–I–S-type Josephson weak links as a function of the applied magnetic field H is defined as $\Delta T_{C0} = T_{C0}(H =$

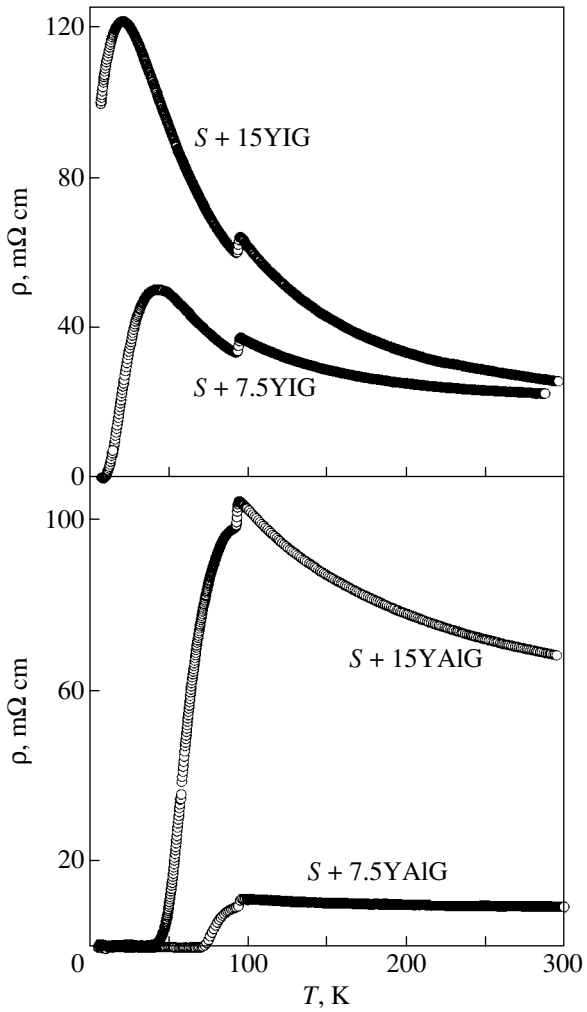

Fig. 1. Temperature dependences of electrical resistivity $\rho(T)$ of samples of HTSC + $Y_3Fe_5O_{12}$ and HTSC + $Y_3Al_5O_{12}$ obtained in the range 4.2–300 K.

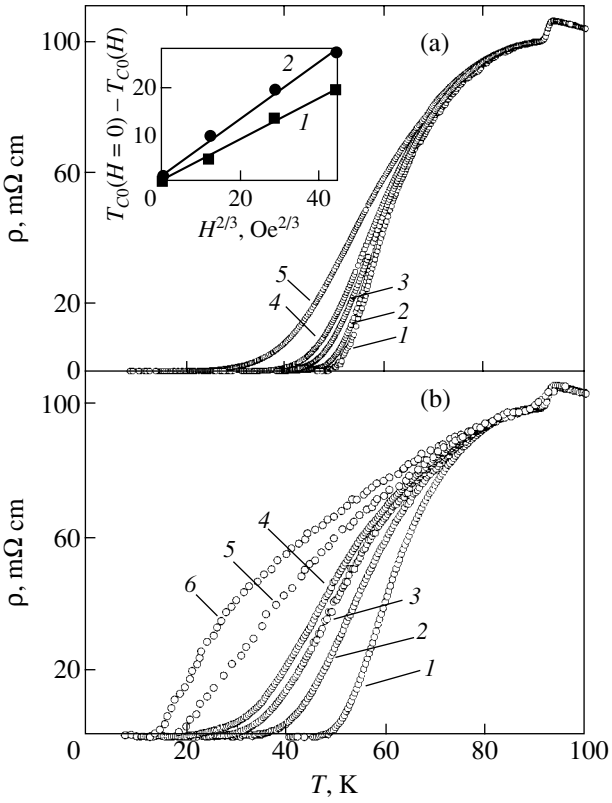

Fig. 2. Temperature dependences of electrical resistivity $\rho(T)$ of samples of HTSC + 15 vol % $Y_3Al_5O_{12}$ (S + 15YAlG) obtained at various values of (a) transport current j and (b) applied magnetic field H. (a) (*1*) j = 3.4, (*2*) 34, (*3*) 170, (*4*) 340, and (*5*) 1000 mA/cm^2; (b) (*1*) H = 0, (*2*) 37, (*3*) 150, (*4*) 292, (*5*) 2000, and (*6*) 60 000 Oe. Measuring current j = 3.4 mA/cm^2. Inset: $\Delta T_{C0} = T_{C0}(H = 0) - T_{C0}(H)$ relations plotted vs. $H^{2/3}$ for R = 0 for (*1*) S + 7.5YAlG and (*2*) S + 15YAlG.

0, R = 0) – $T_{C0}(H, R = 0)$ and scales as $H^{2/3}$. This dependence was observed experimentally on polycrystalline HTSCs [33] and HTSC + CuO composite materials [10]. The inset to Fig. 2a plots $\Delta T_{C0} = T_{C0}(H = 0, R = 0) - T_{C0}(H, R = 0)$ vs. $H^{2/3}$ for samples S + 7.5YAlG and S + 15YAlG. These dependences are seen to be close to linear in fields of up to 300 Oe. Thus, the magnetoresistive properties of the reference composites HTSC + $Y_3Al_5O_{12}$ are similar in character to those of the HTSC + insulator composites [10] and polycrystalline HTSCs [33].

HTSC + ferrimagnet composites exhibit a radically different pattern of transport properties (Figs. 3, 4). Below the temperature T_C at which $Y_{3/4}Lu_{1/4}Ba_2Cu_3O_7$ is transferred to the superconducting state (93.5 K), there is an interval in which the electrical resistivity $\rho(T)$ behaves in a semiconducting manner, as is the case above T_C. The strong dependence of electrical resistivity ρ on transport current j and magnetic field H, which is typical of a Josephson-type weak-link network, is observed only below a certain temperature T_m. The value of T_m depends on the volume concentration of the ferrimagnet in the composite, i.e., on the effective extension of weak links in space [10, 11]. For the S + 15YIG sample, we have $T_m \approx 40$ K; for S + 7.5YIG, $T_m \approx 55$ K; and for S + 3.75YIG, $T_m \approx 65$ K. The I–V curves of the samples are linear in the T_C–T_m range (Fig. 5). For the S + 15YIG sample, there is no critical current j_C at T = 4.2 K; for the S + 7.5YIG sample, j_C(4.2 K) = 0.025 A/cm^2; and for S + 3.75YIG, j_C(4.2 K) = 1.12 A/cm^2. The superconducting properties of the HTSC + ferrimagnet composites are strongly suppressed at relatively small values of the transport current and of the magnetic field. For instance, the temperature behavior of the electrical resistivity $\rho(T)$ of the S + 15YIG sample (Fig. 4) at a threshold transport current j_{cr} = 0.6 A/cm^2 (H = 0) or at a threshold external magnetic field H_{cr} = 1900 Oe (measuring current density j = 0.015 A/cm^2) continues to have the semiconducting character observed in the T_m–T_C interval.

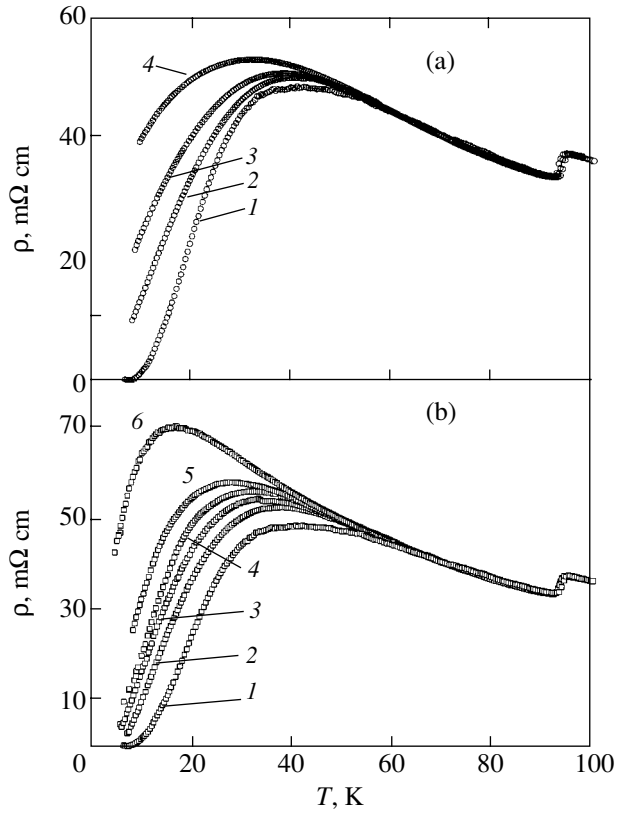

Fig. 3. Temperature dependences of electrical resistivity ρ(*T*) of a sample of HTSC + 7.5 vol % $Y_3Fe_5O_{12}$ (S + 7.5YIG) obtained at various values of (a) transport current *j* and (b) applied magnetic field *H*. (a) (*1*) *j* = 10, (*2*) 50, (*3*) 130, and (*4*) 510 mA/cm^2; (b) (*1*) *H* = 0, (*2*) 40, (*3*) 80, (*4*) 150, (*5*) 290, and (*6*) 2100 Oe. Measuring current *j* = 10 mA/cm^2.

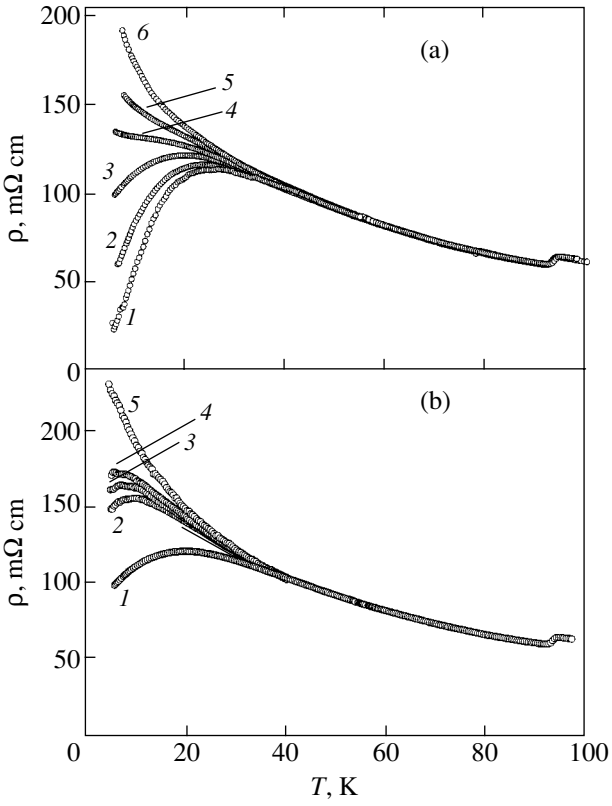

Fig. 4. Temperature dependences of electrical resistivity ρ(*T*) of a sample of HTSC + 15 vol % $Y_3Fe_5O_{12}$ (S + 15YIG) obtained at various values of (a) transport current *j* and (b) applied magnetic field *H*. (a) (*1*) *j* = 1.5, (*2*) 7.7, (*3*) 15, (*4*) 77, (*5*) 150, and (*6*) 600 mA/cm^2; (b) (*1*) *H* = 0, (*2*) 40, (*3*) 80, (*4*) 150, and (*5*) 1900 Oe. Measuring current *j* = 15 mA/cm^2.

Thus, the transport properties of HTSC + ferrimagnet composites differ radically from those of the reference composites HTSC + $Y_3Al_5O_{12}$ nonmagnetic insulator. The data presented in Figs. 1, 3, and 4 show that the *I–V* curves of the HTSC + ferrimagnet Josephson junction network are nonlinear only in the temperature interval below T_m, whereas for the reference composites HTSC + $Y_3Al_5O_{12}$ the *I–V* curves remain nonlinear up to T_C.

We believe that this effect cannot be due to the nonsuperconducting boundaries being distributed in thickness or to the technology of preparation of the composites, because the magnetoresistive properties of the reference composites $Y_{3/4}Lu_{1/4}Ba_2Cu_3O_7$ + $Y_3Al_5O_{12}$ are well described in terms of the TAPS mechanism [32] and thermally activated vortex flow [33]. Moreover, our results correlate with the data obtained in a study [27] of single superconductor–ferromagnet–superconductor Josephson junctions, where niobium served as the superconductor and gadolinium, as the ferromagnet. The ρ(*T*) dependences of a single Nb/Al/Gd/Al/Nb Josephson junction reported on in [27] also exhibit two different regions below the T_C of niobium (≈7.6 K) separated by a temperature T_m. At temperatures below T_m, the *I–V* curves are nonlinear, while in the T_C–T_m interval the values of ρ(*T*) do not depend on the applied transport current *j*. The values of T_m are ≈5.2 K for the Gd thickness 4 nm and ≈4 K for the thickness ≈8 nm.

We propose two possible explanations to account for the unusual transport properties of the HTSC + ferrimagnet composites.

The unusual pattern of the ρ(*T*, *j*) and ρ(*T*, *H*) dependences for the HTSC + $NiTiO_3$ paramagnetic insulator composites was qualitatively interpreted in [17, 18] in terms of a hypothesis assuming the formation of an Abrikosov vortex lattice in HTSC grains. Indeed, the magnetically active component of the composite induces a certain effective field that penetrates in the form of Abrikosov vortices into the HTSC grains to the Josephson penetration depth (~1000 Å [34]). This field at the HTSC/$Y_3Fe_5O_{12}$ interface is approximately equal in magnitude to the effective field (10^6 Oe for $Y_3Fe_5O_{12}$ [35]). In flowing through the composite, the transport current inevitably crosses both the HTSC grains and the ferrimagnet. Therefore, the current should also flow through the region of the HTSC grains where the Abrikosov vortices formed. Assuming that the temperature

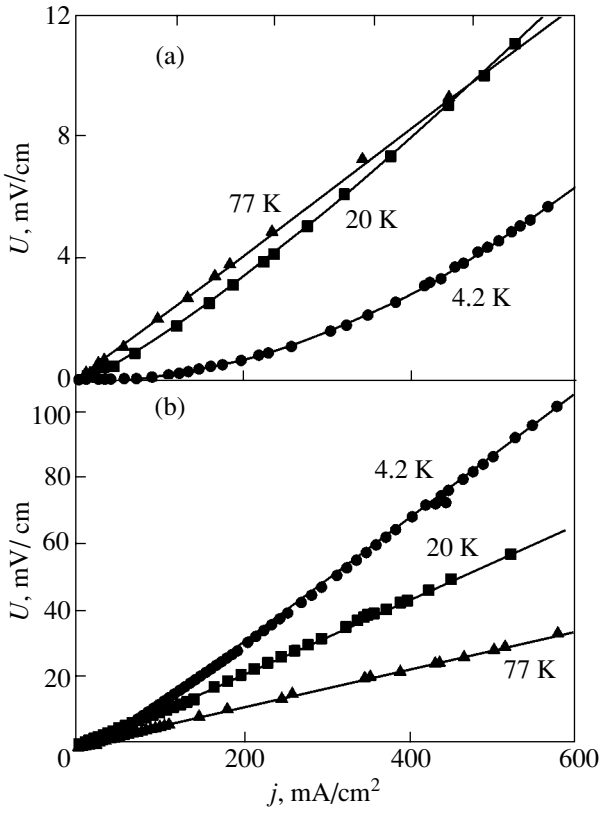

Fig. 5. *I–V* characteristics of samples (a) S + 7.5YIG and (b) S + 15YIG obtained at various temperatures.

T_m observed by us is the melting point of the Abrikosov vortex lattice, this hypothesis can account for the unusual character of the ρ(*T*) dependences of the HTSC + ferrimagnet composites. In the T_C–T_m interval, vortices move without pinning and the resistivity does not depend on the transport current and magnetic field. Below T_m, the vortices are pinned inside the HTSC grains, which results in the *I–V* curves being nonlinear [36]. An increase in the volume concentration of a ferrimagnet in the composite corresponds to an increase in the HTSC/$Y_3Fe_5O_{12}$ interface area, which brings about an increase in the number of Abrikosov vortices and a decrease in the T_m temperature.

Another explanation of the results obtained is conceivable. A theoretical study was made in [21] of the stationary Josephson effect with ordered magnetic moments localized in the barrier. It is believed [21] that the Josephson superconducting current vanishes at a certain critical barrier thickness because of the Cooper pairs being scattered by magnetic moments in the barrier. On the other hand, the TAPS effect [32] accounts for the experimentally observed vanishing of the critical current in the S–I–S structure at temperatures close to the transition temperature of the superconducting banks due to the temperature-induced voltage fluctuations at the junction. Substitution of $I_1 = 0$ (I_1 is the critical current of the S–I–S junction in the absence of thermal fluctuations) into the expression for the *I–V* characteristic in the TAPS model [32] results in a linear *U*(*I*) dependence. The vanishing of the critical current I_1 in the S–F–S Josephson junction network predicted theoretically [21] for a single junction transforms the linear *I–V* curves into nonlinear curves at the temperature T_m. Thus, theory [21] and the TAPS mechanism [32] can provide a qualitative interpretation for the ρ(*T*) behavior of the HTSC + ferrimagnet composites. Unfortunately, theory [21] yields only a very rough estimate, because ferrimagnetic ordering is not taken into consideration. Moreover, the results obtained for HTSCs and low-temperature superconductors may differ from one another, a point mentioned in [25].

3.3. Magnetic Properties of HTSC + Ferrimagnet Composites

Figure 6 presents field dependences of the magnetization *M*(*H*) of samples with different volume contents of nonsuperconducting components, namely, S + 15YIG (on the right) and S + 15YAlG (on the left) measured in the 4.2- to 100-K temperature interval. The hysteresis loops of the sample with $Y_3Al_5O_{12}$ are typical of HTSCs [34]. The *M*(*H*) plots of the sample with $Y_3Fe_5O_{12}$ actually represent a superposition of hysteresis loops of the superconductor and the ferrimagnet, which is clearly seen from the *M*(*H*) graphs recorded at *T* = 61 and 100 K (Fig. 6). Thus, magnetic measurements provide additional evidence for the existence of only two phases in the composite, namely, $Y_{3/4}Lu_{1/4}Ba_2Cu_3O_7$ and $Y_3Fe_5O_{12}$.

Figure 7 specifies the diamagnetic responses *M*(*H*) obtained at *T* = 4.2 K from the HTSC phase in the composites S + 15YIG and S + 15YAlG. To select the diamagnetic response from the HTSC phase in a composite containing a ferrimagnet, the response due to the $Y_3Fe_5O_{12}$ ferrimagnet phase was subtracted from the integral *M*(*H*) curve (Fig. 6, *T* = 4.2 K) with allowance for the temperature dependence *M*(*T*) of this response. As seen from Fig. 7, the diamagnetic response of the HTSC phase present in the composite with the ferrimagnetic insulator (S + 15YIG) is smaller than that for the composite with the nonmagnetic insulator (S + 15YAlG). Because the technology of preparation and the volume concentrations of the components of the composites are the same in both cases, this decrease in the diamagnetic response can be accounted for by suppression of the superconducting properties in the surface layers of HTSC grains under the influence of the ferrimagnet. Indeed, the magnetically active component $Y_3Fe_5O_{12}$ of the composite induces a magnetic field, which penetrates into the HTSC grains and destroys the superconducting state.

As follows from Fig. 7, the superconductor with suppressed superconducting properties takes up 30% of the volume. Assuming the HTSC grains in the composite to have spherical shape with an average diameter of 1.5 μm (as derived from scanning electron microscopy

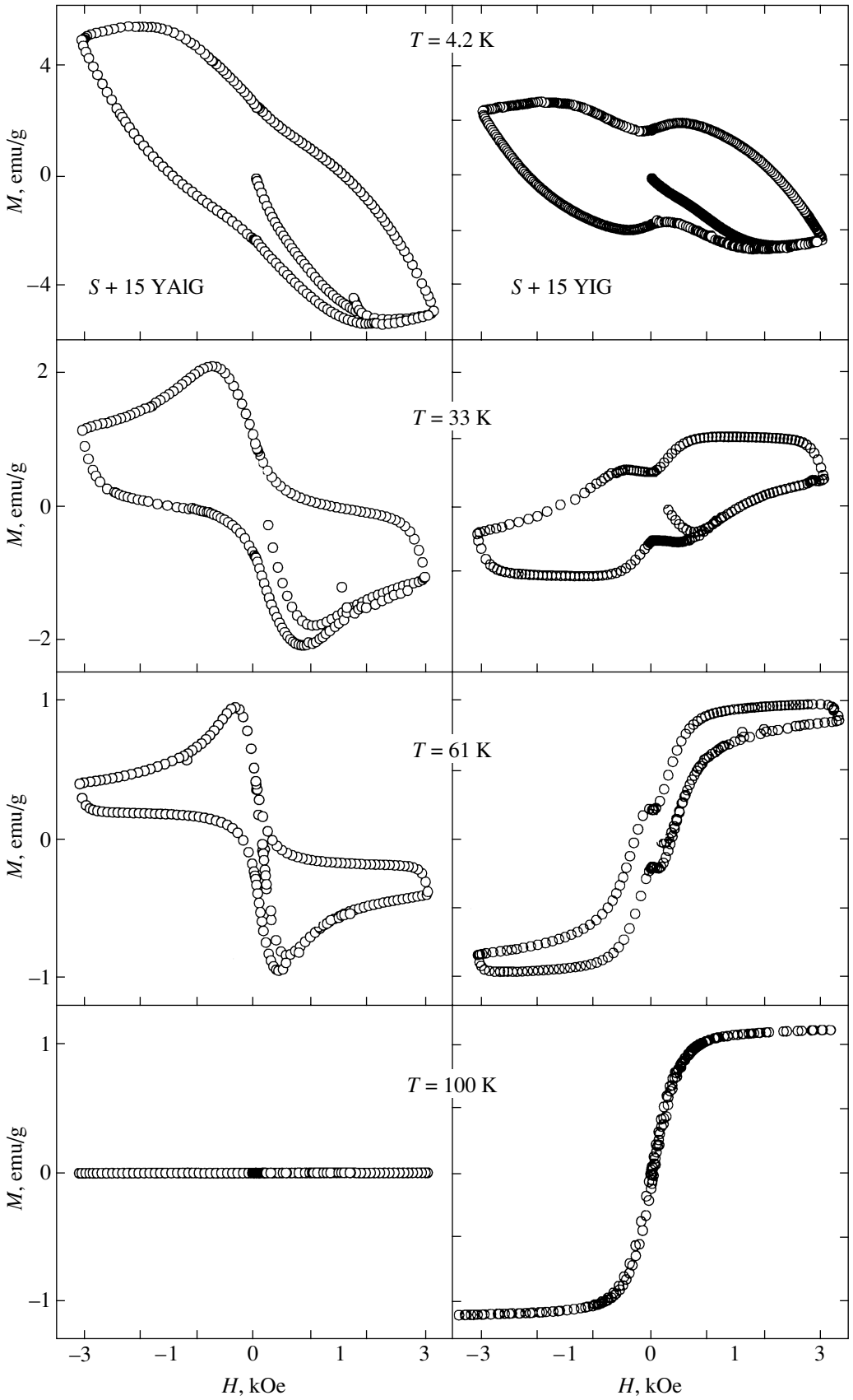

Fig. 6. *M*(*H*) plots of samples S + 15YAlG and S + 15YIG obtained at various temperatures.

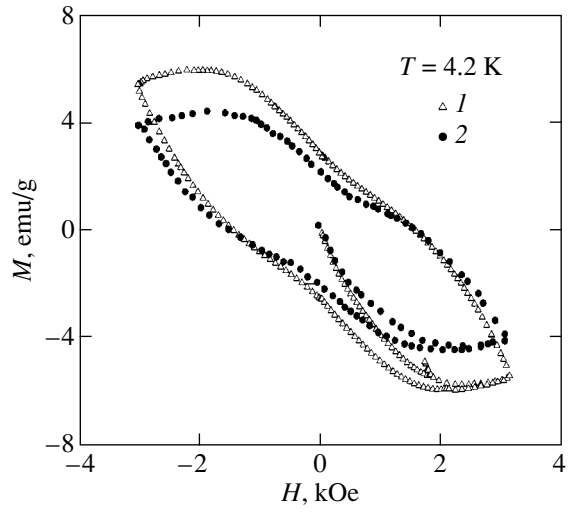

Fig. 7. Diamagnetic response $M(H)$ measured for different HTSC phases in the composites at 4.2 K. (*1*) S + 15YAlG reference composites and (*2*) S + 15YIG composites.

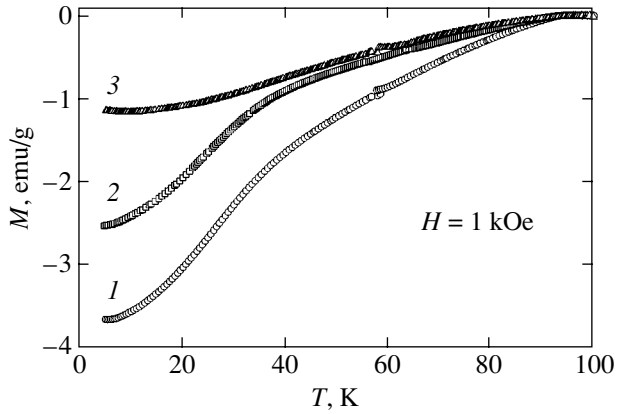

Fig. 8. Diamagnetic response $M(T)$ measured at $H = 1$ kOe for different HTSC phases in the composites. (*1*) S + 15YAlG reference composites, (*2*) S + 15YIG composites, and (*3*) difference between relations *1* and *2*.

data), estimation of the HTSC layer "suppressed" by its proximity to the ferrimagnet yields a thickness of ≈800 Å, a figure that correlates with the penetration depth of ~1000 Å for $YBa_2Cu_3O_7$ [34]. A similar estimate (≈800 Å) is obtained from the temperature dependences of magnetization $M(T)$ (Fig. 8). Figure 8 presents the diamagnetic response $M(T)$ due to the HTSC phases in the S + 15YIG and S + 15YAlG composites, as well as the difference between these curves.

4. CONLUSIONS

Thus, we have studied the transport and magnetic properties of the $Y_{3/4}Lu_{1/4}Ba_2Cu_3O_7 + Y_3Fe_5O_{12}$ composites, which represent a superconductor–ferrimagnet–superconductor Josephson junction network. Besides a strong suppression of transport properties (as compared to the HTSC + $Y_3Al_5O_{12}$ nonmagnetic-insulator reference composites), the HTSC + ferrimagnet composites exhibit radically different temperature dependences of the electrical resistivity. Below the transition temperature in the HTSC grains, the $\rho(T)$ dependence can be divided into two dissimilar ranges by a temperature T_m. At temperatures below T_m, the I–V curves of the HTSC + ferrimagnet composites are nonlinear (a feature characteristic of Josephson-type weak links), whereas within the T_C–T_m interval the behavior of $\rho(T)$ does not depend on the transport current and magnetic field. The resistive state of the HTSC + $Y_3Al_5O_{12}$ reference composites can be readily explained in terms of the thermally activated phase slippage (TAPS) mechanism [32] acting in the S–I–S Josephson junction network.

Magnetic measurements carried out on the composites showed that the diamagnetic response due to the HTSC phase in composites with a ferrimagnetic insulator is smaller than that of the HTSC phase in composites with a nonmagnetic insulator. This decrease in the diamagnetic response can be assigned to suppression of the superconducting properties of HTSC grains in a surface layer of thickness equal to the penetration depth of the magnetic field from the ferrimagnetic component of the composite.

ACKNOWLEDGMENTS

The authors are indebted to A.D. Balaev for his assistance in the magnetic measurements and to A.F. Bovina for x-ray diffraction analysis of the samples.

This study was supported jointly by the Russian Foundation for Basic Research and Krasnoyarsk Science Foundation (project Enisei, no. 02-02-97711) and the Lavrent'ev Competition for Young Scientists (grant, SD RAS, 2002).

REFERENCES

1. G. Xiao, F. H. Stretz, M. Z. Cieplak, *et al.*, Phys. Rev. B **38** (1), 776 (1988).
2. B. R. Weinberger, L. Lynds, D. M. Potrepka, *et al.*, Physica C (Amsterdam) **161**, 91 (1989).
3. J. Koshy, K. V. Paulose, M. K. Jayaraj, and A. D. Damodaran, Phys. Rev. B **47** (22), 15304 (1993).
4. E. Bruneel and S. Hoste, Int. J. Inorg. Mater., No. 1, 385 (1999).
5. D. Berling, B. Loegel, A. Mehdaouli, *et al.*, Supercond. Sci. Technol. **11** (11), 1292 (1998).
6. M. I. Petrov, D. A. Balaev, D. M. Gohfeld, *et al.*, Physica C (Amsterdam) **314**, 51 (1999).
7. D. A. Balaev, D. M. Gokhfel'd, S. I. Popkov, *et al.*, Pis'ma Zh. Tekh. Fiz. **27** (22), 45 (2001) [Tech. Phys. Lett. **27**, 952 (2001)].

8. A. G. Mamalis, S. G. Ovchinnikov, M. I. Petrov, *et al.*, Physica C (Amsterdam) **364–365**, 174 (2001).
9. J. J. Calabrese, M. A. Dubson, and J. C. Garland, J. Appl. Phys. **72** (7), 2958 (1999).
10. M. I. Petrov, D. A. Balaev, K. A. Shaĭkhutdinov, and K. S. Aleksandrov, Fiz. Tverd. Tela (St. Petersburg) **41** (6), 969 (1999) [Phys. Solid State **41**, 881 (1999)].
11. M. I. Petrov, D. A. Balaev, K. A. Shaihutdinov, and K. S. Aleksandrov, Supercond. Sci. Technol. **14** (9), 798 (2001).
12. J. Jung, M. A.-K. Mohamed, I. Isaak, and L. Friedrich, Phys. Rev. B **49** (17), 12188 (1994).
13. B. I. Smirnov, T. S. Orlova, and N. Kudymov, Fiz. Tverd. Tela (St. Petersburg) **36**, 3542 (1994) [Phys. Solid State **36**, 1883 (1994)].
14. M. I. Petrov, D. A. Balaev, S. V. Ospishchev, *et al.*, Phys. Lett. A **237** (1–2), 85 (1997).
15. M. I. Petrov, D. A. Balaev, K. A. Shaĭkhutdinov, and S. G. Ovchinnikov, Fiz. Tverd. Tela (St. Petersburg) **40** (9), 1599 (1998) [Phys. Solid State **40**, 1451 (1998)].
16. M. I. Petrov, D. A. Balaev, S. V. Ospishchev, and K. S. Aleksandrov, Fiz. Tverd. Tela (St. Petersburg) **42** (5), 791 (2000) [Phys. Solid State **42**, 810 (2000)].
17. M. I. Petrov, D. A. Balaev, K. A. Shaĭkhutdinov, and S. I. Popkov, Pis'ma Zh. Éksp. Teor. Fiz. **75** (3), 166 (2002) [JETP Lett. **75**, 138 (2002)].
18. M. I. Petrov, D. A. Balaev, and K. A. Shaihutdinov, Physica C (Amsterdam) **361**, 45 (2001).
19. L. N. Bulaevskiĭ, V. V. Kuziĭ, and A. A. Sobyanin, Pis'ma Zh. Éksp. Teor. Fiz. **25** (7), 314 (1977) [JETP Lett. **25**, 290 (1977)].
20. L. N. Bulaevskii, V. V. Kuzii, and S. V. Panyukov, Solid State Commun. **44** (4), 539 (1982).
21. S. V. Kuplevakhskiĭ and I. I. Fal'ko, Fiz. Nizk. Temp. **10**, 691 (1984) [Sov. J. Low Temp. Phys. **10**, 361 (1984)].
22. S. V. Kuplevakhskiĭ and I. I. Fal'ko, Fiz. Met. Metalloved. **62** (1), 13 (1986).
23. A. S. Borukhovich, Usp. Fiz. Nauk **169** (7), 737 (1999) [Phys. Usp. **42**, 653 (1999)].
24. M. Fogelstrom, Phys. Rev. B **62** (17), 11812 (2000).
25. Y. Tanaka and S. Kashivaya, J. Phys. Soc. Jpn. **69**, 1152 (2000).
26. Yu. Izyumov, Yu. Proshin, and M. G. Khusainov, Usp. Fiz. Nauk **172** (2), 113 (2002) [Phys. Usp. **45**, 109 (2002)].
27. O. Bourgeois, P. Gandit, A. Sulpice, *et al.*, Phys. Rev. B **63**, 064517 (2002).
28. M. Schock, C. Surgers, and H. von Lohneysen, Eur. Phys. J. **14**, 1 (2000).
29. V. V. Ryazanov, V. A. Oboznov, A. Yu. Rusanov, *et al.*, Phys. Rev. Lett. **86** (11), 2427 (2001).
30. A. Barone and G. Paterno, *Physics and Applications of the Josephson Effect* (Wiley, New York, 1982; Mir, Moscow, 1984).
31. A. D. Balaev, Yu. V. Boyarshinov, M. M. Karpenko, and B. P. Khrustalev, Prib. Tekh. Éksp., No. 3, 167 (1985).
32. V. Ambegaokar and B. Halperin, Phys. Rev. Lett. **22**, 1364 (1969).
33. M. Tinkham, Phys. Rev. Lett. **61** (14), 1658 (1988).
34. *Physical Properties of High Temperature Superconductors*, Ed. by D. M. Ginzberg (World Sci., Singapore, 1989; Mir, Moscow, 1990).
35. S. Krupička, *Physik der Ferrite und der Verwandten Magnetischen Oxide* (Vieweg, Braunschweig, 1973; Mir, Moscow, 1976), Vol. 1.
36. M. Charalambous, J. Chaussy, and P. Lejay, Phys. Rev. B **45** (9), 5091 (1992).

Translated by G. Skrebtsov

Physics of the Solid State, Vol. 45, No. 10, 2003, pp. 1874–1883. Translated from Fizika Tverdogo Tela, Vol. 45, No. 10, 2003, pp. 1784–1793.

SEMICONDUCTORS AND DIELECTRICS

Density of States in the Impurity *d* Band and Inelastic Electron Scattering by a System of Mixed-Valence Iron Ions in HgSe : Fe Crystals

I. G. Kuleev, I. I. Kuleev, I. Yu. Arapova, and L. D. Sabirzyanova

Institute of Metal Physics, Ural Division, Russian Academy of Sciences, ul. S. Kovalevskoĭ 18, Yekaterinburg, 620219 Russia

e-mail: kuleev@imp.uran.ru

Received February 19, 2003

Abstract—The resistivity and the Hall coefficient of HgSe : Fe crystals with various iron content are experimentally studied in the temperature range $1.3 \le T \le 300$ K and in magnetic fields up to 60 kOe. The temperature dependences of the density and mobility of conduction electrons in these crystals are determined. The influence of spatial charge ordering in the system of mixed-valence iron ions on impurity states in HgSe : Fe crystals is considered. The density of states in the impurity *d* band is theoretically analyzed, and inelastic electron scattering in which bi- and trivalent iron ions are recharged is discussed. It is shown that the experimentally detected features in the dependence of the density and mobility of electrons on temperature and iron impurity content can be explained by the influence of Coulomb correlations in the mixed-valence iron ion system on the structure of the impurity *d* band. *© 2003 MAIK "Nauka/Interperiodica".*

1. INTRODUCTION

Recently, much attention has been paid to the physical properties of mixed-valence (MV) systems, in which dopants or host ions can be in at least two different charge states [1–5]. Coulomb repulsion between ions in identical charge states causes spatial correlations in their arrangement. Examples of MV systems are lanthanum manganites ($La_{1-x}Sr_xMnO_3$), mercury selenide doped with transition 3*d* elements (iron, chromium, cobalt), gallium arsenide delta-doped with silicon or tin, and 2D structures made on the basis of the latter. Mercury selenide crystals doped with transition elements represent a convenient model system for studying the effects associated with spatial charge ordering in systems of mixed-valence impurities. The influence of spatial charge ordering in the MV system on kinetic effects is most pronounced in HgSe : Fe crystals at low temperatures [5–10]. One of the most remarkable anomalies is a significant increase in the electron mobility observed in the range of liquid-helium temperatures with increasing iron content [6].

Iron impurities in HgSe : Fe crystals form a resonant *d* level at the energy $\varepsilon_d \cong 210$ meV reckoned from the conduction band bottom; i.e., this level is positioned in the continuous energy spectrum of the perfect crystal. When considering resonant *d* states, two competing processes [5] should be taken into account: (i) electron delocalization due to hybridization of localized impurity states with both band and other impurity states and (ii) localization of electrons (*d* holes, i.e., positive charges on iron ions) caused by their Coulomb repulsion tending to retain the local nature of impurity *d* states. In the extreme case of strong interimpurity or *s–d* hybridization overcoming the Coulomb interaction, a state with variable valence arises in the system of impurities. In this case, all impurity lattice sites feature an identical fractional charge and the spatial distribution of impurity charges is uniform. In HgSe : Fe crystals, the *d* level width caused by *s–d* hybridization is smaller than 0.1 meV (judging from the electron spin resonance (ESR) data for Fe^{3+} ions [11–13]), while the Coulomb correlation energy of *d* holes is two orders of magnitude higher. Therefore, the local nature of *d* states persists at low temperatures, and the conditions necessary for initiation of spatial correlations in the MV iron ion system in HgSe : Fe compounds are met. When analyzing the kinetic effects in HgSe : Fe crystals at low temperatures, we use the short-range correlation model [7, 8, 14–16] based on the assumption that the energy of interimpurity Coulomb correlations in the MV iron ion system significantly exceeds the *s–d* hybridization broadening of the impurity level [5, 11–13]. It should be noted that, although the *s–d* hybridization interaction is weak, it can play an important role in inelastic scattering of conduction electrons, resulting in iron ion recharging [10].

The Fe^{3+}–Fe^{2+} mixed-valence state arises in these crystals at contents $N_{Fe} > N^* \cong 4.5 \times 10^{18}$ cm^{-3}, when the Fermi level reaches the iron *d* level ($\varepsilon_d \cong 210$ meV) and is fixed at it [5]. As the iron impurity content increases further, the Fe^{3+} donor concentration remains unchanged ($N_+ = N^*$) and only the content of Fe^{2+} ions (neutral in the lattice) increases ($N_0 = N_{Fe} - N_+$). In the

system of Fe^{2+} and Fe^{3+} ions having the same energy, positive charges on iron ions (d holes) can be redistributed over the lattice sites occupied by iron ions. For this reason, the Coulomb repulsion of d holes in the MV system causes spatial correlations in their arrangement. The higher the iron content N_{Fe}, the larger the number of lattice sites for the d hole redistribution and the higher the degree of ordering of the correlated Fe^{3+} ion system (CIS). Experimental studies of HgSe : Fe crystals (see reviews [5, 7]) have shown that anomalous run of the dependences of kinetic effects on the iron impurity concentration and temperature T is caused by atypical scattering of electrons by the spatially correlated system of MV iron ions.

This study is devoted to the influence of spatial charge ordering in the MV system on the structure of the impurity d band and on electron transport in HgSe : Fe crystals. The conventional approach based on the Anderson model [1, 17], taking into account electron–electron correlations on one impurity, does not allow one to solve this problem, since the Coulomb interaction between impurities in identical charge states is disregarded in this model. In this paper, we suggest a simple method which makes it possible to consider the influence of the Coulomb interimpurity correlations on the structure of the impurity d band and on the kinetic effects in HgSe : Fe crystals at low temperatures. It should be noted that the interaction between oppositely charged donors and acceptors in zero-gap compensated HgCdTe-type semiconductors brings about the formation of a Coulomb pseudogap at the Fermi level, i.e., a minimum density of impurity states with $g_i(\varepsilon_F) > g_e(\varepsilon_F)$ [18, 19]. The analysis of the ESR data for Fe^{3+} ions in HgSe : Fe crystals carried out in [10, 20] within the weak Coulomb correlation model showed that there was a minimum in the density of d states at the Fermi level; however, it was unclear whether a gap or a pseudogap was formed at the Fermi level.

In Section 2, the results of measurements of the resistivity and Hall coefficient for HgSe : Fe crystals with various iron contents are presented. In Section 3, the correlation potential is analyzed and the parameters defining the impurity d band structure are determined. It is shown that, due to the CIS ordering in HgSe : Fe in the presence of strong Coulomb correlations, a correlation gap appears in the density of impurity d states between the populated (Fe^{2+}) and empty (Fe^{3+}) states, where $g_d(\varepsilon) = 0$, and resonance electron scattering is totally suppressed. In Section 4, the density of impurity d states is calculated. Section 5 is devoted to a theoretical analysis of inelastic d-hole scattering in which Fe^{2+} and Fe^{3+} ions are recharged.

2. EXPERIMENTAL RESULTS

The resistivity ρ and the Hall coefficient R of HgSe : Fe crystals of various iron content ($2 \times 10^{18} \le N_{Fe} \le 2 \times 10^{21}$ cm^{-3}) were measured in the temperature range $1.3 \le T \le 300$ K in magnetic fields of up to 60 kOe. The temperature dependences of the density n_e and mobility μ of band electrons were also studied.

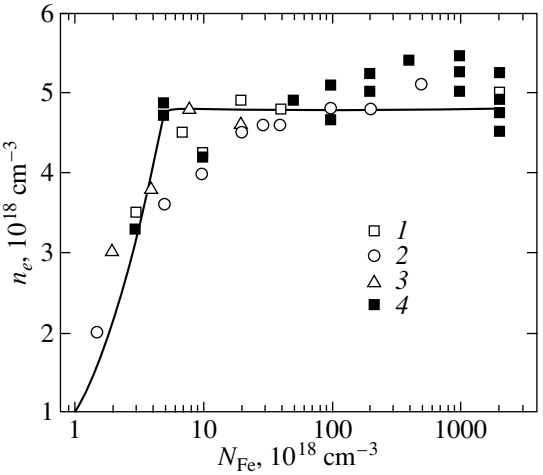

Fig. 1. Dependence of the electron density n_e on the iron impurity content N_{Fe} in HgSe : Fe crystals at T = 4.2 K: (*1*) experimental data from [6], (*2*) [11], (*3*) [12], and (*4*) this study. The solid line is calculated using formulas (20) and (21).

Figure 1 shows the dependence of the electron density n_e on the iron content N_{Fe}. We can see that the electron density is stabilized at the level $n_e \approx (4.7–4.8) \times 10^{18}$ cm^{-3} at $N_{Fe} \ge 5 \times 10^{18}$ cm^{-3}, which conforms to the available published data [5, 6]. This $n_e(N_{Fe})$ dependence indicates that the Fermi level is fixed at the iron donor level. A certain spread in the values of n_e is caused by intrinsic defects, whose concentration is generally ~$(1–2) \times 10^{18}$ cm^{-3} [5, 21]. According to the currently available data [6, 7], the energy of the unperturbed iron donor level is $E_{d0} \cong 210$ meV, which corresponds to $n_e = N^* \cong 4.5 \times 10^{18}$ cm^{-3}. Below, we show that the fact that the electron density exceeds N^* can be explained by the formation of the impurity d band and an increase in the Fermi level due to spatial charge ordering in the system of MV iron ions.

Figure 2 shows the temperature dependences of the electron density n_e in HgSe : Fe crystals of various iron content. We can see that the electron density slightly depends on temperature for all the samples. We note that n_e increases for samples with $N_{Fe} > 3N^*$ and decreases for samples with $N^* < N_{Fe} < 2N^*$ as the temperature is increased. A similar behavior of the $n_e(T)$ dependences for HgSe : Fe crystals was detected in [6], where the experimental and calculated values of n_e were compared. When calculating $n_e(T)$, the density of states in the conduction band for the Kane nonparabolic model was used. An analysis carried out in [6] showed that the calculated and measured values of $n_e(T)$ can be brought into conformity by assuming that ε_{Fe} varies with temperature. We show that these features can be

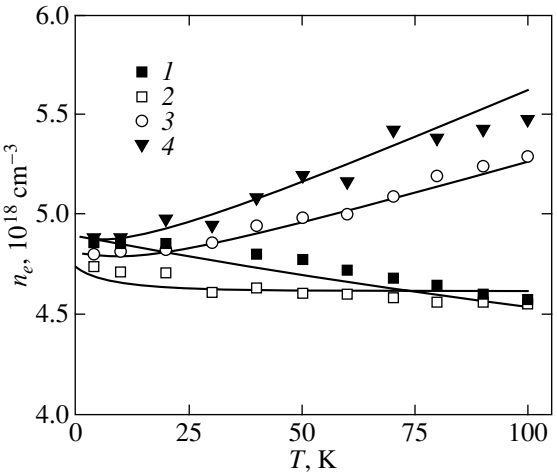

Fig. 2. Temperature dependences of the electron density n_e in HgSe : Fe crystals of various iron content N_{Fe} (10^{18} cm^{-3}): (*1*) 5, (*2*) 10, (*3*) 50, and (*4*) 100. The solid lines are calculated using formulas (16)–(22).

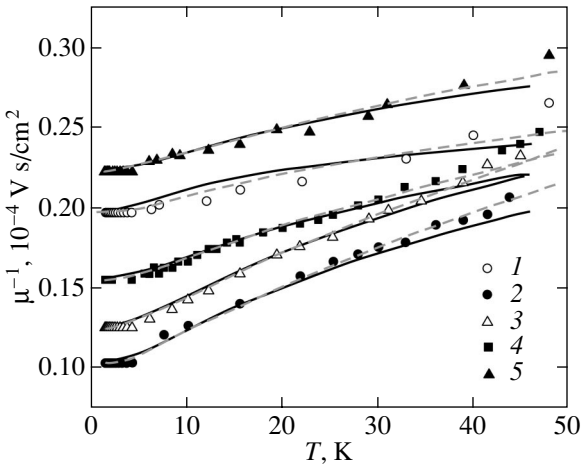

Fig. 3. Temperature dependences of the inverse mobility μ^{-1} for HgSe : Fe crystals with different values of N_{Fe} (10^{18} cm^{-3}): (*1*) 5, (*2*) 20, (*3*) 40, (*4*) 50, and (*5*) 100. Dashed and solid lines are the $\mu^{-1}(T)$ dependences calculated using formulas (23)–(25) and (25)–(28), respectively.

explained by the influence of spatial correlations in the system of MV iron ions on the structure of the impurity *d* band.

Figure 3 shows the temperature dependences of the inverse mobility μ^{-1} of electrons in HgSe : Fe crystals with an iron content $N_{Fe} \geq 5 \times 10^{18}$ cm^{-3} in the temperature range $1.3 \leq T \leq 50$ K. For all samples at very low temperatures ($T \leq 10$ K), there are temperature ranges in which the electron mobility $\mu(T)$ is independent of temperature; the width of these intervals increases with N_{Fe}. In the temperature range $10 < T < 35$ K, the experimental data follow the law $\mu^{-1}(T) \sim T^{\nu}$, where $\nu < 1$. In Section 5, it is shown that the exponent ν is close to 0.5. At $T > 35$ K, a more pronounced increase in μ^{-1} with temperature is observed [$\mu^{-1}(T) \sim T$], which, as follows from [7, 15], is caused by the contribution of electron–phonon scattering.

Below, we theoretically analyze the impurity *d* band structure of the system of MV iron ions and inelastic *d*-hole scattering in which iron ions are recharged.

3. CORRELATION POTENTIAL AND THE STRUCTURE OF THE IMPURITY *d* BAND

We consider the influence of spatial charge ordering in the system of MV iron ions on the impurity *d* band structure in HgSe : Fe crystals. With no ordering effects, the random fields of Fe^{3+} ions cause an energy spread of the *d* states and the formation of an impurity band with a width close to 10 meV. The Fermi level separates empty *d* states (Fe^{3+}) from populated ones (Fe^{2+}). When ordering takes place, any Fe^{3+} ion at a point R_i is subjected to the correlation potential $U_s(R_i)$, which is the result of the self-consistent influence of the potentials of other Fe^{3+} ions [16], and to the field $U_e(R_i)$ of the homogeneous gas of conduction electrons:

$$U(R_i) = U_s(R_i) + U_e(R_i),$$

$$U_s(R_i) = \sum_{j \neq i} V(R_{ij})(g_{++}(R_{ij}) - 1), \qquad (1)$$

$$U_e(R_i) = -4\pi\varepsilon_k(r_s/R_+)^2,$$

where $V(R_{ij})$ is the potential produced by the *j*th Fe^{3+} ion at the point R_i, r_s is the Thomas–Fermi screening length, $\varepsilon_k = e^2/\chi R_+$ is the Coulomb interaction energy between ions spaced at an average distance $R_+ = N_+^{-1/3}$ (N_+ is the Fe^{3+} ion concentration, χ is the permittivity), and $g_{\alpha\beta}(r)$ are the partial pair correlation functions characterizing the spatial distribution of MV iron ions in the Fe^{2+}–Fe^{3+} system [22, 23].

In the case of the screened Coulomb interaction of impurity ions, we have

$$U_s(r) = \frac{2e^2}{\chi\pi}\int_0^\infty \frac{q^2 dq}{q^2 + r_s^{-2}}(S_{++}(q) - 1)\frac{\sin(qr)}{qr}, \qquad (2)$$

where $S_{++}(q)$ is the structure factor of Fe^{3+} ions. Hereafter, we use the structure factors $S_{\alpha\beta}(q)$ for the penetrating solid sphere model, which are defined in [16]. The potential $U_s(r)$ redistributes *d* holes in the Fe^{2+}–Fe^{3+} system so that the potential energy is minimal at the sites of Fe^{3+} donors.

Let us consider the change in the Coulomb interaction energy caused by ordering of the Fe^{3+} ions. The energy gain $\Delta E_c(N_{Fe})$ per Fe^{3+} ion for the ordered distri-

bution (in comparison with the random distribution) can be written in terms of $U_s(0)$ as [14, 24]

$$\Delta E_c = \frac{\Delta E_k}{N_+} = -\frac{1}{2}U_s(0),$$
$$U_s(0) = \frac{2e^2}{\chi\pi}\int_0^\infty \frac{q^2 dq}{q^2 + r_s^{-2}}(S_{++}(q) - 1). \quad (3)$$

For the Coulomb interaction of Fe^{3+} ions, the quantity ΔE_c is immediately expressed in terms of the packing parameter η as [25]

$$U_s(0) = -4\pi\varepsilon_k\left(\frac{d}{R_+}\right)\left\{\frac{0.5 - 0.1\eta + 0.05\eta^2}{1 + 2\eta}\right\}, \quad (4)$$

where $\eta = \frac{\pi}{6}n_+d^3$ and $d = r_c$ is the solid-sphere diameter. For the screened Coulomb interaction, the quantity $U_s(0)$ can be analytically expressed in terms of the parameters η and $\lambda = d/r_s$ as [14, 26]

$$U_s(0) = -4\pi\varepsilon_k\left(\frac{d}{R_+}\right)\{G(\lambda) - \lambda^{-2}\},$$
$$G(\lambda) = \frac{\lambda L(\lambda)}{12\eta[L(\lambda) + S(\lambda)\exp(\lambda)]},$$
$$L(\lambda) = 12\eta[(1 + 0.5\eta)\lambda + 1 + 2\eta], \quad (5)$$
$$S(\lambda) = (1 - \eta)^2\lambda^3 + 6\eta(1 - \eta)\lambda^2$$
$$+ 18\eta^2\lambda - 12\eta(1 + 2\eta).$$

In [8], by comparing the experimental and calculated values of the mobility, the empirical $\eta(N_{Fe})$ dependence was determined to be

$$\eta = \eta_\infty\left[1 - \exp\left(-\frac{\eta}{\eta_\infty}\frac{N_{Fe}}{N_+}\right)\right]. \quad (6)$$

At high iron impurity contents, the function $\eta(N_{Fe}$ tends to a constant: $\eta(N_{Fe} \longrightarrow \infty) = \eta_\infty$. However, the relation $\eta(N_{Fe}) \approx 0.74N_0/N_{Fe}$ was derived in [16] from the balance equation for d holes and neutral centers (with concentration N_0) in a short-range cluster surrounding an Fe^{3+} ion at $N_0 < N_+$. This relation is asymptotically exact in the limit $N_0 \longrightarrow 0$. It follows from empirical equation (6) that, for $N_0 \ll N_+$, we have $\eta(N_{Fe}) \approx 2\eta_\infty N_0/N_{Fe}$, which corresponds to the value $\eta_\infty \approx 0.37$ in Eq. (6). For this reason, we use this value of η_∞ in what follows.

At small values of r ($r < r_c$), the correlation potential $U_s(r)$ can be expanded in powers of r. Keeping only the quadratic terms in this expansion, we obtain from formula (2)

$$U_s(r) = U_s(0) + \Delta U_s(r),$$
$$\Delta U_s(r) \cong \alpha(N_{Fe})r^2 = \alpha^*(N_{Fe})y^2, \quad (7)$$
$$\alpha^*(N_{Fe}) = \alpha(N_{Fe})d^2, \quad y = r/d.$$

We invoke the Laplace transformation similarly to as was done in [26]. For the screened Coulomb interaction, we express the coefficient $\alpha(N_{Fe})$ in terms of the packing parameter η and the screening length r_s:

$$\alpha(N_{Fe}) = \frac{e^2}{3\pi\chi}\int_0^\infty \frac{q^4 dq}{q^2 + r_s^{-2}}(1 - S_{++}(q))$$
$$= \frac{4\pi\varepsilon_k}{3R_+^2} + \frac{1}{6r_s^2}U_s(0). \quad (8)$$

As can be seen from Fig. 4, Eqs. (7) and (8) yield a good approximation for calculating the correlation potential $\Delta U_s(y)$ in the entire correlation sphere ($y \le 1$).

Formulas (4)–(6) allow one to analyze the change in the Coulomb energy ΔE_c associated with ordering of the Fe^{3+} ions as a function of the iron content and the screening length. Such an analysis was carried out in

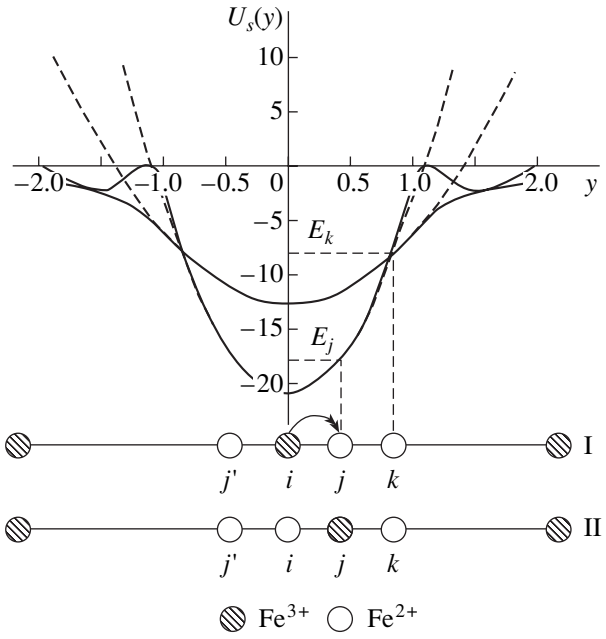

Fig. 4. Potential $U_s(y)$ and the energy diagram of inelastic transitions in a one-dimensional short-range-order cluster of Fe^{3+} and Fe^{2+} ions at different values of the iron content N_{Fe} (10^{18} cm^{-3}): (*1*) 5 and (*2*) 50 ($\chi = 20$). The dashed lines are the approximate $U_s(y)$ dependences calculated using formulas (7) and (8) for the corresponding iron contents. ΔE_{ji} is the energy of the inelastic transition of a d hole from point R_i to point R_j equal to the energy difference for two configurations (I and II) of the short-range-order cluster.

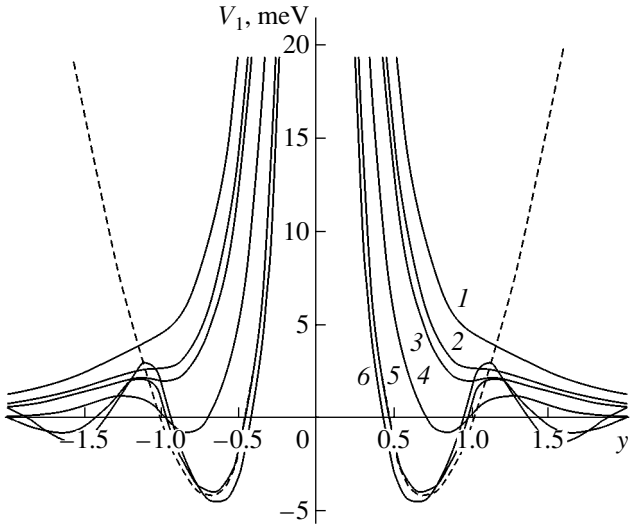

Fig. 5. Potential $V_1(y)$ at different values of the iron content N_{Fe} (10^{18} cm^{-3}): (*1*) 5, (*2*) 5.2, (*3*) 5.3, (*4*) 6, (*5*) 10, and (*6*) 50. The dashed lines are the $V_1(y)$ dependences calculated from the approximated formulas (7) and (8) at $N_{Fe} = 50 \times 10^{18}$ cm^{-3}.

[14, 15]. We note that the steep increase in ΔE_c in the range $N^* < N_{Fe} < 1 \times 10^{19}$ cm^{-3} (see [14, Fig. 5]) is caused by the fact that the distances between *d* holes that are the closest to each other increase initially most significantly with charge ordering in the system of MV iron ions. This yields a maximum gain in the Coulomb energy and causes the formation of correlation spheres surrounding each Fe^{3+} ion, which contain no other positive charges [14]. This circumstance makes it possible to use the model of solid spheres to describe the correlation properties of the system of Fe^{3+} ions statistically. In this model, Fe^{3+} ions cannot be arranged at distances shorter than the correlation sphere radius $r_c = d$ (*d* is the diameter of a solid sphere). The degree of ordering in such a system is characterized by the packing parameter η equal to the ratio of the volume occupied by the solid spheres to the total volume of the system.

The potential $U_s(R_j)$ prevents *d*-hole jumps from Fe^{3+} onto Fe^{2+} ions, thereby promoting their localization at charged centers (Fig. 4). Due to the random distribution of Fe^{2+} ions over lattice sites and, therefore, in short-range-order clusters, the probability of multiparticle transitions of *d* holes is low and the contribution from these transitions can be neglected at low temperatures. Here, we restrict our consideration to single-particle transitions. Let us assume that a *d*-hole transition in a short-range-order cluster from the Fe^{3+} ion located at the point R_i onto an Fe^{2+} ion at the point R_j proceeds in the static field produced by the other Fe^{3+} ions. The inelasticity energy ΔE_{jk} of such a transition is equal to the energy difference of the two configurations (Fig. 4):

$$\Delta E_{ik} = E_i - E_k = U(R_i) - U(R_k). \quad (9)$$

Therefore, the energy levels E_{dk} of Fe^{2+} ions that are neutral in the lattice are distributed over the d_0 band of impurity states. The width of this band is determined by the energy necessary to transfer a *d* hole from the center ($R_i = 0$) to the boundary of the correlation sphere ($R_k = r_c$):

$$W = U_s(r_c) - U_s(0). \quad (10)$$

To determine the energy E_{d0} of the unperturbed *d* level (or the positions of the band edges with respect to the unperturbed level), the potential of the central Fe^{3+} ion should be included and the point r_0 at which the derivative of the total potential with respect to the radius vector is zero should be determined. The total potential $V_1(r) = U_s(r) + V(r)$ is shown in Fig. 5 for various iron impurity contents.

We can see from Fig. 5 that the behavior of the potential $V_1(r)$ qualitatively changes as the degree of spatial ordering in the system of MV iron ions increases: $V_1(r)$ monotonically decreases with increasing distance in the region of weak correlations [$\eta(N_{Fe}) \le 0.125$ or $N_{Fe} \le 5.2 \times 10^{18}$ cm^{-3}], remaining positive over the entire range of values of *r*. As the iron content N_{Fe} increases and becomes higher than 5.2×10^{18} cm^{-3} [$\eta(N_{Fe}) > 0.125$], the $V_1(r)$ dependence exhibits a minimum, whose depth increases with the iron content. When passing to the region of strong spatial correlations [$\eta(N_{Fe}) > 0.185$, $N_{Fe} > 5.8 \times 10^{18}$ cm^{-3}], the potential $V_1(r_0)$ becomes negative. As the iron content increases further, the depth of the $V_1(r_0)$ minimum increases and, at $N_{Fe} > 10^{19}$ cm^{-3}, becomes approximately constant, which is characteristic of a strongly correlated Coulomb liquid. In this case, the value of y_0 is approximately 0.65. It is clear that the force acting on a probing charge placed at the point r_0 is zero ($dV_1(r)/dr = 0$); therefore, the energy of the d_0 level remains unperturbed. The upper (E_1) and lower (E_2) boundaries of the impurity d_0 band are given by

$$E_1 = E_{d0} + \Delta U_s(r_0), \quad E_2 = E_1 - W. \quad (11)$$

Figure 6 shows the dependences of $|U_s(0)|$, *W*, and α^* on the iron content. We can see that the impurity d_0 band width tends to zero as $N_{Fe} \longrightarrow N^*$ ($N_0 \longrightarrow 0$), while at high iron contents ($N_{Fe} \gg N^*$) the band width tends to a constant which exceeds 14.6 meV for $\chi = 27$ and 18.6 meV for $\chi = 20$. The coefficient $\alpha^*(N_{Fe})$ tends to zero as $N_{Fe} \longrightarrow N^*$; when $N_{Fe} \gg N^*$, this coefficient becomes a constant equal to 12.2 meV for $\chi = 27$ and 15.5 meV for $\chi = 20$. The parameter $|U_s(0)|$ exhibits a similar run: at high iron contents, it becomes a constant which is larger than 15.9 meV for $\chi = 27$ and 20 meV for $\chi = 20$. We note that correlation potential $U_s(r)$ is a potential well for *d* holes and a potential barrier for electrons. Hence, a conduction electron must overcome

the potential barrier $|U_s(0)|$ to be trapped by an Fe^{3+} donor center. As can be seen from Figs. 4 and 6, resonant trapping of a conduction electron onto the d level of an Fe^{3+} ion at $N_{Fe} \gg N^*$ requires a high activation energy $U_s(0) \sim 20$ meV, in contrast to scattering with recharging of d centers [10]. Thus, Coulomb interimpurity correlations in the system of MV iron ions suppress resonant electron scattering. The role of resonant scattering of conduction electrons involving the d states in HgSe : Fe compounds at low temperatures has been actively discussed in the literature [5, 13, 20]. Inclusion of this scattering yielded catastrophically low values of the electron mobility in HgSe : Fe [5].

Since iron ions substitute for Hg^{2+} ions at lattice sites, there is a minimum length of d-hole jumps, $\Delta R_{ik} > \Delta R_{min}$ ($R_{min} \sim a_0$, a_0 is the lattice constant). If Coulomb interimpurity correlations at the temperature of sample preparation ($T \sim 10^3$ K) are taken into account, we obtain $R_{min} \sim 2a_0$. Therefore, $\Delta E_{ki} > \Delta E_{min} = \Delta$. If follows from expressions (7) and (8) that

$$\Delta \approx \alpha(N_{Fe})(\Delta R_{min})^2. \quad (12)$$

The quantity Δ tends to zero as $N_{Fe} \longrightarrow N^*$ and becomes constant at $N_{Fe} > 3 \times 10^{19}$ cm^{-3}. In this concentration range, $\Delta \sim 9.3$ K at $\Delta R_{min} \sim 10^{-7}$ cm and $\chi = 20$ and $\Delta \sim 7.3$ K for $\chi = 27$. The estimate of Δ obtained in [27] within the model of a linear chain of Fe^{3+} ions is of the same order of magnitude. The existence of a minimum energy for d-hole jumps means that the populated band of d_0 states (Fe^{2+}) is separated from the empty band of d_+ states (Fe^{3+}) by the finite energy Δ. Thus, spatial charge ordering in the system of MV iron ions removes the degeneracy of the d_0 and d_+ states. In this system, a new mechanism of inelastic electron scattering becomes possible at finite temperatures, in which bi- and trivalent iron ions are recharged [10]. Since the band of d_+ states at $N_{Fe} \gg N^*$ is much narrower than the d_0 band, we approximate the former band by a sharp d level with the energy

$$E_{d+} = E_1 + \Delta. \quad (13)$$

Thus, ordering of the Fe^{3+} ions in the MV system results in the formation of a correlation gap between the populated and empty bands of d states rather than of a Éfros–Shklovskiĭ Coulomb pseudogap [18], as was assumed in [13, 20]. Based on the analysis performed above, we can conclude that the interimpurity Coulomb correlations totally suppress resonant scattering: the density of d states at the Fermi level $g_d(\varepsilon_F)$ is zero, and $\Delta \gg \Gamma_d$, Γ_d is the d-level width due to s–d hybridization; $\Gamma_d < 0.1$ meV, according to [11–13]). The behavior of the carrier mobility in HgSe : Fe at $N_{Fe} \gg N^*$ and $T \longrightarrow 0$ also becomes clear (Fig. 3). At temperatures $T < \Delta$, d-hole jumps are frozen and the electron mobility becomes temperature-independent, as was observed experimentally (see Fig. 3 and [6, 27]). The short-range order in the system of correlated Fe^{3+} ions becomes "frozen," and, in a certain sense, the system of Fe^{3+} ions transfers to a metallic-glass state [28] (a strongly correlated Coulomb liquid of Fe^{3+} ions).

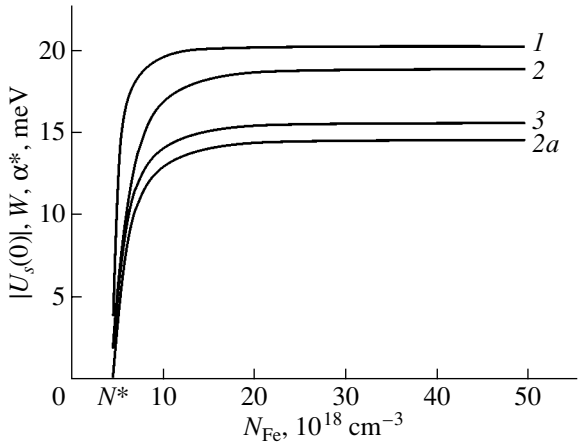

Fig. 6. Dependences of the parameters (*1*) $|U_s(0)|$, (*2*, *2a*) W, and (*3*) α^* on the iron impurity content calculated for the parameters (*1–3*) $\eta_\infty = 0.37$ and $\chi = 20$ and (*2a*) $\chi = 27$.

4. SPATIAL CORRELATIONS AND THE DENSITY OF STATES IN THE IMPURITY d BAND

The density of states in the impurity d band is calculated in two steps. First, we determine the density of states in the d band in the coordinate representation $G_0(r)$ for a known distribution of charges in the short-range-order cluster of a given Fe^{3+} ion. Then, using formulas (7)–(11), we determine the distribution of d_0 states in the correlation sphere according to the above analysis of the correlation potential,

$$E_1 - E_{dj} = \alpha(N_{Fe})r^2, \quad (14)$$

and find the density of states in the d_0 band in the energy representation using the relation

$$G_0(r)dr = G_0(E_{dj})dE_{dj}.$$

from which we obtain

$$G_0(E_{dj}) = G_0(r)dr/dE_{dj},$$
$$r = [(E_1 - E_{dj})/\alpha(N_{Fe})]^{1/2}. \quad (15)$$

To determine $G_0(r)$, we construct a correlation sphere of radius r_c around each Fe^{3+} ion, average over the ensemble of correlation spheres, and come to a description of the system of MV iron ions within the continuous-medium model. To analyze the distribution of charged and neutral particles in a short-range-order cluster, it is convenient to use the partial radial distribution functions $N_{\alpha\beta}(r) = 4\pi r^2 N_\beta g_{\alpha\beta}(r)$ (see [16, Fig. 2]). The quantity $N_{\alpha\beta}(r)dr$ yields the number of particles of type $\beta(0, +)$ within a spherical layer of radius r and

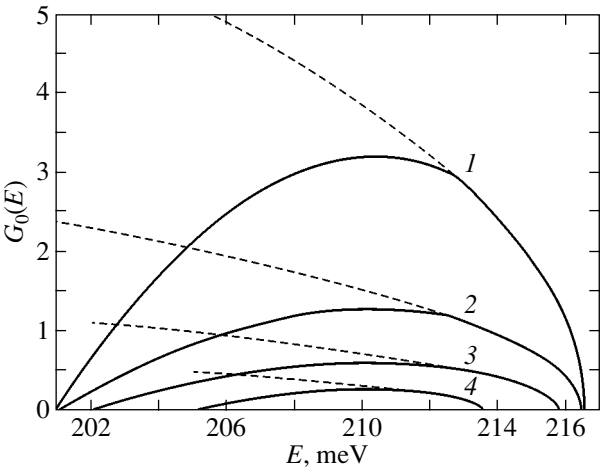

Fig. 7. Density of states in the d_0 band in the energy representation for various values of the iron content N_{Fe} (10^{18} cm^{-3}): (*1*) 50, (*2*) 20, (*3*) 10, and (*4*) 6; $\eta_\infty = 0.37$ and $\chi = 27$. Dashed lines are calculated from formula (16a).

thickness $r + dr$ if a particle of type $\alpha(0, +)$ is placed at its center. In the case of a random distribution of particles, we have $g_{\alpha\beta}(r) = 1$ and the number of particles in a volume Ω_r is equal to the product of the concentration and the volume. Since *d* holes and neutral centers can only exchange sites, the *d* hole sites in the correlation sphere will be occupied by neutral centers. Therefore, at $N_0 \le N_{1+}$, the local density of *d* holes in the correlation sphere is zero and the density of neutral centers is defined by the total iron concentration (see [16, Fig. 2]). The reverse situation arises in the region of the peak corresponding to the first coordination shell: the density of neutral centers is zero, while the density of *d* holes is determined by the total iron concentration. For this reason, both the function $g_{++}(r)$ describing correlations in the system of charged centers (++) and the function $g_{+0}(r)$ describing the correlation in the system (+0) significantly deviate from unity, corresponding to a random distribution of particles in the short-range-order cluster. Thus, the Coulomb repulsion of *d* holes in the system of MV iron impurities gives rise not only to spatial ordering of charged centers (Fe^{3+} ions) but also to correlations in the system (+0).

To determine the function $G_0(r)$, we construct a Wigner–Seitz cell in the correlation sphere; this cell is a sphere of radius $r = d/2$. All neutral centers lying inside this sphere are correlated in position with the central Fe^{3+} ion; therefore, the function $G_0(r)$ is equal to the radial distribution function $N_{+0}(r)$. At $r > d/2$, the neutral centers correlate not only with the central ion but also with the iron ions lying in the spherical layer $d < r < r_1^*$. In this case, the function $G_0(r)$ decreases and then vanishes at $r = d$. As an illustration, we consider the case of a simple cubic (SC) lattice of Fe^{3+} ions over which neutral centers are uniformly distributed with the density N_0. It is easy to verify that, at $r < R_+/2$, the function $G_0(r)$ is equal to the radial distribution function $N_{+0}(r)$; at $R_+/2 < r < R_+/\sqrt{2}$, it decreases in proportion to $r(3R_+/4 - r)$; and in the interval $R_+/\sqrt{2} < r < R_+\sqrt{3}/2$, it decreases quadratically with distance and vanishes at $r = R_+\sqrt{3}/2$.

Thus, in the case of a spherically symmetric charge distribution in the averaged short-range-order cluster in the range $0 < y < 1/2$, we have

$$G_0(r) = 4\pi N_{Fe} d^2 y^2. \tag{16}$$

Using Eq. (15) in the energy representation, we obtain

$$G_0(E_{dj}) = 2\pi d^3 N_{Fe} \frac{\sqrt{E_1 - E_{dj}}}{(\alpha^*(N_{Fe}))^{3/2}}, \tag{16a}$$

$$E_{dj} \le E_d^{(1)} = E_1 - 0.25\alpha^*.$$

In the range $0.5 < y < 1$, based on the results for an SC lattice, we assume that, at $r < R/2$ (where *R* is the distance to a charged center located in the spherical layer), all d_0 states correlate in position with the central Fe^{3+} ion, while at $r > R/2$, the d_0 states correlate with the ion in the spherical layer $d < r < 2d$. Therefore, averaging over the distribution of charged centers in the spherical layer $d < r < 2d$ can be carried out as follows:

$$G_0(r) = \langle G_0(r, R)\rangle = \frac{1}{\langle g_{++}\rangle}\int_d^{2d} G_0(r, R) g_{++}(R) 4\pi R^2 dR,$$

$$\langle g_{++}\rangle = \int_d^{2d} 4\pi R^2 g_{++}(R) dr, \tag{17}$$

$$G_0(r, R) = \begin{cases} 4\pi N_{Fe} d^2 y^2, & y < R/2d \\ 0, & y > R/2d. \end{cases} \tag{18}$$

To simplify further calculations, we restrict our analysis to the first-order approximation in the expansion in powers of the system density and replace $g_{++}(R)$ by a step function: $g_{++}(R) = 0$ at $R < d$ and $g_{++}(R) = 1$ at $R > d$. In this case, Eq. (17) takes the form

$$G_0(r) = \frac{1}{\Delta V_c}\int_d^{2d} G_0(r, R) 4\pi R^2 dR,$$

$$\Delta V_c = 7\frac{4\pi}{3} d^3, \tag{19}$$

where ΔV_c is the volume of the spherical layer $d < r < 2d$. Expressions (14)–(19) allow us to determine the density of states in the d_0 band for various iron contents in the energy representation (Fig. 7). It is noteworthy

that the density of states has a square-root dependence on energy [see relation (16a)] in the energy range $0 < E_1 - E_{dj} \le 4$ meV. We can see from formulas (14) and (15) that this feature of $G_0(E_{dj})$ is related to the quadratic dependence of ΔU_s on the radius r within the correlation sphere. The function $G(E_{dj})$ peaks at the energy $E_{dj} \approx E_{d0}$. This is an indirect confirmation of the fact that the function $G_0(r, R)$ was modeled correctly.

The results obtained above make it possible to analyze the data from Hall effect measurements. At $T = 0$ K, the Fermi level separates the populated and empty states of iron ions and is positioned in the correlation gap:

$$\varepsilon_{F0} = E_1 - \frac{\Delta}{2} \approx E_{d0} + \Delta U_s(r_0). \quad (20)$$

Within the two-band Kane model, the electron density is

$$n_e(N_{Fe}) = N^* \frac{\varepsilon_{F0}(1 + \varepsilon_{F0}/\varepsilon_g)}{\varepsilon_{d0}(1 + \varepsilon_{d0}/\varepsilon_g)}. \quad (21)$$

It is clear that the Fermi level is not fixed at the level ε_{d0} and an increase in the degree of spatial ordering removes the degeneracy of the states d_0 and d_+ in the impurity band and causes an increase in the Fermi level. In this case, the electron density increases from N^* to $n_e \cong 4.8 \times 10^{18}$ cm^{-3}. The calculated density $n_e(N_{Fe})$ is shown in Fig. 1 by solid lines. As is evident from Fig. 1, there is satisfactory agreement with the experimental data. A certain scatter of the n_e values is caused by intrinsic defects, whose typical density is $\sim 10^{18}$ cm^{-3} [5, 21]. The temperature dependence of the electron density at a fixed iron content is determined from the electrical neutrality equation (see, e.g., [29]):

$$n_e(T) = N_+ F_+(\varepsilon_{d+}) + \int_{E_2}^{E_1} d\varepsilon_d g_{d0}(\varepsilon_d)(1 - F_0(\varepsilon)),$$

$$g_{d0}(\varepsilon_d) = N_{Fe} G_0(\varepsilon_d) \left(\int_{E_2}^{E_1} d\varepsilon_d G_0(\varepsilon_d) \right)^{-1}, \quad (22)$$

$$F_+(\varepsilon_{d+}) = \left(1 + 2\exp\left(\frac{\varepsilon_F - \varepsilon_{d+}}{k_B T}\right)\right)^{-1},$$

$$F_0(\varepsilon_d) = \left(1 + \frac{1}{2}\exp\left(\frac{\varepsilon_d - \varepsilon_F}{k_B T}\right)\right)^{-1}.$$

Here, the functions F_+ and $1 - F_0$ allow for population of the d_+ and d_0 states by d holes at finite temperatures and $g_{d0}(\varepsilon_d)$ is the density of states in the d band defined by formulas (16a)–(19). The value of N_+ was determined from the experimental data on the Hall effect at $T = 1.3$ K and from a given iron content. In calculating the $n_e(T)$ dependence, we disregarded the temperature correction to the Fermi energy of electrons, since this correction is of the order of $(k_B T/\varepsilon_F)^2$ and contributes less than 0.1%. Therefore, we calculated n_e from expression (21), which is valid for a degenerate electron gas. The results of the calculation are shown in Fig. 2 by solid lines and are seen to conform well to the experimental data.

Thus, the above analysis of the impurity band structure and the approximate calculation of the density of states in the d_0 band have allowed us to correctly interpret the results of the Hall effect measurements in HgSe : Fe crystals in a wide temperature range. It was shown that the features in the dependence of the electron density on temperature and iron content can be explained in terms of the influence of Coulomb correlations in the system of MV iron ions on the density of states in the impurity d band.

5. INELASTIC SCATTERING OF D HOLES AND THE TEMPERATURE DEPENDENCE OF THE CARRIER MOBILITY

At finite temperatures, the interaction of d holes with phonons or conduction electrons causes migration of d holes between Fe^{2+} and Fe^{3+} ions and gives rise to the following two effects. First, a conduction electron or phonon colliding with an Fe^{3+} ion can transfer to it the energy necessary for the transition of a hole to a neighboring neutral center with higher energy (Fig. 4). For conduction electrons, it is this inelastic scattering mechanism that causes recharging of d centers and should be taken into account. Second, as the temperature increases, inelastic jumps of d holes cause chaotization of the system of Fe^{3+} ions; the degree of spatial ordering and the solid-sphere diameter decrease. In this case, there is a finite probability that a d hole will be at the neutral centers nearest to a given donor. This effect can be taken into account in the approximation of so-called soft spheres [30, 31]:

$$d(T) = d_0(1 - \Delta r(T)/d_0). \quad (23)$$

Here, d_0 is the solid-sphere diameter at $T = 0$ and $\Delta r(T)$ describes the variation of the correlation sphere radius with temperature. The $\Delta r(T)$ dependence can be easily estimated by assuming that all the states of the d_+ and d_0 bands satisfying the condition $\Delta U_s(\Delta r_{ij}) \le (3/2)k_B T$ are equiprobably populated at finite temperatures. In this case, expression (7) immediately yields $\Delta r(T) \sim (3k_B T/\alpha^*)^{1/2}$. Since there is a finite energy gap Δ between the d_+ and d_0 bands, d-hole jumps are frozen at $T < \Delta$. Therefore, the $\Delta r(T)$ dependence can be written in the form

$$\Delta r(T) = AT^{1/2}\exp(-\Delta/k_B T), \quad (24)$$

where the coefficient A is a fitting parameter. Using Eq. (23), the temperature dependence of the electron

mobility can be determined from the $\mu_0(d_0)$ dependence at $T = 0$ to be [32]

$$\frac{1}{\mu(T)} = \frac{1}{\mu(d(T))} \cong \frac{1}{\mu_0} + \frac{1}{\mu^2}\frac{\partial\mu}{\partial d}\Delta r(T), \qquad (25)$$

where $\mu(d(T))$ is defined by formulas (14)–(18) from [32] with $d(T)$ in place of the parameter d_0 and $\mu_0 = \mu(d_0)$. We note that the dependence of the electron mobility on the donor concentration in HgSe crystals and the $\mu(N_{Fe})$ dependence for HgSe : Fe crystals were analyzed in [32]. These dependences were described quantitatively by using a single set of parameters with inclusion of the *s*–*p* hybridization and Bloch amplitudes of the wave functions. Those parameters are also used here to analyze the temperature dependence of the electron mobility. The $\mu^{-1}(T)$ dependence calculated using Eqs. (23)–(25) is shown in Fig. 3 by dashed lines. We can see that the calculated curves fit well with the experimental data in the temperature range 1.3–35 K; within the range $10 < T < 35$ K, the experimental data follow the law $\mu^{-1}(T) \sim T^{1/2}$. It is obvious from formulas (7), (14), and (15) that this dependence is associated with the quadratic dependence of the correlation potential ΔU_s on the radius r within the correlation sphere. At $T > 35$ K, the calculated curves lie below the experimental curves, which is due to the contribution of electron–phonon scattering [15] being disregarded.

The $\Delta r(T)$ dependence can be determined more strictly by using the method suggested in [18, 33, 34]. In contrast to [33, 34], we consider thermally activated jumps (caused by the interaction of *d* holes with either conduction electrons or phonons) rather than tunneling of *d* holes from charged to neutral centers, because the energy of thermal chaotic motion is $k_B T \le \Delta E_{ij}$ in the case under consideration. Unlike [30], we take into account the population of the d_+ and d_0 states according to [33] when considering jumps of *d* holes from charged to neutral centers. In this case, the quantity $\Delta r(T)$ can be found to be

$$\begin{aligned}
\Delta r(T) &= \sum_{i,j} \Delta R_{ij}\Gamma_{ij}, \\
\Gamma_{ij} &= F_i(1-F_j)W_{ij} - F_j(1-F_i)W_{ji}, \\
W_{ij} &= Z_0 w_0 \exp\left(-\frac{\Delta E_{ij}}{k_B T}\right) \\
&= Z_0 w_0 \exp\left(-\frac{\Delta}{k_B T}\right)\exp\left(-\frac{\Delta U_s(r_{ij})}{k_B T}\right), \\
Z_0^{-1} &= \int_0^d d\mathbf{r}_{ij}\exp\left(-\frac{\Delta U_s(r_{ij})}{k_B T}\right).
\end{aligned} \qquad (26)$$

Formula (26) yields, in fact, the average value of Δr obtained by averaging with respect to the Boltzmann distribution, which is defined by the correlation potential and the probability of the population of localized states. In this case, we should take into account not only the transitions of *d* holes from the d_+ level to overlying states of the d_0 band [see Eq. (21)] but also the reverse processes, as well as the transitions of *d* holes between the d_0-band states. The principle of detailed balance allows us to simplify the expression for the probability Γ_{ij}:

$$\Gamma_{ij} = F_i(1-F_j)W_{ij}[1 - \exp(-(\Delta E_{ij}/k_B T))]. \qquad (27)$$

The $\mu^{-1}(T)$ dependence calculated using formulas (25)–(27) is shown in Fig. 3 by solid lines. The parameter w_0 in Eq. (26) and the coefficient A in Eq. (24) are fitting parameters. We can see from Fig. 3 that the calculated curves conform well to the experimental data. An analysis showed that the transitions of *d* holes from the d_+ level to the d_0-band states make a dominant contribution to $\Delta r(T)$ at low temperatures, while the transitions of *d* holes between the d_0-band states make this dominant contribution at $T > 15$ K. Thus, the inclusion of thermally activated jumps of *d* holes, which decrease the degree of spatial ordering in the system of MV iron ions, makes it possible to explain the temperature dependence of the electron mobility.

Let us consider the contribution from inelastic scattering of conduction electrons in which *d* centers are recharged to the resistivity. The inverse electron mobility, with account taken of this contribution, can be written as

$$\frac{1}{\mu(T)} = \frac{1}{\mu(d(T))} + \frac{1}{\Delta\mu_{ne}}, \qquad (28)$$

where $1/\Delta\mu_{ne} = m_F/e\tau_d$ and τ_d^{-1} is defined in [10]. As shown in [10], the inverse relaxation time for the electron transition from state **k** to state **k**' and that for the *d*-hole transition from point $\mathbf{r}_i$ to point $\mathbf{r}_j$ are proportional to the squared overlap integral averaged over the Fermi surface. Since the wave functions of *d* states are spread over distances $\sigma < a_0$, this contribution for jumps with $\Delta r_{ij} > \Delta R_{min} > 2a_0$ is exponentially small (see also [33]): $1/\Delta\mu_{ne} \sim \exp(-2|\Delta r_{ij}|/\sigma)$. For example, by estimating $\Delta r(T)$ from formula (24) at $T = 20$ K, we obtain that the exponent is smaller than minus seven. Therefore, this mechanism makes a very small contribution to the electron momentum relaxation in the low-temperature range and can be neglected.

Thus, the mechanism of inelastic jumps of *d* holes between Fe^{2+} and Fe^{3+} ions causes a decrease in the degree of spatial ordering of the system of Fe^{3+} ions and results in the dependence $\mu^{-1}(T) \sim T^{1/2}$ in the temperature range $10 < T < 35$ K. This mechanism allows a quantitative description of the temperature dependence of the electron mobility in HgSe : Fe crystals.

6. CONCLUSIONS

The correlation potential of a system of mixed-valence iron ions has been calculated and the parameters defining the impurity *d*-band structure have been determined. It was shown that spatial ordering of iron ions in HgSe : Fe in the region of strong Coulomb correlations gives rise to a correlation gap in the density of impurity *d* states, i.e., to the formation of a finite energy gap between populated (Fe^{2+}) and empty (Fe^{3+}) states, as well as to total suppression of resonant electron scattering. The density of states in the impurity *d* band and the inelastic transitions of *d* holes between Fe^{2+} and Fe^{3+} ions due to which the bi- and trivalent iron ions are recharged have been theoretically analyzed. It was shown that the experimentally detected features in the dependences of the electron density and mobility on the temperature and iron content can be explained in terms of the influence of the Coulomb correlations in the system of mixed-valence iron ions on the impurity *d*-band structure.

ACKNOWLEDGMENTS

This study was supported by the Russian Foundation for Basic Research (projects no. 00-02-16299, 02-02-06156), the Dinastiya Foundation, and the International Centre for Fundamental Physics in Moscow (ICFPM).

REFERENCES

1. D. I. Khomskiĭ, Usp. Fiz. Nauk **129** (3), 443 (1979) [Sov. Phys. Usp. **22**, 879 (1979)].
2. M. Yu. Kagan and K. I. Kugel', Usp. Fiz. Nauk **171** (6), 577 (2001) [Phys. Usp. **44**, 553 (2001)].
3. J. M. D. Coey, M. Viret, and S. Molnar, Adv. Phys. **48** (2), 167 (1999).
4. S. K. Park, T. Ishikawa, and Y. Tokura, Phys. Rev. B **58** (7), 3717 (1998).
5. I. M. Tsidil'kovskiĭ, Usp. Fiz. Nauk **162** (2), 63 (1992) [Sov. Phys. Usp. **35**, 85 (1992)].
6. F. Pool, J. Kossut, U. Debska, and R. Reifenberger, Phys. Rev. B **35** (5), 3900 (1987).
7. I. M. Tsidilkovskii and I. G. Kuleyev, Semicond. Sci. Technol. **11**, 625 (1996).
8. I. G. Kuleev, I. I. Lyapilin, and I. M. Tsidil'kovskiĭ, Zh. Éksp. Teor. Fiz. **102** (5), 1652 (1992) [Sov. Phys. JETP **75**, 893 (1992)].
9. I. G. Kuleev, I. I. Lyapilin, A. T. Lonchakov, and I. M. Tsidil'kovskiĭ, Fiz. Tekh. Poluprovodn. (St. Petersburg) **28** (6), 937 (1994) [Semiconductors **28**, 544 (1994)].
10. I. G. Kuleev, I. I. Lyapilin, A. T. Lonchakov, and I. M. Tsidil'kovskiĭ, Zh. Éksp. Teor. Fiz. **106** (4), 1205 (1994) [JETP **79**, 653 (1994)].
11. Z. Wilamowski, A. Mycielski, W. Janstsch, and G. Hendorfer, Phys. Rev. B **38** (5), 3621 (1988).
12. Z. Wilamowski, W. Jantsch, and G. Hendorfer, Semicond. Sci. Technol. **5** (3), S266 (1990).
13. Z. Wilamowski, Acta Phys. Pol. A **77**, 133 (1990).
14. I. G. Kuleev, Fiz. Tverd. Tela (St. Petersburg) **39** (2), 250 (1997) [Phys. Solid State **39**, 219 (1997)].
15. I. G. Kuleev, Fiz. Tverd. Tela (St. Petersburg) **40** (3), 425 (1998) [Phys. Solid State **40**, 389 (1998)].
16. I. G. Kuleev and I. Yu. Arapova, Fiz. Tverd. Tela **43** (3), 403 (2001) [Phys. Solid State **43**, 420 (2001)].
17. P. W. Anderson, Phys. Rev. **124** (1), 41 (1961).
18. B. I. Shklovskiĭ and A. L. Éfros, *Electronic Properties of Doped Semiconductors* (Nauka, Moscow, 1979; Springer, New York, 1984).
19. V. L. Nguen, M. É. Raĭkh, and A. L. Éfros, Fiz. Tverd. Tela (Leningrad) **28**, 1307 (1986) [Sov. Phys. Solid State **28**, 735 (1986)].
20. Z. Wilamowski, K. Swiatek, T. Dietl, and J. Kossut, Solid State Commun. **74** (8), 833 (1990).
21. I. G. Kuleyev, N. K. Lerinman, L. D. Sabirzyanova, *et al.*, Semicond. Sci. Technol. **12**, 840 (1997).
22. J. M. Ziman, *Models of Disorder: The Theoretical Physics of Homogeneously Disordered Systems* (Cambridge Univ. Press, Cambridge, 1979; Mir, Moscow, 1982).
23. R. Balescu, *Equilibrium and Non-Equilibrium Statistical Mechanics* (Wiley, New York, 1975; Mir, Moscow, 1978), Vol. 1.
24. E. I. Khar'kov, V. I. Lysov, and V. E. Fedorov, *Physics of Liquid Metals* (Vishcha Shkola, Kiev, 1979).
25. H. D. Jones, J. Chem. Phys. **55** (6), 2640 (1971).
26. B. Firey and N. W. Ashcroft, Phys. Rev. A **15** (5), 2072 (1977).
27. I. G. Kuleev, N. K. Lerinman, I. I. Lyapilin, *et al.*, Fiz. Tekh. Poluprovodn. (St. Petersburg) **27** (3), 519 (1993) [Semiconductors **27**, 292 (1993)].
28. *Amorphous Solids and the Liquid State*, Ed. by N. H. March, R. A. Street, and M. Tosi (Plenum, New York, 1985).
29. V. M. Askerov, *Electronic Transport Phenomena in Semiconductors* (Nauka, Moscow, 1985).
30. I. G. Kuleev, I. I. Lyapilin, and I. M. Tsidil'kovskiĭ, Fiz. Tverd. Tela (St. Petersburg) **37** (8), 2360 (1995) [Phys. Solid State **37**, 1291 (1995)].
31. P. Protapatas and N. Parlee, High Temp. Sci. **6** (1), 1 (1974).
32. I. G. Kuleev and I. I. Kuleev, Fiz. Tverd. Tela (St. Petersburg) **45** (2), 205 (2003) [Phys. Solid State **45**, 214 (2003)].
33. O. Madelung, *Introduction to Solid State Theory* (Springer, Berlin, 1978; Nauka, Moscow, 1985).
34. A. Miller and E. Abrahams, Phys. Rev. **120** (3), 745 (1960).

Translated by A. Kazantsev

Physics of the Solid State, Vol. 45, No. 10, 2003, pp. 1884–1889. Translated from Fizika Tverdogo Tela, Vol. 45, No. 10, 2003, pp. 1794–1799.

SEMICONDUCTORS AND DIELECTRICS

Simulation of the Stresses Produced in Large-Diameter Silicon Wafers during Thermal Annealing

M. V. Mezhennyĭ*, M. G. Mil'vidskiĭ, and A. I. Prostomolotov*****

** Giredmet State Research Institute for the Rare-Metals Industry, Bol'shoĭ Tolmachevskiĭ per. 5, Moscow, 109017 Russia*

*** Institute for Chemical Problems of Microelectronics, Bol'shoĭ Tolmachevskiĭ per. 5, Moscow, 109017 Russia*

e-mail: icpm@mail.girmet.ru

**** Institute for Problems of Mechanics, Russian Academy of Sciences, Moscow, 109017 Russia*

Received March 11, 2003

Abstract—The three-dimensional problem of stress and strain fields in dislocation-free silicon wafers 200 and 300 mm in diameter placed horizontally on three symmetrical supports and subjected to is gravitational forces and thermal stresses formulated and solved in the isotropic approximation. Under the action of gravitational forces, a wafer is shown to have the lowest total stress when the supports are positioned at a distance of 0.6–0.7*R* from the center of the wafer. The shear-stress fields are calculated for all possible slip systems. The elastic-stress field in a 300-mm wafer is found to be induced mainly by gravitational forces even at a radial temperature gradient of 10 K. At this temperature gradient, the contribution from thermal stresses in a 200-mm wafer is comparable to the contribution from gravitational forces. At radial temperature gradients lower than 5 K, the contribution from thermal stresses can also be neglected for a 200-mm wafer. The maximum shear stresses calculated indicate that one should not neglect possible dislocation generation in the zone of contact between a wafer and the supports during high-temperature annealing of 200-mm and, especially, 300-mm wafers. © *2003 MAIK "Nauka/Interperiodica".*

1. INTRODUCTION

Modern commercial silicon wafers have sharply increased in diameter in recent years; therefore, the problem of elastic stresses in wafers and their possible relaxation through plastic deformation with the formation of dislocations during high-temperature thermal effects has again come to the forefront. The point is that the gravitational forces induced by the weight of a wafer are particularly pertinent in the formation of elastic-stress fields as the wafer diameter increases. Moreover, it is difficult to provide low temperature gradients across the area of a large-diameter wafer during heat treatment. These problems became most important for the production of wafers 200 and 300 mm in diameter.

Wafers are heat-treated in resistive furnaces [1–3] or with halogen incandescent lamps [4]; the latter are most often used for rapid thermal annealing. Upon annealing, wafers are usually placed horizontally on three symmetrically arranged supports. Other methods of fixing wafers are also known: the symmetrical application of four supports or the arrangement of wafers on ring supports. Fisher *et al.* [5] estimated, in a one-dimensional approximation, the maximum shear stresses in 200- and 300-mm silicon wafers caused by gravitational forces for all methods of fixing wafers mentioned above.

In this work, we solve the three-dimensional problem of stressed dislocation-free 200- and 300-mm silicon wafers that are placed horizontally on three symmetrically arranged supports. The wafers are subjected to the gravitational stresses caused by the wafer weight and to thermal stresses caused by a temperature gradient across the wafer area.

2. FORMULATION OF THE PROBLEM

The purpose of this work is to solve the three-dimensional problem of finding the fields of elastic stresses and strains (in the isotropic approximation) in wafers placed horizontally on three symmetrically arranged supports for different values of the distance of the supports from the center of a wafer, namely, 0.5, 0.6, and 0.7*R*, where *R* is the wafer radius.

Upon annealing, a wafer lies freely on three symmetrically arranged supports (Fig. 1). The supports are taken to be perfectly elastic. The wafer can freely slide over the supports; therefore, heating of the wafer does not induce additional stresses related to an increase in the wafer dimensions with an increase in temperature as in the case of a fixed wafer. Taking into account the symmetrical arrangement of the supports, we considered only a 120° sector of the wafer. The equations connecting the fields of displacements u_i, stresses σ_{ij}, and strains ε_{ij} were solved using the finite-element method. The chosen 120° sector of the wafer was divided into a finite number of elements and the size of elements near the point of support was decreased, so that the number of elements increased. The wafer was divided into five elements according to thickness. The wafer thickness

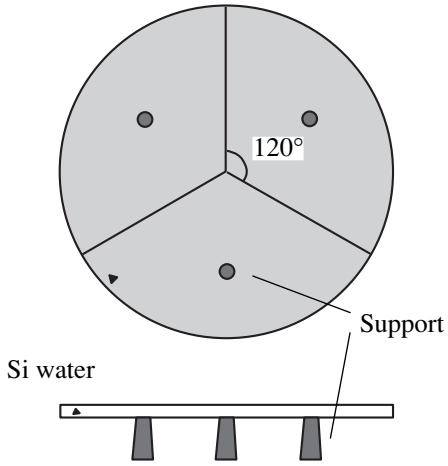

Fig. 1. Division of a wafer into finite elements (schematic).

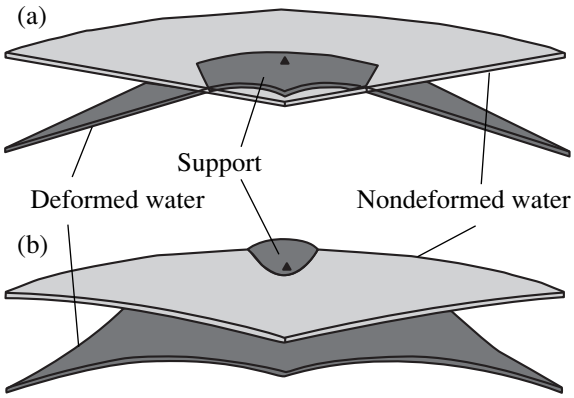

Fig. 2. Calculated patterns of the 300-mm wafer bending (along the *z* axis) under the action of gravitational forces when the supports are located at a distance of (a) 0.5 and (b) 0.7 wafer radius from the center of the wafer.

was taken to be 1000 μm, and the area of the contact surface of a support was ~1 mm^2. It was assumed that the temperature field in the wafer could be determined independently by solving the Laplace equation.

In calculations, we used the following values of the elastic and thermal parameters of silicon: Poisson ratio $\mu = 0.25$, thermal expansion coefficient $\beta = 5.2 \times 10^{-6}$ K^{-1}, shear modulus $G = 6.2 \times 10^4$ MPa, and elastic modulus $E = 2G(1 + \mu) = 1.55 \times 10^5$ MPa (linear approximation of the temperature dependence of the elastic modulus) [6].

3. ANALYSIS OF STRESSES INDUCED BY GRAVITATIONAL FORCES

The simplest estimation of the stresses can be performed by assuming that each support is acted upon by a force equal to one-third of the wafer weight. For a contact area of the wafer and support of 1 mm^2 and a wafer thickness of 1 mm, the maximum working stresses are estimated to be 0.24 and 0.54 MPa for the 200- and 300-mm wafers, respectively. However, this estimation does not take into account the effect of the radial arrangement of the supports. According to rough estimations based on analysis of the balance of the operating forces, the location of the supports at a distance of 0.667*R* from the center of the wafer minimizes stresses in the bulk of the wafer. After completing such rough estimations, we calculated the three-dimensional stress distribution in the wafers.

Figure 2 shows the calculated patterns of a 300-mm wafer bending along the *z* axis (which characterize the bending flexure of the wafer) under the action of gravitational forces when the supports are located at a distance of (a) 0.5 and (b) 0.7 wafer radius from the center of the wafer. These data indicate that the character of deformation of the wafer substantially changes when the supports are shifted radially: as the distance between the supports increases, a positive strain (with respect to the neutral line) in the central part of the wafer changes in magnitude and becomes negative. At the same time, in those peripheral regions of the wafer where the strain is negative and minimal in magnitude, the strain also changes and becomes positive. When the supports are located at a distance of 0.6 wafer radius from the center of the wafer, the displacements are negative in virtually the whole wafer, excluding the regions surrounding the contacts between the supports and the wafer. For the 200-mm wafer, the character of changes in the deformation pattern is similar.

The calculated strains along the *z* axis in the 300-mm wafer for various arrangements of the supports are given in Fig. 3. The deformation pattern has a complex character. The maximum strains, which are observed at the farthest point from the supports at the periphery of the wafer, are seen to decrease as the distance between the support and the center of the wafer increases. A strain is considered to be positive if it is directed opposite to the gravitational forces (i.e., if the wafer bends upward with respect to the neutral plane). A decrease in the wafer diameter from 300 to 200 mm results in a decrease in the maximum strains by a factor of about 4.5.

To characterize the general stressed state of the wafers, we used the Mises stress σ_M [7]. Figure 4 shows the σ_M distribution in the lower plane of the wafer 300 mm in diameter for various radial arrangements of the supports. The stress σ_M is maximum near the supports. When the supports are located at 0.7*R* from the center of the wafer, the maximum stress is $\sigma_M = 1.73$ MPa. When the supports are located at 0.6*R* from the center, the maximum stress decreases to $\sigma_M = 1.37$ MPa. For the supports located at ~0.5*R* from the center of the wafer, the maximum stress is $\sigma_M = 2.76$ MPa. These data show that the wafer as a whole has minimum stresses when the supports are located at (0.6–0.7)*R* from the center of the wafer, which agrees well with the rough estimates performed earlier. Throughout the

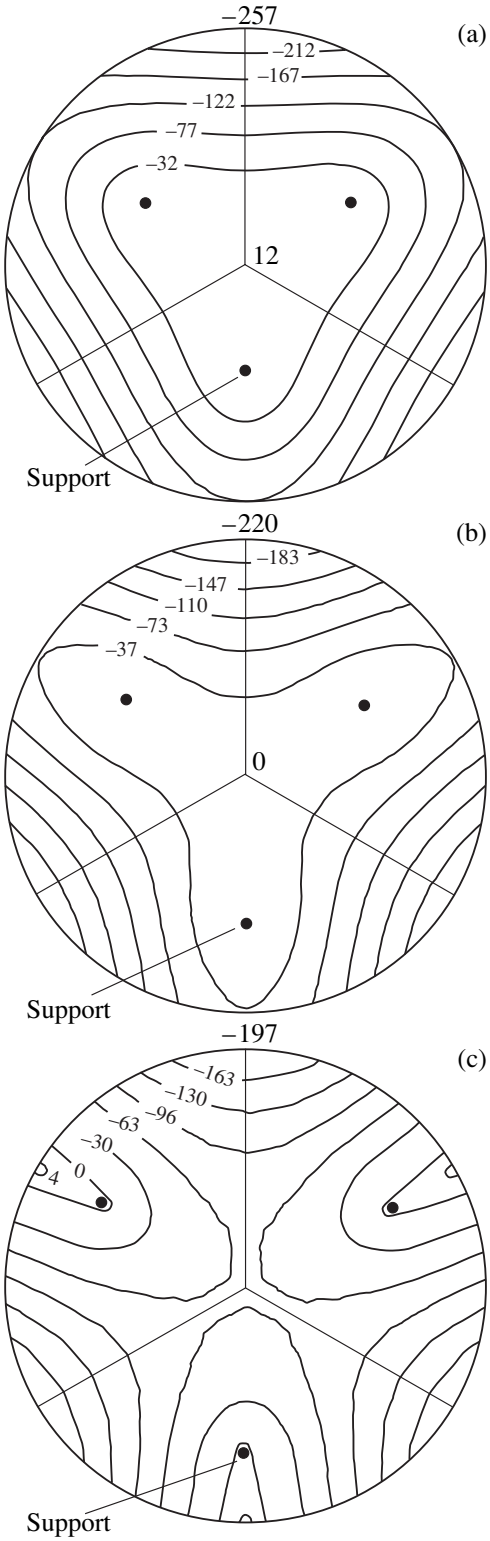

Fig. 3. Strains along the *z* axis caused by the action of gravitational forces in the 300-mm wafer when the supports are located at a distance of (a) 0.5, (b) 0.6, and (c) 0.7 wafer radius from the center of the wafer (numerals on the lines are the strains in the wafer in micrometers; positive numerals correspond to strains directed opposite to the gravitational force, and negative values, to strains directed along this force).

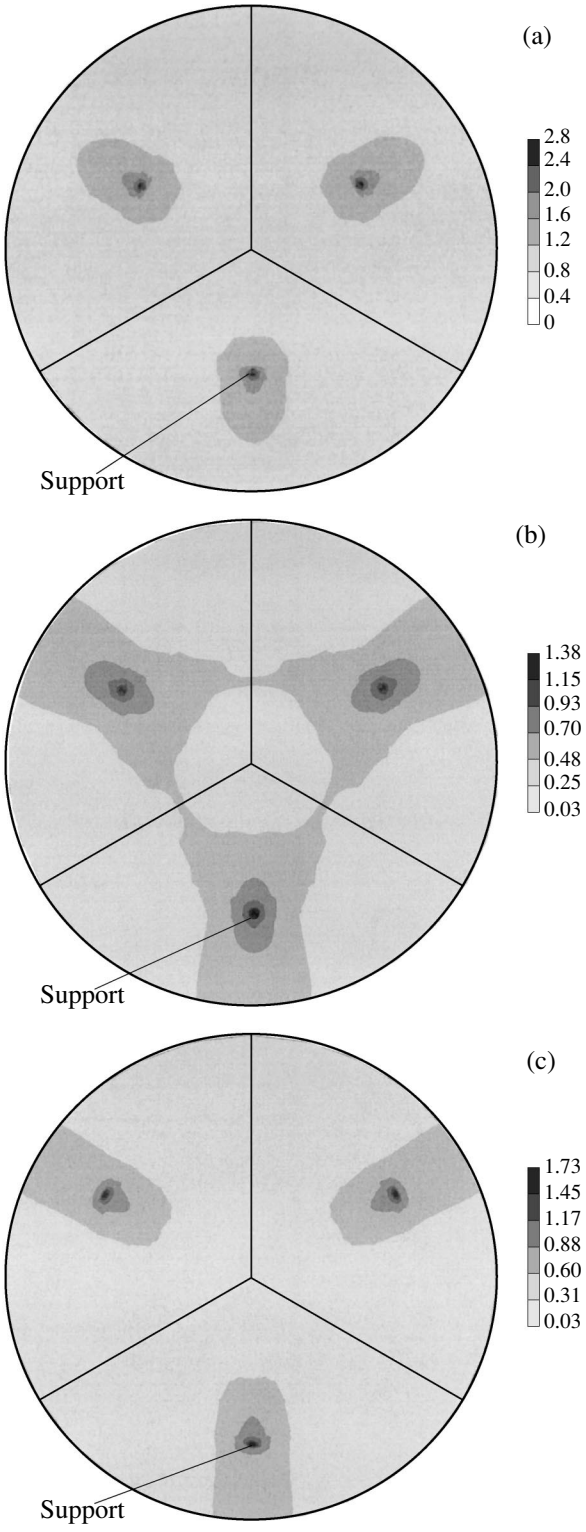

Fig. 4. Distribution of the Mises stresses induced by gravitational forces in the plane of the 300-mm wafer when the supports are located at a distance of (a) 0.5, (b) 0.6, and (c) 0.7 wafer radius from the center of the wafer (numerical values correspond to stresses in megapascals).

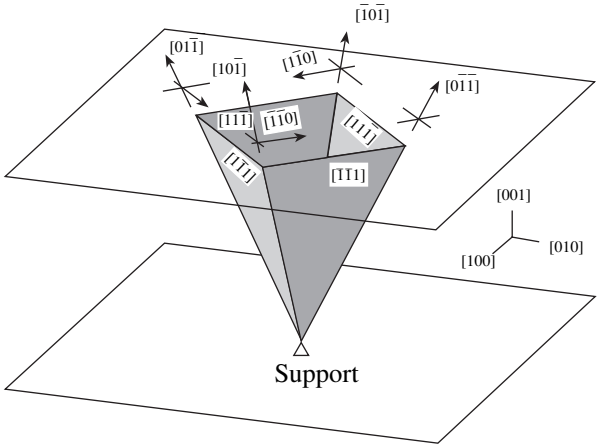

Fig. 5. Arrangement of possible slip systems in a (001) silicon wafer (schematic).

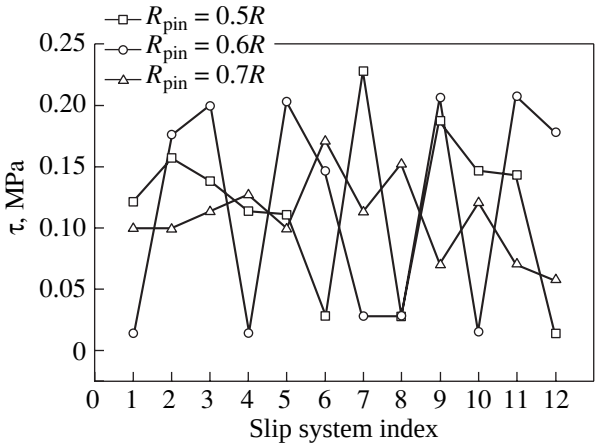

Fig. 6. Maximum shear stresses induced by gravitational forces in the lower surface of the 300-mm wafer at its point of contact with the support for various slip systems and various radial positions of the supports.

greater part of the wafer, stresses do not exceed ~1×10^{-3} MPa. More accurate estimation of the maximum stresses in the contact zone requires a more correct model that takes into account the geometry and material of the supports. The maximum value of σ_M in the 200-mm wafer for the supports located at (0.6–0.7)*R* from the center of the wafer is 0.89 MPa. The working stresses in the majority of the wafer are very low and similar to those in the 300-mm wafer. Thus, the wafer zone near the support has maximum stress and dislocation generation is most probable in this zone.

To estimate the probability of dislocation generation in the wafer, it is necessary to take into account the geometry of possible slip systems. We consider the case of a (001) wafer, which is the most interesting from the practical viewpoint. The scheme of possible slip systems in such a wafer is given in Fig. 5. When calculating the stresses under which dislocations are generated, we have to take into account the shear stress component operating in the plane and direction of easy slip rather than the total operating stresses. When calculating shear stresses, we determined the projection of the calculated resultant vector of the three-dimensional stress field caused by the gravitational forces acting on a slip plane along the easy shear direction. To analyze the propagation of dislocations, we have to answer the question of whether the sign of stresses changes throughout the wafer thickness. In the case where the stresses in the upper and lower surfaces of the wafer differ in sign (the wafer contains a plane with zero stress), dislocations which are nucleated in the wafer–support contact zone can propagate into the bulk of the wafer only to this zero (neutral) plane. If the stresses in the upper and lower surfaces of the wafer are of the same sign, dislocations which are nucleated in the lower surface can propagate throughout the whole wafer thickness. The depth of their penetration depends on the local values of operating stresses.

The shear stresses σ_b were calculated from the formula

$$\sigma_b = \sigma_M \frac{\sigma_x H + \sigma_y K + \sigma_z L}{\sqrt{\sigma_x^2 + \sigma_y^2 + \sigma_z^2}\sqrt{H^2 + K^2 + L^2}} \times \frac{\sigma_x h + \sigma_y k + \sigma_z l}{\sqrt{\sigma_x^2 + \sigma_y^2 + \sigma_z^2}\sqrt{h^2 + k^2 + l^2}}, \quad (1)$$

where σ_x, σ_y, and σ_z are the normal stresses along the *x*, *y*, and *z* axes, respectively; *HKL* are the crystallographic indices of the normal vector to the slip plane;

Possible slip systems used in calculating gravitational stresses in (001) silicon wafers

Slip system index	Slip plane	Slip direction
1	$1\bar{1}\bar{1}$	$\bar{1}0\bar{1}$
2		$0\bar{1}1$
3		110
4	$\bar{1}\bar{1}\bar{1}$	$\bar{1}01$
5		$1\bar{1}0$
6		$01\bar{1}$
7	$11\bar{1}$	101
8		$0\bar{1}\bar{1}$
9		$\bar{1}10$
10	$\bar{1}1\bar{1}$	$10\bar{1}$
11		$\bar{1}\bar{1}0$
12		011

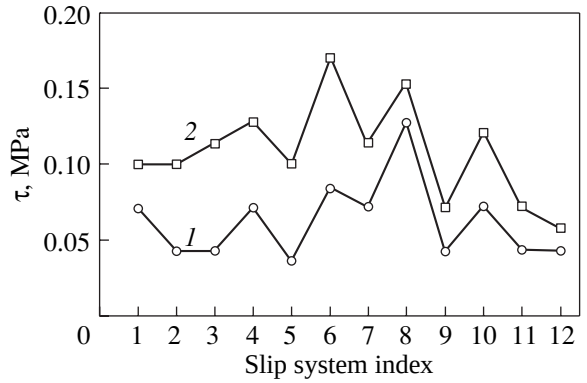

Fig. 7. Maximum shear stresses induced by gravitational forces in the lower surface of the wafers (*1*) 200 and (*2*) 300 mm in diameter at their point of contact with the support for various slip systems. The supports are located at a distance of 0.7*R* from the center of the wafer.

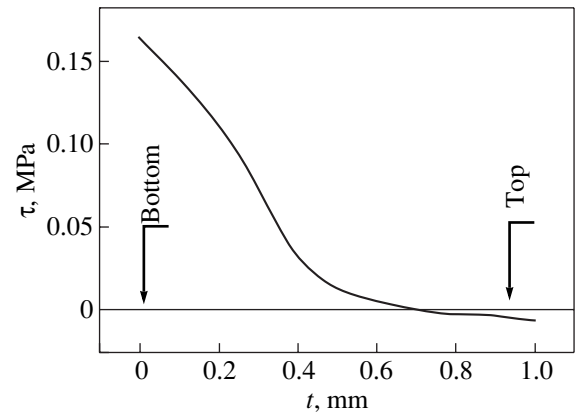

Fig. 8. Distribution of the shear stresses induced by gravitational forces over the thickness of the 300-mm wafer in the cross section that passes through the point of contact of the wafer with the center of the supporting area in the $(\bar{1}\bar{1}\bar{1})[01\bar{1}]$ slip system having the maximum Schmid factor. The supports are located at a distance of 0.7*R* from the center of the wafer.

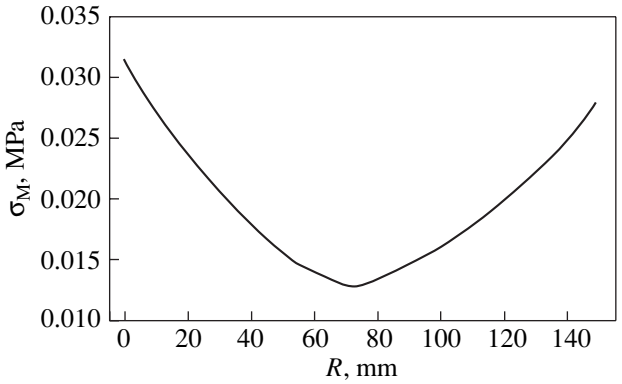

Fig. 9. Radial distribution of thermal stresses σ_M caused by a radial temperature drop of 1 K. The wafer diameter is 300 mm.

and *hkl* are the crystallographic indices of a vector in the slip direction. The first factor in Eq. (1) is the absolute value of the stress vector, the second is the cosine of the angle between the three-dimensional stress vector and its projection on the slip plane (*HKL*), and the third factor is the cosine of the angle between the projection of the three-dimensional stress vector on the slip plane and its projection on the slip direction in this plane. The silicon crystal lattice contains four independent {111} easy-slip planes, each of which contains six pairwise opposite easy-slip directions ⟨110⟩. To estimate the level of stresses, it is sufficient to perform calculations for only 12 slip systems from the 24 possible variants. The slip systems used in calculations are listed in the table.

Even in the isotropic approximation, in order to calculate elastic stresses and determine the shear stresses, we have to know the orientation of the wafer with respect to the supports. The orientation dependence of shear stresses in a slip plane is specified by the mutual crystallographic position of the plate and the three supports. When the wafer rotates about its center, the pyramid formed by the {111} planes (Fig. 5) also rotates around its vertex. Since the shear stresses are maximum at the point of support, the most dangerous sections (from the viewpoint of dislocation generation) for each slip system pass through the point of support. The line of intersection of a slip plane with the wafer surface rotates with respect to the point of support, and the corresponding maximum stress remains unchanged.

Figure 6 shows the calculated maximum shear stresses operating in the corresponding slip systems for the 300-mm wafer at various radial positions of the supports. The shear stresses are maximum in the wafer–support contact zone. Numerals on the abscissa axis show the indices of the corresponding slip systems (see table).

For comparison, Fig. 7 displays the calculated maximum shear stresses in the contact zone for the 200- and 300-mm wafers and the supports located at a distance of 0.7*R* from the center of the wafer. The designation of the slip systems is identical to that in Fig. 6. On average, the shear stresses in the 200-mm wafer are lower than those in the 300-mm wafer by a factor of 1.5–2. It should be noted that the shear stresses near the wafer–support contact zone are an order of magnitude lower than the corresponding values of σ_M.

Figure 8 shows the shear-stress distribution over the wafer thickness in the $(\bar{1}\bar{1}\bar{1})[01\bar{1}]$ slip system, which has the maximum Schmid factor and passes through the point of contact between the wafer and the center of the supporting area. The calculation was conducted for the 300-mm wafer and the supports located at 0.7*R* from the center. This shear-stress distribution indicates that the wafer contains a plane of zero stress positioned at a distance of ~0.7 times the wafer thickness from the lower surface of the wafer. As follows from these data, the maximum shear stress in the lower surface of the

wafer near the contact zone is 0.17 MPa. Such stresses can cause dislocation generation in the region adjacent to the contact zone under heating of the wafers to 1000°C and above. However, dislocations generated in this region can propagate into the wafer only to the neutral plane and cannot reach its upper (working) surface.

4. ANALYSIS OF THERMOELASTIC STRESSES

The cause of thermoelastic stresses is a nonuniform temperature distribution in the wafer plane, which arises under heating. In calculations, we used the traditional approach. As in the case of gravitational forces, we used the Mises stresses σ_M to characterize the stressed state.

As an example, Fig. 9 shows the calculated radial distribution of thermal stresses σ_M in the 300-mm wafer. The radial temperature drop was taken to be 1 K, and the temperature at the center of the wafer was assumed to be 1273 K. At a radial drop of 1 K, the maximum thermal stress σ_M was found to be 0.03 MPa, which is much less than the stresses induced by the gravitational forces. The thermal shear stresses are maximum at the center and periphery of the wafer. Unlike the gravitational stresses, these stresses are minimum near the supports. At the given temperature drop between the center and edge of the 300-mm wafer, the maximum thermal shear stress is ~0.01 MPa. An increase in the radial temperature drop causes a proportional increase in the thermoelastic stresses. The calculations indicate that the maximum thermal shear stresses that appear during thermal annealing are comparable with to maximum stresses caused by the gravitational forces only for the 200-mm wafer and radial temperature drops higher than 10 K. Even at such radial temperature drops, the stresses caused by the gravitational forces in the 300-mm wafer are significantly higher than the thermal stresses.

5. CONCLUSIONS

Thus, we have established that the gravitational forces in the 300-mm wafer play a decisive role in the formation of an elastic-stress field even at a radial temperature drop of 10 K. At this temperature drop, the contribution from thermal stresses in the 200-mm wafer is comparable to the contribution from the gravitational forces. If the radial temperature drop is lower than 5 K, the contribution from thermal stresses can also be neglected for the 200-mm wafer.

The distribution of elastic stresses caused by the gravitational forces in the wafers has been found to be a rather sensitive function of the radial arrangement of the supports. We showed that a wafer has the lowest total stresses when the supports are positioned symmetrically at a distance of (0.6–0.7)*R* from the center of the wafer. The calculated maximum shear stresses indicate that one cannot neglect possible dislocation generation in the zone of contact between a wafer and the supports during high-temperature annealing in 200-mm wafers and, especially, 300-mm wafers.

ACKNOWLEDGMENTS

This work was supported by the Russian Foundation for Basic Research, project no. 01-02-16816.

REFERENCES

1. H. Katsumata, H. Ito, H. Takahashi, *et al.*, U.S. Patent No. 6250914 (2000).
2. M. Hatta, U.S. Patent No. 6032724 (1997).
3. H.-S. Kyung, W.-S. Choi, and J.-H. Shin, U.S. Patent No. 5791895 (1996).
4. K. E. Johnsgard, B. S. Mattson, and J. McDiarmid, U.S. Patent No. 6002109 (1995).
5. A. Fisher, G. Richter, W. Kurner, and P. Kucher, J. Appl. Phys. **87**, 1543 (2000).
6. O. H. Nielsen, Prop. of Silica, EMIS Datarev, Ser. 14 (1987).
7. B. A. Boley and J. H. Weiner, *Theory of Thermal Stresses* (Wiley, New York, 1960; Mir, Moscow, 1964).

Translated by K. Shakhlevich

Physics of the Solid State, Vol. 45, No. 10, 2003, pp. 1890–1892. Translated from Fizika Tverdogo Tela, Vol. 45, No. 10, 2003, pp. 1800–1802.

SEMICONDUCTORS AND DIELECTRICS

The Mechanism of Emission in the Red Photoluminescence Band of Porous Silicon

V. F. Agekyan and A. Yu. Stepanov

Fock Institute of Physics, St. Petersburg State University, ul. Pervogo Maya 100, Petrodvorets, St. Petersburg, 198504 Russia

Received March 20, 2003

Abstract—Porous silicon (PS) exhibits several photoluminescence (PL) bands, whose spectral position and intensity depend strongly on the actual conditions of preparation of PS, its treatment, and subsequent use. The PS PL band peaking at about 1.8 eV and usually assigned to the intrinsic emission of silicon nanocrystals was studied. It was shown that the temperature-induced variation of the PL kinetics in the 80 to 300-K interval follows a complex pattern and depends noticeably on the actual point on the band profile. The temperature behavior of PL decay in the 1.8-eV band is determined by the electron–hole recombination rate within a nanocrystal and the cascade carrier transitions from small to large nanocrystals, with an attendant decrease in energy. *© 2003 MAIK "Nauka/Interperiodica".*

As established in numerous studies, the photoluminescence (PL) spectrum of porous silicon (PS) depends dramatically on the technique of its preparation, its subsequent treatment, and the actual conditions and duration of its storage (see, e.g., [1–5]). There is, however, no consensus on the origin of the individual PS PL bands. Most authors assign the slowly decaying band in the visible region (the so-called *S* band) to the intrinsic radiation of size-quantized silicon crystals [6–10]. The electrons and holes in semiconductor nanocrystals are spaced much closer than those in bulk crystals, which gives rise to a very large increase in exchange coupling. As a result, the exchange splitting of electronic levels in silicon nanocrystals is capable of strongly affecting the temperature dependence of the *S*-band kinetics [10, 11]. Calculations show that the exchange splitting in nanocrystals making up PS can be larger than 10 meV. As a result, at lower temperatures, the luminescence kinetics depends totally on the properties of the lowest component in the exchange doublet, i.e., of the triplet level [11–14]. In this case, the PL decay time τ is long because of the triplet level being metastable. From the good agreement of the experimental $\tau(T)$ dependences for the *S* band with theoretical calculations of the exchange splitting in silicon nanocrystals, some authors drew the conclusion that the contribution of the cascade transitions to the *S*-band formation at low temperatures is insignificant. It should, however, be pointed out that agreement between experimental measurements of the PS PL kinetics with calculations has also been reached with other models. In [15], the slow decay of the *S* band was described by an extended exponential function taking into account the hopping carrier motion on the surface of a silicon nanocrystal; there are also arguments in favor of efficient tunneling migration of electrons and holes between nanocrystals in the interval 70–300 K [16]. This communication reports on a study of specific features in the temperature dependence and spectral response of the PS *S*-band kinetics in the range from 70 K to room temperature.

PS samples with a porosity of about 70% were prepared by anodic etching of crystalline silicon [4] and stored for a long period of time in standard atmospheric conditions. PL was excited by a cw argon laser with a photon energy of 2.41 eV or by nitrogen laser pulses with a photon energy of 3.68 eV, pulse duration of 5 ns, and pulse repetition frequency of 100 Hz. The pulse excitation intensity was about 10^4 W cm^{-2}, and the spectra were taken with a DFS-12 spectrometer and a Boxcar integrator.

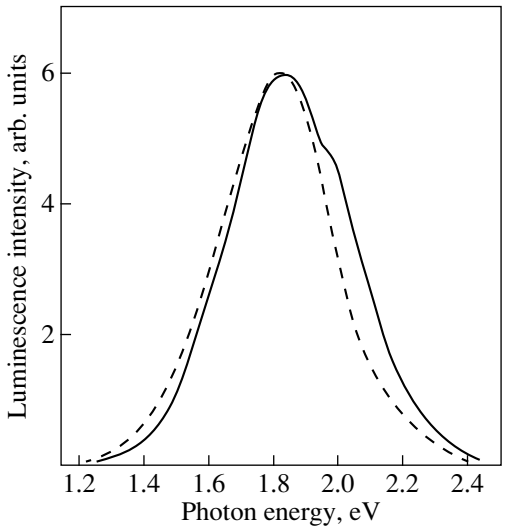

Fig. 1. *S* band in the photoluminescence of PS under pulsed excitation measured during the first 50 μs after the pulse at room temperature (dashed line) and at 77 K (solid line).

1063-7834/03/4510-1890$24.00

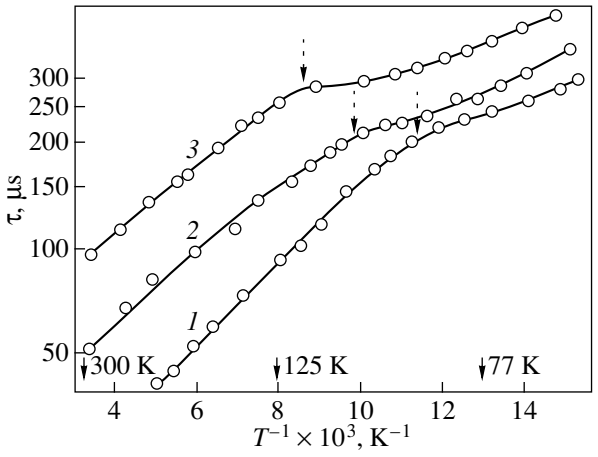

Fig. 2. Temperature dependence of the porous-silicon photoluminescence decay time τ measured (*1*) on the high-energy wing, (*2*) at the maximum, and (*3*) on the low-energy wing of the *S* band. Dashed arrows specify the values of $1/T_c$ corresponding to sharp changes in the $\tau(T)$ relations.

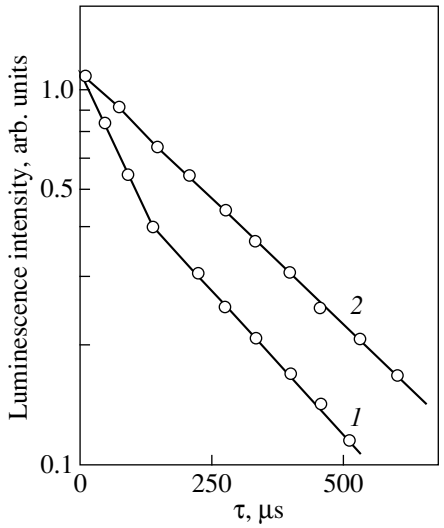

Fig. 3. PS photoluminescence decay kinetics (*1*) on the low-energy wing, at about 1.6 eV, and (*2*) at the maximum, 2.1 eV, of the *S* band measured at 77 K.

The *S* band observed in our samples at room temperature under excitation with a cw argon laser peaks at 1.8 eV and has a halfwidth of 0.35 eV; the peak position and halfwidth vary only weakly in the temperature interval studied. The spectra obtained under pulsed excitation with nanosecond delay times are dominated by a shorter wavelength radiation, which is characteristic of relaxed PS samples and is related to oxides and, possibly, other silicon compounds [17–20], but the spectrum gated with a microsecond scale delay contains the *S* band only. The *S* band measured under pulsed excitation within the first 50-μs gate after the pulse is symmetric at room temperature, but at 77 K its high-energy wing is intensified (Fig. 1). We carried out a comprehensive study of the $\tau(T)$ relation for three energies corresponding to the wings and the maximum of the *S* band (Fig. 2). Since the PL kinetics can be complex and described by more than one exponential, we accepted τ as the characteristic decay time in which the PL intensity dropped *e*-fold. As seen from Fig. 2, each of the three graphs reveals a break with a plateau, but in different temperature intervals. The temperature T_c corresponding to the break in the $\tau(T)$ curve is governed by the recombination dynamics in nanocrystals and by the cascade carrier transitions from small to larger nanocrystals, which involve a decrease in energy. These mechanisms significantly depend on the nanocrystal size. The break point and the plateau shift toward higher temperatures with a decrease in the energy of the photons whose kinetics are being measured. This may be attributed to the fact that the fast temperature-induced decrease in τ for $T > T_c$ is determined largely by carrier migration to larger nanocrystals as a result of enhancement of the cascade transition. Such processes are the most efficient for carriers residing in small nanocrystals (the high-energy wing of the *S* band). The smooth decrease in τ observed to occur under sample heating at lower temperatures originates from the increase in the population of the upper (singlet) component of the exchange doublet. At high temperatures, the characteristic decay time of the electron–hole luminescence decreases because of the enhanced nonradiative relaxation.

The kinetics curves measured at different points on the *S*-band profile support this reasoning. The decay in the low-energy wing at $T = 77$ K is described by a simple exponential that characterizes the electron–hole recombination kinetics, whereas the kinetics related to the high-energy wing contains an additional contribution (Fig. 3), which is apparently accounted for by the cascade migration of carriers involving a decrease in their energy. The $\tau(E)$ relation measured over the *S*-band profile at room temperature turns out to be linear

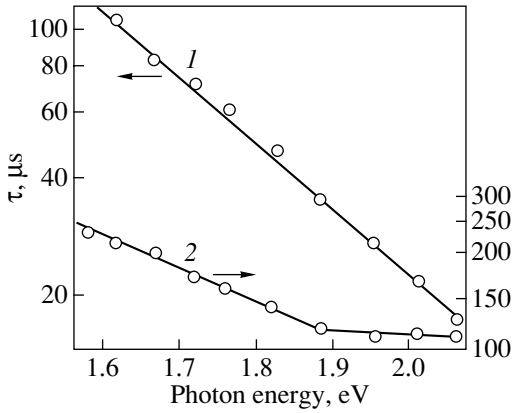

Fig. 4. Spectral response of the photoluminescence decay time τ of porous silicon measured over the *S*-band profile (*1*) at 300 and (*2*) 77 K.

(Fig. 4). The more complex behavior of τ over the band profile observed at 77 K, involving a sharp change at about 1.9 eV, suggests that the relative contribution of the above factors to radiative recombination at low temperatures differs strongly at different points on the *S*-band profile.

ACKNOWLEDGMENTS

This study was supported in part by the Ministry of Education of the Russian Federation, project no. E 02-3.4-426.

REFERENCES

1. A. Bsiesy, J. C. Vial, F. Gaspard, *et al.*, Surf. Sci. **254** (1–3), 195 (1991).
2. L. T. Canham, W. Y. Leong, T. I. Cox, *et al.*, in *Proceedings of the 21st International Conference on Physics of Semiconductors*, Ed. by P. Jiang and H. Z. Zhang (World Sci., Singapore, 1993), p. 1423.
3. V. F. Agekyan, V. V. Emtsev, A. A. Lebedev, *et al.*, Fiz. Tekh. Poluprovodn. (St. Petersburg) **33** (12), 1462 (1999) [Semiconductors **33**, 1315 (1999)].
4. V. F. Agekyan, A. M. Aprelev, R. Laĭkho, and Yu. A. Stepanov, Fiz. Tverd. Tela (St. Petersburg) **42** (8), 1393 (2000) [Phys. Solid State **42**, 1431 (2000)].
5. N. E. Korsunskaya, T. V. Torchinskaya, B. R. Dzhumaev, *et al.*, Fiz. Tekh. Poluprovodn. (St. Petersburg) **31** (8), 908 (1997) [Semiconductors **31**, 773 (1997)].
6. S. Guha, G. Hendershot, D. Peeples, *et al.*, Appl. Phys. Lett. **64** (5), 613 (1994).
7. K. Ito, S. Ohyama, Y. Uehara, and S. Ushiroda, Surf. Sci. **363**, 423 (1996).
8. A. G. Gullis and L. T. Canham, Nature **333** (6342), 335 (1991).
9. G. D. Sanders and Yia-Chung Chang, Phys. Rev. B **45** (16), 9202 (1992).
10. A. G. Gullis, L. T. Canham, and P. D. J. Calcott, J. Appl. Phys. **82** (3), 909 (1997).
11. P. D. J. Calcott, K. J. Nash, L. T. Canham, *et al.*, J. Phys.: Condens. Matter **5** (7), L91 (1993).
12. P. D. J. Calcott, K. J. Nash, L. T. Canham, *et al.*, J. Lumin. **57** (1), 257 (1993).
13. L. Pavesi and M. Ceschini, Phys. Rev. B **48** (23), 17625 (1993).
14. G. Mauckner, K. Tronke, T. Baier, *et al.*, J. Appl. Phys. **75** (8), 4167 (1994).
15. Y. Kanemitsu and T. Ogava, Surf. Rev. Lett. **3** (1), 1163 (1996).
16. T. Suemoto, K. Tanaka, and A. Nakajima, Phys. Rev. B **49** (16), 11005 (1994).
17. L. T. Canham, A. Loni, P. D. J. Calcott, *et al.*, Thin Solid Films **276** (1), 112 (1996).
18. V. F. Agekyan, A. A. Lebedev, Yu. V. Rud', and Yu. A. Stepanov, Fiz. Tverd. Tela (St. Petersburg) **38** (10), 2994 (1996) [Phys. Solid State **38**, 1637 (1996)].
19. L. Tsybeskov, Yu. V. Vandychev, and P. M. Fauchet, Phys. Rev. B **49** (11), 7821 (1994).
20. N. Chiodini, F. Meinardi, F. Mozzaroni, *et al.*, Appl. Phys. Lett. **76** (22), 3209 (2000).

Translated by G. Skrebtsov

Physics of the Solid State, Vol. 45, No. 10, 2003, pp. 1893–1897. Translated from Fizika Tverdogo Tela, Vol. 45, No. 10, 2003, pp. 1803–1806.

SEMICONDUCTORS AND DIELECTRICS

Crystal Structure of Di-(*L*-Serine) Phosphate Monohydrate $[C_3O_3NH_7]_2H_3PO_4H_2O$

Yu. I. Smolin*, A. E. Lapshin*, and G. A. Pankova**

** Grebenshchikov Institute of Silicate Chemistry, Russian Academy of Sciences, ul. Odoevskogo 24/2, St. Petersburg, 199155 Russia*

e-mail: smolin@isc.nw.ru

*** Institute of Macromolecular Compounds, Russian Academy of Sciences, Bol'shoĭ pr. 31, St. Petersburg, 119004 Russia*

Received February 4, 2003

Abstract—The crystal structure of di-(*L*-serine) phosphate monohydrate $[C_3O_3NH_7]_2H_3PO_4H_2O$ is determined by single-crystal x-ray diffraction. The intensities of x-ray reflections are measured at temperatures of 295 and 203 K. The crystal structure is refined using two sets of intensities. It is established that, in the structure, symmetrically nonequivalent molecules of *L*-serine occur in two forms, namely, the monoprotonated positively charged molecule $CH_2(OH)CH(NH_3)^+COOH$ and the zwitterion $CH_2(OH)CH(NH_3)^+COO^-$, which are linked with each other and with the $H_2PO_4^-$ ion through a hydrogen-bond system involving water molecules. © *2003 MAIK "Nauka/Interperiodica".*

1. INTRODUCTION

Owing to their structural features, crystals of inorganic derivatives of proteinic amino acids are of great interest both for searching for new pyroelectric and piezoelectric materials and for understanding the role played by the electrical properties of proteinic amino acids in processes occurring in living organisms. The technique of growing single crystals of amino acids and their inorganic derivatives, tentative x-ray structure characteristics, and the temperature dependence of the piezoresponce of the crystals were described in [1]. The structures of β-alanine, *DL*-alanine, sarcosine, and *L*-alanine phosphates were investigated earlier in [2, 3]. The purpose of this study is to determine the crystal structure of di-(*L*-serine) phosphate monohydrate $[C_3O_3NH_7]_2H_3PO_4H_2O$, which, according to the structural database [4], has not been characterized before.

2. SAMPLE PREPARATION AND EXPERIMENTAL TECHNIQUE

Crystals of $[C_3O_3NH_7]_2H_3PO_4H_2O$ are monoclinic, space group $P2_1$, a = 4.704(5) Å, b = 10.512(5) Å, c = 13.573(3) Å, β = 98.73(5)°, V = 663.4 Å^3, Z = 2, ρ_{calc} = 1.63 g cm^{-3}, λ(MoK_α) = 0.71069 Å, μ = 2.68 cm^{-1}, F(000) = 344, and M = 326.20. Crystals of *L*-serine phosphate monohydrate were prepared by slow cooling of saturated water solutions of *L*-serine and phosphoric acid. The temperature of the solution decreased from room temperature to 8°C at a rate of 1 K/day. A colorless crystal ($0.4 \times 0.35 \times 0.5$ mm in size) suitable for x-ray diffraction analysis was used in the measurements.

The intensities of x-ray reflections were measured on an automated single-crystal diffractometer operating in a perpendicular beam geometry with layer-by-layer analysis (MoK_α radiation, pyrolytic graphite monochromator). The reflections were measured in the ranges h(–7, 7) k(0, 15) l(0, 14) at $2\Theta_{max}$ = 72°. The measurements were carried out for 2037 nonzero nonequivalent reflections with $I > 3\sigma(I)$. The estimation of the integrated intensities and correction for the background were performed using an algorithm of the profile analysis [5].

The stability of the crystal was checked by periodic measurement of the intensity of the standard reflection. The coordinates of the non-hydrogen atoms were determined by direct methods with the AREN software package [6]. All the hydrogen atoms were located in a series of difference syntheses alternating with the least-squares refinement of the positional and thermal parameters of the atoms for the $F^2(hkl)$ set with the SHELXL97 software package [7].[1] The thermal parameters were refined in the anisotropic approximation for the non-hydrogen atoms and in the isotropic approximation for the hydrogen atoms. The final R_1 factor calculated for all the reflections measured is equal to 0.0332 and wR_2 = 0.1047. The total number of parameters refined is 257 and S = 0.97. The results of the refinement, the atomic coordinates, and the equivalent thermal parameters are given in Table 1.

The figure shows the projection of the crystal structure of *L*-serine phosphate monohydrate, which was drawn with the ORTEP III program [8]. The selected

[1] The exact determination of the parameters mentioned in this paper is also given in [7].

Table 1. Fractional coordinates of the atoms and their equivalent thermal parameters

Atom	*x*/*a*	*y*/*b*	*z*/*c*	U_{equiv}/U_{iso} (Å^2)
P(1)	0.05339(5)	0.65189(2)	0.24138(2)	0.01682(5)
O(1)	−0.00540(19)	0.51247(9)	0.22114(8)	0.0264(2)
O(2)	−0.18764(17)	0.72715(9)	0.27598(8)	0.0247(2)
O(3)	0.13069(18)	0.71983(9)	0.14711(8)	0.0244(2)
O(4)	0.32675(17)	0.66183(13)	0.32538(8)	0.0306(2)
O(5)	0.08244(19)	0.20332(11)	0.25228(8)	0.0280(2)
O(6)	0.2747(3)	0.12542(12)	0.40126(10)	0.0395(3)
C(1)	0.2688(2)	0.20107(12)	0.32377(10)	0.0226(3)
C(2)	0.5315(2)	0.28586(12)	0.33227(10)	0.0215(3)
C(3)	0.5730(3)	0.36569(16)	0.42652(12)	0.0306(3)
O(7)	0.3217(3)	0.43459(12)	0.43828(9)	0.0338(3)
N(1)	0.5079(2)	0.36553(10)	0.24097(9)	0.0215(2)
O(8)	0.4607(2)	0.73740(9)	−0.05717(8)	0.0308(2)
O(9)	0.4617(2)	0.59009(10)	0.06228(8)	0.0273(2)
C(4)	0.5370(2)	0.63412(10)	−0.01567(10)	0.0185(2)
C(5)	0.7309(2)	0.55024(10)	−0.06892(9)	0.0164(2)
C(6)	0.5498(2)	0.49113(11)	−0.16007(10)	0.0202(2)
O(10)	0.33541(19)	0.41453(10)	−0.12571(8)	0.0263(2)
N(2)	0.8653(2)	0.44712(9)	−0.00126(8)	0.0190(2)
O(*w*)	0.1285(3)	0.45925(11)	0.61932(10)	0.0386(3)
H(1)	0.246(5)	0.675(3)	0.1226(19)	0.054(7)
H(2)	0.487(8)	0.663(5)	0.311(3)	0.101(12)
H(3)	0.127(7)	0.086(3)	0.391(2)	0.062(8)
H(4)	0.693(4)	0.236(2)	0.334(2)	0.026(5)
H(5)	0.628(4)	0.311(2)	0.485(2)	0.021(4)
H(6)	0.755(5)	0.424(3)	0.424(2)	0.045(6)
H(7)	0.315(7)	0.489(4)	0.396(2)	0.077(10)
H(8)	0.511(5)	0.316(3)	0.181(2)	0.048(7)
H(9)	0.345(4)	0.419(2)	0.236(2)	0.027(5)
H(10)	0.650(5)	0.419(3)	0.242(2)	0.041(6)
H(11)	0.897(4)	0.598(2)	−0.089(2)	0.019(4)
H(12)	0.465(3)	0.560(2)	−0.204(2)	0.006(3)
H(13)	0.666(3)	0.442(2)	−0.197(2)	0.018(4)
H(14)	0.301(5)	0.366(2)	−0.168(2)	0.043(6)
H(15)	1.014(4)	0.416(2)	−0.021(2)	0.024(4)
H(16)	0.732(5)	0.380(3)	−0.000(2)	0.041(6)
H(17)	0.920(4)	0.473(2)	0.062(2)	0.021(4)
H(18)	0.213(5)	0.450(2)	0.577(2)	0.037(6)
H(19)	0.134(4)	0.397(3)	0.661(2)	0.039(6)

interatomic distances and bond angles are presented in Table 2. The structural parameters were also refined using a set of intensities measured at 203 K [a = 4.688(5) Å, b = 10.482(5) Å, c = 13.524(5) Å, β = 98.07(5)°]. Since the coordinates and thermal parameters of the atoms at this temperature differ insignificantly from those obtained for the structure measured at room temperature, Table 2 includes only the atomic coordinates and equivalent thermal parameters for this structure.

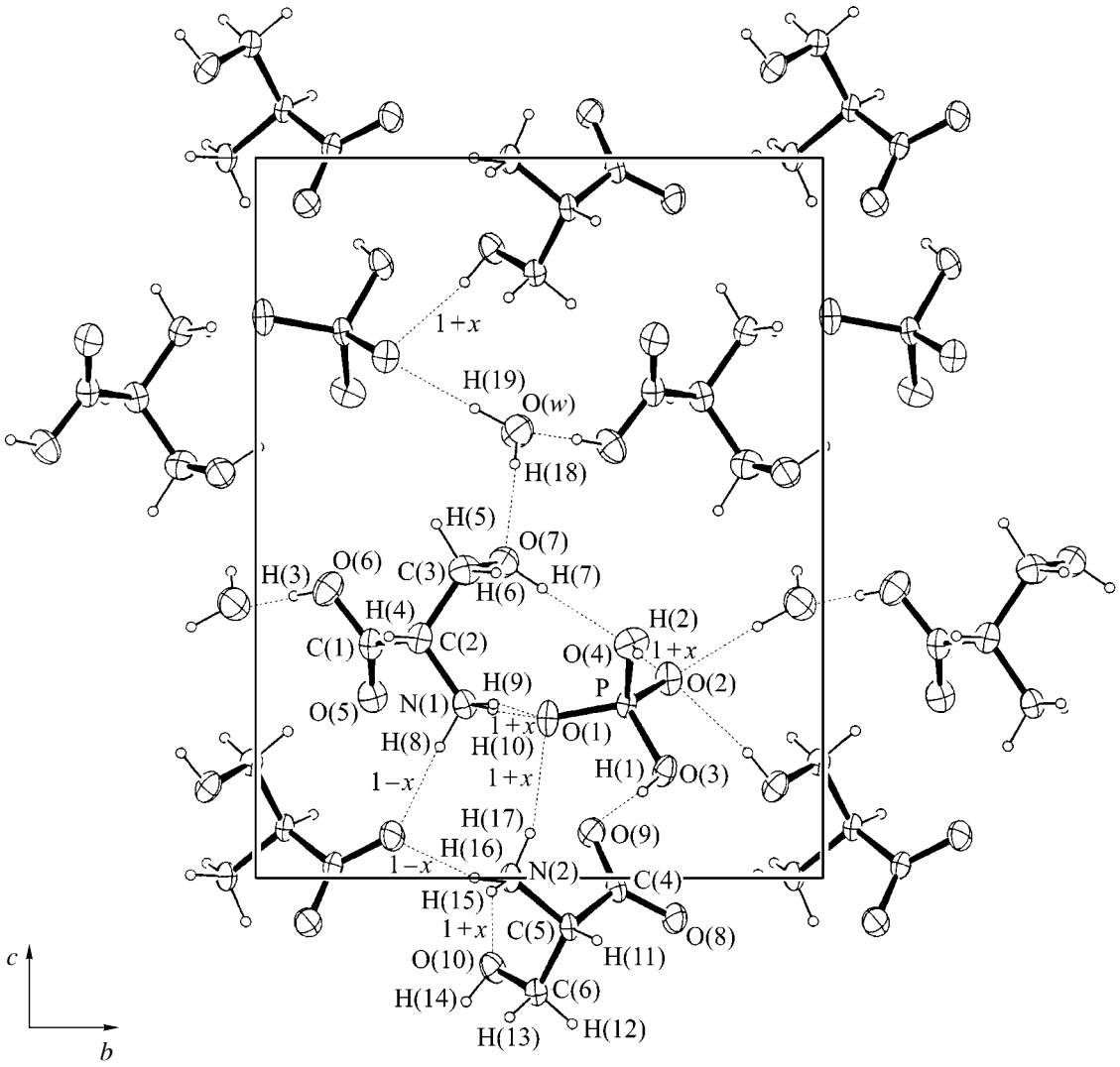

Projection of the crystal structure of di-(*L*-serine) phosphate monohydrate onto the *bc* plane. The non-hydrogen atoms are shown as thermal ellipsoids. The hydrogen atoms are drawn as spheres of arbitrary radius. Dashed lines indicate hydrogen bonds.

The crystallographic data for the structure studied have been deposited with the Cambridge Crystallographic Data Center as supplementary publication no. CCDC 201 068.

3. RESULTS AND DISCUSSION

The structure involves *L*-serine molecules in the form of a monoprotonated molecule of $CH_2(OH)CH(NH_3)^+COOH$ (*L*-serine-1) and a zwitterion of $CH_2(OH)CH(NH_3)^+COO^-$ (*L*-serine-2). The amine group NH_2 in the *L*-alanine-1 molecule is additionally protonated by a hydrogen atom of the phosphate ion. As a consequence, the molecule becomes positively charged. In the zwitterion, an additional protonation of the amine group occurs through the deprotonation of the carboxyl group and the molecule remains electroneutral. The C–C and C–N bond lengths and bond angles in both forms of *L*-serine molecules are close to each other and fall in the predicted ranges (C–C, 1.514(2)–1.527(2) Å; C–N, 1.486(2)–1.497(2) Å) [9, 10]. However, owing to the deprotonation of the carboxyl group in the zwitterion, the C–O bond lengths are close to each other and equal to 1.250(2) and 1.254(2) Å, which are the mean of the relevant bond lengths in the carboxyl group of the *L*-serine-1 molecule [1.205(2) and 1.316(2) Å]. These two forms of *L*-serine molecules are linked by hydrogen bonds. It follows from Table 2 that the $H_2PO_4^-$ ion represents a distorted tetrahedron, because the P–OH distances [1.556 (1) and 1.587(1) Å] are considerably longer than the P–O bonds [1.509(1) and 1.514(1) Å]. The phosphate ions are linked through a hydrogen-bond system with the surrounding *L*-serine molecules. The parameters of the hydrogen bonds are listed in Table 3. The water molecule forms hydrogen bonds with the phosphate ion and

Table 2. Selected bond lengths (Å) and bond angles (deg)

$H_2PO_4^-$			
P(1)–O(1)	1.5089(10)	O(1)–P(1)–O(2)	116.02(5)
P(1)–O(2)	1.5145(9)	O(1)–P(1)–O(3)	110.82(6)
P(1)–O(3)	1.5559(10)	O(2)–P(1)–O(3)	107.14(5)
P(1)–O(4)	1.5872(9)	O(1)–P(1)–O(4)	107.51(6)
		O(2)–P(1)–O(4)	107.81(6)
		O(3)–P(1)–O(4)	107.19(5)
L-Serine-1			
O(5)–C(1)	1.205(2)	O(5)–C(1)–O(6)	125.5(2)
O(6)–C(1)	1.316(2)	O(5)–C(1)–C(2)	122.4(2)
C(1)–C(2)	1.514(2)	O(6)–C(1)–C(2)	112.2(2)
C(2)–N(1)	1.486(2)	N(1)–C(2)–C(1)	108.2(1)
C(2)–C(3)	1.518(2)	N(1)–C(2)–C(3)	112.0(2)
C(3)–O(7)	1.416(2)	C(1)–C(2)–C(3)	112.9(2)
		O(7)–C(3)–C(2)	112.0(2)
L-Serine-2			
O(8)–C(4)	1.250(2)	O(8)–C(4)–O(9)	127.0(2)
O(9)–C(4)	1.254(2)	O(8)–C(4)–C(5)	116.1(1)
C(4)–C(5)	1.527(2)	O(9)–C(4)–C(5)	116.9(1)
C(5)–N(2)	1.497(2)	N(2)–C(5)–C(6)	109.6(1)
C(5)–C(6)	1.524(2)	N(2)–C(5)–C(4)	110.8(1)
C(6)–C(10)	1.423(2)	C(6)–C(5)–C(4)	108.6(1)
		O(10)–C(6)–C(5)	107.5(1)

Table 3. Parameters of the hydrogen bonds

A–H…*D*	*A*–H(*A*)	H…*D*(*A*)	*A*…*D*(*A*)	*AHD* (deg)
O(3)–H(1)–O(9)	0.82(3)	1.66(3)	2.481(2)	174(3)
O(7)–H(7)–O(4)	0.81(4)	2.06(4)	2.840(2)	163(3)
N(1)–H(8)–O(8)^{iii}	0.97(3)	1.90(3)	2.859(2)	172(2)
N(1)–H(9)–O(1)	0.94(2)	1.90(2)	2.845(2)	174(2)
N(1)–H(10)–O(1)^{i}	0.87(3)	1.95(2)	2.808(2)	167(2)
O(10)–H(14)–O(2)^{iv}	0.76(2)	2.08(2)	2.845(2)	176(3)
N(2)–H(15)–O(10)^{i}	0.85(2)	2.23(2)	2.999(2)	151(2)
N(2)–H(16)–O(8)^{iii}	0.95(3)	1.97(3)	2.865(2)	157(2)
N(2)–H(17)–O(1)^{i}	0.90(2)	2.17(2)	3.065(2)	170(2)
O(*w*)–H(18)–O(7)	0.75(3)	2.03(3)	2.758(2)	163(2)
O(*w*)–H(19)–O(2)^{ii}	0.87(3)	1.97(3)	2.816(2)	163(2)
C(2)–H(4)	0.92(2)			
C(3)–H(5)	0.98(2)			
C(3)–H(6)	1.05(3)			
C(5)–H(11)	1.00(2)			
C(6)–H(13)	0.95(2)			
C(6)–H(12)	0.99(2)			

Symmetry codes: (i) $1 + x, y, z$; (ii) $x, y - 1/2, -z + 1$; (iii) $1 - x, y - 1/2, -z$; (iv) $x, y - 1/2, -z$.

the *L*-serine-1 molecule and is coordinated by the hydrogen atom of the carboxyl group of another molecule of *L*-serine-1. Thus, we can conclude that, in addition to electrostatic interactions, the structure is characterized by an extended system of hydrogen bonds.

ACKNOWLEDGMENTS

This work was supported by the Russian Foundation for Basic Research, project no. 01-02-17163.

REFERENCES

1. V. V. Lemanov, S. N. Popov, and G. A. Pankova, Fiz. Tverd. Tela (St. Petersburg) **44** (10), 1840 (2002) [Phys. Solid State **44**, 1929 (2002)].
2. M. T. Averbuch-Pouchot, A. Durif, and J. C. Guite, Acta Crystallogr. C **44**, 1968 (1988).
3. Yu. I. Smolin, A. E. Lapshin, and G. A. Pankova, Kristallografiya **48**, 280 (2003) [Crystallogr. Rep. **48**, 283 (2003)].
4. F. H. Allen, Acta Crystallogr. B **58**, 380 (2002).
5. S. Oatley and S. French, Acta Crystallogr. A **38**, 537 (1982).
6. V. N. Andrianov, Kristallografiya **32** (1), 228 (1987) [Sov. Phys. Crystallogr. **32**, 130 (1987)].
7. G. M. Sheldrick, *SHELXL97: Program for the Refinement of Crystal Structures* (Univ. of Göttingen, Germany, 1997).
8. M. N. Burnett and C. K. Johnson, ORTEP III: Report ORNL-6895 (Oak Ridge National Laboratory, Tennessee, 1996).
9. T. J. Kistenmacher, G. A. Rand, and E. Marsh, Acta Crystallogr. B **30** (11), 2573 (1974).
10. M. N. Frey, M. S. Lenmann, T. F. Koetzle, and W. C. Hamilton, Acta Crystallogr. B **29** (4), 877 (1973).

Translated by N. Korovin

Physics of the Solid State, Vol. 45, No. 10, 2003, pp. 1898–1905. Translated from Fizika Tverdogo Tela, Vol. 45, No. 10, 2003, pp. 1807–1813.

SEMICONDUCTORS AND DIELECTRICS

Electrical Conduction and Polarization in $PbWO_4$ Crystals

V. N. Shevchuk and I. V. Kayun

Franko National University, ul. Lomonosova 8, Lviv, 79005 Ukraine

e-mail: shevchuk@wups.lviv.ua

Received March 7, 2003

Abstract—The regularities of ion–electron processes in an undoped $PbWO_4$ single crystal upon transition to a quasi-equilibrium state in an external dc electric field with a linear variation in the temperature in the range 290–600 K are investigated using different methods. The total conductivity, thermally stimulated polarization current, and thermally stimulated depolarization current are measured. It is assumed that the temperature dependence of the conductivity can be described within the theory of small-radius polarons. The thermally stimulated polarization (depolarization) currents are interpreted in terms of the space-charge (peaks of the current in the range 400–550 K) and dipole (peaks of the current in the range 290–370 K) mechanisms of generation of a polarization charge in the sample. The inference is drawn that the dominant contribution to the dipole polarization is made by dipolons, namely, doubly charged (cation–anion) vacancy pairs coupled through electrostatic interaction. The basic parameters of relaxation phenomena and charge transfer are calculated. © *2003 MAIK "Nauka/Interperiodica".*

1. INTRODUCTION

The considerable scientific interest expressed in $PbWO_4$ crystals is associated with their practical use, in particular, as self-activated scintillators with short afterglow times (see, for example, [1, 2]). The operational characteristics of $PbWO_4$ crystals are determined, to a large extent, by their structural defects. However, to date, there has been no agreement among researchers regarding the nature of defects in the $PbWO_4$ structure. Although the properties of $PbWO_4$ crystals have been investigated by different methods in many works, the electrical characteristics of this compound and their changes under external actions are still not clearly understood, especially in the temperature range 290–600 K.

Groenink and Binsma [3] were among the first to investigate the electrical properties of $PbWO_4$ crystals. They measured dc and ac electrical conductivities of potassium-, yttrium-, and bismuth-doped and undoped $PbWO_4$ crystals grown using the Czochralski method upon heating to 1200 K in air. The electrical characteristics of $PbWO_4$ are also described in the monograph by Mokhosoev and Bazarova [4]. The electrical conductivity of undoped and lanthanum-, praseodymium-, samarium-, and terbium-doped $PbWO_4$ samples, which were prepared by pressing of metal oxide powders followed by their sintering at temperatures of 600–800 K, was measured in [5–7] with the aim of elucidating the role played by the oxygen sublattice in charge transfer. Suszynska *et al.* [8, 9] analyzed the temperature dependence of the conductivity of undoped $PbWO_4$ crystals immediately after the Czochralski growth and upon annealing under vacuum or in air in the temperature range 120–350 K. Huang *et al.* [10] examined the dielectric response of $PbWO_4$ single crystals doped with yttrium and niobium impurities.

However, the nature of the electrically active defects that predominate in $PbWO_4$ single crystals remains unclear. At present, studies of the electrical properties of these crystals and, particularly, thermal polarization effects have been reduced to accumulation of experimental data.

In this work, we elucidated the regularities of ion–electron processes in an undoped $PbWO_4$ single crystal and the behavior of electrically active defects in the $PbWO_4$ structure upon the transition to a quasi-equilibrium state with a linear variation in the temperature T or under isothermal conditions. For this purpose, we investigated the total conductivity σ, thermally stimulated polarization (TSP) currents I_{TSP} in an external dc electric field, and thermally stimulated depolarization (TSD) currents I_{TSD} in the internal field of the crystal in the polarized state.

2. EXPERIMENTAL TECHNIQUE

The crystals used in the measurements were grown by the Czochralski method along the [001] axis. Samples $10 \times 10 \times 0.5$ mm in size were cut normally to the [001] axis. A dc electric field $E = 10^2$–10^4 V/cm was applied to the sample placed in a capacitor measuring cell with Aquadag electrodes and metal leads. The applied field was chosen in such a way as to correspond to a linear portion of the current–voltage characteristics. The experiments were performed in the temperature range $T = 290$–600 K in air. The conduction current I, the thermally stimulated polarization current I_{TSP}, and

1063-7834/03/4510-1898$24.00

the thermally stimulated depolarization current I_{TSD} were measured under changes in the temperature at a constant rate $\beta = 0.1$–0.2 K/s. Experimental data on the electrical conductivity were obtained during heating and cooling in one heating–cooling cycle or several consecutive cycles. In order to determine temperatures at which the polarization substantially affects the dependences $\sigma(T)$, we also measured the electrical conductivity of samples preliminarily cooled in an external electric field. Weak currents were measured on a V7-30 voltmeter electrometer. The temperature was measured using a chromel–alumel thermocouple. The temperature in the quartz measuring cell was maintained constant with an accuracy of ±1 K. The error in the determination of the activation energy for conduction did not exceed ±2–3%. All other details of the experimental procedure and the measuring setup used for studying high-resistance crystals and TSD (TSP) currents were similar to those described in [11].

In our experiments, we varied polarization conditions, i.e., the polarization voltage U_p, polarization temperature T_p, and polarization time τ_p (i.e., the time required for the formation of a spatially nonuniform charge distribution in the sample). This made it possible to control the maximum intensity I_m of thermally stimulated currents and to separate the I_m peaks in the TSD (TSP) spectra. The nature of polarization effects with due regard for the dependences of the intensity I_m on the maximum temperature T_m and the half-width of the peaks under different polarization conditions in the presence of blocking electrodes was analyzed in the framework of the space-charge and dipole models of polarization.

3. ELECTRICAL CONDUCTIVITY

Under normal conditions, the $PbWO_4$ crystals are characterized by a band gap of 4.13 eV along the z direction [12] and a permittivity of 23 [4] and, according to our measurements, exhibit a low conductivity ($\sigma \approx 10^{-11}$–10^{-14} Ω^{-1} cm^{-1}). It should be noted that the conductivities σ obtained in different works can differ from each other, because these characteristics, like other properties, substantially depend on the method and conditions of the crystal growth, the purity of the initial materials, doping, high-temperature annealing of the crystal in various media, and other factors.

The temperature dependence of the electrical conductivity $\sigma(T)$ measured during heating of the $PbWO_4$ crystals in the temperature range 290–600 K (Fig. 1) can be well approximated by the formula

$$\sigma = \sigma_0 \exp(-\Delta E/kT), \quad (1)$$

where k is the Boltzmann constant. Detailed analysis of the curves in Fig. 1c shows that the dependence $\sigma(T)$ involves three portions in the temperature ranges 350–400, 400–520, and 520–600 K with different (even though very close) parameters σ_0 and ΔE (Table 1). Table 1 also presents the data obtained upon cooling of the sample and those determined from the curve $\ln(\sigma T) = f(1/T)$. It can be seen that the results of the measurements upon cooling differ from those upon heating. The curve $\ln\sigma = f(1/T)$ measured during cooling has one straight-line portion in the temperature range 550–350 K. In all cases, except for the experiment presented by curve *2* in Fig. 1b, the samples were preliminarily cooled in the short-circuited state in the absence of an external electric field.

Table 1. Activation energies ΔE for conduction in $PbWO_4$ crystals and preexponential factors σ_0 in different temperature ranges

T, K	ΔE, eV			σ_0, Ω^{-1} cm^{-1}
	cooling		heating	
290–350	0.23	–	–	1.4×10^{-6}
350–400	0.66	0.73*	–	3.9×10^{-4}
400–460	0.72	0.85*	–	3.5×10^{-3}
460–590	0.85	0.93*	–	3.2×10^{-2}
560–350	–	–	0.91	8.6×10^{-2}

* Activation energies ΔE determined from the dependence $\ln(\sigma T) = f(1/T)$.

It can be seen from Figs. 1a and 1b that, in the temperature range 290–350 K, the curve $\sigma(T)$ substantially depends on the relaxation effects (associated with the appearance and disappearance of polarization charges), the history of the sample prior to measurements, the temperature range of heating in the preceding measurement, and the cooling conditions. In this "sensitive" range, the temperature dependence of the TSP current is characterized by a broad intense peak $I_m \sim 10^{-9}$ A at $T_m \approx 310$ K. Under identical conditions, the intensity I_m depends on the number of heating cycles in the course of the measurement. The maximum value of I_m is observed in the first heating–cooling cycle. The behavior of the dependence $\sigma(T)$ depicted by curve *3* in Fig. 1a is due to partial suppression of relaxation processes through several consecutive heating–cooling cycles. The dependence $\ln\sigma = f(1/T)$ measured upon heating of the sample preliminarily cooled in an external electric field (Fig. 1b, curve *2*) changes in the low-temperature range 290–350 K and does not follow the law described by expression (1) in the range 350–400 K. This can be explained by the effect of polarization on the conduction current. It was experimentally found that slow cooling of the sample in the absence of an external field leads to less pronounced variations in the initial dependence $\ln\sigma = f(1/T)$, even though, in this case, also, the relaxation leads to a decrease in the current intensity after repeated heating–cooling cycles.

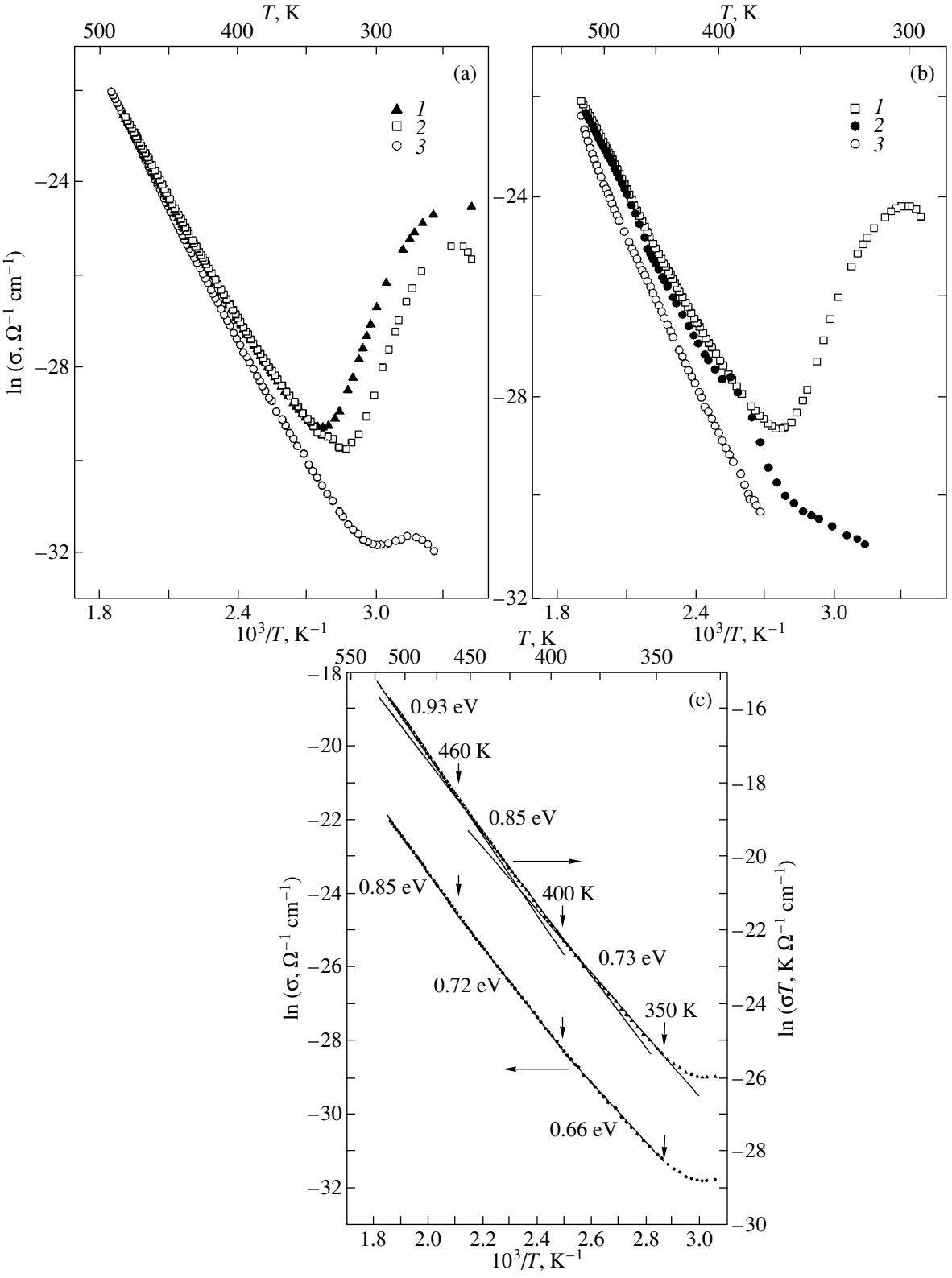

Fig. 1. Experimental temperature dependences of the total conductivity of $PbWO_4$ crystals in the Arrhenius coordinates [the upper curve in panel (c) is obtained in the $1/T$–$\ln(\sigma T)$ coordinates] for (a) different numbers of consecutive heating–cooling cycles and (b) different conditions of preliminary polarization of the samples. Curves $\sigma(T)$ are measured during (a) (*1*) the first heating, (*2*) heating after the first two consecutive heating–cooling cycles, (*3*) heating after several heating–cooling cycles and (b) (*1*) the first heating, (*2*) heating of the sample preliminarily cooled in the external electric field, and (*3*) cooling of the sample preliminarily cooled in the external electric field.

The crystals regain their original characteristics after holding in air at room temperature for approximately 24 h.

The dependence $\sigma(T)$ measured for the sample preliminarily cooled in the electric field (Fig. 1b, curve *2*) exhibits a weak peak with a maximum at ~370 K and an additional low-temperature (290–350 K) straight-line portion in the Arrhenius coordinates. This indicates that, under the given experimental conditions, the relaxation processes proceed rather slowly at temperatures $T < 350$ K and the maximum in the polarization current in the range 290–350 K is virtually absent. Apparently, an increase in the temperature is accompanied only by an activation increase in the conductivity. The values of ΔE and σ_0 in this temperature range differ significantly from those at higher temperatures (Table 1). This can also be judged from the inflection point of the curve $\ln\sigma = f(1/T)$ at $T \sim 350$ K. The observed behavior of the dependences $\sigma(T)$ can be explained by a crossover of the conduction mechanism. It seems likely that, at low temperatures, *n*-type carriers execute hoppings from one defect site to another. At temperatures above 350–400 K, the drastic increase in the intensity of the conduction current can be associated with the change not only in the mobility but also in the concentration of charge carriers. Note that the inflection point in the dependence $\ln\sigma = f(1/T)$ at approximately 450 K has also been experimentally observed for other tungstate crystals of similar compositions [4, 13].

Judging from the activation energies and the temperature dependence $\ln\sigma = f(1/T)$, the steady-state conduction and, in particular, its electronic component are provided by carriers that are thermally activated at local levels in the band gap. The sequential involvement of deep levels in charge transfer leads to a change in the slope of the straight-line portion in the dependence $\ln\sigma = f(1/T)$.

An exponential temperature dependence of the conductivity frequently counts in favor of the formation of small-radius polarons. However, in our case, the formation of polarons calls for further verification and investigation. It is evident that intensive polarization, especially at 290–370 K, and hysteresis effects in the temperature dependence of the conduction current upon heating and cooling can be explained by a considerable contribution to the total conductivity of the sample coming from the ionic component.

4. POLARIZATION EFFECTS

In order to elucidate regularities in the relaxation processes associated with the formation and transformation of a polarized (thermoelectret) state of the $PbWO_4$ crystal and their influence on the steady-state conduction, we investigated thermally stimulated depolarization (thermally stimulated polarization) currents. Under the assumption that deep traps are absent, the stability of the electret state can be governed by the

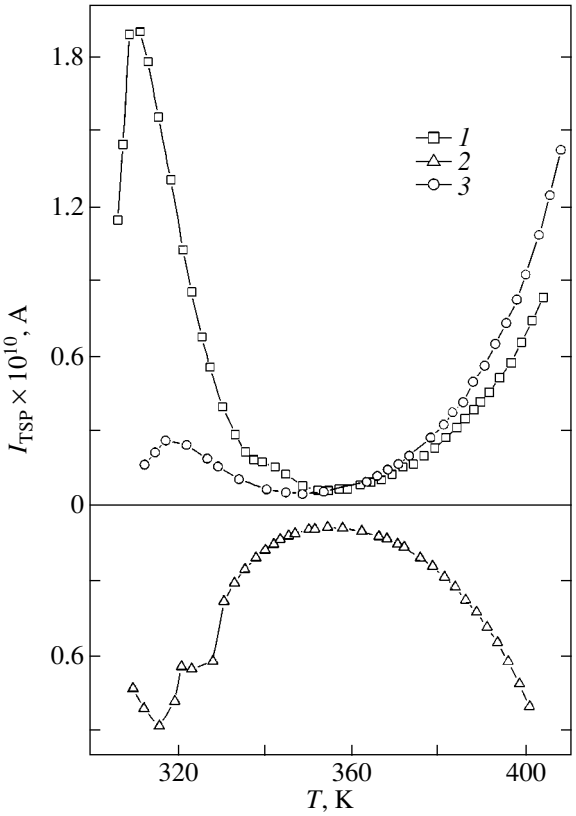

Fig. 2. TSP spectra of $PbWO_4$ crystals in electric fields E = (*1*) $+1.0 \times 10^3$, (*2*) -1.0×10^3, and (*3*) $+1.0 \times 10^3$ V/cm for (*1*) the initial sample and (*2*, *3*) samples preliminarily cooled from 500 to 290 K in the field $E = +1.0 \times 10^3$ V/cm.

Maxwell relaxation time. This time can be estimated from the relationship

$$\tau_\mu = \varepsilon\varepsilon_0/\sigma, \quad (2)$$

where ε is the permittivity of the crystal and ε_0 is the permittivity of free space. In our case, the Maxwell relaxation time at room temperature does not exceed $\sim 10^3$ s.

The typical TSP and TSD spectra with decomposition of the TSD peaks at $T_m > 350$ K into Gaussian components are shown in Figs. 2 and 3, respectively. The relaxation processes can be separated into three main groups in the temperature ranges 290–350, 350–380, and 400–600 K (Fig. 3), which are associated with the corresponding peaks of the current. The resolution of the TSD method is higher than that of the TSP method. For this reason, attention was mainly focused on the TSD spectra. The parameters calculated for relaxors from the TSD spectra are presented in Table 2. The activation energies E_t for thermally stimulated processes were estimated from the expression

$$E_t \cong 27kT_m. \quad (3)$$

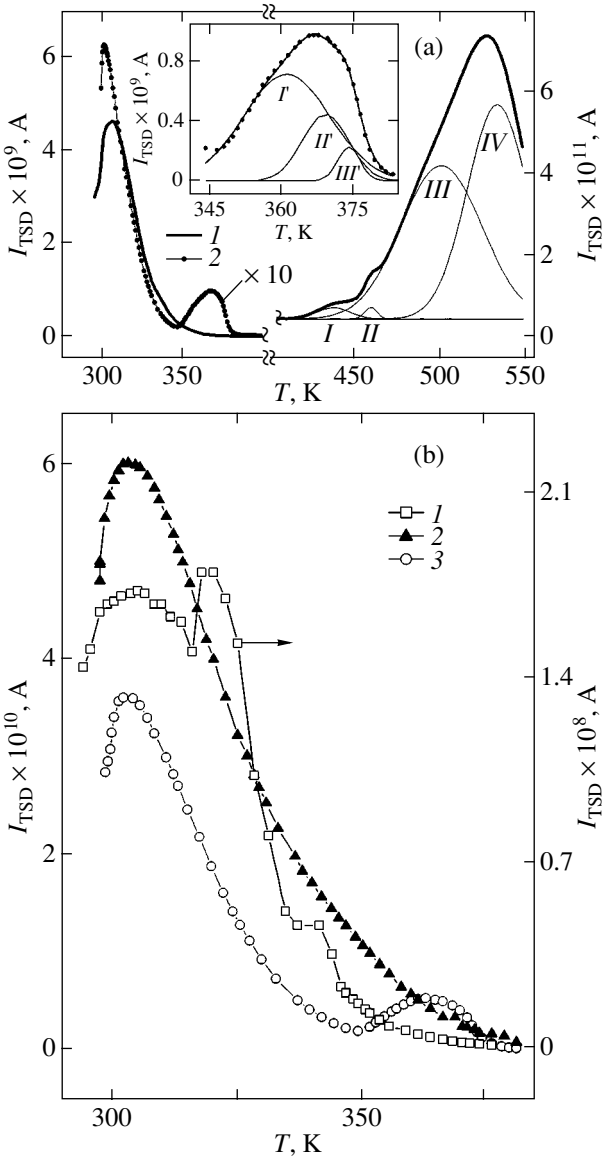

Fig. 3. TSD spectra of $PbWO_4$ crystals polarized under different conditions. (a) U_p = 50 V, τ_p = 5 min, and T_p = (*1*) 335 and (*2*) 320 K. The inset shows the decomposition of the TSD peak into individual components at T = 350–380 K. Closed circles are experimental points. (b) (*1*) T_p = 290 K, U_p = 50 V, and τ_p = 8 min and (*2*, *3*) T_p = 320 K, U_p = 50 V, and τ_p = 5 min (two successive measurements under identical conditions).

The frequency factors ω were evaluated from the maximum condition

$$\omega = (\beta E_t / kT_m^2)\exp(E_t / kT_m) \qquad (4)$$

for the functional dependence $I_{TSD}(T)$ [11] under the assumption that particles of one sort are involved in an elementary relaxation process.

As can be seen from Figs. 2 and 3, the intensities of the TSP and TSD currents exhibit significant peaks with a complex structure in the range 290–350 K. For example, the TSP spectrum (Fig. 2, curve *2*) in this range has at least two maxima at ~312 and ~325 K. According to the experimental data, the intensities of these narrow TSP peaks in the range 290–350 K are interrelated in a complex manner. In particular, the TSP peak at 312 K is dominant upon initial heating. In subsequent heating cycles, the intensity of this peak decreases and only slightly exceeds the intensity of the TSP peak at 325 K. After preliminary polarization of the sample upon cooling, the intensity of the peak at 325 K increases more rapidly than that of the peak at 312 K. For an appropriately chosen polarization temperature T_p, the TSP peaks at 312 and 325 K can become equal to each other in intensity.

In the range 290–350 K, the polarization temperature T_p affects the intensity I_m of TSD currents. As was noted above, the intensity I_m of thermally stimulated currents in the range 290–350 K depend on the prehistory of the sample, specifically on the number of preliminary heating cycles in the course of the measurement, the high-temperature limit of this heat treatment, cooling conditions, the time of relaxation in the short-circuited state, and the time of holding the sample in air prior to measurements. The dependence $I_m(U_p)$ for the broad peak under consideration shows linear behavior. Upon heating at a voltage $+U_p$, the height of this peak for the sample preliminarily polarized at a voltage $-U_p$ appears to be greater than that for the unpolarized sample by a factor of more than two. The total intensity of the peak decreases at $T_p > T_m$. This behavior of the TSD (TSP) currents due to variations in the experimental conditions is characteristic of relaxation processes in a system of point-defect complexes of dipole nature. It is evident that, apart from orientation processes, the dissociation of dipole complexes and an inverse process, namely, the association of point defects into anisotropic complexes, play an important role. A comparison of the experimental data presented in Figs. 1–3 shows that, for each temperature range in which the dominant depolarization activation processes are associated with a particular type of electrically active defects, there is a straight-line portion of the dependence $\ln\sigma = f(1/T)$ with a somewhat different slope (Fig. 1c).

Most likely, the TSD peaks at $T > 400$ K in the range of a drastic increase in conductivity (Figs. 1a, 1b) are attributed to space-charge polarization. This is confirmed by the close values of energies ΔE and E_t at these temperatures. Charge carriers move toward the electrode regions, are trapped in local levels, and give rise to a nonuniform charge distribution in the sample. The local levels correspond to components *I*–*IV* of the TSD peak (Fig. 3a). It can be seen that these components comprise a complex broad high-temperature peak in the range 400–600 K. This peak is associated with the electret state and shifts toward the high-temperature range with an increase in the polarization temperature T_p.

It should be noted that the depolarization phenomena considered in this work are observed in the same temperature ranges as the radiative processes studied earlier by other authors (see, for example, [14–16]). In particular, thermoluminescence peaks were experimentally revealed at temperatures of 280 and 320 K in [14]; 320, 350, 370, and 430 K in [15]; and 330 and 400 K in [16]. In all cases, the peak observed in the temperature range 320–350 K is characterized by a maximum intensity.

Furthermore, thermally stimulated conduction currents in $PbWO_4$ crystals preliminarily exposed to high-energy radiation are also observed in the above temperature ranges of activation of ion–electron processes [17, 18]. Specifically, a number of peaks of thermally stimulated currents were revealed at temperatures ~280 and ~320 K in [17] and in the range 300–320 K in [18]. Moreover, in [18], the authors observed a thermoluminescence peak at ~360 K. From a comparison of the results obtained in the present work and the data available in the literature, the inference can be made that electrically active centers (at least those manifesting themselves in the TSD spectra at $T < 400$ K) serve as trapping centers of nonequilibrium charge carriers and recombination centers simultaneously.

5. DISCUSSION

The dominant relaxation process observed in the temperature range 290–350 K occurs through the dipole mechanism. We assume that dipolons—electrostatically coupled pairs of lead (V_{Pb}^{2-}) and oxygen (V_O^{2+}) doubly charged vacancies—are the most probable dipole centers (responsible for the TSD or TSP peaks in the range 290–350 K) in $PbWO_4$ crystals. These associates have no effective charge, manifest themselves only in the TSD (TSP) spectra, and form the dipole component of the polarization in the crystal. Similar associates in gallium garnet crystals were considered in our earlier work [19]. For these crystals, the TSD peak is observed at 350 K and has a complex structure. Dipole associates of this type in $PbWO_4$ crystals were discussed, in particular, by Lim *et al.* [20], who assigned the absorption band at 350 nm to these associates. Note also that, according to Suszynska *et al.* [8, 9], the TSD peak with a maximum at approximately 330 K can be attributed to dipoles in $PbWO_4$ crystals.

The above assumption regarding the formation of dipolons in $PbWO_4$ crystals and their manifestation in the TSD spectra in the temperature range 290–380 K is supported by the high intensity of peaks *1–3* in Fig. 3 (this intensity cannot be provided by impurities, because their concentration in the crystal is relatively low). Moreover, this assumption is confirmed by the fact that a portion of lead and oxygen always volatilizes during the Czochralski growth [1]. As a result, the crystal has a deficit of lead and oxygen ions, which also leads to the formation of intrinsic color centers [20]. However, the formation of other dipole associates should not be excluded when interpreting the TSD spectrum in the range 290–370 K, especially with due regard for the complex structure of the TSD peak and its evolution with a variation in the polarization conditions. Apart from the aforementioned vacancy pairs, these can be triads with trapped *n*-type carriers for local charge neutralization, etc. Such defect complexes of dipole nature can differ in their energy parameters and correspond to individual TSD peaks. Single vacancies at high depolarization temperatures T_d can also be responsible for the TSD peaks. In particular, these complexes can be responsible for the formation of the three-component TSD peak shown in the inset to Fig. 3a. It is found that the intensities of components *I'–III'* of this peak can be different depending on the experimental conditions. This peak is not observed in the first heating–cooling cycle in a series of successive measurements.

Table 2. Parameters calculated for the main relaxors from the TSD spectra of $PbWO_4$ crystals

Peak no.	T_m, K	E_t, eV	$\omega \times 10^{-9}$, s^{-1}
1	305	0.71	4.7
2	320	0.74	3.5
3	340	0.79	3.7
I	360	0.84	4.0
II	369	0.86	3.9
III	375	0.87	3.3
I	435	1.01	2.8
II	458	1.07	3.2
III	500	1.16	2.4
IV	530	1.23	2.3

Note: TSD peaks *1–3* are determined from spectrum *1* in Fig. 3b.

The nature of the TSP peaks can also be judged from their temperature positions. In the case when thermally stimulated polarization in a crystal can be adequately described within the model of space-charge accumulation due primarily to steady-state conductivity, the theoretical dependence of the current density at the TSP peak on the applied electric field has the form [11]

$$J(T_m) \cong \sigma_0 E \exp(-\Delta E/kT_m - 1). \quad (5)$$

In the framework of the above model, the temperature T_m of the possible TSP peak can be easily calculated from expression (5) for the corresponding temperature range. The calculated temperatures T_m of the peaks (at $T > 350$ K) differ from the experimental values by no more than 5–10 K. This insignificant difference between the calculated and experimental values of

T_m can be associated with the error in determining the parameters σ_0 and ΔE. In the range 290–350 K, the calculated temperature $T_m \approx 235$ K is approximately 80 K less than the experimental value. This disagreement is quite reasonable because the TSP peak at ~320 K is due to the orientation of defect complexes of dipole nature. At the same time, the high-temperature peaks of the electric current are most likely caused by space charges arising from the drift and accumulation of equilibrium carriers in the electrode regions. This is confirmed by the close agreement between the calculated and experimental temperatures T_m for the peaks in the range $T >$ 350 K.

The observed decrease in the intensity of the TSD peak at ~320 K with an increase in the number of heating cycles is consistent with the dipolon concept. Single vacancies predominate at high temperatures. They have no time to associate into pairs upon cooling, which results in a decrease in the dipolon concentration upon repetition of heating–cooling cycles.

Let us now consider the electronic component of the conductivity of $PbWO_4$ crystals. From analyzing the experimental dependence of the electronic component of the total conductivity of $PbWO_4$ crystals on the oxygen partial pressure (the conductivity σ increases with an increase in the oxygen pressure [3]) and experimental data on the photoconductivity of these crystals in the range of the absorption edge [21, 22], it can be assumed that holes are majority charge carriers in the $PbWO_4$ compound. This inference is also confirmed by the increase in the conductivity upon high-temperature annealing of the samples in air. Similar experiments with samples annealed in air were performed earlier in [8, 9]. It was found that, upon annealing, the conductivity increases by a factor of approximately 15 [8, 9]. Our experimental results also suggest that holes whose mobility exceeds the mobility of ions are majority charge carriers in $PbWO_4$ crystals. Therefore, we can draw the conclusion that the $PbWO_4$ crystals with mixed ionic–electronic conductivity exhibit *p*-type properties.

Laguta *et al.* [23] carried out an electron paramagnetic resonance investigation of $PbWO_4$ crystals and observed the formation of WO_4^{3-} centers that remained stable up to 60 K. In the framework of the proposed model, the WO_4^{3-} centers are formed as a result of autolocalization of electrons in the WO_4^{2-} anionic complex. A similar autolocalization at room temperature was also revealed with the use of excited-state absorption in the fundamental absorption range under irradiation with a 0.5-ps pulsed laser [24]. According to the proposed model of the formation of WO_4^{3-} centers, holes are captured by deep traps (most frequently, by V_{Pb}^{2-} centers) and can be delocalized at room and higher temperatures. Electrons detrapped at 60 K recombine with localized holes, which leads to the appearance of thermoluminescence peaks.

It seems likely that, in $PbWO_4$ crystals, hole conduction at room temperature is provided by correlated hoppings of charge carriers from one defect site to an adjacent defect site. The crossover of the mechanism of charge transfer can occur at $T > 350$ K (Fig. 1), which results in a drastic increase in the conduction current with an increase in the temperature *T*. Judging from the change in the slope of the straight-line portions of the dependence $\ln\sigma = f(1/T)$ in the temperature range 350–600 K and from the TSD spectra (Fig. 3a), the charge transfer in the $PbWO_4$ crystal at these temperatures is controlled by several local levels in the band gap.

The reorientation processes associated with the complex dipole associates proceed at temperatures below 350 K. The dissociation of these dipole complexes at $T > 350$ K ensures appropriate conditions for the release of *n*-type carriers and their migration in the external field and, consequently, leads to an activation increase in the conductivity.

By virtue of the *p*-type component of the conductivity of the $PbWO_4$ crystal, the electroneutrality condition can be satisfied only in the case when cation vacancies or oxygen ions occupy interstices. In our opinion, it is more probable that the structure of the $PbWO_4$ crystal involves not interstitial oxygen but cation vacancies. These vacancies are also necessary for the formation of dipole centers, which were proposed in this work to explain the polarization effects.

REFERENCES

1. L. V. Atroshchenko, S. F. Burachas, L. P. Gal'chinetskiĭ, B. V. Grinev, V. D. Ryzhikov, and N. G. Starzhinskiĭ, *Stintillator Crystals and Ionizing-Radiation Detectors on Their Basis* (Naukova Dumka, Kiev, 1998).
2. M. Nikl, Phys. Status Solidi A **178** (2), 595 (2000).
3. J. A. Groenink and H. Binsma, J. Solid State Chem. **29** (2), 227 (1979).
4. M. V. Mokhosoev and Zh. G. Bazarova, *Complex Molybdenum and Tungsten Oxides with Group I–IV Elements* (Nauka, Moscow, 1990).
5. T. Esaka and T. Mina-ai, Solid State Ionics **57** (3–4), 319 (1992).
6. T. Esaka, R. Tachibana, and S. Takai, Solid State Ionics **92** (1–2), 129 (1996).
7. S. Takai, K. Suginura, and T. Esaka, Mater. Res. Bull. **34** (2), 193 (1999).
8. M. Suszynska, B. Macalik, and M. Nikl, Radiat. Eff. Defects Solids **150** (1–4), 35 (1999).
9. M. Suszynska, B. Macalik, and M. Nikl, J. Appl. Phys. **86** (2), 1090 (1999).
10. H. Huang, W. Li, X. Feng, and P. Wang, Phys. Status Solidi A **187** (2), 563 (2001).
11. Yu. A. Gorokhovatskiĭ and G. A. Bordovskiĭ, *Thermally Stimulated Current Spectroscopy of High-Resistance*

Semiconductors and Dielectrics (Nauka, Moscow, 1991).

12. Y. Zhang, N. A. W. Holtzwarth, and R. T. Williams, Phys. Rev. B **57** (20), 12738 (1998).
13. O. V. Ivanov, A. P. Nakhodnova, and V. N. Krivobok, Zh. Neorg. Khim. **27** (3), 587 (1982).
14. E. Auffrau, I. Dafinei, P. Lecoq, and M. Schneegans, Radiat. Eff. Defects Solids **135** (1–4), 343 (1995).
15. M. Nikl, K. Nitsch, S. Baccaro, *et al.*, J. Appl. Phys. **82** (11), 5758 (1997).
16. A. Annenkov, E. Auffrau, M. Korznik, and P. Lecoq, Phys. Status Solidi A **170** (1), 47 (1998).
17. L. Nagornaya, A. Apanasenko, and I. Tupitsina, in *Proceedings of International Conference SCINT-95, Delft, The Netherlands* (Delft Univ. Press, 1996), p. 299.
18. M. Martini, E. Rosetta, G. Spinolo, *et al.*, J. Lumin. **72–74**, 689 (1997).
19. A. E. Nosenko and V. N. Shevchuk, Radiat. Eff. Defects Solids **134** (1–4), 251 (1995).
20. O. Lim, X. Feng, Z. Man, *et al.*, Phys. Status Solidi A **181**, R1 (2000).
21. E. G. Reut, Fiz. Tverd. Tela (Leningrad) **23** (8), 2514 (1981) [Sov. Phys. Solid State **23**, 1476 (1981)].
22. I. M. Sol's'kiĭ, A. S. Voloshinovs'kiĭ, R. V. Gamernik, *et al.*, Ukr. Fiz. Zh. **46** (8), 881 (2001).
23. V. V. Laguta, J. Rosa, M. I. Zaritskii, *et al.*, J. Phys.: Condens. Matter **10**, 7293 (1998).
24. R. T. Williams, K. B. Ucer, G. Xiong, *et al.*, Radiat. Eff. Defects Solids **155** (1–4), 265 (2001).

Translated by O. Borovik-Romanova

Physics of the Solid State, Vol. 45, No. 10, 2003, pp. 1906–1909. Translated from Fizika Tverdogo Tela, Vol. 45, No. 10, 2003, pp. 1814–1817.

SEMICONDUCTORS AND DIELECTRICS

Electronic Structure of Bivalent Copper Off-Center Complexes in SrF_2 Crystals from Data of EPR and ENDOR Spectroscopy

V. A. Ulanov, O. A. Anikeenok, M. M. Zaripov, and I. I. Fazlizhanov

Kazan Physicotechnical Institute, Russian Academy of Sciences, Sibirskiĭ trakt 10/7, Kazan 29, 420029 Tatarstan, Russia
e-mail: ulanov@dionis.kfti.kcn.ru

Received March 25, 2003

Abstract—The electronic structure of bivalent copper off-center complexes in SrF_2 crystals is calculated from experimental data obtained earlier by electron paramagnetic resonance (EPR) and electron–nuclear double resonance (ENDOR) spectroscopy. The electronic structure parameters characterizing the unpaired-electron density in the vicinity of the nucleus of a copper impurity ion are determined, and the parameters of covalent bonds between an impurity copper ion and three groups of the fluorine ions nearest to this impurity are calculated. It is demonstrated that states of the ground electron configuration of the bivalent copper impurity complex involve an admixture of excited electron configurations due to electron transfer from the ligand to 4*s* and 4*p* unfilled shells of the copper ion. *© 2003 MAIK "Nauka/Interperiodica".*

1. INTRODUCTION

This study is a continuation of our experimental works [1, 2] in which the local structure of bivalent copper impurity centers in SrF_2 crystals was investigated by electron paramagnetic resonance (EPR) and electron–nuclear double resonance (ENDOR) spectroscopy. The considerable interest expressed by researchers in bivalent copper impurity centers of SrF_2 crystals stems from the fact that, in these crystals, the Cu^{2+} cation is located at the off-center position; i.e., it is displaced by ≈1 Å from the center of the coordination cube of the substituted Sr^{2+} cation. This leads to the formation of a $[CuF_4F_4]^{6-}$ paramagnetic complex with C_{4v} symmetry and a relatively large electric dipole moment. Since the crystal has cubic symmetry, there exist six equally probable directions of displacement of the Cu^{2+} cation. Consequently, the crystal contains copper centers of six types that are similar in structure but differ in the orientation of the electric dipole moment. It is evident that the dipole moment can be reoriented under external action. This corresponds to a transition of the paramagnetic center from one well of the lower sheet of the adiabatic potential to another well that is equivalent to the former well.

The dynamics of transitions between wells of the adiabatic potential for a copper complex and the dependence of the dynamic properties on the hydrostatic pressure were analyzed in [3, 4]. Hoffmann and Ulanov [3] investigated the dynamic properties of a $[CuF_4F_4]^{6-}$ complex with C_{4v} symmetry under normal pressure and determined the temperature dependence of the spin–lattice relaxation time T_1 from the results of measurements performed by pulsed EPR spectroscopy. From analyzing this dependence, these authors estimated the separation between the lower vibronic energy levels of the complex under investigation. It was revealed that, at temperatures below ≈225 K, the studied complex resides in one of the wells of the adiabatic potential; however, at temperatures above 225 K, the frequency of transitions between wells of the adiabatic potential for this complex increases drastically. In [4], the dependence of the dynamic properties on the hydrostatic pressure was examined by stationary EPR spectroscopy. It was found that an increase in the hydrostatic pressure leads to a decrease in the height of barriers between the wells of the adiabatic potential. As a result, the frequency of both tunneling and over-barrier transitions between wells of the adiabatic potential increases significantly, even though the temperature remains constant.

It should be noted that complexes of this type have been revealed for Ag^{2+} impurity ions in $SrCl_2$ crystals [5] and for Cu^{2+} impurity ions in $SrCl_2$ [6] and BaF_2 [7] crystals. All these objects are impurity complexes of Jahn–Teller origin in which the Jahn–Teller effect observed in the triply degenerate orbital ground state is accompanied by pseudo-Jahn–Teller interaction [8]. Since these complexes are nonanuclear, they are characterized by multimode vibronic interactions. Therefore, it can be assumed that the magnetic and optical properties of these complexes are very sensitive to various external perturbations. Moreover, bivalent off-center complexes of this type exhibit both paramagnetic and paraelastic properties due to a unique combination of the Jahn–Teller effect with pseudo-Jahn–Teller interactions. For the above reasons, the complexes under investigation are of considerable interest from theoretical and practical standpoints.

The purpose of this work is to obtain more detailed information on the electronic structure of $[CuF_4F_4]^{6-}$

impurity complexes with C_{4v} symmetry in SrF_2 crystals. This information can be derived from the parameters of covalent bonds between an impurity copper ion and the fluorine ions (ligands) surrounding this impurity. In turn, the parameters of covalent bonds can be obtained from the tensor components of ligand hyperfine interactions with magnetic nuclei of the fluorine ligands. The tensor components of the ligand hyperfine interactions with nuclei of the fluorine ligands nearest to the Cu^{2+} ion (according to the classification proposed in [1], these ligands are included in group *I*) and the components of the electron Zeeman and hyperfine interaction tensors were determined from the EPR spectra in [1]. The tensor components of the ligand hyperfine interactions with nuclei of four groups of more distant ligands (i.e., ligands of groups *II*–*V* [2]) were obtained from the ENDOR spectra in [2]. In the latter work, we also proposed a model of Cu^{2+} impurity centers in SrF_2 crystals that allows for all the ligands involved in the interactions observed in the samples studied by ENDOR spectroscopy (see [2, Fig. 4]). The parameters of the covalent bonds with the four nearest ligands were obtained in our recent work [4]. In the present study, we determined the parameters of covalent bonds with ligands of groups *II* and *III*. The experimentally observed interactions with nuclei of more distant ligands (i.e., ligands of groups *IV* and *V*) were adequately described by the Hamiltonians of the direct magnetic dipole–dipole interaction, which indicates the lack of covalent bonds of the impurity ion with these ligands.

2. ELECTRONIC STRUCTURE PARAMETERS CHARACTERIZING THE UNPAIRED-ELECTRON DENSITY IN THE VICINITY OF NUCLEI OF THE NEAREST LIGAND GROUP

A theoretical analysis of the experimental data on ligand hyperfine interactions with nuclei of the nearest ligand group [4] demonstrated that the orbital function (molecular orbital) for the ground state of the copper complex is represented primarily by the $d_{x^2-y^2}$ function of the impurity ion (the orbital functions are specified in the *XYZ* coordinate system in which the *Z* axis is parallel to the C_{4v} symmetry axis of the complex and the *X* and *Y* axes are aligned with two ⟨110⟩ crystallographic axes perpendicular to the C_{4v} symmetry axis). The energy level corresponding to the molecular orbital $|XY\rangle$ is located 8600 cm^{-1} above the orbital ground level $|X^2 - Y^2\rangle$. The doubly degenerate level ($|XZ\rangle$, $|YZ\rangle$) lies 900 cm^{-1} above the molecular orbital $|XY\rangle$. The reduction coefficients of the orbital angular momentum are determined from the following equality [4]:

$$k_{MM'} = \frac{\langle 2, M|\mathbf{L}_j|2, M'\rangle}{\langle d_M|\mathbf{L}_j|d_{M'}\rangle}. \quad (1)$$

As a result, we found the reduction coefficients $k_{22} = 0.829$, $k_{11} = 0.912$, and $k_{21} = 0.711$. The parameters of the orbital coupling of the copper ion with any of the four nearest ligands were determined to be $\lambda_s^D = 0.092$, $\lambda_\sigma^D = -0.380$, and $\lambda_\pi^D = 0.227$. The normalizing factors of the molecular orbitals were calculated by ignoring the covalence of bonds between the Cu^{2+} ion and the other three ligands: $N_2 = 1.208$, $N_1 = 1.097$, and $N_0 = 1.093$. The spin–orbital coupling proved to be anisotropic: $\lambda_{1\|} = -687$ cm^{-1}, $\lambda_{2\|} = -758$ cm^{-1}, and $\lambda_{1\perp} = -721$ cm^{-1}.

3. ELECTRONIC STRUCTURE PARAMETERS CHARACTERIZING THE UNPAIRED-ELECTRON DENSITY IN THE VICINITY OF A COPPER NUCLEUS

From the above results obtained earlier in [4], we derive a relationship between the parameters of the tensor of the hyperfine interaction with a copper nucleus and the parameters of the electronic structure of the complex, which characterize the unpaired-electron density in the vicinity of a ^{63}Cu nucleus. For this purpose, we consider the operator of the magnetic interaction of an unpaired electron with a copper nucleus [9]:

$$\mathbf{H}_{hfi} = g_S\beta_e\gamma_n\hbar\langle r^{-3}\rangle \times\left[\frac{3(\mathbf{I}\cdot\mathbf{r}_i)(\mathbf{S}_i\cdot\mathbf{r}_i) - \mathbf{r}_i^2(\mathbf{l}_i\cdot\mathbf{I})}{r_i^5} + \frac{8\pi}{3}(\mathbf{S}_i\cdot\mathbf{I})\delta(\mathbf{r}_i)\right], \quad (2)$$

where r_i is the radius vector of the ith electron with respect to the nucleus. For the term (*L*, *S*) obeying the Hund rule, this operator can be represented as the function of the total orbital and total spin angular momenta [9]:

$$H_{hfi} = g_S\beta_e\gamma_n\hbar\langle r^{-3}\rangle\Big\{(\mathbf{L}\cdot\mathbf{I}) + [\xi L(L+1) - \mathcal{N}](\mathbf{S}\cdot\mathbf{I}) - \frac{3}{2}\xi[(\mathbf{L}\cdot\mathbf{S})(\mathbf{L}\cdot\mathbf{I}) + (\mathbf{L}\cdot\mathbf{I})(\mathbf{L}\cdot\mathbf{S})]\Big\}. \quad (3)$$

Here, $\mathcal{N}$ is the dimensionless constant expressed through the unpaired-electron density at the ion nucleus,

$$\xi = (2l + 1 - 4S)/[S(2l-1)(l+3)(2L-1)],$$

l is the orbital angular momentum of the unpaired electron of the impurity ion ($l = 2$), *S* is the total spin angular momentum ($S = 1/2$), and *L* is the total orbital angular momentum of the impurity ion ($L = 2$).

Since the hyperfine interaction energy rapidly decreases with an increase in the distance between the electron and the nucleus (due to a strong inhomogene-

ity of the nuclear magnetic field), the ligand contributions to the molecular orbital can be ignored in calculations of the parameters of the hyperfine interaction tensor. Within this approximation, we obtain the following equalities for a Cu^{2+} impurity ion in an SrF_2 crystal:

$$a_{\parallel} = P\left[\left(\frac{24}{7}a_1^2 - \frac{32}{7}a_2^2 - \frac{16}{7}a_3^2 + \frac{12}{7}a_2a_3\right) - \mathcal{N}(a_1^2 + a_2^2 - a_3^2)\right], \quad (4)$$

$$a_{\perp} = P\left[\frac{22}{7}a_1a_3 + \frac{4}{7}a_1a_2 - 2\mathcal{N}a_1a_2\right], \quad (5)$$

where $P = 2g_S\beta_e g_n\beta_n\langle r^{-3}\rangle$, $a_1 = \frac{c_1}{\sqrt{N_2}}$, $a_2 = \frac{c_2}{\sqrt{N_2}}$, $a_3 = \frac{c_3}{\sqrt{N_1}}$, $c_1 = 0.9817$, $c_2 = 0.0745$, and $c_3 = 0.0331$ (see [4]).

For the experimental parameters $a_{\parallel} = 360$ MHz and $a_{\perp} = 26$ MHz, we obtain $P = 872$ MHz and $N = 0.36$.

4. ELECTRONIC STRUCTURE PARAMETERS CHARACTERIZING THE UNPAIRED-ELECTRON DENSITY IN THE VICINITY OF NUCLEI OF MORE DISTANT LIGAND GROUPS

The electronic structure parameters characterizing the unpaired-electron density in the vicinity of nuclei of more distant ligand groups can be calculated from the relationships derived in our previous work [4] for ligands of group *I*. Note that the normalizing factors for molecular orbitals corresponding to the ground state of the complex remain as before (because, in the case under consideration, the covalent contributions from ligands of groups *II–V* are disregarded). The ligand hyperfine interaction tensor components (i.e., the left-hand sides of equalities (17) in [4]) can be obtained by subtracting the relevant components of the tensors $A(F_i)$ and $A^d(F_i)$ taken from the table presented in [2] (for $i \longrightarrow II$ or *III*). It should be remembered that equalities (17) in [4] are derived under the conditions where the nonzero spin density at the ligand nuclei is determined by both the covalence of bonds in the complex and the effects of overlap of 3*d* orbitals of the impurity ion with *p* and *s* orbitals of the ligands; i.e., the admixture of excited electron configurations is ignored in these equalities. However, the ground electron configuration of the impurity ion can involve such an admixture, in particular, due to electron transfer from the filled shells of the ligand to the 4*s* unfilled shells of the copper ion. Numerical relationships for these contributions were deduced in [10]. As follows from these relationships, the relative contribution of the above mechanism to the ligand hyperfine interaction is negligible for a small distance between the paramagnetic ion and the ligand but becomes predominant in the case when this distance increases. The necessity of considering these corrections stems from the result of analyzing the parameters given in the table presented in [2]. It can be seen from this table that the experimentally found ligand hyperfine interaction tensor components reverse sign upon changing over from the F(*I*) ligand to the F(*II*) and F(*III*) ligands. This implies that both mechanisms responsible for the nonzero spin density at nuclei of the F(*II*) and F(*III*) ligands must be included in calculations of the tensor components of ligand hyperfine interactions with nuclei of these ligands. In actual fact, when the contributions from the excited electron configurations are ignored in the calculations of the tensor components for ligands of group *II*, we obtain the relationships

$$A_z'(II) = 0.1102\lambda_s^2 a_s + 0.2204\lambda_\sigma^2 a_p - 0.2364\lambda_\pi^2 a_p,$$
$$A_x'(II) \approx A_y'(II) \quad (6)$$
$$= 0.1102\lambda_s^2 a_s - 0.1092\lambda_\sigma^2 a_p + 0.1182\lambda_\pi^2 a_p.$$

Since the ratio of the parameters λ_σ and λ_π is approximately equal in magnitude to the ratio of the relevant overlap integrals, it is evident that relationships (6) cannot provide the inequalities $A_z'(II) < 0$ and $A_x'(II) \approx A_y'(II) > 0$. In order to achieve complete agreement with the experimental values of the ligand hyperfine interaction tensor components, proper allowance must be made for additional contributions to the ligand hyperfine interactions with ligands of this group, i.e., for the electron transfer from the F(*II*) ligand to semifilled and unfilled shells of the impurity ion. The electron transfer from a ligand of this group to the Cu^{2+} $3d^9$ shell corresponds to a higher order of the perturbation theory and, hence, will not substantially affect the situation. However, as was shown earlier in [10, 11], the electron transfer from the ligand to *ns* unfilled shells of the impurity ion can make a contribution comparable to the effects of orbital overlap and the covalence of bonds between the impurity ion and the ligand. According to [10], the appropriate expressions for ligand hyperfine interaction tensor components accounting for the electron transfer from the ligand to the Cu^{2+} 4*s* unfilled shell can be written in the form

$$A_z' = \frac{1.998G(4s, 3d)}{|\Delta_{4s,2s}| \times 5}\gamma_{4s,2s}\lambda_{2s,4s}a_s - \frac{3.997G(4s, 3d)}{|\Delta_{4s,2p}| \times 5}\gamma_{4s,2p}\lambda_{2p,4s}a_p,$$
$$A_x' = \frac{1.998G(4s, 3d)}{|\Delta_{4s,2s}| \times 5}\gamma_{4s,2s}\lambda_{2s,4s}a_s + \frac{1.998G(4s, 3d)}{|\Delta_{4s,2p}| \times 5}\gamma_{4s,2p}\lambda_{2p,4s}a_p, \quad (7)$$
$$A_y' \approx A_x',$$

where *G* is the parameter related to the Coulomb interaction between the 3*d* and 4*s* unpaired electrons. For copper and fluorine ions, the energy separations $\Delta_{4s,2s}$ and $\Delta_{4s,2p}$ are equal to 340 000 and 190 000 cm^{-1},

respectively, and $G(4s, 3d) = 3690$ cm^{-1} [10]. In the case when the copper–fluorine covalent bond is relatively weak, the parameters $\lambda_{2s, 4s}$ and $\lambda_{2p, 4s}$ should be close in magnitude to the overlap integrals $S_{2s, 4s}$ and $S_{2p0, 4s}$, whereas the parameters $\gamma_{4s, 2s}$ and $\gamma_{4s, 2p}$ can be determined from the approximate equalities $\lambda_{2s, 4s} \approx S_{2s, 4s} + \gamma_{4s, 2s}$ and $\lambda_{2p0, 4s} \approx S_{2p0, 4s} + \gamma_{4s, 2p0}$ [9].

We attempted to interpret the available experimental data on ligand hyperfine interactions with nuclei of the F(*III*) ligands under the same assumptions as for the F^-(*II*) ions. As a result, the parallel component of the tensor A_z'(*III*) for ligand hyperfine interactions with nuclei of the F(*III*) ligands was found to be close to the experimental value. However, the perpendicular components A_x'(*III*) and A_y'(*III*) defied description not only in magnitude but also in sign. In order to approach the experimental value, we had to increase the covalence parameter of the σ bond. In our opinion, this increase in the strength of the σ bond can be explained in terms of additional bonding with the participation of the F(*I*) ligand as an intermediate unit.

It should be noted that, for F(*II*) and F(*III*) ligands, the calculated and experimental differences of the perpendicular components $(A_x' - A_y')$ are opposite in sign. This disagreement indicates that the parameters of ligand hyperfine interactions with nuclei of these ligands are substantially affected by the electron transfer from the ligand to the Cu^{2+} 4*p* unfilled shell. The appearance of an electron in this shell is not surprising, because the potential of the crystal field acting on electrons of the impurity copper ion involves odd harmonics, which, in turn, can be responsible for an admixture of the $3d^8 4p$ excited configuration in the $3d^9$ ground configuration. However, according to the results of our calculations, the appearance of an electron at the 4*p* orbitals also becomes possible due to electron transfer from the ligand.

The final results obtained for ligand hyperfine interactions with ligands of groups *II* and *III* are as follows:

(1) For the F(*II*) ligand, the contribution of the 3*d* electron shell to the ligand hyperfine interaction is determined by the parameters $\lambda_s = 0.0061$, $\lambda_\sigma = -0.0212$, $\lambda_\pi = 0.0008$, $S_s^D = 0.000094$, $S_{\sigma s}^D = 0.003437$, $S_{\sigma Z}^D = -0.010874$, and $S_\pi^D = 0.003942$, whereas the contribution of the 4*s* electron shell is governed by the parameters $\gamma_s = 0.004$, $\gamma_\sigma = -0.122$, $S_s^D = 0.079213$, and $S_{\sigma s}^D = -0.111709$.

(2) For the F(*III*) ligand, the contribution of the 3*d* electron shell to the ligand hyperfine interaction is determined by the parameters $\lambda_s = 0.0016$, $\lambda_\sigma = -0.0087$, $\lambda_\pi = 0.0026$, $S_s^D = 0.000011$, $S_{\sigma s}^D = 0.000461$, $S_{\sigma Z}^D = -0.003215$, and $S_\pi^D = 0.000935$, whereas the contribution of the 4*s* electron shell is governed by the parameters $\gamma_s = 0.02$, $\gamma_\sigma = -0.09$, $S_s^D = 0.079$, and $S_{\sigma s}^D = -0.1117$.

REFERENCES

1. M. M. Zaripov and V. A. Ulanov, Fiz. Tverd. Tela (Leningrad) **31** (10), 251 (1989) [Sov. Phys. Solid State **31**, 1796 (1989)].
2. I. I. Fazlizhanov, V. A. Ulanov, and M. M. Zaripov, Fiz. Tverd. Tela (St. Petersburg) **43** (6), 1018 (2001) [Phys. Solid State **43**, 1052 (2001)].
3. S. K. Hoffmann and V. A. Ulanov, J. Phys.: Condens. Matter **12**, 1855 (2000).
4. V. A. Ulanov, M. Krupski, S. K. Hoffmann, and M. M. Zaripov, J. Phys.: Condens. Matter **15**, 1081 (2003).
5. H. Bill and R. Lacroix, in *Proceedings of XVII Congress AMPERE* (1973), p. 233.
6. H. Bill, Phys. Lett. A **44** (2), 101 (1973).
7. M. M. Zaripov and V. A. Ulanov, Fiz. Tverd. Tela (Leningrad) **31** (10), 254 (1989) [Sov. Phys. Solid State **31**, 1798 (1989)].
8. I. B. Bersuker, *Electronic Structure and Properties of Transition Metal Compounds. Introduction to the Theory* (Wiley, New York, 1996).
9. A. Abragam and B. Bleaney, *Electron Paramagnetic Resonance of Transition Ions* (Clarendon, Oxford, 1970; Mir, Moscow, 1973), Vol. 2.
10. O. A. Anikeenok and M. V. Eremin, Fiz. Tverd. Tela (Leningrad) **23** (3), 706 (1981) [Sov. Phys. Solid State **23**, 401 (1981)].
11. O. A. Anikeenok, R. M. Gumerov, and Yu. V. Yablokov, Fiz. Tverd. Tela (Leningrad) **26** (8), 2249 (1984) [Sov. Phys. Solid State **26**, 1365 (1984)].

Translated by O. Borovik-Romanova

Physics of the Solid State, Vol. 45, No. 10, 2003, pp. 1910–1917. Translated from Fizika Tverdogo Tela, Vol. 45, No. 10, 2003, pp. 1818–1824.

DEFECTS, DISLOCATIONS, AND PHYSICS OF STRENGTH

The Influence of Defects in the Crystal Structure on Helium Diffusion in Quartz

T. S. Argunova[1, 5], L. M. Sorokin[1], B. Z. Pevzner[2], V. S. Balitskiĭ[3], M. A. Gannibal[4], J. H. Je[5], Y. Hwu[6], and W.-L. Tsai[6]

[1] *Ioffe Physicotechnical Institute, Russian Academy of Sciences, Politekhnicheskaya ul. 26, St. Petersburg, 194021 Russia*
e-mail: lev.sorokin@mail.ioffe.ru

[2] *Grebenshchikov Institute of Silicate Chemistry, Russian Academy of Sciences, ul. Odoevskogo 24/2, St. Petersburg, 199155 Russia*

[3] *Institute of Experimental Mineralogy, Russian Academy of Sciences, Chernogolovka, Moscow oblast, 142432 Russia*

[4] *Geological Institute, Kola Research Center, Russian Academy of Sciences, ul. Fersmana 14, Apatity, Murmanskaya oblast, 184209 Russia*

[5] *Department of Materials Science and Engineering, Pohang University of Science and Technology, Pohang, Republic of Korea*

[6] *Institute of Physics, Academia Sinica, Nankang, Taipei, Taiwan, Republic of China*

Received February 18, 2003

Abstract—The solubility and diffusion of helium in quartz crystals are investigated as functions of the distribution and density of structural defects. The types of defects in the crystals are identified and their distribution over growth sectors is determined by x-ray diffraction topography and phase radiography with a synchrotron radiation source. The effective solubility and effective diffusion coefficients for helium in quartz are estimated from the experimental data on the amount of helium extracted from samples with different contents of defects. It is revealed that the effective diffusion coefficient of helium depends on the number of dislocations.© *2003 MAIK "Nauka/Interperiodica".*

1. INTRODUCTION

Investigation into the behavior of helium in the subsurface environment can offer a clue to the solution of a number of important problems. A plausible explanation of the accumulation and migration of cosmogenic helium can give impetus to the development of geochronological methods [1]. The high helium content in ground waters makes it possible to elucidate the helium origin and, in particular, to perform environmental monitoring, because one of the sources of helium is grounds where radioactive waste is buried [2]. With knowledge of the migration rate of radiogenic helium in rocks, it is possible to estimate the amount of helium accumulated in ground waters and to determine the concentration of radioactive elements (helium sources). Since quartz is universally present in rocks, the study of helium diffusion in quartz is an important stage in solving the above problem.

Trull *et al.* [3] experimentally determined the diffusion coefficients of ^{3}He and ^{4}He isotopes in quartz from the amount of helium extracted upon annealing of grains prepared by grinding natural quartz. From the experimental data obtained in the temperature range 150–600°C, these authors constructed a linear dependence of the logarithm of the diffusion coefficient on the reciprocal of the temperature (according to the Arrhenius law) and calculated the activation energies. By extrapolating the linear dependence to the low-temperature range, they determined the diffusion coefficients $D^3_{\mathrm{He}} \approx 10^{-18}$ cm^2/s and $D^4_{\mathrm{He}} \approx 10^{-20}$ cm^2/s at 20°C.

Tolstikhin *et al.* [4] studied crystals of natural quartz aged 1.8 billion years. These crystals contained gas microinclusions. The analysis of the isotopic helium composition in microinclusions demonstrated that the isotopic ratios in microinclusions 1–2 cm apart did not level off throughout the above period of time. By assuming that equalization of the concentrations proceeded through the diffusion of helium atoms, these authors solved the diffusion equation and determined the diffusion coefficient ($D^4_{\mathrm{He}} = 10^{-19}$ cm^2/s) at which the calculated and experimental ratios ^{3}He/^{4}He in microinclusions coincide with each other. It was also assumed that a number of microdefects separated by distances comparable to the unit cell size intersect each microinclusion. In this case, an atom has to execute one or several hoppings in order to find its way into a defect and can then almost instantaneously move along the defect. However, although the authors made the assumption that the migration rates of helium atoms in a defect-free lattice and along defects differ from each other, this assumption was ignored when solving the diffusion equation.

The structure of the outer electron shells of helium dissolved in quartz differs from that of the solvent. Hence, it is reasonable to believe that helium atoms should diffuse over interstices. The lattice of low-temperature α-quartz has a close-packed structure, which can be represented as a helical sequence of SiO_4 tetrahedra. One pitch of the helix corresponds to six tetrahedra. Consequently, hexagonal helical channels are formed along the *Z* axis [5]. In quartz, impurity ions can move rather freely through hexagonal channels along the *c* axis, whereas their motion in the direction perpendicular to the *c* axis is substantially hindered. It could be expected that helium atoms will also diffuse along the channels parallel to the *c* axis. However, the small diffusion coefficients of helium atoms [3, 4] suggest that the ordered quartz lattice is virtually impenetrable to helium. This inference is confirmed by the results obtained in [6, 7]. The transverse size of a hexagonal channel is approximately equal to 0.23 nm. According to different estimates, the diameter of a helium atom is equal to 0.18–0.26 nm [8–10]. Therefore, the helium diffusion in an ordered quartz lattice is reduced to the motion of atoms through channels of a comparable diameter and, hence, is accompanied by the overcoming of high energy barriers.

However, geological investigations have demonstrated that, despite the small diffusion coefficient, radiogenic helium formed in rocks finds its way into ground waters and is transported by them. In this respect, the problem of helium migration in quartz calls for further investigation.

In crystals, enhanced diffusion of impurities proceeds over lattice dislocations. Helium migration over dislocations was analyzed by Klyavin [11] in the study of the new phenomenon of dynamic dislocation pipe diffusion. However, this phenomenon is observed only under plastic deformation of materials in a liquid or gaseous medium whose atoms can penetrate into a crystal through generating and moving dislocations. Helium diffusion over dislocations in a stable state was theoretically investigated by Klyavin *et al.* [12]. It was shown that helium can migrate over screw dislocations at $T < 300$ K.

However, experimental data on enhanced migration of helium over dislocations in quartz are unavailable in the literature. In order to fill this gap, we studied the solubility and the desorption kinetics of helium in synthetic quartz samples with different dislocation densities.

2. INVESTIGATION OF DEFECTS IN THE CRYSTAL STRUCTURE

2.1. Sample Preparation

Crystals of synthetic quartz were grown by the thermal gradient method [13]. The quartz crystal without helium was grown in a standard sodium carbonate solution on a seed with *XY* orientation. The crystal saturated with helium was grown in a similar solution in an autoclave with helium. The sizes of the seed with *ZX* orientation were equal to 2, 4, and 140 mm along the *Z*, *X*, and *Y* axes, respectively. The autoclave with a batch was filled with a standard sodium carbonate solution of composition 7 wt % Na_2CO_3 + 0.5 wt % NaOH. For a filling factor of 78%, the autoclave was covered with a lid and was charged with helium through a sealed-in capillary connected to a gas cylinder. When the helium pressure in the autoclave reached 7 MPa, the autoclave was closed hermetically and placed in a vertical furnace with a two-section heater, which provided the required temperature conditions. The temperatures in the lower and upper autoclave zones were equal to 360 and 330°C, respectively. The water pressure in the autoclave was 84 MPa. The crystal was grown for 30 days. The growth rate of the basal face gradually increased from the lower (0.43 mm/day) to the upper (0.53 mm/day) face of the crystal. After cooling the autoclave to room temperature, the residual helium pressure was of the order of 5 MPa. The quartz crystal grown in a helium atmosphere is drawn schematically in Fig. 1.

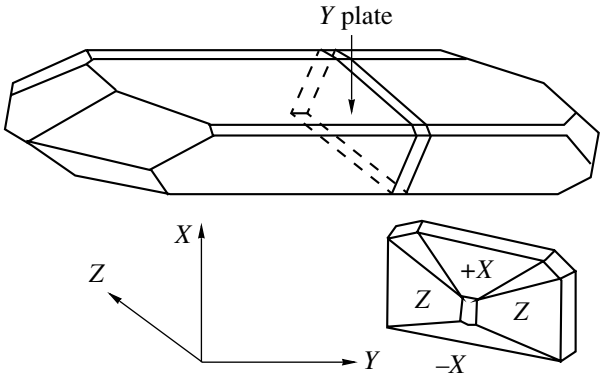

Fig. 1. Schematic drawing of the quartz crystal grown in a helium atmosphere.

The samples suitable for x-ray diffraction investigations were prepared in the forßm of plates cut out along the (0001) and $\{1\bar{1}01\}$ planes. After grinding and polishing, the plate thickness was 0.35 mm.

2.2. Experimental Technique

Structural defects were examined using x-ray diffraction topography with a laboratory source and phase-sensitive radiography with a synchrotron radiation source. The x-ray topographic investigation was performed by the Lang method in Bragg and Laue geometries with the use of CuK_α and MoK_α radiation. The divergence in the scattering plane was of the order of the angular separation between the spectral lines α_1 and α_2. The resolution in the direction normal to the scattering plane was of the order of several microns in the case when the distance between the crystal and a

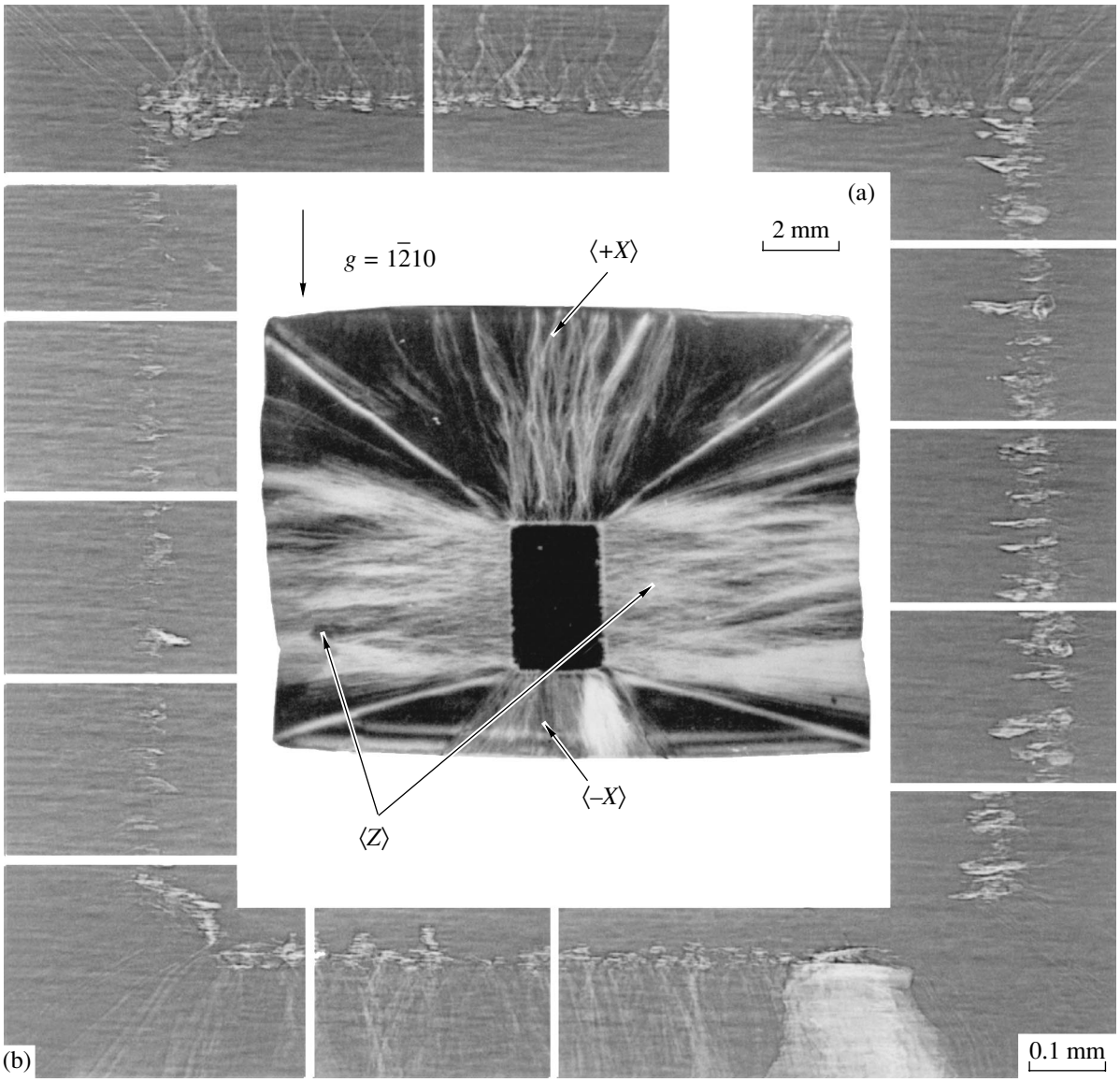

Fig. 2. (a) Lang topogram in a Lauer geometry (MoK_α radiation, $1\bar{2}10$ reflection) for a plate cut out parallel to the $(1\bar{1}00)$ plane from a quartz crystal saturated with helium during growth. The rectangular at the center of the plate indicates the position of the seed. (b) Phase radiograph obtained from a series of images of the crystal–seed boundary. The plate surface is parallel to the $(1\bar{1}00)$ plane.

photographic film amounted to 5–10 mm. The phase radiographic experiments were carried out with the use of nonmonocrhromatic radiation from a synchrotron source (Pohang, Republic of Korea). The effective source size was 60 μm along the vertical and 160 μm along the horizontal direction. The distance from the source to the sample was 30 m. The $CdWO_4$ crystal scintillator mounted behind the sample transformed x-ray radiation into a luminous flux. The distance between the sample and the scintillator varied from several centimeters to 1 m. The images were recorded on a detector with a charge-coupled device matrix. The charge-coupled device matrix had a size of 1392×1040 pixels and a sensitivity of 12 bits. Optical lenses made it possible to change the field of vision from 4×4 to 0.6×0.4 mm.

2.3. Experimental Results

Figure 2a shows a typical topogram of the plate cut out parallel to the $(1\bar{1}00)$ plane of the quartz crystal. The radiograph of this plate is given in Fig. 2b. The crystal was grown in a helium atmosphere. It can be seen from the topogram that the seed is a perfect crystal free of dislocations. However, a large number of dislocations are observed in the crystal beginning from the

boundary with the seed. An analysis of the topograms recorded for different reflections revealed that the dislocation density is maximum (10^5 cm^{-2}) in the growth sector $\langle Z \rangle$ of the (0001) basal plane and in the growth sectors $\langle \pm X \rangle$ of the $\{11\bar{2}0\}$ planes of the trigonal prisms. The dislocation density between the sectors $\langle Z \rangle$ and $\langle +X \rangle$ is lower than that in the sectors by at least three orders of magnitude.

The x-ray topograms of the plate cut from the crystal grown in the absence of helium is shown in Fig. 3. The plate surface is parallel to the (0001) plane. The dislocation density in these samples is relatively low, and images of individual dislocations can be distinguished ed in the topograms. This allows us to determine the Burgers vectors **b** of dislocations. An analysis of the topograms in Fig. 3 shows that a group of dislocations is located in the sector $\langle r \rangle$ of the small rhombohedron. The images were obtained for six reflections from the $\{10\bar{1}1\}$ planes of the rhombohedra. The dislocation lines are almost parallel to the $[\bar{1}011]$ direction. The images of dislocations are characterized by the following features. The dislocations are not observed in the image for the $\bar{1}011$ reflection and are clearly seen in the images for all other reflections. Since the contrast of dislocations is weak even when the condition $\mathbf{g} \cdot \mathbf{b} = 0$ is satisfied, we can make the inference that these are edge dislocations with the Burgers vector $\mathbf{b} = a[1\bar{2}10]$. An analysis of the condition for complete extinction of the image of the dislocation $\mathbf{g} \cdot \mathbf{b} \times \mathbf{l} = 0$ (where **g** is the diffraction vector and **l** is the vector specifying the direction of the dislocation line) demonstrates that the quantity $|\cos\angle(\mathbf{g}, \mathbf{b} \times \mathbf{l})|$ is maximum for the $10\bar{1}1$ reflection and minimum for the $\bar{1}011$ reflection. This explains why the dislocation contrast is maximum for the $10\bar{1}1$ reflection.

A comparison of the topograms displayed in Figs. 2 and 3 shows that the density of dislocations in the crystal grown in the helium atmosphere is higher than the density of dislocations in the crystal grown in the absence of helium. It can be seen from Fig. 2a that dislocations are generated at the boundary with the seed, but the images of dislocation sources are not distinguishable. Figure 2b displays the higher resolution images obtained by phase-sensitive radiography. The image of the crystal–seed boundary is formed from a series of photographs recorded by stepwise moving the sample in the incident beam. The radiograph shows inclusions and etch channels. The channels arose from chemical etching of the plate in a 40 vol % HF solution (at 20°C for 20 h). It is evident that the etch channels are associated with the inclusions at the crystal–seed boundary. The direction and density of etch channels (Fig. 2b) coincide with the direction and density of dislocations (Fig. 2a). Earlier x-ray topographic investigations revealed that etch channels in quartz are formed along lines of dislocations decorated by impurities [14, 15]. Therefore, inclusions bring about the generation of dislocations.

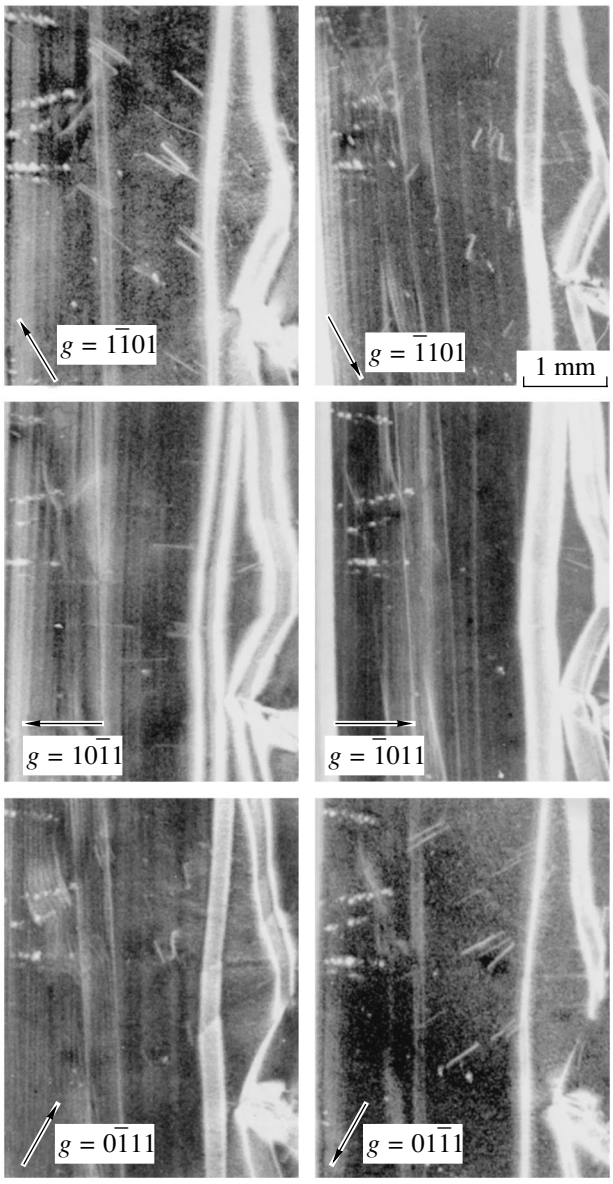

Fig. 3. Lang topograms (MoK_α radiation) illustrating the change in the dislocation contrast with a change in the direction of the diffraction vector **g**. The plate surface is parallel to the (0001) plane. The contrast is opposite to the original.

It can be assumed that the presence of helium in a growth chamber disturbs the physicochemical equilibrium of the system. The primary interaction of the solution with the seed led to a partial dissolution of the seed in the undersaturated solution. The regeneration of the damages caused by the dissolution was accompanied by the formation of inclusions.

The samples used for studying the desorption were prepared from the crystal saturated with helium and

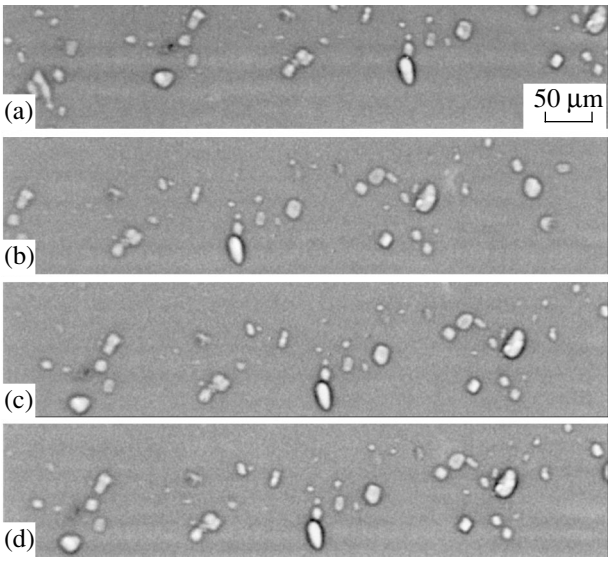

Fig. 4. *In situ* phase radiographs of the sample at temperatures of (a) 20, (b) 350, (c) 420, and (d) 550°C.

could contain inclusions. In the course of desorption, the samples were subjected to heating. Cracks should appear in regions where stresses caused by the pressure of an expanding liquid contained in the formed inclusions exceeded the ultimate stress of the material. With the aim of examining the behavior of inclusions during heating, we performed the following experiment. A polished unetched quartz plate cut out parallel to the $(1\bar{1}00)$ plane was placed in a furnace and was introduced into the incident beam of synchrotron radiation. The plate was slowly heated to 550°C in air. The images of inclusions were recorded at intervals, during each of which the temperature increased by 10°C. The field of vision moved over the plate. In order to observe the spatial arrangement of inclusions, the sample was rotated about the axis perpendicular to the incident beam. The images were also recorded in the course of cooling of the sample and after complete cooling to room temperature. We studied two samples. A number of typical images are given in Fig. 4. Neither cracks nor new inclusions that could be formed as a result of partial healing of cracks were revealed.

Reasoning from the structural-defect distribution determined from the topograms and radiographs, the helium-containing quartz crystal was cut into fragments with different dislocation densities.

3. INVESTIGATION OF THE SOLUBILITY AND DIFFUSION OF HELIUM IN QUARTZ

3.1. Sample Preparation and Experimental Technique

The samples cut from the helium-free crystal were saturated with helium at a pressure of 3.0–3.25 MPa and a temperature of 290–355°C for 100–3000 h. The faces of the samples ~$10 \times 10 \times 10$ and ~$3 \times 3 \times 30$ mm in size were parallel to the (0001), $(1\bar{1}00)$, and $(11\bar{2}0)$ planes. After saturation, the samples were placed in ampules evacuated to a pressure of ~1.333 Pa. The ampules with the samples and empty evacuated ampules were sealed. Immediately prior to analysis, impregnated samples were cut into fragments so that, during saturation, one central fragment was not in contact with helium, whereas the other fragments had different areas in contact with helium.

The crystal grown in the medium containing helium was cut perpendicularly to the *Z* axis into samples 3–4 mm thick. In turn, the samples were cut into fragments corresponding to different growth sectors.

A quantitative analysis of the samples for helium and an investigation into the kinetics of helium desorption were performed using mass spectrometry [16] under different heating conditions (stepwise or isothermal heating and melting). For this purpose, crucibles evacuated to a residual pressure of 1.333×10^{-4} Pa and equipped with sample holders were connected to the inlet and purification system of the mass spectrometer. The samples were dropped in turn into crucibles in which helium was accumulated at specified times and temperatures. The melting temperature of the samples was equal to 1750°C. Extracted helium was fed into the inlet and purification system of the mass spectrometer.

The helium concentration was measured from the peak height on an MI-1201 mass spectrometer. Prior to analysis of each sample, the mass spectrometer was calibrated against a reference sample. The sensitivity of the mass spectrometer for ^{4}He was equal to 5×10^{-5} A/Torr, and the total experimental error was 10%. The helium amount measured after each five or six experiments with the samples was approximately equal to 10^{-9} cm^3. The results of the measurements were corrected to a temperature of 0°C and a pressure of 0.1 MPa.

3.2. Helium Content

The results of the investigation into the extraction of helium from the samples cut from the crystal grown in the absence of helium and then saturated with helium can be summarized as follows. The helium content in the initial crystal was less than 0.5×10^{-9} cm^3/g. The helium content in the ampule after one- to three-month storage of the samples was $(0.3–0.6) \times 10^{-6}$ cm^3/g. Upon melting, the amount of released ^{4}He was equal to $(0.76–1.58) \times 10^{-6}$ cm^3/g. The Ostwald solubility coefficient of helium in quartz was determined to be $S_{Os} = (0.6–1.2) \times 10^{-7}$ cm^3/g atm, which is approximately four orders of magnitude less than that in cristobalite and tridymite [17]. Since the density of dislocations in the samples was relatively low ($<10^2$ cm^{-2}) and the crystal did not contain inclusions, it was inferred that this coefficient characterizes the solubility of helium in the ordered quartz lattice. The amount of helium dis-

solved in the samples did not depend on their orientation, the contact area with helium in the course of saturation, or the saturation time.

3.3. Kinetics of Helium Desorption

The desorption kinetics was studied upon heating of the samples (cut from the crystal saturated with helium during growth) with different dislocation densities. The samples were rapidly heated to temperatures of 300, 350, and 400°C and were isothermally held for 15–30 h. Then, the samples were melted. The time dependences of the amount of extracted helium indicate that the desorption rate initially increases: with an increase in the temperature, the helium amount first increases almost linearly and then reaches saturation. For the samples with the maximum dislocation density, the amount of helium desorbed upon heating is very close to the total amount of helium extracted upon melting. By contrast, the desorption from the samples cut from the crystal regions with a low dislocation density is hindered: only an insignificant amount of dissolved helium can be extracted upon heating during the above period of time. The remaining helium is released (in a considerably larger amount) upon melting.

Let us assume that Q_∞ is the total amount of helium dissolved in the sample and Q_t is the amount of helium desorbed upon heating for the time t. Barker and Vaughan [17] derived the relationship describing the helium diffusion from particles with a total area S and volume V when the diffusion coefficient D depends on the time t; that is,

$$\frac{1}{D}\frac{d}{dt}\left(\frac{Q_t}{Q_\infty}\right)^2 = \frac{4S^2}{\pi V^2}.$$

Therefore, the diffusion coefficient D can be determined from the slope of linear portions of the dependence of Q_t/Q_∞ on $\sqrt{t}$. Our data demonstrate that the ratio Q_t/Q_∞ depends on the density of dislocations in the samples. Consequently, the slope of the dependence of Q_t/Q_∞ on $\sqrt{t}$ can be treated as the effective diffusion coefficient characterizing the dislocation pipes diffusion of helium.

It is expedient to compare the data obtained for samples with different dislocation densities in the case when the samples insignificantly differ in size, are free of internal cracks, and exhibit approximately identical losses through a cracked mosaic layer on the surface. In our experiments, all these conditions were satisfied. As follows from the results of the *in situ* experiment (Fig. 4), the helium desorption from inclusions can proceed only through the diffusion mechanism.

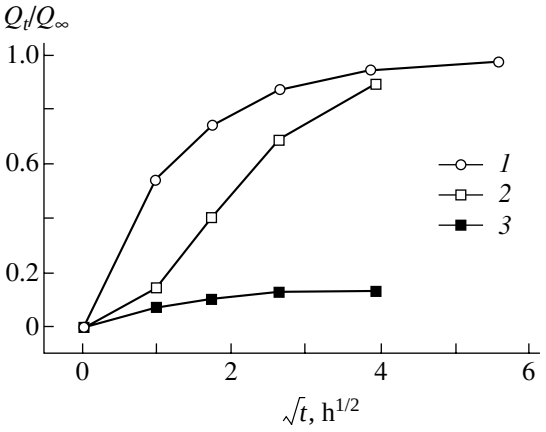

Fig. 5. Dependences of Q_t/Q_∞ on $\sqrt{t}$ upon helium extraction from samples with different dislocation densities ρ at temperatures of (*1*, *3*) 350 and (*2*) 400°C. (*1*, *2*) $\rho \sim 10^5$ and (*3*) $\rho < 10^2$ cm^{-2}.

The experimental dependences of Q_t/Q_∞ on $\sqrt{t}$ are depicted in Fig. 5. It can be seen from this figure that the slopes of the linear portions of curves *1* and *2* are appreciably larger than those of curve *3*. Curves *1* and *2* correspond to the desorption of helium from the samples cut from the growth sectors ⟨*Z*⟩ with the dislocation density $\rho \sim 10^5$ cm^{-2}. Curve *3* was obtained by measuring the extraction of helium from the crystal regions located between the growth sectors ⟨*Z*⟩ and ⟨+*X*⟩. These samples are characterized by the dislocation density $\rho < 10^2$ cm^{-2}. The inference can be made that the diffusion rate of helium is higher and the activation energy of diffusion is lower for the samples with a high dislocation density.

The diffusion coefficient of helium in quartz was calculated from the data obtained for the crystal grown in a standard hydrothermal solution and saturated with helium at a high temperature and a high pressure. The samples used for investigating the extraction had the form of a cube with the characteristic sizes listed in the table. The problem of the helium flux from a cubic sam-

Experimental conditions and typical effective diffusion coefficients

T, °C	Q_∞, 10^{-6} cm^3/g	d, cm	ρ, cm^{-1}	h, cm	K, 10^{-6} s^{-1}	D_{eff}, 10^{-8} cm^2/s
250	0.167	0.62	10	0.1	2.66	2.6
275	0.121	0.63	10	0.1	2.1	2

Note: T is the heating temperature of the sample, Q_∞ is the total amount of helium extracted upon melting, d is the edge length of the cubic fragments, ρ is the dislocation density in the sample, and $h = 1/\rho$ is the diffusion length in the defect-free lattice.

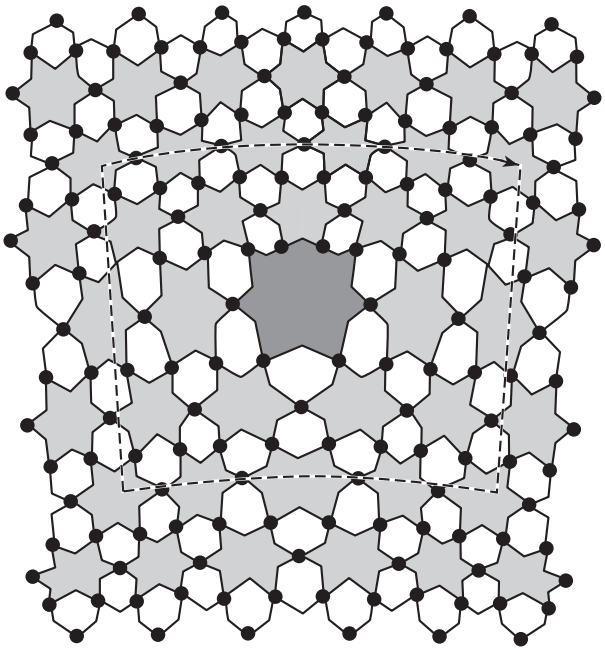

Fig. 6. A model of the edge dislocation with **l** = [0001] and **b** = $a[1\bar{2}10]$ in the projection onto the (0001) plane. Shaded regions correspond to hexagonal channels along the *Z* axis. The dark region at the center of the figure represents the hexagonal channel coinciding with the core of the edge dislocation. Only the Si atoms are shown. The dashed line indicates the Burgers contour.

ple was solved under zero boundary conditions and the assumption of a uniform distribution of helium over the sample volume. The solution was obtained for the coefficient $K = \frac{D_{\text{eff}}}{h^2}$, where D_{eff} is the effective diffusion coefficient and h is the diffusion length. The time dependence of the flux $Q(t, K)$ was calculated and the best agreement between the calculated and experimental data was achieved by varying the coefficient K (see table).

The calculated effective diffusion coefficients D_{eff} are close in order of magnitude to those determined by Trull *et al.* [3]. However, an increase in the dislocation density to 10^5 cm^{-2} should lead to a considerable decrease in the size of defect-free regions and to a change in the diffusion mechanism. In this case, the migration of helium over dislocation pipes should dominate over the interstitial diffusion. An analysis of the contrast in dislocation images demonstrates that, for the most part, the studied crystals involve edge dislocations. An edge dislocation always creates a region of volume expansion in the crystal lattice. In the dislocation core, the upper horizontal rows of atoms are displaced upward to a greater extent than the lower horizontal rows of atoms, which results in a distortion of hexagonal helical channels whose location coincides with dislocation cores (Fig. 6). This leads to an increase in the size of the interstices. It is well known that the activation energy for diffusion of helium-like rare-gas atoms in quartz involves the elastic energy necessary for increasing interstices to sizes large enough for an impurity atom to pass through. An increase in the interstice size due to the presence of dislocations results in a decrease in the energy of impurity migration over dislocation pipes. Since the diffusion is described by the Arrhenius law $D \sim \exp(-W/kT)$ (where W is the activation energy of migration, k is the Boltzmann constant, and T is the absolute temperature), a decrease in the activation energy W leads to a substantial increase in the diffusion coefficient. Moreover, edge dislocations are sinks for vacancies, which, in turn, should enhance the migration of helium atoms.

4. CONCLUSIONS

The main results obtained in this work can be summarized as follows.

Crystals of synthetic quartz were grown in a standard hydrothermal solution in an autoclave with and without helium. The crystals contained different amounts of dislocations and inclusions, whose densities and arrangement were determined using x-ray diffraction topography and phase radiography. The desorption of helium from different crystals was studied by mass spectrometry. It was shown that, for a crystal saturated with helium during growth, the desorption rate of helium from the samples cut from crystal regions with a high dislocation density is higher and the activation energy for diffusion in these samples is lower than those for the samples with a considerably lower dislocation density. The helium diffusion coefficient calculated from the data on the helium desorption from the samples with a dislocation density of 10^2 cm^{-2} was close in order of magnitude to the diffusion coefficients available in the literature. A substantial increase in the diffusion coefficient for the samples with a dislocation density of 10^5 cm^{-2} was explained by the increase in the size of the interstices due to the presence of edge dislocations and by the decrease in the energy of impurity migration over dislocation pipes. The Ostwald solubility coefficient of helium in the real quartz lattice was determined.

ACKNOWLEDGMENTS

We would like to thank I.N. Tolstikhin for providing an opportunity to participate in the studies performed within the Swiss Research Program and for helpful consultations and S.V. Tarakanov for his assistance in processing diffusion data.

This work was supported by the Swiss Research Program "Helium Migration in Subsurface Environments" (N 7SUPJ062127) and the Russian Foundation for Basic Research (project no. 03-02-16613). T.S. Argunova acknowledges the support of the Korean Foundation KISTEP for the opportunity to perform synchrotron investigations in the framework of the Korea–Russia Joint Research Program. J.H. Je acknowledges the support of the National Research Laboratory Program.

REFERENCES

1. B. A. Mamyrin, G. S. Anyfriev, U. L. Kamensky, and I. N. Tolstihin, Geochem. Int. **7**, 498 (1970).
2. I. N. Tolstihin, B. E. Lehmann, H. H. Loosli, and A. Gautschi, Geochim. Cosmochim. Acta **60**, 1497 (1996).
3. T. W. Trull, M. D. Kurz, and W. J. Jenkins, Earth Planet. Sci. Lett. **103**, 241 (1991).
4. I. N. Tolstikhin, É. M. Prasolov, L. V. Khabarin, and I. Ya. Azbel', in *Geochemistry of Radioactive and Radiogenic Isotopes* (Nauka, Leningrad, 1974), pp. 79–90.
5. E. Gorlich, Ceram. Int. **8**, 3 (1982).
6. E. V. Kalashnikov and B. Z. Pevzner, Fiz. Tverd. Tela (St. Petersburg) **44**, 283 (2002) [Phys. Solid State **44**, 294 (2002)].
7. G. G. Boĭko and G. V. Berezhnoĭ, Fiz. Khim. Stekla **29**, 65 (2003).
8. J. F. Shackelfold, J. Non-Cryst. Solids **49**, 299 (1982).
9. R. H. Doremus, *Glass Science* (Wiley, New York, 1973), p. 133.
10. L. Pauling, *The Nature of the Chemical Bond and the Structure of Molecules and Crystals*, 2nd ed. (Cornell Univ. Press, Ithaca, N.Y., 1940; Gostekhizdat, Moscow, 1947).
11. O. V. Klyavin, Fiz. Tverd. Tela (St. Petersburg) **35**, 513 (1993) [Phys. Solid State **35**, 261 (1993)].
12. O. V. Klyavin, P. P. Likhodedov, and A. N. Orlov, Fiz. Tverd. Tela (Leningrad) **28**, 156 (1986) [Sov. Phys. Solid State **28**, 84 (1986)].
13. *Synthesis of Minerals* (VNIISIMS, Aleksandrov, 2000), Vol. 1.
14. A. R. Lang and V. F. Miuscov, J. Appl. Phys. **38**, 2477 (1967).
15. F. Iwasaki, J. Cryst. Growth **39**, 291 (1977).
16. U. L. Kamensky, I. N. Tolstikhin, and V. R. Vetrin, Geochim. Cosmochim. Acta **54**, 3115 (1990).
17. R. M. Barker and D. E. W. Vaughan, Trans. Faraday Soc. **63**, 2275 (1967).

Translated by O. Borovik-Romanova

Physics of the Solid State, Vol. 45, No. 10, 2003, pp. 1918–1925. Translated from Fizika Tverdogo Tela, Vol. 45, No. 10, 2003, pp. 1825–1832.

DEFECTS, DISLOCATIONS, AND PHYSICS OF STRENGTH

Diffuse X-ray Scattering Study of the Formation of Microdefects in Heat-Treated Dislocation-Free Large-Diameter Silicon Wafers

V. T. Bublik*, S. Yu. Matsnev*, K. D. Shcherbachev*, M. V. Mezhennyĭ, M. G. Mil'vidskiĭ***, and V. Ya. Reznik*****

** Moscow Institute of Steel and Alloys, Leninskii pr. 4, Moscow, 117936 Russia*

*** Giredmet State Research Institute for the Rare-Metals Industry, Bol'shoĭ Tolmachevskiĭ per. 5, Moscow, 109017 Russia*

e-mail: icpm@mail.girmet.ru

**** Institute for Chemical Problems of Microelectronics, Bol'shoĭ Tolmachevskiĭ per. 5, Moscow, 109017 Russia*

Received March 11, 2003

Abstract—Diffuse x-ray scattering (DXS) is used to study the formation of microdefects (MDs) in heat-treated dislocation-free large-diameter silicon wafers with vacancies. The DXS method is shown to be efficient for investigating MDs in silicon single crystals. Specific defects, such as impurity clouds, are found to form in the silicon wafers during low-temperature annealing at 450°C. These defects are oxygen-rich regions in the solid solution with diffuse coherent interfaces. In the following stages of decomposition of the supersaturated solid solution, oxide precipitates form inside these regions and the impurity clouds disappear. As a result of the decomposition of the supersaturated solid solution of oxygen, interstitial MDs form in the silicon wafers during multistep heat treatment. These MDs lie in the {110} planes and have nonspherical displacement fields. The volume density and size of MDs forming in the silicon wafers at various stages of the decomposition are determined. © *2003 MAIK "Nauka/Interperiodica".*

1. INTRODUCTION

The processes of microdefect formation in dislocation-free single-crystalline Si wafers are usually studied using optical microscopy (OM) and transmission electron microscopy (TEM). OM provides only very limited possibilities for investigating the nature of microdefect (MD) formation and the transformation of MDs upon annealing of the wafers. Our studies showed that the application of TEM for investigating the early stages of decomposition of a supersaturated solid solution of oxygen in silicon also encounter significant difficulties caused mainly by the fact that MDs forming at these stages induce only small distortions of the crystal lattice. Moreover, the use of TEM implies constraints on the minimum volume density of defects in samples.

Investigation of the microdefect formation in the early stages of decomposition of a supersaturated solid solution of oxygen in silicon makes it possible to reveal not only nucleation mechanisms but also the transformation of the medium with defects when an internal getter is created in a wafer. It is reasonable to suppose that valuable information can be obtained using diffuse x-ray scattering (DXS). In this work, we use DXS to investigate the processes of microdefect formation in heat-treated dislocation-free silicon wafers.

2. EXPERIMENTAL

Defect formation in the early stages of decomposition of a supersaturated solid solution of oxygen in silicon during multistep heat treatment of wafers was studied by DXS on a three-crystal x-ray diffractometer using the dispersion-free scheme (n; $-n$; $+n$) with triple reflection from a monochromator and an analyzer. A 1.5-kW x-ray tube with a copper anode was used. A slit was placed in front of a sample to transmit the $K_{\alpha 1}$ component of the radiation. The irradiated region on a sample was 0.5×7 mm in size. The DXS intensity distribution $I(\mathbf{q})$, where $\mathbf{q} = \mathbf{G} - \mathbf{H}$ is the vector characterizing the deviation of the diffraction vector $\mathbf{G}$ from the reciprocal lattice vector $\mathbf{H}$, was measured in the vicinity of the 004 site. The vector $\mathbf{q}$ components in the diffraction plane are connected with the experimental geometric parameters by the relation

$$(q_z, q_x) = (\Delta\theta_3 \cos\theta_B (2\Delta\theta_2 - \Delta\theta_3) \sin\theta_B)/\lambda, \quad (1)$$

where $\Delta\theta_2$ and $\Delta\theta_3$ are the angular deviations from the exact Bragg position θ_B for the sample and analyzer, respectively; λ is the x-ray wavelength; the Z axis is normal to the sample surface; and the X axis is parallel to the sample surface (both axes lie in the diffraction plane).

1063-7834/03/4510-1918$24.00

According to [1, 2], the DXS intensity distribution is determined by the Fourier transform of the displacement field of a defect $u(q)$:

$$I(\mathbf{q}) \sim |\mathbf{G}\mathbf{u}(\mathbf{q})|^2. \quad (2)$$

If local distortions around defects are small and $\mathbf{G}\mathbf{u}(\mathbf{q}) \ll 1$, the differential cross section of diffuse scattering can be written as [1, 2]

$$S_{\text{dif}}(q) = N|F|^2 e^{-2M}\left(\frac{H^2C^2}{q^2}\sum_i^3 \pi_i\gamma_i + \frac{(HC)^{5/2}}{V_c^2 q}\sqrt{\pi_1\gamma_1}\right), \quad (3)$$

where F is the structure amplitude, N is the number of scattering centers, e^{-2M} is the Debye–Waller temperature factor, and C is the strength of the defect, which characterizes the defect-induced change in the crystal volume ΔV and can be expressed in terms of the defect parameters (shape, size, deformation sign) for a certain type of MD. For a defect producing a displacement field of the Coulomb type $\mathbf{u}(\mathbf{r}) \sim \mathbf{C}(\mathbf{r}_0)/\mathbf{r}^2$, the sign of the defect strength $\mathbf{C}(\mathbf{r}_0)$, which generally depends on the direction of the unit vector $\mathbf{r}_0$ in the real space, is determined by the difference ΔV between the volumes of the matrix and the substitutional defect: if $\Delta V > 0$, then $C > 0$ (and vice versa).

In Eq. (3), γ_i and π_i are defined according to [3]:

$$\begin{aligned}
\pi_1 &= (\mathrm{Tr}\,P_{mn})^2/3,\\
\pi_2 &= \sum_{n>m}(P_{nn} - P_{mm})^2/6,\\
\pi_3 &= 2\sum_{n>m}(P_{mn})^2/3,\\
\gamma_1 &= (\mathrm{Tr}\,T_{ij})^2/3,\\
\gamma_2 &= \sum_{i>j}(T_{ii} - T_{jj})^2/3,\\
\gamma_3 &= \sum_{i>j}(T_{ij} - T_{ji})^2/2,
\end{aligned} \quad (4)$$

where $\mathrm{Tr}P_{mn}$ and $\mathrm{Tr}T_{ij}$ are the traces of the dipole moment tensor P_{mn} and the tensor T_{ij} described by Eq. (6), respectively.

In the case of dislocation loops, the components of the dipole moment tensor $\bar{P}$ are expressed as follows:

$$P_{mn} = (C_{12}\mathrm{Tr}\,\Omega_{mn} + \Omega_{nn}d)\delta_{nm} + 2C_{44}\Omega_{nm}, \quad (5)$$

where $\Omega_{mn} = \frac{1}{2}(F_n b_m + F_m b_n)$, $d = C_{11} - C_{12} - 2C_{44}$, with C_{ij} being the components of the elastic tensor of a cubic crystal in the matrix notation; **b** is the Burgers vector; and **F** is the vector specifying the plane of location of dislocation loops. The tensor T_{ij} is defined as

$$T_{ij} = (h_k/V_c)g_{ij}e_j, \quad (6)$$

where h_k and e_j are the direction cosines of the vectors **H** and **q**, respectively; $g_{ij} = (\sum_{kl} C_{ijkl}e_k e_l)^{-1}$; and V_c is the unit cell volume.

The first term in parentheses in Eq. (3) corresponds to the Huang scattering $S_{\text{dif}}^{\text{H}}(q)$ distributed symmetrically with respect to $S_{\text{dif}}^{\text{H}}(q) = S_{\text{dif}}^{\text{H}}(-q)$. The second term determines the asymmetric part of scattering, $S_{\text{dif}}^{A}(q)$, and leads to a shift in the diffuse scattering distribution toward positive or negative values of q_z depending on the sign of ΔV. For example, for microdefects formed from interstitial atoms, $\Delta V > 0$ and the diffuse scattering distribution shifts toward positive values of q_z, whereas, for defects of the vacancy type ($\Delta V < 0$), it shifts toward negative values of q_z.

Some of the parameters π_i vanish for a certain symmetry of defects. For example, for defects of cubic symmetry, only π_1 is nonzero; in the case of tetragonal symmetry, $\pi_3 = 0$; and in the case of trigonal symmetry, $\pi_2 = 0$ [4]. Moreover, at certain indices m and n corresponding to high-symmetry directions, the values of γ_i also become zero. As a result, the diffuse scattering intensity $S_{\text{dif}}^{\text{ADS}}(q)$ for such directions in the reciprocal space can be zero for a certain symmetry of a defect.

When point defects associate with each other during the course of structural transformations accompanying post-solidification cooling and subsequent anneals, the size of the region of strong distortions around a defect increases. As a result, the range of q values over which the relation $I(q) \sim q^{-2}$ is valid becomes narrower. For strongly distorted regions ($\mathbf{G}\mathbf{u}(\mathbf{q}) \gg 1$), the diffuse scattering intensity can be found using the Stokes–Wilson approximation (asymptotic scattering $S_{\text{dif}}^{\text{ADS}}(q)$). At $q \gg q_0(GC)^{-1/2}$, the cross section of asymptotic diffuse scattering is [2]

$$S_{\text{dif}}^{\text{ADS}}(q) = N|F|^2 e^{-2M}\frac{CH}{V_c^2 q^4}\Psi(\mathbf{m}, \mathbf{n}), \quad (7)$$

where **m** and **n** are the unit vectors of **q** and **H**, respectively, and Ψ is a function depending on the angle between **q** and **H**. Here, the function $\Psi \sim 2$ [2] specifies the anisotropy of the asymptotic scattering distribution, which depends only on the directions of the vectors **H** and **q.**

The angular dependence of the diffuse scattering intensity in the reciprocal space can be conveniently represented in the form of surfaces of equal intensity (isodiffuse surfaces) or their sections made by planes passing through reciprocal lattice sites (isodiffuse curves). For isodiffuse surfaces and small deviations from the diffraction vector, the quantity q can be written as

$$q^2 = \text{const}\sum_i^3 \pi_i\gamma_i. \quad (8)$$

The shape of an isodiffuse surface is substantially determined by the type of defects present, their position in the lattice, and the symmetry of their displacement fields. The general shape of the isodiffuse surfaces allows us to find the symmetry of the displacement field of a point defect and to choose one of the possible displacement configurations [1, 2]. Sometimes, it suffices to consider the DXS intensity distribution along the directions parallel and normal to the diffraction vector.

As the magnitude of the vector **q** increases, the character of the decrease in the differential DXS intensity $I(\mathbf{q})$ changes [1, 5]. In order to analyze changes in the behavior of the $I(\mathbf{q})$ dependence, $\log I = f(\log q)$ plots are conveniently used. There are three **q** magnitude ranges in which the laws of the decrease in $I(\mathbf{q})$ are different.

(1) Huang Scattering Range

X rays are scattered by weak elastic distortions of a crystal lattice caused by elastic displacement fields of the defects. A defect can be considered as a point source of force. The distance **r** from the center of a defect is much greater than the mean radius R_0 of the defect. Under these conditions, $I \sim q^{-2}$. Thus, the slope of the $\log I = f(\log q)$ curve for this scattering range is equal to –2.

(2) Asymptotic Scattering Range

X-ray scattering is caused by rather strong distortions of a crystal lattice and can be described in terms of the elastic-continuum theory without regard for changes in the elastic moduli. A defect cannot be considered as a point source. Here, $I \sim q^{-4}$, which corresponds to a slope of –4. The value q_0 at which the transition occurs from the Huang to asymptotic scattering (inflection point) can be used to estimate the defect strength from the relation [2]

$$q_0 = \frac{1}{\sqrt{HC}}. \quad (9)$$

(3) Range of Scattering by a Defect Core

It is known that the region of $r \le R_0$ (Laue scattering) is difficult to achieve experimentally, since, starting from a certain value $\mathbf{q}_T$, scattering by thermal lattice vibrations predominates over x-ray diffuse scattering by defects if their concentration is low [2]. The intensity of the former scattering is proportional to q^{-2}, which corresponds to a slope of –2. Thermal scattering can be used as an "internal standard" to determine the defect concentration [6].

One of the methods of determining the MD concentration in single crystals is based on the fact that, at scattering vectors with $q < q_0$, the Huang scattering intensity $S^{\mathrm{H}}(q)$ predominates over the thermal diffuse scattering intensity $S^T(q) \sim q^{-2}$. Hence, the quantity $S^T(q)$ can be measured for a crystal under study by using the same experimental procedure as that employed for measuring the intensity $S^{\mathrm{H}}(q)$ at the same reciprocal lattice vector **H**.

Using the expression for $S^T(q)$ from [7], we obtain

$$S^T(q) = N_0|F|^2 e^{-2M}\frac{kTH^2}{V_c q^2}K(\mathbf{m}, \mathbf{n}), \quad (10)$$

where $K(\mathbf{m}, \mathbf{n})$ is the Christoffel determinant [7], N_0 is the number of unit cells in the crystal, k is the Boltzmann constant, and T is the absolute temperature of the sample.

Charniy *et al.* [6] derived a convenient expression for determining the MD concentration n_d in a crystal from the intensity ratio of Huang and thermal scattering:

$$\frac{S^{\mathrm{H}}(\mathbf{q}_{\mathrm{H}})}{S^T(\mathbf{q}_T)} = \frac{n_d(\Delta V)^2}{kT}\frac{|q_T|^2}{|q_{\mathrm{H}}|^2}\frac{\Pi(\mathbf{m}, \mathbf{n})}{K(\mathbf{m}, \mathbf{n})}, \quad (11)$$

where $\mathbf{q}_{\mathrm{H}}$ and $\mathbf{q}_T$ are the wave vectors relating to the angular ranges with predominant Huang or thermal scattering, respectively, and $\Pi(\mathbf{m}, \mathbf{n}) = V_c^2\sum_i^3 \pi_i\gamma_i$. This expression allows us to find absolute values of the measured DXS intensities for the MDs under study without regard for the thickness of the scattering layer, structure amplitude, solid scattering angle, and Debye–Waller factor. Hence, important parameters, such as the symmetry, size, and concentration of MDs, can be determined directly from the experimental data on diffuse scattering by the sample under study.

The $I(\mathbf{q})$ dependences considered above for various scattering ranges relate to the differential intensity. To provide an acceptable light-gathering power, we have to use radiation beams with a vertical divergence. In the presence of a vertical divergence in a three-crystal

x-ray diffractometer, the measured intensity can be written as

$$I(q_x, q_z) = \int_{-q_{y\max}}^{+q_{y\max}} I(\mathbf{q})dq_y, \quad (12)$$

$$q_{y\max} = \varphi_{\max}/\lambda, \quad (13)$$

where $\mathbf{q}_x \parallel (001)$ and $\mathbf{q}_z \parallel (100)$ are the vector $\mathbf{q}$ components in the diffraction plane, the component $\mathbf{q}_y$ is normal to the diffraction plane, and $\varphi_{\max}$ is the maximum angle of deviation of the diffracted rays from the diffraction plane (this angle specifies the effective vertical divergence). The angle $\varphi_{\max}$ is determined by the width of the reflection curve of an analyzer [8]. We will call the intensity distributions $I(q)$ along the $\mathbf{q}_x$ and $\mathbf{q}_z$ directions the q_x and q_z sections, respectively. Thus, the function $I(q)$ should change after integrating with respect to q_y. For example, in the Huang scattering range, the DXS intensity recorded experimentally decreases as q^{-1} and, in the asymptotic scattering range, as q^{-3}. Analysis of the slope of the linearized $\log I = f(\log q)$curve can give information on the nature of a defect, its mean size, and the form of the defect–matrix interface. For quantitative measurements of diffuse scattering with the aim of determining the defect concentration, the limits of integration with respect to q_y should be taken into account.

We studied two series of samples, which were wafers of dislocation-free silicon single crystals (with vacancies) 150 mm in diameter grown by the Czochralski technique along the ⟨100⟩ direction. The concentration of oxygen dissolved in the samples was (7–8) × 10^{17} cm^{-3}, and the resistivity was 1–5 Ω cm. Each series consisted of samples subjected to multistage heat treatment, including low-temperature, stabilizing, and high-temperature annealings. The series differed in the regime of the low-temperature annealing: for the first series, the annealing was performed at 450°C, whereas for the second, at 650°C. The heat-treatment regimes for the wafers under study are given in Table 1. As reference samples, we used as-grown wafers. After heat treatment, the samples were chemically polished in an acid mixture HF(49 vol %) : HNO_3 (70 vol %) = 1 : 6 for 5 min to remove a surface layer ~40 μm thick.

The structure of the samples was examined by OM after selective chemical etching. The concentration of optically active oxygen in the wafers before and after heat treatment was estimated, using infrared spectroscopy, from the measured absorption of ~9-μm radiation. The results are listed in Table 2.

As follows from Table 2, the density of MDs in the as-grown samples is ~8 × 10^5 cm^{-3} (OM data). Heat treatment according to the regimes 1000°C/15 min (sample 2), 1000°C/15 min + 450°C/16 h (sample 3), and 1000°C/15 min + 650°C/16 h (sample 6) did not change the density of visible MDs. Multistage heat treatment according to the regimes for forming an internal getter (samples 5, 9, 10) caused a sharp increase (up to ~3 × 10^9–2 × 10^{10} cm^{-3}) in the MD density in the wafers.

Table 1. Multistep heat treatment regimes for silicon wafers

Sample number	Heat treatment regime
1	As-grown state
2	1000°C/15 min
3	1000°C/15 min + 450°C/16 h
4	1000°C/15 min + 450°C/16 h + 650°C/16 h
5	1000°C/15 min + 450°C/16 h + 650°C/16 h + 1000°C/4 h
6	1000°C/15 min + 650°C/16 h
7	1000°C/15 min + 650°C/4 h + 1000°C/4 h
8	1000°C/15 min + 650°C/16 h + 1000°C/4 h
9	1000°C/15 min + 650°C/4 h + 800°C/4 h + 1000°C/4 h
10	1000°C/15 min + 650°C/16 h + 800°C/4 h + 1000°C/4 h

Table 2. Characteristics of the samples under study

Sample number	Changes in the concentration of optically active oxygen, 10^{-17} cm^{-3}	Microdefect density, cm^{-3} (optical microscopy data)
1	0	~8 × 10^5
2	0.01	~5 × 10^5
3	0.08	~5 × 10^5
4	0.40	–
5	3.62	~3 × 10^9
6	0.03	~5 × 10^5
7	0.09	–
8	0.42	–
9	1.60	~3 × 10^9
10	3.42	~2 × 10^{10}

For the as-grown sample 1, we measured the lattice parameter using the Bond method [9]. The measured value (a = 0.543106 ± 0.0000008 nm) is greater than the lattice parameter of the standard (a = 0.543103 nm) [5]. Since the crystals under study were grown in the vacancy mode and contained 7 × 10^{17} cm^{-3} oxygen atoms, this increase in the lattice parameter can be due to the presence of SiO_2 complexes in the silicon matrix. According to [10], the angle between the Si–O bonds is 100°. By estimating the positive deformation caused by such a complex, it can be found that the observed increase in the lattice parameter [by ~(2–3) × 10^{-6} nm] can be provided by ~(2–3) × 10^{17} cm^{-3} oxygen atoms in the SiO_2 complexes.

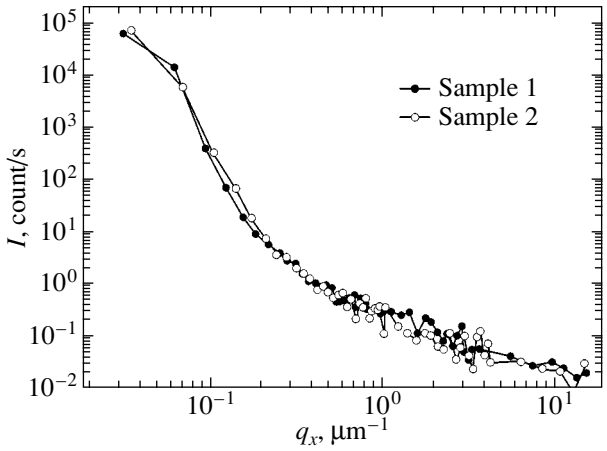

Fig. 1. DXS intensity distributions along the [011] direction for samples 1 and 2.

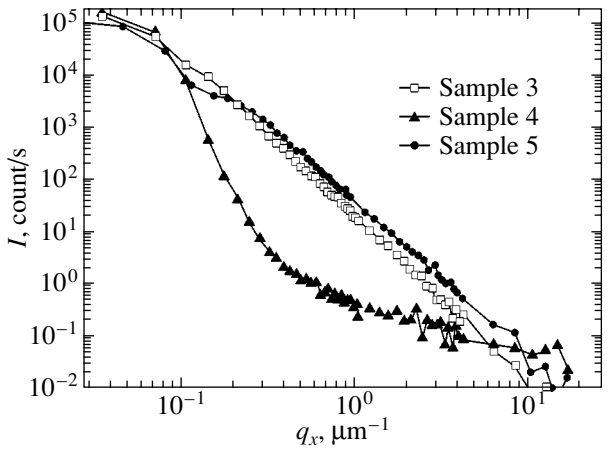

Fig. 2. DXS intensity distributions along the [011] direction for samples 3, 4, and 5.

3. RESULTS AND DISCUSSION

Figure 1 shows the diffuse scattering distribution along the q_x section for samples 1 and 2 (the as-grown state and the state after high-temperature annealing at 1000°C for 15 min, respectively). The curves in Fig. 1 have two pronounced segments: the segment at $q_x < 0.2$ μm^{-1} corresponds to the instrumental function and the segment of the linear $\log I = f(\log q_x)$ dependence at $q_x > 0.6$ μm^{-1} with a slope close to unity. The latter segment corresponds to the Huang scattering by defects smaller than 0.02 μm, since the transition to asymptotic scattering (inflection point) for these defects is beyond the measurement interval. The measurement interval in our case was restricted by a very low DXS intensity, and reliable measurement beyond this interval would require a tenfold increase in the measurement time at each point, which seems inexpedient in this case. The shift of the isodiffuse contour toward positive values of q_z suggests that the defects have a positive strength. These MDs have a nonspherical displacement field, since they contribute to the DXS intensity along the q_x direction [4]. The concentration of point defects forming these MDs in the as-grown samples is ~10^{17} cm^{-3}.

High-temperature annealing at 1000°C (sample 2) is usually performed to dissolve growth MDs existing in the crystal. Analysis of the DXS intensity distribution along the q_x direction in this sample showed no appreciable changes in the concentration of MDs smaller than 0.02 μm after the annealing (Fig. 1). The fact that the density of growth MDs changes only weakly in this case is also indicated by the OM data (Table 2).

The subsequent low-temperature annealing was carried out at 450°C for 16 h (sample 3). At this temperature, oxygen thermodonors form intensely in the silicon wafers. The OM data exhibit no significant changes in the density of MDs in the samples after this annealing. However, the DXS intensity sharply increases in the sample annealed at 450°C (Fig. 2). Analysis of isodiffuse contours (Fig. 3) in this sample indicates that it contains MDs with a positive strength (the asymmetric part of diffuse scattering, which is defined as $[I(q) - I(-q)]/2$ and is dependent on the sign of dilatation, is positive at $q_z > 0$; Fig. 3c). The symmetric component of diffuse scattering $[I(q) + I(-q)]/2$ (Fig. 3b) is specified by the symmetry of the displacement field around MDs. The elongation of the isodiffuse contours in the q_x direction indicates that the symmetry of the displacement field around interstitial MDs is close to orthorhombic, which means that these MDs most likely have a planar shape. A simulation of the distribution of the symmetric DXS component using the formulas from [3, 4] shows that these defects lie along the {110} planes. Using the position of the inflection point $q_0 \approx 0.15$ μm^{-1} in the $\log I = f(\log q_x)$ curve for sample 3 (Fig. 2), the radius of these defects was estimated to be ~2.5 μm. The variation of the slope of the curve for q in the range from 0.2 to 5 μm^{-1} indicates the presence of a size distribution of MDs generated during annealing at 450°C. The volume density of such MDs is ~3.2×10^8 cm^{-3}. The concentration of optically active oxygen in the sample remains virtually unchanged during its annealing (Table 2). Therefore, we can assume, with a fair degree of confidence, that this annealing does not produce oxide precipitates but causes the formation of extended regions of an inhomogeneous solid solution of oxygen in silicon with a diffuse coherent interface ("impurity clouds"), which brings about strong DXS. These regions are likely to be rich in oxygen. It can be assumed that the changes in the concentration of point defects in these regions obey a Gaussian distribution. Similar structural aggregates have been observed in germanium wafers in the early stages of decomposition of a supersaturated solid solution of lithium in germanium [11].

The subsequent annealing at 650°C for 16 h (sample 4) caused significant changes in the character of DXS (Fig. 2). These changes indicate that the large cloudlike MDs disappear in the samples, to be substituted by small MDs with a nonspherical displacement field. The density of these defects exceeds the concentration of small MDs in the as-grown samples by a factor of 1.5–2. It is difficult to estimate the radius of these defects, since the asymptotic scattering range for them was not reached due to a low intensity. We can only assert that they are smaller than 0.02 μm in size. The infrared spectroscopy data indicate that the change in the concentration of optically active oxygen is relatively significant in this sample. All these data suggest that, during annealing at 650°C, small oxygen-containing precipitates (nucleation centers of SiO_2 particles) form in the bulk of the wafers in the regions with maximum oxygen content.

In the final high-temperature (1000°C/4h) stage of the four-step heat treatment of this series of samples (sample 5), further significant structural changes occur in the sample (see the corresponding DXS curve in Fig. 2). The size and density of MDs abruptly increase. Analysis of the isodiffuse contours of x-ray scattering shows that the source of DXS in this sample is MDs having a positive strength (obviously, SiO_2 particles) and a nonspherical displacement field (Fig. 4). Unlike the impurity clouds observed in sample 3, such MDs have a sharp incoherent interface. The shape of isodiffuse contours changed (Fig. 4), which may indicate that the displacement vectors changed. However, the planes of defect location remain the same, namely, {110}. An estimation from the position of the inflection point ($q_0 \approx 0.25$ μm^{-1}) in the $\log I = f(\log q_x)$ curve (Fig. 2) shows that the radius of these MDs is ~1.5 μm. The volume fraction of the MDs is (0.96–1.0) × 10^9 cm^{-3}, which agrees well with the OM data (Table 2).

The data on diffuse scattering in the samples of the second series are displayed in Figs. 5 and 6. An increase in the temperature of the low-temperature step to 650°C (sample 6) leads to a significant (one order of magnitude) decrease in the concentration of the large impurity-cloud defects characteristic of the samples annealed at 450°C (sample 3). Apart from these defects, sample 6 also contains small MDs similar to the defects detected in sample 4, which is indicated by the segment with a slope of ~2 at $q_x > 2$ μm^{-1} in the curve for sample 6 in Fig. 5. The density of these MDs is identical to that in sample 4, as judged from the DXS intensity.

After low-temperature annealing at 650°C, samples 7 and 8 were finally annealed at 1000°C for 4 h; they differed in the duration of the low-temperature step (4 and 16 h, respectively). As follows from the data shown in Fig. 5, the DXS intensity in sample 7 is significantly lower than in sample 8. The density of MDs in sample 8 is substantially higher (7.1 × 10^8 cm^{-3}). The MDs have a positive strength and a nonspherical displacement field. The indistinct inflection point in the curves for

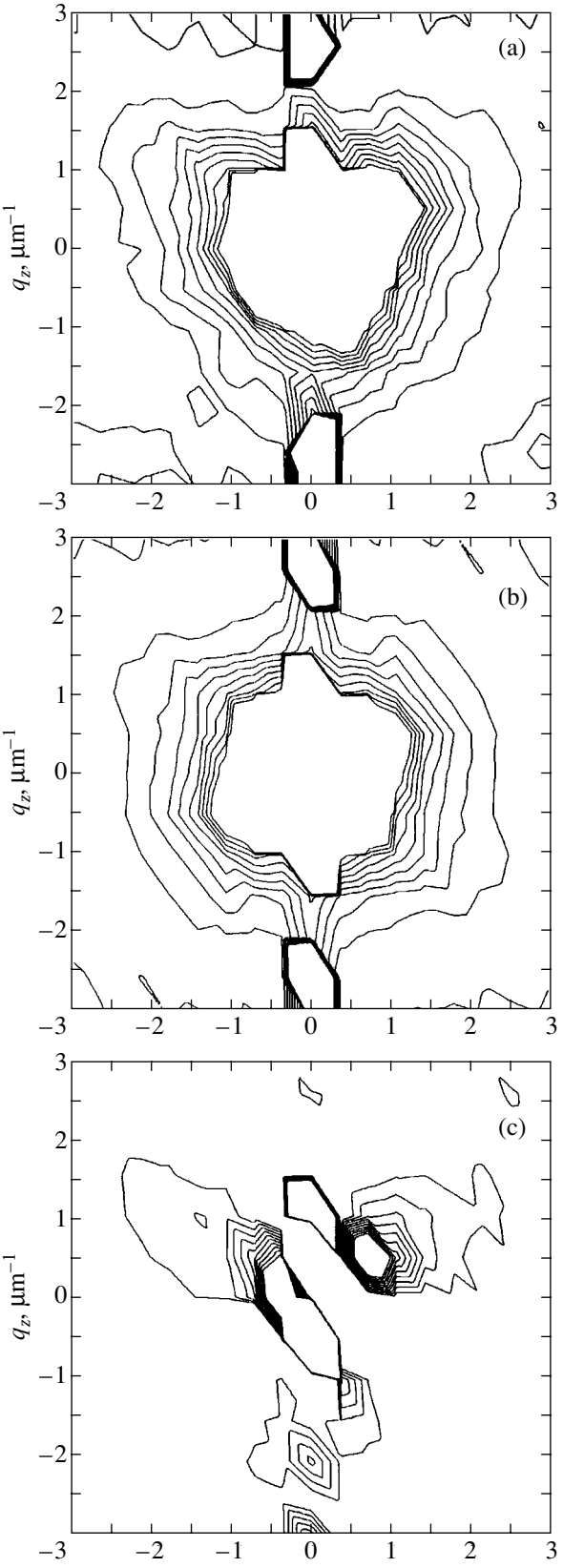

Fig. 3. DXS intensity distribution (isodiffuse contours) in the vicinity of the 400 site for sample 3: (a) experimental contours, (b) symmetric component, and (c) asymmetric component. The DXS intensities on isodiffuse contours vary in 1.0 count/s steps in the range 0.5–9.5 count/s.

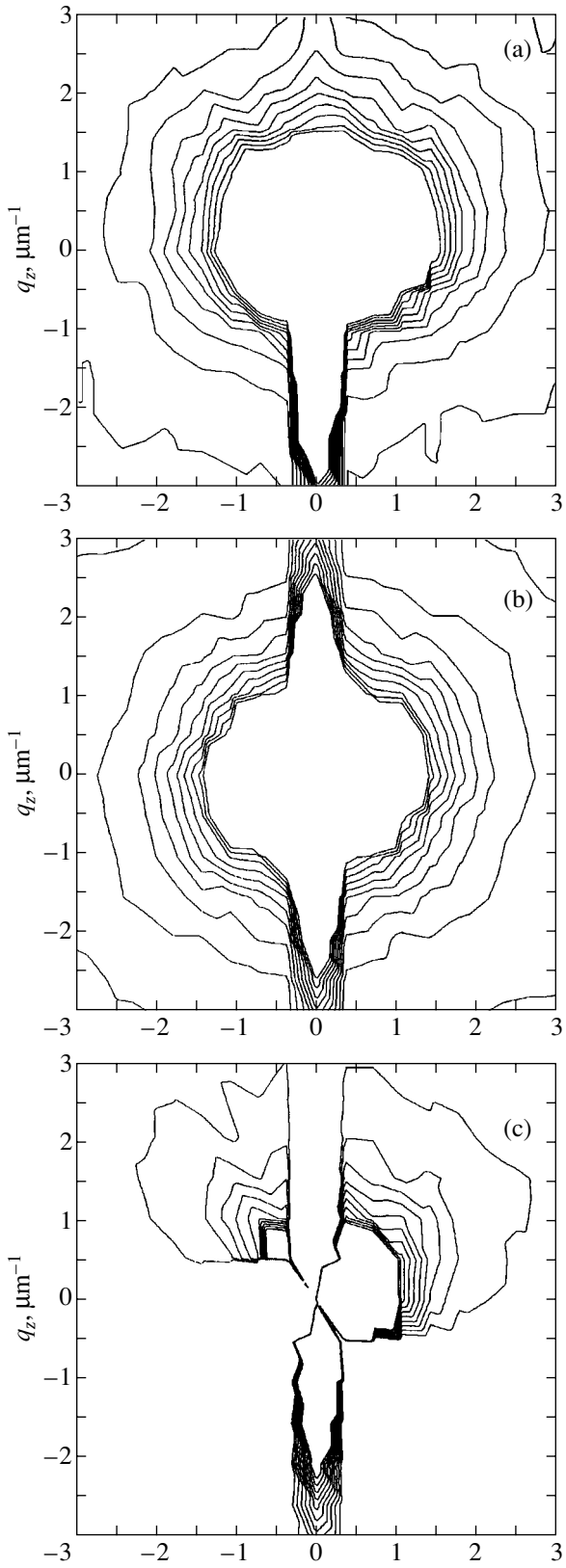

Fig. 4. DXS intensity distribution (isodiffuse contours) in the vicinity of the 400 site for sample 5: (a) experimental contours, (b) symmetric component, and (c) asymmetric component. The DXS intensities on isodiffuse contours vary in 2.0 count/s steps in the range 1–19 count/s.

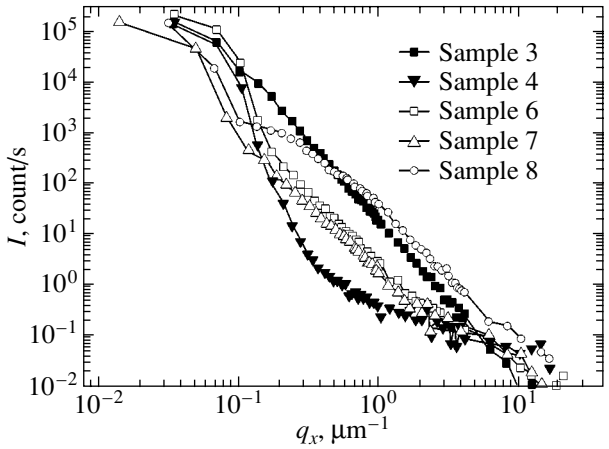

Fig. 5. DXS intensity distributions along the [011] direction for samples 6, 7, and 8. For comparison, the DXS intensity distributions for samples 3 and 4 are also given (according to Fig. 2).

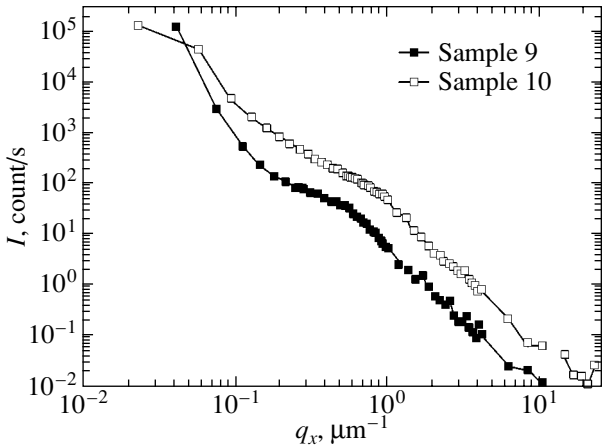

Fig. 6. DXS intensity distributions along the [011] direction for samples 9 and 10.

samples 7 and 8 in Fig. 5 at $q_x > 0.2$ μm^{-1} indicates a large scatter in the sizes of the MDs that form in these samples during heat treatment. The maximum MD size reaches 1.2 μm. Thus, an increase in the annealing time at 650°C from 4 to 16 h results in a significant intensification of the decomposition of the supersaturated solid solution of oxygen to form oxide precipitates. These data correlate well with the observed decrease in the concentration of optically active oxygen in these samples in the course of the three-step heat treatment (Table 2).

Samples 9 and 10 were subjected to the complete cycle of the four-step heat treatment used to form an internal getter. In contrast to the samples discussed above, they were subjected to stabilizing annealing at 800°C for 4 h. As follows from the data shown in Fig. 6, the additional stabilizing annealing leads to a significant increase in the DXS intensity. The density of MDs

substantially increases and becomes equal to 1.2×10^9 cm^{-3} in sample 9 and 2.2×10^{10} cm^{-3} in sample 10. The scatter of the sizes of MDs sharply decreases. The MD size is ~0.4 μm in sample 10 and 0.6 μm in sample 9. Analysis of isodiffuse contours of x-ray scattering indicates MDs having a nonspherical displacement field with a positive strength. It should be noted that the DXS data on the MD density in these samples correlate well with the OM data (Table 2).

4. CONCLUSIONS

Thus, we have obtained the following basic results.

(1) The DXS method is efficient for studying the formation of MDs in silicon single crystals in the stages of their growth and subsequent heat treatment. This method is especially efficient for investigating the early stages of microdefect formation, where TEM cannot provide desirable information.

(2) With the DXS method, we have revealed the formation of specific defects of the impurity-cloud type in silicon wafers during low-temperature annealing at 450°C. These defects are regions of the solid solution enriched in oxygen (and, probably, in intrinsic point defects) with a diffuse coherent interface. These regions reach ~2.5 μm in size and provide strong DXS. In the following stages of decomposition of the supersaturated solid solution of oxygen, oxide precipitates form inside these regions and these regions disappear.

(3) As a result of the decomposition of the supersaturated solid solution of oxygen, interstitial MDs form in the silicon wafers during a multistep heat treatment. These MDs lie in the {110} planes and have nonspherical displacement fields. Precipitates have a platelike shape in the very early stages of their formation. By measuring DXS, we have determined the density and size of MDs forming in the silicon wafers at various stages of decomposition of the supersaturated solid solution of oxygen.

ACKNOWLEDGMENTS

This work was supported by the Russian Foundation for Basic Research, project no. 02-02-16053.

REFERENCES

1. P. H. Dederichs, J. Phys. F **3**, 471 (1973).
2. M. A. Krivoglaz, *Theory of X-ray and Thermal Neutron Scattering by Real Crystals*, 2nd ed. (Plenum, New York, 1969; Naukova Dumka, Kiev, 1983).
3. B. C. Larson and W. Schmatz, Phys. Rev. B **10** (6), 2307 (1974).
4. H. Trinkaus, Phys. Status Solidi B **51**, 307 (1972).
5. V. K. Ovcharov, Candidate's Dissertation (Moscow, 1998).
6. L. A. Charniy, K. D. Scherbachev, and V. T. Bublik, Phys. Status Solidi A **128** (2), 303 (1991).
7. W. A. Wooster, *Diffuse X-ray Reflections from Crystals* (Clarendon, Oxford, 1962; Inostrannaya Literatura, Moscow, 1963).
8. K. D. Shcherbachev and V. T. Bublik, Zavod. Lab. **60** (8), 473 (1994).
9. W. L. Bond, Acta Crystallogr. **13**, 814 (1960).
10. C. Claeys and J. Vanhellemont, in *Proceedings of 2nd International Autumn Meeting on Gettering and Defect Engineering in the Semiconductor Technology, GADEST'87, Garzau, Germany* (1987), p. 3.
11. I. M. Kotina, V. V. Kuryadkov, G. N. Mosina, *et al.*, Fiz. Tverd. Tela (Leningrad) **26** (2), 436 (1984) [Sov. Phys. Solid State **26**, 259 (1984)].

Translated by K. Shakhlevich

Physics of the Solid State, Vol. 45, No. 10, 2003, pp. 1926–1931. Translated from Fizika Tverdogo Tela, Vol. 45, No. 10, 2003, pp. 1833–1838.

DEFECTS, DISLOCATIONS, AND PHYSICS OF STRENGTH

Faceted Grain Boundaries in Polycrystalline Films

S. V. Bobylev and I. A. Ovid'ko

Institute of Problems of Mechanical Engineering, Russian Academy of Sciences, Vasil'evskiĭ ostrov, Bol'shoĭ pr. 61, St. Petersburg, 199178 Russia

e-mail: ovidko@def.ipme.ru

Received November 14, 2002; in final form, April 3, 2003

Abstract—A theoretical model is proposed for describing a new mechanism of misfit-stress relaxation in polycrystalline films, namely, the formation of faceted grain boundaries whose facets are asymmetric tilt boundaries. The ranges of parameters (the film thickness, misfit parameter, angle between facets) in which the nucleation of faceted grain boundaries is energetically favorable are calculated. The nucleation of faceted grain boundaries is shown to be facilitated as the film thickness increases. © *2003 MAIK "Nauka/Interperiodica".*

1. INTRODUCTION

Polycrystalline films are objects of intensive fundamental and applied research, as they are widely applied in modern high-technological production processes. The stability of the physical properties of such films is of primary importance for their technological application and depends significantly on the defects and stress fields in them (see, e.g., reviews [1–5] and papers [6, 7]). For example, a difference between the lattice parameters in substrate and film materials causes internal stresses in the films. These misfit stresses significantly affect the evolution of the structure and the functional properties of the films. When the thickness of a film reaches a certain critical value, misfit stresses, as a rule, are partially accommodated into misfit dislocations at the substrate–film interface [1–15]. However, the presence of grain boundaries in polycrystalline and nanocrystalline films causes alternative efficient mechanisms of relaxation of misfit stresses (and in general, residual stresses of a different nature) via grain-boundary dislocations and disclinations [16–19]. In analyzing these alternative mechanisms, particular attention has been given to the theoretical description of grain-boundary defects in symmetric planar tilt boundaries. In general, however, films also contain asymmetric and faceted grain boundaries [20]. In this work, we propose a theoretical model of a new misfit-stress relaxation mechanism which can operate in polycrystalline films and is related to the formation of faceted grain boundaries whose facets are asymmetric tilt boundaries.

2. FACETED GRAIN BOUNDARIES IN FILMS: MODEL

Let us consider a model of the film–substrate system consisting of a bicrystal film of thickness H and a semi-infinite substrate (Fig. 1). The film and substrate are assumed to be elastically isotropic solids with the same shear modulus G and Poisson ratio ν. The film–substrate interface is characterized by the one-dimensional misfit parameter

$$f = \frac{2(a_f - a_s)}{a_f + a_s}, \quad (1)$$

where a_f and a_s are the lattice parameters of the film and substrate, respectively.

In this work, we analyze two physical states of the film, namely, the state with a straight-line symmetric tilt boundary (Fig. 1a) and the state with a faceted boundary whose facets are asymmetric tilt boundaries (Fig. 1b). For the sake of definiteness, we study low-angle tilt boundaries simulated as ensembles of edge lattice dislocations. However, the results of our consideration can be generalized to the case of a high-angle grain boundary simulated as a grain boundary having dislocations with Burgers vectors of the complete coincidence lattice of the boundary [20]. The plane of the

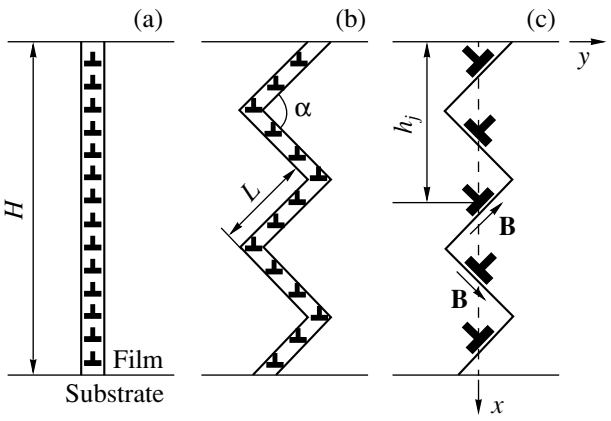

Fig. 1. Dislocation structure of grain boundaries in a bicrystal film: (a) symmetric plane tilt boundary, (b) faceted grain boundary, and (c) faceted grain boundary modeled as a wall of superdislocations having Burgers vectors with alternating directions (schematic).

symmetric tilt boundary is assumed to be normal to the free surface (Fig. 1a). Such a boundary contains M periodically ordered edge dislocations with a Burgers vector **b** parallel to the interface and normal to the plane of the tilt boundary. The misorientation θ of the low-angle symmetric tilt boundary is connected with dislocation parameters by the Frank formula $b = 2(H/M)\sin(\theta/2)$ [20].

A faceted grain boundary consists of facets (segments) having the dislocation structure of an asymmetric tilt boundary (Fig. 1b). For simplicity, we consider facets of only two types, having the same structure and length L; the angle between adjacent facets is α, and their number is N. Like a symmetric boundary, a faceted boundary contains M edge dislocations with a Burgers vector **b** that is parallel to the film–substrate interface. Therefore, the orientations of the crystal lattices far from a faceted boundary are identical to those in the case of a symmetric tilt boundary. Since the Burgers vectors **b** of dislocations making up a faceted grain boundary are not normal to the facet planes, each facet is an asymmetric tilt boundary.

A symmetric tilt boundary and a faceted boundary in the film differ in the spatial arrangement of the dislocation ensemble. This causes the different character of interaction between the grain boundaries under study and the misfit-stress field in the film. The periodic wall of edge dislocations making up a symmetric tilt boundary is essentially characterized by short-range stress fields. The stress fields of dislocations making up a periodic wall (Fig. 1a) completely compensate (shield) each other at distances exceeding the wall period H/M. Therefore, a symmetric tilt boundary with a periodic dislocation structure weakly interacts with the field of misfit stresses.

Dislocations in a faceted boundary are arranged so that the mutual shielding of their stress fields is substantially weakened. Consequently, a faceted boundary is a source of long-range stress fields and strongly interacts with misfit-stress fields in the film. In particular, dislocations in a faceted boundary can provide efficient relaxation of misfit stresses, which decreases the total elastic energy of the system as compared to the case of a symmetric tilt boundary. This decrease is the driving force for the formation of faceted grain boundaries, which have been detected experimentally in films (see, e.g., review [21] and references therein). In this work, we perform a theoretical study of the conditions of formation of faceted boundaries in the context of the model of the dislocation structure of such boundaries shown in Fig. 1c.

If facets are not long, the dislocation structure of each of them responsible for the asymmetry can be simulated, to a first approximation, as one edge superdislocation placed at the center of a facet. The Burgers vector **B** of the superdislocation is parallel to the facet plane, and its magnitude is equal to the sum of the projections of the Burgers vectors of lattice dislocations (the facet elements) along its direction. Thus, a faceted grain boundary in a film subjected to a misfit-stress field is simulated as a vertical wall of N edge superdislocations with alternating Burgers vectors **B** (differing in direction but having the same magnitude) in the misfit-stress field (Fig. 1c).

Within this model, we consider the physical states (Figs. 1a, 1b) as independent states, which are actualized upon film growth. It is assumed that either a symmetric or a faceted grain boundary (depending on the ratio of the elastic energies of the film in these physical states) forms in the film. We do not analyze transformations between these film states or possible energy barriers between them.

A certain similarity between the formation of faceted grain boundaries and the faceting of the free surfaces of crystals should be noted. However, the cause of the spontaneous faceting of a crystal flat surface is an orientation dependence of the surface free energy (see, e.g., [22]), whereas the driving force of the formation of faceted grain boundaries is their involvement in the relaxation of misfit stresses.

3. ENERGY CHARACTERISITCS OF GRAIN BOUNDARIES IN THE FILM

The energy of the film with a faceted grain boundary (Fig. 1b) is higher than the energy of the film with a symmetric boundary (Fig. 1a) by the elastic energy of the superdislocations (Fig. 1c) and by the surface energy of the boundary related to an increase in the boundary length caused by facet formation. In the course of the facet formation, however, misfit stresses relax, which should lead to a decrease in the total energy of the film. The competition of these factors specifies whether the formation of a faceted grain boundary is favorable or not as compared to the symmetric boundary. Thus, the characteristic difference ΔW between the energies of the faceted and symmetric grain boundaries in the film consists of three parts: the elastic energy of superdislocations W^{el} (which includes the energy of superdislocations and the energy of their interactions), the surface energy of the boundary W^{s}, and the interaction energy of the superdislocations with misfit stresses W^{f}:

$$\Delta W = W^{el} + W^{s} + W^{f}. \quad (2)$$

If $\Delta W < 0$, faceting is energetically favorable. Note that the total volume of grains in the film is the same in both physical states (Figs. 1a, 1b).

Below, we calculate the terms in Eq. (2). The energy W^{el} can be represented in the form

$$W^{el} = \sum_{i=1}^{N} W_i^{d} + \frac{1}{2}\sum_{\substack{i,j=1 \\ i\neq j}}^{N} W_{ij}^{d\text{–}d}. \quad (3)$$

Here, W_i^{d} is the self-energy of the ith dislocation and $W_{ij}^{\mathrm{d-d}}$ is the interaction energy between the ith and jth dislocations ($i, j = 1, \ldots, N$, where the first dislocation is the nearest to the free surface and the dislocation index increases as the interface is approached). According to the general procedure for calculating the interaction energy of defects [23], the energy of interaction of two dislocations can be written as the work done in the nucleation of one dislocation in the stress field of the other dislocation (in the coordinate system shown in Fig. 1c):

$$W_{ij}^{\mathrm{d-d}} = -\int_0^{h_j} (B_{jx}\sigma_{xy}^{(i)}(x, y = 0) + B_{jy}\sigma_{yy}^{(i)}(x, y = 0))dx. \quad (4)$$

Here, B_{jx} and B_{jy} are the components of the Burgers vector of the jth dislocation, $\sigma_{xy}^{(i)}$ and $\sigma_{yy}^{(i)}$ are the components of the stress tensor of the ith dislocation, and h_j is the distance from the free surface to the jth dislocation. According to Fig. 1c, h_j can be represented in the form

$$h_j = \frac{2j-1}{2}L\sin\frac{\alpha}{2}. \quad (5)$$

The stress tensor components are sums of the individual contributions from each component of the Burgers vector of a dislocation, i.e., $\sigma_{xy}^{(i)} = \sigma_{xy}^{(ix)} + \sigma_{xy}^{(iy)}$ and $\sigma_{yy}^{(i)} = \sigma_{yy}^{(ix)} + \sigma_{yy}^{(iy)}$. The components of the stress tensor of the ith dislocation near the free surface have the form [23]

$$\sigma_{xy}^{(ix)}(x, y) = \frac{GB_{ix}}{4\pi(1-\nu)}\left(-2\frac{x_1}{r_1^2} + 4\frac{x_1^3}{r_1^4} + 2\frac{x_2}{r_2^2} - 4\frac{x_2^3}{r_2^4} - 2h_i\left[\frac{2}{r_2^2} - 16\frac{x_2^2}{r_2^4} + 16\frac{x_2^4}{r_2^6} + 2h_i\left(6\frac{x_2}{r_2^4} - 8\frac{x_2^3}{r_2^6}\right)\right]\right), \quad (6)$$

$$\sigma_{yy}^{iy}(x, y) = \frac{GB_{iy}}{4\pi(1-\nu)}\left(6\frac{x_1}{r_1^2} - 4\frac{x_1^3}{r_1^4} - 6\frac{x_2}{r_2^2} + 4\frac{x_2^3}{r_2^4} + 2h_i\left[-\frac{2}{r_2^2} + 16\frac{x_2^2}{r_2^4} - 16\frac{x_2^4}{r_2^6} - 2h_i\left(6\frac{x_2}{r_2^4} - 8\frac{x_2^3}{r_2^6}\right)\right]\right), \quad (7)$$

where $x_1 = x - h_i$, $x_2 = x + h_i$, and $r_n^2 = x_n^2 + y^2$, with $n = 1, 2$. The components $\sigma_{xy}^{(iy)}$ and $\sigma_{yy}^{(ix)}$ vanish at $y = 0$ and, hence, are not presented here. Substituting Eqs. (6) and (7) into Eq. (4), we obtain the pair interaction energy

$$W_{ij}^{\mathrm{d-d}} = D(B_{ix}B_{jx} + B_{iy}B_{jy}) \times\left(\ln\frac{h_i + h_j}{|h_i - h_j|} - \frac{2h_ih_j}{(h_i + h_j)^2}\right), \quad (8)$$

where $D = G/2\pi(1 - \nu)$. In our model (Fig. 1c), the components B_{iy} are the same for all dislocations irrespective of their index: $B_{iy} = B\cos(\alpha/2)$. However, the sing of the components B_{ix} alternates with their index; i.e., $B_{ix} = (-1)^iB\sin(\alpha/2)$. Thus, Eq. (8) can be rewritten in the form

$$W_{ij}^{\mathrm{d-d}} = DB^2\left(\cos^2\frac{\alpha}{2} + (-1)^{i+j}\sin^2\frac{\alpha}{2}\right) \times\left(\ln\frac{h_i - h_j}{|h_i - h_j|} - \frac{2h_ih_j}{(h_i + h_j)^2}\right), \quad (9)$$

which is more convenient for further analysis.

Using a calculation procedure similar to that used above to calculate $W_{ij}^{\mathrm{d-d}}$, we find the self-energy W_i^{d} of the ith dislocation at a distance h_i from the free surface to be

$$W_i^{\mathrm{d}} = -\frac{1}{2}\int_0^{h_i - r_0} (B_{ix}\sigma_{xy}^{(i)}(x, y = 0) + B_{iy}\sigma_{yy}^{(i)}(x, y = 0))dx = \frac{DB^2}{2}\left(\ln\frac{2h_i - r_0}{r_0} - \frac{2h_i(h_i - r_0)}{(2h_i - r_0)^2}\right), \quad (10)$$

where r_0 is the dislocation core radius.

Substituting Eqs. (9) and (10) into Eq. (3), we obtain the elastic energy

$$W^{\mathrm{el}} = \frac{DB^2}{2}\sum_{i=1}^{N}\left[2\sum_{\substack{j=1\\ i\neq j}}^{N}\left(\cos^2\frac{\alpha}{2} + (-1)^{i+j}\sin^2\frac{\alpha}{2}\right) \times\left(\ln\frac{h_i + h_j}{|h_i - h_j|} - \frac{2h_ih_j}{(h_i + h_j)^2}\right) + \left(\ln\frac{2h_i - r_0}{r_0} - \frac{2h_i(h_i - r_0)}{(2h_i - r_0)^2}\right)\right]. \quad (11)$$

The difference between the surface energies of the faceted and symmetric boundaries is

$$W^{\mathrm{s}} = N\gamma L - \gamma H = \gamma(NL - H). \quad (12)$$

Here, N is the number of facets, L is the facet length, H is the film thickness, and γ is the surface energy density of the grain boundary.

In general, the interaction energy between the ith dislocation and the misfit stress field is given (by analogy with Eq. (4)) by the formula

$$W_i^{\mathrm{f}} = -\int_0^{h_j} (B_{ix}\sigma_{xy}^{(\mathrm{f})}(x, y = 0) + B_{iy}\sigma_{yy}^{(\mathrm{f})}(x, y = 0))dx, \quad (13)$$

where $\sigma_{xy}^{(\mathrm{f})}$ and $\sigma_{yy}^{(\mathrm{f})}$ are the components of the misfit-stress tensor. Since the off-diagonal components of the misfit-stress tensor are zero and the diagonal ones have the form $\sigma^{(\mathrm{f})} = 4\pi D(1 + \nu)f$ [6], we have from Eq. (13)

$$W_i^{\mathrm{f}} = -B_{iy}\int_0^{h_j}\sigma^{(\mathrm{f})}dx = -4\pi DB\cos\frac{\alpha}{2}(1 + \nu)fh_i. \quad (14)$$

Summing Eq. (14) over i and using Eq. (5), we obtain the energy W^{f}:

$$\begin{aligned} W^{\mathrm{f}} &= \sum_{i=1}^{N} W_i^{\mathrm{f}} = -4\pi DB\cos\frac{\alpha}{2}(1 + \nu)f\sum_{i=1}^{N} h_i \\ &= -4\pi DB\cos\frac{\alpha}{2}(1 + \nu)f\sum_{i=1}^{N}\frac{(2i-1)}{2}L\sin\frac{\alpha}{2} \\ &= -\pi DB(1 + \nu)fL\sin\alpha\sum_{i=1}^{N}(2i-1) \\ &= -\pi DB(1 + \nu)fLN^2\sin\alpha. \end{aligned} \quad (15)$$

Thus, we found all components of the difference between the energies of the faceted and symmetric boundaries, ΔW. Substituting Eqs. (11), (12), and (15) into Eq. (2), we obtain the final expression

$$\begin{aligned} \Delta W = \frac{DB^2}{2}\sum_{i=1}^{N}\Bigg[& 2\sum_{\substack{j=1\\ i\neq j}}^{N}\left(\cos^2\frac{\alpha}{2} + (-1)^{i+j}\sin^2\frac{\alpha}{2}\right) \\ & \times\left(\ln\frac{h_i + h_j}{|h_i - h_j|} - \frac{2h_ih_j}{(h_i + h_j)^2}\right) \\ & + \left(\ln\frac{2h_i - r_0}{r_0} - \frac{2h_i(h_i - r_0)}{(2h_i - r_0)^2}\right)\Bigg] \\ & + \gamma(NL - H) - \pi DB(1 + \nu)fLN^2\sin\alpha. \end{aligned} \quad (16)$$

4. RESULTS OF MODEL CALCULATIONS

Using Eq. (16), derived for the characteristic difference between the energies of the faceted and plane symmetric grain boundaries, we find the dependence of ΔW on the parameters of the system. First, we determine the dependence of ΔW on the misfit parameter f at various values of the Burgers vector of a superdislocation. The following values of the parameters are used: elastic modulus $G = 100$ GPa, $\nu = 0.3$, facet length $L = 10$ nm, angle between adjacent facets $\alpha = 90°$, number of facets $N = 100$ [therefore, the film thickness is $H = NL\sin(\alpha/2) \approx 700$ nm], and surface energy density characteristic of aluminum $\gamma = 0.6$ J/m^2 [24]. The Burgers vector of a superdislocation is $B = nb$, where b is the Burgers vector of a lattice dislocation. The superdislocation core radius is taken to be $r_0 = B$.

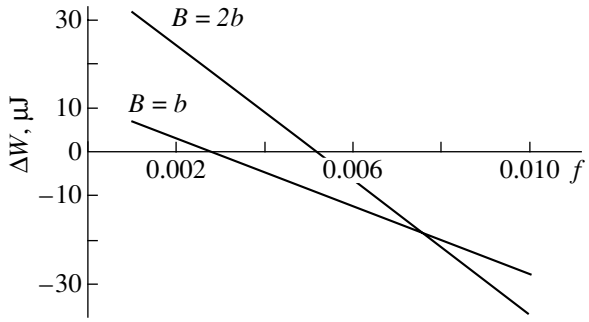

Fig. 2. Dependence of the difference ΔW between the energies of faceted and plane grain boundaries on the misfit parameter f in a film $H = 700$ nm thick at various values of the Burgers vector of superdislocations.

The calculated $\Delta W(f)$ dependence from Eq. (16) at $b = 0.4$ nm and $H = 700$ nm is given in Fig. 2. As the misfit parameter f increases, the energy difference ΔW is seen to decrease linearly and reach negative values, which means that the contribution of the relaxation term is predominant. Therefore, the formation of a faceted boundary becomes energetically favorable as compared to a symmetric tilt boundary. The data in Fig. 2 allow the following conclusion about the effect of the Burgers vectors of superdislocations on ΔW: at small values of the misfit parameter, an increase in the Burgers vector leads to an increase in ΔW, since the elastic energy of superdislocations increases in proportion to B^2 and the interaction energy between superdislocations and the misfit-stress field depends linearly on B. However, at large values of the misfit parameter, when misfit-stress relaxation becomes predominant, an increase in the Burgers vector of a superdislocation decreases ΔW.

The $\Delta W(B)$ dependence calculated from Eq. (16) at various values of f and the system parameters given above is shown in Fig. 3. The value of B was varied from b to $5b$. The plots in Fig. 3 exhibit a very strong dependence of ΔW on the Burgers vector of superdislocations. The maximum value of B at which the formation of a faceted boundary is still favorable as compared to a symmetric tilt boundary is equal to $3b$ at realistic values of the misfit parameter. Figure 4 shows the dependence of ΔW on the film thickness for various values of the misfit parameter at $B = b$. These dependences exhibit three possible types of behavior: (1) a faceted boundary is energetically unfavorable over the whole

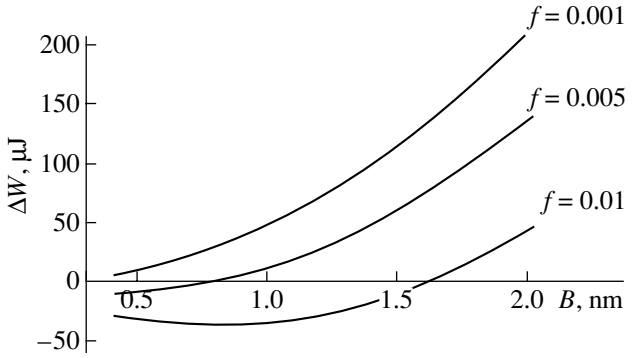

Fig. 3. Dependence of the difference ΔW between the energies of faceted and plane grain boundaries on the Burgers vector of superdislocations in a film H = 700 nm thick at various values of the misfit parameter f.

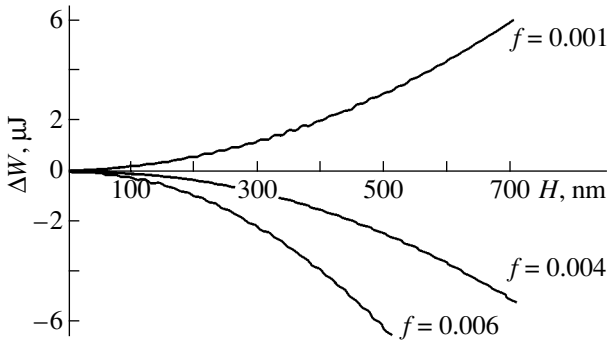

Fig. 4. Dependence of ΔW on the film thickness at various values of the misfit parameter.

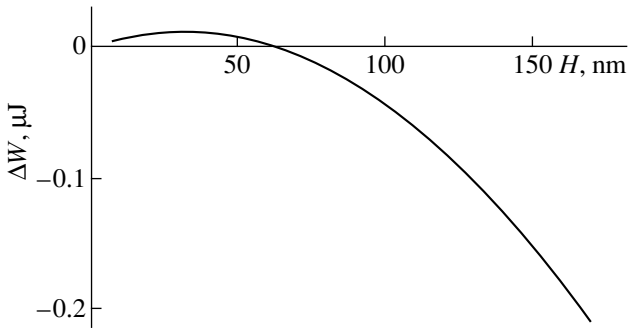

Fig. 5. Dependence of ΔW on the film thickness H at f = 0.004 and $B = b$.

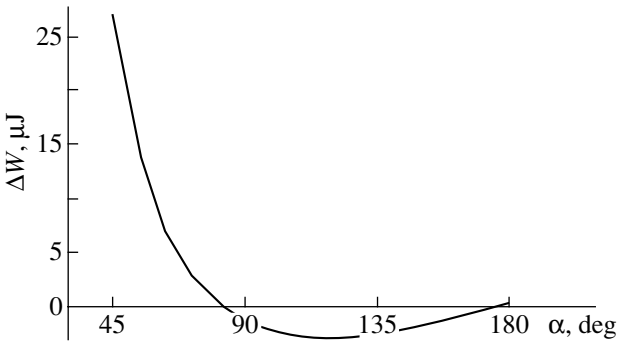

Fig. 6. Dependence of ΔW on the angle α between facets at f = 0.003 and $B = b$.

thickness range (Fig. 1b), (2) a faceted boundary is energetically favorable over the whole thickness range, and (3) a faceted boundary is energetically unfavorable in a thin film and becomes favorable at film thicknesses greater than a certain critical value. The curve at f = 0.004 in Fig. 4 illustrates the third type of behavior. The same curve is shown in Fig. 5 on a larger scale.

The plot in Fig. 6 shows the dependence of ΔW of the angle α between facets (at f = 0.003, $B = b$, $H \cong 700$ nm). Since both the elastic and relaxation terms in ΔW depend on the angle between facets (the latter term vanishes at $\alpha = 180°$), the $\Delta W(\alpha)$ dependence exhibits a minimum corresponding to the most favorable angle between facets.

5. CONCLUSIONS

Thus, in this work, we have theoretically studied a new mechanism of misfit-stress relaxation in polycrystalline films, namely, the formation of faceted grain boundaries whose facets are asymmetric tilt boundaries. We have constructed a model to describe a faceted grain boundary in a film placed on a semi-infinite substrate in the presence of misfit stresses. Using this model, we calculated the difference between the energies characterizing the states of the film with a faceted boundary (Fig. 1b) and a symmetric tilt boundary (Fig. 1a). The parameters of the system that exhibit a significant effect on the formation of faceted grain boundaries in films are the misfit parameter, facet asymmetry (which is characterized by the Burgers vector of a superdislocation), film thickness, and the angle between facets. Within the model proposed, the ranges of the system parameters were found in which faceted grain boundaries are energetically favorable. The model agrees with the experimental data (see review [21] and references therein) on faceted grain boundaries observed in superconducting films. The results obtained within the model can be used to prepare polycrystalline films with a given (faceted or nonfaceted) structure of grain boundaries, which significantly affects the physical (in particular, superconducting [25, 26]) properties of films.

ACKNOWLEDGMENTS

We thank A.G. Sheĭnerman for valuable discussions.

This work was supported by the Russian Foundation for Basic Research (project no. 01-02-16853), the

Office of US Naval Research (grant no. 00014-01-1-1020), the program "Integratsiya" (project no. B0026), the program "Structural Mechanics of Materials and Constructions" of the Russian Academy of Sciences, and the St. Petersburg Scientific Center of the Russian Academy of Sciences.

REFERENCES

1. E. A. Fitzgerald, Mater. Sci. Rep. **7** (1), 87 (1991).
2. J. H. van der Merve, CRC Crit. Rev. Solid State Mater. Sci. **17** (3), 187 (1991).
3. S. C. Jain, A. H. Harker, and R. A. Cowley, Philos. Mag. A **75** (6), 1461 (1997).
4. I. A. Ovid'ko, in *Nanostructured Films and Coatings*, Ed. by G. M. Chow, I. A. Ovid'ko, and T. Tsakalakos (Kluwer, Dordrecht, 2000), p. 231.
5. I. A. Ovid'ko, Rev. Adv. Mater. Sci. **1** (2), 61 (2000).
6. Yu. A. Tkhorik and L. S. Khazan, *Plastic Deformation and Misfit Dislocations in Heteroepitaxial Systems* (Naukova Dumka, Kiev, 1983).
7. M. Yu. Gutkin and I. A. Ovid'ko, *Defects and Mechanisms of Plasticity in Nanostructural and Noncrystalline Materials* (Yanus, St. Petersburg, 2001).
8. S. C. Jain, T. J. Gosling, J. R. Willis, *et al.*, Philos. Mag. A **65** (5), 1151 (1992).
9. T. J. Gosling, R. Bullough, S. C. Jain, and J. R. Willis, J. Appl. Phys. **73** (12), 8267 (1993).
10. U. Jain, S. C. Jain, S. Nijs, *et al.*, Solid State Electron. **36** (3), 331 (1993).
11. T. J. Gosling and J. R. Willis, Philos. Mag. A **69** (1), 65 (1994).
12. F. Bailly, M. Barbé, and G. Cohen-Solal, J. Cryst. Growth **153**, 115 (1995).
13. M. Yu. Gutkin, A. E. Romanov, and E. C. Aifantis, Phys. Status Solidi A **151** (2), 281 (1995).
14. M. Yu. Gutkin, K. N. Mikaelyan, and I. A. Ovid'ko, Fiz. Tverd. Tela (St. Petersburg) **40** (11), 2059 (1998) [Phys. Solid State **40**, 1864 (1998)]; Fiz. Tverd. Tela (St. Petersburg) **43** (1), 42 (2001) [Phys. Solid State **43**, 42 (2001)].
15. M. Yu. Gutkin, I. A. Ovid'ko, and A. G. Sheinerman, J. Phys.: Condens. Matter **12** (25), 5391 (2000).
16. I. A. Ovid'ko, J. Phys.: Condens. Matter **11** (34), 6521 (1999); J. Phys.: Condens. Matter **13** (4), L97 (2001).
17. I. A. Ovid'ko, Fiz. Tverd. Tela (St. Petersburg) **41** (9), 1637 (1999) [Phys. Solid State **41**, 1500 (1999)].
18. S. V. Bobylev, I. A. Ovid'ko, and A. G. Sheinerman, Phys. Rev. B **64**, 224507 (2001).
19. A. L. Kolesnikova, I. A. Ovid'ko, and A. E. Romanov, Solid State Phenom. **87**, 265 (2002).
20. A. P. Sutton and R. W. Balluffi, *Interfaces in Crystalline Materials* (Claredon, Oxford, 1995).
21. S. E. Babcock and J. L. Vargas, Annu. Rev. Mater. Sci. **25** (1), 193 (1995).
22. A. F. Andreev and Yu. A. Kosevich, Zh. Éksp. Teor. Fiz. **81**, 1435 (1981) [Sov. Phys. JETP **54**, 761 (1981)].
23. T. Mura, *Micromechanics of Defects in Solids* (Martinus Nijhoff, Dordrecht, 1987), p. 1.
24. G. C. Hasson and C. Goux, Scr. Metall. **5** (11), 889 (1971).
25. H. Hilgenkamp, J. Mannhart, and B. Mayer, Phys. Rev. B **53**, 14586 (1996).
26. I. A. Ovid'ko, Mater. Sci. Eng. A **313** (1/2), 207 (2001).

Translated by K. Shakhlevich

Physics of the Solid State, Vol. 45, No. 10, 2003, pp. 1932–1934. Translated from Fizika Tverdogo Tela, Vol. 45, No. 10, 2003, pp. 1839–1841.

DEFECTS, DISLOCATIONS, AND PHYSICS OF STRENGTH

Plasticization of NaCl Crystals under the Combined Action of Short Mechanical and Magnetic Pulses

V. A. Morozov

St. Petersburg State University, Universitetskiĭ pr. 28, St. Petersburg, 198504 Russia

e-mail: vaa@math.spbu.ru

Received January 24, 2003; in final form, February 11, 2003

Abstract—The dynamic yield stress of NaCl crystals is found to decrease under loading with a mechanical pulse of submicrosecond duration initiated by an electron beam preceded by a pulse of a vortex electromagnetic field (the time delay is 10^{-6} s). This effect becomes more pronounced as the intensity of loading increases.

The magnetoplastic effect (MPE) was first detected as the motion of individual dislocations in alkali-halide crystals in a magnetic field in the absence of applied load [1]. As was shown later [2–7], this effect can also manifest itself on a macroscopic level as a decrease in the yield stress [5], a decrease in the microhardness [2], a change in the internal friction [4], and an increase in the plastic strain rate [3, 7]. Golovin *et al.* [3] detected a macroscopic effect of softening of NaCl crystals under the simultaneous action of crossed static and microwave magnetic fields. It was found that, when turned on before reaching the yield stress, a microwave magnetic field does not change the stress–strain curve. However, after the yield stress is reached, a microwave magnetic field changes the slope of the stress–strain curve.

All the macroscopic manifestations of the MPE indicated above were observed under either static or quasistatic conditions of magnetic and mechanical actions on nonmagnetic crystals. It is of interest to find out whether this effect manifests itself under short-term actions. This problem was studied in [8] for the motion of individual dislocations in NaCl crystals under the combined action of mechanical and electromagnetic pulses created by an electron beam.

In dynamic experiments, as is well known, it is difficult to construct a dynamic stress–strain curve or to choose the criterion of deviation of this curve from a linear dependence. In [9], this criterion was taken to be a change in the form of a stress wave (pulse form) traveling through a sample. In that work, the flattening of the peak of a stress pulse was related to a nonlinear stress–strain curve, which, in turn, was specified by the changed internal structure of the material, including the dislocation structure. The experiments were carried out on aluminum samples in the microsecond range of loading.

In this work, we examine NaCl crystals that are similar to those used in our earlier work [8] to study the mobility of individual dislocations. The samples were $7 \times 7 \times 1.5$ mm in size. Pulsed loading of the samples was performed on an electron-beam setup [8]. The experimental setup is shown in Fig. 1. A sample can be loaded by both a single mechanical pulse and a combination of a mechanical and an electromagnetic pulse. To this end, in the former case, a sample was placed in a chamber of a ferromagnetic material and, in the latter case, in a chamber of a diamagnetic material (Al). A mechanical pulse was excited by an electron beam in either an aluminum or a steel target in the form of a short rod 8 mm in diameter mounted in the front wall of the chamber, which served as the anode of an electron accelerator, and the pulse was then transferred to the sample. The sample was in acoustic contact with the target through a thin layer of silicone fluid. The mechanical pulse of loading was recorded at both the input and output of the sample using a piezoelectric transducer of lithium iodate. The pulse duration was about 10^{-7} s. The pulse amplitude during the experiment was varied from 15 to 50 MPa by changing the beam current or the target material (Al, Fe). A mag-

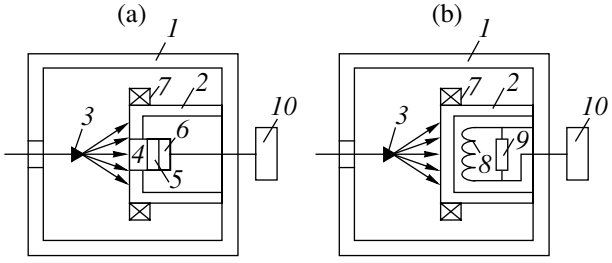

Fig. 1. Experiments (a) with the application of mechanical and magnetic pulses to the crystal and (b) for measuring the magnetic field strength. (*1*) Vacuum chamber of an electron accelerator, (*2*) chamber for samples, (*3*) electron-beam source, (*4*) target, (*5*) sample, (*6*) piezoelectric transducer, (*7*) beam-current meter, (*8*) search coil, (*9*) coil load, and (*10*) oscilloscope.

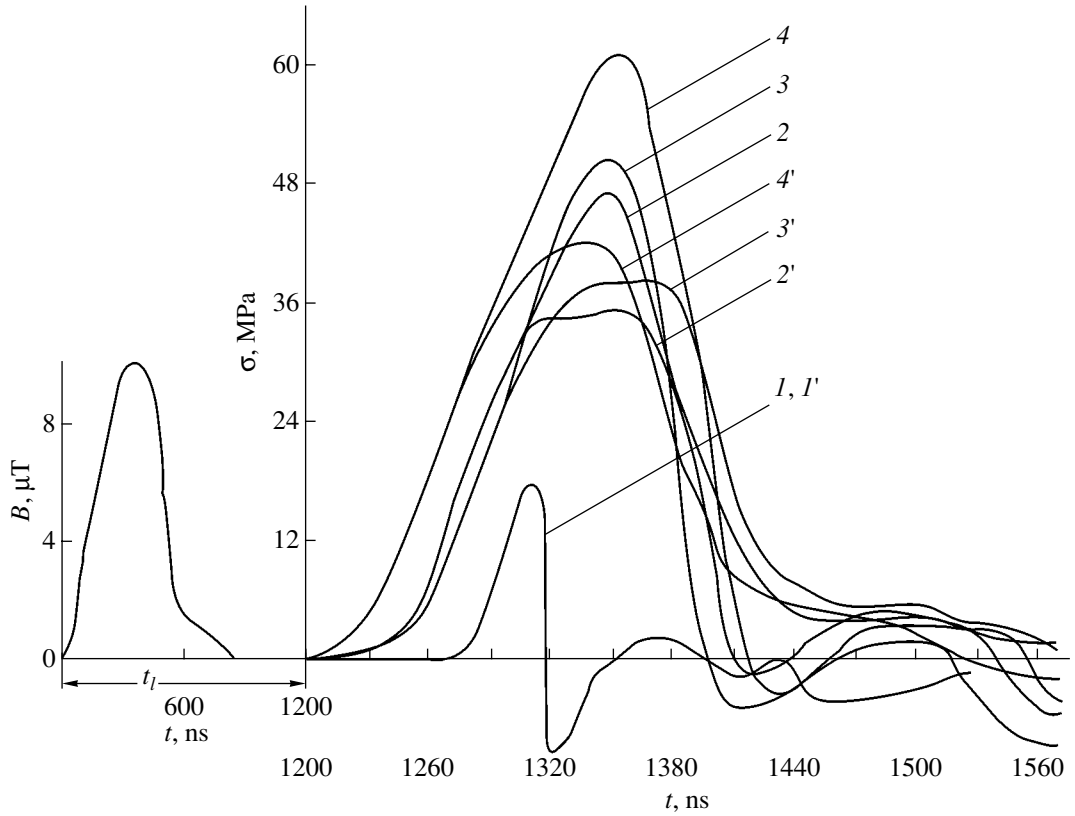

Fig. 2. Oscillograms of pulses of (*1–4*, *1'–4'*) mechanical loading and (*5*) a magnetic field in the NaCl crystal. Loading (*1–4*) in the absence and (*1'–4'*) in the presence of a pulsed magnetic field. t_l is the time delay of the beginning of a mechanical-stress pulse in relation to the beginning of a magnetic pulse.

netic-field pulse was created by an electron-beam current during irradiation of the target. The pulse amplitude was varied in the range $(3.5–10) \times 10^{-6}$ T by changing the current, and its duration was $\sim 3 \times 10^{-7}$ s. In the case of low amplitudes of the mechanical pulse (far from the yield stress of the NaCl sample) initiated in the aluminum target, the magnetic field was about 3.5×10^{-6} T. To excite mechanical pulses of similar low amplitudes in the steel target, we had to use a larger beam current. The magnetic field was about 10^{-5} T. Magnetic pulses were measured using a coil placed in the chamber where an NaCl sample was previously located (Fig. 1). The coil was loaded to a wave impedance of 50 Ω. A signal from the coil was fed to a high-frequency S1-75 oscilloscope and then photographed. To determine the magnetic field strength, the coil was calibrated.

When a mechanical-stress pulse traveled along the target, its beginning was delayed with respect to the magnetic pulse. The delay time t_l could be varied by changing the target thickness. In our experiments, this time was 1.2×10^{-6} s (Fig. 2). Figure 2 shows oscillograms of mechanical-stress pulses with various amplitudes in the NaCl crystal with (curves *1'–4'*) and without (*1–4*) a magnetic pulse. The shape of the magnetic pulse is also shown (curve *5*). When the amplitude of a mechanical pulse in the sample is relatively far from the dynamic yield stress (Fig. 2, curve *1*), the magnetic field does not affect the signal shape as the amplitude of the magnetic field is varied over the range $(3.5–10) \times 10^{-6}$ T. As follows from our earlier experiments [8], individual dislocations move under these conditions. In this case, as well as in the case without applying a magnetic field, the amplitude of the mechanical-stress pulse depends linearly on the current of the electron beam (or on the beam energy introduced into the target; see Fig. 3). As seen from Figs. 2 and 3, the dynamic yield stress of the samples is not reached when using only mechanical loading. Under the experimental conditions employed, the dynamic yield stress was at least above 70 MPa (according to our estimation, it was about 80 MPa). When the amplitude of a mechanical pulse approaches the dynamic yield stress of a sample, the application of a vortex high-frequency magnetic field creates conditions for decreasing the yield stress, which manifests itself as a flattening of the pulse (Fig. 2, curves *2'–4'*) and a deviation from the linear $\sigma(I)$ dependence (Fig. 3, curve *2*).

When the signal intensity increases, the difference between the pulse amplitudes in the presence and in the absence of a magnetic field rises (Figs. 2, 3). The results obtained agree with the data from [9]. However,

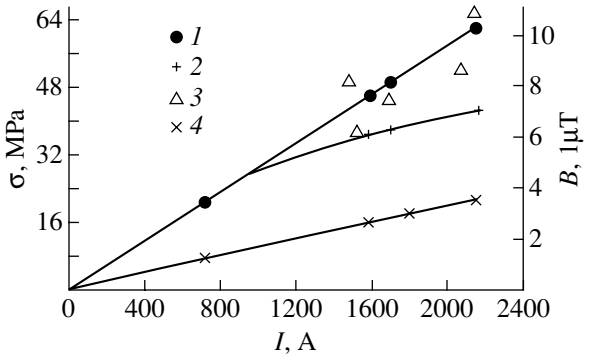

Fig. 3. Dependences of the amplitudes of mechanical-stress pulses $\sigma(I)$ and magnetic field $B(I)$ in the NaCl crystal on the beam current: (*1*) $\sigma(I)$ for the case of a mechanical pulse excited in the Al target in the absence of a magnetic field, (*2*) the same but in the presence of a magnetic field, (*3*) $B(I)$, and (*4*) $\sigma(I)$ for the case of a mechanical pulse excited in a steel target.

the change in the shape of a mechanical pulse and the saturation of its amplitude in that work was related to changes in the internal structure of samples upon annealing, whereas in our work these effects were caused by a magnetic field.

Based on the experimental data obtained, we can draw the following conclusion. Since an electromagnetic pulse was applied to the crystal before a mechanical pulse, dislocations had time to leave impurity paramagnetic centers by the instant of the mechanical pulse was applied. This time is less than 10^{-6} s, which is two orders of magnitude shorter than that obtained in [10]. Moreover, we revealed that a weak pulsed magnetic field could decrease the yield stress of NaCl samples under conditions of high-rate loading.

ACKNOWLEDGMENTS

The author is grateful to B.I. Smirnov for many useful discussions of the results of this work.

REFERENCES

1. V. I. Al'shits, E. V. Darinskaya, T. M. Perekalina, and A. A. Urusovskaya, Fiz. Tverd. Tela (Leningrad) **29** (2), 467 (1987) [Sov. Phys. Solid State **29**, 265 (1987)].
2. Yu. I. Golovin, R. B. Morgunov, D. V. Lopatin, and A. A. Baskakov, Phys. Status Solidi A **160** (2), R3 (1997).
3. Yu. I. Golovin, R. B. Morgunov, V. E. Ivanov, *et al.*, Pis'ma Zh. Éksp. Teor. Fiz. **68** (5), 400 (1998) [JETP Lett. **68**, 426 (1998)].
4. N. A. Tyapunina, V. L. Krasnikov, and E. P. Belozerova, Fiz. Tverd. Tela (St. Petersburg) **41** (6), 1035 (1999) [Phys. Solid State **41**, 942 (1999)].
5. V. I. Al'shits, A. A. Urusovskaya, A. E. Smirnov, and N. N. Bekkauer, Fiz. Tverd. Tela (St. Petersburg) **42** (2), 270 (2000) [Phys. Solid State **42**, 277 (2000)].
6. B. I. Smirnov, N. N. Peschanskaya, and V. I. Nikolaev, Fiz. Tverd. Tela (St. Petersburg) **43** (12), 2154 (2001) [Phys. Solid State **43**, 2250 (2001)].
7. Yu. A. Osip'yan, Yu. I. Golovin, R. B. Morgunov, *et al.*, Fiz. Tverd. Tela (St. Petersburg) **43** (7), 1333 (2001) [Phys. Solid State **43**, 1389 (2001)].
8. V. I. Al'shits, E. V. Darinskaya, M. A. Legen'kov, and V. A. Morozov, Fiz. Tverd. Tela (St. Petersburg) **41** (11), 2004 (1999) [Phys. Solid State **41**, 1839 (1999)].
9. Y. Yasumoto, A. Nakamura, and R. Takeuchi, Acustica **30** (5), 260 (1974).
10. V. I. Al'shits, E. V. Darinskaya, and O. L. Kazakova, Zh. Éksp. Teor. Fiz. **111** (2), 615 (1997) [JETP **84**, 338 (1997)].

Translated by K. Shakhlevich

Physics of the Solid State, Vol. 45, No. 10, 2003, pp. 1935–1939. Translated from Fizika Tverdogo Tela, Vol. 45, No. 10, 2003, pp. 1842–1846.

MAGNETISM AND FERROELECTRICITY

Thermodynamics of a Ladder Ferromagnet with Random Transverse Exchange

P. N. Timonin

Research Institute of Physics, Rostov State University, pr. Stachki 194, Rostov-on-Don, 344090 Russia
e-mail: timonin@aaanet.ru

Received November 6, 2002

Abstract—A model of a ladder ferromagnet with Ising spins that consists of two ferromagnetic chains with interaction of nearest neighbors and a random interaction between the nearest spins of different chains is considered. For properly chosen parameters of the random interaction, the description of the ground-state degeneracy and thermodynamics at $T = 0$ proves to be elementary in terms of the statistics of one-dimensional clusters. Analysis of the field dependences of the thermodynamic parameters has revealed a series of phase transitions associated with changes in the spin configurations of the antiferromagnetic clusters. Numerical investigation of the thermodynamics of the system under consideration at finite temperatures confirms the correctness of the analytical results obtained at $T = 0$. *© 2003 MAIK "Nauka/Interperiodica".*

1. INTRODUCTION

The synthesis of crystals with one-dimensional ladder structures has stimulated investigations into their physical properties [1]. Quasi-one-dimensional structures with different types of disorder are of special interest due to both the possibility of describing real crystals and the large variety of physical processes initiated by disorder. The magnetic properties of quasi-one-dimensional Ising systems are best understood (see, for example, the review by Liebmann [2]). Although quasi-one-dimensional systems with short-range exchange do not undergo magnetic transitions at temperatures $T \neq 0$, they exhibit a number of unusual properties at $T = 0$ due to disorder (such as ground-state degeneracy and transitions in a magnetic field) [2–5]. In turn, this gives rise to singularities in the temperature and field dependences of the physical properties at low temperatures.

The degeneracy of the ground state is a characteristic property of spin-glass phases and mixed phases in which different types of magnetic order and glass disorder coexist. The ground-state degeneracy is associated with nonergodicity of the magnetic phases in disordered magnetic materials (see the review by Binder and Young [6]). In this respect, random (quasi) one-dimensional systems with frustration and ground-state degeneracy have been attracting close research attention. However, only a few of these simplest systems are suitable for rigorous analytical thermodynamic description. Among them are the model of a one-dimensional Ising spin glass with random binary exchange in an external field [3–5], which is characterized by specific forms of the exchange distribution function [7], and ladder glass models with binary exchange [4, 8]. These models made it possible to elucidate the physical cause of the ground-state degeneracy, which is associated with the energy degeneracy of spin states of some magnetic clusters with a particular configuration of exchange interactions [3, 5, 9]. However, the enumeration of these configurations is a nontrivial problem and further progress in the study of the aforementioned models, for example, investigation of the nonergodic dynamics at $T = 0$, is lacking.

Therefore, it is expedient to search for and study other disordered quasi-one-dimensional systems with the degenerate ground state that would be suitable for simple description. In this regard, the application of ladder models offers strong possibilities, in particular, for the experimental verification of theoretical results. In the present work, we consider a model of a ladder ferromagnet with Ising spins that consists of two ferromagnetic chains with interaction of nearest neighbors and a random interaction between the nearest spins of different chains. For properly chosen parameters of the random interaction, the description of the ground-state degeneracy and thermodynamics at $T = 0$ proves to be elementary in terms of the statistics of one-dimensional clusters. Numerical investigation of the thermodynamics of this system at finite temperatures confirms the validity of the analytical results obtained at $T = 0$.

2. THERMODYNAMICS AT $T = 0$

The spin Hamiltonian of the model under consideration has the form

$$\mathcal{H} = -\sum_{i=1}^{N} [J(S_{1i}S_{1i+1} + S_{2i}S_{2i+1}) + J_r S_{1i}S_{2i} + H(S_{1i} + S_{2i})]. \quad (1)$$

1063-7834/03/4510-1935$24.00

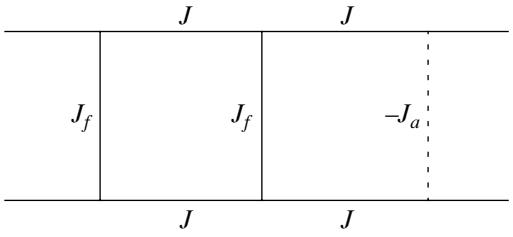

Fig. 1. Schematic drawing of the ladder ferromagnet with random transverse exchange.

Here, $S_{\alpha,i} = \pm 1$; H is the magnetic field ($H > 0$); J is the constant of ferromagnetic exchange of the chains ($J > 0$); and J_r is the constant of random exchange between the nearest spins of different chains, which takes two values, namely, $J_r = -J_a$ with the probability p and $J_r = J_f$ with the probability $1 - p$.

Therefore, for each exchange constant J_r, the system consists of clusters with antiferromagnetic ($-J_a$) and ferromagnetic (J_f) interactions between the chains. Figure 1 presents a schematic drawing of the ladder ferromagnet for a particular random transverse exchange.

Let us now assume that $J_f > 2J$. In this case, the spins in the ground state in ferromagnetic clusters are equal to unity; therefore, it remains to determine the directions of the spins in the antiferromagnetic clusters. We consider the change in the energy of the antiferromagnetic clusters upon the transition from a ferromagnetic state ($S_{1,i}S_{2,i} = 1$) to a configuration with opposite spins in n consecutive cells (if the cells are not consecutive, the energy of the configuration increases); that is,

$$\delta E_n = -2n(J_a - H) + 4J. \quad (2)$$

Under the condition $H > J_a$, the inequality $\delta E_n > 0$ holds and the oppositely directed spins in the cells become energetically unfavorable. As a result, the (only) ground state is a ferromagnetic state with the mean energy per cell:

$$E_f = -2J + pJ_a - (1 - p)J_f - 2H. \quad (3)$$

Under the condition $H < J_a$, the lowest energy is observed in configurations with the largest number of cells n, which coincides with the cluster size ($S_{1,i}S_{2,i} = -1$). This antiferromagnetic ordering is energetically favorable for sufficiently large-sized antiferromagnetic clusters in which the number of cells is greater than or equal to an integral number n_0 satisfying the condition

$$2J/(J_a - H) < n_0 < 1 + 2J/(J_a - H) \quad (4)$$

when $2J/(J_a - H)$ is not an integral number. If $2J/(J_a - H)$ is an integral number, we have $n_0 = 2J/(J_a - H)$; in this case, the clusters belonging to n_0 cells are characterized by equal energies of ferromagnetic and antiferromagnetic ordering.

The ground-state energy at $H < J_a$ is less than the energy E_f by the value of the gain upon transition of the ferromagnetic clusters with $n \geq n_0$ to the antiferromagnetic state:

$$E = E_f + \sum_{n = n_0}^{\infty} N_n \delta E_n. \quad (5)$$

Here, N_n is the mean number of antiferromagnetic clusters in n cells per cell [10]:

$$N_n = p^n (1 - p)^2. \quad (6)$$

Since the antiferromagnetic order of a cluster can be achieved in two ways, the ground state is degenerate with the mean entropy

$$S = \sum_{n = n_0}^{\infty} N_n \ln 2 + \delta_{n_0, 2J/(J_a - H)} N_{n_0} \ln \frac{3}{2}. \quad (7)$$

The last term in formula (7) accounts for the energy degeneracy of the ferromagnetic and antiferromagnetic ordering of n_0 clusters in the case when $2J/(J_a - H)$ is an integral number.

The average magnetization in the ground state at $H < J_a$ can be determined by subtracting the fraction of spins in the clusters with antiferromagnetic ordering from the ferromagnetic magnetization (unity); that is,

$$M = 1 - \sum_{n = n_0}^{\infty} nN_n + \delta_{n_0, 2J/(J_a - H)} \frac{n_0 N_{n_0}}{3}. \quad (8)$$

It should be noted that, unlike the entropy and energy obtained by averaging over all possible configurations of interactions, the average magnetization is determined as the average over the ground states with subsequent averaging over the interactions. The last term in relationship (8) accounts for the degeneracy of the ferromagnetic and antiferromagnetic states of n_0 clusters in the case when $2J/(J_a - H)$ is an integral number. In actual fact, among the $3^{NN_{n_0}}$ states differing in the configuration of n_0 clusters, there exist $2^k \binom{NN_{n_0}}{k}$ states with an antiferromagnetic configuration of spins in k clusters for which the mean number of spins per site in n_0 clusters with antiferromagnetic ordering can be determined according to the formula

$$\sum_{k = 1}^{NN_{n_0}} \frac{n_0 k}{N} 2^k \binom{NN_{n_0}}{k} 3^{-NN_{n_0}} = \frac{2}{3} n_0 N_{n_0},$$

from which follows relationship (8).

Substituting expressions (2) and (6) into formulas (5), (7), and (8), we obtain the following explicit expres-

sions for the mean energy, entropy, and magnetization at $T = 0$:

$$E = -2J[1 - 2p^{n_0}(1-p)] + J_a[p - 2L(n_0, p)] - 2H[1 - 2L(n_0, p)] - (1-p)J_f, \quad (9)$$

$$S = p^{n_0}(1-p)\left[\ln 2 + \delta_{n_0, 2J/(J_a - H)}(1-p)\ln\frac{3}{2}\right], \quad (10)$$

$$M = 1 - L(n_0, p) + \delta_{n_0, 2J/(J_a - H)}\frac{n_0 P^{n_0}(1-p)^2}{3}. \quad (11)$$

Here,

$$L(n_0, p) = \sum_{n = n_0}^{\infty} nN_n = p^{n_0}[p + n_0(1-p)].$$

The field dependences of the entropy and magnetization for the exchange constant $J_a = 3J$ with probabilities $p = 0.3$ and 0.8 (Fig. 2) exhibit a stepwise behavior with jumps at integral values of $2J/(J_a - H)$, which is characteristic of (quasi) one-dimensional Ising magnets with a discrete disorder [2–4]. The physical cause of this behavior is quite obvious: an increase in the magnetic field leads to changes in the spin configurations (from an antiferromagnetic configuration to a ferromagnetic configuration) involving progressively larger clusters with antiferromagnetic interactions. Under the condition $H < J_a$, at the points $H_k = J_a - 2J/k$ ($k = 1, 2, \ldots$), there occurs a series of transitions between phases in which ferromagnetic spin ordering coexists with glass ordering. The energy described by expression (9) is continuous at the transition points. The degree of glass disorder and the ground-state degeneracy (entropy) decrease with an increase in the magnetic field, and, finally, the system becomes ferromagnetic at $H > J_a$. Thus, we have a typical system with disorder-induced frustration; however, unlike the models considered earlier [2–5, 7–9], the description of the properties of a ladder ferromagnet with a random transverse exchange at $T = 0$ and $J_f > 2J$ is quite elementary.

Note that the expressions obtained for the energy and magnetization satisfy the standard thermodynamic relationship

$$2M = -\frac{\partial E}{\partial H},$$

when $2J/(J_a - H)$ is not an integral number. In the case when $2J/(J_a - H)$ is an integral number, this relationship does not hold, because from expression (9) it follows that, at the transition points, the energy has an inflection and its derivative with respect to the magnetic field H does not exist. This is due to a nonuniform (with respect to H) convergence of $\partial E_N/\partial H$ to its limit at $N \longrightarrow \infty$ in the vicinity of these values of H, which makes it impossible to differentiate the limiting value of E with respect to H. In this case the correct result for the magnetization

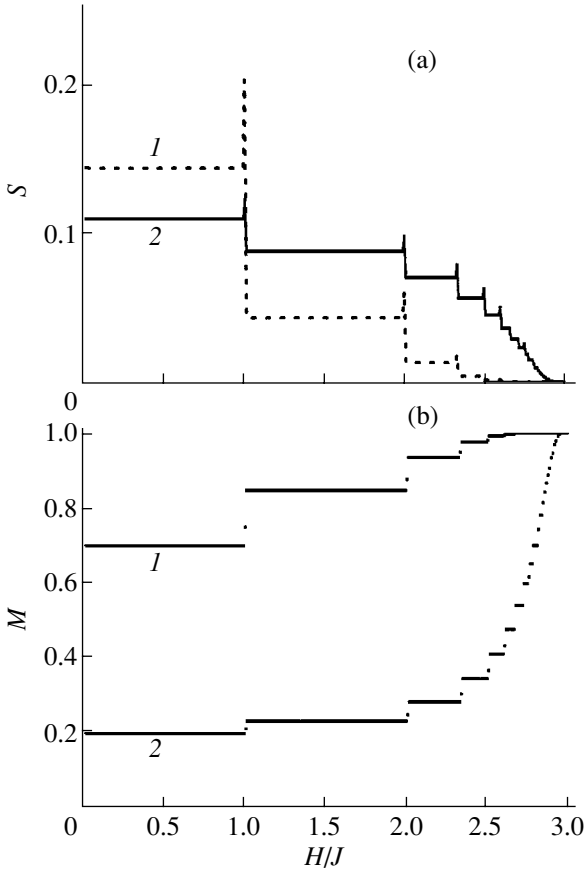

Fig. 2. Field dependences of the thermodynamic parameters at $T = 0$, $J_a = 3J$, and $p = (1)$ 0.3 and 0.8: (a) entropy and (b) magnetization.

coinciding with that defined by relationship (11) can be obtained when the differentiation with respect to H is carried out before the passage to the limit $N \longrightarrow \infty$:

$$2M = -\lim_{N \to \infty} \partial E_N/\partial H.$$

3. THERMODYNAMICS AT FINITE TEMPERATURES

An analysis of the thermodynamics in terms of the above model at finite temperatures can be performed by the standard methods used for studying random quasi-one-dimensional systems with short-range interaction [11]. Let us introduce a partial partition function in the form

$$Z_N(S_1, S_2) = \mathrm{Tr}_{N-1}[\exp(-\beta\mathcal{H})].$$

Here, $\beta = 1/T$ and Tr_{N-1} indicates summation over configurations of all spins, except for the spins of the last cell (S_1, S_2). The quantities $Z_N(S_1, S_2)$ satisfy the following recurrence relationships:

$$Z_{N+1}(\mathbf{S}) = \mathrm{Tr}_{\mathbf{S}'}R(\mathbf{S}, \mathbf{S}')Z_N(\mathbf{S}'), \quad (12)$$

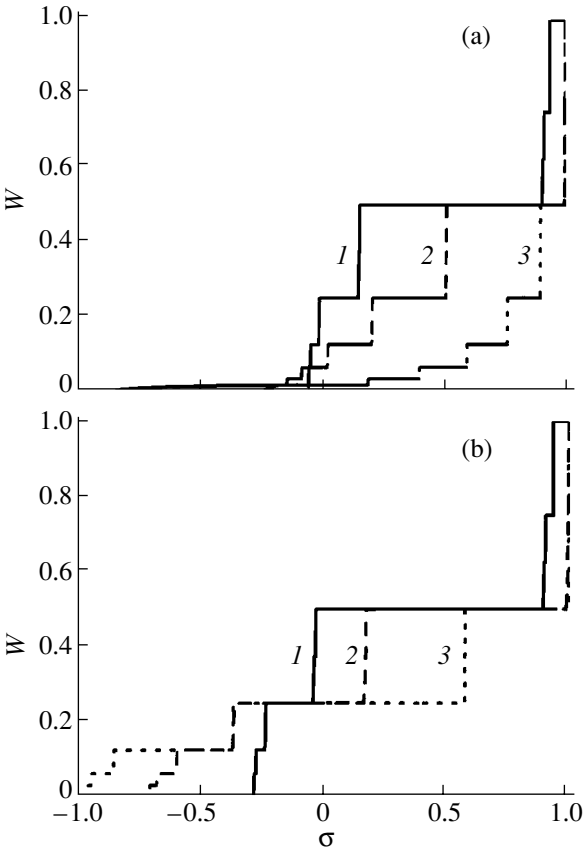

Fig. 3. Integrated distribution function ω(σ) at $p = 0.5$, $J_f = 3J$, J_a = (a) 0.1 and (b) 0.5J, and T = (*1*) 2J, (*2*) J, and 0.5J.

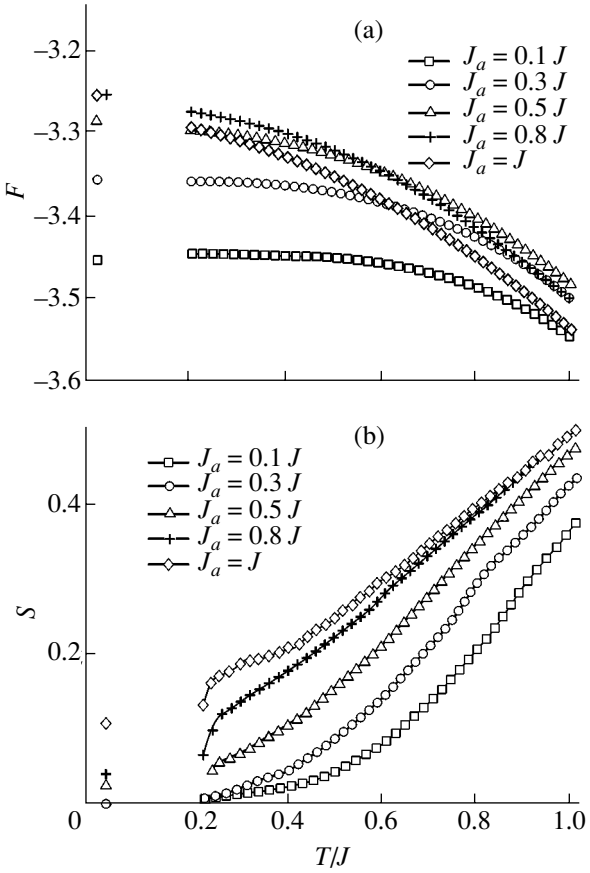

Fig. 4. Temperature dependences of the thermodynamic parameters at $p = 0.5$, $J_f = 3J$ and different values of J_a: (a) thermodynamic potential and (b) entropy.

where $R(\mathbf{S}, \mathbf{S}')$ is the transfer matrix. Below, we will consider the case $H = 0$. Hence, we can write

$$R(\mathbf{S}, \mathbf{S}') = \exp[\beta J(\mathbf{S}, \mathbf{S}') + \beta J_r S_1 S_2].$$

In this case, the partial partition function can be represented in the form

$$Z_N(\mathbf{S}) = \frac{Z_N}{4}(1 + \sigma_N S_1 S_2),$$

where Z_N is a standard partition function,

$$Z_N = \mathrm{Tr}_N[\exp(-\beta\mathcal{H})],$$

and σ_N is the mean product of the spins in a single cell,

$$\sigma_N = \mathrm{Tr}_N(S_1 S_2 e^{-\beta\mathcal{H}})/Z_N \equiv \langle S_1 S_2 \rangle_N.$$

From relationship (12), it follows that

$$Z_{N+1} = 4\cosh^2(\beta J)\cosh(\beta J_r) \times [1 + \tanh^2(\beta J)\tanh(\beta J_r)\sigma_N]Z_N, \quad (13)$$

$$\sigma_{N+1} = \frac{\tanh(\beta J_r) + \tanh^2(\beta J)\sigma_N}{1 + \tanh(\beta J_r)\tanh^2(\beta J)\sigma_N}. \quad (14)$$

In turn, from expression (14), it follows that, when $N \longrightarrow \infty$, the distribution function of the quantity σ takes the form [11]

$$\rho(\sigma) = \int_{-1}^{1} d\sigma' \langle \delta[\sigma - f(\sigma', J_r)] \rangle_{J_r} \rho(\sigma'), \quad (15)$$

where $f(\sigma', J_r)$ is the function on the right-hand side of expression (14),

$$f(\sigma, J_r) = \frac{\tanh(\beta J_r) + \tanh^2(\beta J)\sigma}{1 + \tanh(\beta J_r)\tanh^2(\beta J)\sigma}, \quad (16)$$

and the angular brackets indicate averaging over the random exchange.

After determining the distribution function ρ(σ) from relationship (15), we can calculate the mean ther-

modynamic potential from expression (13); that is,

$$F \equiv -\lim_{N\to\infty}\frac{T}{N}\langle \ln Z_N\rangle$$
$$= -T\ln[4\cosh^2(\beta J)] - T\langle \ln[\cosh(\beta J_r)]\rangle_{J_r} \quad (17)$$
$$-T\int_{-1}^{1} d\sigma\rho(\sigma)\langle \ln[1+\tanh^2(\beta J)\tanh(\beta J_r)\sigma]\rangle_{J_r}.$$

Equation (15) can be solved only numerically. For this purpose, we transform it slightly. By continuing $\rho(\sigma)$ through zero to the region $\sigma^2 > 1$, introducing integration under the averaging sign and integrating, we obtain the relationship

$$\rho(\sigma) = \left\langle \frac{\partial g(\sigma, J_r)}{\partial\sigma}\rho[g(\sigma, J_r)]\right\rangle_{J_r}. \quad (18)$$

Here, $g(\sigma, J_r)$ is the function inverse to the function $f(\sigma, J_r)$ defined by expression (16):

$$g(\sigma, J_r) = \tanh^{-2}(\beta J)\frac{\sigma - \tanh(\beta J_r)}{1-\sigma\tanh(\beta J_r)}.$$

Integrating expression (18) with respect to σ, we obtain

$$w(\sigma) = \langle w[g(\sigma, J_r)]\rangle_{J_r}, \quad (19)$$

where

$$w(\sigma) = \int_{-1}^{\sigma} d\sigma'\rho(\sigma').$$

Unlike the distribution function $\rho(\sigma)$, which can involve delta functions, the integrated distribution function $w(\sigma)$ satisfies the simpler equation (19) and has weaker singularities (jumps). Consequently, the numerical solution to Eq. (19) is significantly simpler and can be obtained by the iteration method. If the initial function is chosen as $w_0(\sigma) = 0.5(1+\sigma)$, convergence to the solution can be reached after five to ten iterations. The function $w(\sigma)$ for $p = 0.5$, $J_f = 3J$, and several temperatures and exchange constants J_a is presented in Fig. 3.

The temperature dependences of the thermodynamic potential F for $p = 0.5$, $J_f = 3J$, and different exchange constants J_a calculated according to formula (17) are shown in Fig. 4a. The entropy obtained by numerical differentiation of the thermodynamic potential $F(T)$ is presented in Fig. 4b. Unfortunately, the computations performed for temperatures $T < 0.2J$ are very time-consuming if one wants to attain a reasonable accuracy. However, the results obtained at $T > 0.2J$ (Fig. 4a) also demonstrate that, at low temperatures, the thermodynamic potential $F(T)$ tends to the corresponding mean values $E(T = 0)$ [expression (9)] represented in this figure. The behavior of the entropy also agrees with the results obtained at $T = 0$ [expression (10)] (Fig. 4b). Thus, the simple analytical relationships derived at $T = 0$ adequately describe the thermodynamics of the model under consideration.

In conclusion, it should be noted that the above model with such a simple but nontrivial thermodynamics at $T = 0$ that exhibits all properties of frustrated disordered systems can serve as a test model for the verification of approximate approaches to the description of more complex low-dimensional disordered magnets. It is evident that the dynamics described by this model at $T = 0$ is also nontrivial and exhibits all effects inherent in nonergodic systems. I believe that, within this model, the description of similar dynamic effects will also be sufficiently simple (even if it is not analytical, it will at least not require time-consuming numerical computations). Note also that this model can be reproduced in practice; for example, random exchange can be created by introducing impurities between ferromagnetic chains.

REFERENCES

1. E. Dagotto, Rep. Prog. Phys. **62** (8), 1525 (1999).
2. R. Liebmann, *Statistical Mechanics of Periodic Frustrated Ising Systems* (Springer, Berlin, 1986), Lect. Notes Phys., Vol. 251.
3. A. Vilenkin, Phys. Rev. B **18** (3), 1474 (1978).
4. B. Derrida, J. Vannimenus, and Y. Pomeau, J. Phys. C **11** (16), 4749 (1978).
5. E. Farhi and S. Guttmann, Phys. Rev. B **48** (13), 9508 (1993).
6. K. Binder and A. P. Young, Rev. Mod. Phys. **58** (4), 801 (1986).
7. J. M. Luck and Th. M. Nieuwenhuizen, J. Phys. A **22** (7), 2151 (1989).
8. D. C. Mattis and P. Paul, Phys. Rev. Lett. **83** (18), 3733 (1999).
9. F. Igloi, J. Phys. A **27** (10), 2995 (1994).
10. D. Stauffer and A. Aharony, *Introduction to Percolation Theory* (Taylor and Francis, London, 1992).
11. D. Andelman, Phys. Rev. B **34** (9), 6214 (1986).

Translated by O. Moskalev

Physics of the Solid State, Vol. 45, No. 10, 2003, pp. 1940–1943. Translated from Fizika Tverdogo Tela, Vol. 45, No. 10, 2003, pp. 1847–1849.

MAGNETISM AND FERROELECTRICITY

Magnetic Structure of a Compensated Ferromagnet–Antiferromagnet Interface

A. I. Morosov

Moscow State Institute of Radio Engineering, Electronics, and Automation (Technical University), pr. Vernadskogo 78, Moscow, 119454 Russia

e-mail: mor-alexandr@yandex.ru

Received March 25, 2003

Abstract—The magnetic structure of a compensated ferromagnet–antiferromagnet interface is considered. It is shown that the rate of decrease in the magnetic order parameters as one goes away from the interface is determined by the type of crystal structure of the layers and by the crystallographic orientation of the interface.

1. A large number of studies have been devoted to the properties of ferromagnet–antiferromagnet interfaces (see, e.g., [1]). The reason for this is that the antiferromagnet-induced shift of ferromagnetic hysteresis loops from their symmetrical position (so-called unidirectional anisotropy, or the exchange-induced bias) has found wide use in magnetoelectronic devices.

The theory of unidirectional anisotropy for the compensated surface of an antiferromagnet was developed by Koon [2]. In the case of a compensated surface, an antiferromagnet atomic plane parallel to the interface has zero magnetic moment. If the compensated surface is coated with a ferromagnetic layer, then, in the absence of an external field in the exchange approximation, the magnetization vector of the ferromagnet is oriented perpendicular to the antiferromagnetism vector of the (two-sublattice) antiferromagnet. Exchange interaction of spins of the bottom atomic layer of the ferromagnet with the spins of the top atomic layer of the antiferromagnet results in spin canting (spin-flop), similar to the sublattice magnetization canting induced by a magnetic field (Fig. 1) [2]. The difference is that, in the nearest neighbor interaction approximation, the exchange field of the ferromagnet acts only on the uppermost atomic spin layer of the antiferromagnet; therefore, the canting angle θ decays as a function of depth in the antiferromagnet.

In addition, the spins of the ferromagnet are slightly tilted in opposite directions from being parallel, which can be interpreted as the appearance of an induced antiferromagnetism vector **L** (Fig. 1). As in the antiferromagnet, the tilting angle φ decreases as a function of depth in the ferromagnet.

The interaction of the magnetization of the ferromagnet with the canting-induced surface magnetic moment of the antiferromagnet, as well as the interaction of the vector **L** of the antiferromagnet with the induced antiferromagnetism vector of the ferromagnet, causes the unidirectional anisotropy. The rotation of the magnetization of the ferromagnet under an external magnetic field creates a domain wall in the antiferromagnet. The bias field of the hysteresis loop can be estimated by equating the Zeeman energy of the ferromagnet to the energy of formation of a domain wall [3, 4] and is found to be

$$B_{ex} = \frac{w_{af}}{Md}, \tag{1}$$

where w_{af} is the surface energy density of a domain wall in the antiferromagnet and M and d are the magnetization and thickness of the ferromagnetic layer, respectively. Here, we assume that the domain-wall energy in

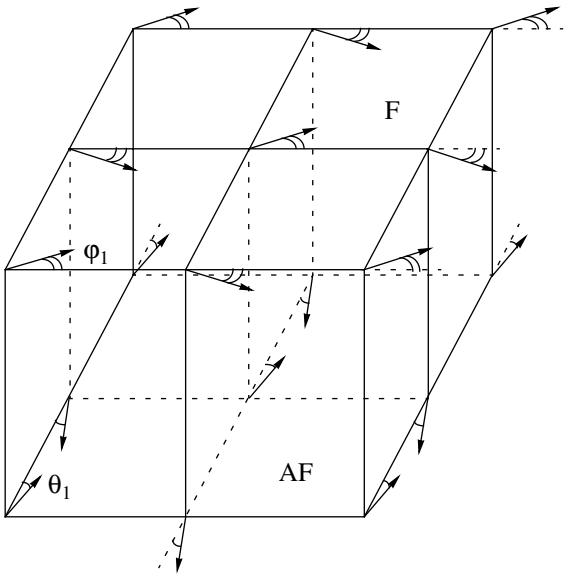

Fig. 1. Orientation of spins in the bottom (F) atomic layer of the ferromagnet and in the top (AF) atomic layer of the antiferromagnet for the (100) cut of a simple cubic lattice.

1063-7834/03/4510-1940$24.00

the ferromagnetic layer is higher than that in the antiferromagnet.

In this publication, we studied the law describing the decay of the angles θ and φ as a function of depth in the respective layers.

2. Since, far from the Curie and Néel temperatures, all characteristic scales of the problem at hand are of the atomic order of magnitude, we consider a discrete spin lattice under the assumption that the type of crystal lattice and its parameters are the same in the ferromagnet and antiferromagnet.

The Heisenberg exchange interaction of adjacent spins in the ferromagnet and antiferromagnet is described by the exchange integrals $J_f > 0$ and $J_{af} < 0$, respectively, while the interaction between a spin in the ferromagnet and its nearest neighbor spins in the antiferromagnet is described by the exchange integral $J_{f, af}$. The computer simulation made in [2] corresponds to the case where all exchange energies are equal. As was indicated in [2], the sublattice canting angle decays quickly with depth in the antiferromagnet and becomes virtually equal to zero in the fifth or sixth atomic layer.

The characteristic decay length of θ and φ depends on the type of crystal lattice and on the crystallographic orientation of the interface. In particular, for a family of atomic planes parallel to the interface and for a given spin, the ratio is of importance between the number of the spin's nearest neighbors *a* located in the adjacent atomic plane and the number of its nearest neighbors *b* in the atomic plane where this spin is located ($2a + b = z$, where *z* is the total number of its nearest neighbors).

Given *a* and *b*, the Heisenberg exchange interaction energy at the ferromagnet–antiferromagnet interface $W_{f, af}$ has the form

$$W_{f, af} = -Na|J_{f, af}|S_f S_{af}\sin(\theta_1 + \varphi_1), \tag{2}$$

where S_f and S_{af} are the average values of the spin of an atom in the ferromagnet and antiferromagnet, *N* is the number of atoms in an atomic plane, θ_1 is the sublattice canting angle in the top atomic plane of the antiferromagnet, and φ_1 is the tilting angle of spins in the bottom atomic plane of the ferromagnet. We assume that the sublattice magnetizations remain unchanged in magnitude. The sign of $J_{f, af}$ determines only the direction of the sublattice canting. At $J_{f, af} > 0$, the magnetization of the top antiferromagnetic atomic layer is parallel to the magnetization of the ferromagnet, and at $J_{f, af} < 0$, it is antiparallel to it [2].

For small values of θ_1 and φ_1, the interaction energy can be represented as the sum of two independent terms. One term, dependent on θ_1, is the interaction energy of the spins of the ferromagnet with the ferromagnetic moment induced in the antiferromagnet. The other term, dependent on φ_1, is the interaction energy of the spins of the antiferromagnet with the induced antiferromagnetism vector of the ferromagnet.

The exchange interaction energy inside the ferromagnet is

$$W_f = -\frac{NJ_f S_f^2}{2}\Bigg\{a\cos(\varphi_1 - \varphi_2) + b\cos 2\varphi_1 + \sum_{j\geq 2}^{\infty}[a\cos(\varphi_j - \varphi_{j-1}) + a\cos(\varphi_j - \varphi_{j+1}) + b\cos 2\varphi_j]\Bigg\}, \tag{3}$$

where φ_j is the tilting angle of spins in the *j*th atomic layer of the ferromagnet (the direction of tilting is the same for all spins located on the same perpendicular to the interface).

The analogous energy inside the antiferromagnet is

$$W_{af} = -\frac{N|J_{af}|S_{af}^2}{2}\Bigg\{a\cos(\theta_1 + \theta_2) + b\cos 2\theta_1 + \sum_{i\geq 2}^{\infty}[a\cos(\theta_i + \theta_{i-1}) + a\cos(\theta_i + \theta_{i+1}) + b\cos 2\theta_i]\Bigg\}, \tag{4}$$

where θ_i is the sublattice canting angle in the *i*th layer of the antiferromagnet (the direction of canting coincides with that in the top atomic layer; see Fig. 1).

Minimization of W_f with respect to the variables φ_j for $j \geq 2$ in the context of the mean-field theory yields the following recurrence formula relating the tilting angles in adjacent layers:

$$a\sin(\varphi_j - \varphi_{j-1}) + a\sin(\varphi_j - \varphi_{j+1}) + b\sin 2\varphi_j = 0. \tag{5}$$

For $\varphi \ll 1$, we assume that

$$\varphi_j = \kappa\varphi_{j-1} \tag{6}$$

and find

$$\kappa = \frac{b}{a} + 1 - \sqrt{\frac{b}{a}\left(\frac{b}{a} + 2\right)}. \tag{7}$$

For noncubic lattices, the value of κ will also depend on the ratio of the exchange integrals corresponding to various interatomic distances.

A similar consideration for the antiferromagnet gives

$$\theta_i = -\kappa\theta_{i-1}, \tag{8}$$

with the same value of κ as for the ferromagnet. Thus, in a real situation, the sublattices in adjacent atomic planes of the antiferromagnet are canted in opposite directions.

Table 1. Parameters characterizing various cuts of cubic crystals

Lattice type	Cut	a	b	κ	γ
SC	(100)	1	4	$5 - \sqrt{24} = 0.101021$	$2 + \sqrt{6} = 4.44949$
SC	(110)	2	2	$2 - \sqrt{3} = 0.267949$	$1 + \sqrt{3} = 2.73205$
BCC	(110)	2	4	$3 - \sqrt{8} = 0.171573$	$2(1 + \sqrt{2}) = 4.82843$

For small values of the canting and tilting angles, the excess energies of the ferromagnet and antiferromagnet associated with the deviation of the spin directions, in view of Eqs. (6) and (8), are reduced to

$$\Delta W_f = NJ_f^2 S_f^2 \left\{ \sum_{j=1}^{\infty} [(b+a)\varphi_j^2 - a\varphi_j\varphi_{j+1}] - \frac{a\varphi_1^2}{2} \right\} = NJ_f S_f^2 \varphi_1^2 \left\{ \frac{b}{1-\kappa^2} + \frac{a(1-\kappa)}{2(1+\kappa)} \right\} \equiv \gamma N J_f^2 S_f^2 \varphi_1^2, \quad (9)$$

$$\Delta W_{af} = N|J_{af}|S_{af}^2 \left\{ \sum_{i=1}^{\infty} [(b+a)\theta_i^2 + a\theta_i\theta_{i+1}] - \frac{a\theta_1^2}{2} \right\} \equiv \gamma N |J_{af}| S_{af}^2 \theta_1^2, \quad (10)$$

where (after certain simplifications)

$$\gamma = \frac{1}{2}[b + \sqrt{b(b+2a)}]. \quad (11)$$

The values of a, b, κ, and γ for several cuts of simple cubic (sc) and body-centered cubic (bcc) lattices are listed in Table 1. The (111) cut in the sc and bcc lattices and the (001) cut in the bcc lattices are not compensated surfaces.

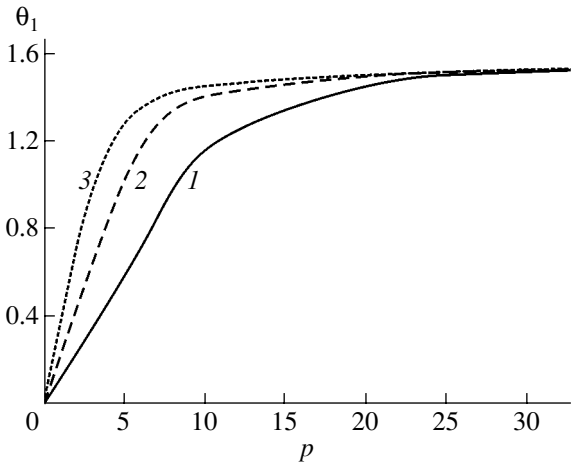

Fig. 2. Sublattice canting angle in the top atomic layer of the antiferromagnet as a function of the interaction energy of the layers for (*1*) $y = 4$, (*2*) 2, and (*3*) 1.

Minimization of the total interaction energy W of the layers

$$W = \Delta W_f + \Delta W_{af} + W_{f,af} \quad (12)$$

with respect to the angles θ_1 and φ_1 gives the following expressions:

$$\theta_1 = \frac{a}{2\gamma} \frac{|J_{f,af}| S_f}{|J_{af}| S_{af}}, \quad (13)$$

$$\varphi_1 = \frac{a}{2\gamma} \frac{|J_{f,af}| S_{af}}{J_f S_f}. \quad (14)$$

Therefore, the interaction energy of the layers W is

$$W = -\frac{a^2 N J_{f,af}^2 S_f^2 S_{af}^2}{4\gamma} \left(\frac{1}{|J_{af}| S_{af}^2} + \frac{1}{J_f S_f^2} \right). \quad (15)$$

This energy is determined by the softest subsystem, i.e., by the layer with the lowest exchange energy of spins.

3. The condition $\varphi_1, \theta_1 \ll 1$ is equivalent to the condition of weak interlayer interaction, $|J_{f,af}| \ll J_f, J_{af}$. Generally (for cubic lattices, only in the case where the exchange integral is the same for all nearest neighbors), the solution of the problem at hand is determined by three dimensionless parameters: $y = b/a$, $p = |J_{f,af}|S_f/|J_{af}|S_{af}$, and $q = |J_{f,af}|S_{af}/J_f S_f$.

For the case of $p \gg 1$ or $q \gg 1$, we have $\theta_1 + \varphi_1 = \pi/2$; i.e., the spins of the bottom atomic layer of the ferromagnet are parallel ($J_{f,af} > 0$) or antiparallel ($J_{f,af} < 0$) to the spins in the top atomic layer of the antiferromagnet. The interaction energy in this case is $W \approx -a|J_{f,af}|NS_f S_{af}$.

If the inequality $q/p \ll 1$ ($p/q \ll 1$) is obeyed, one can assume that $\varphi_1 \approx 0$ ($\theta_1 \approx 0$) and the number of parameters decreases. Numerically calculated $\theta_1(p)$ dependences for the case $q \ll 1$ at various values of y are shown in Fig. 2.

In the limiting case $\theta_1 = \pi/2$, the ratio $|\theta_2|/\theta_1$ is less than κ by a factor of 1.1 to 1.4 and the subsequent reduction of θ_i is described by the dependences obtained for small angles (with an accuracy of better than 1%). The calculated values of θ_i are listed in Table 2.

Formula (1) holds if the total interaction energy of the layers W per area σ of the layers is larger in magnitude than w_{af}. Otherwise, a domain wall does not form.

The main results of this study as follows:

Table 2. Canting angles for the first three atomic planes of the antiferromagnet at $\theta_1 = \pi/2$

y	θ_1	θ_2	θ_3
4	1.5708	0.1125	0.0114
2	1.5708	0.2077	0.0355
1	1.5708	0.3661	0.0976

(1) The sublattices of the antiferromagnet near the ferromagnet–antiferromagnet interface are canted in opposite directions in the adjacent atomic layers parallel to the interface.

(2) The law of the decay of angles θ and φ in depth is the same for the ferromagnetic and antiferromagnetic layers and is determined by the crystallographic orientation of the interface and by the type of crystal lattice of the layers. The decay law is exponential in the case of small angles.

(3) The main contribution to the interaction energy of the layers is connected with the deviations of the spin directions in the layer with a lower exchange interaction energy.

ACKNOWLEDGMENTS

The author would like to thank Yu.V. Pyl'nov for help with the calculations and École Centrale de Lille for providing favorable conditions for productive work.

This study was supported by the CRDF and the Ministry of Education of the Russian Federation (grant no. VZ-010-0) and by the PICS/RFBR (grant no. 1573/02-02-22002).

REFERENCES

1. J. Nogues and I. K. Schuller, J. Magn. Magn. Mater. **192** (2), 203 (1999).
2. N. C. Koon, Phys. Rev. Lett. **78** (25), 4865 (1997).
3. A. P. Malozemoff, Phys. Rev. B **35** (7), 3679 (1987).
4. D. Mauri, H. C. Siegmann, P. S. Bagus, and E. Kag, J. Appl. Phys. **62** (7), 3047 (1987).

Translated by A. Zalesskiĭ

Physics of the Solid State, Vol. 45, No. 10, 2003, pp. 1944–1951. Translated from Fizika Tverdogo Tela, Vol. 45, No. 10, 2003, pp. 1850–1856.

MAGNETISM AND FERROELECTRICITY

Effect of Interstitial Atoms on the Effective Exchange Fields in Ferrimagnetic Rare-Earth and 3*d* Transition Metal Compounds R_2Fe_{17} and $RFe_{11}Ti$

S. A. Nikitin* and I. S. Tereshina**

** Moscow State University, Vorob'evy gory, Moscow, 119992 Russia*

e-mail: nikitin@rem.phys.msu.su

*** Baĭkov Institute of Metallurgy and Materials Sciences, Russian Academy of Sciences, Leninskiĭ pr. 49, Moscow, 117911 Russia*

Received March 25, 2003

Abstract—The magnetic properties (magnetic ordering temperature, magnetization) of the ferrimagnetic compounds R_2Fe_{17} and $RFe_{11}Ti$, as well as of their hydrides and nitrides, were studied. The hydrogenation- and nitrogenation- induced variation of the exchange fields acting on the rare-earth (RE) ions from both the Fe sublattice and other *R*E ions was determined, and the dependence of the Curie temperatures of the starting compounds, their hydrides, and nitrides on the de Gennes factor was revealed. It was found that incorporation of light atoms (H, N) into the crystal lattices of $RFe_{11}Ti$ and R_2Fe_{17} increases the Curie temperature T_C substantially, increases the Fe–Fe exchange coupling, and decreases the *R*–*R* exchange interactions, as well as increases the *R*–Fe intersublattice exchange under hydrogenation and decreases it under nitrogenation, an effect that can be understood as resulting from the attendant changes in the electronic structure of these compounds and in the indirect exchange interactions. © *2003 MAIK "Nauka/Interperiodica".*

1. INTRODUCTION

Rare-earth (RE) and 3*d* transition metal compounds arouse considerable research interest in the physics of magnetic phenomena, because these substances are convenient objects for testing and refining the theoretical concepts used in describing the magnetic ordering in metallic ferro- and ferrimagnets. The electronic system of rare-earth compounds permits a distinct separation into electrons possessing a localized magnetic moment and conduction electrons, and the magnetic system can be separated into two magnetic sublattices, namely, the rare-earth and 3*d* sublattices [1, 2]. On the other hand, many RE compounds of this type have considerable application potential and are already employed in powerful permanent magnets, magnetostrictors, cooling agents in magnetic coolers, etc. [2].

The present communication considers the magnetic properties of the R_2Fe_{17} and $RFe_{11}Ti$ ferrimagnetic compounds, as well as of their hydrides and nitrides, which are obtained from the starting samples by inserting interstitial atoms into their lattices. The best studied to date are the R_2Fe_{17} compounds with such interstitial elements as nitrogen and carbon [3], whereas the $R_2Fe_{17}H_X$ hydrides have thus far attracted less interest. No systematic investigation has been conducted on $RFe_{11}Ti$ compounds with light interstitial elements. The interest in R_2Fe_{17} and $RFe_{11}Ti$ stems from the fact that they are good model ferrimagnets (for heavy rare earths) with two largely localized magnetic sublattices, one of which is made up of iron atoms and the other of rare-earth atoms.

The magnetically active 4*f* subshell of a rare-earth ion is screened by the higher lying $5s^25p^6$ spin-closed electronic shells, thus precluding wave-function overlap of the 4*f* electrons with the 4*f* and 3*d* electrons of the neighboring atoms. In RE and 3*d* intermetallic compounds (including R_2Fe_{17} and $RFe_{11}Ti$), the 3*d* electrons of the iron atoms, which are responsible for the 3*d*-sublattice magnetism, are also localized primarily on the iron atoms; this is indicated by data on the magnetic properties and hyperfine fields [3, 4]. The localized model of magnetic sublattices describes the principal magnetic properties of these compounds fairly well by invoking the molecular-field theory, which considers two (rare-earth, iron) magnetic sublattices coupled by the 3*d*–4*f* exchange interaction [5–9]. It was shown in [5–9] that the exchange interaction between iron atoms on the iron sublattice is the strongest, whereas the exchange (3*d*–4*f*) coupling between the iron and rare-earth sublattices in these compounds is substantially weaker. In contrast to our previous studies, here we attempted to take into account all three kinds of exchange interactions (including those between ions on the RE sublattice) in the hydrides and nitrides. As follows from an analysis of the available publications, the calculations for the hydrides and nitrides performed thus far were conducted under the assumption that the exchange interactions between ions on the RE sublat-

1063-7834/03/4510-1944$24.00

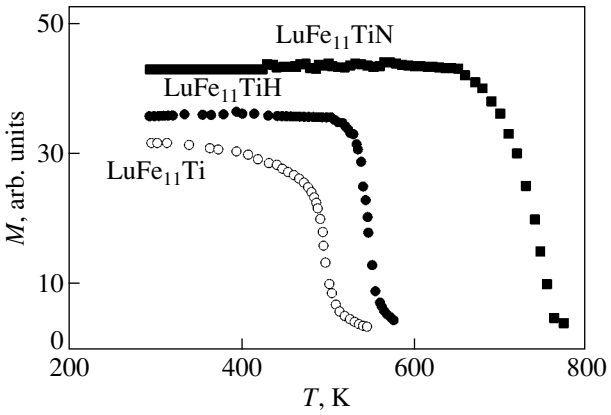

Fig. 1. Thermomagnetic analysis of $LuFe_{11}Ti$ and its hydride and nitride.

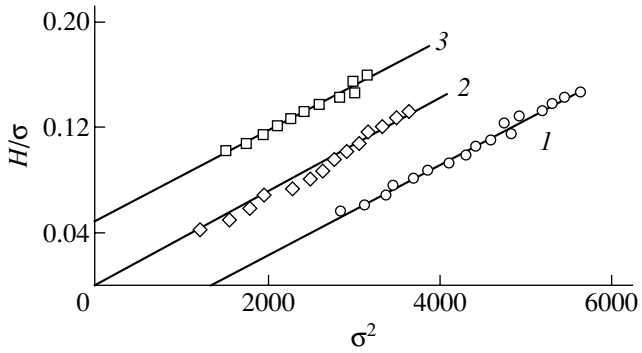

Fig. 2. Belov–Arrott plots calculated for Y_2Fe_{17} at different temperatures near the Curie point: (*1*) 345, (*2*) 340, (*3*) 335 K.

tice may be neglected. This assumption has not been sufficiently substantiated.

Although the exchange interaction model developed for the R_2Fe_{17} and $RFe_{11}Ti$ compounds elucidated the effect of these interactions on the Curie temperatures and the temperature behavior of magnetization [7–9], the nature of the 3*d*–4*f* exchange coupling remains unclear. We consider here itinerant electrons of two types, namely, the *s* electrons (appearing when the 4*s* and 6*s* electrons transfer to the conduction band) and the 3*d* and 5*d* hybridized electrons, as mediators of exchange interaction between the 4*f* and 3*d* electrons. In particular, the model proposed involves the indirect 4*f*–5*d*–3*d* exchange interaction [10]. The importance of investigating this exchange interaction and of determining the corresponding effective exchange fields $H_{\text{eff}2}$ with which the iron sublattice acts on the RE ions (index 1 refers subsequently to the iron sublattice, and index 2, to the RE sublattice) is accounted for by the fact that $H_{\text{eff}2}$ is responsible for the degree of magnetization of the rare-earth sublattice. If the energy of the rare-earth ion magnetic moment in the exchange field $H_{\text{eff}2}$ is higher than the thermal energy, most of the rare-earth ions align with the field $H_{\text{eff}2}$; this is the condition necessary to obtain the giant magnetic anisotropy and magnetostriction observed in RE compounds [6]. The present communication reports on a study of the effects associated with the influence of interstitial hydrogen and nitrogen atoms on the effective exchange fields acting in the R_2Fe_{17} and $RFe_{11}Ti$ RE compounds.

2. TECHNOLOGY OF SAMPLE PREPARATION AND THE MEASUREMENT TECHNIQUE

The starting $RFe_{11}Ti$ alloys (R = Y, Sm, Gd, Tb, Dy, Ho, Er, Lu) were prepared by alloying the charge of 99.95%-pure starting components in an argon atmosphere through RF heating. The growth of single crystals was described in [11]. The hydrogenation and nitrogenation techniques are reported in considerable detail in [12]. The phase composition and lattice parameters were studied by x-ray structural analysis (CuK_α radiation) of the starting samples and their hydrides and nitrides.

The samples for the investigation of R_2Fe_{17} (R = Y, Gd, Tb, Dy, Ho, Er, Lu) were prepared through RF alloying of the charge of 99.95%-pure starting components. The ingots were remelted in an electric resistance furnace with a high temperature gradient and subsequently cooled slowly to increase the grain size. R_2Fe_{17} single crystals were cut from ingots. The hydrogenation and nitrogenation techniques are reported in [13]. X-ray phase characterization showed all samples to be practically single phase and to have the Th_2Ni_{17} structure. The amounts of absorbed H and N in the $R_2Fe_{17}H_X$ and $R_2Fe_{17}N_Y$ compounds corresponded to three hydrogen atoms and two nitrogen atoms per formula unit, respectively.

The Curie temperatures were determined by thermomagnetic analysis. The magnetization of $RFe_{11}TiH$ and $R_2Fe_{17}H_3$ single crystals and magnetic field–oriented $RFe_{11}TiN$ and $R_2Fe_{17}N_2$ powder samples was measured in the 77- to 800-K temperature region in magnetic fields of up to 13 kOe using a pendulum magnetometer.

3. EXPERIMENTAL RESULTS

We determined the Curie temperature as the point of the sharpest drop in magnetization σ experienced in the transition from the ferromagnetic to paramagnetic state, i.e., as the temperature at which $|d\sigma/dT|$ is maximum. Figure 1 illustrates temperature dependences of the magnetic moment of the $LuFe_{11}Ti$ compound and its hydride and nitride measured in a comparatively weak magnetic field, H = 500 Oe. The values of T_C for these compounds were found to be 490, 546, and 738 K, respectively. In some cases, the Curie temperature was derived from Belov–Arrott plots (Fig. 2) relat-

Table 1. Molecular-field coefficients and effective exchange fields for the $R\mathrm{Fe}_{11}\mathrm{Ti(H,N)}_X$ compounds calculated with inclusion of exchange interaction between ions on the rare-earth sublattice ($A_2 \neq 0$)

Composition	ρ, g/cm^3	T_C, K	G	h_{21}, 10^6 Oe	N_{21}	h_{11}, 10^6 Oe	N_{11}	h_{22}, 10^6 Oe
$YFe_{11}Ti$	7.22	540	–	–	–	6.4	6122	–
$GdFe_{11}Ti$	7.81	610	15.75	0.895	764	–	–	0.382
$TbFe_{11}Ti$	7.88	556	10.50	0.895	505	–	–	0.382
$DyFe_{11}Ti$	7.93	535	7.08	0.895	378	–	–	0.382
$HoFe_{11}Ti$	8.06	515	4.50	0.895	298	–	–	0.382
$ErFe_{11}Ti$	8.05	500	2.55	0.895	250	–	–	0.382
$LuFe_{11}Ti$	8.14	486	–	–	–	5.76	5446	–
$YFe_{11}TiH$	7.17	598	–	–	–	6.85	6155	–
$GdFe_{11}TiH$	7.75	658	15.75	0.962	829	–	–	0.379
$TbFe_{11}TiH$	7.79	602	10.50	0.962	551	–	–	0.379
$DyFe_{11}TiH$	7.85	577	7.08	0.962	411	–	–	0.379
$HoFe_{11}TiH$	7.98	553	4.50	0.962	325	–	–	0.379
$ErFe_{11}TiH$	7.99	537	2.55	0.962	271	–	–	0.379
$LuFe_{11}TiH$	8.05	520	–	–	–	5.95	5313	–
$YFe_{11}TiN$	7.10	712	–	–	–	7.76	6480	–
$GdFe_{11}TiN$	7.62	768	15.75	0.834	742	–	–	0.122
$TbFe_{11}TiN$	7.75	750	10.50	0.834	487	–	–	0.122
$DyFe_{11}TiN$	7.78	736	7.08	0.834	365	–	–	0.122
$HoFe_{11}TiN$	7.82	723	4.50	0.834	292	–	–	0.122
$ErFe_{11}TiN$	7.88	713	2.55	0.834	242	–	–	0.122
$LuFe_{11}TiN$	7.93	703	–	–	–	7.66	6373	–

ing the quantity H/σ to squared specific magnetization σ^2 at temperatures close to the Curie point. Here, the Curie point is defined as the temperature at which the H/σ vs. σ^2 straight line passes through the origin. The values of T_C thus obtained practically coincide (to within 1 K) with the data derived with the use of the preceding method (from the maximum value of $|d\sigma/dT|$).

Our data, which agree with the results reported earlier by other authors [3, 7–9], show that hydrogenation and nitrogenation of the $R\mathrm{Fe}_{11}\mathrm{Ti}$ and $R_2\mathrm{Fe}_{17}$ compounds bring about a colossal rise in the Curie temperature (Tables 1, 2) and a substantial increase in the magnetic moment per Fe atom (Table 3) at $T = 4.2$ K. The average increase in the Curie temperature observed to occur, for instance, in the $R\mathrm{Fe}_{11}\mathrm{TiH}$ hydrides and $R\mathrm{Fe}_{11}\mathrm{TiN}$ nitrides compared to the starting compounds is approximately 50 and 200 K, respectively.

In contrast to previous studies, which made use of polycrystalline samples of the hydrides, in this study, the Curie temperatures of the hydrides were derived from measurements of the magnetic properties of single-crystal samples, which improved the accuracy of Curie temperature determination and permitted us to follow the dependence of T_C on the RE ion spin.

4. DISCUSSION OF EXPERIMENTAL DATA ON THE DEPENDENCE OF CURIE TEMPERATURES ON THE DE GENNES FACTOR IN THE $R_2\mathrm{Fe}_{17}$ AND $R\mathrm{Fe}_{11}\mathrm{Ti}$ COMPOUNDS AND THEIR HYDRIDES AND NITRIDES

The effective exchange fields and magnetic ordering of RE metals originate from indirect exchange coupling [1, 2, 14]; this accounts, in particular, for the paramagnetic Curie temperature Θ_p being proportional to the de Gennes factor G, i.e., the average value of the squared RE ion spin projection on the direction of the total angular momentum, with the indirect exchange integral A_{ind} serving as the coefficient of proportionality [14]:

$$\Theta_p = \frac{2}{3} x \frac{A_{\mathrm{ind}}}{k_B} G. \quad (1)$$

Here, x is the RE ion concentration and k_B is the Boltzmann constant. The de Gennes factor G can be represented as

$$G = (g_J - 1)^2 J(J+1), \quad (2)$$

where g_J is the Landé factor and J is the total angular momentum of a rare-earth ion. Experimental investigations of the dependence of Θ_p on the atomic constants of RE ions and their concentrations, conducted using

Table 2. Molecular-field coefficients and effective exchange fields for the $R_2Fe_{17}(H,N,C)_X$ compounds calculated with inclusion of exchange interaction between ions on the rare-earth sublattice ($A_2 \neq 0$)

Composition	ρ, g/cm^3	T_C, K	G	h_{21}, 10^6 Oe	N_{21}	h_{11}, 10^6 Oe	N_{11}	h_{22}, 10^6 Oe
Y_2Fe_{17}	7.35	341	–	–	–	3.81	3076	–
Gd_2Fe_{17}	7.91	492	15.75	0.913	768	–	–	0.359
Tb_2Fe_{17}	8.07	408	10.5	0.913	503	–	–	0.359
Dy_2Fe_{17}	8.15	365	7.08	0.913	376	–	–	0.359
Ho_2Fe_{17}	8.25	322	4.5	0.913	298	–	–	0.359
Er_2Fe_{17}	8.35	302	2.55	0.913	246	–	–	0.359
Lu_2Fe_{17}	8.525	267	–	–	–	2.98	2393	–
$Y_2Fe_{17}H_3$	7.13	490	–	–	–	5.47	4568	–
$Gd_2Fe_{17}H_3$	7.88	582	15.75	1.04	881	–	–	0.340
$Tb_2Fe_{17}H_3$	7.88	495	10.5	1.04	589	–	–	0.340
$Dy_2Fe_{17}H_3$	8.06	460	7.08	1.04	434	–	–	0.340
$Ho_2Fe_{17}H_3$	8.10	426	4.5	1.04	347	–	–	0.340
$Er_2Fe_{117}H_3$	8.18	404	2.55	1.04	287	–	–	0.340
$Lu_2Fe_{17}H_3$	8.35	372	–	–	–	4.15	3412	–
$Y_2Fe_{17}N_{2.5}$	7.00	740	–	–	–	7.70	5848	–
$Gd_2Fe_{17}N_2$	7.61	770	15.75	0.84	751	–	–	0.172
$Tb_2Fe_{17}N_2$	7.61	722	10.5	0.84	502	–	–	0.172
$Dy_2Fe_{17}N_2$	7.77	716	7.08	0.84	371	–	–	0.172
$Ho_2Fe_{17}N_2$	7.92	705	4.5	0.84	292	–	–	0.172
$Er_2Fe_{17}N_2$	8.00	693	2.55	0.84	242	–	–	0.172
$Lu_2Fe_{17}N_2$	8.15	679	–	–	–	7.07	5296	–
$Y_2Fe_{17}C$	7.05	502	–	–	–	5.48	4465	–
$Gd_2Fe_{17}C$	7.74	573	15.75	0.617	536	–	–	0.400
$Tb_2Fe_{17}C$	7.75	537	10.5	0.617	357	–	–	0.400
$Dy_2Fe_{17}C$	7.91	515	7.08	0.617	264	–	–	0.400
$Ho_2Fe_{17}C$	8.01	504	4.5	0.617	209	–	–	0.400
$Er_2Fe_{17}C$	8.09	495	2.55	0.617	173	–	–	0.400
$Lu_2Fe_{17}C$	8.25	486	–	–	–	5.31	4252	–

high-precision measurements of Θ_p on single-crystal samples of RE metals and of their alloys with one another and with yttrium [1, 15], showed that the dependence of Θ_p on the de Gennes factors for individual RE ions can be expressed, in first approximation, by the relation

$$\Theta_p = \frac{2}{3}\frac{A_{\text{ind}}}{k_B}\sum x_i G_i, \qquad (3)$$

where x_i is the concentration of RE ions with the de Gennes factor G_i.

The dependence of the Curie temperatures of ferrimagnetic RE compounds on the de Gennes factor was studied earlier in terms of the molecular-field theory developed for ferrimagnetic compounds with rare-earth and iron sublattices [5–9]. To analyze our experimental data, we write expressions for the temperature dependence of the magnetization of the two oppositely oriented iron (labeled 1) and rare-earth (labeled 2), sublattices:

Table 3. Average values of the magnetic moments μ_{Fe} at $T = 4.2$ K obtained for the $LuFe_{11}Ti$ and Lu_2Fe_{17} compounds and their hydrides and nitrides

Composition	μ_{Fe}, μ_B
$LuFe_{11}Ti$	1.77
$LuFe_{11}TiH$	1.9
$LuFe_{11}TiN$	2.1
Lu_2Fe_{17}	2.0
$Lu_2Fe_{17}H_3$	2.0
$Lu_2Fe_{17}N_2$	2.29

$$\frac{M_1}{M_{10}} = B_{S1}(y_1), \quad \frac{M_2}{M_{20}} = B_{J2}(y_2), \tag{4}$$

where $M_1(T)$ and $M_2(T)$ are the sublattice magnetic moments per mole at temperature T, $M_{10} = N_1\mu_B g_1 S_1$ and $M_{20} = N_2\mu_B g_2 J_2$ are the sublattice magnetic moments at $T = 0$, N_1 is the number of Fe atoms per mole, N_2 is the number of RE atoms per mole, S_1 is the Fe atom spin, J_2 is the total angular momentum of an RE atom, and g_1 and g_2 are the corresponding Landé factors.

The arguments of the Brillouin functions $B_{S1}(y_1)$ and $B_{J2}(y_2)$ can be written as [7, 16]

$$y_1 = \frac{\mu_{10}H}{k_B} + \frac{2\mu_B S_1}{k_B T}H_{\text{eff}1}, \tag{5}$$

$$y_2 = \frac{\mu_{20}H}{k_B T} + \frac{2\mu_B S_2}{k_B T}H_{\text{eff}2}. \tag{6}$$

Here, $\mu_{10} = \mu_B g_1 S_1$; $\mu_{20} = \mu_B g_2 J_2$; and $H_{\text{eff}1}$ and $H_{\text{eff}2}$ are the effective exchange fields acting on the spins of the Fe and RE ions, respectively:

$$H_{\text{eff}1} = h_{11}\sigma_1 + h_{12}\sigma_2, \tag{7}$$

where the exchange parameters are

$$h_{11} = \frac{Z_{11}A_{11}}{\mu_B}, \quad h_{12} = \frac{Z_{12}A_{12}}{\mu_B}; \qquad H_{\text{eff}2} = h_{21}\sigma_1 + h_{22}\sigma_2, \tag{8}$$

with

$$h_{21} = \frac{Z_{21}A_{21}}{\mu_B}, \quad h_{22} = \frac{Z_{22}A_{22}}{\mu_B}.$$

Here, $\sigma_1(T)$ and $\sigma_2(T)$ are the average values of the iron and RE ion spins, respectively; Z_{11} and Z_{22} are the numbers of nearest neighbors for RE ions on sublattices 1 and 2; A_{11} and A_{12} are the exchange interaction integrals for Fe atoms with neighbors on sublattices 1 and 2; and A_{21} and A_{22} are those for RE atoms with neighbors on sublattices 1 and 2, respectively.

Expanding the Brillouin functions in their arguments y_1 and y_2 for a temperature slightly above the magnetic ordering point T_C, where $y_1 \ll 1$ and $y_2 \ll 1$, and solving the system of the corresponding equations linear in M_1 and M_2, we obtain

$$T_C = \frac{1}{2}(\Theta_0 - \Theta_R) + \frac{1}{2}\sqrt{(\Theta_0 + \Theta_R)^2 + 4(\Theta_{RFe}^2 - \Theta_0\Theta_R)}. \tag{9}$$

This relation follows from Néel's theory of ferrimagnetism [17] and was derived and analyzed earlier in [5, 7–9].

Recalling the expressions for the Curie constants C_1 and C_2

$$C_1 = \frac{N_1\mu_B^2 g_1 J_1(J_1+1)}{3k_B}, \quad C_2 = \frac{N_2\mu_B^2 g_2^2 J_2(J_2+1)}{3k_B},$$

one can find the contributions to the Curie temperature due to various exchange interactions:

$$\Theta_0 = C_1\frac{2h_{11}}{N_1\mu_B}\frac{(g_1-1)^2}{g_1^2}, \tag{10}$$

$$\Theta_{RFe}^2 = A_1 h_{21}^2 G, \tag{11}$$

$$\Theta_R = A_2 G, \tag{12}$$

where the coefficients are

$$A_1 = \frac{4\mu_B^2}{9k_B^2}S_1(S_1+1), \tag{13}$$

$$A_2 = \frac{2Z_{22}A_{22}}{3k_B} = \frac{2\mu_B}{3k_B}h_{22}. \tag{14}$$

The Curie temperature of compounds with a zero magnetic moment of the rare-earth sublattice ($\Theta_R = 0$, $\Theta_{RFe} = 0$) is found from the condition

$$T_{C0} = \Theta_0. \tag{15}$$

The goal of our study was to determine the exchange fields and derive the dependence of the Curie temperatures on the de Gennes factor, as well as to find the exchange fields experienced by an RE ion from both the other RE ions and the Fe sublattice. To do this, let us derive the dependence of the Curie temperature of a compound with sublattices of RE and Fe ions on the de Gennes factor.

After squaring relation (9) and making some algebraic transformations, we come to the following expression taking into account the variation of the Curie temperature T_C in an RE compound with the RE sublattice magnetic moment $M_2 \neq 0$ compared to the Curie temperature T_{C0} of a similar compound whose M_2 is zero:

$$\frac{T_C\Delta T_C}{G} = A_1 h_{21}^2 + A_2\Delta T_C, \tag{16}$$

where

$$\Delta T_C = T_C - T_{C0}. \tag{17}$$

The obvious merit of Eq. (16) derived first in [5] (see also [18]) is the explicit dependence of the Curie temperature on the de Gennes factor and the possibility of determining the exchange fields acting on RE ions from both the Fe sublattice (exchange parameter h_{21}) and the surrounding RE ions (parameter A_2).

Figures 3 and 4 display plots of the quantity $T_C\Delta T_C/G$ as a function of $\Delta T_C = T_C - T_{C0}$ derived from

our data for the $R\mathrm{Fe}_{11}\mathrm{Ti}$ and $R_2\mathrm{Fe}_{17}$ compounds and their hydrides and nitrides, with the Curie temperatures of lutetium compounds ($\mathrm{LuFe}_{11}\mathrm{Ti}$, $\mathrm{Lu}_2\mathrm{Fe}_{17}$) substituted for T_{C0}. It is known that the 4*f* electron shell of the Lu^{3+} ion has no magnetic moment because of its being completely filled ($4f^{14}5s^25p^65d^16s^2$). Therefore, in our case, the Lu compounds model the iron sublattice magnetization in the whole series of RE compounds of the type under consideration. Figure 4 also shows the same dependences derived from the data in [3] for $R_2\mathrm{Fe}_{17}$ compounds in which carbon was inserted into the lattice.

As is evident from Figs. 3 and 4, the experimental points derived from the Curie temperature data for the compounds under study fit well to a linear relation $T_C\Delta T_C/G = f(\Delta T_C)$ in full agreement with Eq. (16), which indicates the constancy of the exchange parameters h_{21} and h_{22} in the series of similar compounds and the existence of noticeable exchange coupling between rare-earth ions because $A_2 \neq 0$. The intercept of these straight lines with the vertical axis and the slope of the $T_C\Delta T_C/G = f(\Delta T_C)$ straight line permit one to determine the parameters h_{21} and A_2 using Eq. (16).

Equations (10)–(14) can now be used to calculate the effective exchange fields h_{21}, h_{11}, and h_{22} acting on the ion spins in sublattices 1 and 2; the coefficients N_{11}, N_{21}, and N_{22} of the molecular fields acting on the magnetic moments of these ions are found from the relations [7]

$$N_{11} = \frac{2h_{11}}{N_1\mu_B}\left(\frac{g_1-1}{g_1}\right)^2, \quad N_{22} = \frac{2h_{22}}{N_2\mu_B}\left(\frac{g_2-1}{g_2}\right)^2, \quad (18)$$

$$N_{21} = \frac{2h_{21}}{N_1\mu_B}\frac{(g_1-1)(g_2-1)}{g_1g_2}. \quad (19)$$

The coefficient N_{22} can be derived from the parameter h_{22} using Eq. (14), and coefficient N_{11} can be derived using Eqs. (10) and (18). Coefficient N_{21} is determined from parameter h_{21}. Note that for the Fe sublattice we have $g_1 = 2$; for R = Gd, whose orbital angular momentum $L = 0$, we have $g_2 = 2$, and for RE ions with a nonzero angular momentum, we have $g_2 \neq 0$. The coefficients N_{11}, N_{21}, and N_{22} define the molecular fields H_1 and H_2 acting on the magnetic moments of the iron and RE ions, respectively, and can be found from the relations

$$H_1 = N_{11}M_1 + N_{12}M_2, \quad (20)$$

$$H_2 = N_{21}M_1 + N_{22}M_2, \quad (21)$$

where M_1 is the magnetization of the Fe sublattice and M_2 is the magnetization of the RE ion sublattice.

The results of the calculations are summed up in Tables 1 and 2. An analysis of the results thus obtained permits the following conclusions:

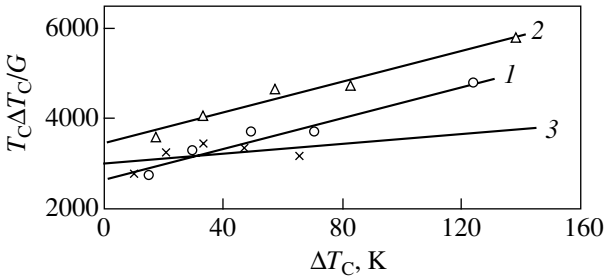

Fig. 3. $T_C\Delta T_C/G$ plotted vs. ΔT_C for (*1*) $R\mathrm{Fe}_{11}\mathrm{Ti}$, (*2*) $R\mathrm{Fe}_{11}\mathrm{TiH}$, and (*3*) $R\mathrm{Fe}_{11}\mathrm{TiN}$.

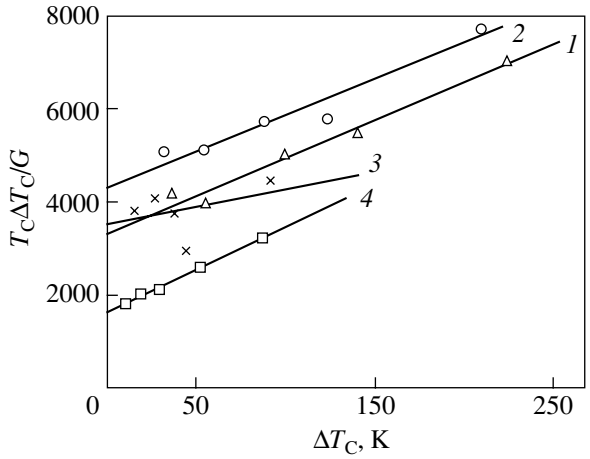

Fig. 4. $T_C\Delta T_C/G$ plotted vs. ΔT_C for (*1*) $R_2\mathrm{Fe}_{17}$, (*2*) $R_2\mathrm{Fe}_{17}\mathrm{H}_3$, (*3*) $R_2\mathrm{Fe}_{17}\mathrm{N}_2$, and (*4*) $R_2\mathrm{Fe}_{17}\mathrm{C}$.

(1) Introduction of hydrogen atoms into the $R\mathrm{Fe}_{11}\mathrm{Ti}$ lattices brings about an increase in the intersublattice exchange field h_{21} (by 7.5% per hydrogen atom). The increase in h_{21} induced by hydrogen incorporation in the $R_2\mathrm{Fe}_{17}$ compounds is smaller (4.5% per hydrogen atom).

(2) By contrast, insertion of nitrogen into the $R\mathrm{Fe}_{11}\mathrm{Ti}$ and $R_2\mathrm{Fe}_{17}$ lattices entails a decrease in the intersublattice exchange field h_{21} (by 6.8 and 4% per nitrogen atom, respectively).

(3) The exchange interactions between ions on the RE sublattice decrease upon incorporation of hydrogen and nitrogen, the latter producing a stronger effect. Indeed, the $R\mathrm{Fe}_{11}\mathrm{Ti}$ compounds exhibit a weak decrease in h_{22} (by 1%) for the $R\mathrm{Fe}_{11}\mathrm{TiH}$ hydrides and a strong decrease (by 68%) for the $R\mathrm{Fe}_{11}\mathrm{TiN}$ nitrides. Hydrogenation of the $R_2\mathrm{Fe}_{17}$ compounds reduces h_{22} by 2%, whereas nitrogenation brings about a decrease by 26%.

(4) Incorporation of carbon into the $R_2\mathrm{Fe}_{17}$ lattices reduces the h_{21} exchange field considerably (by 32% per carbon atom), while the exchange interaction between ions on the RE sublattice exhibits even an

enhancement upon carbon insertion (h_{22} increases by 11%).

The results of calculations conducted for the $R\mathrm{Fe}_{11}\mathrm{Ti}$ compounds under the assumption that exchange interactions between ions on the rare-earth sublattice can be neglected are the same in the case of hydrogenation but are different in the case of nitrogenation (h_{21} decreases by 17%). The calculations carried out for $R_2\mathrm{Fe}_{17}$ produced the following results: hydrogenation increases h_{21} by 1.5%, and nitrogenation reduces h_{21} by 12%, while insertion of carbon reduces this field by 35%. Thus, the interactions between ions on the rare-earth sublattice must be taken into account both for obtaining accurate numerical values of the *R*–Fe exchange coupling and describing the variation of these interactions in the hydrides, nitrides, and carbides of the $R_2\mathrm{Fe}_{17}$ compounds.

Thus, we established that incorporation of light atoms (H, N) into the lattices of the $R\mathrm{Fe}_{11}\mathrm{Ti}$ and $R_2\mathrm{Fe}_{17}$ compounds brings about a substantial increase in the Curie temperature T_C, an enhancement of the Fe–Fe exchange coupling, and a decrease in the *R*–*R* interactions in magnitude; it also results in the *R*–Fe intersublattice interaction increasing under hydrogenation and decreasing under nitrogenation, which can be well accounted for by the attendant variations in the electronic structure of these compounds and in the indirect exchange interactions. According to the theory taking into account spin fluctuations [19], the Curie temperature of band ferromagnets is inversely proportional to the density of states in the subbands near the Fermi level, $N_\uparrow(E_F)$ and $N_\downarrow(E_F)$. The increase in the lattice parameters observed to occur when interstitial atoms (hydrogen, nitrogen) are incorporated gives rise to a decrease in the degree of wave-function hybridization between the 3*d* electrons of Fe atoms and the 5*d* electrons of RE metal atoms and entails a decrease in both the densities of states $N_\uparrow(E_F)$ and $N_\downarrow(E_F)$ [20–23]. This decrease in the degree of hybridization apparently plays an important part in suppressing the spin fluctuations and the increase in the Curie temperature; the main contributions to the latter are due to exchange interactions between ions on the iron sublattice (the exchange field h_{11}), whose magnetism is considerably enhanced by incorporating interstitial light atoms [20] (see Table 3). Because of the localized character of the RE ion 4*f* subshell, the exchange interaction in *R*–Fe compounds between the 4*f* and 3*d* spins is essentially indirect and is mediated by polarized 5*d* electrons, which are hybridized with the 3*d* electrons of Fe [10, 22]. Hydrogenation fills the 3*d* band and magnetizes the 5*d* electrons of the RE atom due to the enhanced polarization of the 3*d* electrons of the transition metal. The contribution of delocalized electrons to the magnetism of hydrogenated compounds increases, thereby increasing the intersublattice exchange field h_{21}, the effect observed by us (Tables 1, 2).

By contrast, insertion of nitrogen and carbon atoms weakens the intersublattice exchange coupling in intermetallic compounds of the 4*f* and 3*d* transition metals of the type $R\mathrm{Fe}_{11}\mathrm{Ti}$ and $R_2\mathrm{Fe}_{17}$. The results obtained by us indicate a weakening of exchange interaction h_{21} in $R\mathrm{Fe}_{11}\mathrm{Ti}$ and $R_2\mathrm{Fe}_{17}$ under nitrogenation and agree with the inelastic neutron scattering experiments conducted on $\mathrm{GdFe}_{11}\mathrm{Ti}$ and $\mathrm{Gd}_2\mathrm{Fe}_{17}$ [24, 25], as well as with the theoretical calculations carried out in [25] in the local spin density approximation within the LMTO theory, which also revealed a decrease in the Gd–Fe exchange interactions under nitrogenation. Interpretation of this result should take into account a number of factors, namely, (i) the volume effect associated with the increase in atomic volume and in the Fe–Fe and *R*–Fe interatomic distances brought about by the presence of interstitial atoms, (ii) the enhanced magnetism of the iron sublattice, (iii) the elastic strains created around an interstitial atom close in size to the octahedral voids (as shown by neutron diffraction measurements [3], at the above-mentioned concentrations, only the octahedral voids are filled), and (iv) the change in the local electron concentration around an interstitial atom (the chemical effect) [25, 26]. It should also be pointed out that, in the $R_2\mathrm{Fe}_{17}$ lattices, the octahedral positions and, hence, the interstitial atoms lie in the basal plane and surround the RE ion, whereas in the $R\mathrm{Fe}_{11}\mathrm{Ti}$ lattices they are arranged along the tetragonal axis *c* (which is perpendicular to the basal plane) both above and below the RE ion.

It can be maintained that the nitrogenation-induced decrease in h_{21} is due to the chemical effect, in which attraction between the nitrogen and RE ion valence orbitals and covalent bonding between the RE and N atoms play the main role [27, 28]. This effect should obviously entail a decrease in the concentration of 5*d* delocalized electrons, which mediate the exchange interaction between the localized RE 4*f* shell and Fe atoms, and, hence, a decrease in the exchange field h_{21}. This mechanism is the most efficient in carbides of the $R_2\mathrm{Fe}_{17}$ compounds.

Exchange interactions between RE ions (field h_{22}) decrease under hydrogenation and nitrogenation (see Tables 1, 2). The $R_2\mathrm{Fe}_{17}\mathrm{C}$ carbides, however, exhibit an increase in h_{22}, which apparently should be assigned to an additional indirect exchange between RE atoms via the carbon 2*p* electrons.

Thus, the analysis of the experimental data obtained shows that it is the specific features in the structure of the outer electronic shell of the interstitial atom that are responsible for the changes in the exchange interactions h_{11}, h_{21}, and h_{22}. Incorporation of interstitial atoms produces additional delocalized band electrons in the 3*d*–5*d* hybridized band in the hydrides and brings about their decrease in number in the nitrides and carbides. This factor affects the exchange interactions because of changes in the concentration and density of the delocal-

ized band electrons, which come primarily from the rare-earth $5d^16s^2$ valence electrons, $4s^2$ valence electrons, and iron $3d$ hybridized electrons.

ACKNOWLEDGMENTS

The authors are indebted to K.P. Skokov for preparing the starting samples and to V.N. Verbetskiĭ and A.A. Salamova for preparing the hydrides and nitrides.

This study was supported by the Russian Foundation for Basic Research (project no. 02-02-16523) and the federal program of support for leading scientific schools (project no. 00-15-96695).

REFERENCES

1. S. A. Nikitin, *Magnetic Properties of Rare-Earth Metals and Their Alloys* (Mosk. Gos. Univ., Moscow, 1989).
2. K. P. Belov, *Rare-Earth Magnets and Their Application* (Nauka, Moscow, 1980).
3. H. Fujii and H. Sun, in *Handbook of Magnetic Materials*, Ed. by K. H. J. Buschow (North-Holland, Amsterdam, 1995), Vol. 9, Chap. 3, pp. 304–404.
4. S. A. Nikitin, V. A. Vasil'kovskiĭ, N. M. Kovtun, *et al.*, Zh. Éksp. Teor. Fiz. **68**, 577 (1975) [Sov. Phys. JETP **41**, 285 (1975)].
5. S. A. Nikitin and A. M. Bisliev, Vestn. Mosk. Gos. Univ., No. 2, 195 (1975).
6. S. A. Nikitin and A. M. Bisliev, Fiz. Tverd. Tela (Leningrad) **15** (12), 3681 (1973) [Sov. Phys. Solid State **15**, 2451 (1973)].
7. K. H. J. Buschow, in *Handbook of Supermagnets: Hard Magnetic Materials*, Ed. by G. J. Long and F. Grandjean (Kluwer Academic, Dordrecht, 1991), Chap. 4, pp. 49–67, NATO Adv. Study Inst. Ser., Ser. C, Vol. 331.
8. E. Belorizky, M. A. Fremy, J. P. Gavigan, *et al.*, J. Appl. Phys. **61** (8), 3971 (1987).
9. B.-P. Hu, H.-S. Li, J. P. Gavigan, and J. M. D. Coey, J. Phys.: Condens. Matter **1**, 755 (1989).
10. M. Brooks, O. Eriksson, and B. Johansson, J. Phys.: Condens. Matter **1**, 5861 (1989).
11. I. S. Tereshina, S. A. Nikitin, T. I. Ivanova, and K. P. Skokov, J. Alloys Compd. **275–277**, 625 (1998).
12. S. A. Nikitin, I. S. Tereshina, V. N. Verbetsky, and A. A. Salamova, J. Alloys Compd. **316**, 46 (2001).
13. S. A. Nikitin, E. A. Ovchenkov, I. S. Tereshina, *et al.*, Metally, No. 2, 111 (1999).
14. P. De Gennes, J. Phys. Radium **23** (8–9), 510 (1962).
15. S. A. Nikitin, Zh. Éksp. Teor. Fiz. **77** (1), 343 (1979) [Sov. Phys. JETP **50**, 176 (1979)].
16. K. P. Belov and S. A. Nikitin, Phys. Status Solidi **12**, 453 (1965).
17. L. Néel, in *Antiferromagnetism* (Inostrannaya Literatura, Moscow, 1956), pp. 56–84.
18. A. S. Andreenko and S. A. Nikitin, Usp. Fiz. Nauk **167** (6), 605 (1997) [Phys. Usp. **40**, 581 (1997)].
19. P. Mohn and E. P. Wohlfarth, J. Phys. F: Met. Phys. **17** (12), 2421 (1987).
20. O. Isnard, S. Miraglia, D. Fruchart, *et al.*, Phys. Rev. B **49** (22), 15692 (1994).
21. S. S. Jaswal, Phys. Rev. B **48** (9), 6156 (1993).
22. G. Givord and D. Courtois, J. Magn. Magn. Mater. **196–197**, 684 (1999).
23. S. Jaswal, W. Yelon, G. Hadjipanayis, *et al.*, Phys. Rev. Lett. **67** (5), 644 (1991).
24. M. Loewenhaupt, P. Tils, D. Middleton, *et al.*, J. Magn. Magn. Mater. **139**, 151 (1994).
25. T. Beuerle, M. Liebs, K. Hummler, and M. Fahnle, J. Magn. Magn. Mater. **132**, L1 (1994).
26. Y. P. Li and J. M. D. Coey, Solid State Commun. **81** (6), 447 (1992).
27. A. Sakuma, J. Phys. Soc. Jpn. **61** (11), 4119 (1992).
28. V. K. Grigorovich, *Metal Bonding and Structure of Metals* (Nauka, Moscow, 1988).

Translated by G. Skrebtsov

Physics of the Solid State, Vol. 45, No. 10, 2003, pp. 1952–1956. Translated from Fizika Tverdogo Tela, Vol. 45, No. 10, 2003, pp. 1857–1861.

MAGNETISM AND FERROELECTRICITY

Electrical and Resonance Properties of Magnetically Inhomogeneous $La_{0.775}Sr_{0.225}MnO_{3-\delta}$ Films

A. I. Tovstolytkin, A. N. Pogorily, I. V. Lezhnenko, A. I. Matviyenko, D. I. Podyalovski, and V. P. Kravchik

Institute of Magnetism, National Academy of Sciences of Ukraine, Kiev, 03142 Ukraine

e-mail: atov@imag.kiev.ua

Received December 17, 2002; in final form, March 27, 2003

Abstract—Electrical properties and magnetic-resonance spectra are studied in $La_{0.775}Sr_{0.225}MnO_{3-\delta}$ thin films obtained on $SrTiO_3$ single-crystal substrates through magnetron sputtering. Below 250 K, the essential influence of the intensity of an electric current flowing through a film on the electrical resistance of the sample is observed. It is experimentally shown that as the current density is increased in the low-temperature range, the semiconducting conduction transforms into metallic conduction. Arguments are advanced in favor of the hypothesis that the strong sensitivity of the film properties to external factors is caused by the coexistence of ferromagnetic metallic and charge- or orbital-ordered phases in a sample. © *2003 MAIK "Nauka/Interperiodica".*

1. INTRODUCTION

Unremitting attention has been given to substituted manganites $La_{1-x}A_xMnO_3$ (*A* is an alkaline-earth element) due to their unusual properties and the variety of types of ordering observed with variation of the composition, temperature, or pressure [1, 2]. Complexity in the electronic and magnetic phase diagrams of manganites is caused by strongly interacting spin, charge, and orbital subsystems; the key role is played by manganese ions of variable valence [2, 3]. Under certain conditions, the energies responsible for the formation of different phases become comparable and an inhomogeneous state characterized by the presence of various phases becomes more favorable in comparison to the homogeneous state [2–4]. Due to the delicacy of the energy balance, the behavior of the material becomes very sensitive to external factors (magnetic and electric fields, mechanical stresses, etc.) and can be changed radically under their action.

For a long period of time (beginning from the mid-1950s), the specific features of these materials were interpreted within the concept of double exchange between Mn^{3+} and Mn^{4+} ions, which favors the delocalization of electrons and stabilizes the ferromagnetic ordering [5]. However, the latest studies have demonstrated that such an approach is oversimplified and that the electron–lattice interaction arising from the Jahn–Teller instability and orbital ordering of 3*d* electrons of Mn^{3+} ions is of great importance [2, 3, 6]. The essential effect of the crystal lattice on the formation of the properties of the electron subsystem has been emphasized in a number of theoretical and experimental studies [2, 6, 7]. Theoretical calculations show that uniform compression of a crystal lattice increases the probability of electron transfer between adjacent sites and favors stabilization of the ferromagnetic metallic state [6]. However, biaxial stresses, occurring, e.g., in an epitaxial film with a lattice parameter different from that of the substrate, strengthen the tendency of electrons to localize. In [8], from a theoretical study on the stability of ferromagnetic metallic state, it was concluded that increased biaxial stresses cause an additional ordering of the Mn ion orbitals, which, in turn, favors the stabilization of an insulating antiferromagnetic state.

The results of Experimental studies performed mainly on epitaxial $La_{1-x}Ca_xMnO_3$ films are in qualitative agreement with theoretical calculations [9–12]. In [9], it was shown that ultrathin (down to 8 nm) $La_{0.73}Ca_{0.27}MnO_3$ films on $SrTiO_3$ substrates are characterized by a weakened magnetic moment, a lower Curie temperature, and an increased electrical resistance (in comparison to that of a bulk sample). Combined studies of the structural, electrical, magnetic, and resonance properties of epitaxial $La_{2/3}Ca_{1/3}MnO_3$ films grown on $SrTiO_3$ substrates were performed in [10]. The experimental results convincingly demonstrated that films of thickness $t \le 50$ nm have a lower T_C, a reduced magnetic moment, and higher electrical resistance. Studies of nuclear magnetic resonance made it possible to separate the phases with different magnetic and electrical properties. It was shown that films simultaneously contain ferromagnetic metallic, ferromagnetic insulating, and nonferromagnetic insulating regions. Recent studies of biaxially stressed $La_{2/3}Ca_{1/3}MnO_3$ films showed that these films possess anisotropic electrical properties, nonlinear current–voltage characteristics, and weakened ferromagnetism and show evidence of antiferromagnetic ordering [11]. It was also shown in [11] that, with increasing the current density, the system transforms into a highly con-

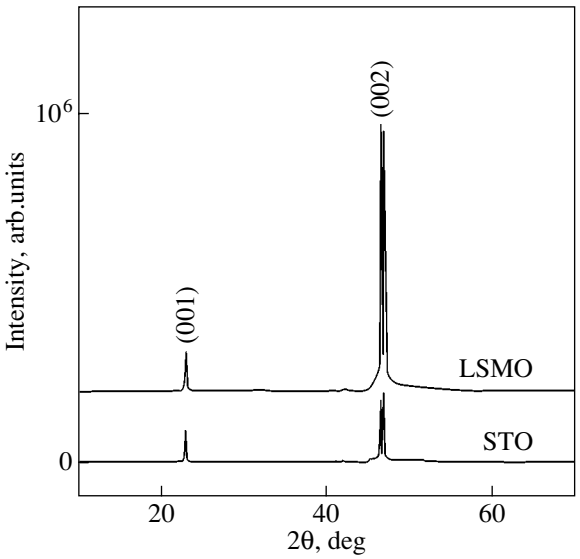

Fig. 1. X-ray diffraction curves of an $La_{0.775}Sr_{0.225}MnO_{3-\delta}$ film (LSMO) and an $SrTiO_3$ substrate (STO).

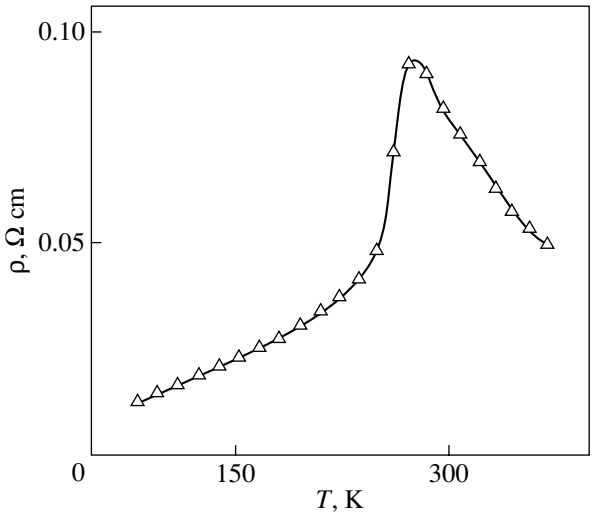

Fig. 2. Temperature dependence of resistivity of LSMO measured at a stabilized current of 5 mA.

ducting state, which is of particular interest for applications of such films in magnetoelectronic devices.

Much fewer studies are devoted to the effect of biaxial stresses on the properties of films of the $La_{1-x}Sr_xMnO_3$ system. Films of this system with x = 0.3 and 0.5 obtained on perovskite substrates with various lattice parameters were studied in detail in [13]. It was shown that the stresses created by substrates could transform the ferromagnetic metallic state into an antiferromagnetic insulating state, which correlates with theoretical calculations [8]. The results of studies of the magnetic, electrical, and crystallographic properties of films with $0.15 \le x \le 0.23$ grown on fluorite and perovskite substrates are presented in [14]. A strong influence of substrate structure on the properties of $La_{1-x}Sr_xMnO_3$ films was attributed to the formation of a ferromagnetic–antiferromagnetic two-phase state. In [15], weak stability of the ferromagnetic metallic phase in the heterostructure $La_{0.80}Sr_{0.20}MnO_3/SrTiO_3$ with respect to external effects was reported; this manifests itself, in particular, in a photoinduced metal–semiconductor transition.

In this paper, we present experimental data which demonstrate an extremely strong dependence of conductivity of $La_{0.775}Sr_{0.225}MnO_{3-\delta}$ films, deposited on $SrTiO_3$ substrates, on the intensity of the electric current flowing through them. It will be shown that the origin of the high sensitivity of the film properties to external factors can be a two-phase magnetic state, the existence of which is confirmed by studies of magnetic-resonance spectra.

2. EXPERIMENTAL

Films $La_{0.775}Sr_{0.225}MnO_{3-\delta}$ (LSMO) 270 nm thick were obtained through magnetron sputtering on single-crystal $SrTiO_3$ substrates oriented in the (001) plane. The target for the preparation of thin-film samples was synthesized by a standard solid-phase reaction [16, 17]. We used films obtained at a substrate temperature of 880°C in an Ar (40%)–O_2 (60%) atmosphere. The gas pressure in the sputtering was 10^{-2} Torr. After preparation, the films were annealed for 6 h at 750°C. X-ray diffraction studies were performed on a DRON 3M diffractometer (CuK_α radiation). The electrical resistance was measured by a dc four-probe method. Measurements of the resistance could be made at a fixed value of the current in the range from 0.01 to 10 mA. A Radiopan spectrometer with a working frequency of $\nu \cong 9.2$ GHz was used to study magnetic-resonance spectra.

3. RESULTS AND DISCUSSION

The x-ray diffraction patterns of one of the obtained films and an $SrTiO_3$ substrate shown in Fig. 1 are indicative of a single-phase state and epitaxial growth of LSMO. It is seen that the film has a *c*-axial texture characterized by high-intense (00*l*) peaks (pseudocubic representation). The intensity A of the (011) and (111) peaks does not exceed 0.8% of $A_{(002)}$. The (002) peak is split both for the film and for the substrate. The diffraction pattern of LSMO does not contain any reflections different from those of the perovskite phase.

The temperature dependence of resistivity ρ of a film measured at a fixed value of the current I = 5 mA is shown in Fig. 2. In the low-temperature range, the value of ρ slightly grows with increasing T, which is typical of metallic-type conductivity; then, the resistivity increases abruptly, beginning from a temperature of 250 K, and reaches a maximum at $T_p \cong 276$ K. The $\rho(T)$ curve obtained at I = 5 mA agrees with similar curves

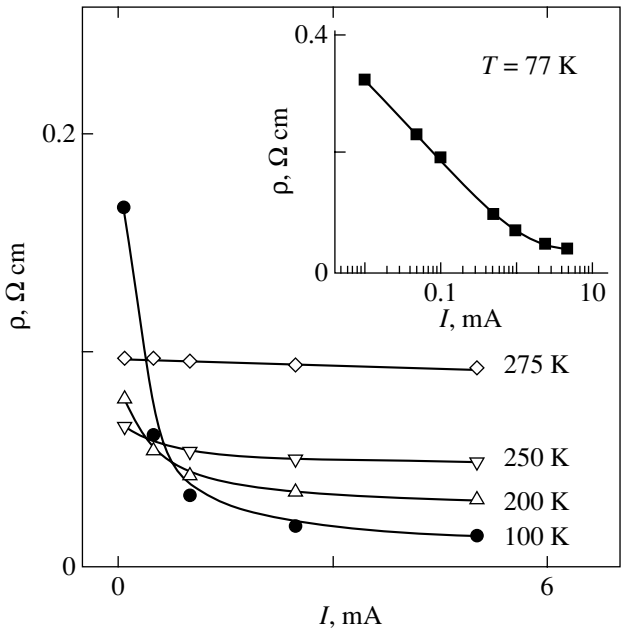

Fig. 3. Resistivity of films as a function of current intensity at various temperatures.

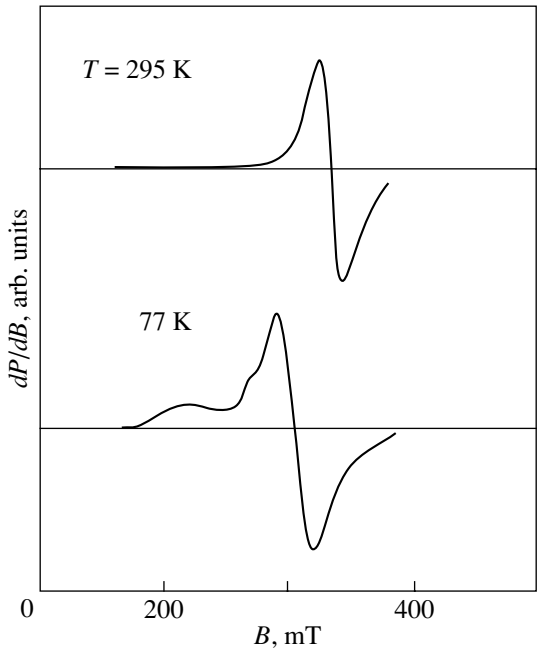

Fig. 4. Magnetic resonance spectra dP/dB at T = 77 and 295 K.

observed for bulk samples of the same composition in which the ferromagnetic metallic phase is completely dominant at low temperatures [1, 16]. However, as we showed previously [18], an decrease in the current flowing through a thin film strongly affects the resistivity, which indicates that the processes occurring in films are more complicated in comparison to those in bulk samples.

The inset to Fig. 3 shows the $\rho(I)$ curve obtained at T = 77 K. To minimize the effect of sample heating due to the electric current [19], the measurements were performed directly in liquid nitrogen. As seen from Fig. 3, a decrease in the strength of the current results in an increase in resistivity, which is particularly pronounced at small values of the current (I < 1 mA).

The curves in Fig. 3, showing the influence of temperature on the $\rho(I)$ dependence, were obtained in the following way. At room temperature, a sample was connected to a stabilized current source and the current was adjusted to a certain value. After cooling to 77 K, the resistance was measured as a function of temperature during heating. Then, the next value of the current was set and the cycle repeated. The $\rho_{T = \text{const}}(I)$ curves were plotted on the basis of the data obtained in accordance with the above procedure. As can be seen from Fig. 3, the resistivity is virtually independent of the current at T = 275 K. However, at lower temperatures ($T \le 250$ K), the $\rho(I)$ dependences noticeably deviate from a horizontal line; the degree of deviation increases significantly as the temperature and the current decrease. According to the effect of the current on resistivity, one can single out two ranges in Fig. 3, which are separated by a boundary located near I = 0.5 mA. This value of the current corresponds to the case when ρ is almost independent of T (for $T \le 250$ K), i.e., when the temperature coefficient of resistance is close to zero. For all values of I larger than 0.5 mA, the resistance gradually decreases on cooling. By contrast, for I < 0.5 mA, the resistance first drops on cooling from 275 K to ~250 K and then begins to increase with a further decrease in T. Thus, in the low-temperature range, a decrease in the current results not only in a significant increase in resistance but also in a transition from the metallic ($d\rho/dT > 0$) to the semiconducting ($d\rho/dT < 0$) type of conductivity.

Figure 4 shows the results of our study of magnetic resonance outside (at 295 K) and inside (at 77 K) the temperature range where the anomalous effect of the current on resistance takes place. At T = 295 K, the absorption spectrum dP/dB obtained with the field parallel to the film surface is represented by a symmetrical line. The integrated curve is well described by a Lorentzian with parameters corresponding to the paramagnetic state of LSMO [4, 20] (resonance field $B_r \cong 331$ mT, line width $w \cong 24$ mT). The main feature of magnetic resonance at T = 77 K is the occurrence of two well-resolved absorption lines. The integrated $P(B)$ curve shown in Fig. 5 is well described by a superposition of two Lorentzian lines with parameters $B_{r1} \cong 239$ mT, $w_1 \cong 70$ mT and $B_{r2} \cong 301$ mT, $w_2 \cong 53$ mT, which is indicative of the occurrence of two magnetic components. Since the conditions of magnetic resonance in a magnetically ordered phase require a smaller external field than in a paramagnetic phase (for materials with magnetic order,

the resonance field is the sum of the external field and the effective internal field), the first line obviously corresponds to the ferromagnetic phase. The position of the second line is slightly shifted relative to the resonance line of the higher temperature paramagnetic phase. However, the data obtained do not allow us to unambiguously determine whether this shift is caused by the magnetic order that might exist in the second phase or is a result of the magnetic field induced by the first phase [20]. In any case, considered the strong correlation between conduction and the degree of magnetic order inherent in substituted manganites, one may expect the electrical characteristics of these phases to be essentially different. By comparing the data on magnetic resonance with the results of electric measurements (Fig. 2) and with the data for bulk samples [1, 16], one can assert that the ferromagnetic phase has a metallic type of conduction. The results of magnetic-resonance studies do not allow one to come to an unambiguous conclusion about the properties of the second phase; however, using all of the collected experimental data, some conclusions can be made about the origin and features of the second phase.

Nonlinear current–voltage characteristics in the samples of substituted manganites are usually associated with the tunneling of charge carriers through insulating or weakly conducting barriers (grain boundaries [21], amorphous regions [22], inclusions of insulating or weakly conducting phases [11, 19, 23], etc). However, in the films studied, not only nonlinearity in the $U(I)$ curves is observed but also dependence of the type of conductance (metallic or semiconducting) on the magnitude of the current flowing through a sample. In our opinion, the whole collection of experimental data can be explained in terms of the hypothesis that two phases with different types of conductivity exist, the amount of each phase being determined by the magnitude of the current flowing through the sample. The latest studies have shown that a similar situation takes place in manganites in the case of coexistence of metallic ferromagnetism with a phase (or phases) in which mutual ordering of the charges and/or of the orbitals of manganese ions of variable valence dominates [19, 24–26]. The possibility of formation of a mixed state of such a type in films and bulk samples of $La_{1-x}Sr_xMnO_3$ partially follows, in particular, from the results obtained in [27, 28]. In [28], magnetic and nuclear elastic neutron scattering was studied in bulk single crystals of the $La_{1-x}Sr_xMnO_3$ system, including samples with $x = 0.23$, which are very close in composition to our films. It was shown that regions with charge or orbital short-range order exist in a single crystal in the entire temperature range below T_C; i.e., these regions coexist with the ferromagnetic metallic phase. Taking into consideration that increased biaxial stresses favor the stabilization of a charge- or an orbital-ordered phase [8, 13], while a current flowing through the sample destroys this phase [2, 19, 20], the unusual properties of

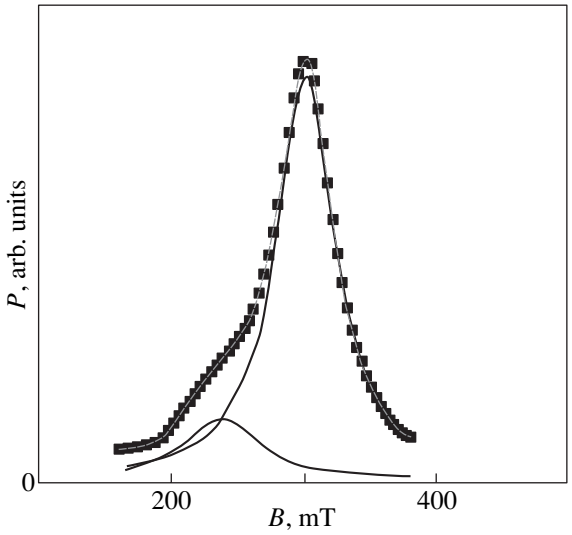

Fig. 5. Integrated magnetic resonance $P(B)$ curve at 77 K.

$La_{0.775}Sr_{0.225}MnO_{3-\delta}$ films can be easily interpreted in terms of the above hypothesis.

4. CONCLUSIONS

Thus, we have found that, at temperatures below 250 K, the conduction of $La_{0.775}Sr_{0.225}MnO_{3-\delta}$ single-crystal films essentially depends on the magnitude of the electric current; this effect becomes considerably enhanced with a decrease in temperature and in the current intensity. It has been shown that a decrease in the current intensity in the low-temperature range results not only in a sharp increase in resistance but also in a transformation from the metallic ($d\rho/dT > 0$) to the semiconducting ($d\rho/dT < 0$) type of conductivity. It was shown experimentally that the films are magnetically inhomogeneous in the low-temperature range. The results obtained can be explained in terms of the hypothesis assuming the coexistence of a ferromagnetic metallic and a charge- or orbital-ordered phase in the volume of a film; the volume fraction of each phase is determined by the current density.

ACKNOWLEDGMENTS

The authors would like to thank A. Belous and O. V'yunov (Institute of General and Inorganic Chemistry, National Academy of Sciences, Ukraine) for manufacturing the targets and help with the x-ray diffraction studies.

This study was supported by the Science and Technology Center in Ukraine, project no. 1086.

REFERENCES

1. A. A. Mukhin, V. Yu. Ivanov, V. D. Travkin, *et al.*, Pis'ma Zh. Éksp. Teor. Fiz. **68** (4), 331 (1998) [JETP Lett. **68**, 356 (1998)].

2. E. Dagotto, T. Hotta, and A. Moreo, Phys. Rep. **344** (1–3), 1 (2001).
3. V. M. Loktev and Yu. G. Pogorelov, Fiz. Nizk. Temp. **26** (3), 231 (2000) [Low Temp. Phys. **26**, 171 (2000)].
4. N. V. Volkov, G. A. Petrakovskiĭ, V. N. Vasil'ev, and K. A. Sablina, Fiz. Tverd. Tela (St. Petersburg) **44** (7), 1290 (2002) [Phys. Solid State **44**, 1350 (2002)].
5. C. Zener, Phys. Rev. **82** (3), 403 (1951).
6. A. J. Millis, T. Darling, and A. Migliori, J. Appl. Phys. **83** (3), 1588 (1998).
7. L. P. Gor'kov, Usp. Fiz. Nauk **168** (6), 665 (1998) [Phys. Usp. **41**, 589 (1998)].
8. Z. Fang, I. V. Solovyev, and K. Terakura, Phys. Rev. Lett. **84** (14), 3169 (2000).
9. H. W. Zandbergen, S. Freisem, T. Nojima, and J. Aarts, Phys. Rev. B **60** (14), 10259 (1999).
10. M. Bibes, L. Balcells, S. Valencia, *et al.***,** Phys. Rev. Lett. **87** (6), 067210 (2001).
11. J. Klein, J. B. Philipp, G. Garbone, *et al.*, Phys. Rev. B **66** (5), 052414 (2002).
12. A. P. Nosov and P. Strobel', Fiz. Met. Metalloved. **93** (3), 50 (2002).
13. Y. Konishi, Z. Fang, M. Izumi, *et al.*, J. Phys. Soc. Jpn. **68** (12), 3790 (1999).
14. O. Yu. Gorbenko, R. V. Demin, A. R. Kaul', *et al.*, Fiz. Tverd. Tela (St. Petersburg) **40** (2), 290 (1998) [Phys. Solid State **40**, 263 (1998)].
15. H. Katsu, H. Tanaka, and T. Kawai, Appl. Phys. Lett. **76** (22), 3245 (2000).
16. V. G. Bar'yakhtar, A. N. Pogorily, N. A. Belous, and A. I. Tovstolytkin, J. Magn. Magn. Mater. **207** (1–3), 118 (1999).
17. A. I. Tovstolytkin, A. N. Pogorily, S. V. Cherepov, *et al.*, Metallofiz. Noveĭshie Tekhnol. **22** (11), 23 (2000).
18. A. I. Tovstolytkin, A. N. Pogorily, I. V. Lezhnenko, *et al.*, in *Abstracts of II International Scientific Conference on Magnetic Materials and Their Application* (Belorus. Gos. Univ., Minsk, 2002), p. 71.
19. A. Guha, N. Khare, A. K. Rayhaudhuri, and C. N. R. Rao, Phys. Rev. B **62** (18), R11941 (2000).
20. F. Rivadulla, M. Freita-Alvite, M. A. Lopez-Quintella, *et al.*, J. Appl. Phys. **91** (2), 785 (2002).
21. R. Gross, L. Alff, B. Büchner, *et al.*, J. Magn. Magn. Mater. **211** (1–3), 150 (2000).
22. J.-M. Liu, G. L. Yuan, Q. Huang, *et al.*, J. Phys.: Condens. Matter **13** (1), 11 (2001).
23. A. Guha, A. K. Rayhaudhuri, A. R. Raju, and C. N. R. Rao, Phys. Rev. B **62** (9), 5320 (2000).
24. C. W. Chang, A. K. Debnath, and J. G. Lin, J. Appl. Phys. **91** (4), 2216 (2002).
25. C. N. R. Rao, A. R. Raju, V. Ponnambalam, *et al.*, Phys. Rev. B **61** (1), 594 (2000).
26. C. W. Chang and J. G. Lin, J. Appl. Phys. **90** (9), 4874 (2001).
27. J. Li, C. K. Ong, J.-M. Liu, *et al.*, Appl. Phys. Lett. **76** (8), 1051 (2000).
28. S. F. Dubinin, V. E. Arkhipov, Ya. M. Mukovskiĭ, *et al.*, Fiz. Met. Metalloved. **93** (3), 60 (2002).

Translated by A. Zalesskiĭ

Physics of the Solid State, Vol. 45, No. 10, 2003, pp. 1957–1965. Translated from Fizika Tverdogo Tela, Vol. 45, No. 10, 2003, pp. 1862–1869.

MAGNETISM AND FERROELECTRICITY

Nongyrotropic Magneto-Optical Effects in Metal–Insulator Magnetic Multilayer Thin Films

V. I. Belotelov, A. K. Zvezdin, V. A. Kotov, and A. P. Pyatakov

Institute of General Physics, Russian Academy of Sciences, ul. Vavilova 38, Moscow, 119991 Russia

e-mail: bvi@nm.ru

Received April 1, 2003

Abstract—Nongyrotropic magneto-optical effects are investigated in metal–insulator magnetic multilayer thin films. These effects manifest themselves in changes in the coefficients of transmission and reflection of electromagnetic radiation from the surface of a multilayer film due to the crossover of the magnetic structure from an antiferromagnetic configuration to a ferromagnetic configuration. The nongyrotropic magneto-optical effect observed in reflected light is analyzed theoretically. It is assumed that the multilayer structure is exposed to radiation of a monochromatic plane wave polarized along the direction of magnetization of the film. The magneto-optical effect is described in terms of the permittivity tensor of the multilayer medium, which depends only on the light frequency. The Boltzmann kinetic equation is treated with allowance made for spin-dependent electron scattering both inside conducting layers and at rough interfaces. Using an Fe/C multilayer as an example, it is demonstrated that the nongyrotropic magneto-optical effect is equal in order of magnitude to the equatorial Kerr effect or other strong magneto-optical effects. © *2003 MAIK "Nauka/Interperiodica".*

1. INTRODUCTION

In recent years, considerable interest has been expressed by researchers in metallic magnetic multilayer films, especially in those exhibiting a giant magnetoresistance [1–6].

As a rule, multilayer structures consist of alternating layers of magnetic and nonmagnetic metals. Under equilibrium conditions, adjacent magnetic layers in a multilayer structure are magnetized in opposite directions, thus forming an antiparallel or so-called antiferromagnetic configuration. In an external magnetic field, the magnetic state of a multilayer sample can change from an antiparallel (antiferromagnetic) configuration to a parallel (ferromagnetic) configuration in which the magnetization vectors in all magnetic layers are collinear to each other. A change in the magnetic state of the multilayer film brings about variations in the conditions of spin-dependent electron scattering in the bulk of conducting layers and at roughnesses of the boundaries (interfaces) between the layers. In turn, this leads to a change in the conductivity of the sample. The effect observed in this case can be significant. For example, the relative change in the resistivity of Co/Cu and Fe/Cr multilayers at appropriate parameters exceeds 50% [2].

Apart from the giant magnetoresistance encountered in multilayer structures, the changes observed in their optical properties due to variations in the magnetic configuration of a multilayer, i.e., magneto-optical effects, have also attracted considerable research attention [7–9]. These effects differ from the well-known magneto-optical Kerr and Faraday (including strong) effects (see, for example, [8, 9]) in that the conventional magneto-optical effects are associated with magnetic gyrotropy of the medium, whereas the effects considered in the present work are not gyrotropic. This implies that the latter effects, like giant magnetoresistance, are governed by the mechanism of spin-dependent electron scattering; i.e., they are determined primarily by the diagonal elements of the permittivity tensor $\hat{\varepsilon}$ of the multilayer medium. In other words, conventional effects depend on the magneto-optical parameter Q, which is determined by the spin–orbit interaction of electrons, whereas the magneto-optical effects discussed in this work do not depend on the parameter Q (they manifest themselves to the zeroth order in Q) and arise predominantly from exchange interactions of electrons.

Nongyrotropic magneto-optical effects (NGMOE) can be used, among other processes, in noncontact probing of materials that exhibit giant magnetoresistance [10].

Jacquet and Valet [11] were the first to investigate the nongyrotropic magneto-optical effect theoretically and to confirm its existence in experiments for Fe/Cr multilayers. Uran *et al*. [12] demonstrated that this effect is clearly observed in the near-IR range and, for an Fe/Cr/Fe trilayer structure, amounts to approximately 0.5%.

Theoretical treatment of the nongyrotropic magneto-optical effect for multilayer structures has been performed in a number of works [7, 11, 13, 14]. In particular, Kubrakov *et al*. [14] theoretically analyzed the magneto-optical effect for a monochromatic electromagnetic plane wave reflected from a multilayer and

polarized along the magnetization direction. It was shown that the nongyrotropic magneto-optical effect expressed through the relative change in the intensity of reflected radiation upon the crossover from the antiferromagnetic configuration of the multilayer to the ferromagnetic configuration reaches several percent.

It can be expected that a similar effect will be observed for metal–insulator multilayer films in which nonmagnetic metal layers are replaced by insulator layers. Actually, in metal–insulator multilayer films, there also arises spin-dependent electron scattering; moreover, the spin-dependent tunneling effect manifests itself at a sufficiently small thickness of the insulator layers. In the present paper, the optical properties of these multilayer structures will be described within a theoretical approach.

The above problem has aroused widespread interest that goes far beyond the properties of multilayer film structures. The optical properties of nanocomposite materials, such as nonmagnetic dielectric or metallic media with embedded magnetic nanoclusters, have been extensively investigated in recent years [15–19]. The experimental data obtained for Cu/Al/O and CoFe/MgF granular films have demonstrated that the nongyrotropic magneto-optical effect in these materials reaches 0.8% and exceeds the magneto-optical effect in metal granular films by a factor of approximately two [15–19]. Note that these magnitudes of the nongyrotropic magneto-optical effect were obtained for nanocomposites with a high metal concentration corresponding to the percolation threshold.

In the majority of cases, the transport and optical properties of nanocomposite materials have been described in the effective-medium approximation. Within this approximation, the effective conductivity and effective permittivity of a composite are determined as functions of the corresponding quantities for each composite component [20–22]. In turn, the nanocomposite components are characterized by the same tensors of conductivity and permittivity as those used for bulk media. However, in the case of granular structures with giant magnetoresistance, in which the grain sizes do not exceed several nanometers, the conditions of applicability of this approach are violated, because the mean free path of electrons in these materials is considerably greater than the mean grain size and spin-dependent scattering and tunneling of electrons become significant. The latter circumstance is a necessary condition for the giant magnetoresistive effect to manifest itself in the material.

Thus, it is evident that the effective-medium approximation, as applied to these systems, is rather contradictory and does not offer an adequate description of their properties. To the best of our knowledge, there has been no consistent theory proposed to date to describe the optical properties of nanocomposite materials. In this respect, investigations into the optical properties of film materials with giant magnetoresistance, for which it possible to construct an adequate and verifiable theoretical model, are of considerable importance for understanding some aspects of the optics of these nanocomposites, especially those associated with spin-dependent transport.

The aim of this work is to develop a theoretical approach to the description of the optical properties of metal–insulator multilayer structures and to investigate the nongyrotropic magneto-optical effect.

2. METHOD OF DESCRIBING THE OPTICAL PROPERTIES OF A MULTILAYER MEDIUM

As was noted above, the effective-medium approach cannot be applied to the multilayer films under consideration. Hence, the permittivity tensor of a multilayer medium in this case should be calculated directly from the kinetic equation for electrons with due regard for spin-dependent scattering and tunneling. The multilayer structure can be treated as a homogeneous anisotropic medium characterized by the permittivity tensor $\hat{\varepsilon}$ [14]. Let us assume that this medium is semi-infinite and occupies a half-space $z > 0$. Under these conditions, the reflection coefficient of an *s* wave (the wave is polarized normally to the plane of incidence) can be determined from the Fresnel formula

$$R = \left| \frac{\cos\varphi - \sqrt{\varepsilon_{xx} - \sin^2\varphi}}{\cos\varphi + \sqrt{\varepsilon_{xx} - \sin^2\varphi}} \right|^2, \quad (1)$$

where $\varepsilon = 1$ is the permittivity above the multilayer (i.e., at $z < 0$) and φ is the angle of light incidence [23].

From the wave equation

$$\nabla^2\mathbf{E} + k_0^2(\varepsilon + i\mu_0 c^2\omega^{-1}\hat{\sigma})\mathbf{E} = 0, \quad (2)$$

it follows that the permittivity tensor element necessary for determining the reflection coefficient R has the form

$$\varepsilon_{xx} = \varepsilon + i\mu_0 c^2\omega^{-1}\sigma_{xx}. \quad (3)$$

Here, ε is the part of the permittivity of the multilayer structure due to the presence of insulator layers; c is the velocity of light; ω is the wave frequency; μ_0 is the permeability of free space; and σ_{xx} is the conductivity (the diagonal element of the tensor $\hat{\sigma}$) relating the longitudinal current J_x, which is averaged over the period of the structure, to the external wave field inducing this current.

Thus, the problem is reduced to determining the conductivity σ_{xx} [involved in formula (3)] from the kinetic equation with allowance made for the behavior of conduction electrons in a multilayer structure.

3. CALCULATION OF THE ELECTRICAL CONDUCTIVITY OF A MULTILAYER STRUCTURE

The metal–insulator multilayer structure is an infinite periodic (along the *z* axis) medium consisting of magnetic conductors of thickness *a* separated by insulator layers of thickness *b*. In this work, we will consider two main configurations of this structure, namely, an antiferromagnetic configuration with a period $L = 2(a + b)$ (Fig. 1a) and a ferromagnetic configuration with a period $L = (a + b)$ (Fig. 1d).

Note that the current $J_{xj}(z)$ in the *j*th conducting layer is the sum of two currents provided by electrons with spins aligned with the *x* axis (↑) and in the opposite direction (↓). At the same time, the potential energy W_j of electrons in the *j*th layer depends on the direction of the electron spin. Therefore, electrons can move in four different potentials depending on the spin orientation and the magnetic configuration of the structure (Figs. 1b–1e). The quantities characterizing the state of an electron in the layer (potential energy *W*, relaxation time τ_0, effective mass *m*) will be designated by the index *a* when the electron spin is aligned with the layer magnetization and by the index *b* when the electron spin is oriented in the opposite direction.

Let us assume that the plane electromagnetic wave $\mathbf{E}^{(i)} = \mathbf{E}_0 \exp(-i\omega t + i\mathbf{k}_0\mathbf{r})$ [where $\mathbf{k}_0 = k_0(0, \sin\varphi, \cos\varphi)$] and $\mathbf{r} = (0, y, z)$] is incident on the multilayer structure at an angle φ and the plane of incidence coincides with the *YZ* plane. The wave is polarized along the *x* axis (*s* polarization). The choice of this direction of polarization somewhat simplifies the theoretical treatment, because, in such a geometry, there appear neither currents in the direction perpendicular to the layers nor effects associated with the spin accumulation [24]. The field of this wave induces the longitudinal current $J_{xj}(z)$ in the *j*th conducting layer of the structure. In this case, the current averaged over the period of the structure

$$J_x = \frac{\sum_j \int J_{xj}(z)\,dz}{L} \qquad (4)$$

is related to the field E_0 through the Ohm law in the differential form

$$J_x = \sigma_{xx} E_0. \qquad (5)$$

Therefore, the conductivity σ_{xx} can be determined as the proportionality factor in relationship (5).

The currents $J_{xj}(z)$ can be calculated from the Boltzmann kinetic equation. Electrons are assumed to be classical particles having a coordinate **r** and a quasimomentum **p**. The nonequilibrium distribution function f_j of electrons in the *j*th layer should satisfy the Boltzmann equation, which, in the relaxation time approximation, has the form

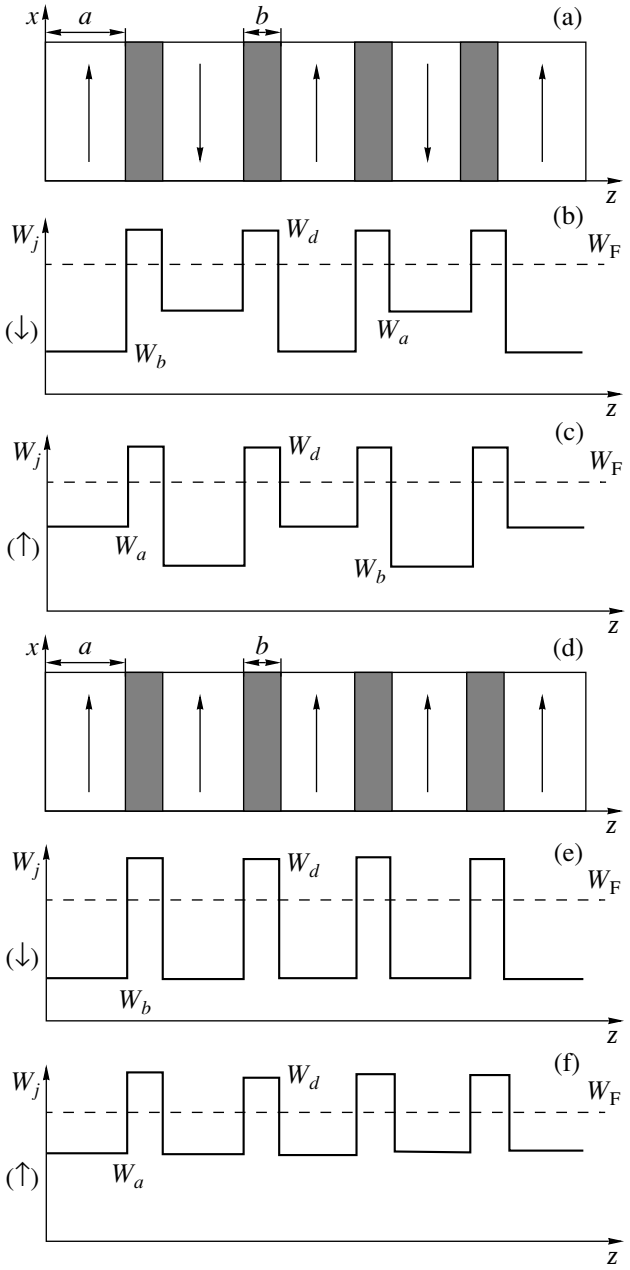

Fig. 1. Schematic diagrams of the magnetic structures of multilayer films with (a) antiferromagnetic and (d) ferromagnetic configurations and (b, c, e, f) functions of the potential energy of electrons with "upward" and "downward" spins in both cases.

$$\frac{\partial f_j}{\partial t} + (\mathbf{v}_j, \nabla_r f_j) + e(\mathbf{E}^{(i)}, \nabla_p f_j) = -\frac{f_j - f_0}{\tau_{0j}}, \qquad (6)$$

where $\mathbf{v}_j = (v_{xj}, v_{yj}, v_{zj})$ is the average velocity of electrons, τ_{0j} is the relaxation time of electrons, $e = 1.6 \times 10^{-19}$ C is the elementary charge, and f_0 is the Fermi–Dirac distribution function.

When solving the kinetic equation, we use the representation $f_j = f_0 + \Psi_j(\mathbf{v}_j, t)$ under the assumption that

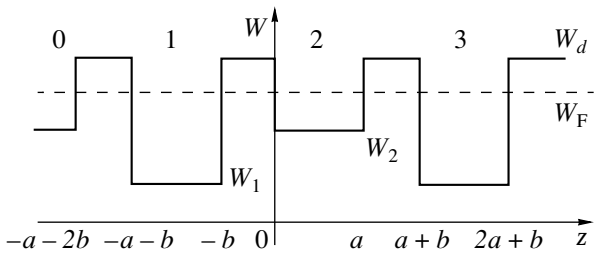

Fig. 2. Function of the potential energy of an electron in the multilayer structure with an antiferromagnetic configuration.

$\Psi_j \sim \exp(-i\omega t + ik_0 y\sin\varphi)$. Then, taking into account the relationship $|v_j|\tau_{0j}k_0 \ll 1$ (the mean free path of electrons is considerably less than the light wavelength), Eq. (6) can be transformed into the following equation for $\Psi_j(\mathbf{v}_j, t)$:

$$\frac{\partial\Psi_j}{\partial z} + \frac{1}{\tau_j v_{zj}}\Psi_j = -eE_0\frac{v_{xj}\exp(ik_0 z)}{v_{zj}}\frac{\partial f_0}{\partial W_e}. \qquad (7)$$

Here, $v_{xj} = v_j\cos\varphi_j\sin\theta_j$ and $v_{zj} = v_j\cos\theta_j$ are the projections of the velocity v_j onto the x and z axes, respectively (where φ_j and θ_j are the spherical coordinates of the velocity v_j); $\tau_j = \tau_{0j}(1 - i\omega\tau_{0j})^{-1}$; and W_e is the energy of electrons.

In order to simplify further calculations, we make two quite obvious assumptions. First, since the condition $|v_{zj}| < v_{Fj} \ll c$ is satisfied, where

$$v_{Fj} = \sqrt{\frac{2(W_e - W_j)}{m_j}}$$

is the Fermi velocity, W_j is the potential energy, and m_j is the effective mass of electrons in the jth layer, the following approximation holds: $\tau_j^{-1} + ik_0 v_{zj} \approx \tau_j^{-1}$. Second, we assume that $\partial f_0/\partial W_e \approx -\delta(W_e - W_F)$, where W_F is the Fermi energy and $\delta(W)$ is the Dirac delta function. As a result, the general solution to Eq. (7) can be represented in the form of two functions:

$$\Psi_j^+(z) = eE_0\left[C_j^+\exp\left(-\frac{z}{\tau_j|v_{zj}|}\right) - \tau_j v_{xj}\right]\delta(W_e - W_F),$$
$$v_{zj} > 0,$$
$$\Psi_j^-(z) = eE_0\left[C_j^-\exp\left(\frac{z}{\tau_j|v_{zj}|}\right) - \tau_j v_{xj}\right]\delta(W_e - W_F),$$
$$v_{zj} < 0. \qquad (8)$$

Since the multilayer has a periodic structure, it is expected that the electron distribution function will also be periodic.

Without a loss in generality, we consider the potential for the antiferromagnetic configuration (Fig. 2). The changeover to the ferromagnetic case becomes possible after the potential energies of electrons in adjacent layers are equated in the final relationships. The constants C_j^+ and C_j^- [involved in formulas (8)] necessary for calculating the functions $\Psi_j^+(z)$ and $\Psi_j^-(z)$ can be determined from the boundary conditions, which are written for four consecutive magnetic layers 0, 1, 2, and 3 in the bulk of the multilayer structure. For convenience, we change over to the coordinate system with the origin located at the interface between the first and second layers (Fig. 2). As a consequence, the boundary conditions take the form

$$\Psi_1^+(-a-b) = P_{10}\Psi_1^-(-a-b) + Q_{01}\Psi_0^+(-a-2b),$$
$$\Psi_1^-(-b) = P_{12}\Psi_1^+(-b) + Q_{21}\Psi_2^-(0),$$
$$\Psi_2^+(0) = Q_{12}\Psi_1^+(-b) + P_{21}\Psi_2^-(0),$$
$$\Psi_2^-(a) = Q_{32}\Psi_3^-(a+b) + P_{23}\Psi_2^+(a), \qquad (9)$$

where P_{jk} is the coefficient of specular reflection of electrons from the interface between the jth and kth adjacent conducting layers and Q_{jk} is the transmission coefficient accounting for the transmission of electrons through a given interface (Fig. 2). It is assumed that the roughness of each interface is described by a random function $\zeta_{jk}(\mathbf{r}_\parallel)$ such that its average over the plane is equal to zero: $\langle\zeta_{jk}(\mathbf{r}_\parallel)\rangle = 0$. The parameter $\eta = \sqrt{\langle\zeta_{jk}^2(\mathbf{r}_\parallel)\rangle}$ characterizing the roughness is assumed to be identical for all interfaces. The expressions for the coefficients P_{jk} and Q_{jk} are known as the Ziman–Soffer generalized formulas [25]

$$P_{jk} = R_{jk}\exp\left[-\left(\frac{2\eta}{\hbar}m_j v_j\cos\theta_j\right)^2\right],$$
$$Q_{jk} = (1 - R_{jk})\exp\left[-\frac{\eta^2}{\hbar^2}(m_j v_j\cos\theta_j - m_k v_k\cos\theta_k)^2\right], \qquad (10)$$

where θ_j and θ_k are the angles of incidence and refraction of electrons at the interface between the jth and kth layers, respectively.

The reflection coefficient R_{jk} can be obtained by solving the quantum-mechanical problem of electron tunneling through the potential barrier $W(x)$ between the jth and kth layers, which depends on the electron spin orientation (Fig. 2). Hence, the reflection coefficient R_{jk} can be represented by the relationship

$$R_{jk} = \left|\frac{(\kappa_j\kappa_k + \kappa^2)\sinh(\kappa a) + i\kappa\cosh(\kappa a)(\kappa_j - \kappa_k)}{(\kappa_j\kappa_k - \kappa^2)\sinh(\kappa a) + i\kappa\cosh(\kappa a)(\kappa_j + \kappa_k)}\right|, \qquad (11)$$

where

$$\kappa_j = \sqrt{\frac{2m_j}{\hbar^2}(W_e - W_j)}\cos\theta_j,$$

$$\kappa_k = \sqrt{\frac{2m_k}{\hbar^2}(W_e - W_k)}\cos\theta_k,$$

$$\kappa = \sqrt{\frac{2m_j}{\hbar^2}\{(W_e - W_j)\sin^2\theta_j + W_d - W_e\}}$$
$$= \sqrt{\frac{2m_k}{\hbar^2}\{(W_e - W_k)\sin^2\theta_k + W_d - W_e\}},$$

and W_d is the potential barrier height for electrons in the dielectric. Note that the angles θ_j and θ_k must obey the refraction law

$$\frac{\sin\theta_j}{\sin\theta_k} = \sqrt{\frac{W_e - W_k}{W_e - W_j}}. \quad (12)$$

For $W_j < W_k$, there exists a critical angle θ_j of incidence such that, if the angles of incidence are greater than the critical angle, there occurs total external reflection; i.e., $R_{jk} = 1$ and $Q_{jk} = 0$.

The periodicity of the structure and symmetry considerations make it possible to obtain the following obvious relationships for the quantities $\Psi_j^+(z)$, $\Psi_j^-(z)$, P_{jk}, and Q_{jk}:

$$\Psi_1^+(-a-b) = \Psi_1^-(-b), \quad \Psi_1^-(-a-b) = \Psi_1^+(-b),$$
$$\Psi_0^+(-a-2b) = \Psi_2^-(0), \quad \Psi_2^-(0) = \Psi_2^+(a),$$
$$\Psi_2^+(0) = \Psi_2^-(a), \quad (13)$$
$$P_{10} = P_{12}, \quad P_{21} = P_{23}, \quad Q_{01} = Q_{21},$$
$$Q_{12} = Q_{32}.$$

According to these relationships, the sought distribution functions can be derived using only two boundary conditions:

$$\Psi_1^-(-b) = P_{12}\Psi_1^-(-a-b) + Q_{21}\Psi_2^-(0),$$
$$\Psi_2^-(a) = Q_{12}\Psi_1^-(-a-b) + P_{21}\Psi_2^-(0). \quad (14)$$

Substitution of expressions (8) into formulas (14) gives the system of equations

$$\begin{bmatrix} \exp\left(-\frac{b}{\tau_1 v_{z1}}\right) - P_{12}\exp\left(-\frac{a+b}{\tau_1 v_{z1}}\right) & -Q_{21} \\ Q_{12}\exp\left(-\frac{a+b}{\tau_1 v_{z1}}\right) & P_{21} - \exp\left(\frac{a}{\tau_2 v_{z2}}\right) \end{bmatrix}$$
$$\times \begin{bmatrix} C_1^- \\ C_2^- \end{bmatrix} = \begin{bmatrix} \tau_1 v_{x1}(1-P_{12}) - \tau_2 v_{x2} Q_{21} \\ -\tau_2 v_{x2}(1-P_{21}) - \tau_1 v_{x1} Q_{12} \end{bmatrix}. \quad (15)$$

By solving this system of equations, we obtain the constants C_1^- and C_2^- in the following form:

$$C_1^- = \frac{(\tau_1 v_{x1}(1-P_{12}) - \tau_2 v_{x2} Q_{21})(P_{21} - \exp(a/\tau_2 v_{z2})) + Q_{21}(-\tau_2 v_{x2}(1-P_{21}) + \tau_1 v_{x1} Q_{12})}{\exp(-(a+b)/\tau_1 v_{z1})[Q_{12}Q_{21} - (P_{12} - \exp(a/\tau_1 v_{z1}))(P_{21} - \exp(a/\tau_2 v_{z2}))]},$$
$$C_2^- = \frac{(\tau_2 v_{x2}(1-P_{12}) - \tau_1 v_{x1} Q_{12})(P_{12} - \exp(a/\tau_1 v_{z1})) + Q_{12}(-\tau_1 v_{x1}(1-P_{12}) + \tau_2 v_{x2} Q_{21})}{[Q_{12}Q_{21} - (P_{12} - \exp(a/\tau_1 v_{z1}))(P_{21} - \exp(a/\tau_2 v_{z2}))]} \quad (16)$$

The constants C_1^+ and C_2^+ are related to the constants C_1^- and C_2^- as follows:

$$C_1^+ = C_1^-\exp\left(-\frac{a+2b}{\tau_1 v_{z1}}\right),$$
$$C_2^+ = C_2^-\exp\left(\frac{a}{\tau_2 v_{z2}}\right). \quad (17)$$

Upon substituting formulas (16) and (17) into relationships (8), we obtain the sought distribution functions.

Knowing the electron distribution functions and using the expressions taken from [26, 27], we determine the currents $J_{xj}(z)$ in conducting layers:

$$J_{xj}(z) = \frac{e}{4\pi}\int_0^\infty \rho_j v_j dW_e \int_0^{2\pi} \cos\varphi d\varphi$$
$$\times \left[\int_0^{\pi/2} \Psi_j^+ \sin^2\theta_j d\theta_j + \int_{\pi/2}^{\pi} \Psi_j^- \sin^2\theta_j d\theta_j\right], \quad (18)$$

where ρ_j is the density of states.

After averaging the current in accordance with relationship (4) and taking into account expression (5), we obtain the conductivity

$$\sigma_{xx} = \frac{a}{2(a+b)}(\sigma_1\xi_1 + \sigma_2\xi_2), \quad (19)$$

where

$$\xi_1 = \frac{3}{2a}\int_0^{\pi/2} C_1^- \sin^2\theta_1 \cos\theta_1 \exp\left(-\frac{b}{\tau_1 v_{z1}}\right) \times\left(1 - \exp\left(-\frac{a}{\tau_1 v_{z1}}\right)\right)d\theta_1 - 1,$$
$$\xi_2 = \frac{3}{2a}\int_0^{\pi/2} C_2^- \sin^2\theta_2 \cos\theta_2 \exp\left(\frac{a}{\tau_2 v_{z2}}\right) \times\left(1 - \exp\left(-\frac{a}{\tau_2 v_{z2}}\right)\right)d\theta_2 - 1, \quad (20)$$

and

$$\sigma_j = \frac{1}{3}e^2\rho_{Fj}\tau_j v_{Fj}^2 = \frac{e^2 m_j^2 \tau_j v_{Fj}^3}{6\pi^2\hbar^3}$$

is the bulk conductivity of the jth layer [3]. By virtue of the used approximation $\partial f_0/\partial W_e \approx -\delta(W_e - W_F)$, it is necessary to set $\nu_j = \nu_{Fj}$ in expressions (10), (16), (20).

For the antiferromagnetic configuration, it is evident that $\sigma_{xx}^{(\uparrow)} = \sigma_{xx}^{(\downarrow)}$; that is,

$$\sigma_{AF} = 2\sigma_{xx}^{(\uparrow)} = \frac{a}{a+b}(\sigma_1^{AF}\xi_1^{AF} + \sigma_2^{AF}\xi_2^{AF}), \quad (21)$$

where $\xi_1^{AF} = \xi_1$, $\xi_2^{AF} = \xi_2$, $\sigma_1^{AF} = \sigma_1$, and $\sigma_2^{AF} = \sigma_2$ upon replacement of the indices $1 \longrightarrow a$ and $2 \longrightarrow b$ in relationships (20) (Figs. 1b, 1c).

In the case when the magnetization vectors are codirectional in the adjacent layers, we have $\sigma_{xx}^{(\uparrow)} \neq \sigma_{xx}^{(\downarrow)}$ and

$$\sigma_F = \sigma_{xx}^{(\uparrow)} + \sigma_{xx}^{(\downarrow)} = \frac{a}{a+b}(\sigma_1^F\xi_1^F + \sigma_2^F\xi_2^F), \quad (22)$$

where $\xi_1^F = \xi_1$ upon replacement of the indices $1 \longrightarrow b$ and $2 \longrightarrow b$, $\xi_2^F = \xi_1$ upon replacement of the indices $1 \longrightarrow a$ and $2 \longrightarrow a$, and $\sigma_1^F = \sigma_1$ and $\sigma_2^F = \sigma_2$ upon replacement of the indices $1 \longrightarrow b$ and $2 \longrightarrow a$ in relationships (20) (Figs. 1e, 1f).

4. NONGYROTROPIC MAGNETO-OPTICAL EFFECT

Making allowance for expressions (3) and (20)–(22), the effective permittivity of the multilayer medium for both configurations of the magnetization can be written in the form

$$\varepsilon^{AF(F)} = \varepsilon - \frac{a}{a+b}\left[\frac{\omega_{p1}^2\xi_1^{AF(F)}}{\omega(\omega + i\gamma_1)} + \frac{\omega_{p2}^2\xi_2^{AF(F)}}{\omega(\omega + i\gamma_2)}\right], \quad (23)$$

where

$$\omega_{pj} = \frac{ecm_j}{\pi}\sqrt{\frac{\mu_0 v_{Fj}^3}{6\hbar^3}}$$

is the plasma frequency of the jth layer and $\gamma_j = \tau_{0j}^{-1}$.

It follows from expression (23) that the frequency dependence of the effective permittivity for the multilayer medium is similar to the frequency dependence of the permittivity for a nonmagnetic homogeneous metal; that is,

$$\varepsilon^M = 1 - \frac{\omega_p^2}{\omega(\omega + i\gamma)}, \quad (24)$$

where

$$\omega_p = \frac{ecm}{\pi}\sqrt{\frac{\mu_0 v_F^3}{3\hbar^3}}.$$

Note that relationship (23) transforms into formula (24) at $b \longrightarrow 0$, $\gamma_a = \gamma_b$, and $W_a = W_b$.

As can be seen from relationship (23), the difference in the effective permittivities for the antiferromagnetic and ferromagnetic multilayer structures is in the nonequality $\xi_j^{AF} \neq \xi_j^F$. According to formula (1), this leads to the magneto-optical effect, which manifests itself in the dependence of the intensity of electromagnetic radiation reflected from the multilayer structure on the configuration of its magnetization. This magneto-optical effect is similar to the magneto-optical effect considered in our earlier work [14] for a multilayer structure consisting of magnetic and nonmagnetic metal layers. In what follows, the nongyrotropic magneto-optical effect will be described as a relative change in the reflection coefficient; that is,

$$\delta = \frac{R_{AF} - R_F}{R_F}. \quad (25)$$

As an example, we consider a multilayer structure composed of Fe magnetic and C insulator layers. For this structure, we have $W_F - W_a = 8.2$ eV, $W_F - W_b = 5.7$ eV, and $W_d - W_F = 1.0$ eV [3, 28]. The effective masses of electrons are assumed to be identical: $m_j = m_e$, where $m_e = 9.1 \times 10^{-31}$ kg. In this case, the Fermi velocities are as follows: $v_{Fa} = 8.5 \times 10^5$ m/s and $v_{Fb} = 7.1 \times 10^5$ m/s. Under the assumption that $\tau_{0a} = 3 \times 10^{-14}$ s and $\tau_{0b} = 6 \times 10^{-14}$ s, the mean free paths of electrons appear to be considerably greater than the layer thicknesses.

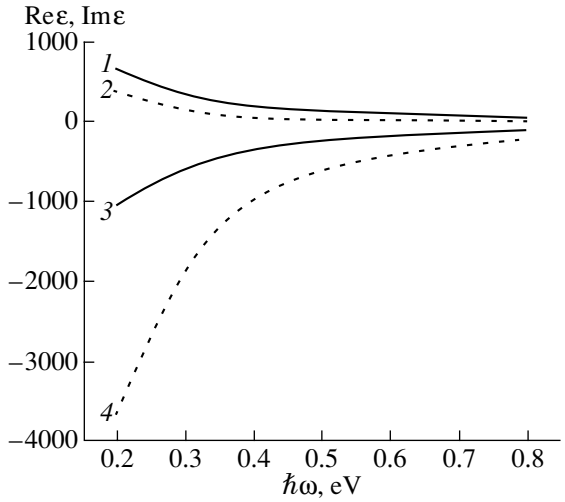

Fig. 3. Dependences of the (*1*, *2*) real and (*3*, *4*) imaginary parts of the effective permittivity on the photon energy $\hbar\omega$ of incident light for the multilayer structure with an antiferromagnetic configuration (solid lines) and the homogeneous nonmagnetic metal (dotted lines). Structural parameters: a = 1 nm, b = 0.2 nm, and η = 1 Å.

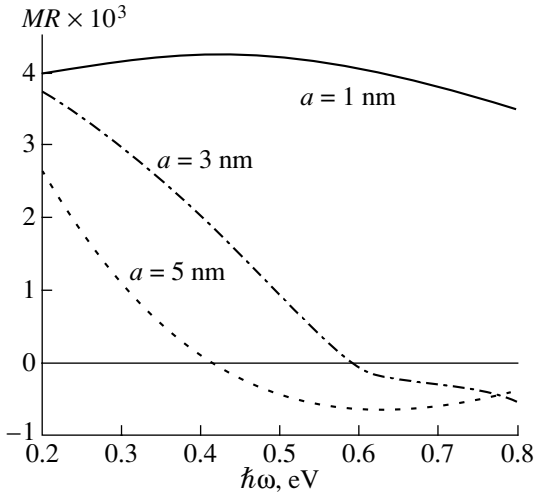

Fig. 4. Dependences of the magnetoresistive effect on the photon energy $\hbar\omega$ of incident light at different thicknesses a of the magnetic layer (b = 0.2 nm, η = 1 Å).

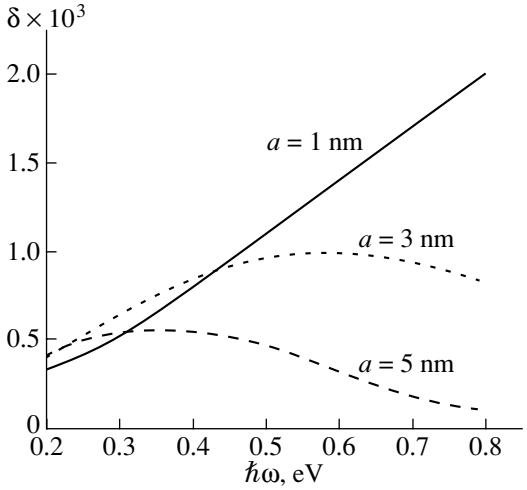

Fig. 5. Dependences of the nongyrotropic magneto-optical effect δ on the photon energy $\hbar\omega$ of incident light at different thicknesses a of the magnetic layer (b = 0.2 nm, η = 1 Å).

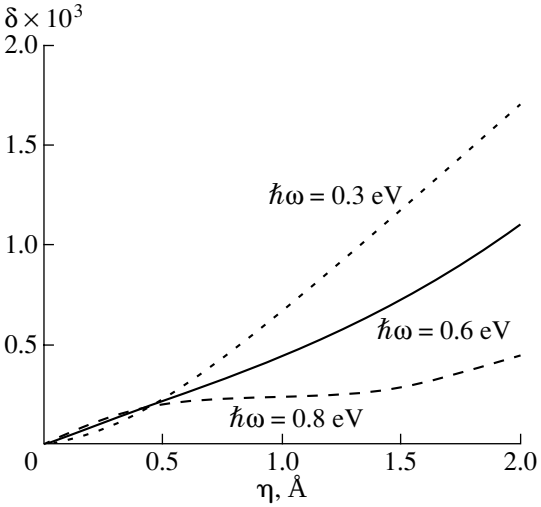

Fig. 6. Dependences of the nongyrotropic magneto-optical effect δ on the interface roughness of the multilayer structure at different photon energies $\hbar\omega$ of incident light. Structural parameters: a = 1 nm and b = 0.2 nm.

The dependences of the real and imaginary parts of the effective permittivity on the photon energy of incident light are shown in Fig. 3.

Figure 4 depicts the dependences of the magnetoresistive effect $MR = \dfrac{\sigma_{AF} - \sigma_F}{\sigma_F}$ on the photon energy of incident light. Here, $\sigma_{AF(F)}$ is the resistance of the multilayer with an antiferromagnetic (ferromagnetic) configuration.

The dependences of the nongyrotropic magneto-optical effect δ on the photon energy of incident light and the interface roughness at different parameters are shown in Figs. 4 and 5, respectively. The effect is absent in the case when the interfaces are perfect, i.e., when they are free of roughnesses (η = 0). Moreover, the nongyrotropic magneto-optical effect virtually disappears when the thickness of the insulator layer increases in order of magnitude to a nanometer. This is associated with the fact that, at $b \longrightarrow 1$ nm, the coefficient of transmission of electrons through the insulator layer is close to zero and electrons appear to be confined in their layers. Note that, in this work, we consider only intraband electron transitions.

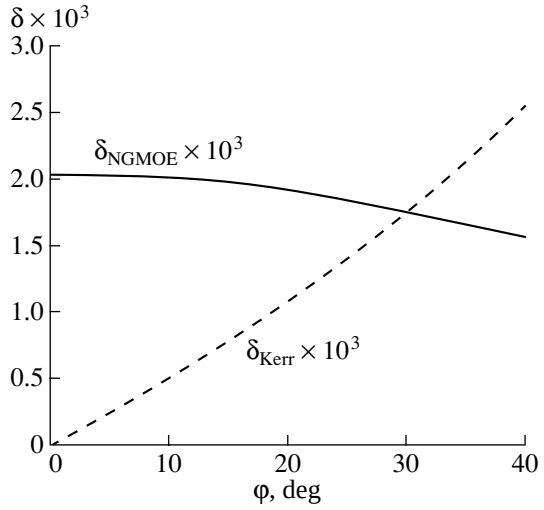

Fig. 7. Dependences of the nongyrotropic magneto-optical effect for the multilayer structure (a = 1 nm, b = 0.2 nm, η = 1.5 Å, $\hbar\omega$ = 0.3 eV) (solid line) and the equatorial magneto-optical Kerr effect for the uniformly magnetized Fe sample with refractive index $n = 2.4 + i \times 3.5$ and magneto-optical parameter $Q = -0.034 + i \times 0.003$ after exposure to p-polarized light [29] (dashed line) on the angle of light incidence φ.

A comparison of the dependences shown in Figs. 4 and 5 demonstrates that, although the optical properties of the multilayer structure are governed by the transport properties, there is no unique correspondence between the magnetoresistive and nongyrotropic magneto-optical effects.

The calculated dependences of the nongyrotropic magneto-optical effect on the angle of light incidence indicate that this effect is maximum at normal incidence of light (Fig. 7). It should be noted that the magneto-optical Kerr effect [8, 9], which also manifests itself in a change in the intensity of reflected light due to a variation in the magnetization of the medium, is characterized by a different angular dependence. As the angle of incidence decreases, the magneto-optical Kerr effect becomes weaker and disappears in the case of normal incidence (Fig. 7). This can be explained by the fact that, as was already noted, the Kerr effect is gyrotropic; i.e., it is determined by the off-diagonal elements of the permittivity tensor, whereas the nongyrotropic magneto-optical effect is related only to the diagonal elements of the permittivity tensor.

5. CONCLUSIONS

Thus, we proposed a theoretical approach to the description of the optical properties of metal–insulator magnetic multilayer films. Consideration was given to the nongyrotropic magneto-optical effect, which manifests itself in a change in the coefficient of reflection of a plane electromagnetic wave (polarized along the magnetization in layers) from the surface of a multilayer film due to the crossover of the magnetic structure from an antiferromagnetic configuration to a ferromagnetic configuration. Within the proposed approach, the permittivity tensor (dependent on the light frequency alone) of the multilayer medium was determined by solving the Boltzmann kinetic equation for free electrons in conducting layers of the multilayer structure.

In the framework of the theoretical model used in this work, it was demonstrated that the nongyrotropic magneto-optical effect is caused primarily by the interface roughness. The effect is absent when the interfaces are ideally smooth and the relaxation times of electrons in all layers are equal to each other.

The nongyrotropic magneto-optical effect under investigation can be used in noncontact probing of materials exhibiting giant magnetoresistance.

ACKNOWLEDGMENTS

This work was supported by the Russian Foundation for Basic Research (project nos. 01-02-16595 and 02-02-17389) and the Federal Program “Physical Properties of Nanostructures.”

REFERENCES

1. M. N. Baibich, J. M. Broto, A. Fert, *et al.*, Phys. Rev. Lett. **61**, 2472 (1988).
2. S. S. P. Parkin, Appl. Phys. Lett. **61**, 1358 (1992).
3. R. Q. Hood and L. M. Falikov, Phys. Rev. B **46**, 8287 (1992).
4. J. Barnas, A. Fuss, R. E. Camily, *et al.*, Phys. Rev. B **42**, 8110 (1990).
5. A. K. Zvezdin and S. N. Utochkin, Pis’ma Zh. Éksp. Teor. Fiz. **57**, 418 (1993) [JETP Lett. **57**, 433 (1993)].
6. X. G. Zhang and W. H. Butler, Phys. Rev. B **51**, 10085 (1995).
7. R. Atkinson, N. F. Kubrakov, A. K. Zvezdin, and K. A. Zvezdin, J. Magn. Magn. Mater. **156**, 169 (1996).
8. A. K. Zvezdin and V. A. Kotov, *Magneto-Optics of Thin Films* (Nauka, Moscow, 1988).
9. A. Zvezdin and V. Kotov, *Modern Magneto-Optics and Magneto-Optical Materials* (IOP, Bristol, 1997).
10. V. G. Kravets, D. Bozec, J. A. D. Matthew, *et al.*, Phys. Rev. B **65**, 054415 (2002).
11. J. C. Jacquet and T. Valet, Mater. Res. Soc. Symp. Proc. **384**, 477 (1995).
12. S. Uran, M. Grimsditch, E. Fullerton, and S. D. Bader, Phys. Rev. B **57**, 2705 (1998).
13. G. M. Genkin, Phys. Lett. A **241**, 293 (1998).
14. N. F. Kubrakov, A. K. Zvezdin, K. A. Zvezdin, and V. A. Kotov, Zh. Éksp. Teor. Fiz. **114** (3), 1101 (1998) [JETP **87**, 600 (1998)].
15. I. V. Bykov, E. A. Ganshina, A. B. Granovskiĭ, and V. S. Gushchin, Fiz. Tverd. Tela (St. Petersburg) **42** (3), 487 (2000) [Phys. Solid State **42**, 498 (2000)].
16. I. Bykov, E. Ganshina, V. Guschin, *et al.*, in *Moscow Book of Abstracts: Moscow International Symposium on Magnetism* (Editorial URSS, Moscow, 2002), p. 68.

17. D. Bozec, V. G. Kravets, J. A. D. Matthew, and S. M. Thompson, J. Appl. Phys. **91**, 8795 (2002).

18. A. Granovskiĭ, V. Gushchin, I. Bykov, *et al.*, Fiz. Tverd. Tela (St. Petersburg) **45** (5), 867 (2003) [Phys. Solid State **45**, 911 (2003)].

19. A. Granovskiĭ, M. Kuzmichev, and J. P. Clerc, Zh. Éksp. Teor. Fiz. **116** (5), 1762 (1999) [JETP **89**, 955 (1999)].

20. D. A. G. Bruggeman, Ann. Phys. (Leipzig) **24**, 636 (1935).

21. M. Wu, H. Zhang, Xi Yao, and L. Zhang, J. Phys. D **34**, 889 (2001).

22. A. B. Granovsky, M. V. Kuzmichev, J. P. Clerc, and M. Inoue, in *Moscow Book of Abstracts: Moscow International Symposium on Magnetism* (Editorial URSS, Moscow, 2002), p. 69.

23. M. Born and E. Wolf, *Principles of Optics*, 4th ed. (Pergamon, Oxford, 1969; Nauka, Moscow, 1970).

24. T. Valet and A. Fert, Phys. Rev. B **48**, 7099 (1993).

25. *The Physics of Metals*, Vol. 1: *Electrons*, Ed. by J. M. Ziman (Cambridge Univ. Press, Cambridge, 1969; Mir, Moscow, 1972).

26. A. F. Abrikosov, *Introduction to the Theory of Normal Metals* (Nauka, Moscow, 1972).

27. V. Bezak, M. Kedro, and A. Pevala, Thin Solid Films **23**, 305 (1974).

28. J. C. Slonczewski, Phys. Rev. B **39**, 6995 (1989).

29. V. I. Belotelov, A. P. Pyatakov, S. A. Eremin, *et al.*, Opt. Spektrosk. **91**, 663 (2001) [Opt. Spectrosc. **91**, 626 (2001)].

Translated by O. Borovik-Romanova

Physics of the Solid State, Vol. 45, No. 10, 2003, pp. 1966–1971. Translated from Fizika Tverdogo Tela, Vol. 45, No. 10, 2003, pp. 1870–1874.

MAGNETISM AND FERROELECTRICITY

Thin *W'* and *W* Domain Walls in Ferroelastic $Pb_3(PO_4)_2$

V. A. Nepochatenko* and E. F. Dudnik**

** Belotserkovskiĭ State Agricultural University, Belaya Tserkov', 09117 Ukraine*

*** Dnepropetrovsk National University, Dnepropetrovsk, 49050 Ukraine*

e-mail: aaa@btsau.kiev.ua

Received February 27, 2003

Abstract—A model of ferroelastic domain walls consisting of matching interlayers of crystal lattices is proposed. The dependences of the parameters of the interlayers and of the parameters of the equations for *W'* and *W* domain walls on the crystal lattice parameters of the ferroelastic phase in $Pb_3(PO_4)_2$ are determined. The problem concerning the number of possible orientational states and their interaction in a polydomain crystal is considered. © *2003 MAIK "Nauka/Interperiodica".*

1. INTRODUCTION

A model of the structure of a ferroelastic domain wall that consists of an induced phase (interlayer) matching the crystal lattices of the adjacent domains and a first-order phase transition between the interlayer and the ferroelectric phase was proposed in [1]. This model makes it possible to determine the parameters and symmetry of an interlayer for different types of domain walls in $Pb_3(PO_4)_2$, provided the orientation of a particular domain wall in the coordinate system of the α phase is known from the experiment. It was demonstrated that the interlayer of the *W'* domain wall has the symmetry of the paraphase (*P*-type twinning), the interlayer of the *W* domain wall has the symmetry of the ferroelastic phase (*F*-type twinning), and the orientation of the domain walls corresponds to lost elements of the symmetry of the β phase.

It is of interest to solve a similar problem for any temperature of the α phase on the basis of the results obtained in [1] without invoking experimental data on the orientation of the domain walls involved and also to explain the angular relationships between different domain walls in a polydomain crystal.

This problem will be solved in three stages. First, we will deduce the equations determining the orientation and parameters of the matching interlayers for *W'* and *W* domain walls at an arbitrary temperature of the α phase. Second, we will perform analogous calculations for the domain walls at 20°C in order to compare the obtained results with available experimental data. Third, we will analyze the interaction of the orientational states in a polydomain crystal.

Lead orthophosphate $Pb_3(PO_4)_2$ is a pure improper ferroelastic. At a temperature of 180°C, this crystal undergoes a phase transition ($\bar{3}mF2/m$) from the rhombohedral β phase to the monoclinic α phase [2, 3]. In this crystal, there can exist both normal *W* and oblique *W'* domain walls [4–6].

The symmetry of interlayers cannot be lower than monoclinic [1]. Therefore, all the phases will be described in terms of monoclinic or pseudomonoclinic symmetry. Let us introduce the following designations: a_0, b_0, c_0, and $\varphi_0 = \beta_0 - 90°$ are the parameters of the β phase; a_1, b_1, c_1, and $\varphi_1 = \beta_1 - 90°$ are the parameters of the α phase; a_2, b_2, c_2, and $\varphi_2 = \beta_2 - 90°$ are the parameters of the interlayer; and C_1, C_2, and C_3 are the orientational states.

The formulated problem will be solved using an orthogonal coordinate system in which the *X* axis is parallel to the *c* axis, the *Y* axis is parallel to the *b* axis, and the *Z* axis makes an angle φ with the *a* axis.

2. STRUCTURE OF THE *W'* DOMAIN WALL

Let us consider a domain wall *W'* separating the C_1 and C_2 orientational states in the coordinate system of the C_1 orientational state. Since a first-order phase transition occurs in the domain wall, the interlayer matches the adjacent orientational states through two interphase boundaries whose orientation coincides with the domain-wall orientation. According to the results obtained in our earlier work [7], the equation for the interphase boundary matching two monoclinic cells with the parameters a_1, b_1, c_1, and $\varphi_1 = \beta_1 - 90°$ and a_2, b_2, c_2, and $\varphi_2 = \beta_2 - 90°$ in the coordinate system of the first phase has the form

$$X_1^2 A_{11} + Y_1^2 A_{22} + Z_1^2 A_{33} + 2X_1 Z_1 A_{13} = 0, \qquad (1)$$

where

$$A_{11} = 1 - (c_2/c_1)^2, \quad A_{22} = 1 - (b_2/b_1)^2,$$

$$A_{13} = -\frac{c_2}{c_1 \cos\varphi_1}\left(\frac{c_2}{c_1}\sin\varphi_1 - \frac{a_2}{a_1}\sin\varphi_2\right),$$

$$A_{33} = 1 - \frac{1}{\cos^2\varphi_1} \times \left(\left(\frac{a_2}{a_1}\right)^2 \cos^2\varphi_2 + \left(\frac{c_2}{c_1}\sin\varphi_1 - \frac{a_2}{a_1}\sin\varphi_2\right)^2\right).$$

In the coordinate system of the second phase, the equation for the interphase boundary takes the form

$$X_2^2 B_{11} + Y_2^2 B_{22} + Z_2^2 B_{33} + 2X_2 Z_2 B_{13} = 0,$$

$$B_{11} = 1 - (c_1/c_2)^2, \quad B_{22} = 1 - (b_1/b_2)^2,$$

$$B_{13} = -\frac{c_1}{c_2\cos\varphi_2}\left(\frac{c_1}{c_2}\sin\varphi_2 - \frac{a_1}{a_2}\sin\varphi_1\right), \qquad (2)$$

$$B_{33} = 1 - \frac{1}{\cos^2\varphi_2} \times \left(\left(\frac{a_1}{a_2}\right)^2 \cos^2\varphi_1 + \left(\frac{c_1}{c_2}\sin\varphi_2 - \frac{a_1}{a_2}\sin\varphi_1\right)^2\right).$$

Under the condition

$$\det\{B_{ij}\} = 0, \qquad (3)$$

expression (2) corresponds to the equation of two intersecting planes:

$$X + BY + CZ = 0, \qquad (4)$$

$$X - BY + CZ = 0, \qquad (5)$$

where $B = \sqrt{-B_{22}/B_{11}}$ and $C = B_{13}/B_{11}$.

The W' domain wall is oriented along the lost twofold axis. Therefore, the equation for this wall can be written in the form

$$X_0 + \sqrt{3}Y_0 + A_3 Z_0 = 0, \qquad (6)$$

where A_3 is the temperature-dependent parameter.

Since the interphase boundary has the same orientation as the domain wall, expressions (4) and (6) coincide with each other. Consequently, we have

$$\sqrt{-B_{22}/B_{11}} = \sqrt{3}, \qquad (7)$$

$$B_{13}/B_{11} = A_3. \qquad (8)$$

The symmetry of the interlayer coincides with the symmetry of the paraphase. As a result, the spontaneous strain of the interlayer is equal to zero. Hence, we can write

$$e_{11}^S = 0, \qquad (9)$$

$$e_{13}^S = 0. \qquad (10)$$

From relationships (7)–(10), we obtain the system of equations

$$\sqrt{-B_{22}/B_{11}} = \sqrt{3}, \quad A_3 = B_{13}/B_{11}, \quad e_{11}^S = 0, \quad e_{13}^S = 0. \qquad (11)$$

After solving this system, we obtain the following expressions:

$$b_2 = b_1\sqrt{1+3F^2}/2, \qquad (12)$$

$$c_2 = c_1\sqrt{1+3F^2}/2F, \qquad (13)$$

$$A_3 = -\frac{2mF}{\sqrt{4F^2 + m^2(1-F^2)}}, \qquad (14)$$

$$\tan\varphi_2 = (c\sqrt{P}\tan\varphi_1 - A_3(1-c^2))/c^2, \qquad (15)$$

$$a_2 = a_1\cos\varphi_1/(\sqrt{P}\cos\varphi_2), \qquad (16)$$

$$c = \frac{c_1}{c_2}, \quad F = \frac{b_0 c_1}{b_1 c_0}, \quad P = 1 - \frac{A_3^2(1-c^2)}{c^2},$$

$$m = \frac{2F\sqrt{1+3F^2}}{\cos\varphi_1(1-F^2)}\left(\sin\varphi_1 - \frac{c_1}{3a_1}\right).$$

From expressions (12)–(16), we can determine the parameters of the interlayer. Then, from these data, we calculate the strain tensor P' with respect to the parameters of the β phase and the strain tensor D' with respect to the parameters of the α phase. Substituting the parameters of the interlayer into Eq. (1), we obtain the equation for the W' domain wall in the coordinate system of the α phase:

$$X_1 + DY_1 + KZ_1 = 0,$$

$$D = \sqrt{3}\frac{b_0 c_1}{b_1 c_0}, \quad K = A_3\sqrt{\frac{1+3F^2}{4F^2 - A_3^2(1-F^2)}}. \qquad (17)$$

Since equations for the W' domain wall in the two coordinate systems are known [expressions (6), (17)], we can determine the matrix T_1' of rotation from the coordinate system of the β phase to the α phase.

The problem for the adjacent orientational state C_2 can be solved in a similar way. As a result, we obtain a similar interlayer but rotated through an angle of 120° about the Z axis. This interlayer is described by the rotation matrix T_2'. Taking into account the symmetry, these interlayers are identical to each other and a common interlayer matches the crystal lattices of the adjacent domains. According to the thickness criterion of

the ferroelastic domain wall in this model [1], we obtain the domain-wall thickness $d \approx 20$ Å.

The surface density of the elastic energy of the domain wall can be determined from the formula

$$E = \frac{d}{2} c_{ijkl} e_{ij} e_{kl}, \tag{18}$$

where d is the domain-wall thickness, e_{ij} are the components of the strain tensor D', and c_{ijkl} are the elastic constants [8, 9].

From the matrices T_1' and T_2', we calculate the matrix K' specifying the mutual arrangement of the coordinate axes in the C_1 and C_2 orientational states separated by the W' domain wall:

$$K' = (T_1')^T B T_2', \tag{19}$$

where B is the matrix of rotation of the coordinate system about the Z axis through an angle of 120°.

Let us now return to Eq. (5). The interphase boundary described by this equation corresponds to the W' domain wall separating the C_1 and C_3 orientational states. The equation for this wall

$$X_0 - \sqrt{3} Y_0 + A_3 Z_0 = 0 \tag{20}$$

is taken as the initial equation. As a result, according to expressions (12)–(16), we obtain an interlayer similar to that used in the preceding case.

Thus, upon formation of the W' domain wall, each orientational state can take two similar orientations that correspond to the matrices T_1' and T_2'.

3. STRUCTURE OF THE W DOMAIN WALL

Let us consider a domain wall W separating the C_1 and C_2 orientational states. The equation for this domain wall in the coordinate system of the β phase corresponds to the lost symmetry plane:

$$X_0 - \sqrt{3}/3 Y_0 = 0. \tag{21}$$

According to [1], the matching interlayer in this domain wall satisfies the condition $e_{13} \neq 0$. Therefore, in order to match the interlayers corresponding to the C_1 and C_2 orientational states, it is necessary to rotate each of these interlayers together with the domain about its own Y axis through an angle $\alpha = -2 \arctan e_{13}$. By applying this operation of rotation, we deduce the following equation for the W domain wall in the coordinate system of the interlayer:

$$\begin{aligned} X_1 - \sqrt{3}/3 B_2 Y_1 + B_3 Z_1 &= 0, \\ B_2 = \sqrt{1 + 4e_{13}^2}, \quad B_3 &= -2e_{13}. \end{aligned} \tag{22}$$

By analogy with the derivation of the equations for the W' domain wall, we use expression (22) as the initial equation and derive the system of equations

$$\begin{aligned} \sqrt{-B_{22}/B_{11}} &= \sqrt{3}/3 B_2, \\ B_{13}/B_{11} &= B_3, \\ e_{11}^S &= 0, \\ e_{13} &= (c_2 + 3a_2 \cos\beta_2)/(6a_2 \sin\beta_2). \end{aligned} \tag{23}$$

By solving the system of equations (23), we obtain

$$e_{13} = \sqrt{\frac{-T \pm \sqrt{D}}{8F^2}}, \tag{24}$$

$$b_2 = b_1 \sqrt{\frac{1 + B_2^2 F^2}{1 + B_2^2}}, \tag{25}$$

$$c_2 = \frac{c_1}{F} \sqrt{\frac{1 + B_2^2 F^2}{1 + B_2^2}}, \tag{26}$$

$$\tan\varphi_2 = (c\sqrt{H} \tan\varphi_1 - B_3(1 - c^2))/c^2, \tag{27}$$

$$a_2 = \frac{a_1 \cos\varphi_1}{\sqrt{H} \cos\varphi_2}, \tag{28}$$

$$c = \frac{c_1}{c_2}, \quad F = \frac{b_0 c_1}{b_1 c_0}, \quad H = 1 - \frac{B_3^2 (1 - c^2)}{c^2},$$

$$n = \frac{c_1}{6a_1 \cos\varphi_1} - \frac{1}{2} \tan\varphi_1,$$

$$T = 3 + F^2 + 12n^2 - (4nF)^2, \quad D = T^2 + 64F^4 n^2.$$

After determining the parameters of the interlayer [expressions (24)–(28)], we can calculate the strain tensor P with respect to the parameters of the β phase and the strain tensor D with respect to the parameters of the α phase. Substituting the parameters of the interlayer into expression (1), we obtain the equation for the W domain wall with respect to the coordinate system of the ferroelastic phase:

$$\begin{aligned} X_2 - D_2 Y_2 + D_3 Z_2 &= 0, \\ D_2 &= \frac{\sqrt{3} F}{3} \sqrt{1 + 4e_{13}^2}, \\ D_3 &= -2e_{13}/\sqrt{c^2 - 4e_{13}^2 (1 - c^2)}. \end{aligned} \tag{29}$$

From relationships (21) and (29), we determine the matrix T_1 of rotation from the coordinate system of the α phase to the β phase.

Now, we solve a similar problem for the adjacent orientational state C_2 and obtain an interlayer similar to that found in the preceding case but rotated through an angle of 120° about the Z axis of the β phase. This inter-

Table 1. Parameters of the interlayers in the domain walls W' and W at $t = 20°C$

Parameter	W' domain wall	Parameter	W domain wall
a_2, Å	13.8938	a_2, Å	13.8243
b_2, Å	5.5136	b_2, Å	5.6346
c_2, Å	9.5491	c_2, Å	9.7587
β_2, deg	103.244	β_2, deg	102.903
$P' \times 10^{-3}$	$\begin{pmatrix} -6.06 & 0 & 0 \\ & -6.06 & 0 \\ & & -1.84 \end{pmatrix}$	$P \times 10^{-3}$	$\begin{pmatrix} 15.76 & 0 & 6.16 \\ & 15.76 & 0 \\ & & -5.46 \end{pmatrix}$
$D' \times 10^{-3}$	$\begin{pmatrix} 11.29 & 0 & -6.36 \\ & -31.17 & 0 \\ & & 3.64 \end{pmatrix}$	$D \times 10^{-3}$	$\begin{pmatrix} 33.49 & 0 & -0.21 \\ & -10.46 & 0 \\ & & 0.005 \end{pmatrix}$
T_1'	$\begin{pmatrix} 0.99984 & -0.01756 & -0.0019 \\ 0.01753 & 0.99976 & -0.0134 \\ 0.00213 & 0.01338 & 0.99991 \end{pmatrix}$	T_1	$\begin{pmatrix} 0.99978 & 0.0186 & -0.0096 \\ -0.01854 & 0.99981 & 0.0056 \\ 0.00969 & -0.005478 & 0.99994 \end{pmatrix}$
T_2'	$\begin{pmatrix} 0.99984 & 0.01756 & -0.0019 \\ -0.01753 & 0.99976 & 0.0134 \\ 0.00213 & -0.01338 & 0.99991 \end{pmatrix}$	T_2	$\begin{pmatrix} 0.99978 & -0.0186 & -0.0096 \\ 0.01854 & 0.99981 & -0.0056 \\ 0.00969 & 0.005478 & 0.99994 \end{pmatrix}$
K'	$\begin{pmatrix} -0.4693 & -0.883 & -0.0087 \\ 0.883 & -0.4694 & 0.0052 \\ -0.0087 & -0.0052 & 0.99995 \end{pmatrix}$	K	$\begin{pmatrix} -0.5316 & -0.8467 & 0.0195 \\ 0.8467 & -0.5319 & -0.0108 \\ 0.0195 & 0.0108 & 0.99975 \end{pmatrix}$
E', J/m^2	3.7358	E, J/m^2	13.338

layer corresponds to the rotation matrix T_2. Since the W domain wall consists of two interlayers, its thickness is two times greater than that of the W' domain wall. Therefore, the elastic energy in the W domain wall should increase significantly.

By analogy with the derivation of relationship (20), we use the matrices T_1 and T_2 in order to determine the matrix K describing the mutual arrangement of the coordinate axes in the adjacent domains separated by the W domain wall:

$$K = (T_1)^T B T_2. \quad (30)$$

Thus, the proposed model of a domain wall makes it possible to obtain the parameters of the interlayers; equations for domain walls in different coordinate systems; the matrices T_1', T_2', K', T_1, T_2, and K; the strain tensors P', D', P, and D; and the energy of the domain walls at any temperature of the ferroelastic phase. It remains to verify whether this model is consistent with the experimental data. For this purpose, we carried out analogous calculations for the domain walls at 20°C according to the data taken from [10]. The results obtained are presented in Table 1.

4. INTERACTION OF THE ORIENTATIONAL STATES IN A POLYDOMAIN CRYSTAL

As was shown in [11], each orientational state in a single-domain sample can take two similar orientations depending on which interphase boundary forms this state. It was demonstrated that, when a single domain wall is formed in a crystal, each orientational state can take four similar orientations that correspond to the matrices T_1, T_2, T_1', and T_2'. In this case, the domain walls are oriented along the symmetry elements of the β phase that are lost upon the phase transition, which is consistent with the results obtained by Shuvalov [12]. This inference can be extended to the case where several parallel single-type domain walls are observed in the crystal (stripe domain structure).

Table 2. Matrices of rotation of the coordinate system corresponding to different pairs of domain walls (t = 20°C)

Matrix	Adjacent domain walls			
	W'_{12}–W_{12}	W'_{12}–W'_{13}	W'_{12}–W_{13}	W_{12}–W_{13}
M	$\begin{pmatrix} 0.9993 & -0.0361 & 0.0079 \\ 0.0363 & 0.99917 & -0.019 \\ -0.0072 & 0.019 & 0.99979 \end{pmatrix}$	$\begin{pmatrix} 0.99938 & -0.0351 & 0.00047 \\ 0.0351 & 0.99902 & -0.0268 \\ 0.00047 & 0.0268 & 0.99964 \end{pmatrix}$	$\begin{pmatrix} 0.99997 & 0.0001 & 0.0077 \\ -0.00094 & 0.99997 & -0.0078 \\ -0.0077 & 0.0078 & 0.99994 \end{pmatrix}$	$\begin{pmatrix} 0.9993 & 0.037 & 0.0002 \\ -0.037 & 0.9992 & 0.011 \\ 0.0002 & -0.011 & 0.99994 \end{pmatrix}$

Let us analyze how the orientational states interact with each other when different domain walls are formed in a crystal. It is assumed that the crystal consists of three domains: the C_1 domain located at the center is separated from the C_2 domain by the W'_{12} domain wall on one side and from the C_3 domain by the W'_{13} domain wall on the other. The parameters of the equation for the W'_{12} domain wall with respect to the coordinate systems of the β and α phases are related by the expression

$$X_{0i} = T'_1 X_{1j}. \quad (31)$$

The analogous expression for the W'_{13} domain wall has the form

$$X'_{0i} = T'_2 X_{1j}. \quad (32)$$

From relationships (31) and (32), we obtain

$$X_{0i} = M X'_{0j},$$

$$M = T'_1 (T'_2)^T. \quad (33)$$

The matrix M describes the rotation of one coordinate system relative to the other coordinate system and, hence, the rotation of the equations for domain walls obtained above. For different variants of adjacent domains and domain walls, we determined the appropriate matrices M (Table 2).

5. RESULTS AND DISCUSSION

The matching interlayer corresponding to the W' domain wall is a compressed paraphase (see parameters P'_1 in Table 1). An almost opposite situation is observed in the matching interlayer of the W domain wall: the paraphase is extended along the X and Y axes and is compressed in the direction of the Z axis; moreover, there arises a shear strain e_{13} responsible for monoclinic symmetry. The surface density of the elastic energy E in the W domain wall is approximately 3.6 times higher than that in the W' domain wall; consequently, the W' domain wall is more energetically favorable.

From analyzing the temperature dependence of the parameters of the domain walls, we obtained the following results: (1) the equations for the W' domain wall change with variations in the temperature, and the equation for the W domain wall remains unchanged with respect to the coordinate system of the β phase but changes with respect to the coordinate system of the α phase; and (2) the energy of the domain walls is proportional to the square of the spontaneous strain.

The difference between the structures of the domain walls leads to the difference in the orientation and shape of the domains. From the matrix K (Table 1), we found that the angle between the twofold axes of the adjacent domains separated by the W domain wall is α = 57.86° (58° ± 1°) (the experimental value [5] is given in parentheses), whereas the angle between the (100) monoclinic planes is γ = 178.7° (178.6° ± 0.1°). Similarly, from the matrix K', we determined the angles α = 117.99° (118° ± 1°) and γ = 179.42° (180°; the accuracy is not specified). As can be seen, the coplanarity of the domains separated by the W' domain wall is not confirmed.

It follows from the analysis of the matrices M (Table 2) that, upon the formation of different domain walls in the crystal, there occurs rotation of the crystallographic axes and domain walls. For example, the angle between the traces of the domain walls W'_{12} and W_{12} on the plane (100) differs from 90° by 2.2° (2° ± 0.5°) and the angle between the domain walls W'_{12} and W_{13} differs from 30° by 0.45° (0 ± 0.5°). This interaction is one of the factors responsible for the existence of 92° domain walls in the crystal.

6. CONCLUSIONS

Thus, the results obtained within the model of thin domain walls allowed us to conclude that, in lead orthophosphate, different types of domain walls differ in the symmetry of the interlayer, the thickness, and the energy and mechanism of twinning. When one or several parallel domain walls are formed in the crystal, each orientational state at a given temperature can take four similar orientations depending on the type of domain wall and the orientation of the adjacent domain. The symmetry elements of the paraphase, which are lost in the course of the phase transition, become the

elements of domain twinning. If a more complex domain structure is formed in the crystal, there occur additional rotations of the crystallographic axes, which result in an increase in the number of possible orientations of the domains and domain walls.

REFERENCES

1. V. A. Nepochatenko, Kristallografiya **48** (2), 324 (2003) [Crystallogr. Rep. **48**, 290 (2003)].
2. K. Aizu, J. Phys. Soc. Jpn. **27**, 387 (1969).
3. V. Keppler, Z. Kristallogr. **132**, 228 (1970).
4. L. H. Brixner, P. E. Bierstedt, W. F. Jaep, and J. R. Barkley, Mater. Res. Bull. **8**, 497 (1973).
5. M. Chabin and F. Gilletta, J. Appl. Cryst. **10**, 247 (1977).
6. E. F. Dudnik, E. V. Sinyakov, V. V. Gene, and S. V. Vagin, Fiz. Tverd. Tela (Leningrad) **17**, 1846 (1975) [Sov. Phys. Solid State **17**, 1212 (1975)].
7. E. F. Dudnik and V. A. Nepochatenko, Kristallografiya **25** (5), 984 (1980) [Sov. Phys. Crystallogr. **25**, 564 (1980)].
8. Cao-Xuan An, G. Hauret, and J. P. Chapelle, C. R. Acad. Sci. Paris, Ser. B **280** (5), 543 (1975).
9. J. Torres, J. Primot, A. M. Pougnet, and J. Aubree, Ferroelectrics **26** (1–4), 689 (1980).
10. C. Joffren, J. P. Benoit, L. Deschamps, and M. Lambert, J. Phys. (Paris) **38** (2), 205 (1977).
11. V. A. Nepochatenko, Kristallografiya **47** (3), 514 (2002) [Crystallogr. Rep. **47**, 467 (2002)].
12. L. A. Shuvalov, Izv. Akad. Nauk SSSR, Ser. Fiz. **43** (8), 1554 (1979).

Translated by O. Moskalev

Physics of the Solid State, Vol. 45, No. 10, 2003, pp. 1972–1977. Translated from Fizika Tverdogo Tela, Vol. 45, No. 10, 2003, pp. 1875–1879.

MAGNETISM AND FERROELECTRICITY

Specific Features in the Permittivity of Polycrystalline Ferroelectrics: The Role of Schottky Regions

A. N. Pavlov, I. P. Raevskiĭ, and V. P. Sakhnenko

Research Institute of Physics, Rostov State University, pr. Stachki 194, Rostov-on-Don, 344104 Russia

Received March 3, 2003

Abstract—This paper reports on the results of investigations into the influence of Schottky regions formed in the vicinity of crystallite boundaries in polycrystalline ferroelectrics on their permittivity. The dependence of the dielectric properties of the Schottky regions on the orientation of the spontaneous polarization in the adjacent region of the crystallite is taken into consideration. It is demonstrated that nonmonotonic dependences of the permittivity and its relative change on the crystallite size under uniaxial compression are associated with the presence of the domain structure in polycrystalline ferroelectrics. *© 2003 MAIK "Nauka/Interperiodica".*

1. INTRODUCTION

It is known that breaking of chemical bonds at crystallite boundaries of polycrystalline ferroelectrics brings about the formation of localized states of the acceptor type. Upon filling of these states, the crystallite boundaries acquire a localized positive charge and Schottky regions depleted in negative charge are formed in the vicinity of the charged crystallite boundaries. In these regions, the electric field is sufficiently strong to affect the ratio of the permittivity inside the Schottky region (ε_s) to the permittivity in the bulk region of the crystallite (ε_v) [1]. In a number of works concerned with description of the dielectric properties of ferroelectric polycrystals and thin films, the authors examined a surface region with specific dielectric characteristics (as compared to those of the bulk regions of the crystallite) [2, 3] but ignored the influence of the domain structure of the ferroelectrics on the properties of this region. In the present study, we consider the domain structure of polycrystalline ferroelectrics in terms of the concentration of Schottky regions with the aim of describing some anomalies in the dielectric properties of polycrystals: (i) the nonmonotonic behavior of the permittivity ε with a decrease in the crystallite size d (Fig. 1) [4, 5] and (ii) the dependence of the sign of the relative change in the permittivity $\Delta\varepsilon/\varepsilon$ on the crystallite size d under the pressure σ (Fig. 2) [6, 7].

2. DESCRIPTION OF THE MODEL

In [2, 3], the influence of the crystallite surface on the permittivity ε was described under the assumption that the surface layer exhibits dielectric properties with a low permittivity ε_s. This implies that only the polarizing effect of the electric field of localized surface charges in a Schottky region is taken into account (see Fig. 3a, configuration *1*). In polarization regions of the ferroelectric material, the polarization P is close to saturation. Consequently, the permittivity of these regions is less than the permittivity of the bulk regions of the crystallite. However, in Schottky regions, the ferroelectric material undergoes not only polarization but also polarization switching (Fig. 3a, configurations *2*, *3*). These processes result in an efficient screening of the surface electric field and, correspondingly, in a high permittivity ε_s [8]. In ferroelectric semiconductors, a local increase in the permittivity ε in the Schottky region affects the transfer of mobile charge carriers, which manifests itself in posistor [9], varistor, and pho-

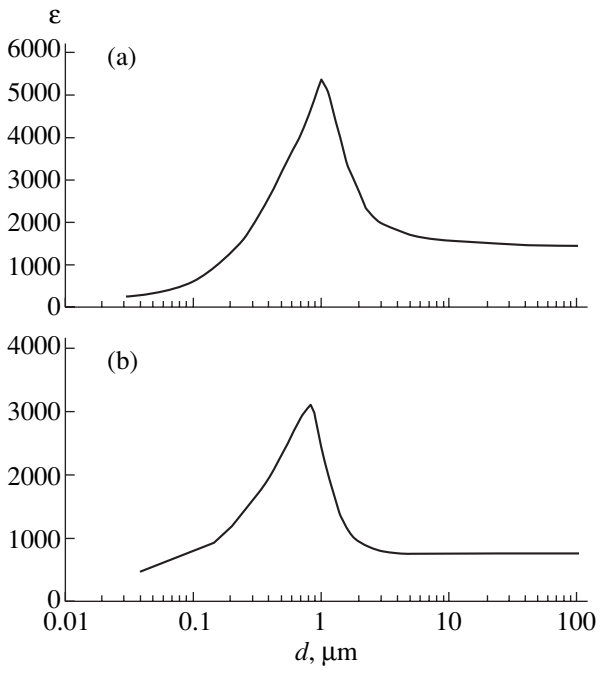

Fig. 1. Dependences of the permittivity ε on the crystallite size d according to the results of (a) measurements for $BaTiO_3$ [4, 5] and (b) calculations.

1063-7834/03/4510-1972$24.00 © 2003 MAIK "Nauka/Interperiodica"

tovoltaic [10] effects and in asymmetry of the current–voltage characteristics [11].

Let us consider the permittivity ε of an unpolarized crystallite in the form of a rectangular parallelepiped (with edges aligned parallel to the crystallographic axes) in a weak measuring field E_m with a strength less than that of the coercive field. The main configurations of the orientations of the spontaneous polarization P_s for the tetragonal phase in the crystallite bulk with respect to a particular crystallite surface in a zero measuring field ($E_m = 0$) are depicted in Fig. 3a. Moreover, the main configurations can be obtained from configuration *3* (Fig. 3a) by rotating the polarization vector P_s through angles of 90°, 180°, and 270°, provided the vector P_s remains parallel to the chosen surface of the crystallite. It is assumed that the measuring field is perpendicular to the chosen surface of the crystallite (Fig. 3b, where l_s is the thickness of the Schottky region). In this case, configurations *1* and *2* correspond to *c* domains, whereas configuration *3* is associated with *a* domains [2]. The dielectric properties of a polycrystal can be described in the framework of the capacitor model [1–3] under the assumption that all configurations shown in Fig. 3a are equally probable in the polycrystal. Within this model, the permittivity ε of the crystallite can be represented by the expression

$$\varepsilon = \frac{1}{6}(\varepsilon_1 + \varepsilon_2 + 4\varepsilon_3). \quad (1)$$

Here, the permittivities ε_1, ε_2, and ε_3 corresponding to configurations *1–3* (Fig. 3a) are defined by the relationships

$$\frac{1}{\varepsilon_i} = \frac{2l_s}{\varepsilon_{si}d} + \frac{d-2l_s}{\varepsilon_{vi}d}; \quad 2l_s < d \le 2l_s + l_d, \quad i = 1, 2, 3; \quad (2)$$

$$\frac{1}{\varepsilon_i} = \frac{2l_s}{\varepsilon_{si}d} + \frac{l_d}{\varepsilon_{vi}d} + \frac{d-2l_s-l_d}{6d}\left(\frac{1}{\varepsilon_{v1}} + \frac{1}{\varepsilon_{v2}} + 4\frac{1}{\varepsilon_{v3}}\right), \quad 2l_s + l_d < d, \quad i = 1, 2, 3, \quad (3)$$

where ε_{si} (i =1–3) are the permittivities of the Schottky region for configurations *1–3*, ε_{vi} (i =1–3) are the permittivities of the bulk region of the crystallite for configurations *1–3*, and l_d is the domain size. The thickness l_s of the Schottky region is determined by electroneutrality condition (4) given below. By virtue of the locality of the processes involved, the change observed in the depolarizing field due to polarization switching is compensated for by the space-charge field of the Schottky region. As a result, the change in the polarization ΔP in the polarization switching regions and the thickness l_s of the Schottky region can be related by the expressions

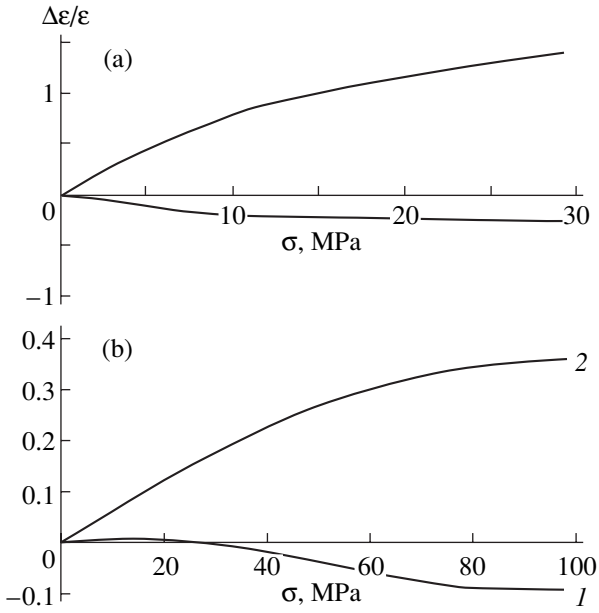

Fig. 2. Experimental dependences of the relative change in the permittivity Δε/ε on the pressure σ for (a) single-crystal and (b) polycrystalline $BaTiO_3$ samples [7] measured under (*1*) uniaxial compression and (*2*) biaxial tension.

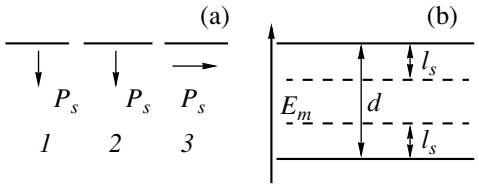

Fig. 3. Schematic diagram of the orientations of (a) the spontaneous polarization P_s in the bulk of the crystallites and (b) the measuring field E_m with respect to the crystallite surface (the designations are given in the text).

$$l_s = \frac{qn_s}{Q}, \quad (4)$$

$$\Delta P \approx l_s Q. \quad (5)$$

Here, n_s is the density of occupied localized states at the crystallite surface, Q is the space-charge density of the Schottky region, and q is the elementary electric charge. Under the condition $2P_s > qn_s > P_{ss}$, expressions (4) and (5) lead to the relationship $2P_s > \Delta P > P_s$. Consequently, upon polarization switching P_s in the electric field of the Schottky region, the saturation state is attained for configuration *3* (Fig. 3a); however, for configuration *2*, the saturation state is not achieved,

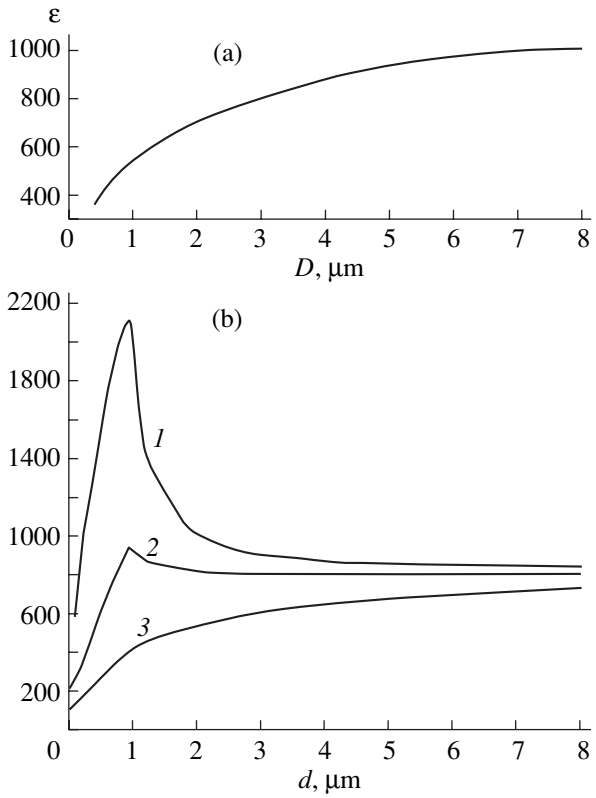

Fig. 4. (a) Experimental dependence of the permittivity ε on the thickness D of a $BaTiO_3$ polycrystalline ferroelectric film [2] and (b) calculated dependences of the permittivity ε on the crystallite size d for $\varepsilon_{s1} = \varepsilon_{s3} =$ (*1*) 100, (*2*) 30, and (*3*) 10.

which results in the permittivity $\varepsilon_{s2} \sim 10^4$–$10^5$. The permittivity ε_{s2} was estimated from the expression

$$\varepsilon_{s2} \approx \frac{\Delta P}{\varepsilon_0 E_c} \approx \frac{P_s}{\varepsilon_0 E_c}, \quad (6)$$

where ε_0 is the permittivity of free space, $E_c \sim 10^5$–10^6 V/m is the strength of the coercive field in the Schottky region [8], and $P_s \sim 0.1$ C/m^2 [12].

Thus, configurations *1* and *3* are characterized by a saturation state. The corresponding permittivities are estimated as $\varepsilon_{s1} \sim \varepsilon_{s3} \sim$ 10–100 [1]. According to [12], we have $\varepsilon_{v1} \sim \varepsilon_{v2} \sim 300$ for *c* domains and $\varepsilon_{v3} \sim 10^4$ for *a* domains. Making allowance for the above estimates of the permittivities ε_{si} and ε_{vi}, we can write the relationship

$$\varepsilon_{s1}, \varepsilon_{s3} < \varepsilon_{v1}, \quad \varepsilon_{v2} \ll \varepsilon_{v3}, \varepsilon_{s2}. \quad (7)$$

3. COMPUTATIONAL RESULTS

Let us now analyze the asymptotic behavior of the permittivity ε in terms of relationships (1)–(3). For a thick crystallite plate ($d > l_d > l_s$), according to condition (7), we obtain the expression describing the portion of the dependence ε(d) in which the permittivity ε remains unchanged at large values of d (Fig. 1):

$$\varepsilon \approx 3\varepsilon_{v1}. \quad (8)$$

For a thin crystallite plate ($d > l_d$), according to the conditions $l_s < d < l_s(\varepsilon_{v3}/\varepsilon_{s3}) < l_d$ and $l_s < d < l_d < l_s(\varepsilon_{v3}/\varepsilon_{s3})$, we can write the expression

$$\varepsilon = \frac{1}{3}\varepsilon_{v1} + \frac{2}{3}\varepsilon_{s3}\frac{d}{2l_s} - \frac{1}{6}\varepsilon_{v1}\frac{\varepsilon_{v1}}{\varepsilon_{s1}}\frac{1l_s}{d}. \quad (9)$$

Expression (9) accounts for the effect of Schottky regions on the initial increase in the permittivity ε with an increase in the crystallite size d (Fig. 1).

Under the condition $l_s(\varepsilon_{v3}/\varepsilon_{s3}) < d < l_d$, the permittivity ε_{v3} reaches a larger value due to configuration *3* (*a* domains) (Fig. 3a). In this case, we obtain the relationship

$$\varepsilon = \frac{2}{3}\varepsilon_{v3} - \frac{2}{3}\varepsilon_{v3}\frac{\varepsilon_{v3}}{\varepsilon_{s3}}\frac{2l_s}{d}. \quad (10)$$

From this relationship, it follows that the permittivity ε drastically increases to ~10^3–10^4 at $d \sim l_d \sim 10^{-6}$ m (Fig. 1).

Such a drastic increase in the permittivity ε upon changing over from coarse-grained ($d \sim 10^4$ m) to fine-grained ($d \sim 10^{-6}$ m) polycrystals was explained by Buessem *et al.* [13] as resulting from the increase in the elastic stress of the polycrystalline material with a decrease in the crystallite size d, which, in turn, should lead to a decrease in the degree of tetragonality of the crystal lattice. However, this explanation contradicts the experimental results obtained by Bradley [14], according to which the degree of tetragonality of the lattice of fine-grained polycrystals is equal to that of powders prepared by grinding these polycrystals. Goswami *et al.* [15] explained the high permittivity ε observed for fine-grained materials in terms of reducing effects of saturation of the depolarizing fields, which is also highly improbable due to compensating for the depolarizing fields by free charges. The results of our calculations of the dependence ε(d) (Fig. 1b) are in satisfactory agreement with the experimental curve (Fig. 1a). These calculations were performed at the parameters $l_s = 10^{-8}$ m, $l_d = 5 \times 10^{-7}$ m, $\varepsilon_{s1} = 200$, $\varepsilon_{s2} = 9000$, $\varepsilon_{s3} = 250$, $\varepsilon_{v1} = \varepsilon_{v2} = 300$, and $\varepsilon_{v3} = 7000$. The experimental dependence of the permittivity ε on the thickness D of a $BaTiO_3$ polycrystalline ferroelectric film (Fig. 4a) [2], unlike the curve obtained in [5] (Fig. 1a), does not exhibit nonmonotonic behavior with a sharp maximum, even though the mean crystallite size decreases with a decrease in the film thickness [2]. This can be explained by the fact that, in the case under consideration, the relationship $l_s(\varepsilon_{v3}/\varepsilon_{s3}) < d < l_d$, which is a necessary condition for asymptotic equation (10) to be satisfied, does not hold. The theoretical dependences of the permittivity ε on the crystallite size d for different values

of ε_{s1} and ε_{s3} (Fig. 4b, curves *1–3*) were calculated according to relationships (1)–(3) at the parameters $l_s = 10^{-8}$ m, $l_d = 5 \times 10^{-7}$ m, $\varepsilon_{s2} = 9000$, $\varepsilon_{v1} = \varepsilon_{v2} = 300$, and $\varepsilon_{v3} = 7000$. An analysis of these dependences demonstrates that agreement with the experimental data (Fig. 4a) can be achieved by varying the permittivity ε_s in the Schottky region.

Now, we investigate how the pressure affects the permittivity ε of ferroelectrics. Figure 5a presents the experimental results obtained for single-crystal and polycrystalline $BaTiO_3$ samples under hydrostatic compression in the case when any transformation of the domain structure is ruled out. In this situation, an increase in the permittivity ε is caused by changes in ε_{si} and ε_{vi} with a decrease in the phase transition temperature T_c under pressure. The calculated dependences of the relative change in the permittivity $\Delta\varepsilon/\varepsilon$ on the pressure σ at a temperature $T = T_c - 50$ for $l_s = 10^{-7}$ m and $l_d = 10^{-6}$ m (Fig. 5b) agree well with the experimental data (Fig. 5a). The calculations for a single crystal and a polycrystal were performed using crystallite sizes $d = 10^{-4}$ and 4×10^{-6} m, respectively. It turned out that the relative change in the permittivity $\Delta\varepsilon/\varepsilon$ of polycrystalline materials is less than that of single crystals. This can be explained by the fact that, for polycrystals, the contribution of ε_{v1} to the permittivity ε decreases, whereas the contribution of ε_{v3} increases. It is worth noting that, unlike the quantity ε_{v1}, the quantity ε_{v3} decreases with an increase in the pressure under hydrostatic compression (see table). The permittivities ε_{v1} and ε_{si} (i =1–3) were calculated with the use of the thermodynamic potential [16]

$$\begin{aligned}\Phi = {} & \frac{1}{2}\alpha(P_1^2 + P_2^2 + P_3^2) + \frac{1}{4}\beta_1(P_1^4 + P_2^4 + P_3^4) \\ & + \beta_2(P_1^2P_2^2 + P_2^2P_3^2 + P_1^2P_3^2) + \frac{1}{6}\gamma_1(P_1^6 + P_2^6 + P_3^6) \\ & + \gamma_2(P_1^4(P_2^2 + P_3^2) + P_2^4(P_1^2 + P_3^2) + P_3^4(P_1^2 + P_2^2)) \\ & + \gamma_3P_1^2P_2^2P_3^2 - (E_1P_1 + E_2P_2 + E_3P_3) \\ & - q_{11}(\sigma_1P_1^2 + \sigma_2P_2^2 + \sigma_3P_3^2) \\ & - q_{12}(\sigma_1(P_2^2 + P_3^2) + \sigma_2(P_1^2 + P_3^2) + \sigma_3(P_1^2 + P_2^2)) \\ & - q_{44}(\sigma_4P_2P_3 + \sigma_5P_1P_3 + \sigma_6P_1P_2).\end{aligned} \quad (11)$$

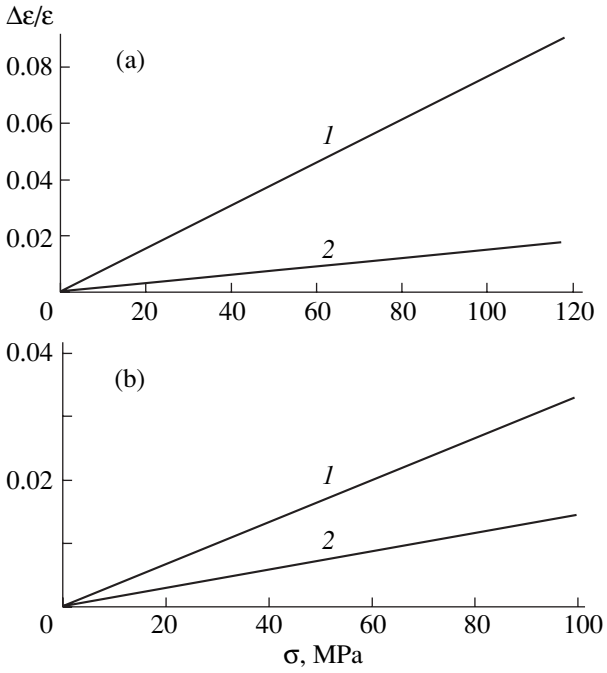

Fig. 5. (a) Experimental and (b) calculated dependences of the relative change in the permittivity $\Delta\varepsilon/\varepsilon$ on the pressure σ under hydrostatic compression for (*1*) single-crystal and (*2*) polycrystalline $BaTiO_3$ samples [7] with crystallite sizes d = (*1*) 1×10^{-4} and (*2*) 4×10^{-6} m.

In these calculations, the electric field strength in the Schottky region was taken to be equal to 10^7 V/m [2].

Let us now elucidate how the permittivity ε is affected by uniaxial compression and biaxial tension (Fig. 2). Changes in the permittivity ε under these actions are several times greater than those under hydrostatic pressure and, hence, cannot be explained by the effect of pressure on the quantities ε_{si} and ε_{vi}. As was shown by Dudkevich *et al.* [17], the domain structure of polycrystalline ferroelectrics undergoes a transformation under uniaxial or biaxial pressure. Below, we will analyze the influence of this phenomenon on the permittivity ε. Let us consider the situation where the direction of uniaxial compression coincides with the direction of the external measuring field E_m (Fig. 3b). In this case, the fraction of *c* domains decreases (Fig. 3a, configurations *1*, *2*) and the fraction of *a* domains increases (Fig. 3a, configuration *3*). As a consequence,

Calculated permittivities ε_v for different orientations of the spontaneous polarization P_s (Fig. 3a)

ε_v	σ, MPa					
	0		20		100	
	$T = T_c - 50$	$T = T_c - 100$	$T = T_c - 50$	$T = T_c - 100$	$T = T_c - 50$	$T = T_c - 100$
ε_{v1}	302	162	307	164	331	170
ε_{v3}	1424	4133	1394	3845	1290	3093

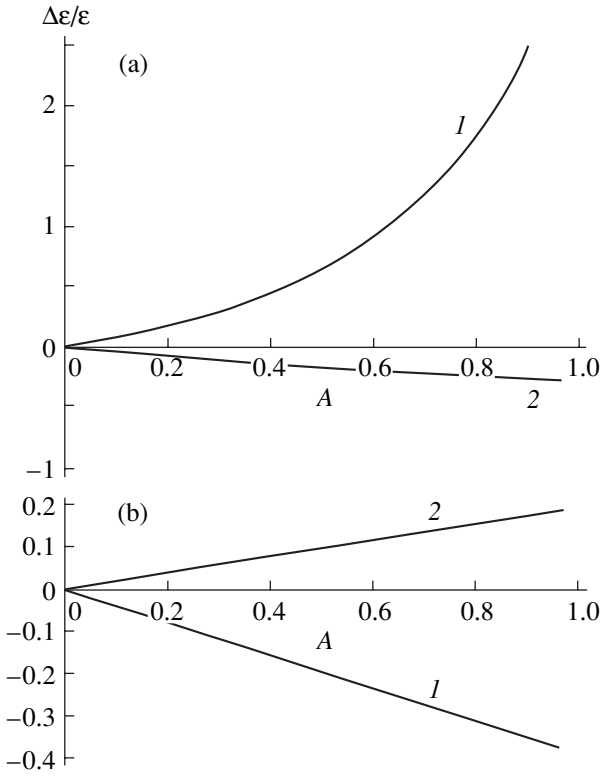

Fig. 6. Calculated dependences of the relative change in the permittivity $\Delta\varepsilon/\varepsilon$ on the fraction of domains A under (*1*) uniaxial compression and (*2*) biaxial tension for crystallite sizes d = (*1*) 1×10^{-4} and (*2*) 4×10^{-6} m.

the effect of pressure on the permittivity ε can be adequately described by the relationships

$$\varepsilon = \frac{1}{6}\varepsilon_1(1-A) + \frac{1}{6}\varepsilon_2(1-A) + \frac{2}{3}\varepsilon_3\left(1+\frac{A}{2}\right), \quad (12)$$

$$\frac{1}{\varepsilon_i} = \frac{2l_s}{\varepsilon_{si}d} + \frac{d-2l_s}{\varepsilon_{vi}d}, \quad 2l_s < d \le 2l_s + l_d, \quad i = 1, 2, 3, \quad (13)$$

$$\frac{1}{\varepsilon_i} = \frac{2l_s}{\varepsilon_{si}d} + \frac{l_d}{\varepsilon_{vi}d} + \frac{d-2l_s-l_d}{6d} \times\left(\frac{1-A}{\varepsilon_{v1}} + \frac{1-A}{\varepsilon_{v2}} + 4\frac{1+0.5A}{\varepsilon_{v3}}\right), \quad 2l_s + l_d < d, \quad i = 1, 2, 3. \quad (14)$$

Here, A is the fraction of domains in which 90° rotations of the polarization P_s occur under pressure ($0 \le A \le 1$).

Figure 6 shows the theoretical dependences of the relative change in the permittivity $\Delta\varepsilon/\varepsilon$ on the degree of transformation of the domain structure. These dependences were calculated from relationships (12)–(14) at the parameters $l_s = 7 \times 10^8$ m, $l_d = 8 \times 10^{-7}$ m, $\varepsilon_{s1} = 10$, $\varepsilon_{s2} = 9000$, $\varepsilon_{s3} = 10$, $\varepsilon_{v1} = \varepsilon_{v2} = 300$, and $\varepsilon_{v3} = 7000$. The calculations for a single crystal and a polycrystal were performed using crystallite sizes $d = 10^{-4}$ and 4×10^{-6} m, respectively. As can be seen, the calculated dependences are in qualitative agreement with the experiment (Fig. 2). From relationships (12)–(14), we obtain the following expression for an approximate description of the quantity $\Delta\varepsilon/\varepsilon$ under uniaxial compression:

$$\frac{\Delta\varepsilon}{\varepsilon} \approx \mp A. \quad (15)$$

Here, the signs "–" and "+" refer to thin and thick crystallite plates, respectively. An increase in the permittivity ε for thick crystallite plates is associated with an increase in the fraction of *a* domains under uniaxial compression. As the crystallite size decreases, the role played by the Schottky regions in the behavior of the permittivity ε becomes increasingly important. Therefore, we can infer that the relative change $\Delta\varepsilon/\varepsilon$ in the permittivity for thin crystallite plates is determined by the decrease in the permittivity of the Schottky regions due to a transformation of the domain structure under uniaxial compression.

Now, we analyze the response of the permittivity ε to biaxial tension in the case where the measuring field E_m (Fig. 3b) is oriented along one of the directions of tension. Under these conditions, the relationships describing the effect of pressure on the permittivity ε take the form

$$\varepsilon = \frac{1}{6}\varepsilon_1\left(1+\frac{A}{2}\right) + \frac{1}{6}\varepsilon_2\left(1+\frac{A}{2}\right) + \frac{1}{3}\varepsilon_3\left(1+\frac{A}{2}\right) + \frac{1}{3}\varepsilon_3(1-A), \quad (16)$$

$$\frac{1}{\varepsilon_i} = \frac{2l_s}{\varepsilon_{si}d} + \frac{d-2l_s}{\varepsilon_{vi}d}, \quad 2l_s < d \le 2l_s + l_d, \quad i = 1, 2, 3, \quad (17)$$

$$\frac{1}{\varepsilon_i} = \frac{2l_s}{\varepsilon_{si}d} + \frac{l_d}{\varepsilon_{vi}d} + \frac{d-2l_s-l_d}{6d} \times\left(\frac{1+0.5A}{\varepsilon_{v1}} + \frac{1+0.5A}{\varepsilon_{v2}} + 2\frac{1+0.5A}{\varepsilon_{v3}} + 2\frac{1-A}{\varepsilon_{v3}}\right), \quad 2l_s + l_d < d, \quad i = 1, 2, 3. \quad (18)$$

The theoretical dependences of the relative change in the permittivity $\Delta\varepsilon/\varepsilon$ on the degree of transformation of the domain structure (Fig. 6), which were calculated from relationships (16)–(18), agree qualitatively with the experiment (Fig. 2). From relationships (16)–(18),

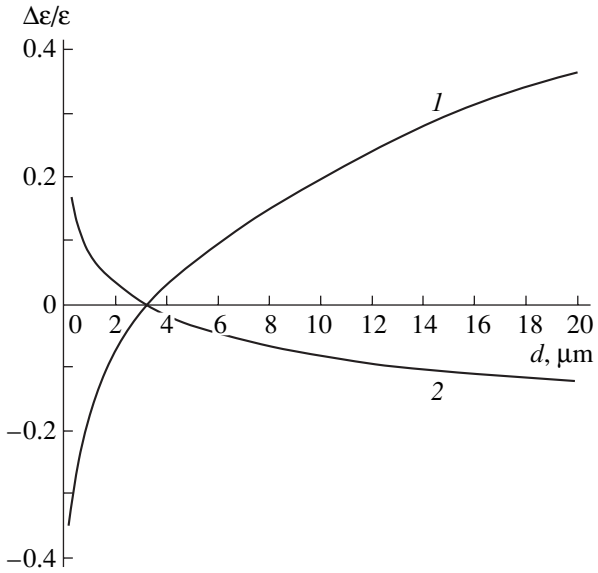

Fig. 7. Calculated dependences of the relative change in the permittivity $\Delta\varepsilon/\varepsilon$ on the crystallite size d under (*1*) uniaxial compression and (*2*) biaxial tension for the fraction of domains $A = 0.5$.

we obtain the following expression for an approximate description of the quantity $\Delta\varepsilon/\varepsilon$ under biaxial tension:

$$\frac{\Delta\varepsilon}{\varepsilon} \approx \pm\frac{A}{2}, \qquad (19)$$

where the signs "+" and "–" refer to thin and thick crystallite plates, respectively.

As follows from relationship (19), the responses of the permittivity ε to compression and tension of thick and thin crystallite samples are opposite in sign. This also manifests itself in the experimental dependences of the relative change in the permittivity $\Delta\varepsilon/\varepsilon$ on the pressure (Fig. 2). Figure 7 depicts the calculated dependences of $\Delta\varepsilon/\varepsilon$ on d under uniaxial compression and biaxial tension for $A = 0.5$ ($l_s = 7 \times 10^{-8}$ m, $l_d = 8 \times 10^{-7}$ m, $\varepsilon_{s1} = 10$, $\varepsilon_{s2} = 9000$, $\varepsilon_{s3} = 10$, $\varepsilon_{v1} = \varepsilon_{v2} = 300$, and $\varepsilon_{v3} = 7000$). As the crystallite size d decreases, the relative change in the permittivity $\Delta\varepsilon/\varepsilon$ reverses sign at $d \sim l_d$ under both uniaxial compression and biaxial tension.

4. CONCLUSIONS

Thus, the presence of Schottky regions and domain structure in polycrystalline ferroelectrics is responsible for a large variety of phenomena observed in these materials. In particular, under the condition $l_s(\varepsilon_{v3}/\varepsilon_{s3}) < d < l_d$, the dependence of the permittivity ε on the crystallite size d exhibits a nonmonotonic behavior. In this case, the permittivity ε reaches a large value for *a* domains. As the fraction of *a* domains increases under pressure, the permittivity of the bulk regions of the crystallite increases, whereas the permittivity of the Schottky regions decreases. Consequently, the relative changes in the permittivity $\Delta\varepsilon/\varepsilon$ for single-crystal and polycrystalline materials under uniaxial compression are opposite in sign.

REFERENCES

1. F. M. Fridkin, *Ferroelectric Semiconductors* (Nauka, Moscow, 1976).
2. V. P. Dudkevich and E. G. Fesenko, *Physics of Ferroelectric Films* (Rostov. Gos. Univ., Rostov-on-Don, 1979).
3. A. K. Tagantsev, Ferroelectrics **184**, 79 (1996).
4. G. Arlt, D. Hennings, and G. de With, J. Appl. Phys. **58** (4), 1619 (1985).
5. R. Waser, Integr. Ferroelectr. **15** (1), 39 (1997).
6. I. A. Izhak, Zh. Tekh. Fiz. **27** (5), 953 (1957) [Sov. Phys. Tech. Phys. **2**, 872 (1958)].
7. Ya. M. Ksendzov and B. A. Rotenberg, Fiz. Tverd. Tela (Leningrad) **1** (4), 637 (1959) [Sov. Phys. Solid State **1**, 579 (1959)].
8. A. N. Pavlov, I. P. Raevskiĭ, and V. P. Sakhnenko, Fiz. Tverd. Tela (St. Petersburg) **42** (11), 2060 (2000) [Phys. Solid State **42**, 2123 (2000)].
9. A. N. Pavlov, Fiz. Tverd. Tela (St. Petersburg) **36** (3), 579 (1994) [Phys. Solid State **36**, 319 (1994)].
10. A. N. Pavlov and I. P. Raevsky, Ferroelectrics **214**, 157 (1998).
11. A. N. Pavlov, I. P. Raevsky, M. A. Malitskaya, and I. A. Sizkova, Ferroelectrics **174**, 35 (1995).
12. G. A. Smolenskiĭ, V. A. Bokov, V. A. Isupov, N. N. Kraĭnik, R. E. Pasynkov, and M. S. Shur, *Ferroelectrics and Antiferroelectrics* (Nauka, Leningrad, 1971).
13. W. R. Buessem, L. E. Cross, and A. K. Goswami, J. Am. Ceram. Soc. **49** (1), 33 (1966).
14. F. M. Bradley, J. Am. Ceram. Soc. **51** (5), 293 (1968).
15. A. K. Goswami, L. E. Cross, and W. R. Buessem, J. Phys. Soc. Jpn. **24** (2), 279 (1968).
16. J. S. Capurso and W. A. Schulze, J. Am. Ceram. Soc. **81** (2), 347 (1998).
17. V. P. Dudkevich, V. V. Kuleshov, and A. V. Turik, Zh. Tekh. Fiz. **47** (10), 2168 (1977) [Sov. Phys. Tech. Phys. **22**, 1259 (1977)].

Translated by O. Borovik-Romanova

Physics of the Solid State, Vol. 45, No. 10, 2003, pp. 1978–1983. Translated from Fizika Tverdogo Tela, Vol. 45, No. 10, 2003, pp. 1880–1885.

LATTICE DYNAMICS AND PHASE TRANSITIONS

Phase Transition in the Isotropic *m*-Vector Model on a Random Graph

P. N. Timonin and V. P. Sakhnenko

Research Institute of Physics, Rostov State University, pr. Stachki 194, Rostov-on-Don, 344090 Russia

e-mail: timonin@aaanet.ru, sakh@ip.rsu.ru

Received February 19, 2003

Abstract—The thermodynamics of a phase transition is investigated within an isotropic *m*-vector model on a graph with sparse random connections. This model adequately describes superconductivity and superfluidity ($m = 2$), Heisenberg magnets ($m = 3$), and some structural transitions in different systems with macroscopic disorder (gels, composites, and porous media). It is demonstrated that the phase transition is characterized by classical effective-field anomalies. The thermodynamics of the phase transition is also analyzed in terms the proposed model at low temperatures. The dependences of the thermodynamic parameters on the external field, the mean coordination number, and the dimension of the order parameters are determined. © *2003 MAIK "Nauka/Interperiodica".*

1. INTRODUCTION

The study of phase transitions in disordered structures is an important field of the physics of condensed matter. This is related to the large variety of disordered structures, such as crystalline solid solutions, composites, gels, porous media, etc. There exist many types of phase transitions in disordered structures owing to different forms of ordering elements (magnetic moments, atomic displacements, and wave functions for a condensate). There also occur purely geometric percolation transitions due to the formation of macroscopic connected clusters.

Investigations of the phase transitions in the framework of disordered-lattice models using renormalization-group analysis [1] have revealed qualitative features in the critical behavior due to disorder, in particular, changes in the critical exponents in models with a second-order phase transition (see, for example, [2]). Examinations of another class of models that describe the macroscopic structural disorder in porous media, gels, and composites and are, as a rule, represented by different types of random graphs have demonstrated that, in many cases, the geometry of a random medium plays a decisive role in the thermodynamics of the phase transition. In the framework of the Ising and Potts models in random graphs, it has been established that variations in the geometric properties of the graph can lead not only to changes in the critical exponents [3, 4] and the type of transition [3–6] but also to its splitting [7] or vanishing [8].

Among the previously considered models of macroscopically disordered media, the simplest model is a graph with sparse random connections [9]. Within this model, it is assumed that any pair of N points can have connections with a probability p/N. The parameter p has the meaning of the mean coordination number; at $p = 1$, there occurs a percolation transition [10].

The phase transition in the Ising model on this graph was studied by Viana and Bray [11] and Kanter and Sompolinsky [12]. It was established that the specific features in the behavior of the thermodynamic quantities in the vicinity of the temperature $T_c(p)$ have an effective-field character. Moreover, the phase diagram was examined within this model with a random exchange responsible for the formation of the glass phase. The undoubted merits of these models are that they offer an exhaustive description of the thermodynamics in the range of applicability of the effective-field approximation and a generalization of the methods used to other types of random graphs [3, 4].

Moreover, there are many experimental works concerned with the phase transitions in disordered media that are adequately described by multicomponent order parameters (for example, superconducting, structural, and magnetic transitions in crystalline solid solutions and porous media [13–15]). The renormalization-group analysis of these transitions is limited by the disordered-lattice models and the small vicinity of the transition [1, 2]. To the best of our knowledge, description of the thermodynamics of phase transitions over wider ranges of variations in the temperature and disorder parameters, as well as for different types of random graphs, has been performed only in the framework of the Ising and Potts models [3–8]. In this respect, the purpose of the present work was to investigate the thermodynamics of a phase transition within an isotropic *m*-vector model in a graph with random sparse connections that can describe the superconductivity and superfluidity ($m = 2$), Heisenberg magnets ($m = 3$), and some

1063-7834/03/4510-1978$24.00

structural transitions in different media with macroscopic disorder.

2. REPLICA FORMALISM

The Hamiltonian of the model under consideration has the form

$$\mathcal{H} = -\frac{1}{2}\sum_{i\neq j}^{N} J_{ij}\mathbf{S}_i\mathbf{S}_j - \mathbf{H}\sum_{i=1}^{N}\mathbf{S}_i,$$

where $\mathbf{S}_i$ are the unit *m*-component vectors,

$$\mathbf{S}_i\mathbf{S}_i = 1,$$

$\mathbf{H}$ is the conjugated field, and J_{ij} is the constant of the random exchange interaction with the distribution function

$$P(J_{ij}) = \left(1-\frac{p}{N}\right)\delta(J_{ij}) + \frac{p}{N}\delta(J_{ij}-J).$$

In order to determine the thermodynamic potential averaged over the random exchange and other thermodynamic parameters, we will use the replica technique consisting in calculating the averaged *n*th-power partition function with subsequent passage to the limit $n \longrightarrow 0$; that is,

$$\langle Z^n\rangle_C = \int\prod_{j\neq j}^{N} dJ_{ij}P(J_{ij})\int\prod_{\alpha,i} d\mathbf{S}_{\alpha,i}\exp -\beta\sum_{\alpha=1}^{n}\mathcal{H}_\alpha.$$

In this expression, integration with respect to the unit *m*-component vector $\mathbf{S}_i$ satisfies the condition

$$\int d\mathbf{S}_i = 1.$$

For $N \longrightarrow \infty$, the averaged partition function $\langle Z^n\rangle_C$ can be represented as

$$\langle Z^n\rangle_C = \int\prod_{\alpha,i} d\mathbf{S}_{\alpha,i}e^{-\beta\mathcal{H}_r}.$$

Here, the replica Hamiltonian has the form

$$\mathcal{H}_r \approx -\frac{pT}{2N}\sum_{j\neq j}^{N}[\exp(K\mathbf{S}_{i\alpha}\mathbf{S}_{j\alpha}) - 1] - \mathbf{H}\sum_{i,\alpha}\mathbf{S}_{i\alpha}$$

with summation over the replica index α ranging from 1 to *n* and $K = \beta J$.

According to Leone *et al.* [4], the calculation of the averaged partition function $\langle Z^n\rangle_C$ can be reduced to a single-particle problem. For this purpose, we introduce the function

$$w(\{\boldsymbol{\sigma}\},\{\mathbf{S}\}) = \frac{1}{N}\sum_{i=1}^{N}\prod_{\alpha=1}^{n}\delta(\boldsymbol{\sigma}_\alpha - \mathbf{S}_{i,\alpha}).$$

With this function, we can eliminate summation over pairs of nodes in the replica Hamiltonian by representing it in the following form:

$$\mathcal{H}_r \approx -\frac{pTN}{2}\int\prod_{\alpha=1}^{n} d\boldsymbol{\sigma}_\alpha d\boldsymbol{\sigma}'_\alpha \exp(K\boldsymbol{\sigma}_\alpha\boldsymbol{\sigma}'_\alpha)w(\{\boldsymbol{\sigma}\},\{\mathbf{S}\})$$

$$\times w(\{\boldsymbol{\sigma}'\},\{\mathbf{S}\}) + \frac{pTN}{2} - \mathbf{H}\sum_{i,\alpha}\mathbf{S}_{i\alpha}.$$

Next, we use the identity

$$\int D\rho(\{\boldsymbol{\sigma}\})\delta[\rho(\{\boldsymbol{\sigma}\}) - w(\{\boldsymbol{\sigma}\},\{\mathbf{S}\})] = 1$$

and represent the partition function $\langle Z^n\rangle_C$ in the form of a continual integral,

$$\langle Z^n\rangle_C = \int D\rho(\{\boldsymbol{\sigma}\})U[\rho(\{\boldsymbol{\sigma}\})]\exp[-\beta NE[\rho(\{\boldsymbol{\sigma}\})]],$$

where

$$E[\rho(\{\boldsymbol{\sigma}\})] = -\frac{pT}{2}\int\prod_{\alpha=1}^{n} d\boldsymbol{\sigma}_\alpha d\boldsymbol{\sigma}'_\alpha \exp(K\boldsymbol{\sigma}_\alpha\boldsymbol{\sigma}'_\alpha)$$

$$\times\rho(\{\boldsymbol{\sigma}\})\rho(\{\boldsymbol{\sigma}'\}) + \frac{pT}{2},$$

$$U[\rho(\{\boldsymbol{\sigma}\})] = \int\prod_{\alpha}(d\mathbf{S}_\alpha e^{\beta\mathbf{H}\mathbf{S}_\alpha})\delta[\rho(\{\boldsymbol{\sigma}\}) - w(\{\boldsymbol{\sigma}\},\{\mathbf{S}\})].$$

In the last expression, the delta function can be represented in the form of a (continual) exponential integral. Consequently, we obtain

$$U[\rho(\{\boldsymbol{\sigma}\})] = \int D\tilde{\rho}(\{\boldsymbol{\sigma}\})\exp[N\Sigma(\rho,\tilde{\rho})],$$

where

$$\Sigma(\rho,\tilde{\rho}) = -\int\prod_{\alpha} d\boldsymbol{\sigma}_\alpha\tilde{\rho}(\{\boldsymbol{\sigma}\})\rho(\{\boldsymbol{\sigma}\})$$

$$+\ln\left(\int\prod_{\alpha} d\mathbf{S}_\alpha\exp\left[\beta\mathbf{H}\sum_{\alpha}\mathbf{S}_\alpha + \tilde{\rho}(\{\mathbf{S}\})\right]\right).$$

As a result, the averaged partition function $\langle Z^n\rangle_C$ is represented in the form of a continual integral of the functions $\rho(\{\boldsymbol{\sigma}\})$ and $\tilde{\rho}(\{\boldsymbol{\sigma}\})$:

$$\langle Z^n\rangle_C = \int D\rho(\{\boldsymbol{\sigma}\})D\tilde{\rho}(\{\boldsymbol{\sigma}\})\exp[-N\beta\Phi(\rho,\tilde{\rho})],$$
$$\Phi(\rho,\tilde{\rho}) = E(\rho) - T\Sigma(\rho,\tilde{\rho}). \quad (1)$$

For $N \longrightarrow \infty$, the integral in expression (1) is determined by the function $\Phi(\rho, \tilde{\rho})$ at the stationary point.

The functional equations for the stationary functions ρ and $\tilde{\rho}$ have the form

$$\tilde{\rho}(\{\boldsymbol{\sigma}\}) = p\int\prod_{\alpha} d\boldsymbol{\sigma}'_{\alpha}\exp(K\boldsymbol{\sigma}_{\alpha}\boldsymbol{\sigma}'_{\alpha})\rho(\{\boldsymbol{\sigma}'\}), \quad (2)$$

$$\rho(\{\boldsymbol{\sigma}\}) = \tilde{Z}^{-1}\exp\left[\tilde{\rho}(\{\boldsymbol{\sigma}\}) + \beta\mathbf{H}\sum_{\alpha}\boldsymbol{\sigma}_{\alpha}\right], \quad (3)$$

where $\tilde{Z}$ is the normalizing constant determined by the condition

$$\int\prod_{\alpha} d\boldsymbol{\sigma}_{\alpha}\rho(\{\boldsymbol{\sigma}\}) = 1.$$

By solving Eqs. (2) and (3), we can determine the averaged thermodynamic potential

$$F = -TN^{-1}\lim_{n\to 0} n^{-1}\ln\langle Z^n\rangle = \lim_{n\to 0} n^{-1}\Phi(\rho,\tilde{\rho}). \quad (4)$$

As follows from the above consideration, $\rho(\{\boldsymbol{\sigma}\})$ is the distribution function for the single-particle parameters dependent on $\mathbf{S}_i$ at a single node (when $n \longrightarrow 0$). In particular, we obtain the order parameter

$$\mathbf{M} \equiv \langle\langle \mathbf{S}_i\rangle_T\rangle_C = \lim_{n\to 0}\int\prod_{\alpha} d\boldsymbol{\sigma}_{\alpha}\rho(\{\boldsymbol{\sigma}\})\boldsymbol{\sigma}_1 \quad (5)$$

and the Edwards–Anderson parameter

$$\hat{Q} \equiv \langle\langle \mathbf{S}_i\rangle_T : \langle \mathbf{S}_i\rangle_T\rangle_C = \lim_{n\to 0}\int\prod_{\alpha} d\boldsymbol{\sigma}_{\alpha}\rho(\{\boldsymbol{\sigma}\})\boldsymbol{\sigma}_1\boldsymbol{\sigma}_2. \quad (6)$$

It is evident that Eqs. (2) and (3) at $\mathbf{H} = 0$ always have a trivial "paramagnetic" solution,

$$\rho(\{\boldsymbol{\sigma}\}) = 1,$$

$$\tilde{\rho}(\{\boldsymbol{\sigma}\}) = pR_m^n(K),$$

where

$$R_m(K) = \int d\mathbf{S}\exp(K\mathbf{S}\mathbf{S}') = \Gamma\left(\frac{m}{2}\right)\left(\frac{2}{K}\right)^{\frac{m-2}{2}} I_{\frac{m-2}{2}}(K). \quad (7)$$

Here, $I_{\frac{m-2}{2}}(K)$ is the Bessel function of the imaginary argument. The function $R_m(K)$ satisfies the equation

$$R''_m + \frac{m-1}{K}R'_m - R_m = 0. \quad (8)$$

In order to describe the transition to the phase with an order parameter $M \neq 0$, it is necessary to find another solution giving a lower thermodynamic potential at temperatures $T < T_c$ as compared to the potential provided by the paramagnetic solution. Unfortunately, in Eqs. (2) and (3), it is impossible to change over directly to the limit $n \longrightarrow 0$ with the assumption of the replica symmetry, as has been done in similar equations for the Ising model in a random graph [4, 12]. This substantially hampers the solution of Eqs. (2) and (3). However, at $T \longrightarrow T_c$ and $T \longrightarrow 0$, one can obtain explicit analytical results in the framework of the above model.

3. THERMODYNAMICS IN THE VICINITY OF THE PHASE TRANSITION

Since the hypothetical transition to the phase with an order parameter $M \neq 0$ is associated with the breaking of symmetry, it can be assumed that this transition is a second-order transition. Therefore, in the vicinity of the temperature T_c and at small values of H, the solution to Eqs. (2) and (3) differs only insignificantly from the paramagnetic solution. In this case, the functions $\rho(\{\boldsymbol{\sigma}\})$ and $\tilde{\rho}(\{\boldsymbol{\sigma}\})$ should depend on a particular vector $\mathbf{f}$ determining the spontaneous breaking of symmetry. By virtue of the isotropy, this dependence can be expressed only through scalar products of the form

$$f_{\alpha} = \mathbf{f}\boldsymbol{\sigma}_{\alpha}.$$

Under the assumption that the vector magnitude f is small, the distribution function $\rho(\{\boldsymbol{\sigma}\})$ can be represented in the form of the following expansion in terms of f_{α}:

$$\rho = a + \sum_{\alpha} f_{\alpha} + b_1\sum_{\alpha} f_{\alpha}^2 + b_2\sum_{\alpha\neq\beta} f_{\alpha}f_{\beta}$$

$$+ c_1\sum_{\alpha} f_{\alpha}^3 + c_2\sum_{\alpha\neq\beta} f_{\alpha}^2 f_{\beta} + c_3\sum_{\alpha\neq\beta\neq\gamma} f_{\alpha}f_{\beta}f_{\gamma} \quad (9)$$

$$+ d_1\sum_{\alpha} f_{\alpha}^4 + d_2\sum_{\alpha\neq\beta} f_{\alpha}^2 f_{\beta}^2.$$

Here, we used the assumption of replica symmetry, according to which the distribution function $\rho(\{\boldsymbol{\sigma}\})$ (and $\tilde{\rho}(\{\boldsymbol{\sigma}\})$) should be symmetric with respect to the permutation of the replica indices. Moreover, in expansion (9), we retain only the fourth order f_{α} terms which contribute to the thermodynamic potential.

Substituting expansion (9) into relationships (2) and (3), we obtain the following equations for $\mathbf{f}$:

$$(\tau + uf^2)\mathbf{f} = \beta\mathbf{H}, \quad (10)$$

where

$$\tau = 1 - p/p_c(K),$$

$$p_c(K) = R_m/R'_m = I_{\frac{m-2}{2}}(K)/I_{\frac{m}{2}}(K),$$

$$u = \frac{1}{m(p_c(K)-1)} + \frac{1}{m(m+2)(1-\lambda(K))} + \frac{1}{m+2},$$

$$\lambda(K) \equiv p_c(K) - m/K = I_{\frac{m+2}{2}}(K)/I_{\frac{m}{2}}(K).$$

It follows from the recurrence relationships for $I_m(K)$ [16] that

$$p_c(K) > 1, \quad \lambda(K) < 1.$$

As a result, Eq. (10) at $\mathbf{H} = 0$ has a nonzero solution for $\tau < 0$ or $p > p_c(K)$: $f^2 = -\tau/u$.

The equality $p = p_c(K)$ determines the phase transition temperature as a function of the mean coordination number p. The transition takes place only when $p > 1$; at $p \longrightarrow 1$, the temperature $T_c(p)$ tends to zero,

$$T_c(p) \approx 2J(p-1)/(m-1).$$

This stems from the fact that the graph has a macroscopic connected cluster only when $p > 1$ [9].

At $p \longrightarrow \infty$, the phase transition temperature $T_c(p)$ increases proportionally to p; that is,

$$T_c(p) \approx Jp/m.$$

The coefficients of $\rho(\{\boldsymbol{\sigma}\})$ in expansion (9) at $p \longrightarrow p_c$ and $n \longrightarrow 0$ have the following form:

$$2b_1 = (1-\lambda)^{-1}, \quad b_2 = p_c/2(p_c-1),$$

$$c_1 = \frac{K(1+2\lambda)}{6(m+2)\lambda(1-\lambda)}, \quad c_2 = \frac{p_cK(1+p_c-2\lambda)}{2m(p_c-1)(1-\lambda)},$$

$$c_3 = \frac{p_c(1+2\lambda)}{6(p_c-1)(1-\lambda)},$$

$$d_1 = \frac{K^2}{4}\frac{4c_1 + 2(b_1-1)^2 - 1}{K^2(1-p_c) + (m+2)[2K-(m+4)\lambda]},$$

$$d_2 = \frac{p_c}{4(p_c-\lambda^2)}[4c_2 + 2(b_1-1)^2 + 4(b_2-1)^2 - 3].$$

It follows from relationships (5), (6), and (9) that

$$\mathbf{M} = \mathbf{f}/m,$$

$$\hat{Q} = 2b_2\mathbf{f}:\mathbf{f}/m^2.$$

Moreover, we obtain

$$\langle\langle \mathbf{S}_i : \mathbf{S}_i\rangle_T\rangle_C = \frac{\hat{I}}{m} + \frac{2b_1}{m^2(m+2)}(m\mathbf{f}:\mathbf{f} - f^2\hat{I}),$$

$$\langle\langle \mathbf{S}_i\rangle_T : \langle \mathbf{S}_j\rangle_T\rangle_C = \langle\langle \mathbf{S}_i : \mathbf{S}_i\rangle_T\rangle_C = \mathbf{f}:\mathbf{f}/m^2, \quad i \neq j.$$

Note that the equality of the two correlators in the last expression holds accurate only to terms of the order of N^{-1}, which, in this case, are disregarded.

Differentiating expression (10) with respect to $\mathbf{H}$ we obtain the following relationship for the susceptibility:

$$\hat{\chi} = \frac{\partial \mathbf{M}}{\partial \mathbf{H}} = \chi_\perp\left(\hat{I} - \frac{\mathbf{H}:\mathbf{H}}{H^2}\right) + \chi_\parallel\frac{\mathbf{H}:\mathbf{H}}{H^2},$$

$$\chi_\perp = M/H, \quad \chi_\parallel = (\tau + 3uf^2)^{-1}.$$

For $T > T_c(p)$ and $H = 0$, we have

$$\chi_\perp = \chi_\parallel = \tau^{-1} \approx \frac{\vartheta(p)}{T - T_c(p)},$$

where the Curie constant is defined as

$$\vartheta(p) = (\partial\tau/\partial T)^{-1}$$
$$= pT_c(p)[K_c(p)(p^2-1) - (m-1)p]^{-1}.$$

For $T < T_c(p)$ and $H = 0$, the susceptibility $\chi_\parallel$ also adheres to the Curie–Weiss law with the Curie constant reduced by half.

In the case when $p \longrightarrow 1$, the quantity $\vartheta(p)$ tends to a constant,

$$\vartheta(p) \approx 2J/(m-1),$$

and when $p \longrightarrow \infty$, the Curie constant $\vartheta(p)$ takes the form

$$\vartheta(p) \approx T_c(p) = pJ/m.$$

From relationship (4), we obtain an equilibrium thermodynamic potential in the vicinity of the transition; that is,

$$F = -\frac{pT}{2}\ln R_m(K) - \frac{\mathbf{Hf}}{2m} - \frac{T\nu f^4}{2m^2(m+2)}.$$

Here,

$$\nu = b_1(b_1-1) + m\{d_1[1 - p_c + 3m(m+2)\lambda/K^2]$$
$$- c_1 - 1/12\} + (m+2)[d_2(2\lambda - \lambda^2/p_c - 1)$$
$$+ c_2 + (b_2-1)^2].$$

For the entropy, we derive the following expression:

$$S = \frac{p}{2}\ln R_m(K) + \frac{pK}{2p_c(K)} + \frac{T\nu f^2}{m^2(m+2)\vartheta u}.$$

According to this expression, the entropy is continuous at the transition point, whereas the heat capacity exhibits a jump:

$$\Delta C = \frac{T_c^2(p)\nu}{m^2(m+2)\vartheta^2u^2}.$$

At $p \longrightarrow 1$, we have

$$u \approx \frac{m^2 + 4m + 1}{m(m+1)(m+2)(p-1)},$$

$$v \approx \frac{1}{(p-1)^2}\left[(m+2)\left(1+\frac{1}{4m}\right)\right.$$
$$+\frac{(m-1)^2(5m^2+10m+4)}{4m(m+1)^2(m+2)}$$
$$\left.+\frac{72m^4+188m^3+245m^2+212m+108}{24(m+1)^2(m+2)(m+3)(3m+1)}\right],$$

Hence, the heat capacity satisfies the relationship $\Delta C \propto T_c(p)^2 \propto (p-1)^2$.

At $p \longrightarrow \infty$, we obtain the following expressions:

$$u \approx \frac{m+1}{m(m+2)}, \quad v \approx mp/12,$$

$$\Delta C \approx \frac{p}{12}\left[1-\frac{1}{(m+1)^2}\right].$$

Therefore, in the vicinity of the phase transition, the model under consideration is characterized by a classical effective-field thermodynamics inherent in models with an infinite interaction range. The results obtained above are valid for $f \ll 1$.

4. THERMODYNAMICS AT LOW TEMPERATURES

An analytical description of the thermodynamics in terms of the given model can also be obtained at $T \longrightarrow 0$ and $H \neq 0$ or $M \neq 0$. In this case, the function $\rho(\{\mathbf{S}\})$, which is an approximate solution to Eqs. (2) and (3), can be represented as the sum of the constant $(1-Q)$ and the function $\rho'(\{\mathbf{S}\})$ characterized by a sharp peak at $\mathbf{S}_\alpha = \mathbf{M} \equiv \langle \mathbf{S}_i \rangle$; that is,

$$\rho(\{\mathbf{S}\}) = 1 - Q + \rho'(\{\mathbf{S}\}).$$

By substituting this expression into formula (2) and using the aforementioned property of the function $\rho'(\{\mathbf{S}\})$, we obtain the relationship

$$\tilde{\rho}(\{\mathbf{S}\}) \approx p(1-Q)R_m^n(K) + pQ\exp\left(K\mathbf{M}\sum_\alpha \mathbf{S}_\alpha\right).$$

In turn, upon substituting this relationship into expression (3) and separating the constant out from the function $\rho(\{\mathbf{S}\})$, we derive the expression for the function $\rho'(\{\mathbf{S}\})$,

$$\rho'(\{\mathbf{S}\}) = \tilde{Z}^{-1}\exp[p(1-Q)R_m^n(K)]$$
$$\times\left\{\exp\left[pQ\exp\left(K\mathbf{M}\sum_\alpha \mathbf{S}_\alpha\right)+\beta\mathbf{H}\sum_\alpha \mathbf{S}_\alpha\right]-1\right\}, \quad (11)$$

and the equation for the parameter Q,

$$1-Q = \tilde{Z}^{-1}\exp[p(1-Q)R_m^n(K)].$$

Integrating expression (11) with respect to $\mathbf{S}_\alpha$, we obtain the normalizing constant at $n \longrightarrow 0$,

$$\tilde{Z} = e^p$$

and the equation for the parameter Q (also at $n \longrightarrow 0$),

$$1-Q = e^{-pQ}. \quad (12)$$

It follows from expression (12) that the parameter Q has the meaning of the fraction of nodes belonging to a macroscopic connected cluster, because expression (12) coincides with the corresponding equation of the percolation theory in the given graph [9]. This equation has a nontrivial positive solution when $p > 1$.

The function $\rho'(\{\mathbf{S}\})$ defined by relationship (11) has a sharp maximum at $\mathbf{S}_\alpha + \mathbf{M}$ under the condition

$$\max(JM, H) \gg T. \quad (13)$$

Consequently, the range of applicability of the results presented below is limited by this condition. It follows from expression (11) that the order parameter $\mathbf{M}$ is parallel to the field $\mathbf{H}$ and its magnitude can be determined from the formula

$$M = Q + (1-Q)\frac{R_m'(H/T)}{R_m(H/T)}. \quad (14)$$

The first term in formula (14) corresponds to the spontaneous order parameter and differs from zero when $p > 1$. The second term describes the contribution from the isolated nodes.

The transverse and longitudinal susceptibilities have the form

$$\chi_\perp = M/H,$$

$$\chi_\parallel = (1-Q)\left[\frac{1}{T}\left(1-\frac{R_m'^2(H/T)}{R_m^2(H/T)}\right)-\frac{(m-1)R_m'(H/T)}{HR_m(H/T)}\right].$$

It should be noted that the longitudinal susceptibility $\chi_\parallel$ differs from conventional paramagnetic susceptibility only by the factor $(1-Q)$.

From expressions (4) and (11), we obtain the following relationship for the thermodynamic potential in the region specified by condition (13):

$$F \approx -J\left[p(1-Q)+\frac{pQ}{2}(1+pQ-p^2Q^2)M\right]-QH$$
$$-T\ln R_m(H/T)+\frac{m-1}{2}\left[Q+\frac{p}{2}(1-Q)(2-Q)\right]T\ln\frac{J}{T}.$$

For the entropy, we have

$$S \approx -\frac{m-1}{2}\left[Q+\frac{p}{2}(1-Q)(2-Q)\right]\ln\frac{J}{T}.$$

As in models with continuous spins, in this case, we also obtain the entropy $S \longrightarrow \infty$ at $T \longrightarrow 0$, because the phase space with an ensemble of spins tends to zero.

The heat capacity is positive when $T \longrightarrow 0$ and tends to a constant,

$$C \approx \frac{m-1}{2}\left[Q + \frac{p}{2}(1-Q)(2-Q)\right].$$

From a comparison of the analytical results with the experimental data, one can judge the degree of accuracy to which the model of a graph with sparse random connections describes the macroscopic disorder in a particular porous medium or composite. However, we should note that the solutions presented above are by no means the only possible solutions. The point is not only that we restricted our consideration to the case of replica-symmetric solutions. The analysis of the bifurcations of the paramagnetic solutions for the functions $\rho(\{\mathbf{S}\})$ and $\tilde{\rho}(\{\mathbf{S}\})$ demonstrated that very similar solutions can be obtained at $T < T_c$, specifically at temperatures determined by the condition $p = p_c^l(K)$, (l = 2, 3, …). The same situation occurs with the Ising model of the graph under study [11]. Unfortunately, we failed to determine the stability region of all solutions to Eqs. (2) and (3). This requires detailed analysis of the applicability of the saddle point method for continual integrals; however, at present, the validity of this method has not been justified. We can only assume that, among the set of solutions to Eqs. (2) and (3), there exist solutions stable in some regions of variation in temperatures T and fields H, which describe the possible metastable states in terms of this model. Elucidation of the properties of these states can provide an adequate description of the kinetics of the given model at $T < T_c$ [17].

Note also that this model can be generalized by introducing a random exchange (or random external fields) and anisotropy and by specifying the distribution function of the coordination numbers of the graph nodes [3, 4]. These modifications should lead to the formation of new phase states and, in a number of cases, to variations in the critical behavior of the model. This offers rich possibilities for describing the whole variety of critical phenomena in macroscopically disordered media described by multicomponent order parameters.

ACKNOWLEDGMENTS

This work was supported by the International Association of Assistance for the promotion of co-operation with scientists from the New Independent States of the former Soviet Union (INTAS), project no. 2001-0826.

REFERENCES

1. R. B. Stinchcomb, in *Phase Transitions and Critical Phenomena*, Ed. by C. Domb and J. L. Lebowitz (Academic, London, 1983), Vol. 7.
2. D. E. Khmel'nitskiĭ, Zh. Éksp. Teor. Fiz. **68**, 1960 (1975) [Sov. Phys. JETP **41**, 981 (1975)].
3. S. N. Dorogovtsev, A. V. Goltsev, and J. F. F. Mendes, cond-mat/0203227.
4. M. Leone, A. Vazquez, A. Vespignani, and R. Zecchina, cond-mat/0203416.
5. S. N. Dorogovtsev, A. V. Goltsev, and J. F. F. Mendes, cond-mat/0204596.
6. F. Igloi and L. Turban, Phys. Rev. E **66**, 036140 (2002).
7. J. Machta, Phys. Rev. Lett. **66**, 169 (1991).
8. H. Rieger and T. R. Kirkpatrick, Phys. Rev. B **45**, 9772 (1992).
9. M. E. J. Newman, cond-mat/0202208.
10. D. Stauffer and A. Aharony, *Introduction to Percolation Theory* (Taylor and Francis, London, 1992).
11. L. Viana and A. J. Bray, J. Phys. C **18**, 3037 (1985).
12. I. Kanter and H. Sompolinsky, Phys. Rev. Lett. **58**, 164 (1987).
13. I. V. Golosovsky, I. Mirebeau, G. Andre, *et al.*, Phys. Rev. Lett. **86**, 5783 (2001).
14. E. V. Charnaya, C. Tien, K. J. Lin, *et al.*, Phys. Rev. B **58**, 467 (1998).
15. A. V. Fokin, Yu. A. Kumzerov, N. M. Okuneva, *et al.*, cond-mat/0205303.
16. I. S. Gradshteĭn and I. M. Ryzhik, *Table of Integrals, Series, and Products*, 4th ed. (Fizmatgiz, Moscow, 1963; Academic, New York, 1980), Chap. 8.
17. P. N. Timonin, Zh. Éksp. Teor. Fiz. **119**, 1198 (2001) [JETP **92**, 1038 (2001)].

Translated by O. Moskalev

Physics of the Solid State, Vol. 45, No. 10, 2003, pp. 1984–1989. Translated from Fizika Tverdogo Tela, Vol. 45, No. 10, 2003, pp. 1886–1891.

LATTICE DYNAMICS AND PHASE TRANSITIONS

Phase States and Dielectric Properties of Sodium–Potassium Niobate Solid Solutions

M. P. Ivliev, I. P. Raevskiĭ, L. A. Reznichenko, S. I. Raevskaya, and V. P. Sakhnenko

Research Institute of Physics, Rostov State University, pr. Stachki 194, Rostov-on-Don, 344090 Russia

e-mail: rip@ip.rsu.ru

Received March 11, 2003

Abstract—The temperature dependence of dielectric constant ε for single crystals of $Na_{1-x}K_xNbO_3$ ($0.04 \lesssim x \lesssim 0.15$) is studied for the first time. From the shape of the ε(*T*) anomalies corresponding to rotational phase transitions, the type of interaction between the order parameters and the polarization is determined. A phenomenological model is developed which adequately describes the experimentally observed sequence of high-temperature ($T > 300$°C) phase transitions, the dielectric anomalies associated with these transitions, and the changes in the phase states under the action of external factors (pressure, electric field). *© 2003 MAIK "Nauka/Interperiodica".*

1. INTRODUCTION

Sodium niobate $NaNbO_3$ (NN) belongs to the large family of crystals with perovskite structure and is characterized by a rich variety of structural phase transitions. At present, six disymmetric phases are known to exist in NN [1]. From the crystallographic standpoint, the sequence of the structural transitions is caused by the instability of a cubic lattice with respect to distortions of two kinds: shifts of anions of the oxygen sublattice, which may be interpreted as rotation (tilting) of octahedrons, and shifts of cations from their centrosymmetrical positions, leading to the occurrence of ferroelectric and antiferroelectric states [2–5].

In sodium niobate, three higher temperature phase transitions are caused by the rotation of octahedrons and the next three transitions, by a combination of rotation and polarization of octahedrons with the formation of two antiferroelectric complex ordered phases (*P*, *R*) and of one ferroelectric (low-temperature) phase. The whole set of disymmetric phases, except the *P* and *R* phases, can be described by three three-component order parameters, two of which, ψ and φ, characterize the rotation of NbO_6 octahedrons corresponding to lattice vibration modes M_3 and R_{25} and one of which, *p*, describes uniform ($\mathbf{k} = 0$) polarization arising as a result of shifts of Nb cations from the centers of octahedrons (Γ_{15} mode). The order parameters ψ and φ belong to the following stars of vectors **k**: ψ belongs to the triple-ray star of $\mathbf{k} = \frac{1}{2}(\mathbf{b}_1 + \mathbf{b}_2)$, and φ, to the single-ray star of $\mathbf{k} = \frac{1}{2}(\mathbf{b}_1 + \mathbf{b}_2 + \mathbf{b}_3)$, where $\mathbf{b}_i$ are vectors of the reciprocal lattice; these parameters transform according to irreducible representations τ_3 and τ_8 (in the notation from [6]).

The variety of lattice instabilities occurring in NN also determines the complex polymorphism of NN-based solid solutions, among them $Na_{1-x}K_xNbO_3$ (NKN), which is widely used as a piezoelectric material. Up to the mid-1970s, quite adequate studies of the structures of phases observed in NKN had been made and the *x–T* phase diagram for this system had been constructed [7, 8] (Fig. 1). Subsequently, the main fea-

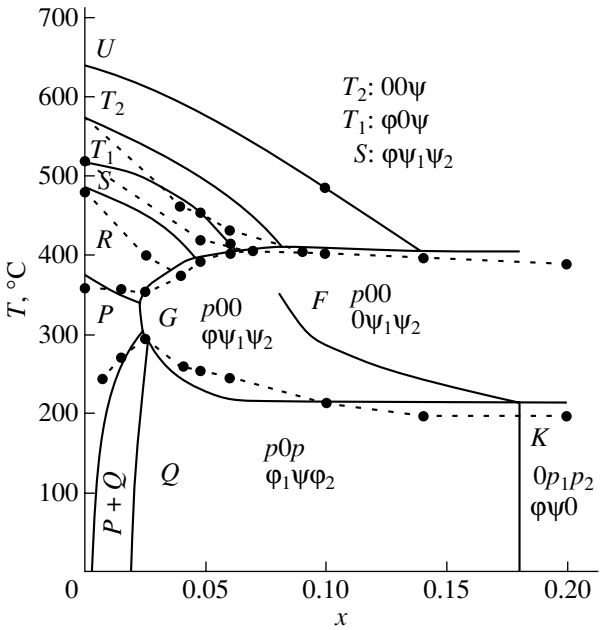

Fig. 1. Experimental *x–T* phase diagram of $Na_{1-x}K_xNbO_3$ solid solutions. The notation of phases is the same as that in [3, 4, 7, 8]. Solid lines are data from [7, 8] for ceramics. Dashed lines are the phase transition lines based on the experimental data on the dielectric properties of single crystals (filled circles).

1063-7834/03/4510-1984$24.00

tures of this phase diagram were interpreted in the context of the Landau theory [9], although some essential details remained unexplained, which, as shown in this paper, was associated with the inadequacy of the thermodynamic model suggested in [9], as well as with the inadequate (in our opinion) description of the interaction of several critical order parameters.

In crystals that exhibit various types of instabilities, the structure of the disymmetric phases is determined by the order in which the condensation of the phonon modes associated with the order parameters occurs and by the interactions between these modes. In this study, the parameters characterizing the interaction of the order parameters φ and ψ are obtained from the structural data given in [3] and information on the interaction of the rotational order parameters with polarization is obtained from an analysis of the temperature dependence of the dielectric constant ε. Studies of the dielectric properties of compounds of this type have shown that these properties strongly depend on the method of sample preparation [10]. It has been found that in single crystals the anomalies in ε(*T*) are pronounced much stronger and the reproducibility of the results is much better than in ceramics. In what follows, the results of measuring ε in $Na_{1-x}K_xNbO_3$ single crystals ($0.04 \lesssim x \lesssim 0.15$) in the temperature range 300–500°C with a step of 1–3°C are presented. It is precisely in thes ranges of *T* and *x* that anomalies in the dielectric properties caused by condensation of the rotational modes are observed. The analysis of these and other ε(*T*) anomalies is made in the framework of the Landau theory. The data thus obtained are then used for more comprehensive (than in [9]) thermodynamic description of NKN and the construction of a refined *x*–*T* phase diagram for these solid solutions.

2. EXPERIMENTAL RESULTS

Crystals of $Na_{1-x}K_xNbO_3$ were grown through mass crystallization from the melt using $NaBO_2$ as a solvent [11]. The crystal faces were parallel to the (001) planes of the perovskite structure. The composition was determined by a Camebax-Micro x-ray microanalyzer. Crystals with $x \lesssim 0.15$ were chosen for measurements. Optical analysis showed that all crystals are strongly twinned at room temperature. The dielectric constant ε of platelike crystals 0.2–0.3 mm thick with edges 1.5–2 mm long was measured at a frequency of 100 kHz with the aid of an R5083 ac bridge in the process of continuous heating or cooling at a rate of 2–3 K/min. Aquadag electrodes were applied to the (001) natural crystal faces.

Measurements of the ε(*T*) dependences for NKN single crystals with $x \approx 0.04$, 0.05, 0.06, 0.1, and 0.15 were made for the first time. The results are shown in Fig. 2. The following features in the behavior of ε(*x*, *T*) are worth noting. In the range of $x \approx 0.04$–0.06, a strong increase in the transition temperature to the ferroelectric state (determined from the position of the maximum in the ε(*T*) curve) is observed with increasing *x*. This effect is accompanied by a noticeable decrease in the temperature hysteresis of ε(*T*), and, in addition, the shape of the ε versus temperature curve is changed and (particularly at $x \sim 0.1$) becomes similar to that typical of second-order phase transitions.

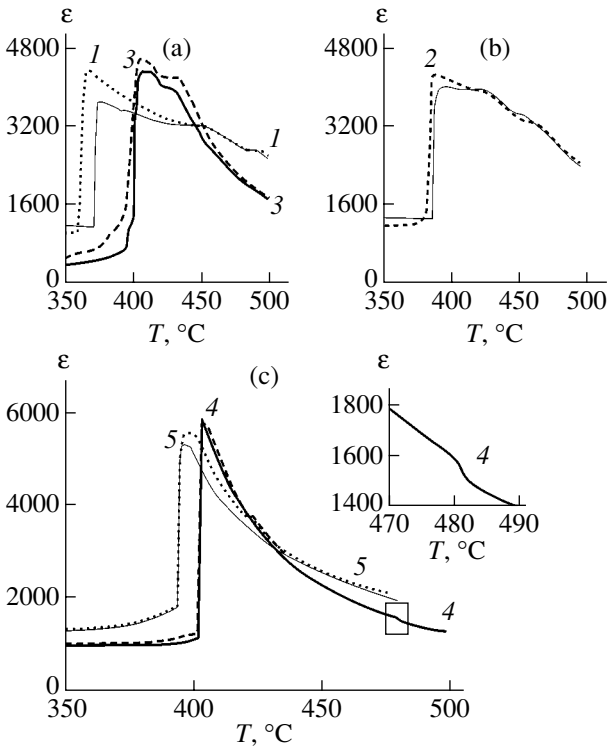

Fig. 2. Temperature dependence of dielectric constant ε of $Na_{1-x}K_xNbO_3$ single crystals for different values of *x*: (*1*) ≈0.04, (*2*) ≈0.05, (*3*) ≈0.06, (*4*) ≈0.1, and (*5*) ≈0.15.

3. PHASE DIAGRAM AND PHENOMENOLOGICAL THEORY

The phase states observed in the NKN system at $x \approx 0.04$–0.50 are described by three-component order parameters. However, for the description of the ordered phases in the range $T \geq 300$°C at $x \approx 0.04$–0.15, we require two components of the order parameter ψ (ψ_2, ψ_3) in various combinations and one component for φ and *p*, namely, φ_1 and p_1 (p_i denotes the polarization along the axis *i*; ψ_j and φ_k characterize rotations around the axes *j* and *k*). Therefore, the nonequilibrium thermodynamic potential can be simplified by retaining only those components of the order parameters that are required for the description of the observed ordered states. In this case, the model thermodynamic potential has the form

$$\Phi = \Phi_P + \Phi_R + \Phi_M + \Phi_{\text{int}}, \quad (1)$$

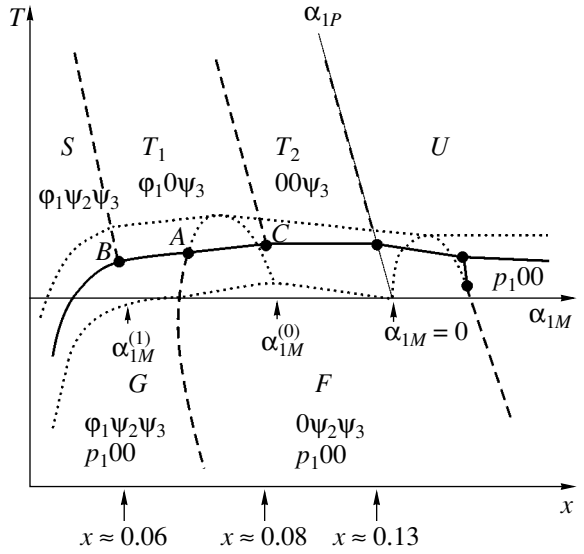

Fig. 3. Phase diagram described by the thermodynamic potential (1). Solid lines are the first-order phase transition lines, dashed lines are the second-order phase transition lines, and dotted lines are the stability boundaries of the phases.

where

$$\Phi_P = \alpha_{1P}p_1^2 + \alpha_{2P}p_1^4 + \alpha_{3P}p_1^6 + \ldots,$$

$$\Phi_R = \alpha_{1R}\varphi_1^2 + \alpha_{2R}\varphi_1^4 + \ldots,$$

$$\Phi_M = \alpha_{1M}g_1 + \alpha_{2M}g_1^2 + \beta_{1M}g_2 + \beta_{2M}g_2^2 + \delta_M g_1 g_2 + \ldots,$$

$$g_1 = \psi_2^2 + \psi_3^2, \quad g_2 = \psi_2^2\psi_3^2,$$

$$\Phi_{\text{int}} = \gamma_{PM}p_1^2 g_1 + \kappa_{PM}p_1^2 g_2 + \gamma_{PR}p_1^2\varphi_1^2 + \gamma_{MR}\varphi_1^2 g_1^2 + \ldots.$$

This potential contains the terms that characterize the contribution of each order parameter, Φ_L ($L = P, M, R$), and mixed invariants that describe the interaction between them, Φ_{int}. The potentials Φ_P and Φ_M are written to within terms that allow one to describe the first-order phase transition close to that of second order with respect to the order parameter p and to analyze solutions of the type $\psi_2 \neq \psi_3$, respectively.

The equilibrium phase diagram for the thermodynamic potential (1) is shown in Fig. 3 for various relations between α_{1M} and α_{1P}. To illustrate the accordance (on a qualitative level) between the α_{1M}–α_{1P} diagram and the experimental x–T diagram (Fig. 1), we show approximate values of the concentration x in Fig. 3. It was taken into account that α_{1P} depends on x only weakly for $x \gtrsim 0.06$, while α_{1M} and α_{1R} are strongly dependent on x (the temperatures at which the order parameters ψ and φ become nonzero decrease by 15–20°C as x is increased by 1% [7, 9]).

The phase diagram is obtained under the conditions $\alpha_{1M} \lesssim \alpha_{1R}$, $\alpha_{1R} = a + b\alpha_{1M}$, $a \gtrsim 0$, $b \sim 1$, $\alpha_{2P} \lesssim 0$, $\alpha_{2M} > 0$, $\alpha_{2R} > 0$, $\gamma_{PM} < 0$, $\gamma_{MR} < 0$, $\gamma_{PR} > 0$, $\kappa_{PM} < 0$, $\beta_{2M} > 0$, and $|\gamma_{MR}| \ll (\alpha_{2M}, \alpha_{2R})$. The relation between α_{1R} and α_{1M} means that first the parameter ψ and then the parameter φ become nonzero with a decrease in temperature. The quantities a and b characterize the relative softness of modes M_3 and R_{25}. From the analysis that follows it will be seen that the above conditions are quite justified and suitable for the description of the system under consideration.

In the region $\alpha_{1P} \gg 0$, the thermodynamic potential (1) describes not only the symmetric cubic phase U ($\varphi = \psi = p = 0$, $\alpha_{1M} > 0$) but also three disymmetric paraelectric ($p_{1M} = 0$) phases:

(1) phase T_2 with $\varphi_1 = \psi_2 = 0$, $\psi_3^2 = -\alpha_{1M}/2\alpha_{2M}$, $\alpha_{1M}^{(0)} \leq \alpha_{1M} \leq 0$;

(2) phase T_1 with $\psi_2 = 0$, $\psi_3 \neq 0$, $\varphi_1^2 = \dfrac{b}{2\alpha_{2R}}(\alpha_{1M}^{(0)} - \alpha_{1M})$, $\alpha_{1M}^{(1)} \leq \alpha_{1M} \leq \alpha_{1M}^{(0)}$;

(3) phase S with $\varphi_1 \neq 0$, $\psi_2 \neq 0$, $\psi_3 \neq 0$, $\alpha_{1M} \leq \alpha_{1M}^{(1)}$, $4\alpha_{2M}\beta_{2M} - \delta_M^2 > 0$, $\alpha_{1M}^{(0)} \cong -\dfrac{a}{b}\left(1 + \dfrac{\gamma_{MR}}{2b\alpha_{2M}}\right)$, $\alpha_{1M}^{(1)} = \dfrac{4\alpha_{2M}\alpha_{2R}\beta_{1M} - b\delta_M\gamma_{MR}\alpha_{1M}^{(0)}}{2\alpha_{2R}\delta_M}$.

It should be noted that solutions of the type $\psi_2 \neq \psi_3$, which characterize the phases S, G, and F, can be obtained only with inclusion of the eight-power invariant g_2^2 in the thermodynamic potential (1); therefore, within the model considered in [9], it was impossible to describe these phases adequately.

The paraelectric phases are stable with respect to polarization in the following regions:

for the cubic phase $U(000)$,

$$\chi_U = \alpha_{1P} \geq 0;$$

for phase $T_2(00\psi_3)$,

$$\chi_{T_2} = \alpha_{1P} + \gamma_{MP}\psi_3^2 \geq 0; \quad (2)$$

for phase $T_1(\varphi_1 0\psi_3)$,

$$\chi_{T_1} = \alpha_{1P} + \gamma_{MP}\psi_3^2 + \gamma_{RP}\varphi_1^2 \geq 0; \quad (3)$$

and for phase $S(\varphi_1\psi_2\psi_3)$,

$$\chi_S = \alpha_{1P} + \gamma_{MP}\psi_3^2 + \gamma_{RP}\varphi_1^2 + \left(\kappa_{MR} - \frac{\gamma_{MP}\delta_M}{2\alpha_{2M}}\right)\psi_2^2\psi_3^2 \geq 0, \quad (4)$$
$$\psi_2 \ll \psi_3,$$

where $\chi_i = \varepsilon_i^{-1}$ is the reciprocal dielectric constant of the ith phase.

The transition from the cubic phase to the phase $F(p_1, \varphi_1 = 0, \psi_2, \psi_3)$ is a complex first-order phase transition with the order parameter p_1, which destabilizes the system with respect to ψ_2 and ψ_3 becoming nonzero ($\psi_2 \neq \psi_3$). The softness with respect to the parameter ψ in the region $\alpha_{1M} \sim 0$ increases the jump in the order parameter at the U–F and T_2–F transitions. However, as one goes away from the point $\alpha_{1M} = 0$, the T_2–F transition becomes less pronounced.

The transition from the T_1 phase to the phase $G(p_1, \varphi_1, \psi_2, \psi_3)$ is also a complex first-order phase transition accompanied by the appearance (in addition to the parameter p_1) of the nonzero parameter ψ_2. Ferroelectric phases G and F have a common second-order transition line determined by the condition

$$\alpha_{1M} - \alpha_{1M}^{(0)} = \frac{-\gamma_{PR}}{b}p^2,$$

where

$$p^2 = \frac{-h + \sqrt{h^2 - 24\alpha_{3P}\alpha_{2M}m}}{12\alpha_{3P}\alpha_{2M}}, \quad h = 4\alpha_{2P}\alpha_{2M} - \gamma_{PM}^2,$$
$$m = 2\alpha_{2M}\alpha_{1P} - \gamma_{PM}\alpha_{1M}.$$

The coefficient γ_{PR} determines the relative position of the T_2–T_1 and F–G interphase boundaries near the transition line to the ferroelectric state. Since $\gamma_{PR} > 0$, the triple-phase point A is located to the left of the triple point C (Fig. 3). The same relative position of these points is obtained by extrapolating the experimentally observed F–G interphase boundary. It should be mentioned that, due to the specific structure of the phase diagram in the vicinity of point A (Fig. 3), on cooling along the $\alpha_{1M}'' = \text{const}$ line, where $\alpha_{1M}^{(A)} \leqslant \alpha_{1M}'' \ll \alpha_{1M}^{(C)}$ (i.e., $x'' = \text{const}$, $x_A \leqslant x'' \ll x_C$), the sequence of phases is $T_1 \longrightarrow F$, while on heating we have $F \longrightarrow G \longrightarrow T_1$. The G phase arises in the region of metastability of the F phase (i.e., above the AC line) as a result of the loss of stability of the F phase with respect to φ_1.

From a comparison of the α_{1M}–α_{1P} diagram (Fig. 3) with the experimental x–T diagram (Fig. 1), it is seen that they are qualitatively similar in terms of their basic elements, such as the set of phase states and the arrangement of these states on the phase plane. This suggests that our choice of the coefficients in thermodynamic potential (1) suits the description of the entire range of phase transitions observed in the region studied. Therefore, we will use this thermodynamic potential in our further analysis of the anomalies in dielectric properties.

4. DIELECTRIC PROPERTIES

As mentioned above, an increase in x in the range from 0.04 to 0.06 results in a strong rise in the ferroelectric phase transition temperature and a decrease in the temperature hysteresis of $\varepsilon(T)$. In addition, the $\varepsilon(T)$ dependence in the range 400–500°C, i.e., above the transition to a polar phase, demonstrates two well-pronounced kinks associated with rotational phase transitions. It should be emphasized that the analogous anomaly observed in crystals with $x \approx 0.1$ at $T \approx 485$°C is much weaker (Fig. 2).

First, we consider the change in the dielectric properties caused by the transitions between paraelectric phases. According to Eqs. (2)–(4), for the phase transition from paraelectric phase i to the paraelectric phase j characterized by an order parameter σ, the following relation holds:

$$\chi_j = \chi_i + d\sigma^2, \quad \text{where} \quad \chi_n^{-1} = \varepsilon_n, \quad (5)$$

from which it follows that the difference in magnitude between χ_j and χ_i becomes progressively more pronounced with decreasing χ_i. Therefore, in the vicinity of a transition to a polar phase, the dielectric anomalies caused by a phase transition between paraelectric phases are much more pronounced than those observed far from this transition. This can be clearly seen from a comparison of the anomalies in $\varepsilon(T)$ that accompany the T_2–T_1, T_1–S ($x \sim 0.04$–0.06), and U–T_2 ($x \sim 0.1$, $T \approx$ 485°C) phase transitions (Fig. 2). In the range 400–500°C, the first kink on the $\varepsilon(T)$ curve (Fig. 2) upon cooling is caused by the T_2–T_1 phase transition and the second kink, by the T_1–S phase transition. The T_2–T_1 transition is either second order or first order but very close to second order [3, 12]. The T_1–S transition is a first-order phase transition at which the order parameter ψ_2 arises in a jump but $\psi_2 \ll \psi_1$ [3]. The appearance of φ_1 at the T_2–T_1 phase transition results in a reduction in the slope of the $\varepsilon(T)$ curve. Consequently, according to Eq. (5), $\gamma_{PR} > 0$. The fact that ψ_2 becoming nonzero in the T_1–S transition is accompanied by an increase in the slope of the $\varepsilon(T)$ curve suggests that $\kappa_{PR} < 0$. The condition $\gamma_{PR} > 0$ means that the presence of the order parameter φ_1 hinders the appearance of p_1 and, as a consequence, the T_1–G phase transition temperature decreases with increasing φ (with a decrease in x). Similarly, the slope of the S–G interphase boundary with respect to the T_1–S boundary should become smaller (since $\kappa_{PR} < 0$), but actually it increases [7]. This means that the decrease in the S–G transition temperature is

caused by the fact that the $\alpha_{1P}(T, x) = 0$ line shifts dramatically toward lower temperatures with decreasing x.

Now, we consider variations in the dielectric properties at the transitions to a polar phase. The observed strong decrease in the ferroelectric phase transition temperature with a decrease in x ($x < 0.06$) can be caused by the following: (i) by weakening of the interaction responsible for the occurrence of polarization, which results in an increase in α_{1P}, and (ii) by the appearance of the order parameter φ in a polar phase. The second reason becomes essential if one assumes that the line along which φ becomes nonzero in the polar phase passes in such a way that the triple-phase point A lies slightly left of point B; i.e., $x_A \sim 0.06$ (Fig. 3). This means that both of the above reasons become important simultaneously and enhance the effect. In this case, on cooling along the line $x \gtrsim x_A$ we will have the sequence of phases $S \longrightarrow F$ and on heating, $F \longrightarrow G \longrightarrow S$, with the $F \longrightarrow G$ transition taking place in the region of metastability of these phases and being accompanied by a decrease in ε. The $\varepsilon(T)$ curve for $x \sim 0.06$ (Fig. 2) for heating (somewhat lower than the transition point from the polar phase) exhibits a small anomaly, which can be explained as a consequence of the phase transition from F to the G phase. However, extrapolation of the F–G interphase boundary shows that the A point should be located on the boundary of the phase T_1 near $x \sim 0.07$.

The decrease in temperature hysteresis with an increase in x from 0.04 to 0.06 (the maxima of $\varepsilon(T)$ in this range are almost of the same size) is caused by a decrease in the potential barrier separating the phases and by a reduction of the region of coexistence of the phases. The latter factor is caused by the slope of the S–G interphase boundary decreasing with increase in x and transforming into a plateau at $x > 0.06$, where the cross section of the region of coexistence of the S and G phases by the x = const path orthogonal to the phase transition line becomes the smallest.

In the range $x \sim 0.06$–0.15, the ferroelectric phase transition temperature changes insignificantly. For $x \sim 0.1$, the temperature hysteresis decreases markedly in comparison with the case of $x \sim 0.06$, the maximum value of ε increases noticeably, and the shape of the $\varepsilon(T)$ peak more closely resembles that of a second-order phase transition (Fig. 2). This fact suggests that a first-order, but close to a second-order, phase transition takes place at $x \sim 0.1$ (the Curie–Weiss temperature is shifted from the temperature of the $\varepsilon(T)$ maximum by ~20°C). In addition, the $\varepsilon(T)$ curve for $x \sim 0.1$ exhibits a small, weakly pronounced discontinuity in slope at $T \sim 485$°C, which, as was mentioned above, is caused by the rotational phase transition from the cubic (U) phase to the T_2 phase (Fig. 2). The shape and the small magnitude of this discontinuity support the idea about the character and relative weakness of the interaction between the order parameters p and ψ. As to the possible existence of a critical point in the vicinity of $x \sim 0.1$ at which the first-order-transition line transforms into a second-order-transition line similar to that observed in PZT [4, 5, 13], one should bear in mind the following. If we assume that such a point exists on the line of transitions to the polar phase, then it turns out that two such points must exist because they limit the line of second-order transitions to the polar phase; however, in the vicinity of this line, the phase with p_1, $\varphi_1 = \psi_2 = 0$, and ψ_3 should exist rather than the phase with p_1, $\varphi_1 = 0$, ψ_2, and ψ_3 (Fig. 3). No such phase has been observed to date.

For $x \sim 0.15$, the peak on the $\varepsilon(T)$ curve becomes smaller and the temperature hysteresis slightly increases (Fig. 2). This means that at $x \sim 0.15$ a first-order phase transition occurs which is not very close to a second-order transition (the Curie–Weiss temperature is shifted from T_m by ~40°C). Thus, the experimental data obtained agree with the prediction of the theory that the least pronounced transition to the polar phase will take place at $\alpha_{1M}^{(0)} \lesssim \alpha_{1M} < 0$. Our estimations give that $\alpha_{1M}^{(0)}$ corresponds to $x \sim 0.08$–0.09.

5. EFFECT OF EXTERNAL FACTORS ON PHASE TRANSITIONS

Given the picture of phase states analyzed above, one may anticipate how it will change under the action of external factors. For example, a hydrostatic pressure stimulates rotational phase transitions (increasing their temperature) and suppresses ferroelectric transitions [14]. As a result, the U–T_2, T_2–T_1, and T_1–S transition temperatures between the paraelectric phases increase. In contrast, the temperatures of the transitions to a ferroelectric state decrease and the magnitude of the jump in the order parameter p also decreases; i.e., the transitions become less pronounced. The latter circumstance may transform part of the line of the first-order transitions to the ferroelectric state into a second-order-transition line limited by critical points and also generate an intermediate phase (between the T_2 and F phases) with the order parameters p_1, $\varphi_1 = \psi_2 = 0$, and ψ_3. The transformations of the phase states are accompanied by changes in the physical parameters. This is likely the cause of the strong dependence of the properties of ferroelectric niobate ceramics on the thermodynamic history of the samples, since there are always residual stresses with a considerable hydrostatic component in ceramics [15].

The effect of external electric fields on the phase states is also a topical problem.

For example, a field with components ($E_1$00) transforms the U phase into the phase with parameters p_1 and $\varphi_1 = \psi_2 = \psi_3 = 0$ (U_E' phase); the T_2 phase, into the phase with p_1, $\varphi_1 = \psi_2 = 0$, and ψ_3 (T_{2E}' phase); the phase T_1, either into the phase with p_1, $\varphi_1 = \psi_2 = 0$, and

ψ_3 (T_{1E}' phase) or the phase with p_1, $\varphi_1 = 0$, φ_2, $\psi_2 = 0$, and ψ_3 (T_{1E}'' phase); and the phase S, into the phase with p_1, φ_1, ψ_2, and ψ_3 (S_E' phase). In the phases F and G, only the value of p is changed. The phase S_E' is isostructural to the phase G. As $E_1 \longrightarrow 0$, the phases T_{1E}' and T_{1E}'' transform into domains of the phase T_1 ($\varphi 0 \psi_3$, $0 \varphi \psi_3$). In order to decide which of these domains is more stable in the case of $E_1 \neq 0$, additional study is required. Henceforth, T_{1E}' will denote the more stable phase state arising from the phase T_1 in a field E_1. By taking into account the character of interaction of the polarization with the rotational order parameters discussed above, it can be shown that, with an increase in the applied field, the temperatures of the U_E'–T_{2E}', T_{1E}'–S_E', S_E'–G, T_{1E}'–F, T_{1E}'–G, T_{2E}'–F, and U_E'–F phase transitions increase, while the temperatures of the T_{2E}'–T_{1E}' and F–G transitions become lower. It is worth noting that the transition temperatures to the phases F and G increase to a greater extent than for the remaining transitions. This indicates that the regions of existence of the phases U_E' and T_{1E}' become smaller, while the regions of existence of the phases T_{2E}' and T_{1E}' and particularly of the phases F and G become larger. In sufficiently strong fields, the phase T_{1E}' disappears due to its being "forced out" by the phases T_{2E}', S_E', and F; the boundary between the phases S_E' and G disappears, while a common boundary is formed between the phases T_{2E}' and G. Such an approach, among other things, allows one to describe the processes occurring in NKN piezoelectric ceramics subjected to strong electric fields in the course of polarization and service.

The examples considered above are part of the general problem of the influence of external factors on the formation of phase states in the process of synthesis and treatment of materials that exhibit several structural instabilities. This problem is of particular topical interest in connection with the strong dependence of the physical properties of such materials on the preparation technology [10]. This dependence is largely caused by the fact that the instabilities that induce various order parameters are differently affected by the external factors. Under certain conditions, this feature can drastically change the regions of existence of different phases, the phases themselves, and, consequently, the entire range of physical properties. The examples given above show that such a possibility really exists.

6. CONCLUSIONS

Thus, the analysis of the obtained experimental data on the temperature dependence of the dielectric constant in NKN single crystals made it possible to clarify the character of the interaction of rotational order parameters with the polarization. This has allowed us to develop a thermodynamic model which adequately describes not only the variety of phase states, their location on the phase plane, and structural transformations but also the changes in the dielectric constant caused by these transformations. In addition, on the basis of this model, it becomes possible to make a detailed analysis of the changes of the phase states in NKN under various external actions, particularly, under a hydrostatic pressure and an electric field.

ACKNOWLEDGMENTS

This study was supported in part by the Russian Foundation for Basic Research, project no. 02-02-17781.

REFERENCES

1. H. Megaw, Ferroelectrics **7** (1–2), 87 (1974).
2. L. E. Cross and B. J. Nicholson, Philos. Mag. **46** (376), 453 (1955).
3. R. Ishida and G. Honjo, J. Phys. Jpn. **34** (11), 1279 (1973).
4. K. S. Aleksandrov, A. T. Anistratov, B. V. Beznosikov, and N. V. Fedoseeva, *Phase Transitions in Crystals of ABX_3 Halogen Compounds* (Nauka, Novosibirsk, 1981).
5. G. A. Smolenskiĭ, V. A. Bokov, V. A. Isupov, N. N. Kraĭnik, R. E. Pasynkov, A. I. Sokolov, and N. K. Yushin, *The Physics of Ferroelectric Phenomena* (Nauka, Leningrad, 1985).
6. O. V. Kovalev, *Irreducible Representations of Space Groups* (Akad. Nauk Ukr. SSR, Kiev, 1961).
7. M. Ahtee and A. M. Glazer, Acta Crystallogr. A **32** (3), 434 (1976).
8. M. Ahtee and A. W. Hewat, Acta Crystallogr. A **34** (2), 309 (1978).
9. C. N. W. Darlington, Philos. Mag. **31** (5), 1159 (1975).
10. I. P. Raevskiĭ, M. P. Ivliev, L. A. Reznichenko, *et al.*, Zh. Tekh. Fiz. **72** (6), 120 (2002) [Tech. Phys. **47**, 772 (2002)].
11. I. P. Raevskiĭ, L. A. Reznichenko, M. P. Ivliev, *et al.*, Kristallografiya **48** (3), 531 (2003) [Crystallogr. Rep. **48**, 486 (2003)].
12. C. N. W. Darlington and K. S. Knigth, Acta Crystallogr. B **55** (1), 24 (1999).
13. V. V. Eremkin, V. G. Smotrakov, and E. G. Fesenko, Fiz. Tverd. Tela (Leningrad) **31** (6), 156 (1989) [Sov. Phys. Solid State **31**, 1002 (1989)].
14. T. Hidaka, Phys. Rev. B **17** (11), 4363 (1978).
15. I. P. Raevskiĭ, L. A. Reznichenko, and A. N. Kalitvanskiĭ, Zh. Tekh. Fiz. **50** (9), 1983 (1980) [Sov. Phys. Tech. Phys. **25**, 1154 (1980)].

Translated by A. Zalesskiĭ

Physics of the Solid State, Vol. 45, No. 10, 2003, pp. 1990–1992. Translated from Fizika Tverdogo Tela, Vol. 45, No. 10, 2003, pp. 1892–1894.

LOW-DIMENSIONAL SYSTEMS AND SURFACE PHYSICS

Long-Wavelength Optical Phonons in the ZnTe/$Zn_{0.8}Cd_{0.2}Te$ Superlattice

L. K. Vodop'yanov, S. P. Kozyrev, and Yu. G. Sadof'ev

Lebedev Physical Institute, Russian Academy of Sciences, Leninskiĭ pr. 53, Moscow, 119991 Russia

e-mail: vodopian@sci.lebedev.ru

Received March 3, 2003

Abstract—The lattice IR reflection spectra of a ZnTe/$Zn_{0.8}Cd_{0.2}Te$ superlattice measured at temperatures of 300 and 10 K are analyzed. The ZnTe/$Zn_{0.8}Cd_{0.2}Te$ superlattice is grown by molecular-beam epitaxy on a GaAs substrate with a ZnTe buffer layer. It is found that the lattice IR reflection spectra of the studied structure exhibit only one reflection band. Dispersion analysis of the experimental spectrum has revealed the presence of one lattice TO mode close in frequency to the mode of pure ZnTe. This result is explained by a shift in the frequency of the lattice modes of the ZnTe and $Zn_{0.8}Cd_{0.2}Te$ layers of the superlattice toward each other. In turn, this shift is caused by internal elastic stresses in the superlattice due to a mismatch between the lattice parameters of the materials of these layers. © *2003 MAIK "Nauka/Interperiodica".*

1. INTRODUCTION

Although superlattices based on II–VI semiconductor compounds have attracted considerable research interest, there are only a few works concerned with the study of their phonon properties. In particular, Perkowitz *et al.* [1] and Kozyrev [2] investigated the lattice properties of HgTe/CdTe superlattices on a $Cd_{0.96}Zn_{0.04}Te$ substrate, which are formed by components with nearly identical lattice parameters. The condition of matched lattice parameters provided a means for interpreting the lattice reflection spectra of HgTe/CdTe superlattices in terms of the properties of bulk lattice modes of the Hg–Te and Cd–Te vibrations in $Hg_{1-x}Cd_xTe$ alloys. The analysis of the lattice IR reflection spectra made it possible to construct a model of the real superlattice that allows for the interdiffusion of Hg and Cd atoms in the adjacent layers and the formation of an HgCdTe alloy near the interface.

A more complex situation in studying the lattice properties occurs with superlattices based on components with mismatched lattice parameters. The lack of lattice matching gives rise to elastic stresses that significantly affect the physical properties of these structures. In our recent work [3], we analyzed the lattice IR reflection spectra of ZnSe/$Zn_{1-x}Cd_xSe$ (x = 0.2, 0.4) strained superlattices on a GaAs substrate. Earlier [4], we demonstrated that solid solutions in the $Zn_{1-x}Cd_xSe$ system are characterized by a single-mode transformation of the vibrational spectrum. Owing to the single-modality of $Zn_{1-x}Cd_xSe$ solid solutions, the lattice IR reflection spectrum of the superlattice exhibits only one lattice mode at an intermediate frequency rather than the two expected IR-active lattice modes of the ZnSe and $Zn_{1-x}Cd_xSe$ layers. This result is explained by the fact that the lattice modes of the layers approach each other in frequency under the effect of internal elastic stresses.

2. SUPERLATTICE GROWTH AND MEASUREMENTS

The ZnTe/$Cd_xZn_{1-x}Te$ (x = 0.2) superlattices were grown by molecular-beam epitaxy in a Katun' apparatus. The epitaxy was performed on exactly oriented (100) substrates of semi-insulating gallium arsenide through evaporation of special-purity (6*N*) elements for all the substances used. The surface of the GaAs substrate was cleaned from a layer of natural oxides by heating to 580°C in a ultrahigh vacuum chamber during preliminary preparation of the samples. After cooling to the temperature of epitaxial growth of the ZnTe buffer layer, the substrate was placed in the growth chamber and was then held in zinc vapors at an equivalent pressure of 3×10^{-5} Pa for about 2 min. A 1.5- to 2-μm-thick ZnTe buffer layer was grown at a substrate temperature of 350°C. The quantum-confined part of the ZnTe/CdZnTe structure was grown at a lower temperature (280°C) in order to prevent reevaporation of cadmium and, where possible, to provide the formation of abrupt interfaces between the layers. The ratio of the equivalent pressure of the tellurium molecular beam to the total pressure of Cd and Zn molecular beams was chosen close to two in order to ensure the coexistence of the superstructure consisting of a mixture of $(1 \times 2) + c(2 \times 2)$ reconstructions and the superstructure corresponding to the conditions of the highest extent of stoichiometric growth on the surface. The growth rate was kept equal to 0.2 nm/s for the ZnTe buffer layer and decreased to 0.1 nm/s before the growth of the quantum-confined part of the structure. The composition of the layers grown was checked against the change in the oscillation period of reflections in the high-energy electron diffraction patterns, which correspond to the growth of ZnTe and CdZnTe, and also against the posi-

tion of the emission lines of single quantum wells grown in a series of experiments on the calibration of molecular beam sources.

The lattice IR reflection spectra of the superlattice were recorded on a laboratory grating infrared spectrometer and a Bruker IFS-66 Fourier spectrometer with a resolution better than 1 cm^{-1}.

3. RESULTS AND DISCUSSION

The experimental lattice IR reflection spectrum of the $ZnTe/Zn_{0.8}Cd_{0.2}Te$ superlattice at 300 K is shown by the thin line in Fig. 1. The thick line in this figure represents the theoretical spectrum calculated using the dispersion analysis. It can be seen from Fig. 1 that the short-wavelength band corresponds to the lattice mode of the GaAs substrate, whereas the spectrum of the superlattice contains only one band, which is confirmed by the mathematical analysis. The reflection curve exhibits frequent oscillations (with a period of 2.5 cm^{-1}) associated with the interference on a 400-μm-thick GaAs substrate.

The dispersion analysis of the lattice IR reflection spectra of the superlattices was carried out using a model structure formed by a thin film (a superlattice and a buffer layer) on a semi-infinite substrate. In the framework of this model for a film of thickness L with a dielectric function $\varepsilon_f(\omega)$ and a substrate with a dielectric function $\varepsilon_s(\omega)$ in normally incident light, the amplitude reflectivity has the form [5]

$$r_{1fs}(\omega) = \frac{r_{1f}(\omega) + r_{fs}(\omega)\exp(i2\beta)}{1 + r_{1f}(\omega)r_{fs}(\omega)\exp(i2\beta)}, \qquad (1)$$

where

$$r_{1f}(\omega) = \frac{1 - \sqrt{\varepsilon_f(\omega)}}{1 + \sqrt{\varepsilon_f(\omega)}}, \; r_{fs}(\omega) = \frac{\sqrt{\varepsilon_f(\omega)} - \sqrt{\varepsilon_s(\omega)}}{\sqrt{\varepsilon_f(\omega)} + \sqrt{\varepsilon_s(\omega)}},$$

$$\text{and} \quad \beta = \frac{2\pi L\sqrt{\varepsilon_f(\omega)}}{\lambda}.$$

Here, λ is the wavelength $\left(=\frac{10\,000}{\omega}\right)$. The reflectivity is defined by the formula $R(\omega) = |r_{1fs}(\omega)|^2$.

The dielectric function $\varepsilon_f(\omega)$ of the film was considered in the classical additive form:

$$\varepsilon_f(\omega) = \varepsilon_\infty + \sum_j \frac{S_j\omega_{tj}^2}{\omega_{tj}^2 - \omega^2 - i\omega\gamma_j}. \qquad (2)$$

From the dispersion analysis of the lattice IR reflection spectrum of the superlattice at room temperature, we obtained only one lattice mode of the superlattice at a frequency of 177 cm^{-1}, which is close to the frequency of the lattice TO mode (179 cm^{-1}) for pure ZnTe. Since the difference between the frequencies of the TO modes for the ZnTe and $Zn_{0.8}Cd_{0.2}Te$ layers is small (~6 cm^{-1}), these modes can be unresolved because of the large attenuation parameters (of approximately 3 cm^{-1}) at room temperature. In order to separate the contributions from individual layers of the $ZnTe/Zn_{0.8}Cd_{0.2}Te//GaAs$ superlattice, the lattice IR reflection spectra were measured at a temperature of 10 K. The experimental lattice IR reflection spectrum of the $ZnTe/Zn_{0.8}Cd_{0.2}Te$ superlattice at 10 K is depicted by the thin line in Fig. 2. The thick line in this figure represents the theoretical spectrum calculated using the dispersion analysis. As can be seen, the spectrum shape does not change qualitatively. Within the limits of the spectral resolution of the spectrometer, we revealed only one lattice TO mode at a frequency of 181 cm^{-1}. This value is close to the frequency of the TO mode (182 cm^{-1}) for pure ZnTe at a temperature of 4.2 K. The shoulder observed in the low-frequency range of the TO mode of the superlattice is not related to an IR-active mode but is caused, more likely, by the interference in a layer consisting of the superlattice and buffer. This assumption is confirmed by the frequent oscillations associated with the interference on the substrate. These oscillations can be observed only in the transparency region of the substrate and multilayer structure. The mode in the vicinity of 146 cm^{-1}, which corresponds to a vibration of the two-mode system of $Zn_{1-x}Cd_xTe$ solid solutions that is similar to the vibration in CdTe, is not observed because of its weakness.

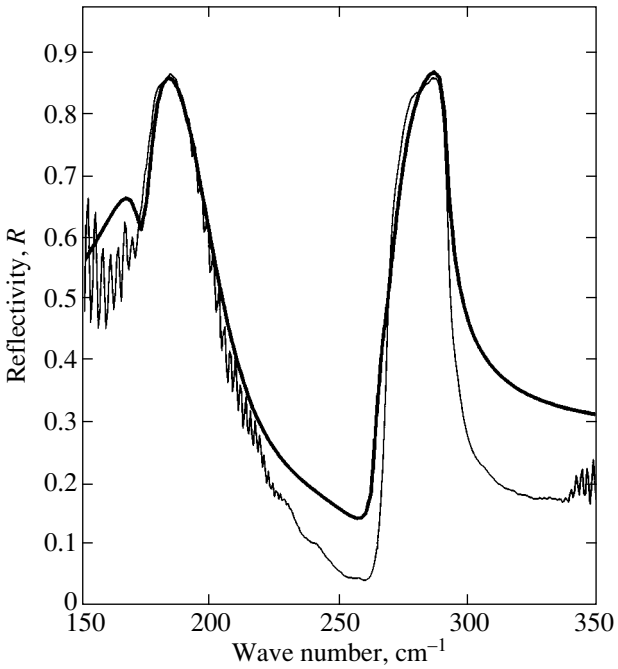

Fig. 1. Lattice IR reflection spectra of the $ZnTe/Zn_{0.8}Cd_{0.2}Te$ superlattice at a temperature of 300 K. The thin and thick lines represent the experimental and calculated spectra, respectively.

Let us elucidate why only one transverse optical mode is observed in the experiment. As was shown in

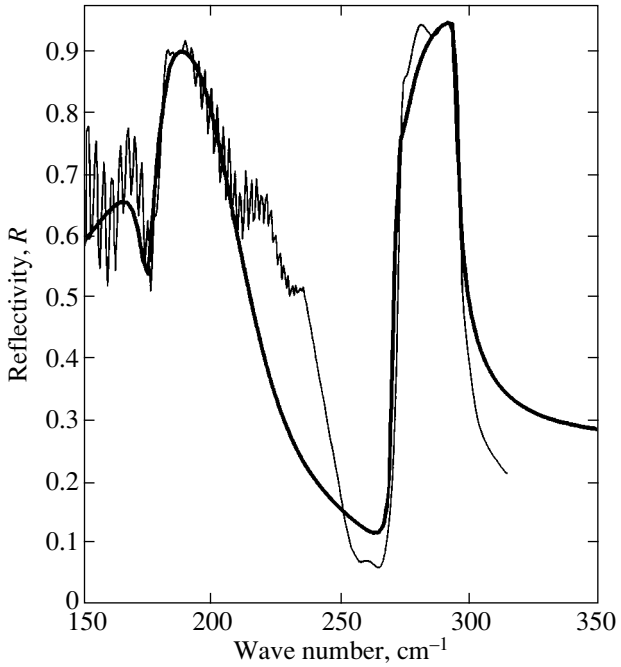

Fig. 2. Lattice IR reflection spectra of the $ZnTe/Zn_{0.8}Cd_{0.2}Te$ superlattice at a temperature of 10 K. The thin and thick lines represent the experimental and calculated spectra, respectively.

our earlier works [6, 7], the frequencies of the TO modes for bulk ZnTe and $Zn_{0.8}Cd_{0.2}Te$ crystals at room temperature are equal to 179 and 173 cm^{-1}, respectively. The difference in these frequencies (~6 cm^{-1}), even if not very large, could be found experimentally. However, it should be remembered that the frequencies of vibrational modes for the superlattice undergo shifts under the effect of internal elastic stresses. Now, we estimate these shifts within the approach used in [3, 8]. The elastic strains can be calculated under the condition of equilibrium of two mutually strained layers forming the superlattice. To the best of our knowledge, no elastic constants for $Zn_{0.8}Cd_{0.2}Te$ are available in the literature. Therefore, they were calculated using the extrapolation $C_{ik}(x) = C_{ik}(0)(a/a(x))^3$ [8], where $C_{ik}(0)$ and $C_{ik}(x)$ are the elastic constants of ZnTe and the solid solution, respectively, and a and $a(x)$ are the lattice constants of ZnTe and the solid solution, respectively. For $Zn_{0.8}Cd_{0.2}Te$, the coefficient $K(x)$ accounting for the relative change in the frequency of TO modes polarized along the layers and for the strain in the same direction was calculated using a linear interpolation between these coefficients for CdTe ($x = 0$) and ZnTe ($x = 1$). From these calculations, we obtained the following shifts and final frequencies: $\Delta\omega_{TO} = -2.7$ cm^{-1} and $\omega_{TO} = 176.3$ cm^{-1} for ZnTe layers subjected to tensile strain and $\Delta\omega_{TO} = 4$ cm^{-1} and $\omega_{TO} = 177$ cm^{-1} for $Zn_{0.8}Cd_{0.2}Te$ layers subjected to compressive strain. The difference in these frequencies (0.7 cm^{-1}) is considerably less than the attenuation constant (~3 cm^{-1}) and is unlikely to be found experimentally. The estimates obtained account for the manifestation of only one TO mode in our experiments.

4. CONCLUSIONS

Thus, the above analysis of the lattice IR reflection spectra of $ZnTe/Zn_{0.8}Cd_{0.2}Te$ and other superlattices based on II–VI compounds confirmed our assumption that the phonon spectrum of multilayer structures depends on the nature of the chemical bonds. In particular, it was established that individual properties of each layer manifest themselves in superlattices based on III–V compounds in which short-range covalent bonds dominate. As a result, the vibrational spectra exhibit modes typical of superlattices, such as confined, folded, and boundary phonons [9]. In multilayer structures based on II–VI compounds, in which the long-range ionic bonds dominate, the phonon frequencies of adjacent layers belong to a common mode and vibrational modes characteristic of superlattices do not manifest themselves.

ACKNOWLEDGMENTS

This work was supported by the Russian Foundation for Basic Research, project no. 03-02-7110.

REFERENCES

1. S. Perkowitz, R. S. Sudharsanan, and S. Yom, J. Vac. Sci. Technol. A **5**, 3157 (1987).
2. S. P. Kozyrev, Fiz. Tverd. Tela (St. Petersburg) **36** (10), 3008 (1994) [Phys. Solid State **36**, 1601 (1994)].
3. V. S. Vinogradov, L. K. Vodop'yanov, S. P. Kozyrev, and Yu. G. Sadof'ev, Fiz. Tverd. Tela (St. Petersburg) **43** (7), 1310 (2001) [Phys. Solid State **43**, 1365 (2001)].
4. L. K. Vodop'yanov, S. P. Kozyrev, and Yu. G. Sadof'ev, Fiz. Tverd. Tela (St. Petersburg) **41** (6), 982 (1999) [Phys. Solid State **41**, 893 (1999)].
5. H. W. Verleur, J. Opt. Soc. Am. **58**, 1356 (1968).
6. L. K. Vodop'yanov, E. A. Vinogradov, and A. E. Tsurkan, Zh. Prikl. Spektrosk. **21** (2), 321 (1974).
7. E. A. Vinogradov and L. K. Vodop'yanov, Fiz. Tverd. Tela (Leningrad) **17** (11), 3161 (1975) [Sov. Phys. Solid State **17**, 2088 (1975)].
8. V. S. Vinogradov, L. K. Vodop'yanov, S. P. Kozyrev, and Yu. G. Sadof'ev, Fiz. Tverd. Tela (Leningrad) **41** (11), 1948 (1999) [Phys. Solid State **41**, 1786 (1999)].
9. H. Shin, D. Lackwood, and P. Pool, Appl. Phys. Lett. **77** (2), 229 (2000).

Translated by N. Korovin

Physics of the Solid State, Vol. 45, No. 10, 2003, pp. 1993–2000. Translated from Fizika Tverdogo Tela, Vol. 45, No. 10, 2003, pp. 1895–1902.

LOW-DIMENSIONAL SYSTEMS AND SURFACE PHYSICS

Effect of Oxidation on the Electrical Properties of Granular Copper Nanostructures

V. M. Kozhevin, D. A. Yavsin, I. P. Smirnova, M. M. Kulagina, and S. A. Gurevich

Ioffe Physicotechnical Institute, Russian Academy of Sciences, Politekhnicheskaya ul. 26, St. Petersburg, 194021 Russia

e-mail: vmk@pltec.ioffe.rssi.ru

Received March 7, 2003

Abstract—The structural and electrical properties of thin granular metal films obtained by laser electrodispersion were studied. Such structures, which consist of amorphous copper grains 5 nm in size, were established to be extremely stable against oxidation. For instance, when oxidized in air, copper grains were covered by Cu_2O oxide shells about 1 nm thick after a period of a few days, after which further growth of the oxide in thickness stopped. The oxidized close-packed structures conduct current through intergrain tunneling electron transitions, whereas in partially oxidized structures the conduction involves tunneling electron hopping between conducting ensembles made up of several nanoparticles. It was shown that the size of the nanoparticles and of the conducting ensembles can be found by analyzing the temperature dependence of the conductivity and, independently, from the *I–V* characteristics of the films. © *2003 MAIK "Nauka/Interperiodica".*

1. INTRODUCTION

Granular metals, i.e., structures made up of nanosized metal particles, can serve as a basis for developing novel nanoelectronic devices [1] and new types of solid-state catalysts [2] and can also be employed to advantage in other areas of nanotechnology [3]. The electrical properties of such structures depend, to a considerable extent, on the size of the conducting nanoparticles and on their (bulk or surface) packing density. If the structure-averaged particle density is low, the dc conductivity of such a medium will be very low. In the opposite extreme case of a very high density, where a sizable fraction of particles are in contact [4], fairly extended conducting ensembles can form in the structure [5], with its conduction taking on a metallic pattern. Of particular interest are structures with an intermediate density, in which the average distance between particles is on the order of their dimensions, i.e., about a few nanometers. In this case, the conductivity of the medium derives from electron tunneling through the gaps separating the particles. The tunneling probability depends on the particle size; the height, width, and shape of the tunneling barriers; and the temperature of the medium [6]. The tunneling conductivity of metallic nanostructures is also governed substantially by such factors of structural and energy disorder as the spread in particle size, the pattern of the correlations in their positions, and the existence of a random potential on the particles [7]. The above-mentioned parameters of the structures may strongly vary depending on the technology used in their preparation, thus considerably complicating the problem of describing conduction in such media.

This communication reports on a study of granular copper nanostructures prepared by laser electrodispersion [8]. This method is based essentially on laser ablation of a metal (copper) target. The conditions of ablation are chosen so that the molten-metal drops injected from the target surface into the laser torch plasma become charged to the threshold of capillary instability and break up into smaller particles. It was shown in [8] that under certain conditions the drops undergo cascade fission to form finally copper nanoparticles. Nanoparticles thus formed cool rapidly; they are extracted by an electric field from the plasma zone and directed onto the substrate. Depending on the deposition time, substrate coatings with different particle densities and of different thickness can be prepared. Copper particles produced by this method typically have a small spread in size; indeed, for an average particle size of 5 nm, the relative spread does not exceed ≈20%. After preparation of the granular films in vacuum was complete, the structures were exposed to air and oxidized gradually, with the formation of oxide shells on the surface of the copper nanoparticles. It is assumed that these shells, along with the air gaps separating the particles, act as barriers in electron tunneling.

We studied the conductivity of granular copper films prepared by laser electrodispersion. The conductivity of the films was measured in lateral geometry. The conductivity of closely packed structures is shown to be extremely sensitive both to the pattern of mutual arrangement of particles in the bulk of a film and to the degree of oxidation of the structure. In particular, the specific features of self-organization of particles in the films under study account for the very sharp transition from tunneling to metallic conduction. The conductivity measurements also suggest that natural oxidation of

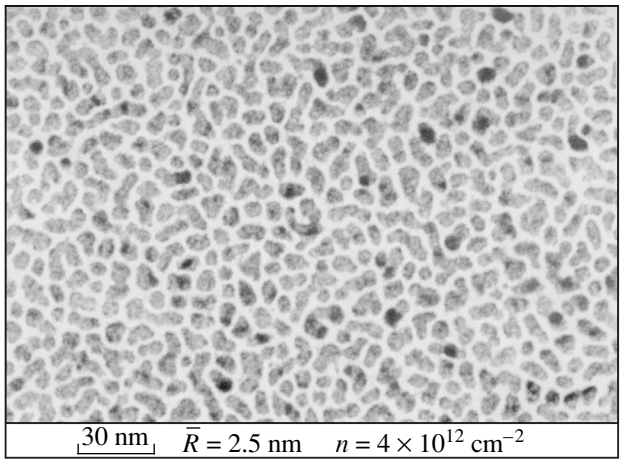

Fig. 1. TEM image of a granular copper film (top view). Film deposition time 3 min.

copper nanoparticles in air proceeds very slowly. This finding is in accord with observations made by other authors [9] in structural studies. The slow oxidation of copper nanoparticles is apparently a consequence of their having amorphous structure. We also derived a simple relation for the conductivity of granular films which is valid in both weak and strong fields. This relation is used to analyze the *I–V* characteristics and the temperature behavior of the conductivity, which permits us to establish the dependence of the characteristic size of a conducting ensemble on the oxidation time of the structure.

2. STRUCTURAL PROPERTIES OF FILMS

The structural properties of films were studied by transmission electron microscopy (TEM) and x-ray photoelectron spectroscopy (XPS). The film substrates were silicon plates coated with a layer of thermal oxide, with the surface-oxide relief depth not exceeding 2 nm. Figure 1 presents a TEM image of a structure deposited for 3 min. As follows from an analysis of this image and the diffraction patterns of transmitted electrons, this structure consists of copper grains about 5 nm in size and the particles are amorphous. The particle images in the photomicrograph are seen not to overlap, which suggests that for the given deposition time the particles are arranged in one layer on the substrate. The layer is nonuniform; indeed, it is seen to be made up of ensembles (islands) consisting of several particles in close contact. The photograph also reveals a network of gaps separating the islands. The gaps are practically of the same size, about 3 nm. There is also a small number of particles (they appear as darker colored in Fig. 1) belonging to the second layer. The particles of the second layer fall primarily into gaps between the islands.

That the second layer of particles in films deposited by laser electrodispersion starts to fill only after the filling of the first layer is complete is borne out by studies conducted earlier using atomic force microscopy [8]. The layer-by-layer formation of structures, as well as the formation of islands in the first particle layer, was suggested in [10] to be due to Coulomb interaction between charged particles impinging on the substrate and the particles deposited on its surface during the previous laser pulses. Note that, in order for TEM images to provide reliable information on the film structure, the images have to be obtained at the lowest possible electron beam current. When the current is too high, the particles are charged through electron absorption and migrated over the substrate surface, thus giving rise to a noticeable modification of the structures.

The structures prepared by laser electrodispersion in a vacuum chamber were subsequently exposed to air, which resulted in natural oxidation. The oxygen content in the structures was determined by XPS. The photoelectron spectra obtained within a broad range of kinetic energies clearly revealed the oxygen line $1s_{1/2}$ in addition to the lines characteristic of adsorbed carbon and water and to those due to the presence of silicon in the substrate. In the case under study, where the surface of a substrate consisting of SiO_2 silicon dioxide is coated with a fairly dense layer of copper grains, the presence of this line can be associated with the oxygen accumulated in the granular film during oxidation. The validity of this explanation is also supported by the small electron escape depth measured by XPS (see, e.g., [11]). The oxygen concentration was derived from the intensity of this line. The measured oxygen concentration in a film deposited for 2 min and exposed subsequently to air for 30 min was approximately 16 vol %. To exclude the contribution of the surface-adsorbed oxygen, the photoelectron spectra were also recorded after a short-time etching of the sample by Ar^+ ions, a procedure which removed a 0.5-nm layer from the surface. As a result of the etching, the oxygen content decreased to ≈10 vol %. To understand the results obtained, one has to make assumptions concerning the structure of the oxide thus formed.

It is known that oxidation of bulk copper samples develops primarily through diffusion of copper atoms across the growing oxide film to the surface and occurs through the reaction $Cu \longrightarrow Cu_2O \longrightarrow CuO$ [12]. Oxidation of copper particles a few nanometers to tens of nanometers in size was shown in [9, 13] to proceed by the same scenario; the general conclusion obtained in many studies consists, however, in that the room-temperature oxidation rate decreases with decreasing particle size. For copper particles a few nanometers in size, the time needed to reach the final stage of oxidation, the CuO oxide, can be very long; in fact, it can be longer than the reasonable observation time. Thus, it may be suggested that in our case, after exposure of a film to air for a few tens of minutes to several days, the product of oxidation will be Cu_2O, cuprous oxide. Assuming also that nanoparticles are of spherical shape and that the thickness of the oxide shell is uniform over the structure, the above experimental data permit the conclusion

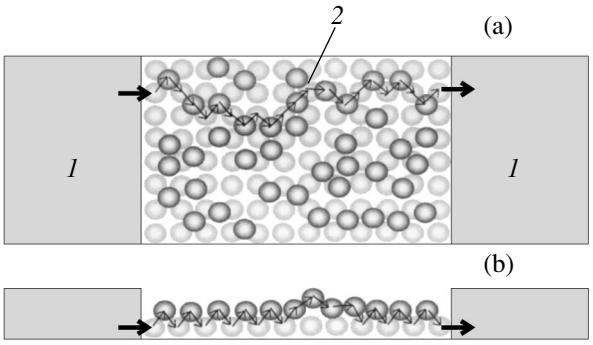

Fig. 2. Formation of a continuous current channel in a structure with a partially filled second grain layer. (a) Top view and (b) side view along the current path. (*1*) Metallic contact and (*2*) current path.

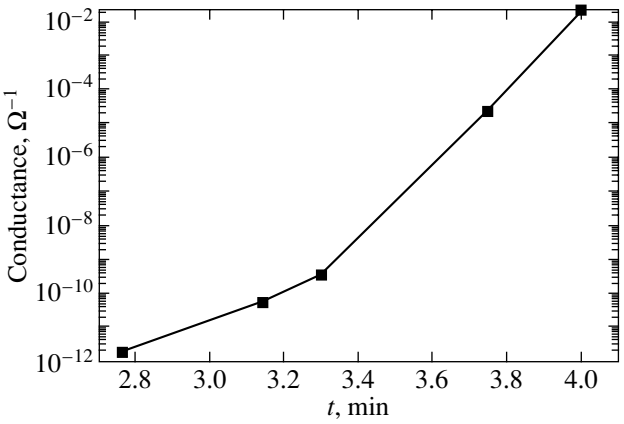

Fig. 3. Film conductance plotted vs. deposition time *t*.

that the thickness of the cuprous-oxide coating around a copper particle is, on the average, 0.8 nm. Thus, the nanoparticles under study contain an amorphous-copper core 4 nm in size which is coated with a cuprous-oxide layer 0.8 nm thick (the thickness of a cuprous-oxide monolayer is ~0.4 nm).

3. DEPENDENCE OF THE CONDUCTIVITY ON FILM THICKNESS AND OXIDATION TIME

As already mentioned, self-organization of particles in the course of deposition makes the structures under study locally nonuniform. Monolayer films have an islandlike structure. Within an island, the particles are in close contact with one another; as a result, the probability of electron transitions between particles in the island is sufficiently high. At the same time, the islands are separated by gaps about 3 nm in dimension, which practically excludes the possibility of interisland tunneling. Thus, the conductivity of monolayer coatings should be very low. Continuous current paths in the film plane can appear only when particles of the second layer appear to close the gaps between the islands. The formation of current paths in a structure is shown schematically in Fig. 2. The number of current paths and the film conductivity are determined primarily by the extent to which the second layer is filled. In addition, the conductivity of a film with a partially filled second layer of particles should obviously be very sensitive to the magnitude of the dielectric gaps between particles in islands and between particles of the first and second layer. Accordingly, the variation of the film conductivity caused by varying the magnitude of these dielectric gaps can be employed to monitor the degree of oxidation of a structure.

The longitudinal conductance of the films was measured on specially prepared test samples. To prepare these samples, a Cr layer 30 nm thick was first deposited on the oxidized silicon surface of a substrate and 400×400 μm contact pads were produced by explosive lithography, with the distance between these pads being varied on the same sample from 5 to 200 μm. Next, a granular copper film was deposited in the gaps between the contacts. Prior to measurements, all samples were exposed to air for the same time (30 min). Measurements were conducted at room temperature. Figure 3 displays the dependence of the film conductance on deposition time. The time threshold for the onset of conduction (determined from the sensitivity threshold of the measuring system, $\sim 10^{-12}\ \Omega^{-1}$) is seen to be about 2.8 min. This time correlates well with our notions on the structural properties of the films and can be identified with the beginning of formation of the second particle layer. As is evident from Fig. 3, as the second layer is filled, i.e., during the time interval of deposition of three to four minutes, the conductance of the structures rises by nine orders of magnitude. It can be readily seen that the surface density of particles changes only by ~25%. Note that, when the conductance rose to $\sim 10^{-3}\ \Omega^{-1}$, the film conduction was metallic, despite the short-time oxidation. Thus, because of the specific organization of particles the thin granular films under study, the insulator–metal transition occurs in them very quickly during the filling of the second layer of nanoparticles.

Figure 4 plots the conductance of films with a partially filled second layer of grains versus the time of exposure of the structure to air. We readily see that the pattern of conductance variation with time depends noticeably on the degree of filling of the second layer by grains or, what amounts to the same thing, on the initial conductance of the samples. For instance, the time to reach the time-independent conductance in films with a high initial conductance is about 15 days, whereas for films with a lower conductance (i.e., with a smaller number of grains in the second layer) the stage of fast conductance variation comes to an end after two days. After the first stage of oxidation, the film conductance stabilizes. Check measurements showed that, in thin films with a relatively small number of grains in the second layer, the conductance that was reached after the first stage of oxidation practically did not

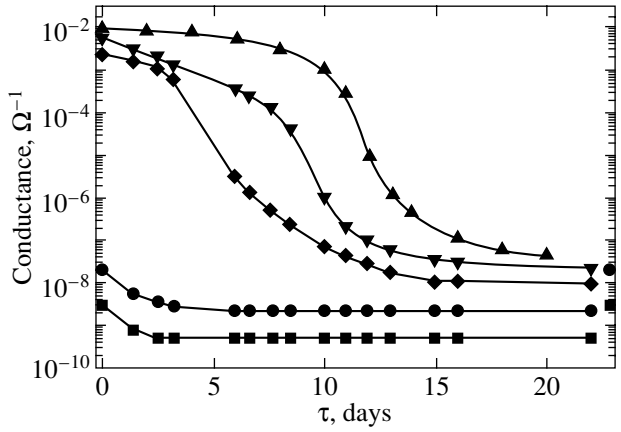

Fig. 4. Film conductance plotted vs. exposure time τ to air at room temperature.

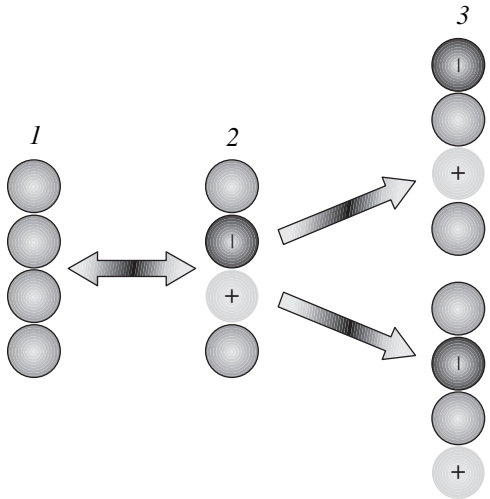

Fig. 5. Two-stage grain ionization process: (1 ⟶ 2) formation of a charged-grain dipole, (2 ⟶ 1) recombination of a charged-grain dipole, and (2 ⟶ 3) formation of a pair of independent charged grains.

change for two to three months from the date of manufacture of the structure. This means that the nanoparticle cores remained metallic during this long period of time and that the thickness and composition of the oxide shells practically did not change.

Studies of the conductivity of films consisting of two or more grain layers showed that it has a metallic pattern and approaches that of a thin continuous copper film. The resistivity of granular films of thickness in excess of 15 nm (consisting of three or more layers of particles) remained constant during the whole observation time period after deposition (up to three years). This effect can be attributed to the upper layer of grains preventing oxidation of the lower lying ones, so that no oxide shells form on the grains making up the lower layers and they are in direct contact, providing metallic conduction of the film as a whole. Note that a low activity of copper nanoparticles to oxidation has been observed by some authors [9, 14], but in most cases the experimental conditions and the properties of the particles themselves were different, which does not permit one to establish a one-to-one correspondence between the oxidation rate and the grain size. The extremely high stability of copper structures to oxidation revealed in our experiments can be assigned to the fact that nanoparticles prepared by laser electrodispersion have amorphous structure. This conjecture is in agreement with the observation that amorphous metals are more stable to corrosion than conventional metals with polycrystalline structure [15].

4. TEMPERATURE BEHAVIOR OF THE CONDUCTIVITY AND CURRENT–VOLTAGE CHARACTERISTICS OF OXIDIZED FILMS

Positively and negatively charged particles can appear in granular metal nanostructures both in tunneling transitions of electrons between originally neutral adjacent grains and as a result of electron (hole) injection from the electrodes. In the case of high ionization energies or comparatively low temperatures, the system contains only singly charged particles, i.e., particles with one excess electron or lacking an electron. It is this case that will be considered below. If a system contains a certain amount of charged particles, an electric field will initiate the drift of charges resulting from tunneling transitions. The current density in the film is given by the well-known expression

$$j = e(n_- v_- + n_+ v_+), \quad (1)$$

where e is the electronic charge; n_- and n_+ are the densities of negatively and positively charged grains, respectively; and $v_\pm$ are the drift velocities of electrons (–) or holes (+) in an external electric field.

The density of charged grains is determined by the charge generation and recombination rates. In weak electric fields, the thermal activation mechanism of generation dominates; the corresponding relation for the density of charged particles can be derived in this case by using a statistical approach [16]. In strong fields, field ionization of neutral grains can also play a substantial part. To find the charged particle density within a broad range of applied fields, we consider the generation–recombination balance with due account of thermal and field ionization.

Figure 5 is a schematic representation of the process of ionization of originally neutral grains. The ionization is seen to proceed in two stages; initially, a dipole of two oppositely charged neighboring particles forms through electron exchange between adjacent neutral grains (transition 1 ⟶ 2), after which the dipole breaks up to form two independent charged grains (transitions 2 ⟶ 3). If, conversely, charge migration

brings positively and negatively charged grains to neighboring positions, the charges can recombine.

In general, the rate of tunneling transitions of electrons between neighboring metal grains separated by a dielectric gap s wide can be written as [6]

$$r = \frac{\gamma}{h}\exp(2\chi s)\frac{\Delta}{1-e^{-\Delta/kT}} = A\frac{\Delta}{1-e^{-\Delta/kT}}, \qquad (2)$$

where γ is a geometry factor depending on particle shape, $\chi = [2m\phi/\hbar^2]^{1/2}$ is a tunneling constant, ϕ is the effective dielectric-barrier height, Δ is the change in the electrostatic energy of the grain system caused by the given transition, and $A \equiv \frac{\gamma}{h}\exp(-2\chi s)$. In the $1 \longrightarrow 2$ transition, the electrostatic energy of the grain system changes by $\Delta_{12} = eU_d - E_{12}$, where U_d is the potential difference of the neighboring grains between which the transition takes place and E_{12} is the energy of the dipole thus formed. For the reverse transition $2 \longrightarrow 1$, i.e., for the dipole recombination, we have $\Delta_{21} = E_{12} - eU_d$. Similarly, the change in energy occurring in the $2 \longrightarrow 3$ transition is $\Delta_{23} = eU_d - 2E + E_{12}$, where E is the work that has to be done for an electron to be transported from infinity to a neutral grain. It was shown in [6] that $E \approx E_{12}$; hence, $\Delta_{12} = -\Delta_{21} \approx \Delta_{23} = eU_d - E$. The corresponding transition rates calculated from Eq. (2) are

$$r_{12} = r_{23} = A\frac{eU_d - E}{1-\exp\left(\frac{E-eU_d}{kT}\right)},$$
$$r_{21} = A\frac{E-eU_d}{1-\exp\left(\frac{eU_d-E}{kT}\right)}. \qquad (3)$$

These relations for the transition rates can be used to find the rate of the two-stage ionization process $r_i = r_{12}r_{23}/(r_{21} + r_{23})$. Because the electrostatic energy of a singly charged nanoparticle 5 nm in size is $E \approx 200$ meV and eU_d in our experiments does not exceed 20 meV, the ionization rate at close to room temperature ($kT \leq 25$ meV) can be described by a simple relation,

$$r_i \approx AE\exp\left[\frac{2(eU_d - E)}{kT}\right]. \qquad (4)$$

In general, an electron can make a tunneling transition at an angle φ to the electric field vector. To include this possibility, one has to replace U_d in Eq. (4) by $U_d\cos\varphi$ and average the expression for r_i over the angle φ. The averaging over angles complicates Eq. (4), but it can be shown that correcting the quantity r_i reduces in this case to introducing a factor on the order of $\frac{kT}{kT + 2eU_d}$ that does not greatly differ from unity. Finally, knowing the ionization rate, one can calculate the generation rate of charged particles of both signs, $\Gamma_i = 2n_0r_i$, where n_0 is the density of neutral grains.

Electron tunneling from the newly formed negatively charged particle to a neighboring neutral particle or from a neutral to a neighboring positively charged grain produces charge migration in the bulk of the film. If this migration brings charges of opposite sign to neighboring grains, these charges recombine in a very short time $1/r_{21}$. The recombination rate of charged particles is given by the relation $\Gamma_r = 2n\nu_T\sigma$, where n is the density of positively or negatively charged particles, $\nu_T = dr|_{\Delta\to 0} = AdkT$ is the thermal velocity of charge motion due to thermally activated electron tunneling, and $\sigma \approx d$ is the recombination cross section (equal to the distance between the centers of neighboring conducting particles). The relation for ν_T thus obtained is valid if the particle size is fixed and the tunneling-gap dimensions along the current paths are constant. In this case, one can assume that, in the absence of an external field, the electron tunnels from a charged to a neighboring neutral particle without any change in energy. It is these properties that characterize the monodisperse structures under study here, in which the tunneling gaps are determined by the thickness of the grain oxide shell. For only partially oxidized structures, this approach also turns out to be applicable, because the tunneling transition probabilities cannot vary strongly along a chosen current path [5].

In a steady state, the generation rate is equal to the charge recombination rate, i.e.; $\Gamma_i = \Gamma_r$. If the density of charged particles is low ($n \ll n_0$), this relation readily transforms to

$$n \approx n_0\sqrt{\frac{E}{kT + 2eU_d}}\exp\left(\frac{eU_d - E}{kT}\right). \qquad (5)$$

Substituting the experimental values $E \approx 200$, $U_d \approx 20$, and $kT \approx 25$ meV ($T \approx 300$ K) into Eq. (5) yields an estimate of the density of charged particles $n \approx 10^{-3}n_0$, which bears out the validity of the above assumption. Note that, because the ionization process under study produces negatively and positively charged particles in equal numbers and their recombination rates are equal, a stationary homogeneous system is always in the state of charge neutrality, $n_- = n_+ = n$.

To find the drift velocities $\nu_\pm$ in Eq. (1), one has to consider the electron (hole) tunneling in the presence of an external field in more detail. We assume, as before, that all particles are of the same size and form a close-packed structure with tunneling gaps of a fixed width. If the electron migrates in an external field by tunneling from a negatively charged to a neutral grain, the change in energy of the system due to the transition is $\Delta = eU_d\cos\varphi$, where φ is the angle between the direction of transition and the electric field vector. (A hole transition

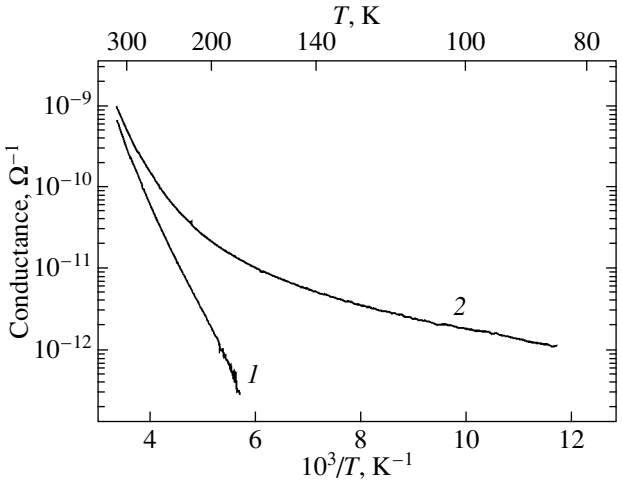

Fig. 6. Temperature dependences of the film conductance measured at different instants of time: (*1*) after exposure to air for a week and (*2*) immediately after film deposition.

involves the same change in energy.) Accordingly, the rate of charge displacements r_{dr} in various directions is

$$r_{dr} = A\frac{eU_d\cos\varphi}{1-\exp\left(-\frac{eU_d\cos\varphi}{kT}\right)}. \quad (6)$$

By averaging r_{dr} over all directions, one can calculate the directed velocity of charge motion:

$$\nu_{\pm} = \frac{d}{2\pi}\int_0^{2\pi} r_{dr}\cos\varphi d\varphi. \quad (7)$$

Integration yields

$$\nu_{\pm} = \frac{1}{4}AeU_d d. \quad (8)$$

Substituting Eqs. (5) and (8) into Eq. (1) yields the current density:

$$j = \frac{1}{2}Ae^2 dn_0 U_d\sqrt{\frac{E}{kT+2eU_d}}\exp\left(\frac{eU_d-E}{kT}\right). \quad (9)$$

The average voltage drop between neighboring grains in the direction of the field is $U_d = Ud/L$, where U is the voltage applied to the contacts and L is the interelectrode gap. Therefore, from Eq. (9), we obtain

$$j \propto U\sqrt{\frac{E}{kT+2eUd/L}}\exp\left(\frac{eUd/L-E}{kT}\right). \quad (10)$$

Relation (10) defines the current–voltage characteristics and the temperature dependence of conductivity of granular films.

Consider first the temperature behavior of the conductivity and the effect of film oxidation on this relation. Figure 6 presents temperature dependences of the conductance of the same film measured immediately after film preparation and following exposure of the sample to air for one week, which was sufficient for the film conductance to stabilize (Fig. 4). The measurements were conducted at a fixed voltage $U = 1$ V across the interelectrode gap. As follows from Eq. (10), the conductance measured at a fixed voltage and at a constant energy E over the structure should exhibit a close to activated temperature behavior, which yields a linear dependence when expressed in the $\ln\sigma$ vs. $1/T$ coordinates.[1] In the experiment, this relation was observed to hold for an oxidized film. The value of E derived from the slope of curve *1* in Fig. 6 is 200 meV. Using an approximate expression for this energy, $E \approx e^2/3\pi\varepsilon\varepsilon_0 D$ (ε is the effective permittivity of the medium and D is the particle diameter), obtained in the dipole approximation [18], one comes to the characteristic size of conducting particles $D \approx 5$ nm, which agrees with the main dimension of copper nanoparticles in such structures (see Section 2). Therefore, the dielectric gaps between all grains (including the grains in the first-layer islands) in the films whose conductance stabilized in time formed uniformly over the structure.

The nonlinear temperature dependence of conductance shown by curve *2* in Fig. 6 obviously corresponds to the case of temperature-dependent E. As seen from the shape of this curve, at low temperatures, the current paths in as-prepared films pass over ensembles of particles or conducting islands of a comparatively large size, for which the effective value of E is small. At high temperatures, the current paths pass over smaller grains as well. It thus follows that as-prepared films have only fragments of the network of dielectric gaps that forms after the structure has completely oxidized.

Equation (10) also shows that the slope of the temperature dependence of conductance plotted in the $\ln\sigma$–$1/T$ coordinates is determined by the difference $E - eUd/L$, i.e.; hence, at low voltages, the slope of the curve is dominated by the magnitude of E and starts to decrease with increasing voltage. Indeed, as seen from Fig. 7, the slope of the temperature dependence of conductance of an oxidized film decreases as the voltage at which it is measured increases.

Consider the current–voltage characteristics of the films. As follows from Eq. (10), the dependence of the current on voltage is dominated by the factor $U\exp\left(\frac{eUd}{kTL}\right)$. This relation can be conveniently analyzed by using a normalized characteristic. Introducing the parameters $i = I/I_{max}$ and $u = U/U_{max}$, where I_{max} is

[1] Another important condition for the temperature dependence of the conductance to be linear consists in the smallness of the random-potential amplitude on the grains [17]. This condition is also met in the structures under study.

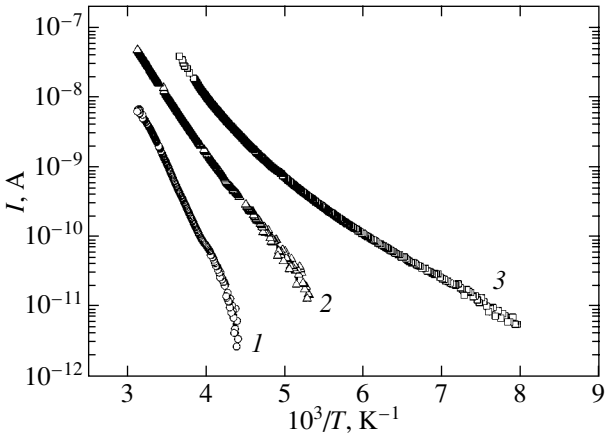

Fig. 7. Temperature dependences of the film conductance measured at three different voltages: (*1*) 1, (*2*) 10, and (*3*) 40 V. Gap width 5 μm.

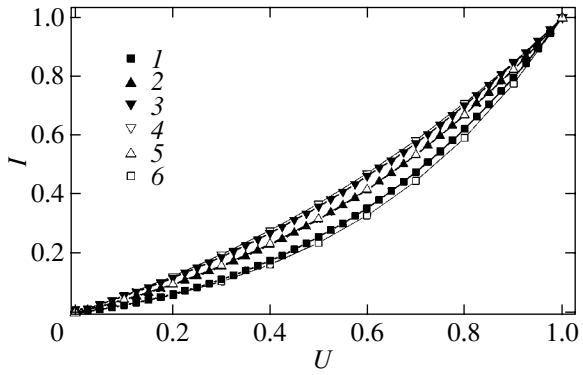

Fig. 8. Normalized current–voltage characteristics measured after different film exposures to air. Experiment: (*1*) $I_{max} = 1.6 \times 10^{-7}$ A for an as-prepared film, (*2*) $I_{max} = 6.8 \times 10^{-9}$ A three days later, and (*3*) $I_{max} = 3.1 \times 10^{-9}$ A seven days later. Calculated curves correspond to β equal to (*4*) 0.6, (*5*) 0.9, and (*6*) 1.5.

the maximum current at the maximum voltage U_{max}, we obtain

$$i = \frac{I}{I_{max}} = \frac{U}{U_{max}} \exp\left[\frac{ed(U - U_{max})}{kTL}\right] = u \exp[\beta(u-1)], \quad (11)$$

where $\beta = edU_{max}/kTL$. As is evident from Eq. (11), the curvature of the current–voltage characteristic plotted in the *u*–*i* coordinates depends on the only parameter, β. Note that the magnitude of parameter β for fixed values of U_{max}, *L*, and *T* is determined by the value of *d* only.

Experimental studies of the current–voltage characteristics revealed that their curvature decreases with increasing exposure time of as-prepared films to air. This effect is well illustrated in Fig. 8, which displays several normalized characteristics of the same film measured at different instants of time. The best fit between the theoretical and the experimental characteristic obtained immediately after the film deposition is reached for $\beta = 1.5$, which corresponds to a film with an average distance between the centers of conducting ensembles $d \approx 18$ nm. Such ensembles may consist of three to four contacting grains 5 nm in size. After the exposure of a film to air for three days, parameter ν decreases to 0.9. In this case, $d \approx 10.8$ nm, which means that the conducting ensembles are made up primarily of two grains. Oxidation of the film in air for seven days brings about a further decrease in the nonlinearity of the experimental characteristic. Its comparison with the theoretical curve yields $\beta = 0.6$ and $d \approx 7.2$ nm, which corresponds practically to close packing of 5-nm copper nanoparticles. Thus, the shape of the current–voltage characteristics also leads one to conclude that prolonged oxidation of a structure in air results in the formation of uniform dielectric gaps around all grains in the structure.

5. CONCLUSIONS

Thus, it has been shown that the conductivity of granular metallic structures depends substantially on the packing density and the pattern of mutual arrangement of conducting particles, as well as on the degree of their oxidation, i.e., on the presence, dimensions, and properties of dielectric barriers between individual particles or ensembles of particles. One of the most essential conclusions obtained in this study is that granular structures prepared by laser electrodispersion and made up of close-packed amorphous-copper particles 5 nm in size oxidize extremely slowly in air. A fairly long oxidation (a few to ten days) coats all particles by approximately 1-nm thick Cu_2O oxide shells, after which further growth of the oxide layer in thickness stops. The conduction in such completely oxidized structures occurs, provided the particles are closely packed, through tunneling transitions of electrons between individual grains. Current flow in partially oxidized structures involves tunneling electron hopping between conducting ensembles, which may consist of a few grains. It has been shown that the parameters of a granular film that are responsible for conduction can be determined by analyzing the temperature behavior of the conductance and, independently, from the shape of the current–voltage characteristics.

ACKNOWLEDGMENTS

This study was supported by the Russian Foundation for Basic Research (project nos. 01-02-17827, 02-03-32609), ISTC (project no. B 678), and the Ministry of Science, Industry, and Technologies of the Russian Federation ("Technology of Low-Dimensional Objects and Systems", project no. 40.072.1.1.1178).

REFERENCES

1. R. H. Chen and K. K. Likharev, Appl. Phys. Lett. **72**, 61 (1998).
2. V. M. Kozhevin, D. A. Yavsin, M. A. Zabelin, *et al.*, in *Proceedings of 10th International Symposium on Nanostructures: Physics and Technology, St. Petersburg, Russia* (2002), p. 41.
3. A. L. Buchachenko, *Problems and Advances in the Physics, Chemistry, and Engineering Science of Nanomaterials* (Moscow, 2002), Vol. 1, p. 15.
4. K. Deppert and L. Samuelson, Appl. Phys. Lett. **68** (10), 1409 (1996).
5. B. I. Shklovskiĭ and A. L. Éfros, *Electronic Properties of Doped Semiconductors* (Nauka, Moscow, 1979; Springer, New York, 1984).
6. B. Abeles, P. Sheng, M. D. Coutts, and Y. Arie, Adv. Phys. **24**, 407 (1975).
7. E. Guevas, M. Ortuno, and J. Ruiz, Phys. Rev. Lett. **71**, 1871 (1993).
8. V. M. Kozhevin, D. A. Yavsin, V. M. Kouznetsov, *et al.*, J. Vac. Sci. Technol. B **18**, 1402 (2000).
9. R. van Wijk, P. C. Gorts, A. J. M. Mens, *et al.*, Appl. Surf. Sci. **90**, 261 (1995).
10. V. M. Kozhevin, D. A. Yavsin, S. A. Gurevich, *et al.*, in *Proceedings of 7th International Symposium on Nanostructures: Physics and Technology, St. Petersburg, Russia* (1999), p. 205.
11. M. P. Seah and W. A. Dench, Surf. Interface Anal. **1**, 2 (1979).
12. B. V. Nekrasov, *Fundamentals of General Chemistry* (Khimiya, Moscow, 1970), Vol. 3.
13. A. Yanase, H. Matsue, K. Tanaka, and H. Komiyama, Surf. Sci. **219**, L601 (1989).
14. M. Diociaiuti, A. Bascelli, and L. Paoletti, Vacuum **43**, 575 (1992).
15. *Glassy Metals*, Ed. by H. S. Güntherodt and H. Beck (Springer, Berlin, 1981; Mir, Moscow, 1983).
16. E. Z. Mekhlikhov, Zh. Éksp. Teor. Fiz. **120**, 712 (2001) [JETP **93**, 625 (2001)].
17. D. A. Zakgeĭm, I. V. Rozhanskiĭ, I. P. Smirnova, and S. A. Gurevich, Zh. Éksp. Teor. Fiz. **118**, 637 (2000) [JETP **91**, 553 (2000)].
18. D. A. Zakgeĭm, I. V. Rozhanskiĭ, and S. A. Gurevich, Pis'ma Zh. Éksp. Teor. Fiz. **70**, 100 (1999) [JETP Lett. **70**, 105 (1999)].

Translated by G. Skrebtsov

Physics of the Solid State, Vol. 45, No. 10, 2003, pp. 2001–2011. Translated from Fizika Tverdogo Tela, Vol. 45, No. 10, 2003, pp. 1903–1912.

LOW-DIMENSIONAL SYSTEMS AND SURFACE PHYSICS

An Analog of the Kubo Formula for Conductivity of Spatially Inhomogeneous Media in Spatially Inhomogeneous Electric Fields

S. T. Pavlov[1, 2], I. G. Lang[3], and L. I. Korovin[3]

[1]*Escuela de Fisica de la UAZ, Apartado Postal c-580, 98060 Zacatecas, Mexico*
e-mail: pavlov@ahobon.reduaz.mx
[2]*Lebedev Institute of Physics, Russian Academy of Sciences, Leninskiĭ pr. 53, Moscow, 117924 Russia*
[3]*Ioffe Physicotechnical Institute, Russian Academy of Sciences, Politekhnicheskaya ul. 26, St. Petersburg, 194021 Russia*
e-mail: korovin@mail.ioffe.ru
Received March 27, 2003

Abstract—The average densities of currents and charges induced by a weak electromagnetic field in spatially inhomogeneous systems at a finite temperature are calculated. The Kubo formula for the electrical conductivity tensor is generalized to spatially inhomogeneous systems and spatially inhomogeneous fields. The contributions containing electric fields and derivatives of the fields with respect to coordinates are separated. It is shown that semiconductor quantum wells, wires, and dots can be treated as spatially inhomogeneous systems. © *2003 MAIK "Nauka/Interperiodica".*

1. INTRODUCTION

In recent years, great interest has been expressed by researchers in experimental and theoretical investigations of low-dimensional semiconductor objects, such as quantum wells, wires, and dots. In this respect, the development of a basic theory of interaction between electromagnetic fields and spatially inhomogeneous systems is an important problem.

The Kubo formula for the electrical conductivity tensor [1] is applicable for spatially homogeneous systems and electric fields independent of spatial coordinates. This formula correctly accounts for the interaction of charge carriers with a medium and, hence, can be used in solving particular problems of electrical conductivity in the solid-state theory. In the present work, we generalize the Kubo formula to the case of spatially inhomogeneous systems and spatially inhomogeneous fields. For this purpose, we preliminarily calculate the average densities of currents and charges induced by an electromagnetic field in a spatially inhomogeneous medium.

The Kubo formula [1] was derived using the operator for the interaction of charge carriers with the electric field in the following form:

$$U_K = -\sum_i e_i \mathbf{r}_i \mathbf{E}(t), \qquad (1)$$

where e_i is the charge of the ith particle, $\mathbf{r}_i$ is the radius vector of the ith particle, and $\mathbf{E}(t)$ is a time-dependent but spatially homogeneous electric field. However, it follows from the Maxwell equations that the time-dependent electric field necessarily depends on the coordinates. Therefore, the use of relationship (1) is always an approximation as applied to the field $\mathbf{E}$ dependent on t. In the case of spatially inhomogeneous systems, the field can strongly depend on the coordinates.

The problem is to take into account the homogeneity of a medium and to obtain additional terms involving derivatives of the electric field with respect to coordinates in the Kubo formula.

The operator for the interaction of an electromagnetic field with a system of charged particles is expressed through the vector $\mathbf{A}(\mathbf{r}, t)$ and scalar $\varphi(\mathbf{r}, t)$ potentials (see, for example, [2, p. 68]) but is not expressed in terms of the electric $\mathbf{E}(\mathbf{r}, t)$ and magnetic $\mathbf{H}(\mathbf{r}, t)$ fields (except for specific cases, for example, a constant electric field). Correspondingly, the current-density operator $\mathbf{j}_1(\mathbf{r}, t)$ and the charge-density operator $\rho_1(\mathbf{r}, t)$ within an approximation linear in the vector and scalar potentials are not expressed through the fields $\mathbf{E}(\mathbf{r}, t)$ and $\mathbf{H}(\mathbf{r}, t)$. However, the averages $\langle \mathbf{j}_1(\mathbf{r}, t)\rangle$ and $\langle \rho_1(\mathbf{r}, t)\rangle$ should be expressed in terms of the fields, because these quantities are observables. At a finite temperature T, the average can be defined by the expression [1, 3, 4]

$$\langle \ldots \rangle = \frac{\mathrm{Sp}\{\exp(-\beta\mathcal{H})\ldots\}}{\mathrm{Sp}\{\exp(-\beta\mathcal{H})\}}, \quad \beta = \frac{1}{kT}, \qquad (2)$$

where $\mathcal{H}$ is the Hamiltonian without regard for the interaction of particles with a weak electromagnetic field.

1063-7834/03/4510-2001$24.00

In our recent study [5], we deduced relationships for the averages $\langle 0|\mathbf{j}_1(\mathbf{r}, t)|0\rangle$ and $\langle 0|\rho_1(\mathbf{r}, t)|0\rangle$ at $T = 0$, when the average $\langle\ldots\rangle$ transforms into the average $\langle 0|\ldots|0\rangle$ over the ground state $|0\rangle$. In the present work, we continue our investigation and, hence, use the designations and many of the results obtained in [5].

The problem of expressing the averages $\langle \mathbf{j}_1(\mathbf{r}, t)\rangle$ and $\langle \rho_1(\mathbf{r}, t)\rangle$ in terms of electric and magnetic fields is very important, because the average $\langle \mathbf{j}_1(\mathbf{r}, t)\rangle$ expressed through the vector and scalar potentials includes the term $-(e/mc)\langle\rho(\mathbf{r})\rangle\mathbf{A}(\mathbf{r}, t)$, where $e = e_i$ is the charge of particles, $m = m_i$ s the mass of particles, c is the velocity of light, and $\rho(\mathbf{r})$ is the charge-density operator within the zeroth approximation in the fields [see formula (9)]. This term leads to difficulties in solving particular problems, such as the reflection and absorption of light in semiconductor quantum wells. These difficulties can be avoided if the averages $\langle \mathbf{j}_1(\mathbf{r}, t)\rangle$ and $\langle \rho_1(\mathbf{r}, t)\rangle$ are expressed in terms of the electric fields and their derivatives with respect to coordinates.

The question as to what kind of interaction (involving the vector potential or the electric field) is more convenient to use was previously discussed in [6] as applied to the problem of light scattering in bulk crystals. Zeyher *et al.* [6] were likely the first to change over from the velocity operators $\mathbf{v}_i$ to the coordinate operators $\mathbf{r}_i$ of particles according to the quantum relationship $\mathbf{v}_i = (i/\hbar)[\mathcal{H}, \mathbf{r}_i]$. As a result, these authors succeeded in changing over from expressions containing the vector potential to expressions including the electric field. However, since we need to solve other problems of spatially inhomogeneous systems, it is necessary to return to this question.

We will consider the case of a finite temperature and use the mathematical approaches proposed in [1, 3]. Our results will be compared with the inferences made by Konstantinov and Perel' [4], who developed the quantum theory of spatial dispersion of the electric and magnetic susceptibilities. It is assumed that charges and currents are absent at infinity and the fields $\mathbf{E}(\mathbf{r}, t)$ and $\mathbf{H}(\mathbf{r}, t)$ are equal to zero at $t \longrightarrow -\infty$, which corresponds to their adiabatic switching-on.

2. HAMILTONIAN OF THE SYSTEM AND THE CURRENT-DENSITY AND CHARGE-DENSITY OPERATORS

Let us consider a system composed of N particles with a charge e and a mass m in an arbitrary weak electromagnetic field characterized by the intensities $\mathbf{E}(\mathbf{r}, t)$ and $\mathbf{H}(\mathbf{r}, t)$. We introduce the vector $\mathbf{A}(\mathbf{r}, t)$ and scalar $\varphi(\mathbf{r}, t)$ potentials through which the fields can be expressed in the form

$$\begin{aligned}\mathbf{E}(\mathbf{r}, t) &= -\frac{1}{c}\frac{\partial\mathbf{A}(\mathbf{r}, t)}{\partial t} - \operatorname{grad}\varphi(\mathbf{r}, t),\\ \mathbf{H}(\mathbf{r}, t) &= \operatorname{curl}\mathbf{A}(\mathbf{r}, t).\end{aligned} \tag{3}$$

The fields are assumed to be classical, and the gauge of the potentials $\mathbf{A}$ and φ is arbitrary. To generalize the problem, we assume that the system of particles resides in a constant magnetic field $\mathbf{H}_c$ that can be relatively strong. This field is described by the vector potential $\mathbf{A}_c(\mathbf{r})$, so that $\mathbf{H}_c = \operatorname{curl}\mathbf{A}_c(\mathbf{r})$. The total Hamiltonian $\mathcal{H}_{\text{tot}}$ can be written in the form

$$\begin{aligned}\mathcal{H}_{\text{tot}} &= \frac{1}{2m}\sum_i\left(\mathbf{P}_i - \frac{e}{c}\mathbf{A}_c(\mathbf{r}_i) - \frac{e}{c}\mathbf{A}(\mathbf{r}_i, t)\right)^2\\ &+ V(\mathbf{r}_1, \ldots, \mathbf{r}_N) + e\sum_i\varphi(\mathbf{r}_i, t),\end{aligned} \tag{4}$$

where $\mathbf{P}_i = (\hbar/i)(\partial/\partial\mathbf{r}_i)$ is the generalized momentum operator and $V(\mathbf{r}_1, \ldots, \mathbf{r}_N)$ is the potential energy, including the interaction between particles and the external potential. The noncommutativity of $\mathbf{P}_i$ with $A_c(\mathbf{r}_i)$ and $\mathbf{A}(\mathbf{r}_i, t)$ should be taken into account in relationship (4). Next, the interaction energy U of particles with the electromagnetic field is separated in the total Hamiltonian (4) and the interaction with the strong magnetic field is included in the main Hamiltonian; that is,

$$\mathcal{H}_{\text{tot}} = \mathcal{H} + U, \tag{5}$$

where

$$\begin{aligned}\mathcal{H} &= \frac{1}{2m}\sum_i\mathbf{p}_i^2 + V(\mathbf{r}_1, \ldots, \mathbf{r}_N),\\ \mathbf{p}_i &= \mathbf{P}_i - \frac{e}{c}\mathbf{A}_c(r_i),\end{aligned} \tag{6}$$

$$\begin{aligned}U &= U_1 + U_2,\\ U_1 &= -\frac{1}{c}\int d^3r\mathbf{j}(\mathbf{r})\mathbf{A}(\mathbf{r}, t) + \int d^3r\rho(\mathbf{r})\varphi(\mathbf{r}, t),\\ U_2 &= \frac{e}{2mc}\int d^3r\rho(\mathbf{r})\mathbf{A}^2(\mathbf{r}, t).\end{aligned} \tag{7}$$

Here, we also introduce the current-density operator

$$\begin{aligned}\mathbf{j}(\mathbf{r}) &= \sum_i\mathbf{j}_i(\mathbf{r}),\\ \mathbf{j}_i(\mathbf{r}) &= (e/2)[\delta(\mathbf{r} - \mathbf{r}_i)\mathbf{v}_i + \mathbf{v}_i\delta(\mathbf{r} - \mathbf{r}_i)],\\ \mathbf{v}_i &= \mathbf{p}_i/m,\end{aligned}$$

and the charge-density operator

$$\rho(\mathbf{r}) = \sum_i\rho_i(\mathbf{r}), \quad \rho_i(\mathbf{r}) = e\delta(\mathbf{r} - \mathbf{r}_i).$$

The operators $\mathbf{j}_i(\mathbf{r})$ and $\rho_i(\mathbf{r})$ are related by the continuity equation

$$\begin{aligned}\operatorname{div}\mathbf{j}_i(\mathbf{r}) + \dot{\rho}_i(\mathbf{r}) &= 0,\\ \dot{\rho}_i(\mathbf{r}) &= (i/\hbar)[\mathcal{H}, \rho(\mathbf{r})],\end{aligned} \tag{8}$$

which will be used in further calculations. Note that the operator U_2 will not appear below, because it is quadratic in the vector potential and its inclusion is beyond the scope of an approximation linear in the fields.

Additions linear in the potentials $\mathbf{A}(\mathbf{r}, t)$ and $\varphi(\mathbf{r}, t)$ to the current-density and charge-density operators in the Heisenberg representation can be written as follows:

$$\begin{aligned} j_{1\alpha}(\mathbf{r}, t) &= -\frac{e}{mc}\rho(\mathbf{r}, t)A_\alpha(\mathbf{r}, t) \\ &+ \frac{i}{\hbar}\int_{-\infty}^{t} dt'[U_1(t'), j_\alpha(\mathbf{r}, t)], \\ \rho_1(\mathbf{r}, t) &= \frac{i}{\hbar}\int_{-\infty}^{t} dt'[U_1(t'), \rho(\mathbf{r}, t)], \end{aligned} \tag{9}$$

where subscript 1 indicates the approximation linear in the fields; $\rho(\mathbf{r}, t)$, $\mathbf{j}(\mathbf{r}, t)$, and $U_1(t)$ are the operators in the interaction representation, for example,

$$\rho(\mathbf{r}, t) = \exp(i\mathcal{H}t/\hbar)\rho(\mathbf{r})\exp(-i\mathcal{H}t/\hbar);$$

and $[F, Q] = FQ - QF$. Substitution of expression (7) for U_1 into formulas (9) gives

$$\begin{aligned} j_{1\alpha}(\mathbf{r}, t) &= -\frac{e}{mc}\rho(\mathbf{r}, t)A_\alpha(\mathbf{r}, t) \\ &+ \frac{i}{\hbar c}\int d^3r' \int_{-\infty}^{t} dt'[j_\alpha(\mathbf{r}, t), j_\beta(\mathbf{r}', t')]A_\beta(\mathbf{r}', t') \\ &- \frac{i}{\hbar}\int d^3r' \int_{-\infty}^{t} dt'[j_\alpha(\mathbf{r}, t), \rho(\mathbf{r}', t')]\varphi(\mathbf{r}', t'), \end{aligned} \tag{10}$$

$$\begin{aligned} \rho_1(\mathbf{r}, t) &= \frac{i}{\hbar c}\int d^3r' \int_{-\infty}^{t} dt'[\rho(\mathbf{r}, t), j_\beta(\mathbf{r}', t')]A_\beta(\mathbf{r}', t') \\ &- \frac{i}{\hbar c}\int d^3r' \int_{-\infty}^{t} dt'[\rho(\mathbf{r}, t), \rho(\mathbf{r}', t')]\varphi(\mathbf{r}', t'). \end{aligned} \tag{11}$$

3. AVERAGES OF THE INDUCED DENSITIES OF CURRENTS AND CHARGES

In our previous work [5], we considered the problem at $T = 0$ and operators (10) and (11) averaged over the ground state of the system. In [7, p. 84], it was shown that the averaging should be performed using the wave functions $|0\rangle$ of the ground state without regard for the interaction U. In [5], we rearranged the expressions for the averages $\langle 0|j_{1\alpha}(\mathbf{r}, t)|0\rangle$ and $\langle 0|\rho_1(\mathbf{r}, t)|0\rangle$ and obtained the relationships

$$\begin{aligned} &\langle 0|j_{1\alpha}(\mathbf{r}, t)|0\rangle \\ &= \langle 0|j_{1\alpha}(\mathbf{r}, t)|0\rangle_E + \langle 0|j_{1\alpha}(\mathbf{r}, t)|0\rangle_{\partial E/\partial \mathbf{r}}, \\ &\langle 0|\rho_1(\mathbf{r}, t)|0\rangle = \langle 0|\rho_1(\mathbf{r}, t)|0\rangle_E + \langle 0|\rho_1(\mathbf{r}, t)|0\rangle_{\partial E/\partial \mathbf{r}}, \end{aligned} \tag{12}$$

where the subscripts E and $\partial E/\partial \mathbf{r}$ designate the terms containing the electric field and the derivatives of the field with respect to the coordinates, respectively. When turning to consideration of the system at a finite temperature, we replace the averaging $\langle 0|\ldots|0\rangle$ over the ground state in formulas (12) by the averaging $\langle\ldots\rangle$ defined by expression (2). The correctness of this replacement will be proved by comparing our data with the results obtained in [1, 3, 4].

According to [5], we have

$$\begin{aligned} \langle j_{1\alpha}(\mathbf{r}, t)\rangle_E &= \frac{i}{\hbar}\int d^3r' \\ &\times \int_{-\infty}^{t} dt'\langle[j_\alpha(\mathbf{r}, t), d_\beta(\mathbf{r}', t')]\rangle E_\beta(\mathbf{r}', t'), \end{aligned} \tag{13}$$

$$\begin{aligned} \langle \rho_1(\mathbf{r}, t)\rangle_E &= \frac{i}{\hbar}\int d^3r' \\ &\times \int_{-\infty}^{t} dt'\langle[\rho_\alpha(\mathbf{r}, t), d_\beta(\mathbf{r}', t')]\rangle E_\beta(\mathbf{r}', t'), \end{aligned} \tag{14}$$

$$\begin{aligned} \langle j_{1\alpha}(\mathbf{r}, t)\rangle_{\partial E/\partial \mathbf{r}} &= \frac{e}{mc}\langle d_\beta(\mathbf{r})\rangle\frac{\partial a_\beta(\mathbf{r}, t)}{\partial r_\alpha} - \frac{i}{\hbar c}\int d^3r' \\ &\times \int_{-\infty}^{t} dt'\langle[j_\alpha(\mathbf{r}, t), Y_{\beta\gamma}(\mathbf{r}', t')]\rangle\frac{\partial a_\beta(\mathbf{r}', t')}{\partial r'_\gamma}, \end{aligned} \tag{15}$$

$$\begin{aligned} \langle \rho_1(\mathbf{r}, t)\rangle_{\partial E/\partial \mathbf{r}} &= -\frac{i}{\hbar c}\int d^3r' \\ &\times \int_{-\infty}^{t} dt'\langle[\rho(\mathbf{r}, t), Y_{\beta\gamma}(\mathbf{r}', t')]\rangle\frac{\partial a_\beta(\mathbf{r}', t')}{\partial r'_\gamma}. \end{aligned} \tag{16}$$

Here, we introduced the designations

$$\mathbf{d}(\mathbf{r}) = \mathbf{r}\rho(\mathbf{r}), \quad Y_{\beta\gamma}(\mathbf{r}) = r_\beta j_\gamma(\mathbf{r}), \tag{17}$$

$$\mathbf{a}(\mathbf{r}, t) = -c\int_{-\infty}^{t} \mathbf{E}(\mathbf{r}, t')dt'. \tag{18}$$

Now, we rearrange the derived relationships in such a way as to obtain the Kubo formula for spatially homogeneous systems and an electric field independent of

coordinates. For this purpose, we invoke the expression [1, 3]

$$\frac{i}{\hbar}\langle [F(t), Q(t')]\rangle = \int_0^\beta d\lambda \left\langle \frac{dQ(t')}{dt'} F(t + i\hbar\lambda)\right\rangle, \quad (19)$$

which is valid for any pair of operators F and Q. With the use of expression (19), from formula (13), we find

$$\langle j_{1\alpha}(\mathbf{r}, t)\rangle_E = \int d^3r' \int_{-\infty}^{t} dt' \times \int_0^\beta d\lambda \left\langle \frac{\partial d_\beta(\mathbf{r}', t')}{\partial t'} j_\alpha(\mathbf{r}, t + i\hbar\lambda)\right\rangle E_\beta(\mathbf{r}', t'). \quad (20)$$

It can be shown that the following equality holds:

$$\partial s_\beta(\mathbf{r}, t)/\partial t = -r_\beta \frac{\partial j_\gamma(\mathbf{r}, t)}{\partial r_\gamma}. \quad (21)$$

Substitution of formula (21) into relationship (20) and integration over the variable $\mathbf{r}'$ by parts give

$$\langle j_{1\alpha}(\mathbf{r}, t)\rangle_E = \int d^3r' \int_{-\infty}^{t} dt' \int_0^\beta d\lambda \langle j_\beta(\mathbf{r}', t') j_\alpha(\mathbf{r}, t + i\hbar\lambda)\rangle E_\beta(\mathbf{r}', t') + \int d^3r' \int_{-\infty}^{t} dt' \int_0^\beta d\lambda \langle Y_{\beta\gamma}(\mathbf{r}', t') j_\alpha(\mathbf{r}, t + i\hbar\lambda)\rangle \frac{\partial E_\beta(\mathbf{r}', t')}{\partial r'_\gamma}. \quad (22)$$

Expression (15) for $\langle j_{1\alpha}(\mathbf{r}, t)\rangle_{\partial E/\partial \mathbf{r}}$ involves two terms. The first term remains unchanged. In the second term, we perform integration over the variable t' by parts and use expression (19). As a result, we obtain

$$\langle j_{1\alpha}(\mathbf{r}, t)\rangle_{\partial E/\partial \mathbf{r}} = \frac{e}{mc}\langle d_\beta(\mathbf{r})\rangle \frac{\partial a_\beta(\mathbf{r}, t)}{\partial r_\alpha} - \frac{1}{c}\int d^3r' \int_0^\beta d\lambda \langle Y_{\beta\gamma}(\mathbf{r}') j_\alpha(\mathbf{r}, i\hbar\lambda)\rangle \frac{\partial a_\beta(\mathbf{r}', t)}{\partial r'_\gamma} - \int d^3r' \int_{-\infty}^{t} dt' \int_0^\beta d\lambda \langle Y_{\beta\gamma}(\mathbf{r}', t') j_\alpha(\mathbf{r}, t + i\hbar\lambda)\rangle \frac{\partial E_\beta(\mathbf{r}', t')}{\partial r'_\gamma}. \quad (23)$$

After combining expressions (22) and (23), the last terms on the right-hand side of both relationships cancel each other out. The resultant expression can be separated into two terms,

$$\langle j_{1\alpha}(\mathbf{r}, t)\rangle = \langle j_{1\alpha}(\mathbf{r}, t)\rangle^{(1)} + \langle j_{1\alpha}(\mathbf{r}, t)\rangle^{(2)}. \quad (24)$$

As a result, the first term contains the electric field and the second term involves the derivatives of the field with respect to the coordinates; that is,

$$\langle j_{1\alpha}(\mathbf{r}, t)\rangle^{(1)} = \int d^3r' \int_{-\infty}^{t} dt' \times \int_0^\beta d\lambda \langle j_\beta(\mathbf{r}', t') j_\alpha(\mathbf{r}, t + i\hbar\lambda)\rangle E_\beta(\mathbf{r}', t'), \quad (25)$$

$$\langle j_{1\alpha}(\mathbf{r}, t)\rangle^{(2)} = \frac{e}{mc}\langle d_\beta(\mathbf{r})\rangle \frac{\partial a_\beta(\mathbf{r}, t)}{\partial r_\alpha} - \frac{1}{c}\int d^3r' \int_0^\beta d\lambda \langle Y_{\beta\gamma}(\mathbf{r}') j_\alpha(\mathbf{r}, i\hbar\lambda)\rangle \frac{\partial a_\beta(\mathbf{r}', t)}{\partial r'_\gamma}. \quad (26)$$

It is evident that relationship (24) does not coincide with expression (12), which is convenient only at $T = 0$.

In a similar way, from expressions (14) and (16), we find

$$\langle \rho_1(\mathbf{r}, t)\rangle = \langle \rho_1(\mathbf{r}, t)\rangle^{(1)} + \langle \rho_1(\mathbf{r}, t)\rangle^{(2)}, \quad (27)$$

$$\langle \rho_1(\mathbf{r}, t)\rangle^{(1)} = \int d^3r' \int_{-\infty}^{t} dt' \times \int_0^\beta d\lambda \langle j_\beta(\mathbf{r}', t')\rho(\mathbf{r}, t + i\hbar\lambda)\rangle E_\beta(\mathbf{r}', t'), \quad (28)$$

$$\langle \rho_1(\mathbf{r}, t)\rangle^{(2)} = -\frac{1}{c}\int d^3r' \int_0^\beta d\lambda \langle Y_{\beta\gamma}(\mathbf{r}')\rho(\mathbf{r}, i\hbar\lambda)\rangle \frac{\partial a_\beta(\mathbf{r}', t)}{\partial r'_\gamma}. \quad (29)$$

After the derivation of relationships (24)–(29), we achieved our objective. To be more specific, we separated the basic contributions with the superscript (1) to the average induced densities of currents and charges and showed that the additional contributions with the superscript (2) involve derivatives of the electric field with respect to the coordinates. The reason for separating the contributions into basic and additional ones is that, when solving problems with a spatially inhomogeneous field $\mathbf{E}(\mathbf{r}, t)$, it is possible to estimate the additional contributions and to determine whether they should be allowed for or can be rejected. As in the case of $T = 0$, the obtained relationships contain the coordinate operators $\mathbf{r}_i$ of particles, in contrast to the initial expressions (10) and (11), which do not involve these operators.

4. COMPARISON WITH THE RESULTS OBTAINED IN [4]

Nakajima [3] and Konstantinov and Perel' [4] obtained expressions for $\langle \mathbf{j}_1(\mathbf{r}, t)\rangle$ that differ from our expressions derived in the present work. Moreover, we carried out similar calculations for the quantity $\langle \rho_1(\mathbf{r}, t)\rangle$, which was not considered in [1, 3, 4], even though this quantity and the average current density enter into the Maxwell equations on equal terms. Note that the authors considered a homogeneous medium in [1, 3] and an inhomogeneous medium in [4]. By solving the equation for the density matrix, the authors of [3, 4] derived the formula that can be obtained from expression (10) if the averaging $\langle\ldots\rangle$ defined by relationship (2) is performed on the right- and left-hand sides. It is evident that a similar expression for $\langle \rho_1(\mathbf{r}, t)\rangle$ can be deduced through the averaging on both sides of formula (11).

Then, the authors of [3, 4] rearranged the expression for the average induced current density in such a way that the electric field $\mathbf{E}(\mathbf{r}, t)$ appears but the vector potential $\mathbf{A}(\mathbf{r}, t)$ is also retained in this expression. An analogous procedure performed with the initial relationship for the average induced charge density results in an expression similar to formula (27) in which the contribution $\langle \rho_1(\mathbf{r}, t)\rangle^{(1)}$ is defined by formula (28) and the contribution $\langle \rho_1(\mathbf{r}, t)\rangle^{(2)}$ is written in the form

$$\langle \rho_1(\mathbf{r}, t)\rangle^{(2)} = \frac{1}{c}\int d^3r' \int_0^\beta d\lambda \langle j_\beta(\mathbf{r}')\rho(\mathbf{r}, i\hbar\lambda)\rangle A_\beta(\mathbf{r}', t). \quad (30)$$

In [3, 4], expression (25) was obtained for the contribution $\langle j_{1\alpha}(\mathbf{r}, t)\rangle^{(1)}$ on the right-hand side of relationship (24) and the formula

$$\langle j_{1\alpha}(\mathbf{r}, t)\rangle^{(2)} = -\frac{e}{mc}\langle \rho(\mathbf{r})\rangle A_\alpha(\mathbf{r}, t) + \frac{1}{c}\int d^3r' \int_0^\beta d\lambda \langle j_\beta(\mathbf{r}') j_\alpha(\mathbf{r}, i\hbar\lambda)\rangle A_\beta(\mathbf{r}', t) \quad (31)$$

was derived for the additional contribution.

Furthermore, in [4], the time derivative of the contribution $\langle j_{1\alpha}(\mathbf{r}, t)\rangle^{(2)}$ was expressed through the electric field with the use of expression (31). By integrating this derivative over the time, we obtain

$$\langle j_{1\alpha}(\mathbf{r}, t)\rangle^{(2)} = -\frac{e}{mc}\langle \rho(\mathbf{r})\rangle a_\alpha(\mathbf{r}, t) + \frac{1}{c}\int d^3r' \int_0^\beta d\lambda \langle j_\beta(\mathbf{r}') j_\alpha(\mathbf{r}, i\hbar\lambda)\rangle a_\beta(\mathbf{r}', t) \quad (32)$$

and, similarly,

$$\langle \rho_1(\mathbf{r}, t)\rangle^{(2)} = \frac{1}{c}\int d^3r' \int_0^\beta d\lambda \langle j_\beta(\mathbf{r}')\rho(\mathbf{r}, i\hbar\lambda)\rangle a_\beta(\mathbf{r}', t). \quad (33)$$

Thus, there exist two types of formulas for the additional contributions: formulas (26) and (29), which contain the derivatives of the electric field with respect to the coordinates, and formulas (32) and (33), which involve the electric field.

Let us demonstrate how expression (26) can be transformed into relationship (32) and expression (29) can be rearranged to give relationship (33). In the last term in expression (26), we perform integration over the variable r'_γ by parts. Then, we use the equality

$$\frac{dY_{\beta\gamma}(\mathbf{r})}{dr_\gamma} = j_\beta(\mathbf{r}) + r_\beta\frac{\partial j_\gamma(\mathbf{r})}{\partial r_\gamma} = j_\beta(\mathbf{r}) - r_\beta\dot{\rho}(\mathbf{r}). \quad (34)$$

As a result, from expression (26), we have

$$\langle j_{1\alpha}(\mathbf{r}, t)\rangle^{(2)} = \frac{e}{mc}\langle d_\beta(\mathbf{r})\rangle\frac{\partial a_\beta(\mathbf{r}, t)}{\partial r_\alpha} + \frac{1}{c}\int d^3r' \int_0^\beta d\lambda \langle j_\beta(\mathbf{r}') j_\alpha(\mathbf{r}, i\hbar\lambda)\rangle a_\beta(\mathbf{r}', t) - \frac{1}{c}\int d^3r' r'_\beta \int_0^\beta d\lambda \langle \dot{\rho}(\mathbf{r}') j_\alpha(\mathbf{r}, i\hbar\lambda)\rangle a_\beta(\mathbf{r}', t). \quad (35)$$

In the last term, we use relationship (19) and integrate over the variable $\mathbf{r}'$, which leads to the formula

$$-\frac{ie}{\hbar c}\left\langle\left[j_\alpha(\mathbf{r}), \sum_i r_{i\beta}a_\beta(\mathbf{r}_i, t)\right]\right\rangle = -\frac{e}{mc}\left[\langle \rho(\mathbf{r})\rangle a_\alpha(\mathbf{r}, t) + \langle d_\beta(\mathbf{r})\rangle\frac{\partial a_\beta(\mathbf{r}, t)}{\partial r_\alpha}\right]. \quad (36)$$

Substituting this formula into relationship (35) gives expression (32), which is the required result. Relationship (29) for $\langle \rho_1(\mathbf{r}, t)\rangle^{(2)}$ is rearranged in a similar manner. The only difference is that, instead of formula (36), we have

$$-\frac{ie}{\hbar c}\left\langle\left[\rho(\mathbf{r}), \sum_i r_{i\beta}a_\beta(\mathbf{r}_i, t)\right]\right\rangle = 0$$

and transform expression (29) into relationship (33).

Thus, a comparison of our data with the results obtained in [3, 4] shows the applicability of expressions (26) and (29) for the additional contributions to the average induced current and charge densities, which contain only the derivatives of the electric field with respect to the coordinates.

5. ANALYSIS OF THE FORMULAS FOR AN ADDITIONAL CONTRIBUTION TO THE AVERAGE CURRENT DENSITY

The three expressions (26), (31), and (32) were derived for the quantity $\langle j_{1\alpha}(\mathbf{r}, t)\rangle^{(2)}$. Some properties of this quantity are given in [4]. Now, we deduce the fourth expression for $\langle j_{1\alpha}(\mathbf{r}, t)\rangle^{(2)}$ through the derivatives of the vector potential $\mathbf{A}(\mathbf{r}, t)$ with respect to the coordinates. In the second term in formula (31), relationship (34) is used for $j_\beta(\mathbf{r}')$. As a result, this second term is separated into two terms. In the first term, we carry out integration over the variable r'_γ by parts. In the second term, we use the relationship

$$\frac{i}{\hbar}\langle [F, Q]\rangle = \int_0^\beta d\lambda \langle \dot{Q}F(i\hbar\lambda)\rangle, \tag{37}$$

which follows from expression (19) at $t' = t$. By calculating the commutator, we obtain

$$\langle j_{1\alpha}(\mathbf{r}, t)\rangle^{(2)} = \frac{e}{mc}\langle d_\beta(\mathbf{r})\rangle \frac{\partial A_\beta(\mathbf{r}, t)}{\partial r_\alpha} - \frac{1}{c}\int d^3r' \int_0^\beta d\lambda \langle Y_{\beta\gamma}(\mathbf{r}') j_\alpha(\mathbf{r}, i\hbar\lambda)\rangle \frac{\partial A_\beta(\mathbf{r}', t')}{\partial r'_\gamma}. \tag{38}$$

In order to derive the fifth expression for the additional contribution to the current density, we use relationship (34) for $j_\alpha(\mathbf{r}, i\hbar\lambda)$ in formula (31) and the following modification of formula (37):

$$\frac{i}{\hbar}\langle [F, Q]\rangle = \int_0^\beta d\lambda \langle F\dot{Q}(i\hbar\lambda)\rangle. \tag{39}$$

Then, we obtain

$$\langle j_{1\alpha}(r, t)\rangle^{(2)} = -\frac{e}{mc}\frac{\partial}{\partial r_\beta}\{\langle d_\alpha(\mathbf{r})\rangle A_\beta(\mathbf{r}, t)\} + \frac{1}{c}\frac{\partial}{\partial r_\gamma}\left\{\int d^3r' \int_0^\beta d\lambda \langle j_\beta(\mathbf{r}') Y_{a\gamma}(\mathbf{r}, i\hbar\lambda)\rangle A_\beta(\mathbf{r}', t)\right\}. \tag{40}$$

From expression (40), it follows that the integral of $\langle j_{1\alpha}(\mathbf{r}, t)\rangle^{(2)}$ over the entire space is equal to zero [4].

6. DERIVATION OF EXPRESSIONS INVOLVING A MAGNETIC FIELD

Let us derive the sixth expression for the additional contribution $\langle j_{1\alpha}(\mathbf{r}, t)\rangle^{(2)}$ and introduce the magnetic field. We separate relationship (38) into two parts:

$$\langle j_{1\alpha}(\mathbf{r}, t)\rangle^{(2)} = \langle j_{1\alpha}(\mathbf{r}, t)\rangle^{(-)} + \langle j_{1\alpha}(\mathbf{r}, t)\rangle^{(+)}, \tag{41}$$

$$\langle j_{1\alpha}(\mathbf{r}, t)\rangle^{(\pm)} = \frac{e}{2mc}\langle d_\beta(\mathbf{r})\rangle\left(\frac{\partial A_\beta(\mathbf{r}, t)}{\partial r_\alpha} \pm \frac{\partial A_\alpha(\mathbf{r}, t)}{\partial r_\beta}\right) - \frac{1}{2c}\int d^3r' \int_0^\beta d\lambda \langle Y_{\beta\gamma}(\mathbf{r}') j_\alpha(\mathbf{r}, i\hbar\lambda)\rangle \times\left(\frac{\partial A_\beta(\mathbf{r}', t)}{\partial r'_\gamma} \pm \frac{\partial A_\gamma(\mathbf{r}', t)}{\partial r'_\beta}\right). \tag{42}$$

Since $\mathbf{H} = \mathrm{curl}\mathbf{A}$, the quantity $\langle j_{1\alpha}(\mathbf{r}, t)\rangle^{(-)}$ can be expressed through the magnetic field; that is,

$$\langle j_{1\alpha}(\mathbf{r}, t)\rangle^{(-)} = -\frac{e}{2mc}(\mathbf{H}(\mathbf{r}, t)\times\mathbf{r})_\alpha\langle\rho(\mathbf{r})\rangle + \frac{1}{2c}\int d^3r' \int_0^\beta d\lambda (\mathbf{H}(\mathbf{r}', t)\times\mathbf{r}')_\beta \langle j_\beta(\mathbf{r}') j_\alpha(\mathbf{r}, i\hbar\lambda)\rangle. \tag{43}$$

The quantity $\langle j_{1\alpha}(\mathbf{r}, t)\rangle^{(+)}$ can be expressed in terms of the second derivatives of the vector potential with respect to the coordinates in the following way:

$$\langle j_{1\alpha}(\mathbf{r}, t)\rangle^{(+)} = -\frac{e}{2mc}\langle\rho(\mathbf{r})\rangle r_\beta r_\gamma \frac{\partial^2 A_\beta}{\partial r_\alpha \partial r_\gamma} + \frac{1}{2c}\int d^3r' r'_\beta r'_\delta \int_0^\beta d\lambda \langle j_\gamma(\mathbf{r}') j_\alpha(\mathbf{r}, i\hbar\lambda)\rangle \frac{\partial^2 A_\beta}{\partial r'_\gamma \partial r'_\delta}. \tag{44}$$

Relationship (44) was obtained from expression (42) as follows. In formula (42), we used the relationship $Y_{\beta\gamma}(\mathbf{r}') = r'_\beta j_\gamma(\mathbf{r}')$ and expression (34) for $j_\gamma(\mathbf{r}')$. Then, in the term containing $\partial Y_{\gamma\delta}(\mathbf{r}')/\partial r'_\delta$, we performed integration over the variable r'_δ by parts. In the term involving $\dot{d}_\gamma(\mathbf{r}')$, we used expression (39), integrated over the variable $\mathbf{r}'$, and calculated the commutator.

It can be shown that the individual quantities $\langle j_{1\alpha}(\mathbf{r}, t)\rangle^{(+)}$ and $\langle j_{1\alpha}(\mathbf{r}, t)\rangle^{(-)}$ possess the properties

$$\mathrm{div}\langle \mathbf{j}_1(\mathbf{r}, t)\rangle^{(\pm)} = 0, \quad \int d^3r \langle j_{1\alpha}(\mathbf{r}, t)\rangle^{(\pm)} = 0. \tag{45}$$

Now, we demonstrate that the contribution $\langle j_{1\alpha}(\mathbf{r}, t)\rangle^{(+)}$ can be expressed through the second derivatives of the electric field with respect to the coordinates. For this purpose, the relationship for the vector potential [following from formula (3)]

$$\mathbf{A}(\mathbf{r}, t) = \mathbf{a}(\mathbf{r}, t) - c\int_{-\infty}^t dt' \partial\varphi(\mathbf{r}, t')/\partial\mathbf{r} \tag{46}$$

is substituted into expression (42). Then, in the quantities $\langle j_{1\alpha}(\mathbf{r}, t)\rangle^{(\pm)}$, it is possible to separate the contributions of the scalar potential

$$\langle j_{1\alpha}(\mathbf{r}, t)\rangle^{(\pm)} = \langle j_{1\alpha}(\mathbf{r}, t)\rangle_E^{(\pm)} + \langle j_{1\alpha}(\mathbf{r}, t)\rangle_\varphi^{(\pm)}, \quad (47)$$

which are designated by the subscript φ.

From these relationships, it immediately follows that

$$\langle j_{1\alpha}(\mathbf{r}, t)\rangle_\varphi^{(-)} = 0, \quad (48)$$

$$\langle j_{1\alpha}(\mathbf{r}, t)\rangle_\varphi^{(+)} = \int_{-\infty}^{t} dt' \left[-\frac{e}{m}\langle d_\beta(\mathbf{r})\rangle \frac{\partial^2 \varphi(\mathbf{r}, t')}{\partial r_\alpha \partial_\beta} + \int d^3 r' \int_0^\beta d\lambda \langle Y_{\beta\gamma}(\mathbf{r}') j_\alpha(\mathbf{r}, i\hbar\lambda)\rangle \frac{\partial^2 \varphi}{\partial r'_\beta \partial r'_\gamma} \right]. \quad (49)$$

In the second term in formula (49), we doubly integrate by parts: initially, over the variable r'_γ and then over the variable r'_β. Finally, with the use of the continuity equation (8) and relationship (37), we find that the second term in expression (49) is equal to the first term with the opposite sign and

$$\langle j_{1\alpha}(\mathbf{r}, t)\rangle_\varphi^{(+)} = 0. \quad (50)$$

With due regard for expressions (48) and (50), from relationships (47) and (42), we derive

$$\langle j_{1\alpha}(\mathbf{r}, t)\rangle^{(\pm)} = \langle j_{1\alpha}(\mathbf{r}, t)\rangle_E^{(\pm)} = \frac{e}{2mc}\langle d_\beta(\mathbf{r})\rangle \left(\frac{\partial a_\beta(\mathbf{r}, t)}{\partial r_\alpha} \pm \frac{\partial a_\alpha(\mathbf{r}, t)}{\partial r_\beta} \right) - \frac{1}{2c}\int d^3 r' \int_0^\beta d\lambda \langle Y_{\beta\gamma}(\mathbf{r}') j_{1\alpha}(\mathbf{r}, i\hbar\lambda)\rangle \times \left(\frac{\partial a_\beta(\mathbf{r}', t)}{\partial r'_\gamma} \pm \frac{\partial a_\gamma(\mathbf{r}', t)}{\partial r'_\beta} \right). \quad (51)$$

By using the Maxwell equation $\mathrm{curl}\mathbf{E} = -(1/c)(\partial\mathbf{H}/\partial t)$ and definition (18) of the vector $\mathbf{a}(\mathbf{r}, t)$, we are again led to expression (43) for $\langle j_{1\alpha}(\mathbf{r}, t)\rangle^{(-)}$ and also obtain

$$\langle j_{1\alpha}(\mathbf{r}, t)\rangle^{(+)} = -\frac{e}{2mc}\langle \rho(\mathbf{r})\rangle r_\beta r_\gamma \frac{\partial^2 a_\beta(\mathbf{r}, t)}{\partial r_\alpha \partial r_\gamma} + \frac{1}{2c}\int d^3 r' \int_0^\beta d\lambda r'_\beta r'_\gamma \langle j_\gamma(\mathbf{r}') j_\alpha(\mathbf{r}, i\hbar\lambda)\rangle \frac{\partial^2 a_\beta(\mathbf{r}', t)}{\partial r'_\gamma \partial r'_\delta}. \quad (52)$$

According to definition (18), we find that the quantity $\langle j_{1\alpha}(\mathbf{r}, t)\rangle^{(+)}$ is expressed through the second derivatives of the electric field with respect to the coordinates. As a result, the sixth (and last) formula for the additional contribution $\langle j_{1\alpha}(\mathbf{r}, t)\rangle^{(2)}$ is determined by the combination of expressions (43) and (52).

7. ELIMINATION OF THE DIAGONAL ELEMENTS OF THE $\mathbf{r}_i$ OPERATORS

Unlike expressions (32) and (33), relationships (26) and (29) for the additional contributions to the average induced current and charge densities involve the coordinate operators $\mathbf{r}_i$ of particles. Actually, definitions (17) can be rewritten in the form

$$\mathbf{d}(\mathbf{r}) = e\sum_i \mathbf{r}_i \delta(\mathbf{r} - \mathbf{r}_i), \quad (53)$$

$$Y_{\beta\gamma} = (e/2)\sum_i (r_{i\beta} j_{i\gamma} + j_{i\gamma} r_{i\beta}). \quad (54)$$

However, the averages $\langle \mathbf{j}_1(\mathbf{r}, t)\rangle$ and $\langle \rho_1(\mathbf{r}, t)\rangle$ should not depend on the position of the reference point of the coordinates $\mathbf{r}_i$. This means that relationships (26) and (29) contain only off-diagonal elements of the operators $\mathbf{r}_i$ and the diagonal elements can be eliminated. Now, we demonstrate that this is the case.

For this purpose, we transform expression (54) so that the operator $r_{i\beta}$ appears only on the left-hand side; that is,

$$Y_{\beta\gamma}(\mathbf{r}) = -(i\hbar/2m)\delta_{\beta\gamma}\rho(\mathbf{r}) + \sum_i r_{i\beta} j_{i\gamma}(\mathbf{r}). \quad (55)$$

Substitution of expressions (53) and (55) into relationship (26) gives

$$\langle \mathbf{j}_{1\alpha}(\mathbf{r}, t)\rangle^{(2)} = \frac{i\hbar}{2mc}\int d^3 r' \int_0^\beta d\lambda \langle \rho(\mathbf{r}') j_\alpha(\mathbf{r}, i\hbar\lambda)\rangle \mathrm{div}\,\mathbf{a}(\mathbf{r}', t) + \frac{e^2}{mc}\sum_i \langle r_{i\beta}\delta(\mathbf{r} - \mathbf{r}_i)\rangle \frac{\partial a_\beta(\mathbf{r}, t)}{\partial r_\alpha} - \frac{1}{c}\int d^3 r' \int_0^\beta d\lambda \sum_i \langle r_{i\beta} j_{i\gamma}(\mathbf{r}') j_{1\alpha}(\mathbf{r}, i\hbar\lambda)\rangle \frac{\partial a_\beta(\mathbf{r}', t)}{\partial r'_\gamma}. \quad (56)$$

In formula (56), the first two terms remain unchanged and the operator $\mathbf{r}_i$ in the last term is separated into two parts:

$$\mathbf{r}_i = \mathbf{r}_i^{\mathrm{d}} + \mathbf{r}_i^{\mathrm{nd}}, \quad (57)$$

where superscripts "d" and "nd" indicate the diagonal and off-diagonal contributions, respectively. The operator $\mathbf{r}_i^{\mathrm{d}}$ is determined through the matrix elements:

$$\langle n|\mathbf{r}_i^{\mathrm{d}}|m\rangle = \langle n|\mathbf{r}_i|m\rangle\langle n|m\rangle, \quad (58)$$

where $|n\rangle$ are the eigenfunctions of the Hamiltonian $\mathcal{H}$. The commutativity property

$$[\mathcal{H}, \mathbf{r}_i^{\mathrm{d}}] = 0.$$

is obvious. Let us consider the contribution of the operator r_i^{d} to the last term in expression (56). This contribution will be denoted as $I_\alpha(\mathbf{r}, t)$. We perform integration over the variable r'_γ by parts, use the continuity equation (8), and obtain

$$I_\alpha(\mathbf{r}, t) = -(1/c)\int d^3r' \int_0^\beta d\lambda \times \sum_i \langle r_{i\beta}^{\mathrm{d}} \dot{\rho}_i(\mathbf{r}') j_\alpha(\mathbf{r}, i\hbar\lambda)\rangle a_\beta(\mathbf{r}', t). \quad (59)$$

Since the operator $\mathbf{r}_i^{\mathrm{d}}$ commutes with the Hamiltonian $\mathcal{H}$, relationship (59) can be rewritten in the following form:

$$I_\alpha(\mathbf{r}, t) = -(1/c)\int d^3r' \int_0^\beta d\lambda \times \sum_i \langle \dot{\rho}_i(\mathbf{r}') j_\alpha(\mathbf{r}, i\hbar\lambda) r_{i\beta}^{\mathrm{d}}(i\hbar\lambda)\rangle a_\beta(\mathbf{r}', t). \quad (60)$$

Substitution of the expression $r_{i\beta}^{\mathrm{d}} = r_{i\beta} - r_{i\beta}^{\mathrm{nd}}$ into formula (60) leads to separation of the contribution $I_\alpha(\mathbf{r}, t)$ into two parts:

$$I_\alpha(\mathbf{r}, t) = I'_\alpha(\mathbf{r}, t) + I_\alpha^n(\mathbf{r}, t), \quad (61)$$

where

$$I'_\alpha(\mathbf{r}, t) = -(1/c)\int d^3r' \int_0^\beta d\lambda \times \sum_i \langle \dot{\rho}_i(\mathbf{r}') j_\alpha(\mathbf{r}, i\hbar\lambda) r_{i\beta}(i\hbar\lambda)\rangle a_\beta(\mathbf{r}', t), \quad (62)$$

$$I''_\alpha(\mathbf{r}, t) = (1/c)\int d^3r' \int_0^\beta d\lambda \times \sum_i \langle \dot{\rho}_i(\mathbf{r}') j_\alpha(\mathbf{r}, i\hbar\lambda) r_{i\beta}^{\mathrm{nd}}(i\hbar\lambda)\rangle a_\beta(\mathbf{r}', t). \quad (63)$$

With due regard for relationship (37), expression (62) transforms into the formula

$$I'_\alpha(\mathbf{r}, t) = -(i/\hbar c)\int d^3r' \sum_i \langle [j_\alpha(\mathbf{r}) r_{i\beta}, \rho(\mathbf{r}')]\rangle a_\beta(\mathbf{r}', t). \quad (64)$$

Integration over the variable $\mathbf{r}'$ and calculation of the commutator give the relationship

$$I'_\alpha(\mathbf{r}, t) = -\frac{e^2}{mc}\sum_i \langle r_{i\beta}\delta(\mathbf{r} - \mathbf{r}_i)\rangle \frac{\partial a_\beta(\mathbf{r}, t)}{\partial r_\alpha}, \quad (65)$$

which is canceled by the second term in expression (56). Then, we rearrange the remaining quantity $I''_\alpha(\mathbf{r}, t)$ with the use of the continuity equation (8), integrate over the variable r'_γ by parts, and obtain

$$I''_\alpha(\mathbf{r}, t) = \frac{1}{c}\int d^3r' \int_0^\beta d\lambda \times \sum_i \langle j_{i\gamma}(\mathbf{r}') j_\alpha(\mathbf{r}, i\hbar\lambda) r_{i\beta}^{\mathrm{nd}}(i\hbar\lambda)\rangle \frac{\partial a_\beta(r', t)}{\partial r'_\gamma}. \quad (66)$$

By using relationships (61), (65), and (66), we derive the final expression for the additional contribution to the average induced current density without diagonal matrix elements of the operator $\mathbf{r}_i$; that is,

$$\langle j_{1\alpha}(\mathbf{r}, t)\rangle^{(2)} = \frac{i\hbar}{2mc}\int d^3r' \times \int_0^\beta d\lambda \langle \rho(\mathbf{r}') j_\alpha(\mathbf{r}, i\hbar\lambda)\rangle \operatorname{div}\mathbf{a}(\mathbf{r}', t) + \frac{1}{c}\int d^3r' \int_0^\beta d\lambda \sum_i \langle j_{i\gamma}(\mathbf{r}') j_\alpha(\mathbf{r}, i\hbar\lambda) r_{i\beta}^{\mathrm{nd}}(i\hbar\lambda) - r_{i\beta}^{\mathrm{nd}} j_{i\gamma}(\mathbf{r}') j_\alpha(\mathbf{r}, i\hbar\lambda)\rangle \frac{\partial a_\beta(r', t)}{\partial r'_\gamma}. \quad (67)$$

Similarly, we obtain

$$\langle \rho(\mathbf{r}, t)\rangle^{(2)} = \frac{i\hbar}{2mc}\int d^3r' \times \int_0^\beta d\lambda \langle \rho(\mathbf{r}')\rho(\mathbf{r}, i\hbar\lambda)\rangle \operatorname{div}\mathbf{a}(\mathbf{r}', t) + \frac{1}{c}\int d^3r' \int_0^\beta d\lambda \sum_i \langle j_{i\gamma}(\mathbf{r}')\rho(\mathbf{r}, i\hbar\lambda) r_{i\beta}^{\mathrm{nd}}(i\hbar\lambda) - r_{i\beta}^{\mathrm{nd}} j_{i\gamma}(\mathbf{r}')\rho(\mathbf{r}, i\hbar\lambda)\rangle \frac{\partial a_\beta(\mathbf{r}', t)}{\partial r'_\gamma}. \quad (68)$$

8. THE ELECTRICAL CONDUCTIVITY TENSOR

The Fourier transform of the electric field can be represented as

$$E_\alpha(\mathbf{k}, \omega) = \int d^3r \int_{-\infty}^{\infty} dt E_\alpha(\mathbf{r}, t) e^{-i(\mathbf{kr} - \omega t)}, \quad (69)$$

$$E_\alpha(\mathbf{r}, t) = (2\pi)^{-4}\int d^3k\int_0^\infty d\omega E_\alpha(\mathbf{k}, \omega)e^{i(\mathbf{kr}-\omega t)} + \text{c.c.} \quad (70)$$

The average induced current density can be written in the following form:

$$\langle j_{1\alpha}(\mathbf{r}, t)\rangle = (2\pi)^{-4}\int d^3k\int_0^\infty d\omega\sigma_{\alpha\beta}(\mathbf{k}, \omega|\mathbf{r}) \times E_\beta(\mathbf{k}, \omega)e^{i(\mathbf{kr}-\omega t)} + \text{c.c.}, \quad (71)$$

where $\sigma_{\alpha\beta}(\mathbf{k}, \omega|\mathbf{r})$ is the electrical conductivity tensor dependent on the spatial coordinates (the designation following from [8]).

From expressions (25) and (67) for the basic and additional contributions to the average induced current density, we obtain

$$\sigma_{\alpha\beta}(\mathbf{k}, \omega|\mathbf{r}) = \sigma^{(1)}_{\alpha\beta}(\mathbf{k}, \omega|\mathbf{r}) + \sigma^{(2)}_{\alpha\beta}(\mathbf{k}, \omega|\mathbf{r}), \quad (72)$$

where

$$\sigma^{(1)}_{\alpha\beta}(\mathbf{k}, \omega|\mathbf{r}) = \int d^3r'\int_0^\infty dt\int_0^\beta d\lambda\langle j_\beta(\mathbf{r}-\mathbf{r}', -i\hbar\lambda)j_\alpha(\mathbf{r}, t)\rangle \times \exp[-i(\mathbf{kr}'-\omega t)], \quad (73)$$

$$\sigma^{(2)}_{\alpha\beta}(\mathbf{k}, \omega|\mathbf{r}) = \frac{i\hbar k_\beta}{2m\omega}\int d^3r' e^{-i\mathbf{kr}'}\int_0^\beta d\lambda\langle\rho(\mathbf{r}-\mathbf{r}', -i\hbar\lambda)j_\alpha(\mathbf{r})\rangle + \frac{k_\gamma}{\omega}\int d^3r' e^{-i\mathbf{kr}'}\int_0^\beta d\lambda\sum_i\langle j_{i\gamma}(\mathbf{r}-\mathbf{r}', -i\hbar\lambda)j_\alpha(\mathbf{r})r^{\text{nd}}_{i\beta} - r^{\text{nd}}_{i\beta}(-i\hbar\lambda)j_{i\gamma}(\mathbf{r}-\mathbf{r}', -i\hbar\lambda)j_\alpha(\mathbf{r})\rangle. \quad (74)$$

At $T = 0$, instead of formula (72), we have

$$\sigma_{\alpha\beta,0}(\mathbf{k}, \omega|\mathbf{r}) = \sigma^{\text{I}}_{\alpha\beta}(\mathbf{k}, \omega|\mathbf{r}) + \sigma^{\text{II}}_{\alpha\beta}(\mathbf{k}, \omega|\mathbf{r}) + \sigma^{\text{III}}_{\alpha\beta}(\mathbf{k}, \omega|\mathbf{r}), \quad (75)$$

where

$$\sigma^{\text{I}}_{\alpha\beta}(\mathbf{k}, \omega|\mathbf{r}) = \frac{i}{\hbar}\int d^3r'\int_0^\infty dt e^{-i(\mathbf{kr}'-\omega t)} \times\sum_i\langle 0|j_\alpha(\mathbf{r}, t)\rho_i(\mathbf{r}-\mathbf{r}')r^{\text{nd}}_{i\beta} - r^{\text{nd}}_{i\beta}\rho_i(\mathbf{r}-\mathbf{r}')j_\alpha(\mathbf{r}, t)|0\rangle, \quad (76)$$

$$\sigma^{\text{II}}_{\alpha\beta}(\mathbf{k}, \omega|\mathbf{r}) = \frac{e^2k_\alpha}{m\omega}\sum_i\langle 0|r^{\text{nd}}_{i\beta}\delta(\mathbf{r}-\mathbf{r}_i)|0\rangle - \frac{ik_\gamma}{\hbar\omega}\int d^3r'\int_0^\infty dt e^{-i(\mathbf{kr}'-\omega t)}\sum_i\langle 0|j_\alpha(\mathbf{r}, t)j_{i\gamma}(\mathbf{r}-\mathbf{r}')r^{\text{nd}}_{i\beta} - r^{\text{nd}}_{i\beta}j_{i\gamma}(\mathbf{r}-\mathbf{r}')j_\alpha(\mathbf{r}, t)|0\rangle, \quad (77)$$

$$\sigma^{\text{III}}_{\alpha\beta}(\mathbf{k}, \omega|\mathbf{r}) = \frac{k_\beta}{2m\omega}\int d^3r'\int_0^\infty dt e^{-i(\mathbf{kr}'-\omega t)} \times\langle 0|[j_\alpha(\mathbf{r}, t), \rho(\mathbf{r}-\mathbf{r}')]_+|0\rangle, \quad (78)$$

and $[F, Q]_+ = FQ + QF$. Expression (75) transforms into relationship (72) when the averaging $\langle 0|\ldots|0\rangle$ in formulas (76)–(78) is replaced by the averaging $\langle\ldots\rangle$ and formula (37) is used.[1]

9. APPROXIMATION OF A SPATIALLY HOMOGENOUS ELECTRIC FIELD

In some cases, we can disregard the contributions containing the derivatives of the electric field with respect to the coordinates to the average induced current and charge densities; i.e., we can assume that

$$\mathbf{E}(\mathbf{r}, t) \simeq \mathbf{E}(t). \quad (79)$$

For example, this was done in [1], even though, in the strict sense, only a time-independent field $\mathbf{E}$ can be homogeneous in space. Under assumption (79), we take the Fourier transform

$$E_\alpha(\omega) = \int_{-\infty}^\infty dt e^{i\omega t}E_\alpha(t). \quad (80)$$

Hence, we can write

$$\langle j_{1\alpha}(\mathbf{r}, t)\rangle_\hbar = (1/2\pi)\int_0^\infty d\omega\sigma_{\alpha\beta}(\omega|\mathbf{r})E_\beta(\omega)e^{-i\omega t} + \text{c.c.}, \quad (81)$$

where the subscript h indicates the spatially homogeneous field. It is evident that the following equality holds:

$$\sigma_{\alpha\beta}(\omega|\mathbf{r}) = \sigma_{\alpha\beta}(\mathbf{k} = \mathbf{0}, \omega|\mathbf{r}). \quad (82)$$

[1] In our earlier work [5], the formula for the electrical conductivity tensor at $T = 0$ does not coincide with formula (75). This is explained by the fact that only the diagonal elements $\langle 0|\mathbf{r}_i|0\rangle$ are eliminated and the operator $\mathbf{r}_i = \mathbf{r}_i - \langle 0|\mathbf{r}_i|0\rangle$ differing from the operator r^{nd}_i is introduced in [5].

Next, from expressions (72)–(74), we obtain

$$\sigma_{\alpha\beta}(\omega|\mathbf{r}) = \int_0^\infty dt \int_0^\beta d\lambda \langle J_\beta(-i\hbar\lambda) j_\alpha(\mathbf{r}, t)\rangle e^{i\omega t}, \quad (83)$$

where we introduced the current operator

$$J_\alpha = e\sum_i \dot{r}_{i\alpha}. \quad (84)$$

Expression (83) is a generalization of the Kubo formula to the case of a spatially inhomogeneous medium when the electrical conductivity tensor depends on **r**.

Let us consider a spatially homogeneous medium in which averages cannot depend on the coordinates **r**. In this case, the tensor $\sigma_{\alpha\beta}(\omega|\mathbf{r})$ does not depend on **r** and, from relationship (83), we have

$$\sigma_{\alpha\beta}(\omega) = V_0^{-1}\int_0^\infty dt \int_0^\beta d\lambda \langle J_\beta(-i\hbar\lambda) J_\alpha(t)\rangle e^{i\omega t}, \quad (85)$$

where V_0 is the normalized volume. The derived formula coincides with the Kubo formula [1] if ω on the right-hand side is replaced by –ω and it is remembered that $V_0 = 1$ in [1].

10. THE CASE OF A CONSTANT MAGNETIC FIELD

We now analyze the case when the external weak electromagnetic field is reduced to a magnetic field $\mathbf{H}(\mathbf{r}, t) = \mathbf{H}$ that is constant in space and time and the electric field $\mathbf{E}(\mathbf{r}, t) = 0$. Recall that the vector potential $\mathbf{A}_c(\mathbf{r})$ corresponding to the constant magnetic field $\mathbf{H}_c$ was included in Hamiltonian (6). In this section, we assume that $\mathbf{H}_c = 0$, $\mathbf{A}_c(\mathbf{r}) = 0$, and the field $\mathbf{H} = \text{const}$ is so weak that only the contributions linear in field to the induced current and charge densities can be taken into account. Then, according to formula (25), we have $\langle \mathbf{j}_1(\mathbf{r}, t)\rangle^{(1)} = 0$ for the main contribution to the induced current density, because $\mathbf{E}(\mathbf{r}, t) = 0$. The vector potential can be chosen in the form

$$\mathbf{A}(\mathbf{r}) = (1/2)(\mathbf{H}\times\mathbf{r}). \quad (86)$$

It follows from expression (44) that $\langle j_1(\mathbf{r}, t)\rangle^{(+)} = 0$, because this expression contains the second derivatives of $\mathbf{A}(\mathbf{r})$ with respect to the coordinates. As a result, only the contribution $\langle \mathbf{j}_1(\mathbf{r}, t)\rangle^{(-)}$ given by relationship (43) turns out to be nonzero. Thus, we succeeded in expressing the induced current density through the magnetic field intensity at $\mathbf{H} = \text{const}$ in the linear-field approximation. Now, the diagonal matrix elements of the operators $\mathbf{r}_i$ can be eliminated from the expression for $\langle \mathbf{j}_1(\mathbf{r}, t)\rangle$ at $\mathbf{H} = \text{const}$. For this purpose, we use relationship (67), in which the vector $\mathbf{a}(\mathbf{r}, t)$ can be replaced by the vector potential $\mathbf{A}(\mathbf{r}, t)$, because the initial expression (26) can be replaced by relationship (38). Substitution of formula (86) into expression (67) gives

$$\begin{aligned}\langle j_{1\alpha}(\mathbf{r}, t)\rangle &= -\frac{e^2}{2mc}\sum_i \langle (\mathbf{H}\times\mathbf{r}_i^{\text{nd}})_\alpha \delta(\mathbf{r}-\mathbf{r}_i)\rangle \\ &- \frac{ie}{2\hbar c}\sum_i \langle j_\alpha(\mathbf{r}) H_\beta(\mathbf{r}_i^{\text{nd}}\times\mathbf{r}_i^{\text{nd}})_\beta\rangle \quad (87)\\ &+ \frac{e}{2c}\int_0^\beta d\lambda \sum_i \langle (\mathbf{H}\times\mathbf{r}_i^{\text{nd}})_\beta v_{i\beta} j_\alpha(\mathbf{r}, i\hbar\lambda)\rangle.\end{aligned}$$

Note that, since the projections $r_{i\alpha}^{\text{nd}}$ with different subscripts α do not commute with each other, the condition for the vector $\mathbf{r}_i^{\text{nd}}\times\mathbf{r}_i^{\text{nd}} \neq 0$ is satisfied and we have, for example,

$$(\mathbf{r}_i^{\text{nd}}\times\mathbf{r}_i^{\text{nd}})_z = [\mathbf{r}_{ix}^{\text{nd}}, \mathbf{r}_{iy}^{\text{nd}}]. \quad (88)$$

11. CONCLUSIONS

The main results obtained in this work can be summarized as follows. It was demonstrated that the average densities of the current and charge induced by a weak electromagnetic field in spatially inhomogeneous systems at finite temperatures can be expressed in terms of electric fields and their derivatives with respect to coordinates. The contributions expressed through the electric field were referred to as the basic contributions, and the contributions expressed through the derivatives of the electric field were termed the additional contributions.

Six pairs of different expressions were derived for the additional contributions to the average induced current and charge densities. Two of these expressions for the current density coincide with those obtained in [4]. However, the expressions determined in [4] contain the electric fields or the vector potentials rather than their derivatives with respect to the coordinates, which complicates the estimation of the additional contributions. In general, integration over the variable **r**' by parts makes it possible to eliminate the derivatives $\partial E_\beta(\mathbf{r}', t)/\partial r_\gamma'$ and to obtain formulas that involve only the fields rather than their derivatives. However, the reverse procedure, namely, the changeover from the field to the derivatives, is not necessarily possible and the fields are always retained in the basic contributions.

The sixth expression (deduced in Section 6) for the additional contribution to the average induced current density includes two terms. The first term with the index (–) is expressed only through the magnetic field $\mathbf{H}(\mathbf{r}, t)$, and the second term with the index (+) is expressed through the second derivatives of the electric field with respect to the coordinates. A similar result was obtained for the average induced charge density. In

the case when the additional contributions are expressed in terms of the derivatives of the electric fields, the corresponding formulas necessarily involve the coordinate operators $\mathbf{r}_i$ of particles. This result can seem absurd, because the coordinate $\mathbf{r}_i$ depends on the reference point. However, as was shown in Section 7, the diagonal matrix elements $\langle n|\mathbf{r}_i|n\rangle$ do not enter into the expressions for the average induced current and charge densities and the off-diagonal elements do not depend on the reference point.

The basic and additional contributions to the electrical conductivity tensor for spatially inhomogeneous systems and spatially inhomogeneous fields were calculated in Section 8. It was shown that only the basic contributions are retained within the approximation of spatially homogeneous electric fields dependent on time (Section 9). In this approximation, the modified Kubo formula was derived for the electrical conductivity tensor dependent on the frequency ω and the coordinates $\mathbf{r}$. This formula transforms into the Kubo formula [1] for spatially homogeneous systems.

Finally, the expression for the average induced current density in the case when the weak electromagnetic field is reduced to the constant magnetic field was obtained in Section 10.

From relationship (74), it follows that the additional contributions to the electrical conductivity contain the factor k_γ/ω. When the field $\mathbf{E}(\mathbf{r}, t)$ is considered a plane wave propagating at the velocity of light (under monochromatic irradiation) or a wave packet (under pulsed irradiation), $k \simeq \omega/c$ and the additional contributions contain a small factor v/c (where v is the particle velocity in the system) as compared to the basic contributions. However, this estimate is not necessarily correct for spatially inhomogeneous systems, such as semiconductor quantum wells, wires, or dots. The field $\mathbf{E}(\mathbf{r}, t)$ can be treated as an external or exciting field only in the case when the induced current and charge densities are calculated to the lowest order in the interaction of the field with the system of charged particles. Such an approximation is applicable for quantum wells if the condition $\gamma_r \ll \gamma$ is satisfied, where $\gamma_r(\gamma)$ is the radiative (nonradiative) reciprocal lifetime of the electronic excitation [9, 10].

Otherwise, at $\gamma_r \gg \gamma$, the interaction of the field with particles to all orders should be taken into account. In this case, the field $\mathbf{E}(\mathbf{r}, t)$ is the true field inside a low-dimensional object. This field cannot be represented as a superposition of plane waves for which $k = \omega/c$. For example, the true field considerably changes in magnitude inside a quantum well along the z axis perpendicular to the quantum well plane if the incident light propagates along the z axis and the frequency ω is at resonance with one of the discrete excitation levels of the electronic system in the well [11, 12]. In this case, the quantities $kd \simeq 1$ become significant (where d is the well width) and, instead of the small factor v/c, there appears the factor

$$M \simeq \frac{v}{d\omega} = \frac{v\lambda}{2\pi c d}.$$

At wavelengths $\lambda \gg d$, the factor M can be considerably larger than v/c. In specific cases, it is necessary to estimate the magnitude of this factor. In [11, 12], it was assumed that $M \ll 1$ and the additional contributions to the average induced current and charge densities were disregarded (at $T = 0$).

In principle, substitution of the obtained expressions for the average current and charge densities into the Maxwell equations makes it possible to determine the true fields inside and outside semiconducting low-dimensional objects. This provides a way of calculating the coefficients of reflection and absorption of light by these objects (see, for example, [11, 12]).

ACKNOWLEDGMENTS

We are grateful to M. Harkins for careful reading of the manuscript and critical remarks.

REFERENCES

1. R. J. Kubo, Phys. Soc. Jpn. **12** (6), 570 (1957); R. Kubo, in *Problems of Quantum Theory of Irreversible Processes*, Ed. by V. L. Bonch-Bruevich (Inostrannaya Literatura, Moscow, 1961).
2. L. D. Landau and E. M. Lifshitz, *The Classical Theory of Fields*, 6th ed. (Nauka, Moscow, 1973; Pergamon, Oxford, 1975).
3. S. Nakajima, Proc. Phys. Soc. **69**, 441 (1965).
4. O. V. Konstantinov and V. I. Perel', Zh. Éksp. Teor. Fiz. **37** (3), 786 (1959) [Sov. Phys. JETP **10**, 560 (1959)].
5. I. G. Lang, L. I. Korovin, J. A. de la Cruz-Alcaz, and S. T. Pavlov, Zh. Éksp. Teor. Fiz. **123** (2), 305 (2003) [JETP **96**, 268 (2003)]; cond-mat/0212549.
6. R. Zeyher, H. Bilz, and M. Cardona, Solid State Commun. **19** (1), 57 (1976).
7. A. A. Abrikosov, L. P. Gor'kov, and I. E. Dzyaloshinskiĭ, *Methods of Quantum Field Theory in Statistical Physics* (Prentice Hall, Englewood Cliffs, N.J., 1963; Dobrosvet, Moscow, 1998).
8. R. Enderlien, K. Peuker, and F. Bechstedt, Phys. Status Solidi B **92** (1), 149 (1979).
9. L. C. Andreani, F. Tassone, and F. Bassani, Solid State Commun. **77** (11), 641 (1991).
10. L. C. Andreani, G. Panzarini, A. V. Kavokin, and M. R. Vladimirova, Phys. Rev. B **57** (8), 4670 (1998).
11. L. I. Korovin, I. G. Lang, D. A. Contreras-Solorio, and S. T. Pavlov, Fiz. Tverd. Tela (St. Petersburg) **43** (11), 2091 (2001) [Phys. Solid State **43**, 2182 (2001)]; cond-mat/0104262.
12. L. I. Korovin, I. G. Lang, D. A. Contreras-Solorio, and S. T. Pavlov, Fiz. Tverd. Tela (St. Petersburg) **44** (11), 2084 (2002) [Phys. Solid State **44**, 2181 (2002)]; cond-mat/0203390.

Translated by O. Borovik-Romanova

Physics of the Solid State, Vol. 45, No. 10, 2003, pp. 2012–2016. Translated from Fizika Tverdogo Tela, Vol. 45, No. 10, 2003, pp. 1913–1916.

LOW-DIMENSIONAL SYSTEMS AND SURFACE PHYSICS

Electrostatic Response and Surface Electron States of a Ca(001) Face-Centered Cubic Film

G. V. Wolf and D. V. Fedorov

Physicotechnical Institute, Ural Division, Russian Academy of Sciences, ul. Kirova 132, Izhevsk, 426001 Russia

e-mail: wolf@otf.fti.udmurtia.su

Received January 22, 2003

Abstract—The electron response of a Ca(001) face-centered cubic film to an external electrostatic field is calculated. The results of calculations are compared with the previously obtained data on the electron response of a Cu(001) film. The energy location of occupied and unoccupied excited surface states of the Ca(001) film is determined. © *2003 MAIK "Nauka/Interperiodica".*

1. INTRODUCTION

Investigation of the electron response of an anisotropic metal to an external electrostatic field in the framework of the electron-density-functional theory is of considerable scientific interest. This is associated not only with the necessity of interpreting the results of experiments that are sensitive to changes in the surface distribution of the electron density and the potential [1] but also with the need to solve a number of general problems in the inhomogeneous electron gas theory. It seems likely that, at present, only within this approach can the exchange–correlation effects be properly accounted for in the electron response of inhomogeneous systems with a complex band structure [2]. In principle, the electron-density-functional theory leads to exact results in the long-wavelength limit [3] and offers an independent verification and evaluation of the approximations used in diagram techniques for determining the low-frequency electron response.

The screening of an electrostatic field by the surface of a particular metal is substantially affected by the metal electronic structure, which, in turn, depends on a large number of different factors in a complex manner. Among these are the composition and the structure of the crystal, the orientation of its surface, relaxation processes occurring in the surface layer, etc. In order to elucidate the influence of all these factors on the phenomenon under investigation, it is expedient to perform a comparative analysis of the systems differing from each other by a minimum number of factors that have a significant effect on the electron response. For this purpose, in the present work, we analyzed the evolution of electron states of Cu(001) and Ca(001) face-centered cubic films in an external electrostatic field.

2. COMPUTATIONAL TECHNIQUE, RESULTS, AND DISCUSSION

The occupancies of electron states of copper and calcium atoms of these isostructural metals differ only in that the 3*d* electron states are completely occupied in copper atoms and completely unoccupied in calcium atoms. It is known that, in a copper bulk crystal, the Fermi level E_F lies above the *s*–*d* hybridized states and the dominant contribution to the density of states at the Fermi level E_F is made by the 4*s* states [4].

In crystalline calcium, the Fermi level E_F lies below the main group of 3*d* electron states. However, according to the results of our calculations[1] (Fig. 1), the partial densities of states $n_p(E_F)$ and $n_d(E_F)$ are comparable in magnitude. This makes it possible to elucidate the role played by 3*d* electrons in the electrostatic response of the metal.

In this work, the electronic structures of electroneutral and charged Cu(001) and Ca(001) films were calculated using a new method in the framework of the electron-density-functional theory. Within this approach, the electron screening of the metal surface is efficiently included in the calculation (the method was described in detail in our previous work [6]). The system of self-consistent equations (in atomic units with the energy expressed in rydbergs) to be solved has the following form [7]:

$$\{-\Delta + V[\rho; \mathbf{r}, q]\}\Psi_{n\mathbf{k}}(\mathbf{r}, q) = E_n(\mathbf{k}, q)\Psi_{n\mathbf{k}}(\mathbf{r}, q),$$
$$\Psi_{n\mathbf{k}}(\mathbf{r}, q) = \exp(-i\mathbf{k}\mathbf{R}_n)\Psi_{n\mathbf{k}}(\mathbf{r} + \mathbf{R}_n, q),$$
$$\int_\Omega |\Psi_{n\mathbf{k}}(\mathbf{r}, q)|^2 d\mathbf{r} = 1, \qquad (1)$$
$$\rho(\mathbf{r}, q) = \sum_{n,\mathbf{k}} |\Psi_{n\mathbf{k}}(\mathbf{r}, q)|^2,$$

[1] The calculations of the densities of states for a calcium bulk crystal were carried out by the self-consistent *q*-spin-polarized relativistic Korringa–Kohn–Rostoker (SPR–KKR) code for calculating solid-state properties [5].

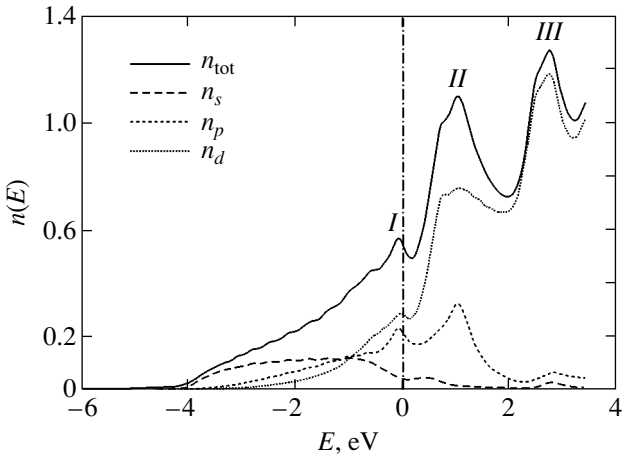

Fig. 1. Total (n_{tot}) and partial (n_s, n_p, n_d) densities of states of the copper bulk crystal (the energy expressed in electronvolts is reckoned from the Fermi level).

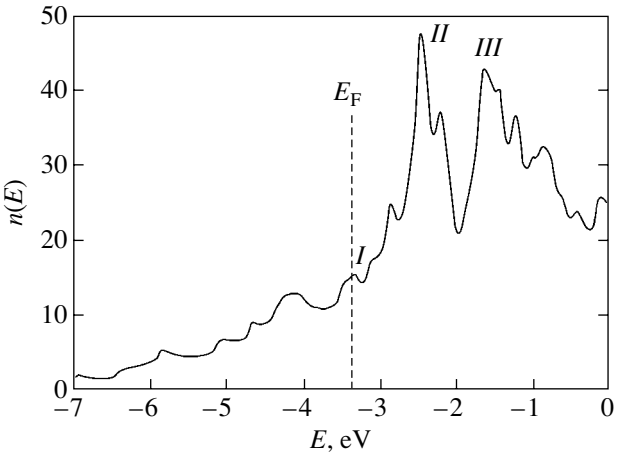

Fig. 2. Density of states of the Ca(001) five-layer film (the energy expressed in electronvolts is reckoned from the vacuum zero).

where **k** is the two-dimensional reduced quasi-momentum, $\mathbf{R}_n$ is the translational vector of the Bravais lattice of the film under consideration, and q is the number of uncompensated electrons in the unit cell of the film Ω. When calculating the electron density $\rho(\mathbf{r}, q)$, summation was performed over all states with energies $E_n(\mathbf{k}, q)$ lying below the Fermi level $E_F(q)$.

The effective potential $V[\rho; \mathbf{r}, q]$ represents the sum of the Coulomb and exchange–correlation contributions. The Coulomb contribution was determined by the method used in our earlier work [8]. The exchange–correlation contribution was obtained within the local-density approximation in the form of a Hedin–Lundqvist potential with the parameters taken from [9].

The lattice constants of copper and calcium films were assumed to be equal to those of copper and calcium bulk crystals: $A_{Cu} = 6.8309$ au and $A_{Ca} = 10.5296$ au.

It is known that calculated values of the work function W are very sensitive to changes in the electron-density distribution in the vicinity of the metal surface. The difference between theoretical and experimental values of the work function serves as a severe criterion of applicability of both the model and the method used in solving the system of equations (1). The work functions calculated in this study for Cu(001) and Ca(001) five-layer films were compared (see Table 1) with the available experimental data and the results of other self-consistent calculations [10–19]. It turned out that our data on the work function of the Cu(001) film coincide very closely with the experimental values obtained by Delchar [16] and Strayer *et al.* [18]. As regards the theoretical data, our value of the work function of the copper film is in best agreement with the result (5.18 eV) of the precision calculation carried out by Bross and Kauzmann [13]. Unfortunately, experimental data available in the literature on the work function of the Ca(001) surface are more scarce. The work function calculated for the Ca(001) film in our case differs by 0.5 eV from the result of the self-consistent calculation performed within the pseudopotential approach for a Ca(001) seven-layer film by Ley *et al.* [14]. It should be noted that the experimental value of 2.87 eV (Table 1) was obtained by Gaudart and Rivoira [15] for a polycrystalline sample.

Figure 2 presents the results of our calculations of the density of states for the Ca(001) five-layer film. A comparison of these data with the calculated density of states for a bulk calcium crystal (Fig. 1) shows that, upon changing over from the film to the bulk crystal, the energies corresponding to maxima *I* and *II* vary only slightly. The shift in these maxima does not exceed 0.2 eV. The energy position of maximum *III* changes more significantly and lies 0.98 eV closer to the Fermi level in the film as compared to that in the bulk crystal.

The calculation of the electrostatic response of Cu(001) films [6] and examination of the electron screening of the (001) surfaces of Al, Ni, and Ag semi-infinite crystals [20, 21] demonstrated that the induced charge is localized in a very thin surface region contain-

Table 1. Work functions of Cu(001) and Ca(001) films (in eV)

Film	Our calculation	Other calculations	Experiment
Cu(001)	5.11	4.50 [10]	5.16 ± 0.054 [16]
		4.94 [11]	4.59 ± 0.054 [17]
		4.91 [12]	5.10 ± 0.030 [18]
		5.18 [13]	4.77 ± 0.050 [19]
Ca(001)	3.38	2.90 [14]	2.87 ± 0.06 [15]

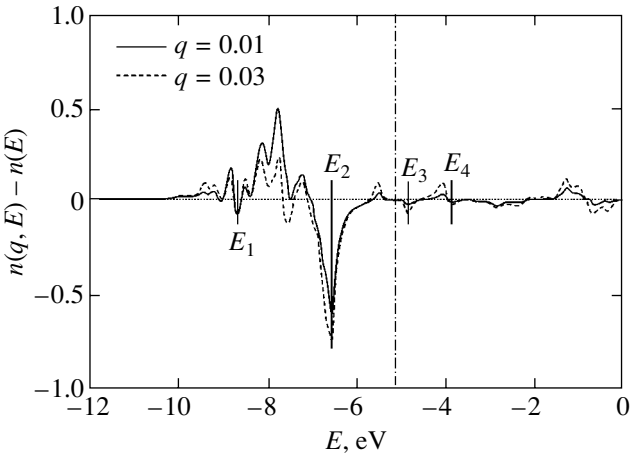

Fig. 3. Difference in the densities of states of the charged and electroneutral Cu(001) films. The dot-dashed line corresponds to the energy at the Fermi level E_F of the electroneutral film (the energy expressed in electronvolts is reckoned from the vacuum zero).

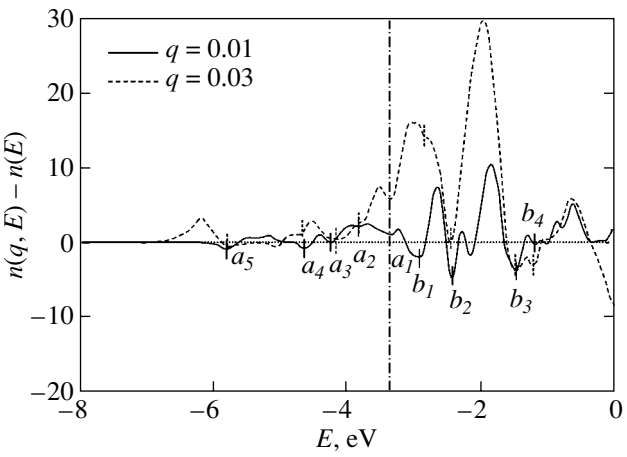

Fig. 4. Difference in the densities of states of the charged and electroneutral Ca(001) films. The dot-dashed line corresponds to the energy at the Fermi level E_F of the electroneutral film (the energy expressed in electronvolts is reckoned from the vacuum zero).

ing only one or two atomic layers. The Stark shift $C(q)$, which is determined by the dipole moment of the charge of the surface region, is nearly identical for all bulk states [8]. Consequently, after the energy shift, the difference between the densities of states of the charged and electroneutral films,

$$\Delta n(q, E) = n(E + C(q), q) - n(E, 0), \qquad (2)$$

becomes equal to the difference between the surface-state densities of these films,

$$\Delta n^{(s)}(q, E) = n^{(s)}(E + C(q), q) - n^{(s)}(E, 0). \qquad (3)$$

The contribution $n^{(s)}(E + C(q), q)$ of the surface-state density of the charged film leads to an insignificant change in the energy location of the specific features (which are associated with the maxima in the surface-state density of the electroneutral film) in the curve $\Delta n(q, E)$ as compared to the energy location of the corresponding features in the curve $n^{(s)}(E, 0)$. In order to decrease this error, we calculated the difference $\Delta n(q, E)$ for several values of the uncompensated charge. In these calculations, proper allowance was made only for the specific features in the curve $\Delta n^{(s)}(q, E)$ that are not very sensitive to changes in the number q of uncompensated electrons per unit cell of the film, which suggests a weak energy dependence $n^{(s)}(E + C(q), q)$ in the vicinity of the corresponding maxima in the curve $n^{(s)}(E, 0)$.

The differences between the surface-state densities of Cu(001) and Ca(001) five-layer films are presented in Figs. 3 and 4, respectively. For the Cu(001) film, the positions of all minima in the curve $\Delta n(q, E)$ at $q = 0.01$ and 0.03 almost coincide with each other. From the above it follows that they correspond in energy to the maxima in the surface-state density of the electroneutral film. Our results are in good agreement with available theoretical [10] and experimental [22] data on the energy location of Cu(001) occupied surface states. In particular, the positions of minima at the energies $E_1 = -3.55$ eV and $E_2 = -1.45$ eV (the energies are reckoned from the Fermi level of the electroneutral film) coincide to within several hundredths of an electronvolt with the

Table 2. Energy location of occupied surface states of the Ca(001) film (the energies expressed in electronvolts are reckoned from the Fermi level of the electroneutral film)

		Specific features of $\Delta n(q, E)$				
		a_1	a_2	a_3	a_4	a_5
Our calculation	$q = 0.01$	0.00	–0.48	–0.89	–1.29	–2.46
	$q = 0.03$	0.00	–0.46	–0.81	–1.31	–2.44
Calculation [14]		–0.1	–	–	–1.4	–2.5
Experiment [14]		–	–0.6	–	–1.6	–2.4

positions of the peaks in the difference between the densities of states of the surface and central layers of the Cu(001) nine-layer film [10]. The surface-state density in the vicinity of the Fermi level for the copper film is negligible.

For the Ca(001) film, the surface electron states contribute significantly to the density of states at the Fermi level. In this case, the position of the local maximum in the surface-state density $n^{(s)}(E, 0)$ virtually coincides with the energy at the Fermi level E_F of the electroneutral film (Fig. 4, minimum a_1). A comparison of our results with data available in the literature on the energy location of occupied surface states of the Ca(001) film is given in Table 2.

It can be seen from Table 2 that, as in the case of the Cu(001) surface, the results of our calculations for the Ca(001) film are in satisfactory agreement with theoretical and experimental data obtained by other authors. Moreover, from these results, we can predict an increased density of surface states lying 0.8–0.9 eV below the Fermi level.

An analysis of the specific features revealed in the curve $\Delta n(q, E)$ makes it possible to determine the energy location of unoccupied surface states. As can be seen from Fig. 3, the curve $\Delta n(q, E)$ for the Cu(001) film is characterized by two minima at the energies E_3 = 0.29 eV and E_4 = 1.26 eV (the energies are reckoned from the Fermi level of the electroneutral film). The energy E_4 agrees with the experimental results and the calculated data obtained by Hulbert *et al.* [23], who found the surface resonance band in the energy range from 0.8 to 2.4 eV above the Fermi level. The energy E_3 only slightly exceeds the Fermi level E_F. This is in qualitative agreement with the results of the precision angle-resolved photoelectron emission experiments performed by Kevan *et al.* [22] and the band structure calculations carried out by Euceda *et al.* [12], who revealed a surface state with a binding energy of 0.06 eV (0.07 eV) and effective mass $m^* = 0.16m_e$ ($0.2m_e$) at the $\bar{X}$ point of the Cu(001) two-dimensional Brillouin zone.[2]

From the results of our calculations (Fig. 4), it is possible to estimate the energies corresponding to the maximum density of unoccupied surface states of the Ca(001) film (Table 3). In Table 3, the designations of the specific features of the curve $\Delta n^{(s)}(q, E)$ are the same as in Fig. 4. The relative error in the determination of the maximum density of surface states is equal to several hundredths of an electronvolt (Table 3), which is comparable to the error in the calculation of the electronic structure.

The electrostatic response of the calcium film is of special interest. This stems from the fact that, under hydrostatic compression at a pressure of approximately 200 kbar, the calcium bulk crystal undergoes a transition to a semiconductor state with zero energy gap [24, 25]. The observed changes in the bulk contribution to the density of states in the near-Fermi region of the Ca(001) film (Figs. 1, 2) suggests that calcium films can also exhibit a similar effect. The surface contribution to the density of states at the Fermi level in the Ca(001) film, unlike the Cu(001) film, is significant and depends on the strength of the external electrostatic field. Therefore, it is quite possible that the charge state of the calcium film can affect the above transition.

Table 3. Energy location of unoccupied surface states of the Ca(001) film (the energies expressed in electronvolts are reckoned from the Fermi level of the electroneutral film)

q	b_1	b_2	b_3	b_4
0.01	0.43	0.92	1.88	2.16
0.03	0.51	0.91	1.87	2.14

[2] The results of calculations are given in parentheses.

REFERENCES

1. P. J. Feibelman, Prog. Sufr. Sci. **12**, 287 (1982).
2. A. Williams and U. Barth, in *Theory of the Inhomogeneous Electron Gas*, Ed. by S. Lundqvist and N. H. March (Plenum, New York, 1983; Mir, Moscow, 1987).
3. D. J. W. Gerdart, M. Rasolt, and R. Taylor, Solid State Commun. **10**, 279 (1972).
4. V. V. Nemoshkalenko and V. N. Antonov, in *Methods of Computational Physics in the Theory of Solids: The Band Theory of Metals* (Naukova Dumka, Kiev, 1985), p. 238.
5. H. Ebert, in *Electronic Structure and Physical Properties of Solids*, Ed. by H. Dreysse (Springer, Berlin, 2000), Lect. Notes Phys., Vol. 535, p. 191.
6. G. V. Wolf and D. V. Fedorov, Fiz. Tverd. Tela (St. Petersburg) **43** (3), 385 (2001) [Phys. Solid State **43**, 401 (2001)].
7. V. Kohn and P. Vashishta, in *Theory of the Inhomogeneous Electron Gas*, Ed. by S. Lundqvist and N. H. March (Plenum, New York, 1983; Mir, Moscow, 1987).
8. G. V. Wolf and D. V. Fedorov, Poverkhnost, No. 5, 105 (1998).
9. O. Gunnarson and B. I. Lundqvist, Phys. Rev. B **13**, 4274 (1976).
10. J. R. Smith, J. G. Gay, and F. J. Arlinghaus, Phys. Rev. B **21**, 2201 (1980).
11. D. S. Wang, A. J. Freeman, and H. Krakauer, Phys. Rev. B **26**, 1340 (1982).
12. A. Euceda, D. M. Bylander, L. Kleinman, and K. Mednick, Phys. Rev. B **27**, 659 (1983).
13. H. Bross and M. Kauzmann, Phys. Rev. B **51**, 17135 (1995).
14. L. Ley, G. P. Kerker, and N. Martensson, Phys. Rev. B **23**, 2710 (1981).
15. L. Gaudart and R. Rivoira, Appl. Opt. **10**, 2336 (1971).

16. T. A. Delchar, Surf. Sci. **27**, 11 (1971).
17. P. O. Gartland, S. Berge, and B. J. Slagsvold, Phys. Rev. Lett. **28**, 738 (1972).
18. R. W. Strayer, W. Macki, and L. W. Swanson, Surf. Sci. **34**, 225 (1973).
19. G. G. Tibbets, J. M. Burkstand, and J. C. Tracy, Phys. Rev. B **15**, 3652 (1977).
20. J. E. Inglesfield and G. A. Benesh, Phys. Rev. B **37**, 6682 (1988).
21. G. C. Aers and J. E. Inglesfields, Surf. Sci. **217**, 367 (1989).
22. S. D. Kevan, N. G. Stoffel, and N. Y. Smith, Phys. Rev. B **31**, 3348 (1985).
23. S. L. Hulbert, P. D. Johnson, M. Weinert, and R. F. Garrett, Phys. Rev. B **33**, 760 (1986).
24. R. A. Stager and H. G. Drickamer, Phys. Rev. **131**, 2524 (1963).
25. J. W. McCaffrey, J. R. Anderson, and D. A. Papaconstantopoulos, Phys. Rev. B **7**, 674 (1973).

Translated by O. Borovik-Romanova